frontiers | Research Topics

Clinical application of medical imaging for functional evaluation in orthopaedics

Edited by
Tsung-Yuan Tsai, Huiwu Li, Yan Yu, Seung-Hoon Baek and Tengbo Yu

Published in
Frontiers in Surgery

FRONTIERS EBOOK COPYRIGHT STATEMENT

The copyright in the text of individual articles in this ebook is the property of their respective authors or their respective institutions or funders. The copyright in graphics and images within each article may be subject to copyright of other parties. In both cases this is subject to a license granted to Frontiers.

The compilation of articles constituting this ebook is the property of Frontiers.

Each article within this ebook, and the ebook itself, are published under the most recent version of the Creative Commons CC-BY licence. The version current at the date of publication of this ebook is CC-BY 4.0. If the CC-BY licence is updated, the licence granted by Frontiers is automatically updated to the new version.

When exercising any right under the CC-BY licence, Frontiers must be attributed as the original publisher of the article or ebook, as applicable.

Authors have the responsibility of ensuring that any graphics or other materials which are the property of others may be included in the CC-BY licence, but this should be checked before relying on the CC-BY licence to reproduce those materials. Any copyright notices relating to those materials must be complied with.

Copyright and source acknowledgement notices may not be removed and must be displayed in any copy, derivative work or partial copy which includes the elements in question.

All copyright, and all rights therein, are protected by national and international copyright laws. The above represents a summary only. For further information please read Frontiers' Conditions for Website Use and Copyright Statement, and the applicable CC-BY licence.

ISSN 1664-8714
ISBN 978-2-8325-3584-4
DOI 10.3389/978-2-8325-3584-4

About Frontiers

Frontiers is more than just an open access publisher of scholarly articles: it is a pioneering approach to the world of academia, radically improving the way scholarly research is managed. The grand vision of Frontiers is a world where all people have an equal opportunity to seek, share and generate knowledge. Frontiers provides immediate and permanent online open access to all its publications, but this alone is not enough to realize our grand goals.

Frontiers journal series

The Frontiers journal series is a multi-tier and interdisciplinary set of open-access, online journals, promising a paradigm shift from the current review, selection and dissemination processes in academic publishing. All Frontiers journals are driven by researchers for researchers; therefore, they constitute a service to the scholarly community. At the same time, the *Frontiers journal series* operates on a revolutionary invention, the tiered publishing system, initially addressing specific communities of scholars, and gradually climbing up to broader public understanding, thus serving the interests of the lay society, too.

Dedication to quality

Each Frontiers article is a landmark of the highest quality, thanks to genuinely collaborative interactions between authors and review editors, who include some of the world's best academicians. Research must be certified by peers before entering a stream of knowledge that may eventually reach the public - and shape society; therefore, Frontiers only applies the most rigorous and unbiased reviews. Frontiers revolutionizes research publishing by freely delivering the most outstanding research, evaluated with no bias from both the academic and social point of view. By applying the most advanced information technologies, Frontiers is catapulting scholarly publishing into a new generation.

What are Frontiers Research Topics?

Frontiers Research Topics are very popular trademarks of the *Frontiers journals series*: they are collections of at least ten articles, all centered on a particular subject. With their unique mix of varied contributions from Original Research to Review Articles, Frontiers Research Topics unify the most influential researchers, the latest key findings and historical advances in a hot research area.

Find out more on how to host your own Frontiers Research Topic or contribute to one as an author by contacting the Frontiers editorial office: frontiersin.org/about/contact

Clinical application of medical imaging for functional evaluation in orthopaedics

Topic editors

Tsung-Yuan Tsai — Shanghai Jiao Tong University, China
Huiwu Li — Department of Orthopaedic, Shanghai Ninth People's Hospital, China
Yan Yu — Tongji University School of Medicine, China
Seung-Hoon Baek — Kyungpook National University, Republic of Korea
Tengbo Yu — Qingdao Municipal Hospital, China

Citation

Tsai, T.-Y., Li, H., Yu, Y., Baek, S.-H., Yu, T., eds. (2023). *Clinical application of medical imaging for functional evaluation in orthopaedics*. Lausanne: Frontiers Media SA. doi: 10.3389/978-2-8325-3584-4

Table of contents

frontiers | Frontiers in Surgery

TYPE Original Research
PUBLISHED 26 August 2022
DOI 10.3389/fsurg.2022.1003757

Check for updates

OPEN ACCESS

EDITED BY
Yan Yu,
Tongji University School of Medicine, China

REVIEWED BY
Da-Long Yang,
Third Hospital of Hebei Medical University, China
Huo Zhenxin,
Tianjin Hospital, China

*CORRESPONDENCE
Shi-Bao Lu
spinelu@163.com

SPECIALTY SECTION
This article was submitted to Orthopedic Surgery, a section of the journal Frontiers in Surgery

RECEIVED 26 July 2022
ACCEPTED 10 August 2022
PUBLISHED 26 August 2022

CITATION
Wang D-F, Zhu W-G, Wang W, Li X-Y, Kong C, Liu C-X, Shi B and Lu S-B (2022) The discrepancy between preoperative cervical sagittal vertical axis and T1 slope predisposes inferior clinical outcomes in patients with cervical spondylotic myelopathy after cervical laminoplasty.
Front. Surg. 9:1003757.
doi: 10.3389/fsurg.2022.1003757

COPYRIGHT
© 2022 Wang, Zhu, Wang, Li, Kong, Liu, Shi and Lu. This is an open-access article distributed under the terms of the Creative Commons Attribution License (CC BY). The use, distribution or reproduction in other forums is permitted, provided the original author(s) and the copyright owner(s) are credited and that the original publication in this journal is cited, in accordance with accepted academic practice. No use, distribution or reproduction is permitted which does not comply with these terms.

The discrepancy between preoperative cervical sagittal vertical axis and T1 slope predisposes inferior clinical outcomes in patients with cervical spondylotic myelopathy after cervical laminoplasty

Dong-Fan Wang[1,2], Wei-Guo Zhu[1,2], Wei Wang[1,2], Xiang-Yu Li[1,2], Chao Kong[1,2], Cheng-Xin Liu[1,2], Bin Shi[1,2] and Shi-Bao Lu[1,2]*

[1]Department of Orthopedics, Xuanwu Hospital, Capital Medical University, Beijing, China, [2]National Clinical Research Center for Geriatric Diseases, Xuanwu Hospital, Capital Medical University, Beijing, China

Objective: Cervical sagittal parameters have been widely used to predict clinical outcomes in patients with cervical spondylotic myelopathy (CSM). This study aims to coin a novel cervical sagittal parameter defined as the ratio of cervical sagittal vertical axis to T1 slope (CSVA/T1S) and to investigate the correlation between CSVA/T1S and postoperative HRQOL after laminoplasty.
Methods: A total of 102 CSM patients treated with cervical laminoplasty from our database were retrospectively reviewed. All patients were followed up for >12 months. Radiological parameters were measured using lateral cervical radiographs, including occiput-C2 lordosis (OC2), cervical lordosis (CL), CSVA, and T1S. Clinical parameters included the Japanese Orthopedic Association (JOA) score, neck disability index (NDI), and JOA recovery rate. Patients were grouped by preoperative T1S, T1S-CL, and CSVA/T1S value, respectively. Clinical and radiological outcomes were compared between the groups.
Results: Patients with high CSVA/T1S had greater OC2 and CSVA but lower CL than those in the low CSVA/T1S group pre-and postoperatively. With respect to HRQOL results, the final NDI was 12.46 ± 9.11% in the low CSVA/T1S group, which was significantly lower than that in the high CSVA/T1S group (17.68 ± 8.81%, $P = 0.040$). Moreover, only CSVA/T1S was detected to be significantly correlated with final NDI ($r = 0.310$, $P = 0.027$). No significant correlation was found between clinical results and other cervical sagittal parameters, including T1S, CSVA, and T1S-CL.
Conclusions: Preoperative CSVA/T1S was correlated with postoperative NDI in patients with CSM after cervical laminoplasty. Patients with low preoperative CSVA/T1S achieved better neurological function improvement after cervical laminoplasty. Cervical laminoplasty could be an appropriate choice for patients with lower preoperative CSVA/T1S.

KEYWORDS

cervical sagittal vertical axis, t1 slope, cervical laminoplasty, clinical outcomes, sagittal alignment

Introduction

Cervical spondylotic myelopathy (CSM) is a common cervical degenerative disorder with an incidence of about 4.04 per 100,000 person-years (1, 2), which is the leading cause of spinal cord dysfunction, including upper extremity numbness, weakness, decreased manual dexterity, and gait disturbance (3). Surgical intervention is usually indicated to halt neurological function deterioration and improve living quality for patients unresponsive to conservative treatment. Surgeries through anterior and posterior approaches are both important methods for the treatment of CSM. Compared with the anterior procedure, the posterior surgery is particularly well adapted to multi-level stenosis with spinal cord injury (4). Cervical laminoplasty, as the primary technique of posterior procedure, allows for direct posterior decompression in patients with myelopathy secondary to congenital cervical stenosis or hypertrophy of ligament flava and also affords indirect anterior decompression in patients with multiple disk herniations or ossification of the posterior longitudinal ligament (OPLL) (5).

However, cervical laminoplasty has its major defects that impair the cervical posterior muscle-ligament complex, which would lead to loss of cervical lordosis and then the cervical sagittal imbalance (5). It has been well documented that the cervical sagittal alignment, which could be reflected by cervical lordosis (CL), T1 slope (T1S), cervical sagittal axis (CSVA), the ratio of CL to T1S (CL/T1S), and T1S minus CL mismatch (T1S-CL), is correlated with patients' health-related quality of life (HRQOL) (6, 7). Among all the cervical parameters, CSVA was believed to be the primary factor influencing patients' self-reported outcomes such as neck pain and neurological symptoms before and after laminoplasty. In the *post hoc* analysis of a prospective and multicenter study, Smith et al. found that the preoperative modified Japanese Orthopedic Association (JOA) scores were correlated with CSVA in 56 patients with CSM (8). Kato et al. reported that the improvement in SF-36 physical component summary was significantly lower in patients with CSVA $\geq$ 35 mm after laminoplasty and concluded that CSVA could lead to poor postoperative HRQOL results and axial neck pain (9). Xu et al. also discovered that preoperative CSVA was significantly related to the neurological outcome after laminoplasty in their retrospective OPLL case study (10).

Therefore, figuring out the risk factors of cervical sagittal decompensation and suboptimal surgical outcome after cervical laminoplasty could serve as a significant reference for clinical practice. Like the decrease of sacral slope (SS) playing an essential role in compensating for global sagittal imbalance, T1S represents the compensatory capacity of the upper thoracic for cervical sagittal malalignment (11). We speculate that the preoperative relationship between CSVA and T1S, represented by the ratio of CSVA to T1S (CSVA/T1S), could reflect the possibility of spontaneous compensation of cervical sagittal malalignment and predict the clinical outcome after laminoplasty. We conduct the present study with the following aims: (1) to coin a novel cervical sagittal parameter CSVA/T1S and (2) to investigate the correlation between CSVA/T1S and postoperative HRQOL after laminoplasty.

Materials and methods

Patient population

After being approved by the Ethics Committee of Capital Medical University Xuanwu Hospital (approval number: 2018014), a retrospective review of patients who underwent cervical laminoplasty between March 2018 and February 2021 was performed. Patients with cervical myelopathy secondary to OPLL, congenital cervical stenosis, or multilevel cervical disk herniation were included in this study (5). Thereinto, those with the following manifestations were recommended for surgical treatment: (1) rapid progression of clinical signs and symptoms, (2) presence of the signs of myelopathy with or without radiculopathy for six months or longer, (3) compression ratio (canal diameter/vertebra diameter) approaching 0.4, and (4) with neutral to lordotic cervical sagittal alignment (12). Patients who met the inclusion criteria below were enrolled: (1) age >18 years, (2) complete preoperative and postoperative radiographic data, (3) followed up for at least 12 months. Patients with spinal tumors, tuberculosis, trauma, a history of spinal surgery or non-horizontal gaze when taking lateral cervical x-rays were excluded. A horizontal gaze was defined as $-10° \leq$ chin-brow to vertical angle $\leq 10°$ (13). A total of 102 patients were finally included in this study.

Operative procedure

All the surgeries were performed based on the Hirabayashi method by the same spinal surgeon (14). Patients were positioned cranially 15–20° up in a prone position. The Mayfield skull clamp was used for immobilizing the head position. The incision was made on the posterior midline of the cervical skin. The spinous process, lamina, and bilateral lateral mass were exposed. Part of the spinous processes was removed using a rongeur for bone grafting on the hinge side. The paraspinal muscle of C2, especially the semispinalis, was preserved. A high-speed drill was used to create gutters on the bilateral laminae at the border of the laminae and facets. The lamina of the side with more significant clinical symptoms was completely cut and used as the open side; the other side of the lamina was partially cut with the ventral cortex

preserved to form the hinge side. A thin-bladed Kerrison rongeur was used to remove ligamentum flava at the cranial and caudal ends of the intended laminar expansion to facilitate opening the lamina. Suitable Centerpiece laminoplasty plates (Medtronic Sofamor Danek) were respectively fixed on the lateral masses and laminae. Spacer height was dependent on the degree of canal stenosis. C-arm fluoroscopy was used to confirm the position of the plates. Additional bleeding can be stopped with the use of bipolar coagulation forceps and thrombinated gelfoam. A negative pressure drainage tube was indwelt on the open side. All patients were told to wear a collar for 4–6 weeks postoperatively. Postoperative rehabilitation was done as early as possible.

Radiological parameters

A standing neutral lateral radiograph of the cervical spine was obtained with patients facing forward and in horizontal gaze before surgery and at the last follow-up. The following radiological parameters were measured: occiput-C2 lordosis (OC2, the angle between the McGregor line and the inferior endplate of the C2), CL (the angle between the inferior endplate of C2 and the inferior endplate of C7), T1S (the angle between a horizontal line and the superior endplate of T1), CSVA (the distance from the posterior, superior corner of C7 to the plumbline from the centroid of C2). To patients with invisible T1S on the cervical radiography, the value of superior C7 slope was utilized to substitute for T1S (15). All parameters were measured and calculated by 2 spine surgeons who were not involved in the program. For investigating the correlation between preoperative cervical sagittal parameters and HRQOL indicators after laminoplasty, all patients were grouped according to the median of preoperative T1S, T1S-CL, and CSVA/T1S, respectively. **Figure 1** illustrated the cervical sagittal parameters measured in this study.

Clinical parameters

The Japanese Orthopedic Association (JOA) score and neck disability index (NDI) were used to postoperative HRQOL (16, 17). The JOA recovery rate, calculated as (postoperative JOA score − preoperative JOA score)/(full score − preoperative JOA score) × 100%, was used to evaluate the improvement of cervical neurological function. A JOA recovery rate of 100% indicated being cured; >60% indicated significantly effective; 25%–60% indicated effective; <25% indicated ineffective. An NDI < 10% indicated no disability; 10%–30% indicated mild disability; 30%–50% indicated moderate disability; 50%–70% indicated severe disability; >70% indicated complete disability.

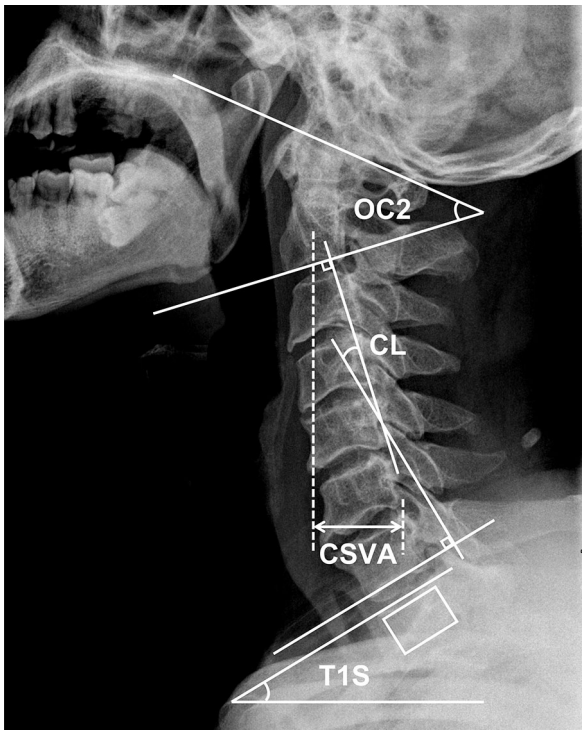

FIGURE 1
Measurements of cervical sagittal parameters utilized in this study.

Preoperative data were extracted from the medical charts. Postoperative data were collected from outpatient follow-up.

Statistical analysis

All data were analyzed using SPSS Statistics (version 26.0, IBM Corp., Armonk, NY, USA). Data are presented as means ± standard deviations. Continuous variables were compared between groups using the independent-samples *t*-test, Mann-Whitney *U* test, and paired-sample *t*-test. The chi-square test was used to compare composition ratios. The correlations among the parameters were analyzed with Pearson correlation coefficient. Statistical significance was set at a level of $P < 0.05$.

Results

Baseline data of the whole cohort

A total of 102 patients were included in this study. They were 56 males and 46 females with an average age of 64.69 ± 9.73 years. The mean follow-up period was 17.88 ± 6.43 months. In terms of cervical sagittal parameters, OC2 angle was significantly increased from 23.34 ± 6.87° to 27.53 ± 7.21° ($P < 0.001$) whereas CL was significantly decreased from

13.99 ± 8.23° to 10.12 ± 7.78° ($P < 0.001$) after laminoplasty. As to clinical parameters, JOA score and NDI were both obviously improved. There were no significant differences between T1S and CSVA before and after surgery (Table 1).

Comparisons of cervical sagittal parameters and HRQOL outcomes between low T1S group and high T1S group

As shown in Table 2, the high T1S group had greater CL than the low T1S group pre-and postoperatively. Patients with high T1S tended to match high CSVA, though the data did not vary significantly between groups. Moreover, OC2 was significantly increased, while CL was decreased in both groups after surgery. Concerning the clinical parameters, no significant difference was found in terms of the JOA score, JOA recovery rate, and NDI between the two groups.

Comparisons of cervical sagittal parameters and HRQOL outcomes between low T1S-CL group and high T1S-CL group

Patients with high T1S-CL corresponding to greater OC2 and CSVA but lower CL than those with low T1S-CL. No significant difference was showed in T1S between groups. OC2 was increased and CL was decreased from the preoperative measurements through the final follow-up in both groups. JOA score, NDI, and JOA recovery rate were similar between the two groups (Table 3).

TABLE 1 Comparison of cervical sagittal parameters and patient-reported outcome indicators pre- and postoperatively.

Parameters	Preoperative ($n = 102$)	Final follow-up ($n = 102$)	*P*
OC2 (°)	23.34 ± 6.87	27.53 ± 7.21	0.000**
CL (°)	13.99 ± 8.23	10.12 ± 7.78	0.000**
T1S (°)	24.52 ± 6.37	23.33 ± 6.86	0.167
CSVA (mm)	23.11 ± 11.97	24.65 ± 12.12	0.465
JOA score	12.01 ± 1.23	14.61 ± 1.18	0.000**
NDI (%)	29.54 ± 17.23	15.02 ± 9.26	0.000**

OC2, occiput-C2 lordosis; CL, cervical lordosis; T1S, T1 slope; CSVA, cervical sagittal vertical axis; JOA, Japanese orthopedic association; NDI, neck disability index.
**$P < 0.01$.

Comparisons of cervical sagittal parameters and HRQOL outcomes between low CSVA/T1S group and high CSVA/T1S group.

Table 4 detailed the comparison of sagittal and clinical parameters between patients with different CSVA/T1S. Compared with the low CSVA/T1S group, OC2 and CSVA were significantly greater and CL was significantly lower in the high CSVA/T1S group. Both CSVA and CSVA/T1S were increased in the Low CSVA/T1S group after surgery ($P = 0.028$), while they were not obviously changed in the high CSVA/T1S group. With respect to HRQOL results, the final NDI was 12.46 ± 9.11% in the low CSVA/T1S group, which was significantly lower than that in the High CSVA/T1S group (17.68 ± 8.81%, $P = 0.040$).

TABLE 2 Comparison of cervical sagittal parameters and HRQOL indicators between the low T1S group and the high T1S group.

Parameters	Low T1S ($n = 51$)	High T1S ($n = 51$)	*P*
Age (years)	63.92 ± 8.28	66.56 ± 10.43	0.207
Follow-up (months)	17.46 ± 6.55	18.32 ± 6.40	0.638
Operation segments			0.602
C3–C6	8	10	
C4–C7	13	9	
C3–C7	30	32	
OC2 (°)			
Pre-op	25.12 ± 6.78	24.11 ± 7.18	0.610
Final	27.82 ± 6.84***	27.43 ± 8.24***	0.853
CL (°)			
Pre-op	10.60 ± 7.73	17.54 ± 8.11	0.003**
Final	7.00 ± 7.78***	13.73 ± 7.69***	0.003**
T1S (°)			
Pre-op	19.47 ± 3.73	29.21 ± 3.85	0.000**
Final	19.05 ± 5.74	27.79 ± 5.12	0.000**
CSVA (mm)			
Pre-op	20.04 ± 9.30	26.59 ± 13.90	0.053
Final	21.21 ± 10.83	27.62 ± 13.65	0.069
JOA score			
Pre-op	12.15 ± 1.83	11.84 ± 1.95	0.556
Final	14.62 ± 1.30	14.60 ± 1.08	0.964
NDI (%)			
Pre-op	29.15 ± 15.94	31.76 ± 20.98	0.619
Final	15.77 ± 8.78	13.20 ± 9.56	0.171
JOA recovery rate (%)	51.25 ± 23.66	50.28 ± 20.39	0.876

OC2, occiput-C2 lordosis; CL, cervical lordosis; T1S, T1 slope; CSVA, cervical sagittal vertical axis; JOA, Japanese orthopedic association; NDI, neck disability index.
**$P < 0.01$.
***There is a significant difference compared with preoperative parameter ($P < 0.05$).

TABLE 3 Comparison of cervical sagittal parameters and HRQOL indicators between the low T1S-CL group and the high T1S-CL group.

Parameters	Low T1S-CL ($n = 51$)	High T1S-CL ($n = 51$)	*P*
Age (years)	63.08 ± 10.40	66.36 ± 8.87	0.232
Follow-up (months)	19.62 ± 7.13	17.08 ± 5.15	0.058
Operation segments			0.567
C3–C6	11	7	
C4–C7	10	12	
C3–C7	30	32	
OC2 (°)			
Pre-op	22.61 ± 6.75	26.72 ± 6.59	0.033*
Final	25.26 ± 7.88***	30.09 ± 6.30***	0.020*
CL (°)			
Pre-op	19.01 ± 7.59	8.80 ± 6.18	0.000**
Final	13.86 ± 8.76***	6.60 ± 6.20***	0.001**
T1S (°)			
Pre-op	22.92 ± 6.14	25.62 ± 6.04	0.121
Final	23.78 ± 7.44	23.77 ± 5.85	0.995
CSVA (mm)			
Pre-op	18.45 ± 12.06	30.49 ± 10.08	0.000**
Final	16.51 ± 9.85	30.27 ± 10.21	0.000**
T1S-CL (°)			
Pre-op	3.91 ± 4.98	16.82 ± 5.03	0.000**
Final	9.93 ± 5.37***	17.18 ± 7.34	0.000**
JOA score			
Pre-op	12.42 ± 1.92	11.56 ± 1.76	0.101
Final	14.77 ± 1.21	14.04 ± 1.15	0.326
NDI (%)			
Pre-op	32.08 ± 17.68	28.72 ± 19.42	0.521
Final	14.23 ± 10.53	15.84 ± 7.85	0.538
JOA recovery rate (%)	51.76 ± 23.65	49.55 ± 20.36	0.747

OC2, occiput-C2 lordosis; CL, cervical lordosis; T1S, T1 slope; CSVA, cervical sagittal vertical axis; JOA, Japanese orthopedic association; NDI, neck disability index.
*$P < 0.05$.
**$P < 0.01$.
***There is a significant difference compared with preoperative parameter ($P < 0.05$).

TABLE 4 Comparison of cervical sagittal parameters and HRQOL indicators between the low CSVA/T1S group and the high CSVA/T1S group.

Parameters	Low CSVA/T1S ($n = 51$)	High CSVA/T1S ($n = 51$)	*P*
Age (years)	63.88 ± 8.76	65.60 ± 9.99	0.334
Follow-up (months)	18.58 ± 6.40	17.16 ± 6.50	0.437
Operation segments			0.266
C3–C6	7	11	
C4–C7	9	13	
C3–C7	35	27	
OC2 (°)			
Pre-op	21.69 ± 6.66	27.68 ± 5.89	0.001**
Final	24.67 ± 7.71***	30.71 ± 5.94***	0.003**
CL (°)			
Pre-op	17.82 ± 7.89	10.03 ± 7.52	0.001**
Final	13.03 ± 8.50***	7.46 ± 7.39***	0.016*
T1S (°)			
Pre-op	24.64 ± 4.83	23.83 ± 7.42	0.645
Final	24.30 ± 7.03	22.33 ± 6.67	0.310
CSVA (mm)			
Pre-op	15.48 ± 9.06	31.34 ± 9.33	0.000**
Final	20.05 ± 12.72***	30.83 ± 10.98	0.011*
CSVA/T1S			
Pre-op	0.63 ± 0.36	1.35 ± 0.29	0.000**
Final	0.86 ± 0.54***	1.30 ± 0.38	0.001**
JOA score			
Pre-op	12.04 ± 1.89	11.96 ± 1.90	0.883
Final	14.77 ± 1.24	14.44 ± 1.12	0.326
NDI (%)			
Pre-op	27.15 ± 19.62	33.84 ± 16.84	0.199
Final	12.46 ± 9.11	17.68 ± 8.81	0.040*
JOA recovery rate (%)	51.30 ± 24.56	50.23 ± 19.24	0.863

OC2, occiput-C2 lordosis; CL, cervical lordosis; T1S, T1 slope; CSVA, cervical sagittal vertical axis; JOA, Japanese orthopedic association; NDI, neck disability index.
*$P < 0.05$.
**$P < 0.01$.
***There is a significant difference compared with preoperative parameter ($P < 0.05$).

Correlation analysis

Table 5 summarized the correlations between cervical sagittal parameters and clinical results. Only CSVA/T1S was detected to be correlated with final NDI ($r = 0.310$, $P = 0.027$). No significant correlation was found between clinical results and T1S, CSVA, or T1S-CL.

Discussion

Posterior cervical laminoplasty has been proven to be a classical surgical technique for CSM, which can generate an indirect decompression by allowing the spinal cord to migrate dorsally. However, this technique always has a major defect damaging the posterior muscular-ligament complex, which often leads to the loss of cervical sagittal lordosis and a tendency of tilting forward (manifest as CSVA increasing) (18). In a retrospective study including 108 patients with CSM, Pan et al. found that the CL decreased from 13.9° to 10.7°, and the CSVA increased from 21 mm to 25 mm after cervical laminoplasty (19). Lin et al. also reported a significant increase in CSVA from 20.8 mm to 25.7 mm and a decrease of C3–C7 curvature from 11.6° to 7.8° in 37 patients with CSM treated by open-door laminoplasty (20). In the present

TABLE 5 Correlations between T1S, CSVA, T1S-CL, CSVA/T1S, final JOA score, JOA recovery rate, final NDI.

		Final JOA score	JOA recovery rate	Final NDI
CSVA/T1S	Pearson coefficients	−0.096	−0.111	0.310
	P	0.501	0.439	0.027*
T1S-CL	Pearson coefficients	−0.003	0.153	−0.068
	P	0.984	0.284	0.635
CSVA	Pearson coefficients	−0.168	0.024	0.264
	P	0.237	0.870	0.062
T1S	Pearson coefficients	−0.038	0.170	−0.133
	P	0.790	0.233	0.351

CSVA, cervical sagittal vertical axis; T1S, T1 slope; CL, cervical lordosis; JOA, Japanese orthopedic association; NDI, neck disability index.
*$P < 0.05$.

study, 71.5% (73 / 102) of patients underwent a decrease in CL after cervical laminoplasty. The mean CL angle was decreased from $13.99 \pm 8.23°$ to $10.12 \pm 7.78°$ ($P < 0.001$). Cervical sagittal malalignment has been demonstrated to have an impact on surgical outcomes, including neck pain and neurological symptoms after laminoplasty (21).

T1S plays an essential role in the evaluation of cervical sagittal alignment after laminoplasty. Kim et al. prospectively analyzed the effect of T1S on kyphotic alignment change after cervical laminoplasty in 51 patients with CSM and found that those with high T1S had more postoperative kyphotic alignment changes (22). Zhang et al. further demonstrated that preoperative T1S had a positive correlation with postoperative loss of cervical lordosis (LCL) after laminoplasty (23). However, patients with high T1S and those with low T1S underwent a similar extent of CL decreasing and final HRQOL indicators in this study (**Tables 2**, **5**). Consistent with our results, Cho et al. illustrated that the aggravation of cervical sagittal alignment and changes in HRQOL indicators were not associated with preoperative T1S in patients with CSM who underwent cervical laminoplasty (24). Furthermore, T1S in both groups did not differ significantly before and after surgery (**Table 2**). If CL decreasing could not be compensated by T1S, the cervical spine would present anterior malalignment in the sagittal plane, which always has negative effects on surgical outcomes, especially the HRQOL scores (6, 25).

Like the relationship between SS and LL, the harmony between cervical alignment and cervicothoracic alignment is the objective that spinal surgeons are trying to obtain. Previous studies have proven that the preoperative mismatch between CL and T1S would induce inferior outcomes before and after laminoplasty. In patients with OPLL who underwent laminoplasty, Kim et al. found that lower T1S-CL was significantly associated with more postoperative CL decreasing (26). Li et al.'s results showed that the JOA recovery rate after cervical laminoplasty in 78 CSM patients with extreme CL/T1S was significantly lower than that in patients with fair CL/T1S, which indicated that patients with high CL/T1S ratio would have inferior HRQOL results (27). Similarly, Rao et al. found that patients with T1S-CL mismatching are more likely to have postoperative kyphotic alignment changes, cervical sagittal imbalance, and unsatisfied self-reported outcomes (28). In the current study, the cervical alignment of the high T1S-CL group showed a relatively anterior malalignment. The CL decreased significantly after laminoplasty in both groups. However, there were no significant differences in clinical parameters between groups according to our research, and the T1S-CL was not correlated with the final JOA score, JOA recovery rate, and NDI (**Tables 3**, **5**).

Compared with CL, CSVA would have more relevance with HRQOL scores. We speculate that the match between CSVA and T1S could be more efficient in predicting the clinical outcome after laminoplasty. In this study, we put forward a novel cervical sagittal parameter CSVA/T1S, which could represent the capacity of T1S to compensate for cervical sagittal malalignment. Interestingly, we found that high preoperative CSVA/T1S was correlated with worse NDI at the final follow-up in patients with CSM who underwent cervical laminoplasty, while CSVA was not (**Table 5**). In addition, results indicated that T1S had little difference, but CSVA was quite various between the high and low CSVA/T1S groups (15.48 ± 9.06 vs. 31.34 ± 9.33, $P < 0.001$), which meant the change of CSVA/T1S was mainly affected by CSVA (**Table 4**). Therefore, the effect of CSVA on clinical outcomes after cervical laminoplasty was amplified by matching with T1S. Moreover, though CSVA in the low CSVA/T1S group increased after surgery, it was still significantly lower than that in the high CSVA/T1S group and closer to the normal range as reported by Hardacker et al. in asymptomatic patients of 16.8 ± 11.2 mm (29). High CSVA/T1S refers to the condition that cervical sagittal malalignment might be beyond the compensatory power of T1S. Then the residual malalignment would increase the spinal cord intramedullary pressures and the tension in the neck muscle, which contribute to unsatisfied neurological function recovery and inferior postoperative HRQOL results (30). For those with Low CSVA/T1S, the upper thoracic spine had sufficient potential to halt anterior cervical malalignment, which would be helpful for maintaining better sagittal balance after laminoplasty. Thus, the final NDI result in the low CSVA/T1S group was superior.

The present study used CSVA/T1S to predict the HRQOL after cervical laminoplasty for the first time. According to our research, patients with high preoperative CSVA/T1S had higher NDI at the final follow-up after cervical laminoplasty. Inversely, patients with low preoperative CSVA/T1S corresponded to better neurological function recovery from cervical laminoplasty. In summary, results indicated that

patients with low preoperative CSVA/T1S might be better candidates for cervical laminoplasty. There are still several limitations to our study that need to be considered. Firstly, our research is retrospective, only the data contained in the medical records can be analyzed. Secondly, the sample size was relatively limited and from a single center. Thirdly, the thoracolumbar and the lower limb parameters, which might influence the cervical spine alignment, were not included. Further studies will be necessary to assess the effect of CSVA/T1S on clinical outcome predicting and surgical decision-making. Despite these, our findings could still serve as a reference for spinal surgeons when making a surgical plan for patients with CSM.

Patient presentation

Patient 1 (Low CSVA/T1S, C3–7 laminoplasty; Figure 2): A 65-year-old male with a 17-month follow-up. The preoperative CSVA/T1S value was 0.66 (CSVA: 15.4 mm, T1S: 23.4°). Preoperative JOA score and NDI were 12 and 28.9%, respectively. At the final follow-up, the change of CSVA was +2.1 mm. JOA score increased from 12 to 16, while NDI decreased from 28.9% to 12%. The JOA recovery rate was 80%.

Patient 2 (Low CSVA/T1S, C4–7 laminoplasty; Figure 3): A 60-year-old male with a 19-month follow-up. The preoperative CSVA/T1S value was 0.47 (CSVA: 9.7 mm, T1S: 20.7°). Preoperative JOA score and NDI were 11 and 26%, respectively. At the final follow-up, the change of CSVA was +1.3 mm. JOA score increased from 11 to 15, while NDI decreased from 26% to 14%. The JOA recovery rate was 67%.

Patient 3 (High CSVA/T1S, C4–7 laminoplasty; Figure 4): A 63-year-old male with an 18-month follow-up.

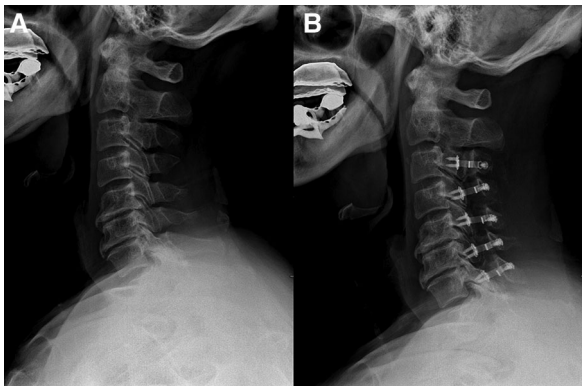

FIGURE 2
A 65-year-old male patient treated with C3–C7 laminoplasty. (A) Preoperative lateral cervical radiograph (CSVA = 15.4 mm, T1S = 23.4°). (B) Lateral cervical radiograph at final follow-up (17 months after surgery, CSVA = 17.5 mm).

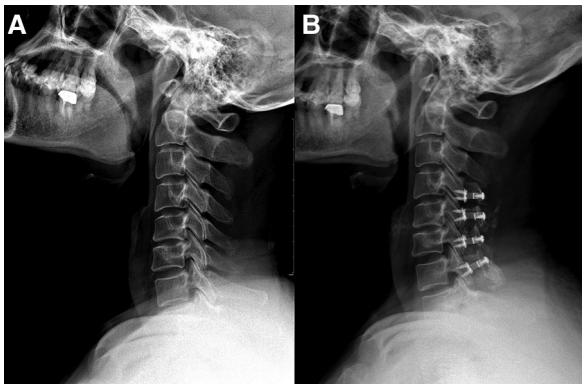

FIGURE 3
A 60-year-old male patient treated with C4–C7 laminoplasty. (A) Preoperative lateral cervical radiograph (CSVA = 9.7 mm, T1S = 20.7°). (B) Lateral cervical radiograph at final follow-up (19 months after surgery, CSVA = 11 mm).

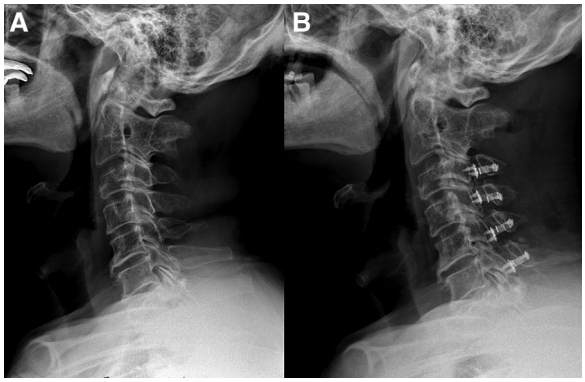

FIGURE 4
A 63-year-old male patient treated with C4–C7 laminoplasty. (A) Preoperative lateral cervical radiograph (CSVA = 29.5 mm, T1S = 21.8°). (B) Lateral cervical radiograph at final follow-up (18 months after surgery, CSVA = 30.9 mm).

The preoperative CSVA/T1S value was 1.35 (CSVA: 29.5 mm, T1S: 21.8°). Preoperative JOA score and NDI were 10 and 30%, respectively. At the final follow-up, the change of CSVA was +1.4 mm. JOA score increased from 10 to 15, while NDI decreased from 30% to 18%. The JOA recovery rate was 71%.

Patient 4 (High CSVA/T1S, C3–6 laminoplasty; Figure 5): A 58-year-old male with a 17-month follow-up. The preoperative CSVA/T1S value was 1.34 (CSVA: 37.6 mm, T1S: 28°). Preoperative JOA score and NDI were 10 and 28%, respectively. At the final follow-up, the change of CSVA was +3.6 mm. JOA score increased from 10 to 14, while NDI decreased from 28% to 17.7%. The JOA recovery rate was 57%.

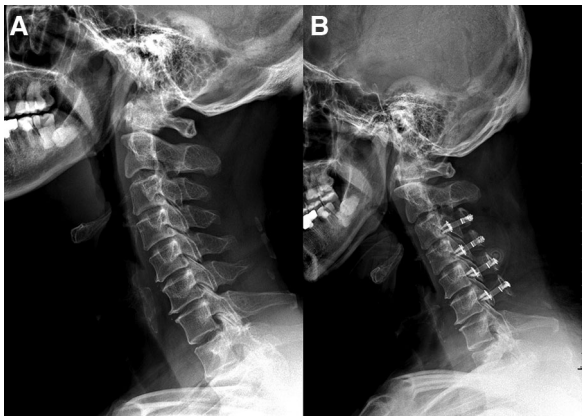

FIGURE 5
A 58-year-old male patient treated with C3–C6 laminoplasty. (A) Preoperative lateral cervical radiograph (CSVA = 37.6 mm, T1S = 28°). (B) Lateral cervical radiograph at final follow-up (17 months after surgery, CSVA = 41.2 mm).

Conclusion

Preoperative CSVA/T1S was significantly correlated with postoperative NDI in patients with CSM after cervical laminoplasty. Patients with low preoperative CSVA/T1S achieved better neurological function improvement after cervical laminoplasty. Cervical laminoplasty could be an appropriate choice for patients with lower preoperative CSVA/T1S.

Data availability statement

The original contributions presented in the study are included in the article/Supplementary Material, further inquiries can be directed to the corresponding author/s.

Ethics statement

The studies involving human participants were reviewed and approved by Ethics Committee of Capital Medical University Xuanwu Hospital. Written informed consent for participation was not required for this study in accordance with the national legislation and the institutional requirements.

Author contributions

D-FW: Writing, Reviewing, Editing, Methodology and Data Curation; W-GZ, WW, X-YL: Writing, Data Curation and Supervision; C-XL, BS: Resources; C K: Validation and software; S-BL: Supervision. All authors contributed to the article and approved the submitted version.

Conflict of interest

The authors declare that the research was conducted in the absence of any commercial or financial relationships that could be construed as a potential conflict of interest.

Publisher's note

All claims expressed in this article are solely those of the authors and do not necessarily represent those of their affiliated organizations, or those of the publisher, the editors and the reviewers. Any product that may be evaluated in this article, or claim that may be made by its manufacturer, is not guaranteed or endorsed by the publisher.

References

1. Bernhardt M, Hynes RA, Blume HW, White AA. Cervical spondylotic myelopathy. *J Bone Joint Surg Am*. (1993) 75(1):119–28. doi: 10.2106/00004623-199301000-00016

2. Wu JC, Ko CC, Yen YS, Huang WC, Chen YC, Liu L, et al. Epidemiology of cervical spondylotic myelopathy and its risk of causing spinal cord injury: a national cohort study. *Neurosurg Focus*. (2013) 35(1):E10. doi: 10.3171/2013.4.FOCUS13122

3. Emery SE. Cervical spondylotic myelopathy: diagnosis and treatment. *J Am Acad Orthop Surg*. (2001) 9(6):376–88. doi: 10.5435/00124635-200111000-00003

4. Chiba K, Ogawa Y, Ishii K, Takaishi H, Nakamura M, Maruiwa H, et al. Long-term results of expansive open-door laminoplasty for cervical myelopathy–average 14-year follow-up study. *Spine*. (2006) 31(26):2998–3005. doi: 10.1097/01.brs.0000250307.78987.6b

5. Cho SK, Kim JS, Overley SC, Merrill RK. Cervical laminoplasty: indications, surgical considerations, and clinical outcomes. *J Am Acad Orthop Surg*. (2018);26(7):e142–e52. doi: 10.5435/JAAOS-D-16-00242

6. Hyun SJ, Han S, Kim KJ, Jahng TA, Kim HJ. Assessment of T1 slope minus cervical lordosis and C2-7 sagittal vertical axis criteria of a cervical spine deformity classification system using long-term follow-up data after multilevel posterior cervical fusion surgery. *Oper Neurosurg*. (2019) 16(1):20–6. doi: 10.1093/ons/opy055

7. Stegen S, van Gastel N, Carmeliet G. Bringing new life to damaged bone: the importance of angiogenesis in bone repair and regeneration. *Bone*. (2015) 70:19–27. doi: 10.1016/j.bone.2014.09.017

8. Smith JS, Lafage V, Ryan DJ, Shaffrey CI, Schwab FJ, Patel AA, et al. Association of myelopathy scores with cervical sagittal balance and normalized spinal cord volume: analysis of 56 preoperative cases from the AOSpine North America myelopathy study. *Spine*. (2013) 38(22 Suppl 1):S161–70. doi: 10.1097/BRS.0b013e3182a7eb9e

9. Kato M, Namikawa T, Matsumura A, Konishi S, Nakamura H. Effect of cervical sagittal balance on laminoplasty in patients with cervical myelopathy. *Global Spine J*. (2017) 7(2):154–61. doi: 10.1177/2192568217694011

10. Xu C, Zhang Y, Dong M, Wu H, Yu W, Tian Y, et al. The relationship between preoperative cervical sagittal balance and clinical outcome of laminoplasty treated cervical ossification of the posterior longitudinal ligament patients. *Spine J*. (2020) 20(9):1422–9. doi: 10.1016/j.spinee.2020.05.542

11. Lee DH, Ha JK, Chung JH, Hwang CJ, Lee CS, Cho JH. A retrospective study to reveal the effect of surgical correction of cervical kyphosis on thoraco-lumbo-pelvic sagittal alignment. *Eur Spine J*. (2016) 25(7):2286–93. doi: 10.1007/s00586-016-4392-9

12. Petraglia AL, Srinivasan V, Coriddi M, Whitbeck MG, Maxwell JT, Silberstein HJ. Cervical laminoplasty as a management option for patients with cervical spondylotic myelopathy: a series of 40 patients. *Neurosurgery*. (2010) 67 (2):272–7. doi: 10.1227/01.NEU.0000371981.83022.B1

13. Scheer JK, Tang JA, Smith JS, Acosta Jr FL, Protopsaltis TS, Blondel B, et al. Cervical spine alignment, sagittal deformity, and clinical implications: a review. *J Neurosurg Spine*. (2013) 19(2):141–59. doi: 10.3171/2013.4.SPINE12838

14. Hirabayashi K, Watanabe K, Wakano K, Suzuki N, Satomi K, Ishii Y. Expansive open-door laminoplasty for cervical spinal stenotic myelopathy. *Spine* (1983) 8(7):693–9. doi: 10.1097/00007632-198310000-00003

15. Tamai K, Buser Z, Paholpak P, Sessumpun K, Nakamura H, Wang JC. Can C7 slope substitute the T1 slope?: an analysis using cervical radiographs and kinematic MRIs. *Spine*. (2018) 43(7):520–5. doi: 10.1097/BRS.0000000000002371

16. Kato S, Oshima Y, Oka H, Chikuda H, Takeshita Y, Miyoshi K, et al. Comparison of the Japanese Orthopaedic Association (JOA) score and modified JOA (mJOA) score for the assessment of cervical myelopathy: a multicenter observational study. *PLoS One*. (2015) 10(4):e0123022. doi: 10.1371/journal.pone.0123022

17. Howell ER. The association between neck pain, the Neck Disability Index and cervical ranges of motion: a narrative review. *J Can Chiropr Assoc*. (2011) 55(3):211–21.

18. Aita I, Wadano Y, Yabuki T. Curvature and range of motion of the cervical spine after laminaplasty. *J Bone Joint Surg Am*. (2000) 82(12):1743–8. doi: 10.2106/00004623-200012000-00008

19. Pan Y, Ma X, Feng H, Chen C, Qin Z, Huang Y. Effect of posterior cervical expansive open-door laminoplasty on cervical sagittal balance. *Eur Spine J*. (2020) 29(11):2831–7. doi: 10.1007/s00586-020-06563-9

20. Lin S, Zhou F, Sun Y, Chen Z, Zhang F, Pan S. The severity of operative invasion to the posterior muscular-ligament complex influences cervical sagittal balance after open-door laminoplasty. *Eur Spine J*. (2015) 24(1):127–35. doi: 10.1007/s00586-014-3605-3

21. Zhang X, Gao Y, Gao K, Yu Z, Lv D, Ma H, et al. Factors associated with postoperative axial symptom after expansive open-door laminoplasty: retrospective study using multivariable analysis. *Eur Spine J*. (2020) 29 (11):2838–44. doi: 10.1007/s00586-020-06494-5

22. Kim TH, Lee SY, Kim YC, Park MS, Kim SW. T1 slope as a predictor of kyphotic alignment change after laminoplasty in patients with cervical myelopathy. *Spine*. (2013) 38(16):E992–7. doi: 10.1097/BRS.0b013e3182972e1b

23. Zhang JT, Li JQ, Niu RJ, Liu Z, Tong T, Shen Y. Predictors of cervical lordosis loss after laminoplasty in patients with cervical spondylotic myelopathy. *Eur Spine J*. (2017) 26(4):1205–10. doi: 10.1007/s00586-017-4971-4

24. Cho JH, Ha JK, Kim DG, Song KY, Kim YT, Hwang CJ, et al. Does preoperative T1 slope affect radiological and functional outcomes after cervical laminoplasty? *Spine*. (2014) 39(26):E1575–81. doi: 10.1097/BRS.0000000000000614

25. Knott PT, Mardjetko SM, Techy F. The use of the T1 sagittal angle in predicting overall sagittal balance of the spine. *Spine J*. (2010) 10(11):994–8. doi: 10.1016/j.spinee.2010.08.031

26. Kim B, Yoon DH, Ha Y, Yi S, Shin DA, Lee CK, et al. Relationship between T1 slope and loss of lordosis after laminoplasty in patients with cervical ossification of the posterior longitudinal ligament. *Spine J*. (2016) 16(2):219–25. doi: 10.1016/j.spinee.2015.10.042

27. Li XY, Kong C, Sun XY, Guo MC, Ding JZ, Yang YM, et al. Influence of the ratio of C2-C7 cobb angle to T1 slope on cervical alignment after laminoplasty. *World Neurosurg*. (2019) 124:e659–66. doi: 10.1016/j.wneu.2018.12.181

28. Rao H, Huang Y, Lan Z, Xu Z, Li G, Xu W. Does preoperative T1 slope and cervical lordosis mismatching affect surgical outcomes after laminoplasty in patients with cervical spondylotic myelopathy? *World Neurosurg*. (2019) 130: e687–e93. doi: 10.1016/j.wneu.2019.06.193

29. Hardacker JW, Shuford RF, Capicotto PN, Pryor PW. Radiographic standing cervical segmental alignment in adult volunteers without neck symptoms. *Spine*. (1997) 22(13):1472–80; discussion 80. doi: 10.1097/00007632-199707010-00009

30. Tang JA, Scheer JK, Smith JS, Deviren V, Bess S, Hart RA, et al. The impact of standing regional cervical sagittal alignment on outcomes in posterior cervical fusion surgery. *Neurosurgery*. (2015) 76(Suppl 1):S14–21; discussion S. doi: 10.1227/01.neu.0000462074.66077.2b

frontiers | Frontiers in Surgery

TYPE Original Research
PUBLISHED 01 September 2022
DOI 10.3389/fsurg.2022.966617

Check for updates

OPEN ACCESS

EDITED BY
Songqiao Liu,
Southeast University, China

REVIEWED BY
Minwei Zhao,
Peking University Third Hospital, China
Xiang Li,
People's Liberation Army General Hospital, China

*CORRESPONDENCE
Liao Wang
wang821127@163.com
Tsung-Yuan Tsai
tytsai@sjtu.edu.cn

†These authors have contributed equally to this work and share first authorship

SPECIALTY SECTION
This article was submitted to Orthopedic Surgery, a section of the journal Frontiers in Surgery

RECEIVED 11 June 2022
ACCEPTED 12 August 2022
PUBLISHED 01 September 2022

CITATION
Jiang Z, Cheng R, Kernkamp WA, Xia C, Liang J, Wang L and Tsai T-Y (2022) The midcortical-line is more reliable than the T-line in predicting stem anteversion in patients with developmental hip dysplasia after total hip arthroplasty.
Front. Surg. 9:966617.
doi: 10.3389/fsurg.2022.966617

COPYRIGHT
© 2022 Jiang, Cheng, Kernkamp, Xia, Liang, Wang and Tsai. This is an open-access article distributed under the terms of the Creative Commons Attribution License (CC BY). The use, distribution or reproduction in other forums is permitted, provided the original author(s) and the copyright owner(s) are credited and that the original publication in this journal is cited, in accordance with accepted academic practice. No use, distribution or reproduction is permitted which does not comply with these terms.

The midcortical-line is more reliable than the T-line in predicting stem anteversion in patients with developmental hip dysplasia after total hip arthroplasty

Ziang Jiang[1,2,3†], Rongshan Cheng[1,2,3†], Willem Alexander Kernkamp[4], Chunjie Xia[3,5], Junjie Liang[1,6], Liao Wang[1,2*] and Tsung-Yuan Tsai[1,2,3*]

[1]School of Biomedical Engineering and Med-X Research Institute, Shanghai Jiao Tong University, Shanghai, China, [2]Department of Orthopaedic Surgery, Shanghai Ninth People's Hospital, Jiao Tong University School of Medicine, Shanghai, China, [3]Engineering Research Center of Digital Medicine and Clinical Translation, Ministry of Education, Shanghai, China, [4]Department of Orthopaedic Surgery, Leiden University Medical Center, Leiden, Netherlands, [5]School of Mechanical Engineering, Shanghai Jiao Tong University, Shanghai, China, [6]Guangxi Clinical Research Center for Digital Medicine and 3D Printing, Guigang City People's Hospital, Guigang, China

Background: Precise preoperative planning improves postoperative outcomes in total hip arthroplasty (THA), especially in developmental dysplasia of the hip (DDH) cases. Previous studies used the T-line and midcortical-line as preoperative landmarks to predict postoperative stem anteversion (PSA). However, the most reliable landmark in predicting PSA in DDH patients remains unclear. To find the most reliable measurement to predict the PSA in DDH patients, this study compared the midcortical-line and T-line at different femoral neck levels.

Methods: Pre- and postoperative Computed Tomography (CT) scans of 28 hips in 21 DDH patients who received THA were obtained for three-dimensional femoral models. The preoperative CT scan was used to measure the anteversion of the midcortical-line on the axial cross-sectional plane images (AM-CT), the anteversion of the midcortical-line from 3D models (AM-3D), and the T-line from 3D models (AT-3D) at simulated osteotomy planes at 5 and 10 mm heights proximal to the base of the lesser trochanter. The correlation between the preoperative femoral anteversion (AM-CT, AM-3D, AT-3D) and the PSA was assessed to evaluate the prediction accuracy.

Results: The correlations between the AM-CT and the PSA were 0.86 (mean difference (MD) = 1.9°) and 0.92 (MD = –3.0°) at 5 and 10 mm heights, respectively. The correlation between the AM-3D and the PSA were 0.71 (MD = –11.6°) and 0.61 (MD = –12.9°) at 5 and 10 mm heights. The AT-3D was significantly greater (MD = 15.4°) than the PSA (p-value <0.01) at 5 mm cutting

Abbreviations

DDH, developmental dysplasia of the hip; CT, computed tomography; THA, total hip arthroplasty; ICC, interclass correlation coefficient; AM-CT, the anteversion using the midcortical-line based on CT; AM-3D, the anteversion using the midcortical-line based on 3D models; AT-3D, the anteversion using the T-line based on 3D models; PSA, postoperative stem anteversion; LCEA, lateral center-edge angle; ISB, international society of biomechanics; ROM, range of motion; IMI, The intersection of midcortical-line with the inferior margins of the plane; NFA, native femoral anteversion.

height, and the correlation between the AT-3D and the PSA was 0.57 (MD = 7.8°) at 10 mm cutting height.
Conclusions: The AM-CT at the 10 mm height had the strongest correlation with the PSA and was more reliable in predicting the PSA when compared with the AM-3D and the AT-3D in DDH patients.

KEYWORDS

midcortical-line, T-line, postoperative stem anteversion, developmental dysplasia of the hip (DDH), total hip arthroplasty (THA)

Introduction

Appropriate postoperative stem anteversion (PSA) in total hip arthroplasty (THA) is critical to achieving implant stability, the optimal range of motion (ROM), and avoiding impingement (1–8). The combined anteversion technique, which considers the sum of acetabular cup anteversion and femoral anteversion, has been clinically proven to prevent implant impingement if controlled in a safe zone of 25°–50° (8–11). The stem anteversion is more challenging to control during surgery, or to predict preoperatively. Therefore, the "femur-first" technique (9, 12) was developed. The cup anteversion can then be intraoperatively calculated to the stem anteversion and match the safe zone. Therefore, the prediction of PSA can play a decisive role in the implantation target of the acetabular cup, which can optimize the combined anteversion of the preoperative planning process. Accurate predictions of the PSA may improve surgical outcomes after THA.

Few studies have used the anatomical landmarks of medical images to predict the PSA prior to THA implantation. Suh et al. (13) reported that the midcortical-line is compatible with the true femoral anteversion using a single slice of CT. However, Tsukeoka et al. (14, 15) demonstrated that the stem tended to retroversion compared with the midcortical-line on the cut surface of the femoral neck. These differences in the reliability of the midcortical-line could attribute to different methodologies. Others used the lesser trochanter to estimate the PSA intraoperatively which has shown to have a mean difference of <5° (16). However, it is difficult to evaluate the version of the lesser trochanter using a surgical incision other than the posterior approach. The T-line landmark that connects the trochanteric fossa and the inferior margins on the cut surface was found to be a reliable and reproducible intraoperative reference to produce a stable and functional THA (15). During THA surgery, the T-line reproduces the native femoral anteversion (NFA) in osteoarthritis and DDH patients (14, 15). Through the definition of femoral stem torsion in THA simulation surgery, the T-line was also validated that the accuracy of using a T-line to guide version during implantation of the femoral stem would not be affected by the degree of subluxation of the femoral head (15). 3D analyzes are thought to better simulate the intraoperative view before THA. Detailed 3D information may be particularly helpful in complex preoperative planning in patients with developmental dysplasia of the hip (DDH) (5, 14, 15, 17). However, 3D analysis requires intensive work and is therefore not practical in daily practice. The relatively convenient use of CT images for PSA prediction has also not been evaluated for its efficiency in DDH patients.

Furthermore, the level of the CT images selected in predicting the PSA also affected the accuracy. Yu et al. (3) showed that AM-CT, which selected the CT images at a proximal level, accurately predicted PSA for Crowe type II/III DDH patients with a posterolateral approach and "acetabular-first" technique. Tsukeoka et al. (15) simulated the osteotomy process on 3D femoral models, which showed that the AT-3D at 5 mm cutting height proximal to the lesser trochanter reproduced the NFA better than that at 10 mm. However, the effect of different osteotomy levels using the T-line measurement on predicting the PSA for DDH patients remains unknown, and the confirmation of the optimal femoral neck level requires further investigation.

This study aimed to investigate: (1) whether the midcortical-line or the T-line was more reliable in predicting the PSA in DDH patients; (2) to find the optimal femoral neck level at which the T-line and midcortical-line could better predict PSA in DDH patients.

Materials and methods

Patient demographics

The Internal Review Board approved this study. 28 hips were enrolled in this study retrospectively. The inclusion criteria were: patients with DDH Crowe grade I to IV who had undergone cementless THA and had received pre-and postoperative femoral CT scans between May 2013 and September 2015. The exclusion criteria were: patients who underwent an osteotomy lower than the lesser trochanter level during surgery, patients without femoral head or neck, patients who had prior hip surgery, patients who missed the pre-operative or postoperative lower limb CT images, and

TABLE 1 Characteristics in DDH patients.

Parameters	Mean ± SD
Age	64.5 ± 8.9
Weight (kg)	64.0 ± 10.2
Height (m)	1.6 ± 0.1
BMI (kg/m^2)	24.7 ± 3.1

patients who had a surgical complication of dislocation or component subluxation on the implanted hips. A total of 17 hips were Crowe type I (<50% subluxation); 6 Crowe type II/III (50%–75%/75%–100% subluxation); and 5 Crowe type IV (>100% subluxation) (18) (**Table 1**). According to the guideline of Crowe classification, the dysplasia with the lateral center-edge angle (LCEA) of the participants was less than 20° measured from a radiograph.

Surgical procedure

All DDH hips received cementless THA prostheses (Stryker Secur-Fit, Mahwah, New Jersey, United States; DePuy SUMMIT, Warsaw, IN, United States) with metaphyseal fit stems by the same experienced arthroplasty surgeon (ZZ) using a posterolateral approach. Intraoperatively, the femoral stem was implanted using the "femur-first" technique (9, 12), in combination with the evaluation of the medullary cavity, femoral geometry, and acetabular position (19), and experience.

Measurements based on CTs

The pre- and postoperative CT scans were obtained using 128-slices CT scanners (Somatom Definition Flash®, Siemens Healthcare, Germany) with 1 mm slice thickness and in-plane resolution of 0.98 mm. The preoperative CT images at 5 mm and 10 mm heights above the lesser trochanter were selected (**Figure 1A**). The midcortical-line was defined as the anterior and posterior cortex's angular bisector (3, 13). The AM-CT is the angle between the midcortical-line and Posterior Condylar Axis (PCA) on each level as proposed (3) (**Figure 1B**). The PSA was measured as the angle between the femoral stem neck axis on the axial CT images and the PCA from the postoperative CTs (**Figure 1C**). The anatomical coordinate system referred to the International Society of Biomechanics (ISB) recommendations (20).

Measurements based on 3D models

The pre- and postoperative CT images were imported into commercial software (Amira 6.7, Thermo Fisher Scientific, Waltham, MA, United States) to reconstruct the 3D surface

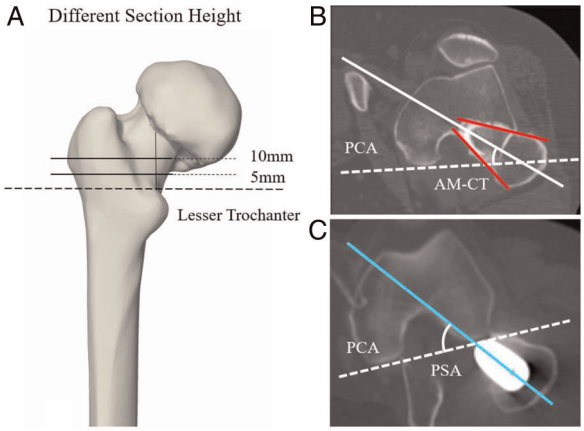

FIGURE 1
The schematic illustration of the measurements based on CT. (A) The selection of two different CT section height on femur, which are 5 mm and 10 mm height above the proximal end of the lesser trochanter. (B) AM-CT was defined as the angle between the PCA (white dotted line) and the midcortical-line (white solid line), which is the angular bisector of anterior cortex and posterior cortex (red solid line). (C) PSA was defined as the angle between the PCA and the femoral stem neck axis (bright sky-blue solid line).

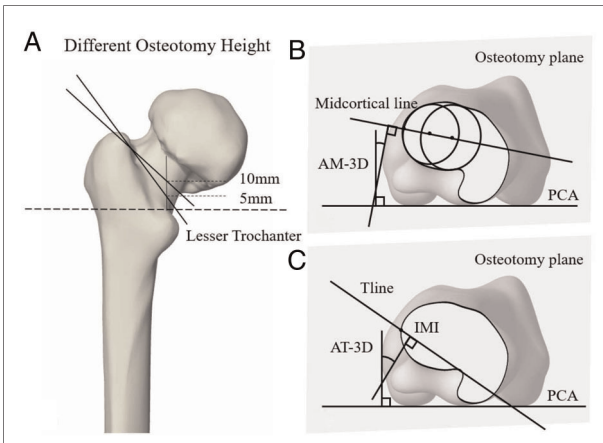

FIGURE 2
The schematic illustration of the measurements based on 3D model. (A) The simulated osteotomy plane pass through the center of piriformis fossa and the location at the 5 mm and 10 mm heights above the lesser trochanter. (B) AM-3D was defined as the angle between the midcortical-line and the PCA. (C) AT-3D was defined as the angle between the PCA and the T-line. IMI was the intersection of midcortical-line with the inferior margins of the osteotomy plane.

models (21). The anteversion using the midcortical-line and T-line were measured based on the 3D models (AM-3D; AT-3D) (14). The simulated osteotomy plane was determined through the center of the piriformis fossa and the 5 and 10 mm cutting heights proximal to the lesser trochanter (**Figure 2A**). AM-3D was defined as the angle between the midcortical-line (the connecting line between the center of the

best fitting circles obtained from the medial and inferior margins of the simulated osteotomy plane) and the PCA (14) (**Figure 2B**). AT-3D was defined as the angle between the T-line (the line connecting the trochanteric fossa and the inferior margins of the plane) and the PCA (14) (**Figure 2C**).

Statistical analysis

All data met the normal distribution, and the measurements were calculated using Excel 2016 (Microsoft Excel, Redmond, WA, United States). The data were analyzed using the mean values ± standard deviation of PSA, AM-CT, AM-3D, and AT-3D. The differences between AM-CT, AM-3D, AT-3D, and PSA were calculated by the mean difference (MD). Interobserver and intraobserver reliability of the measurements was estimated by the intraclass correlation coefficient (ICC). Pearson correlation coefficients (r) were used to evaluate the correlations between AM-CT, AM-3D, AT-3D, and PSA. The student's t-test was used to determine differences between parameters at 5 and 10 mm heights. The statistical significance level (α) was set at 0.05.

Results

The ICC for intra-observer and interobserver reliabilities were >0.9 for all measurements. The two-tailed Pearson correlation coefficients are statistically significant for all measures.

A strong correlation was found for the AM-CT and the PSA at the 5 and 10 mm heights (respectively, $r = 0.86$ with p-value = 0.000 and $r = 0.92$ with p-value = 0.000), and no statistically significant difference was found (p-value = 0.662 and 0.495). The mean difference (MD) between the AM-CT at 5 mm height (31.8° ± 15.3°) and the PSA (29.8° ± 17.7°) was 1.9° ± 8.8°, and the MD between the AM-CT at 10 mm height (26.8° ± 14.9°) and PSA was −3.0° ± 7.1° (**Table 2**).

A moderate correlation was found between the AM-3D and the PSA at the 5 and 10 mm cutting heights respectively, $r = 0.71$ (p-value = 0.000) and $r = 0.61$ (p-value = 0.001). The mean AM-3D was 18.3° ± 12.5° at 5 mm and 16.9° ± 12.3° at 10 mm cutting height, which both were significantly smaller than the PSA (p-value = 0.007 and 0.003) (**Table 2**).

A moderate correlation was also found between the AT-3D and the PSA at 5 and at 10 mm cutting heights, respectively, which were $r = 0.56$ (p-value = 0.001) and $r = 0.57$ (p-value = 0.001) in 5 and 10 mm groups. The mean AT-3D was 45.2° ± 17.5° and was significantly greater than the PSA (p-value <0.010) at 5 mm cutting height. The mean AT-3D was 37.6° ± 15.2° and no significant difference was found between AT-3D and PSA (p-value = 0.084) at 10 mm cutting height (**Table 2**).

Discussion

The main finding of this study was that midcortical-line had higher accuracy in predicting the PSA compared to the T-line. Second, the 10 mm osteotomy level for AM-CT may best predict the PSA compared to the AM-3D or AT-3D in DDH patients. The AM-CT on the axial CT images at the 10 mm height had the strongest correlation ($r = 0.92$) and the smallest difference with PSA (−3.0° ± 7.1°) compared to the other methods. Therefore, clinical use of AM-CT to predict PSA (4, 8, 10) can best determine the anteversion of the acetabular cup and help to control the combined anteversion in the safe zone.

We found that the prediction of anteversion using the T-line showed a moderate correlation with the PSA ($r = 0.56$ and $r = 0.57$ in the 5 and 10 mm groups) and can even be significantly greater than the PSA (MD reached 15.4° in the 5 mm group). This difference may be explained by the conception of the T-line. The T-line is adjusted to get a larger anteversion compared with the midcortical-line. The adjustment corrected the proximal femoral deformity of DDH patients due to the disease. Therefore, T-line can be a useful intraoperative reference that helps reproduce the NFA as the high correlation with the NFA reported in the article of Tsukeoka et al. (15). The anteversion reference can be

TABLE 2 The different anteversions simulated based on various reference landmarks.

Parameters	Height (mm)	Angle (°)[a]	Difference (°)[a]	t-test p-value	r	Pearson correlation p-value
AM-CT	5	31.8 ± 15.3	1.9 ± 8.8	0.662	0.86	0.000**
	10	26.8 ± 14.9	−3.0 ± 7.1	0.495	0.92	0.000**
AM-3D	5	18.3 ± 12.5	−11.6 ± 12.5	0.007*	0.71	0.000**
	10	16.9 ± 12.3	−12.9 ± 14.2	0.003*	0.61	0.001**
AT-3D	5	45.2 ± 17.5	15.4 ± 16.5	0.002*	0.56	0.001**
	10	37.6 ± 15.2	7.8 ± 15.5	0.084	0.57	0.001**
PSA	N/A	29.8 ± 17.7	N/A	N/A	N/A	N/A

Difference = (AM-CT/AM-3D/AT-3D) − PSA; t-test = student's t-test; r = correlation coefficient.
[a]Expressed as mean ± standard deviation.
*Indicates the difference is statistically significant in student's t-test (p-value <0.05).
**Indicates the Pearson correlation coefficient is statistically significant (p-value <0.01).

extremely meaningful in clinical application for the implantation of prostheses like SROM for DDH patients, especially for patients in severe situations. However, the orientation of the cementless femoral stem in implanting was mainly dependent on the geometric shape of the proximal medullary cavity. The intraoperative twist and press-fit result in a certain pathological anteversion but lead to the deviation from the anteversion of the T-line landmark.

On the other hand, the midcortical-line was strongly correlated with the PSA of DDH patients, which is consistent with the previous studies (3, 13). This may be because the midcortical-line is created between the anterior and posterior cortical line and met an actual axis of femoral anteversion (13), which may influence the orientation of the cementless stem in THA during implanting. Moreover, the patients selected in this study included DDH patients with the posterolateral approach, which expands the application range of the conclusion that the AM-CT could be a reliable landmark for predicting the PSA of DDH patients.

The height of the anatomic landmark is critical to the accuracy of prediction. According to the previous studies (3, 13, 15), 5 and 10 mm heights proximal to the base of the lesser trochanter are commonly chosen for osteotomy, which can preserve bone mass and prevent trochanteric fractures. In this study, we observed a strong correlation between the AM-CT at the two levels (5 and 10 mm height proximal to the lesser trochanter) and the PSA. We found the AM-CT at 10 mm height was better than that at 5 mm for predicting the PSA for DDH patients. These results may be because morphological characteristics of the distal femoral medullary cavity in DDH femurs tend to be more circular or elliptical (6, 22), which created more difficulties in confirming the anterior and posterior cortex. Therefore, 5 mm height proximal to the base of the lesser trochanter of the CT slices may cause a slight deviation in confirming the midcortical-line compared to the 10 mm height group. Moreover, the circinal or elliptical medullary cavity in the distal location can provide a relatively greater adjustive range for stem implantation, which resulted in the difference between PSA and predicted stem anteversion (23). Therefore, the CT images at 10 mm above the proximal end of the lesser trochanter are advised to use in preoperative planning for DDH patients accurately.

The explanation of these phenomena is that the design of cementless femoral stems is mainly based on the medullary cavity morphology according to CT images (24). Therefore, the postoperative anteversion of cementless stems with adaptation in implanting may be relatively consistent with the positional relationship between the stem and the proximal femoral medullary canal observed on CT images. This may also explain why the midcortical-line from cross-sectional CT planes can be better correlated with PSA than the 3D models. Therefore, the AM-CT based on the axis CT images was more appropriate for predicting the PSA than the AM-3D based on the 3D models in the preoperative planning. Furthermore, although using the 3D models can simulate the THA surgical procedure, we did not find other landmarks from the osteotomy planes of the 3D femoral model that have high effectiveness in predicting PSA in this study. Therefore, we believe preoperative planning based on CT images provides a good solution for predicting the PSA.

This study has several limitations. First, the sample size of this study was small. However, the Pearson correlation coefficient is statistically significant at the 0.05 level (two-tailed), which verified the validity of the sample. The sample size of this experiment has certain reliability. Limited by the sample size, it is hard for us to make a sub-group analysis separately according to different Crowe types. Nevertheless, the PSA is mainly depending on the cavity morphology, which shared a similar trend in Crowe I–IV proximal femur in the transverse section (23). Moreover, the selected plane for obtaining the landmarks involved minimal areas that were influenced by excessive deformation caused by DDH with different severity, such as the femoral head and neck. Thus, the difference caused by DDH Crowe types in conclusion should be limited in this research. Second, even though the cementless stem was reported as one of the most extensively used stems in younger patients, the use of only one type of femoral stem in this study was limited to a certain extent (22, 25). The cementless stem design mainly relies on the profile of the femoral medullary cavity based on the CT cross-section (26, 27). Other femoral stem types may affect the femoral anteversion after implantation.

In conclusion, this study found that the AM-CT was the most reliable preoperative reference guide for predicting the PSA when compared to the AM-CT and the AT-3D in DDH patients. The AM-CT at 10 mm height was better able to predict the PSA than the 5 mm height proximal to the base of the lesser trochanter in DDH patients. These findings further underscore the importance of preoperative planning, as it may be challenging to find reliable intraoperative landmarks which can accurately predict the PSA for DDH patients.

Data availability statement

The original contributions presented in the study are included in the article/supplementary material, further inquiries can be directed to the corresponding author/s.

Ethics statement

The studies involving human participants were reviewed and approved by Three-Dimensional Acetabular Orientation Measurement in a Reliable CoordinateSystem Among One Hundred Chinese. The patients/participants provided their written informed consent to participate in this study.

Author contributions

ZJ: study design, data acquisition, analysis, data interpretation, manuscript writing, manuscript revision, and final approval of the submitted version. RC: study design, data acquisition, data interpretation, manuscript revision, and final approval of the submitted version. WAK: data interpretation, manuscript revision, and final approval of the submitted version. CX: data acquisition, data interpretation, manuscript revision, and final approval of the submitted version. JL: data acquisition, data interpretation. LW: study design, data interpretation, manuscript revision, and final approval of the submitted version. T-YT: study design, data interpretation, and manuscript revision and final approval of the submitted version. All co-authors have seen and agree with the contents of the manuscript. The manuscript has not been submitted or is not simultaneously being submitted elsewhere. All authors contributed to the article and approved the submitted version.

Funding

This study was sponsored by the National Key Technology Research and Development Program of the Ministry of Science and Technology of China (grant no. 2019YFC0120600), and the Shanghai Association for Science and Technology (grant no. 21DZ2208200).

Acknowledgments

The authors would like to thank orthopedic surgeon Dr. Zhenan Zhu for the assistance in surgical procedures.

Conflict of interest

The authors declare that the research was conducted in the absence of any commercial or financial relationships that could be construed as a potential conflict of interest.

Publisher's note

All claims expressed in this article are solely those of the authors and do not necessarily represent those of their affiliated organizations, or those of the publisher, the editors and the reviewers. Any product that may be evaluated in this article, or claim that may be made by its manufacturer, is not guaranteed or endorsed by the publisher.

References

1. Hidaka R, Matsuda K, Nakamura M, Nakamura S, Kawano H. Optimal combined anteversion range for obtaining a wider range of motion without prosthetic impingement after total hip arthroplasty: a three-dimensional analysis study. *J Orthop Surg Res.* (2022) 17:1–10. doi: 10.1186/s13018-022-03112-6

2. Li G, Peng Y, Zhou C, Jin Z, Bedair H. The effect of structural parameters of total hip arthroplasty on polyethylene liner wear behavior: a theoretical model analysis. *J. Orthop. Res.* (2020) 38(7): 1587–95. doi: 10.1002/jor.24577

3. Yu D, Zeng Y, Li H, Zhu Z, Liu F, Mao Y. Prediction of postoperative stem anteversion in crowe type II/III developmental dysplasia of the hip on preoperative two-dimensional computed tomography. *J Arthroplasty.* (2020) 35:457–64. doi: 10.1016/j.arth.2019.09.037

4. Tezuka T, Heckmann ND, Bodner RJ, Dorr LD. Functional safe zone is superior to the Lewinnek safe zone for total hip arthroplasty: why the Lewinnek safe zone is not always predictive of stability. *J Arthroplasty.* (2019) 34:3–8. doi: 10.1016/j.arth.2018.10.034

5. Inoue D, Kabata T, Maeda T, Kajino Y, Fujita K, Hasegawa K, et al. Value of computed tomography-based three-dimensional surgical preoperative planning software in total hip arthroplasty with developmental dysplasia of the hip. *J Orthop Sci.* (2015) 20:340–6. doi: 10.1007/s00776-014-0683-3

6. Huang C, Tan H, Kernkamp WA, Cheng R, Liang J, Zhu Z, et al. Effect of altered proximal femoral geometry on predicting femoral stem anteversion in patients with developmental dysplasia of the hip. *J Orthop Surg Res.* (2019) 14:1–9. doi: 10.1186/s13018-018-1031-7

7. Belzunce MA, Henckel J, Di Laura A, Hart A. Uncemented femoral stem orientation and position in total hip arthroplasty: a CT study. *J Orthop Res.* (2020) 38:1486–96. doi: 10.1002/jor.24627

8. Yoshimine F. The safe-zones for combined cup and neck anteversions that fulfill the essential range of motion and their optimum combination in total hip replacements. *J Biomech.* (2006) 39:1315–23. doi: 10.1016/j.jbiomech.2005.03.008.

9. Renkawitz T, Haimerl M, Dohmen L, Gneiting S, Wegner M, Ehret N, et al. Minimally invasive computer-navigated total hip arthroplasty, following the concept of femur first and combined anteversion: design of a blinded randomized controlled trial. *BMC Musculoskelet Disord.* (2011) 12:1–6. doi: 10.1186/1471-2474-12-192

10. Imai H, Miyawaki J, Kamada T, Takeba J, Mashima N, Miura H. Preoperative planning and postoperative evaluation of total hip arthroplasty that takes combined anteversion. *Eur J Orthop Surg Traumatol.* (2016) 26:493–500. doi: 10.1007/s00590-016-1777-8.

11. Dorr LD, Malik A, Dastane M, Wan Z. Combined anteversion technique for total hip arthroplasty. *Clin Orthop Relat Res.* (2009) 467:119–27. doi: 10.1007/s11999-008-0598-4

12. Renkawitz T, Weber M, Springorum H, Sendtner E, Woerner M, Ulm K, et al. Impingement-free range of movement, acetabular component cover and early clinical results comparing "femur-first"navigation and "conventional"minimally invasive total hip arthroplasty: a randomised controlled trial. *Bone Joint J.* (2015) 97:890–8. doi: 10.1302/0301-620X.97B7.34729

13. Suh KT, Kang JH, Roh HL, Moon KP, Kim HJ. True femoral anteversion during primary total hip arthroplasty: use of postoperative computed tomography–based sections. *J Arthroplasty.* (2006) 21:599–605. doi: 10.1016/j.arth.2005.04.042

14. Tsukeoka T, Tsuneizumi Y, Lee TH. The T-line as an intraoperative landmark for reproducing the native femoral anteversion during hip arthroplasty. *Arch Orthop Trauma Surg.* (2014) 134:873–9. doi: 10.1007/s00402-014-1978-8.

15. Tsukeoka T, Tsuneizumi Y, Lee TH. A useful anatomical reference guide for stem anteversion during total hip arthroplasty in the dysplastic hip. *J Arthroplasty.* (2015) 30:1393–6. doi: 10.1016/j.arth.2015.03.030

16. Dimitriou D, Tsai T-Y, Kwon Y-M. The effect of femoral neck osteotomy on femoral component position of a primary cementless total hip arthroplasty. *Int Orthop.* (2015) 39:2315–21. doi: 10.1007/s00264-015-2739-1

17. Tsai T-Y, Dimitriou D, Li G, Kwon Y-M. Does total hip arthroplasty restore native hip anatomy? Three-dimensional reconstruction analysis. *Int Orthop*. (2014) 38:1577–83. doi: 10.1007/s00264-014-2401-3

18. Crowe JF, Mani VJ, Ranawat CS. Total hip replacement in congenital dislocation and dysplasia of the hip. *J Bone Jt Surg Am Vol*. (1979) 61:15. doi: 10.2106/00004623-197961010-00004

19. Capello WN. Uncemented total hip replacement. *Tech Orthop*. (1986) 1:12–21. doi: 10.1097/00013611-198610000-00006

20. Wu G, Siegler S, Allard P, Kirtley C, Leardini A, Rosenbaum D, et al. ISB recommendation on definitions of joint coordinate system of various joints for the reporting of human joint motion—Part I: ankle, hip, and spine. *J Biomech*. (2002) 35:543–8. doi: 10.1016/S0021-9290(01)00222-6

21. Rongshan C, Muyin H, Alexander KW, Huiwu L, Zhenan Z, Liao W, et al. The severity of developmental dysplasia of the hip does not correlate with the abnormality in pelvic incidence. *BMC Musculoskelet Disord*. (2021) 21(1):623. doi: 10.1186/s12891-020-03632-4

22. Hailer NP, Garellick G, Kärrholm J. Uncemented and cemented primary total hip arthroplasty in the Swedish hip arthroplasty register: evaluation of 170,413 operations. *Acta Orthop*. (2010) 81:34–41. doi: 10.3109/17453671003685400

23. Zhang M, Liu B-L, Qi X-Z, Yang Q-Q, Sun J-Y, Zheng Q-Y, et al. The three-dimensional morphology of femoral medullary cavity in the developmental dysplasia of the hip. *Front Bioeng Biotechnol*. (2021) 9:546. doi: 10.3389/fbioe.2021.684

24. Spitzer AI. The S-ROM cementless femoral stem: history and literature review. *Orthopedics*. (2005) 28:S1117–24. doi: 10.3928/0147-7447-20050902-24

25. Hwang K-T, Kim Y-H, Kim Y-S, Choi I-Y. Total hip arthroplasty using cementless grit-blasted femoral component: a minimum 10-year follow-up study. *J Arthroplasty*. (2012) 27:1554–61. doi: 10.1016/j.arth.2012.02.005

26. Stulberg SD, Stulberg BN, Wixson RL. The rationale, design characteristics, and preliminary results of a primary custom total hip prosthesis. *Clin Orthop Relat Res*. (1989) 249:79–96. PMID: 2684468

27. Walker PS, Robertson DD. Design and fabrication of cementless hip stems. *Clin Orthop Relat Res*. (1988) 235:25–34. PMID: 3416530

frontiers | Frontiers in Surgery

TYPE Original Research
PUBLISHED 05 September 2022
DOI 10.3389/fsurg.2022.975026

Check for updates

OPEN ACCESS

EDITED BY
Yan Yu,
Tongji University School of Medicine, China

REVIEWED BY
Osvaldo Mazza,
Bambino Gesù Children's Hospital (IRCCS), Italy
Harvinder Singh Chhabra,
Indian Spinal Injuries Centre, India

*CORRESPONDENCE
Tailin Wu
TL_spine@163.com

†These authors have contributed equally to this work and share last authorship

SPECIALTY SECTION
This article was submitted to Orthopedic Surgery, a section of the journal Frontiers in Surgery

RECEIVED 21 June 2022
ACCEPTED 04 August 2022
PUBLISHED 05 September 2022

CITATION
Luo J, Yang K, Yang Z, Feng C, Li X, Luo Z, Tao H, Duan C and Wu T (2022) Optimal immediate sagittal alignment for kyphosis in ankylosing spondylitis following corrective osteotomy.
Front. Surg. 9:975026.
doi: 10.3389/fsurg.2022.975026

COPYRIGHT
© 2022 Luo, Yang, Yang, Feng, Li, Luo, Tao, Duan and Wu. This is an open-access article distributed under the terms of the Creative Commons Attribution License (CC BY). The use, distribution or reproduction in other forums is permitted, provided the original author(s) and the copyright owner(s) are credited and that the original publication in this journal is cited, in accordance with accepted academic practice. No use, distribution or reproduction is permitted which does not comply with these terms.

Optimal immediate sagittal alignment for kyphosis in ankylosing spondylitis following corrective osteotomy

Jianzhou Luo[1], Kai Yang[2], Zili Yang[1], Chaoshuai Feng[2], Xian Li[1], Zhenjuan Luo[1], Huiren Tao[1], Chunguang Duan[1†] and Tailin Wu[1,3*†]

[1]Department of Orthopaedics, Shenzhen University General Hospital, Shenzhen, China, [2]Department of Orthopaedics, Xi'an Red Cross Hospital, Xi'an, China, [3]The Key Laboratory of Biomedical Information Engineering of Ministry of Education, School of Life Science and Technology, Xi'an Jiaotong University, Xi'an, China

Purpose: To investigate the optimal immediate sagittal alignment of kyphosis in ankylosing spondylitis (AS) following corrective osteotomy.
Methods: Seventy-seven AS patients who underwent osteotomy were enrolled. Radiographic parameters, including global kyphosis (GK), lumbar lordosis (LL), T1 spinopelvic inclination (T1SPI), sagittal vertical axis (SVA), T1 pelvic angle (TPA), pelvic incidence (PI), pelvic tilt (PT), sacral slope (SS), and PI and LL mismatch (PI−LL), were collected. The clinical outcome was evaluated using the Scoliosis Research Society-22 (SRS-22) questionnaire and Oswestry Disability Index (ODI). At the final follow-up, SVA > 5 cm was regarded as sagittal imbalance, and a total ODI ≤ 20 or total SRS-22 score ≥4 was considered to indicate a good clinical outcome.
Results: Seventy-seven patients with an average age of 37.4 ± 8.6 years were followed up for 29.4 ± 4.2 months. At the final follow-up, GK, LL, PT, SS, TPA, and T1SPI showed some degree of correction loss ($P < 0.05$). The follow-up parameters could be predicted with the immediate postoperative parameters through their linear regression equation ($P < 0.05$). The postoperative immediate T1SPI, TPA, SVA, and PI were also highly correlated with the clinical outcome (ODI and/or SRS-22) at the final follow-up ($P < 0.05$). Based on the relationship, the optimal immediate sagittal alignment for obtaining good clinical outcome was determined: T1SPI ≤ 0.9°, TPA ≤ 31.5°, and SVA ≤ 9.3cm. AS patients with PI ≤ 49.2° were more likely to achieve the optimal alignment and obtained lower ODI and a lower incidence of sagittal imbalance than those with PI > 49.2° at the final follow-up ($P < 0.05$).
Conclusion: Postoperative immediate parameters could be used to predict the final follow-up parameters and clinical outcome. The optimal postoperative immediate sagittal alignment of AS patients was T1SPI ≤ 0.9°, TPA ≤ 31.5°, and SVA ≤ 9.3 cm, providing a reference for kyphosis correction and a means for clinical outcome evaluation. Patients with a lower PI (≤49.2°) were more likely to achieve optimal alignment and obtain satisfactory clinical outcomes.

Abbreviations
AS, ankylosing spondylitis; ASD, adult spinal deformity; AUC, area under the curve; GK, global kyphosis; LL, lumbar lordosis; ODI, Oswestry Disability Index; PI, pelvic incidence; PI-LL, pelvic incidence and lumbar lordosis mismatch; PT, pelvic tilt; ROC, receiver operating characteristic curve; SRS-22, Scoliosis Research Society-22; SS, sacral slope; SVA, sagittal vertical axis; TPA, T1 pelvic angle; T1SPI, T1 spinopelvic inclination.

KEYWORDS
ankylosing spondylitis, kyphosis, optimal sagittal alignment, osteotomy, clinical outcome

Introduction

Ankylosing spondylitis (AS) is a chronic inflammatory disease. In advanced stages, AS is usually complicated by total spinal stiffness, thoracolumbar kyphosis, and pelvic retroversion. Individuals with AS might have trouble looking horizontally, lying flat, and standing or walking upright, seriously impairing their daily activities and quality of life (1). Osteotomy is the only effective method for correcting these deformities and providing these individuals with the opportunity for a normal life. However, for AS patients with kyphosis, the correction standard is elusive and the optimal postoperative immediate sagittal alignment following osteotomy is still not well understood (2).

Schwab et al. (3) proposed a sagittal vertical axis (SVA) <5.0 cm, pelvic tilt (PT) <25°, and pelvic incidence and lumbar lordosis mismatch (PI–LL) = ±9° as realignment objectives for adult spinal deformity (ASD). However, these values are different in AS patients. Recently, Huang et al. (4) reported PT < 24°, spinosacral angle >108°, T1 pelvic angle (TPA) < 22°, and spinopelvic angle >152° as the optimal sagittal objectives for AS patients at the 2-year follow-up. Notably, Huang proposed these values as goals for the 2-year follow-up; however, the optimal values for immediate alignment after surgery are still unknown and could be more pragmatic and meaningful for guiding kyphosis correction.

Therefore, in this study, we (1) determined the relationship between the immediate postoperative parameters and final follow-up parameters and clinical outcome in AS patients, (2) investigated an optimal immediate sagittal alignment based on the relationship, and (3) clarified the influence of PI on sagittal alignment and clinical outcome at the final follow-up.

Materials and methods

Subjects

Consecutive AS patients who underwent modified three-column osteotomy from January 2010 to July 2019 were reviewed retrospectively. The inclusion criteria were as follows: (1) age between 18 and 65 years old, (2) global kyphosis (GK) over 50°, (3) completed radiographs and clinical outcome measurements, and (4) a minimum of 2 years of follow-up. Patients with a history of previous spinal surgery, ankylosed hip or knee joints, postoperative pseudarthrosis, or instrumentation failure during the follow-up were excluded. Finally, a total of 77 AS patients, including 57 who underwent one-level osteotomy and 20 who underwent two-level osteotomy, met the criteria and were enrolled in this study.

The study was performed in accordance with the Declaration of Helsinki and approved by the institutional review board of Shenzhen University General Hospital. Informed consent was obtained from all participants before surgery.

Data collection

Standing anteroposterior and lateral radiographs of the whole spine were obtained preoperatively, immediately postoperatively (3–4 weeks after surgery), and at the final follow-up (a minimum of 2 years after surgery). Several parameters were measured using lateral radiographs, including GK, LL, SVA, T1 spinopelvic inclination (T1SPI), TPA, pelvic incidence (PI), PT, sacral slope (SS), and PI–LL (**Figure 1**). The clinical outcome was evaluated using the Scoliosis Research Society-22 (SRS-22) questionnaire and Oswestry Disability Index (ODI). Data were collected before and after surgery as well as at the final follow-up. At the final follow-up, an SVA of >5 cm was regarded as sagittal imbalance (3), and a total ODI ≤ 20 or total SRS-22 score ≥4.0 was considered to indicate a good clinical outcome (4–6).

Surgical technique

The modified three-column osteotomy was usually performed in the apical region of kyphosis so that substantial kyphosis correction could be achieved. The whole procedure was performed under somatosensory-evoked potential and motor-evoked potential monitoring. The resection area of the corrective osteotomy included the spinous process, the upper part of the lamina and superior articular processes of the osteotomized vertebra, as well as the lower part of the lamina and inferior articular processes of the cranially adjacent vertebra. The transverse process of the osteotomized vertebra was exposed and resected; then, subtotal resection was performed along the upper part of the pedicles to the front of the vertebral body, which usually involved resecting 1/3–1/2 of the upper part of the vertebral body together with the cranially adjacent intervertebral disc. The lower half of the vertebral pedicle, part of the lamina, and the intact inferior articular processes of the osteotomized vertebra were preserved.

Temporary rods were implanted after finishing the osteotomy. Before correction, the spinal cord was slightly shortened in advance by compressing the rods, with the aim of preserving the space for potential spinal cord lengthening

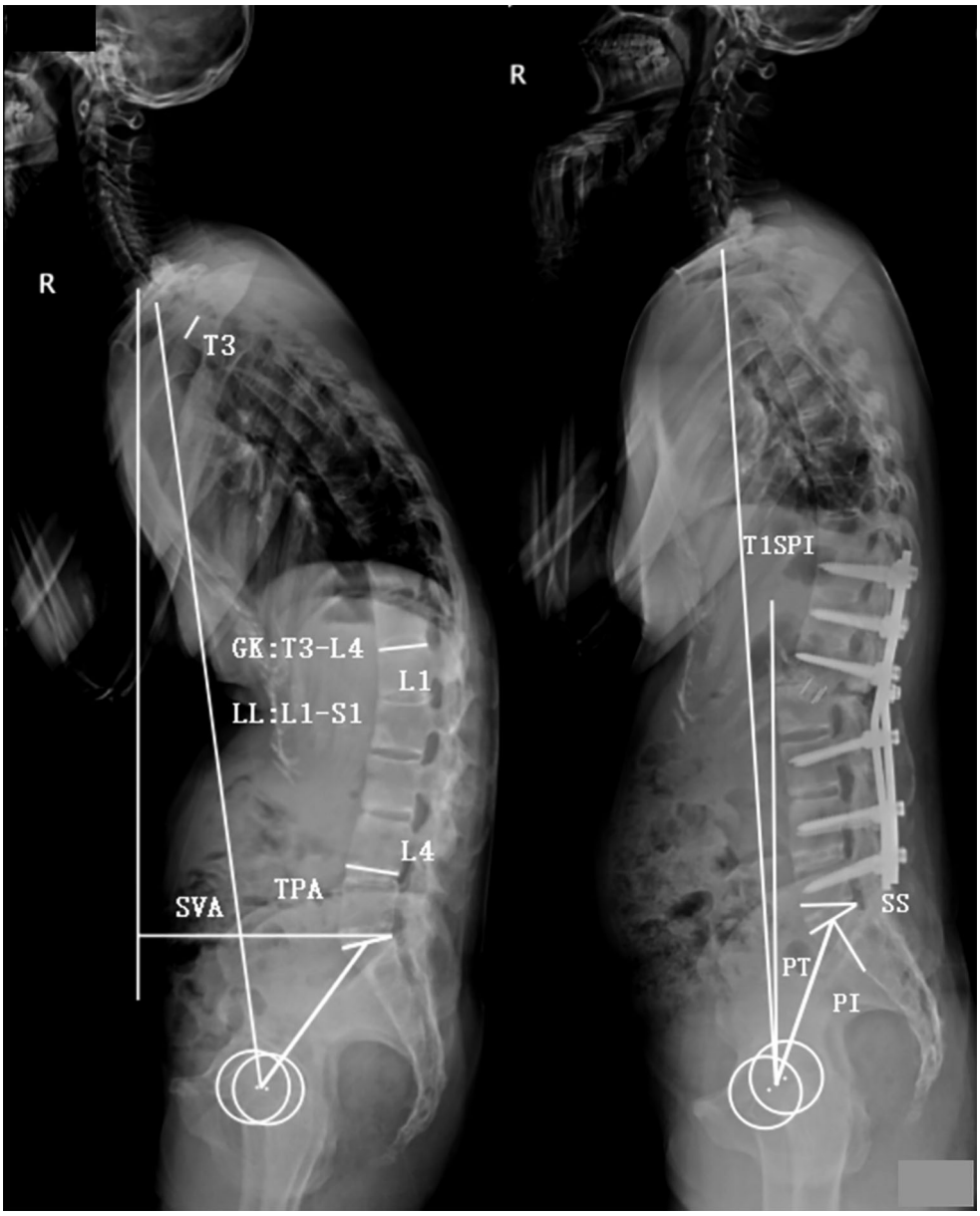

FIGURE 1
Illustration of radiographic parameters. Global kyphosis (GK): the angle between the superior endplate of the maximally tilted upper-end vertebra and the inferior endplate of the maximally tilted lower-end vertebra. Lumbar lordosis (LL): the Cobb angle from the L1 upper endplate to the S1 upper endplate (negative number represents lordosis, and positive number represents kyphosis). Sagittal vertical axis (SVA): the distance between the C7 plumb line and the posterior-superior corner of S1. T1 pelvic angle (TPA): the angle between a line joining the center of T1 and the femoral head axis and a line from the center of the femoral head axis to the midpoint of the S1 upper endplate. T1 spinopelvic inclination (T1SPI): the angle between the vertical line and a line from the center of the femoral head axis to the center of the T1 vertebral body (a negative number represents that T1 is posterior to the femoral head, and a positive number represents that T1 is anterior to the femoral head). Pelvic tilt (PT): the angle between the vertical line and the line from the center of the S1 upper endplate to the center of the femoral head axis. Pelvic incidence (PI): the angle between the perpendicular line to the S1 upper endplate and the line from the center of the S1 upper endplate to the center of the femoral head axis. Sacral slope (SS): the angle between the S1 upper endplate and the horizontal line. Pelvic incidence and lumbar lordosis mismatch (PI−LL): pelvic incidence value minus lumbar lordosis value.

during correction. Sequentially, kyphosis was corrected gradually by lifting up the patient's shoulders while simultaneously bending the rods. After achieving satisfying correction, the temporary rods were replaced with precontoured rods successively. Subsequently, a local bone graft and a cage filled with autogenetic bone were implanted sequentially in the osteotomy space, further compressing the rods. The bone autograft was spread on the surface of the lamina to facilitate spinal fusion. Postoperatively, the patients were allowed to ambulate with a customized

thoracolumbosacral orthosis 3 days after surgery, which was typically maintained for 6 months.

Statistical analysis

Measurement data are expressed as the mean ± standard deviation. Statistical analysis was performed using SPSS software (version 22.0, SPSS, Inc., Chicago, IL, USA). Paired *t*-tests were used to compare differences in the radiographic parameters and clinical outcome before and after surgery as well as at follow-up. The relationship between postoperative immediate parameters and final follow-up parameters was assessed with linear regression analysis. Correlations between postoperative immediate parameters and clinical outcome were evaluated using Pearson's correlation coefficient. Optimal thresholds of clinically relevant parameters were evaluated using receiver operating characteristic (ROC) curve analysis. Multiple stepwise linear regression analysis was performed to determine the key clinically relevant parameter and establish a predictive model for the total SRS-22 score. The difference between groups which was divided by the threshold of PI was using two independent *t*-tests and χ^2 tests. A difference with a *P*-value <0.05 was considered statistically significant.

Results

General data

Seventy-seven AS patients (67 men and 10 women) with an average age of 37.4 ± 8.6 years (range, 20–64 years) and an average follow-up of 29.4 ± 4.2 months (range, 24–84 months) were included. The postoperative immediate GK, LL, PT, SS, PI–LL, TPA, T1SPI, and SVA were significantly improved ($P < 0.01$). At the final follow-up, GK, LL, PT, SS, TPA, and T1SPI showed some degree of correction loss ($P < 0.05$). Although the difference was not statistically significant, PI–LL ($P = 0.078$) and SVA ($P = 0.115$) also showed some loss of correction at the final follow-up. There was no significant difference in PI before and after surgery ($P > 0.05$) (Table 1).

Relationship between postoperative immediate parameters and final follow-up parameters

Linear regression analysis showed that the postoperative immediate GK, LL, PT, SS, PI–LL, TPA, T1SPI, and SVA were positively correlated with the corresponding parameters at the final follow-up ($R^2 = 0.835$, 0.817, 0.742, 0.551, 0.818, 0.857, 0.427, and 0.554, respectively, all $P < 0.001$, Figure 2). All these parameters at the final follow-up could be predicted with the immediate postoperative parameters through their linear regression equation.

Correlation between postoperative immediate parameters and clinical outcome

At the final follow-up, 29 patients (37.7%) had ODI ≤ 20 and 32 patients (41.6%) had SRS-22 ≥ 4.0, which were considered to have achieved a good clinical outcome. All domains of the SRS-22 and ODI were significantly improved at the final follow-up ($P < 0.05$) (Table 2). The correlation between the immediate postoperative parameters and the final follow-up clinical outcomes (ODI and SRS-22) was examined. The results showed that the postoperative

TABLE 1 Differences of radiographic parameters in ankylosing spondylitis patients after surgery.

Parameters	Preoperative	Postoperative immediate	Final follow-up	Loss of correction
GK (°)	84.7 ± 24.8	32.9 ± 15.4**	35.1 ± 16.7	2.2 ± 6.8*
LL (°)	5.9 ± 21.9	−33.8 ± 17.2**	−31.7 ± 17.6	2.2 ± 7.6*
PT (°)	38.6 ± 11.5	28.5 ± 9.7**	31.0 ± 8.8	3.3 ± 5.2*
PI (°)	48.9 ± 13.5	48.5 ± 12.0	48.0 ± 11.2	0.5 ± 4.3
SS (°)	10.3 ± 12.8	20.2 ± 11.7**	15.8 ± 13.0	4.6 ± 8.5*
PI–LL (°)	53.9 ± 21.8	15.0 ± 15.4**	16.7 ± 16.4	1.7 ± 7.0
TPA (°)	57.9 ± 19.4	30.1 ± 11.6**	32.5 ± 10.9	1.7 ± 4.6*
T1SPI (°)	18.5 ± 16.8	1.8 ± 5.8**	0.3 ± 5.8	1.5 ± 4.8*
SVA (cm)	23.0 ± 9.0	9.5 ± 5.5**	8.6 ± 5.8	0.9 ± 4.1

GK, global kyphosis; LL, lumbar lordosis; PT, pelvic tilt; PI, pelvic incidence; SS, sacral slope; PI–LL, pelvic incidence and lumbar lordosis mismatch; TPA, T1 pelvic angle; T1SPI, T1 spinopelvic inclination; SVA, sagittal vertical axis.
*A statistically significant difference in parameters between postoperatively and at the final follow-up ($P < 0.05$).
**A statistically significant difference in parameters between preoperatively and postoperatively ($P < 0.01$).

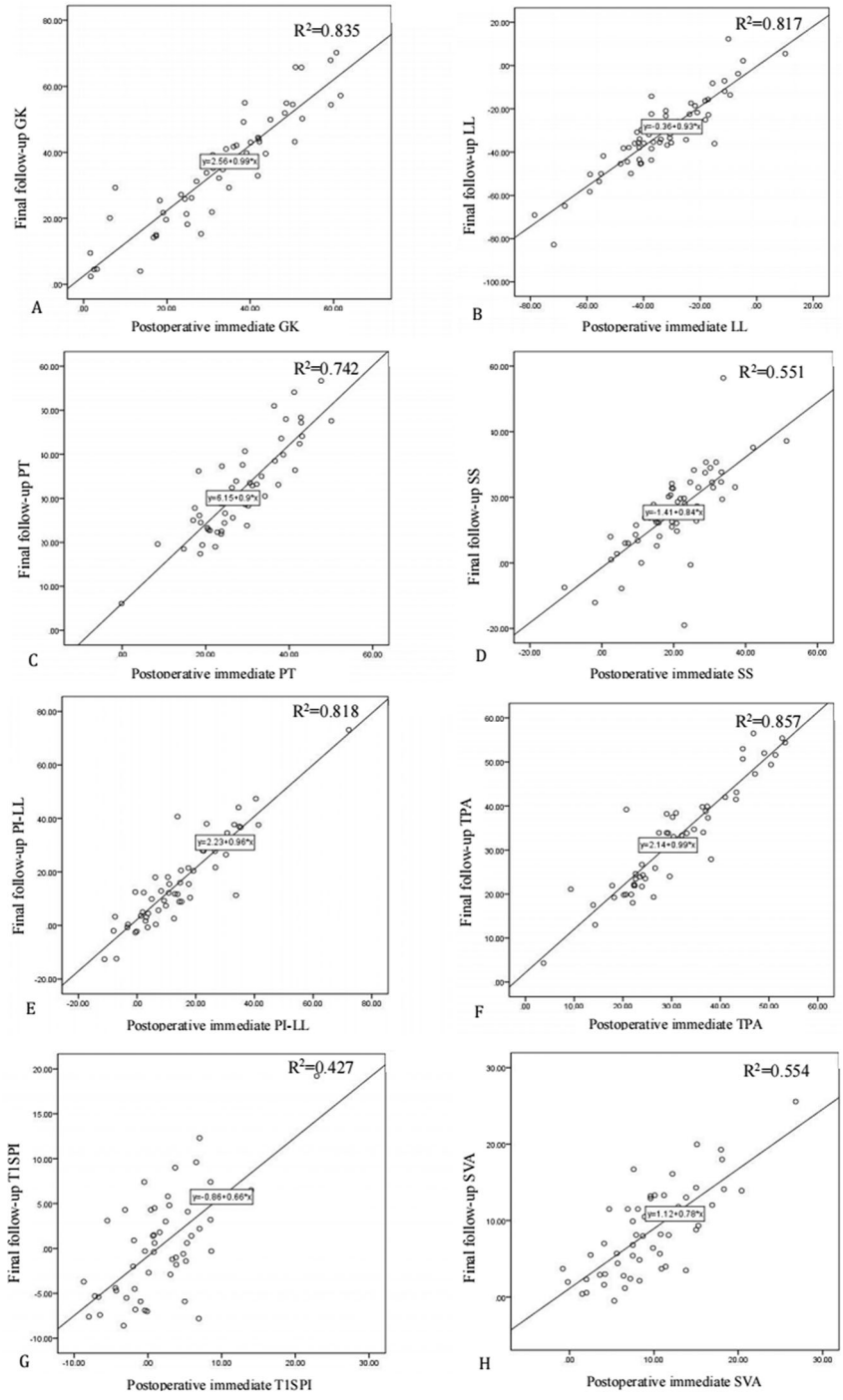

FIGURE 2
Linear regression analysis of postoperative immediate parameters and final follow-up parameters. (**A**) Final follow-up global kyphosis (GK) = 2.56 + 0.99 × postoperative immediate GK, $R^2 = 0.835$; (**B**) final follow-up lumbar lordosis (LL) = −0.36 + 0.93 × postoperative immediate LL, $R^2 = 0.817$; (**C**) final follow-up pelvic tilt (PT) = 6.15 + 0.9 × postoperative immediate PT, $R^2 = 0.742$; (**D**) final follow-up sacral slope (SS) = −1.41 + 0.84 × postoperative immediate SS, $R^2 = 0.551$; (**E**) final follow-up pelvic incidence and lumbar lordosis mismatch (PI−LL) = 2.23 + 0.96 × postoperative immediate PI−LL, $R^2 = 0.818$; (**F**) final follow-up T1 pelvic angle (TPA) = 2.14 + 0.99 × postoperative immediate TPA, $R^2 = 0.857$; (**G**) final follow-up T1 spinopelvic inclination (T1SPI) = −0.86 + 0.66 × postoperative immediate T1SPI, $R^2 = 0.427$; and (**H**) final follow-up sagittal vertical axis (SVA) = 1.12 + 0.78 × postoperative immediate SVA, $R^2 = 0.554$.

immediate PI, SS, T1SPI, and SVA values significantly correlated with the total ODI (all $P < 0.05$), while the postoperative immediate T1SPI, SVA, and TPA values significantly correlated with the total SRS-22 score (all $P < 0.05$) (Table 3). This means that the clinical outcomes at the final follow-up could be assessed and predicted with the immediate postoperative parameters.

Optimal thresholds of the clinically relevant parameters

The clinically relevant parameters (PI, SS, T1SPI, SVA, and TPA) were subjected to ROC curve analysis to determine the optimal thresholds for obtaining good clinical outcomes. With total ODI as a state variable, only the PI showed a statistical significance ($P < 0.05$), while the SS, T1SPI, and SVA showed no significant difference (all $P > 0.05$). The optimal value of PI was ≤49.2° for obtaining good clinical outcome with a sensitivity of 99.8% and a false-positive rate of 36.7% (Figure 3A). With total SRS-22 as a state variable, all of the postoperative immediate T1SPI, TPA, and SVA were significantly different (all $P < 0.05$). The optimal value of T1SPI was ≤0.9° for obtaining good clinical outcome with a sensitivity of 70.0% and a false-positive rate of 17.6% (Figure 3B). The optimal value of TPA was ≤31.5° for obtaining good clinical outcome with a sensitivity of 63.3% and a false-positive rate of 11.8% (Figure 3C). The optimal value of SVA was ≤9.3 cm for obtaining good clinical outcome with a sensitivity of 63.3% and a false-positive rate of 11.8% (Figure 3D).

TABLE 2 Clinical outcomes of Oswestry Disability Index and Scoliosis Research Society-22 score after surgery.

Items	Preoperative	Final follow-up	Improvement	*P*-value
ODI-walking	1.72 ± 1.21	0.66 ± 1.02	1.06 ± 1.46	<0.001*
ODI-sitting	1.40 ± 1.10	1.04 ± 0.76	0.36 ± 1.26	0.043*
ODI-standing	2.34 ± 1.27	0.94 ± 0.93	1.40 ± 1.35	<0.001*
Total ODI	40.02 ± 18.20	21.45 ± 11.85	18.57 ± 20.45	<0.001*
SRS-22-pain	3.28 ± 0.91	3.89 ± 0.72	0.61 ± 0.91	<0.001*
SRS-22-function	2.80 ± 0.85	3.41 ± 0.63	0.60 ± 0.79	<0.001*
SRS-22-appearance	2.00 ± 0.71	3.88 ± 0.64	1.87 ± 0.91	<0.001*
SRS-22-mental health	2.93 ± 0.87	3.98 ± 0.77	1.05 ± 0.91	<0.001*
SRS-22-satisfaction	2.61 ± 0.90	4.42 ± 0.59	1.81 ± 1.06	<0.001*
Total SRS-22	2.62 ± 0.60	3.98 ± 0.44	1.36 ± 0.66	<0.001*

ODI, Oswestry Disability Index; SRS-22, Scoliosis Research Society-22.
*A statistically significant difference between preoperatively and at the final follow-up ($P < 0.05$).

Identifying the key clinically relevant parameters for total SRS-22

Multiple stepwise linear regression analysis was performed to determine the important clinically relevant parameters. With the total SRS-22 score as the dependent variable, the postoperative immediate T1SPI, TPA, and SVA were entered into the analysis. Finally, the SVA was the only parameter included in the regression model. The linear regression equation was total SRS-22 score = 4.247–0.033 × postoperative immediate SVA (adjusted $R^2 = 0.125$, $P = 0.006$), which indicates that the model explains 12.5% of the variability in the cohort (Table 4).

TABLE 3 Correlation between postoperative immediate parameters and final follow-up Oswestry Disability Index and Scoliosis Research Society-22 scores.

Items	GK	PT	PI	SS	LL	PI–LL	TPA	T1SPI	SVA
ODI-walking	0.184	0.073	0.466**	0.440**	−0.238	0.107	0.177	0.231	0.184
ODI-sitting	0.277*	0.016	0.304*	0.314*	−0.269*	−0.047	0.081	0.132	0.106
ODI-standing	0.139	0.158	0.232	0.110	0.038	0.211	0.206	0.136	0.130
Total ODI	0.208	0.085	0.364**	0.326**	−0.238	−0.029	0.240	0.340*	0.330*
SRS-22-pain	−0.223	−0.164	−0.116	0.021	−0.068	−0.155	−0.286*	−0.297*	−0.335*
SRS-22-function	−0.216	−0.197	−0.247	−0.091	0.068	−0.115	−0.373**	−0.414**	−0.424**
SRS-22-appearance	−0.046	0.014	−0.023	−0.036	0.001	−0.017	−0.123	−0.269	−0.249
SRS-22-mental health	−0.254	−0.119	−0.100	−0.002	0.088	0.016	−0.178	−0.150	−0.183
SRS-22-satifacton	0.044	−0.039	−0.215	−0.199	0.148	−0.010	−0.128	−0.191	−0.183
Total SRS-22	−0.204	−0.143	−0.189	−0.076	0.062	−0.078	−0.301*	−0.360**	−0.377**

GK, global kyphosis; PT, pelvic tilt; PI, pelvic incidence; SS, sacral slope; LL, lumbar lordosis; PI–LL, pelvic incidence and lumbar lordosis mismatch; TPA, T1 pelvic angle; T1SPI, T1 spinopelvic inclination; SVA, sagittal vertical axis; ODI, Oswestry Disability Index; SRS-22, Scoliosis Research Society-22.
*A statistically significant correlation ($P < 0.05$).
**A statistically significant correlation ($P < 0.01$).

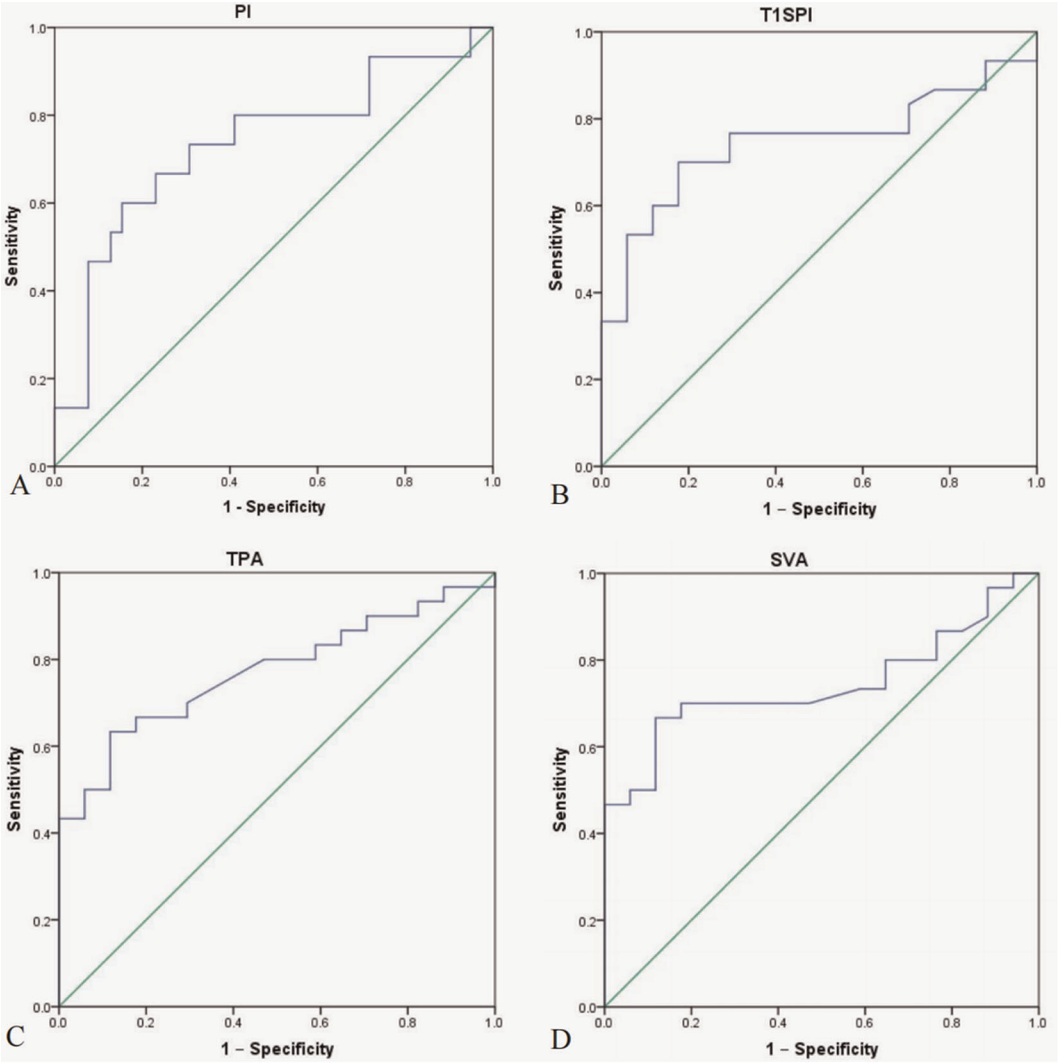

FIGURE 3
Receiver operating characteristic (ROC) curve analysis of clinically relevant parameters for the optimal threshold value. (**A**) The area under curve (AUC) for pelvic incidence (PI) was 0.733, the optimal threshold of PI was ≤49.2° for obtaining good clinical outcome with sensitivity of 73.3% and false-positive rate (1-Specificity) of 30.8%. (**B**) The AUC for T1 spinopelvic inclination (T1SPI) was 0.746, and the optimal threshold of T1SPI was ≤0.9° for obtaining a good clinical outcome with a sensitivity of 70.0% and a false-positive rate of 17.6%. (**C**) The AUC for T1 pelvic angle (TPA) was 0.772, and the optimal threshold of TPA was ≤31.5° for obtaining good clinical outcome with a sensitivity of 63.3% and a false-positive rate of 11.8%. (**D**) The AUC for sagittal vertical axis (SVA) was 0.741, and the optimal threshold of SVA was ≤9.3 cm for obtaining good clinical outcome with a sensitivity of 66.7% and a false-positive rate of 11.8%.

TABLE 4 Multiple stepwise linear regression analysis for the key clinically relevant parameter with total Scoliosis Research Society-22 as the dependent variable.

Variable	*B*	Standard error	Standardized beta coefficient	*t*	*P*-value
(Constant)	4.247	0.131		32.359	0.000
Postoperative immediate SVA	−0.033	0.012	−0.377	−2.878	0.006

With adjusted $R^2 = 12.5\%$.
SVA, sagittal vertical axis.

Comparing differences between groups with different pelvic incidences

The cohort was divided into two groups according to the PI threshold of 49.2°. Forty-four patients with PI ≤ 49.2° were in group A, and 33 patients with PI > 49.2° were in group B. Preoperatively, group A had smaller PI, PT, SS, PI–LL, T1SPI, and TPA than group B ($P < 0.05$); there was no significant difference in all domains of ODI and SRS-22 ($P > 0.05$). Postoperatively, the PI, PT, SS, LL, PI–LL, TPA, and

SVA were smaller in group A than in group B ($P < 0.05$). The average values of postoperative immediate T1SPI, TPA, and SVA in group A met the standard of optimal sagittal alignment (T1SPI ≤ 0.85°, TPA ≤ 31.5°, and SVA ≤ 9.3 cm), while all of them were over the threshold values in group B. At the final follow-up, the total ODI was lower in group A than in group B ($P < 0.05$), while there was no significant difference in SRS-22 ($P > 0.05$). The incidence of sagittal imbalance at the final follow-up was also lower in group A than in group B (Table 5 and Figure 4).

Discussion

Sagittal realignment in AS patients after the corrective osteotomy is a primary determinant of clinical outcome measures and is a complex challenge for surgeons (4, 7, 8). Failure to achieve optimal immediate sagittal alignment might result in residual kyphosis, increasing the risk of sagittal imbalance, instrumental failure, and even reoperation (8). However, until now, few studies have explored the immediate postoperative sagittal alignment in AS patients with kyphosis after corrective osteotomy. The goals for AS kyphosis correction are still unclear, which seriously limits preoperative planning and impairs postoperative clinical outcomes.

In this study, correction loss occurred in GK, LL, PT, SS, TPA, and T1SPI at the final follow-up. However, all the final follow-up parameters linearly correlated with their immediate postoperative parameters. This meant that sagittal alignment at the mid- or long-term follow-up could be evaluated and predicted with some parameters immediately after surgery and made it possible to intervene to prevent severe correction loss early. Furthermore, the postoperative immediate parameters were also significantly correlated with the clinical outcome (ODI and SRS-22) at the final follow-up. Among them, the pelvic parameters (PI and SS) and sagittal global parameters (T1SPI, TPA, and SVA) were closely correlated with ODI and/or SRS-22 scores, which were also consistent with the findings reported by Schwab and Lafage (3, 9). The results also revealed that the reconstruction of sagittal realignment (T1SPI, TPA, and SVA) and unique parameters (PI) could be used to assess and predict the clinical outcome measures at the final follow-up. The ROC analysis indicated that when postoperative immediate T1SPI ≤ 0.9°, TPA ≤ 31.5°, SVA ≤ 9.3 cm, and PI ≤ 49.2°, the AS patients were more likely to obtain a good clinical outcome at the final follow-up.

The T1SPI reflects the position of T1 relative to the pelvis through the hips. This parameter might be more pragmatic and accurate than the SVA in noncalibrated radiographs. In this study, the optimal T1SPI for achieving a satisfactory clinical outcome was ≤0.9°, while the normative value was −1.4° ± 2.7° (10). This means that corrective osteotomy should

TABLE 5 Differences in radiographic parameters and clinical outcomes with different pelvic incidences.

Variables	Group A (PI ≤ 49.2°, *n* = 44)	Group B (PI > 49.2°, *n* = 33)	*P*-value
Preoperative GK (°)	82.1 ± 19.6	88.6 ± 30.1	0.250
Preoperative PI (°)	40.5 ± 7.6	59.8 ± 11.3	<0.001*
Preoperative PT (°)	35.2 ± 9.8	43.2 ± 12.2	0.002*
Preoperative SS (°)	5.4 ± 10.3	16.8 ± 12.9	<0.001*
Preoperative LL (°)	9.0 ± 20.8	1.8 ± 22.8	0.158
Preoperative PI–LL (°)	49.5 ± 21.4	59.6 ± 21.2	0.044*
Preoperative T1SPI (°)	14.9 ± 14.5	23.1 ± 18.5	0.032*
Preoperative TPA (°)	51.4 ± 17.9	66.4 ± 17.7	<0.001*
Preoperative SVA (cm)	21.2 ± 8.5	25.2 ± 9.1	0.057
Preoperative ODI-walking	1.79 ± 1.10	1.64 ± 1.35	0.667
Preoperative ODI-sitting	1.29 ± 1.12	1.52 ± 1.08	0.443
Preoperative ODI-standing	2.36 ± 1.34	2.32 ± 1.22	0.917
Preoperative total ODI	37.65 ± 20.65	42.37 ± 19.81	0.400
Preoperative SRS-22-pain	3.39 ± 0.93	3.16 ± 0.89	0.373
Preoperative SRS-22-function	2.94 ± 0.97	2.66 ± 0.67	0.224
Preoperative SRS-22-appearance	1.99 ± 0.79	2.01 ± 0.61	0.910
Preoperative SRS-22-mental health	2.86 ± 1.07	3.00 ± 0.61	0.567
Preoperative SRS-22-satisfaction	2.82 ± 0.93	2.38 ± 0.82	0.073
Preoperative total SRS-22	2.80 ± 0.70	2.64 ± 0.50	0.356
Postoperative immediate GK (°)	34.2 ± 14.7	32.8 ± 15.5	0.700
Postoperative immediate PI (°)	40.6 ± 6.7	59.3 ± 8.8	<0.001*
Postoperative immediate PT (°)	25.3 ± 9.1	32.1 ± 9.2	0.002*
Postoperative immediate SS (°)	15.3 ± 9.6	26.8 ± 11.1	<0.001*
Postoperative immediate LL (°)	−29.5 ± 13.3	−40.6 ± 20.8	0.006*
Postoperative immediate PI–LL (°)	11.1 ± 12.5	18.3 ± 18.8	0.048*
Postoperative immediate T1SPI (°)	0.2 ± 5.1	2.6 ± 6.4	0.075
Postoperative immediate TPA (°)	25.8 ± 9.1	35.9 ± 12.3	<0.001*
Postoperative immediate SVA (cm)	7.9 ± 4.9	11.2 ± 5.9	0.011*
Final follow-up ODI-walking	0.30 ± 0.53	1.13 ± 1.26	0.006*
Final follow-up ODI-sitting	0.80 ± 0.55	1.29 ± 0.91	0.025*
Final follow-up ODI-standing	0.73 ± 0.69	1.21 ± 1.10	0.059
Final follow-up total ODI	19.29 ± 11.29	28.69 ± 15.10	0.012*
Final follow-up SRS-22-pain	4.03 ± 0.60	3.73 ± 0.83	0.143
Final follow-up SRS-22-function	3.52 ± 0.58	3.27 ± 0.66	0.139
Final follow-up SRS-22-appearance	3.92 ± 0.65	3.80 ± 0.64	0.490
Final follow-up SRS-22-mental health	4.03 ± 0.82	3.92 ± 0.71	0.607
Final follow-up SRS-22-satisfaction	4.53 ± 0.58	4.29 ± 0.59	0.138
Final follow-up total SRS-22	4.01 ± 0.46	3.80 ± 0.51	0.122
Incidence of sagittal imbalance at the final follow-up	56.8% (25/44)	81.8% (27/33)	0.020*

GK, global kyphosis; PI, pelvic incidence; PT, pelvic tilt; SS, sacral slope; LL, lumbar lordosis; PI–LL, pelvic incidence and lumbar lordosis mismatch; T1SPI, T1 spinopelvic inclination; TPA, T1 pelvic angle; SVA, sagittal vertical axis. ODI, Oswestry Disability Index; SRS-22, Scoliosis Research Society-22.
*A statistically significant difference between group A and group B ($P < 0.05$).

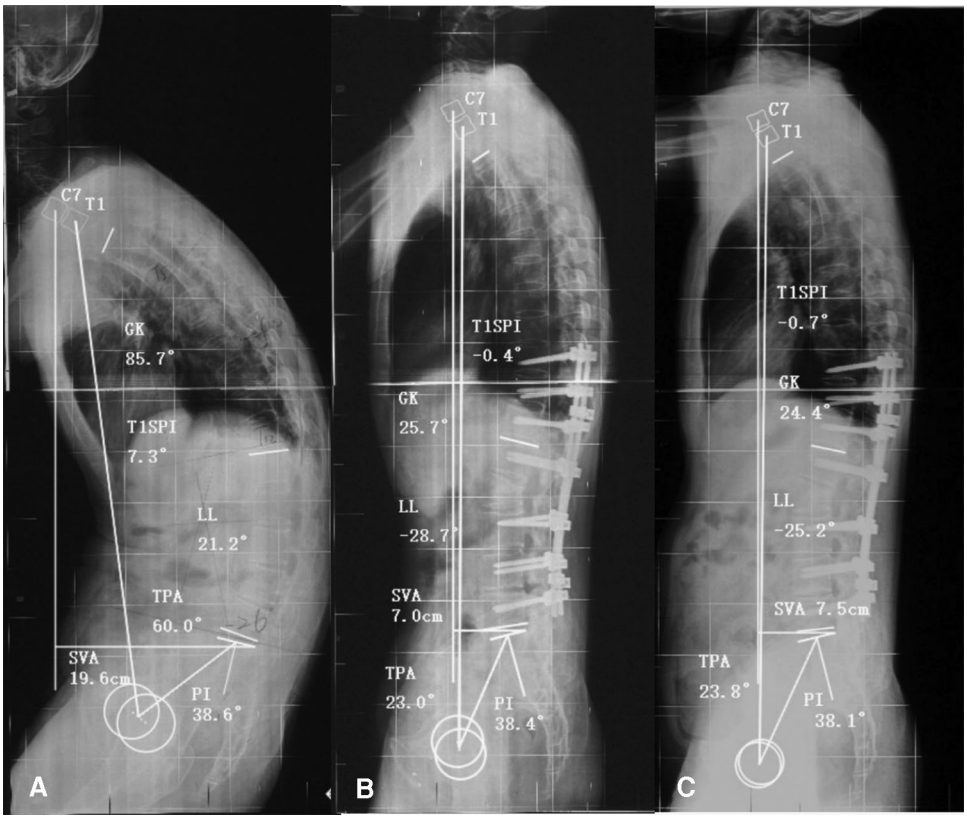

FIGURE 4
A 37-year-old man with ankylosing spondylitis kyphosis for 11 years. (**A**) The preoperative sagittal parameters were pelvic incidence (PI) = 38.6°, T1 spinopelvic inclination (T1SPI) = 7.3°, T1 pelvic angle (TPA) = 60.0°, and sagittal vertical axis (SVA) = 19.6 cm. (**B**) After L2 corrective osteotomy, the immediate postoperative sagittal parameters were PI = 38.4° (<49.2°), T1SPI = −0.4° (<0.9°), TPA = 23.0° (<31.5°), and SVA = 7.0 cm (<9.3 cm), all of which met the optimal parameter threshold values. (**C**) At the 25-month follow-up, the correction was well maintained, with PI = 38.1°, T1SPI = −0.7°, TPA = 23.8°, and SVA = 7.5 cm. The patient presented with a favorable health-related quality of life (total Oswestry Disability Index (ODI) = 0, total Scoliosis Research Society-22 (SRS-22) = 4.85).

be performed to keep AS patients with a relatively low T1SPI to achieve a good clinical outcome because a large T1SPI might displace the trunk anteriorly relative to the femoral heads, resulting in malpositioning of the trunk in terms of its gravity and causing pain and disability (9). However, few studies have focused on the influence of T1SPIs on AS patients until now.

The goal for postoperative SVA varies among previous studies. Kim et al. (11) reported that the maintenance of SVA < 8 cm was important for ultimate sagittal reconstruction in fixed sagittal imbalance. Van Royen et al. (12) reported that the postoperative SVA ideally ranged from 5 cm to 10 cm, while Schwab et al. (13) reported that a postoperative SVA of more than 10 cm could be considered to indicate failed realignment. In this study, the optimal SVA was ≤9.3 cm for a good clinical outcome. In patients with ankylosed cervical vertebrae, sagittal alignment cannot be corrected perfectly to be within a normal range because a chin-brow vertical angle in the range of 10°–20° needs to be ensured and horizontal vision needs to be maintained for patients postoperatively (14). Meanwhile, although there may be some residual deformity in these patients, it might not affect their ability to perform basic daily tasks, and the corrections are maintained well over the follow-up period. Therefore, it might not be necessary to correct the SVA to a normal value with excessive expanding operations, placing these patients at an increased risk for various surgical complications. Thus, an immediate postoperative SVA of 9.3 cm or less might be sufficient for the correction of severe kyphosis in AS.

Moreover, the postoperative SVA was found to be a key clinically relevant parameter by multiple linear regression analysis, which is in agreement with the findings of previous studies (9, 13). A predictive model of the postoperative SRS-22 score was calculated, i.e., total SRS-22 score = 4.247–0.033 × postoperative immediate SVA. This equation allows the follow-up total SRS-22 score to be predicted in AS patients, whereas only ODI predictive methods have been reported in previous studies (4, 7, 13).

Unlike the SVA, the TPA is an angle reflecting global sagittal alignment, which does not vary on the basis of pelvic retroversion or patient standing posture (15, 16). To date, the optimal TPA for AS patients after the corrective

osteotomy is still unclear. Protopsaltis et al. (15) found that TPA > 20° might result in severe disability (ODI > 40) for ASD, and they recommended TPA < 14° as a postoperative target (ODI < 20). However, Banno et al. (16) investigated 656 elderly healthy volunteers and determined that a TPA of 26° was the threshold value for an ODI of 40, while a TPA of 20° was the threshold value for an ODI of 20. Their study also noted that the optimal TPA varies widely by race, sex, and disease (16). Recently, Huang et al. (4) reported TPA < 22° as a goal in AS patients to achieve a satisfactory clinical outcome (ODI < 20) following osteotomy. According to our data, the optimal TPA was <31.5°, which was calculated on the basis of a total SRS-22 score ≥4.0. Several reasons could explain the difference between this optimal TPA and that reported by Huang et al. (4). First, the patients in this study had more severe deformities than those in the study by Huang and were thus hard to correct perfectly but still satisfied with the improvement in quality of life. Second, the optimal threshold value for the TPA in this study was calculated by ROC curve analysis based on a total SRS-22 score ≥4.0, while Huang used linear regression equations to calculate the TPA based on ODI <20.

PI is a constant morphological parameter that is unique regardless of the rotation of the pelvis (7, 8, 17). Our data indicated that PI plays a key role in sagittal alignment reconstruction and significantly affects clinical outcome measures. Although PI showed no change after surgery, it was highly correlated with the recovery of clinically relevant parameters (1, 8, 17). For patients with a large PI value, it is difficult to achieve spinal and pelvic balance, leading to a negative clinical outcome and potentially even large correction loss at the final follow-up (7, 18, 19). Qian et al. (8) reported that patients with PI ≤ 50° were more likely to achieve spinopelvic matching and decrease the chance of sagittal imbalance on follow-up. Similar to the study by Qian et al. (8), this study validated the conclusion that AS patients with PI ≤ 49.2° achieved optimal immediate postoperative sagittal alignment and obtained better clinical outcomes and a lower incidence of sagittal imbalance than those with PI > 49.2° at the final follow-up. These results further confirmed that PI is a critical parameter for sagittal realignment that affects global balance achievement and clinical outcome restoration in AS patients after osteotomy. Therefore, the surgeon should pay more attention to PI in reconstructing sagittal alignment to achieve optimal sagittal alignment and should choose appropriate osteotomy techniques and the number of osteotomy segments to obtain enough correction for correction (3, 19).

Of the four key radiographic parameters determined in this study, the T1SPI, TPA, and SVA represent spinal alignment and can be corrected directly with surgical treatment; although PI, as a pelvic parameter, cannot be changed by surgery, it can influence the spine and pelvis harmony, affecting the maintenance of spinopelvic balance. Therefore, the spinal and pelvic parameters should be taken into consideration for a good clinical outcome while reconstructing an optimal sagittal alignment.

Limitations

First, this was a retrospective study in which a limited number of patients were enrolled. Second, the influence of one-level and two-level osteotomy on the postoperative sagittal alignment was not compared separately. Third, radiographic parameter evaluation is only one aspect in evaluating the clinical outcome in AS patients. The surgery itself might influence the clinical outcome, and other potential factors, such as age, sex, and comorbidities, might also affect the clinical outcome reported by patients. Finally, although most of the AS patients who underwent osteotomy were in an inflammatory static state, AS did affect the quality of life on follow-up. In the future, a prospective study with a larger sample size is required to further confirm the conclusions.

Conclusion

The results of this study demonstrated that the immediate postoperative parameters could be used to evaluate and predict the final follow-up parameters and clinical outcome in AS patients. In particular, the PI and postoperative immediate T1SPI, TPA, and SVA significantly correlated with the clinical outcome measures. The optimal postoperative immediate sagittal alignment was T1SPI ≤ 0.9°, TPA ≤ 31.5°, and SVA ≤ 9.3 cm, providing a reference for kyphosis correction and a means for clinical outcome evaluation. Patients with lower PI values (≤49.2°) are more likely to achieve better sagittal alignment and clinical outcomes after corrective osteotomy.

Data availability statement

The raw data supporting the conclusions of this article will be made available by the authors, without undue reservation.

Ethics statement

The studies involving human participants were reviewed and approved by the Human Investigation Committee of Shenzhen University General Hospital. The patients/participants provided their written informed consent to participate in this study. Written informed consent was obtained from the individual(s) for the publication of any potentially identifiable images or data included in this article.

Author contributions

JL, KY, ZY, and CF collected the radiographic and clinical data and measured the parameters. XL and ZL analyzed the clinical data and measurements; JL wrote the manuscript; HT, CD, and TW revised the manuscript; CD and TW conceived the idea and designed the study. All authors reviewed the manuscript. All authors contributed to the article and approved the submitted version.

Funding

Natural Science Foundation of Guangdong Province (2020A1515010726), Basic Research of Shenzhen Science and Technology Project (JCYJ20180305124242438), Shenzhen Major Project of Fundamental Research (JCYJ20200109114233670), Key Research and Development Program of Guangdong Province (2020B0909020002), Sanming Project of Medicine in Shenzhen (SZSM201911011), and the Shenzhen Key Laboratory Foundation (ZDSYS20200811143757022).

Conflict of interest

The authors declare that the research was conducted in the absence of any commercial or financial relationships that could be construed as a potential conflict of interest.

Publisher's note

All claims expressed in this article are solely those of the authors and do not necessarily represent those of their affiliated organizations, or those of the publisher, the editors and the reviewers. Any product that may be evaluated in this article, or claim that may be made by its manufacturer, is not guaranteed or endorsed by the publisher.

References

1. Shin JK, Lee JS, Goh TS, Son SM. Correlation between clinical outcome and spinopelvic parameters in ankylosing spondylitis. *Eur Spine J*. (2014) 23(1):242–7. doi: 10.1007/s00586-013-2929-8

2. Koller H, Koller J, Mayer M, Hempfing A, Hitzl W. Osteotomies in ankylosing spondylitis: where, how many, and how much? *Eur Spine J*. (2018) 27(Suppl 1):70–100. doi: 10.1007/s00586-017-5421-z

3. Schwab F, Patel A, Ungar B, Farcy JP, Lafage V. Adult spinal deformity-postoperative standing imbalance: how much can you tolerate? An overview of key parameters in assessing alignment and planning corrective surgery. *Spine (Phila Pa 1976)*. (2010) 35(25):2224–31. doi: 10.1097/BRS.0b013e3181ee6bd4

4. Huang JC, Qian BP, Qiu Y, Wang B, Yu Y, Qiao M. What is the optimal postoperative sagittal alignment in ankylosing spondylitis patients with thoracolumbar kyphosis following one-level pedicle subtraction osteotomy? *Spine J*. (2020) 20(5):765–75. doi: 10.1016/j.spinee.2019.11.005

5. Baldus C, Bridwell KH, Harrast J, Edwards C 2nd, Glassman S, Horton W, et al. Age-gender matched comparison of SRS instrument scores between adult deformity and normal adults: are all SRS domains disease specific? *Spine (Phila Pa 1976)*. (2008) 33(20):2214–8. doi: 10.1097/BRS.0b013e31817c0466

6. Smith JS, Shaffrey CI, Lafage V, Schwab F, Scheer JK, Protopsaltis T, et al. Comparison of best versus worst clinical outcomes for adult spinal deformity surgery: a retrospective review of a prospectively collected, multicenter database with 2-year follow-up. *J Neurosurg Spine*. (2015) 23(3):349–59. doi: 10.3171/2014.12.Spine14777

7. Schwab FJ, Blondel B, Bess S, Hostin R, Shaffrey CI, Smith JS, et al. Radiographical spinopelvic parameters and disability in the setting of adult spinal deformity: a prospective multicenter analysis. *Spine (Phila Pa 1976)*. (2013) 38(13):E803–12. doi: 10.1097/BRS.0b013e318292b7b9

8. Qian BP, Jiang J, Qiu Y, Wang B, Yu Y, Zhu ZZ. Radiographical predictors for postoperative sagittal imbalance in patients with thoracolumbar kyphosis secondary to ankylosing spondylitis after lumbar pedicle subtraction osteotomy. *Spine (Phila Pa 1976)*. (2013) 38(26):E1669–75. doi: 10.1097/BRS.0000000000000021

9. Lafage V, Schwab F, Patel A, Hawkinson N, Farcy JP. Pelvic tilt and truncal inclination: two key radiographic parameters in the setting of adults with spinal deformity. *Spine (Phila Pa 1976)*. (2009) 34(17):E599–606. doi: 10.1097/BRS.0b013e3181aad219

10. Vialle R, Levassor N, Rillardon L, Templier A, Skalli W, Guigui P. Radiographic analysis of the sagittal alignment and balance of the spine in asymptomatic subjects. *J Bone Joint Surg Am*. (2005) 87(2):260–7. doi: 10.2106/jbjs.D.02043

11. Kim YJ, Bridwell KH, Lenke LG, Cheh G, Baldus C. Results of lumbar pedicle subtraction osteotomies for fixed sagittal imbalance: a Minimum 5-year follow-up study. *Spine (Phila Pa 1976)*. (2007) 32(20):2189–97. doi: 10.1097/BRS.0b013e31814b8371

12. Van Royen BJ, De Gast A, Smit TH. Deformity planning for sagittal plane corrective osteotomies of the spine in ankylosing spondylitis. *Eur Spine J*. (2000) 9 (6):492–8. doi: 10.1007/s005860000183

13. Schwab FJ, Patel A, Shaffrey CI, Smith JS, Farcy JP, Boachie-Adjei O, et al. Sagittal realignment failures following pedicle subtraction osteotomy surgery: are we doing enough? Clinical Article. *J Neurosurg Spine*. (2012) 16(6):539–46. doi: 10.3171/2012.2.Spine11120

14. Song K, Su X, Zhang Y, Liu C, Tang X, Zhang G, et al. Optimal chin-brow vertical angle for sagittal visual fields in ankylosing spondylitis kyphosis. *Eur Spine J*. (2016) 25(8):2596–604. doi: 10.1007/s00586-016-4588-z

15. Protopsaltis T, Schwab F, Bronsard N, Smith JS, Klineberg E, Mundis G, et al. Thet1 pelvic angle, a novel radiographic measure of global sagittal deformity, accounts for both spinal inclination and pelvic tilt and correlates with health-related quality of life. *J Bone Joint Surg Am*. (2014) 96(19):1631–40. doi: 10.2106/jbjs.M.01459

16. Banno T, Hasegawa T, Yamato Y, Kobayashi S, Togawa D, Oe S, et al. T1 pelvic angle is a useful parameter for postoperative evaluation in adult spinal deformity patients. *Spine (Phila Pa 1976)*. (2016) 41(21):1641–8. doi: 10.1097/brs.0000000000001608

17. Sato T, Yonezawa I, Inoue H, Tada K, Kobayashi S, Hayashi E, et al. Relationship between characteristics of spinopelvic alignment and quality of life in Japanese patients with ankylosing spondylitis: a cross-sectional study. *BMC Musculoskelet Disord*. (2020) 21(1):41. doi: 10.1186/s12891-020-3040-z

18. Liu ZJ, Qian BP, Qiu Y, Mao SH, Jiang J, Wang B. Does postoperative PI-LL mismatching affect surgical outcomes in thoracolumbar kyphosis associated with ankylosing spondylitis patients? *Clin Neurol Neurosurg*. (2018) 169:71–6. doi: 10.1016/j.clineuro.2018.04.006

19. Sun XY, Zhang XN, Hai Y. Optimum pelvic incidence minus lumbar lordosis value after operation for patients with adult degenerative scoliosis. *Spine J*. (2017) 17(7):983–9. doi: 10.1016/j.spinee.2017.03.008

frontiers | Frontiers in Surgery

TYPE Original Research
PUBLISHED 14 September 2022
DOI 10.3389/fsurg.2022.965505

Check for updates

OPEN ACCESS

EDITED BY
Tsung-Yuan Tsai,
Shanghai Jiao Tong University, China

REVIEWED BY
Qian Kun Ni,
Southwest Sports Medicine Center, China
Pengfei Zheng,
Nanjing Children's Hospital, China

*CORRESPONDENCE
Haobo Wu
2505014@zju.edu.cn
Zengfeng Xin
osxinzf@zju.edu.cn

†These authors have contributed equally to this work

SPECIALTY SECTION
This article was submitted to Orthopaedic Surgery, a section of the journal Frontiers in Surgery

RECEIVED 09 June 2022
ACCEPTED 31 August 2022
PUBLISHED 14 September 2022

CITATION
Liu A, Ye X, Li C, Yang W, Yan S, Xin Z and Wu H (2022) Preoperative excessive lateral anterior tibial subluxation is related to posterior tibial tunnel insertion with worse sagittal alignment after anterior cruciate ligament reconstructions. Front. Surg. 9:965505.
doi: 10.3389/fsurg.2022.965505

COPYRIGHT
© 2022 Liu, Ye, Li, Yang, Yan, Xin and Wu. This is an open-access article distributed under the terms of the Creative Commons Attribution License (CC BY). The use, distribution or reproduction in other forums is permitted, provided the original author(s) and the copyright owner(s) are credited and that the original publication in this journal is cited, in accordance with accepted academic practice. No use, distribution or reproduction is permitted which does not comply with these terms.

Preoperative excessive lateral anterior tibial subluxation is related to posterior tibial tunnel insertion with worse sagittal alignment after anterior cruciate ligament reconstructions

An Liu[1†], Xiaojun Ye[2†], Congsun Li[1], Weinan Yang[1], Shigui Yan[1], Zengfeng Xin[1*] and Haobo Wu[1*]

[1]Department of Orthopedics, the Second Affiliated Hospital, Zhejiang University School of Medicine, Hangzhou, China, [2]Department of Ultrasound, Hangzhou Women`s Hospital, Hangzhou, China

Objective: To investigate whether preoperative lateral anterior tibial subluxation (LATS) measured from magnetic resonance imaging (MRI) can influence tibial insertion and postoperative sagittal alignment after anterior cruciate ligament reconstructions (ACLRs).

Methods: 84 patients who underwent single-bundle ACLRs were retrospectively investigated. Among them, 39 patients (LATS of <6 mm) 23 patients (LATS of ≥6 mm and <10 mm) and 22 patients (excessive LATS of ≥10 mm) were defined as group 1, 2 and 3, respectively. LATS, the position of graft insertion into tibia as ratio of anterior-posterior width (AP ratio) and the sagittal graft angle (SGA) were postoperatively assessed from MRI at 2-year follow-up. Following linear regression analyses were employed.

Results: The group 3 exhibited the largest preoperative LATS and remained the most postoperative LATS. Moreover, the group 3 possessed the most posteriorly located tunnel insertion with the largest AP ratio and the most vertical graft orientation. Of all included patients, a moderate correlation was demonstrated between pre- and postoperative LATS ($r = 0.635$). A low correlation was observed between preoperative LATS and AP ratio ($r = 0.300$) and a moderate correlation was displayed between AP ratio and SGA ($r = 0.656$).

Conclusion: For ACL injuries with excessive LATS (≥10 mm), most posteriorly located tibial insertion was found out, and worse sagittal alignment containing high residual LATS was associated with more vertical graft orientation following ACLRs.

KEYWORDS

lateral anterior tibial subluxation, tibial tunnel insertion, graft orientation, anterior cruciate ligament, magnetic resonance imaging

Introduction

For single-bundle anterior cruciate ligament (ACL) reconstructions (ACLRs), a general consensus exists that restoring native ACL insertion site and graft orientation can restore knee kinematics, maintain knee stability, and decrease anteroposterior and rotatory instability (1, 2). Anterior tibial subluxation (ATS) in extension, also known as "resting pivoted position", was radiological abnormal sagittal alignment between femur and tibia following the ACL injury (3). It was reported that lateral ATS (LATS) based on magnetic resonance imaging (MRI) could predict high-grade rotatory knee instability (4) and patients with LATS (≥6 mm) had much more cases of high-grade pivot shift (5).

In order to control LATS and restore rotatory stability postoperatively, numerous researches focus on the location of femoral site during ACLRs. Compared with transtibial (TT) technique, anteromedial portal (AMP) technique can independently create more anatomical femoral tunnel rather than relying on tibial tunnel orientation (6, 7). However, less attention has been paid to the relationship between tibial tunnel insertion and postoperative knee stability. For achieving ideal tibial tunnel site, anatomic references such as a residual stump, anterior horn of lateral meniscus (AHLM), or medial tibial spine were used (8). But it was noteworthy that a significant locating error in tibial tunnel placement persisted using contemporary anatomic ACLR techniques (9), and improper placement of the tibial tunnel insertion could lead to potentially devastating consequences (10).

One study found that an anterior tibial tunnel site controlled Lachman and pivot-shift movements better than a relative posterior tibial footprint (11). Posteriorly placed tibial site might change graft orientation and vertical graft trajectory which could result in rotational knee laxity (12) with aggravating the incidence of early arthrosis (13). Nevertheless, the anterior footprint increased the risk of graft impingement in extension, particularly in positive pivot-shift cases (14). Given close relation between pivot shift and LATS, preoperative LATS raise concerns regarding tibial tunnel malpositioning under ACLRs. However, whether preoperative LATS can influence the tibial tunnel insertion and follow-up sagittal knee alignment has been scarcely investigated following single-bundle ACLRs. Preoperative LATS might be a clue for surgeons to predict postoperative sagittal alignment and knee stability.

The purpose of this study was to investigate whether preoperative LATS can influence the tibial insertion and analyze the sagittal knee alignment. It was hypothesized that (1) preoperative excessive LATS (≥10 mm) would be related to posterior tibial tunnel site, and (2) worse sagittal alignment with residual postoperative LATS in two-year follow-up visit.

Methods

Patient selection

From January 2017 to October 2019, 202 consecutive patients with noncontact ACL injuries who subsequently underwent primary single-bundle ACLRs in our department were retrospectively investigated. The exclusion criteria was set as follows: (1) partial ACL injury; (2) comitant PCL, medial collateral ligament, or posterolateral corner injury; (3) general joint laxity [more than 5 of 9 on Beighton score (15)] or significant knee hyperextension (>10°); (4) lost to a follow-up visit, follow-up time <2 years; (5) lack of available magnetic resonance imaging (MRI) data. Based on the exclusion criteria, 84 patients were left for subsequent allocation based on our Institutional Ethics Board.

Surgical technique and rehabilitation procedures

All single-bundle ACLRs were performed by a single senior surgeon (HW) using 4-strand hamstring tendon autografts. Autografts have a diameter ranging from 8.0 to 9.0 mm. If 4-strand hamstring tendon autografts were less than 8.0 mm, allograft augmentation was conducted to achieve a diameter ranging from 8.0–9.0 mm. The femoral tunnel was independently drilled using the AMP technique with the knee in 120° of flexion, and the tibial tunnel placement was guided according to a combination of anatomic landmarks, with the ACL tibial stump being as the most commonly referenced landmark. The TightRope® suspensory fixation (Arthrex, USA) and Milagro® interference screw (DePuy Mitek, USA) were employed for femoral and tibial tunnel fixations, respectively.

All patients received the same rehabilitation protocol. During the first four weeks, a hinged knee brace was employed and unlocked to allow a passive range of motion from 0° to 90°, emphasizing early passive extension stretching. After four weeks postoperatively, partial weight-bearing was permitted. Full weight-bearing was not started until eight weeks following surgery. Patients were recommended to resume sporting activities at their pre-injury level nine months after surgery.

Data extraction

Preoperative data were individually extracted, including patient demographics [age, sex, body mass index (BMI), the period from injury to surgery, the follow-up time], MRI assessments of preoperative and follow-up LATS, the position

of graft insertion into tibia as ratio of anterior-posterior width (AP ratio), the sagittal graft angle (SGA) and the meniscal tears during arthroscopic observation.

All selected patients were supine and scanned using a 1.5-T MRI (Discovery 750, GE Medical Systems) with knee extension in the neutral position on the admission day before ACLR. The images contained sagittal, coronal, and axial sections with T1- and T2-weighted phases. For LATS measurement, the protocol for LATS was according to the method previously described by Tanaka et al (16).

Briefly, a best-fit circle tangent to the lateral posterior femoral condyle border was first drawn on the sagittal section of the most medial edge of the fibula. Along the posterior margin of the circle, a straight line was depicted vertically to the tibial plateau. After that, another parallel line was drawn across the posterior cortex of tibia. The distance between these two lines was identified as LATS. They were performed on both preoperative (**Figure 1A**) and follow-up MRIs (**Figure 1B**).

For tibial tunnel insertion, a line vertical to the tibia's axis was drawn from the anterior tibial cortex to the posteriormost part of posterior intercondylar margin to confirm the tibia's total AP distance. The AP ratio was defined as the distance between anterior tibial margin to the center of tibial graft insertion/the tibia's total AP distance (**Figure 1C**). As to graft orientation, SGA was defined as the angle between the tangent to the graft and a line perpendicular to the tibia's long axis (**Figure 1D**) (17, 18).

Two investigators separately measured and recorded the MRI data. Additionally, an independent investigator performed all MRI remeasurements on each selected patient twice within two weeks. The intraclass correlation coefficients (ICCs) were calculated to determine the inter- and intra-observer reliability of measurement by randomly choosing 30 patients (10 from each group). The details regarding inter- and intra-observer ICCs (with 95% confidence intervals) are given in **Table 1**.

A previous cadaveric study indicated that 6 mm of LATS was necessary to produce a pivot shift and 10 mm of LATS was the mean amount of subluxation in grade I pivot shift (19). Therefore, preoperative LATS was classified into three grade in the present study: <6 mm for low grade, ≥ 6 mm and <10 mm for high grade, ≥ 10 mm for excessive grade.

TABLE 1 Intraobserver and interobserver intraclass correlation for MRI measurement.[a]

	Preoperative LATS	Postoperative LATS	AP ratio	SGA
Intra-observer	0.83	0.82	0.82	0.80
ICC (95% CI)	(0.80–0.86)	(0.79–0.84)	(0.78–0.85)	(0.76–0.83)
Inter-observer	0.79	0.80	0.80	0.78
ICC (95% CI)	(0.76–0.82)	(0.77–0.83)	(0.77–0.84)	(0.75–0.81)

[a]ICC, intraclass correlation coefficient; CI, confidence interval; LATS, lateral anterior tibial subluxation; AP ratio, anteroposterior ratio; SGA, sagittal graft angle.

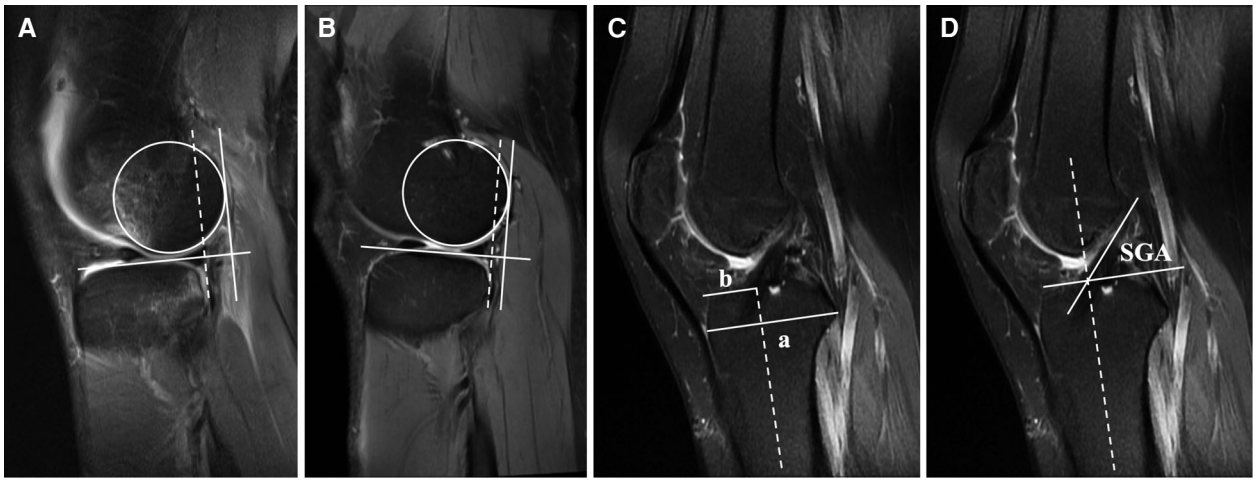

FIGURE 1
For MRI measurement (**A**) preoperative and (**B**) postoperative LATS, the slice showing the most medial edge of the fibula was chosen. Following that, a best-fit circle tangent to the lateral posterior femoral condyle border was first drawn. Along the posterior margin of this circle, a straight line was depicted vertical to the tibial plateau, and another parallel line (dotted line) was drawn across the posterior cortex of the tibia. The distance between these two lines was defined as the amount of LATS. (**C**) AP ratio was defined as the distance between the anterior tibial margin to the center of tibial graft insertion/the tibia's total AP distance (b/a). A line vertical to the tibia's axis (dotted line) was drawn from the anterior tibial cortex to the posteriormost part of posterior intercondylar margin to confirm the tibia's total AP distance. (**D**) SGA was defined as the angle between the tangent to the graft and a line perpendicular to the tibia's long axis (dotted line). LATS, lateral anterior tibial subluxation. AP ratio, anteroposterior ratio; SGA, sagittal graft angle.

Statistical analyses

Statistical analyses were conducted using SPSS software (version 20.0, IBM Corp., USA). Individual variables were tested for normality. Descriptive statistics were calculated for patient demographic data, preoperative and follow-up LATS, SGA, AP ratio and meniscal tears. The Student t-test was used to evaluate continuous variables. The Fisher exact test or the Pearson chi-square test was used to compare categorical variables. Linear regression analyses were performed to test the relationship between pre- and postoperative LATS, AP ratio, respectively. The correlation between AP ratio and SGA was also analyzed. Correlation strength was defined as follows: r value of 0.1–0.3 = weak; 0.3–0.5 = low; 0.5–0.7 = moderate and over 0.7 = high (20). The significant difference was set as $p < 0.05$. For determining the power of this study, the software G*Power 3.1 (Universität Düsseldorf, Germany) was used to performed *post hoc* power analysis (21). An effect size was calculated based on the pre- and postoperative LATS. With the underlying effect size and α of 0.05, a power of 1.0 was obtained.

Results

Preoperative characteristics of patients

39 patients who has low LATS (<6 mm) were selected as group 1 and left 45 patients were subsequently divided into two groups: high LATS (≥6 mm and <10 mm) (group 2, $n = 23$) and excessive LATS of ≥ 10 mm (group 3, $n = 22$) (Figure 2).

Table 2 compared the preoperative characteristics of patients with different grades of LATS. The group 3 with excessive LATS (≥10 mm) exhibited significantly larger LATS than the group 2 and the group 1 (10.6 (10.0–11.1) mm vs. 7.0 (6.6–7.3) mm, $p < 0.001$; 10.6 (10.0–11.1) mm vs. 2.4 (1.8–3.1) mm, $p < 0.001$), respectively. Moreover, the group 3 (LATS ≥ 10 mm) contained more cases of high-grade (Grade 2&3) pivot shift than those in the group 1 ((LATS <6 mm) with significance ($p = 0.019$). However, no differences were found in age, sex, BMI, period from injury to surgery and lateral meniscus tear among three groups.

Assessment of postoperative LATS

For postoperative follow-ups (Table 3), postoperative LATS of all three groups were reduced after ACLRs. Whereas, the group 3 remained more residual LATS than the group 2 and the group 1 (6.5 (5.2–7.9) mm vs. 3.8 (2.7–4.9) mm, $p = 0.002$; 6.5 (5.2–7.9) mm vs. 2.1 (1.3–2.9) mm, $p < 0.001$), respectively.

Measurement of tibial tunnel insertion and graft orientation

In terms of the tibial tunnel insertion, the group 3 had a posteriorly located tibial tunnel site with the AP ratio of 44.1 (41.9–46.3)%. Moreover, its exhibited more vertical sagittal graft orientation with larger SGA [58.3 (55.8–60.8)°] than those of other two groups. However, the comparison between the group 1 and the group 2 revealed no significant difference on AP ratio [40.9 (39.3–42.6)% vs. 41.2 (39.6–42.9)%, $p = 0.804$] or SGA [53.4 (51.4–55.4) ° vs. 54.0 (52.2–55.9) °, $p = 0.670$, Table 3].

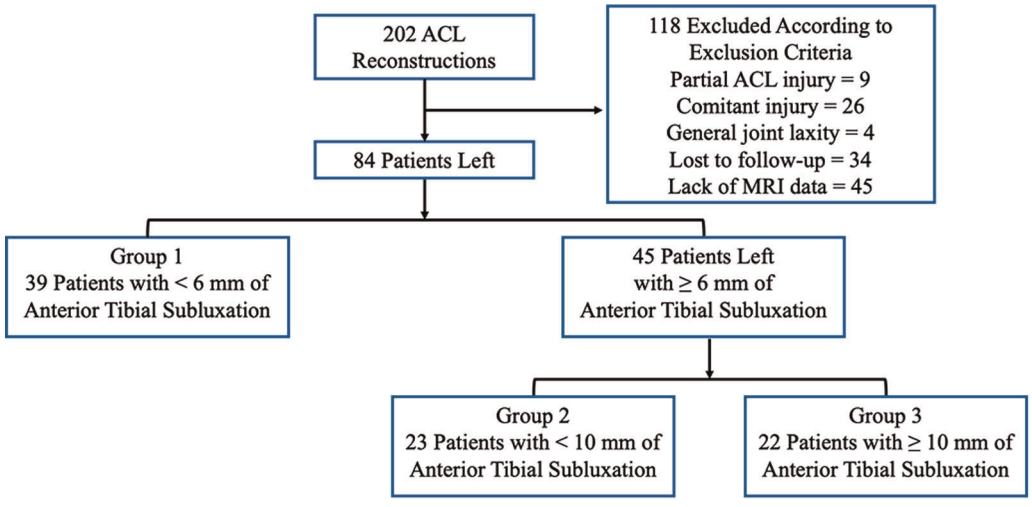

FIGURE 2
A flowchart for the group allocation. ACL, anterior cruciate ligament.

TABLE 2 Preoperative comparisons among different grades of LATS.[a]

	Group 1 ($n = 39$)	Group 2 ($n = 23$)	Group 3 ($n = 22$)	p value[b]		
				p_1	p_2	p_3
Age, y	27.7 (26.2–29.2)	26.1 (24.9–28.2)	27.0 (23.8–30.2)	0.197	0.649	0.618
Sex, M/F	26/13	17/6	17/5	0.584	0.560	>0.999
BMI, kg/m^2	24.5 (23.2–25.7)	23.9 (22.7–25.1)	23.6 (22.0–25.2)	0.510	0.363	0.750
Period from injury to surgery, months	6.1 (3.3–9.0)	6.0 (3.6–8.5)	6.5 (4.3–8.6)	0.964	0.865	0.781
LATS, mm	2.4 (1.8–3.1)	7.0 (6.6–7.3)	10.6 (10.0–11.1)	**<0.001**	**<0.001**	**<0.001**
Lateral meniscus tears, n				0.596	0.181	0.554
Present	15	11	13			
Absent	24	12	9			
Pivot-shift, n				0.426	**0.019**	0.231
Grade 1	25	12	7			
Grade 2&3	14	11	15			

[a]Data are expressed as mean (95%CI) or n; Bold values indicate statistical significance ($p < 0.05$); CI, confidence interval; M/F, male/female; BMI, body mass index; LATS, lateral anterior tibial subluxation.
[b]p_1 = Group 2 vs. Group 1; p_2 = Group 3 vs. Group 1; p_3 = Group 3 vs. Group 2.

TABLE 3 Postoperative comparisons among different grades of LATS.[a]

	Group 1 ($n = 39$)	Group 2 ($n = 23$)	Group 3 ($n = 22$)	p value[b]		
				p_1	p_2	p_3
Follow-up time, months	28.9 (27.6–30.2)	29.0 (27.5–30.6)	28.4 (26.6–30.1)	0.865	0.631	0.548
LATS, mm	2.1 (1.3–2.9)	3.8 (2.7–4.9)	6.5 (5.2–7.9)	**0.011**	**<0.001**	**0.002**
AP ratio, %	40.9 (39.3–42.6)	41.2 (39.6–42.9)	44.1 (41.9–46.3)	0.804	**0.021**	**0.035**
SGA, °	53.4 (51.4–55.4)	54.0 (52.2–55.9)	58.3 (55.8–60.8)	0.670	**0.003**	**0.006**

[a]Data are expressed as mean (95%CI); Bold values indicate statistical significance ($p < 0.05$); CI, confidence interval; LATS, lateral anterior tibial subluxation; AP ratio, anteroposterior ratio; SGA, sagittal graft angle.
[b]p_1 = Group 2 vs. Group 1; p_2 = Group 3 vs. Group 1; p_3 = Group 3 vs. Group 2.

Analysis of linear correlation

In all included patients ($n = 84$), a moderate correlation was shown between preoperative and postoperative LATS [Figure 3A; r = 0.635 (0.487–0.748), $p < 0.001$]. For tibial insertion analysis, there was a low correlation between preoperative LATS and AP ratio [Figure 3B; r = 0.300 (0.090–0.482), $p = 0.006$]. Regarding the follow-up sagittal graft orientation, moderate correlation with statistical significance was demonstrated between AP ratio and SGA [Figure 3C; r = 0.656 (0.514–0.763), $p < 0.001$].

Discussion

The current study's findings indicated that for single-bundle ACLRs, ACL injuries with preoperative excessive LATS (≥10 mm) was related to increased posterior tibial tunnel insertion with worse sagittal alignment (postoperative LATS of >6 mm) and more vertical graft orientation at two-year follow-up time.

Several researches have reported that preoperative LATS was found to be a risk factor for predicting the grade of pivot shift in acute ACL injuries (4, 5), and preoperative pivot shift was found to be a risk factor for residual pivot shift following ACLRs (22, 23). Song et al. demonstrated that excessive preoperative ATS for both lateral and medial sides (>10 mm) could not be reduced with anatomic ACLRs with high residual LATS (>6 mm) (24), which was in accordance with our results [6.5 (5.2–7.9) mm].

As previously stated, sufficient coverage of the native ACL footprint is critical for successful restoration of normal knee kinematics (25), but whether the LATS can influence the tibial insertion needs to be investigated. Several studies revealed that tibial site was located at an average AP ratio of 38.5% to 40.7% (26, 27), which was consistent with our results from the group 1 and group 2. However, the group 3 with excessive LATS contained a larger AP ratio indicating that the tibial insertion was posteriorly placed and a low

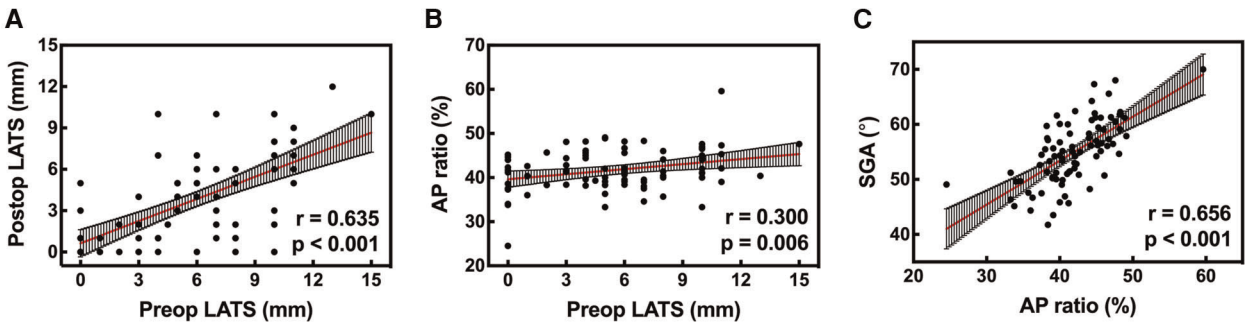

FIGURE 3
(A) A moderate correlation was found between preoperative and postoperative LATS [r = 0.635 (0.487–0.748), $p < 0.001$]. (B) A low correlation was found between preoperative LATS and AP ratio [r = 0.300 (0.090–0.482), $p = 0.006$]. (C) It was demonstrated that SGA was moderately correlated with AP ratio [r = 0.656 (0.514–0.763); $p < 0.001$]. LATS, lateral anterior tibial subluxation; AP ratio, anteroposterior ratio; SGA, sagittal graft angle.

correlation between preoperative LATS and AP ratio (r = 0.300). Therefore, preoperative excessive LATS may be a factor for posteriorly locating tibial insertion.

It was found that a significant positioning error in tibial tunnel placement posterior to the native ACL footprint remains with by using contemporary surgical technique for anatomic ACLRs (9). For ACL injuries with excessive LATS, the subluxated relationship between tibia and femur may mislead surgeons` observation and judgement and aggravate the positioning error. Furthermore, excessive LATS (≥10 mm) could give rise to the concern of possible notch impingement and loss of extension. Consequently, relative posterior tibial tunnel placement might be a compromise on graft impingement that would weaken the knee stability. And for graft orientation, our results find that the group 3 exhibited the most vertical graft angle and moderate correlation was shown between the AP ratio and SGA (r = 0.656, $p < 0.001$) for all cases. Therefore, the angle of graft orientation might be increased due to posteriorly placed tibial tunnel site, which resulted in worse control of AP subluxation and tibial rotation that were previously reported (28, 29).

Surgical techniques for eliminating LATS in ACL injuries remain controversial. One study reported that a single-bundle ACLR was sufficient to restore ATS and tibial rotation (30), and another research demonstrated that an anatomic ACLR covering the central 2/3 of native ACL footprint could restore knee stability with preoperative Grade-3 pivot shift (31). Unfortunately, our results about postoperative LATS in the excessive group appeared to contradict the above conclusions. Anterolateral ligament (ALL) were reported to be crucial to control LATS as they were secondary stabilizers after ACL injuries to maintain anterolateral stability (22). It is noticeable that several authors (32, 33) recommended that ALL reconstruction or augmentation combined with ACLR could reduce ATS for initially restoring tibiofemoral alignment. Further studies focusing on the potential effect of the ALL reconstruction to the placement of tibia tunnel insertion are required.

We acknowledge that this study contains the following limitations: first, although ATS was 2-dimensionally evaluated using MRI with standard protocol, the measurements may be confounded by leg rotation and knee flexion variations. Second, no immediate postoperative MRI scans were conducted on included patients. After ACLR, the sagittal tibiofemoral alignment was possibly restored to normal at time 0 and then deteriorated over time.

Conclusion

For ACL injuries with excessive LATS (≥10 mm), most posteriorly located tibial insertion was found out, and worse sagittal alignment containing high postoperative LATS was associated with more perpendicular graft orientation following single-bundle ACLRs.

Data availability statement

The original contributions presented in the study are included in the article/Supplementary Material, further inquiries can be directed to the corresponding author/s.

Ethics statement

The studies involving human participants were reviewed and approved by Second Affiliated Hospital, School of

Medicine, Zhejiang University . Written informed consent for participation was not required for this study in accordance with the national legislation and the institutional requirements.

Author contributions

AL, XY prepared original materials and wrote the manuscript. CL and WY made statistics. ZX and SY made commentary and revision. All authors have read and approved the manuscript. HW planned the study project and made supervision. All authors contributed to the article and approved the submitted version.

Conflict of interest

The authors declare that the research was conducted in the absence of any commercial or financial relationships that could be construed as a potential conflict of interest.

Publisher's note

All claims expressed in this article are solely those of the authors and do not necessarily represent those of their affiliated organizations, or those of the publisher, the editors and the reviewers. Any product that may be evaluated in this article, or claim that may be made by its manufacturer, is not guaranteed or endorsed by the publisher.

References

1. Zaffagnini S, Signorelli C, Bonanzinga T, Roberti Di Sarsina T, Grassi A, Budeyri A, et al. Technical variables of ACL surgical reconstruction: effect on post-operative static laxity and clinical implication. *Knee Surg Sports Traumatol Arthrosc.* (2016) 24:3496–506. doi: 10.1007/s00167-016-4320-x

2. Zantop T, Herbort M, Raschke MJ, Fu FH, Petersen W. The role of the anteromedial and posterolateral bundles of the anterior cruciate ligament in anterior tibial translation and internal rotation. *Am J Sports Med.* (2007) 35:223–7. doi: 10.1177/0363546506294571

3. Almekinders LC, De Castro D. Fixed tibial subluxation after successful anterior cruciate ligament reconstruction. *Am J Sports Med.* (2001) 29:280–3. doi: 10.1177/03635465010290030301

4. Lian J, Novaretti JV, Sheean AJ, Patel NK, Whaley S, Popchak A, et al. Static lateral tibial plateau subluxation predicts high-grade rotatory knee laxity in anterior cruciate ligament–deficient knees. *Am J Sports Med.* (2019) 47:277–84. doi: 10.1177/0363546518812435

5. Song GY, Zhang H, Zhang J, Liu X, Xue Z, Qian Y, et al. Greater static anterior tibial subluxation of the lateral compartment after an acute anterior cruciate ligament injury is associated with an increased posterior tibial slope. *Am J Sports Med.* (2018) 46:1617–23. doi: 10.1177/0363546518760580

6. Liu A, Sun M, Ma C, Chen Y, Xue X, Guo P, et al. Clinical outcomes of transtibial versus anteromedial drilling techniques to prepare the femoral tunnel during anterior cruciate ligament reconstruction. *Knee Surg Sports Traumatol Arthrosc.* (2017) 25:2751–9. doi: 10.1007/s00167-015-3672-y

7. Youm YS, Cho SD, Lee SH, Youn CH. Modified transtibial versus anteromedial portal technique in anatomic single-bundle anterior cruciate ligament reconstruction: comparison of femoral tunnel position and clinical results. *Am J Sports Med.* (2014) 42:2941–7. doi: 10.1177/0363546514551922

8. Kassam AM, Tillotson L, Schranz PJ, Mandalia VI. The lateral meniscus as a guide to anatomical tibial tunnel placement during anterior cruciate ligament reconstruction. *Open Orthop J.* (2015) 9:542–7. doi: 10.2174/1874325001509010542

9. Pedneault C, Laverdière C, Hart A, Boily M, Burman M, Martineau PA. Evaluating the accuracy of tibial tunnel placement after anatomic single-bundle anterior cruciate ligament reconstruction. *Am J Sports Med.* (2019) 47:3187–94. doi: 10.1177/0363546519873633

10. Hosseini A, Lodhia P, Van de Velde SK, Asnis PD, Zarins B, Gill TJ, et al. Tunnel position and graft orientation in failed anterior cruciate ligament reconstruction: a clinical and imaging analysis. *Int Orthop.* (2012) 36:845–52. doi: 10.1007/s00264-011-1333-4

11. Bedi A, Maak T, Musahl V, Citak M, O'Loughlin PF, Choi D, et al. Effect of tibial tunnel position on stability of the knee after anterior cruciate ligament reconstruction: is the tibial tunnel position most important? *Am J Sports Med.* (2011) 39:366–73. doi: 10.1177/0363546510388157

12. Lee MC, Seong SC, Lee S, Chang CB, Park YK, Jo H, et al. Vertical femoral tunnel placement results in rotational knee laxity after anterior cruciate ligament reconstruction. *Arthroscopy.* (2007) 23:771–8. doi: 10.1016/j.arthro.2007.04.016

13. Scanlan SF, Blazek K, Chaudhari AMW, Safran MR, Andriacchi TP. Graft orientation influences the knee flexion moment during walking in patients with Anterior cruciate ligament reconstruction. *Am J Sports Med.* (2009) 37:2173–8. doi: 10.1177/0363546509339574

14. Zuiderbaan HA, Khamaisy S, Nawabi DH, Thein R, Nguyen JT, Lipman JD, et al. Notchplasty in anterior cruciate ligament reconstruction in the setting of passive anterior tibial subluxation. *Knee.* (2014) 21:1160–5. doi: 10.1016/j.knee.2014.08.011

15. Redler LH, Dennis ER, Mayer GM, Kalbian IL, Nguyen JT, Shubin Stein BE, et al. Does ligamentous laxity protect against chondral and osteochondral injuries in patients with patellofemoral instability? *Orthop J Sports Med.* (2022) 10:23259671221107609. doi: 10.1177/23259671221107609

16. Tanaka MJ, Jones KJ, Gargiulo AM, Delos D, Wickiewicz TL, Potter HG, et al. Passive anterior tibial subluxation in anterior cruciate ligament-deficient knees. *Am J Sports Med.* (2013) 41:2347–52. doi: 10.1177/0363546513498995

17. Stäubli HU, Rauschning W. Tibial attachment area of the anterior cruciate ligament in the extended knee position. Anatomy and cryosections in vitro complemented by magnetic resonance arthrography in vivo. *Knee Surg Sports Traumatol Arthrosc.* (1994) 2:138–46. doi: 10.1007/BF01467915

18. Konarski A, Strang M, Jain N. The natural orientation of the Anterior Cruciate Ligament compared to the tibial plateau on magnetic resonance imaging scans. *J Orthop.* (2020) 22:422–6. doi: 10.1016/j.jor.2020.09.010

19. Bedi A, Musahl V, Lane C, Citak M, Warren RF, Pearle AD. Lateral compartment translation predicts the grade of pivot shift: a cadaveric and clinical analysis. *Knee Surg Sports Traumatol Arthrosc.* (2010) 18:1269–76. doi: 10.1007/s00167-010-1160-y

20. Scheffel PT, Henninger HB, Burks RT. Relationship of the intercondylar roof and the tibial footprint of the ACL: implications for ACL reconstruction. *Am J Sports Med.* (2013) 41:396–401. doi: 10.1177/0363546512467955

21. Zhang Z, Zhang H, Song G, Wang X, Zhang J, Zheng T, et al. A high-grade J sign is more likely to yield higher postoperative patellar laxity and residual maltracking in patients with recurrent patellar dislocation treated with derotational distal femoral osteotomy. *Am J Sports Med.* (2020) 48:117–27. doi: 10.1177/0363546519884669

22. Ueki H, Nakagawa Y, Ohara T, Watanabe T, Horie M, Katagiri H, et al. Risk factors for residual pivot shift after anterior cruciate ligament reconstruction: data from the MAKS group. *Knee Surg Sports Traumatol Arthrosc.* (2018) 26:3724–30. doi: 10.1007/s00167-018-5005-4

23. McDonald LS, van der List JP, Jones KJ, Zuiderbaan HA, Nguyen JT, Potter HG, et al. Passive anterior tibial subluxation in the setting of anterior cruciate ligament injuries. *Am J Sports Med.* (2017) 45:1537–46. doi: 10.1177/0363546516688673

24. Song GY, Zhang H, Zhang J, Zhang ZJ, Zheng T, Feng H. Excessive preoperative anterior tibial subluxation in extension is associated with Inferior knee stability after anatomic anterior cruciate ligament reconstruction. *Am J Sports Med.* (2020) 48:573–80. doi: 10.1177/0363546519900158

25. Araujo PH, Asai S, Pinto M, Protta T, Middleton K, Linde-Rosen M, et al. ACL graft position affects in situ graft force following ACL reconstruction. *J Bone Joint Surg Am*. (2015) 97:1767–73. doi: 10.2106/JBJS.N.00539

26. Lee JK, Lee S, Seong SC, Lee MC. Anatomy of the anterior cruciate ligament insertion sites: comparison of plain radiography and three-dimensional computed tomographic imaging to anatomic dissection. *Knee Surg Sports Traumatol Arthrosc*. (2015) 23:2297–305. doi: 10.1007/s00167-014-3041-2

27. Parkinson B, Gogna R, Robb C, Thompson P, Spalding T. Anatomic ACL reconstruction: the normal central tibial footprint position and a standardised technique for measuring tibial tunnel location on 3D CT. *Knee Surg Sports Traumatol Arthrosc*. (2017) 25:1568–75. doi: 10.1007/s00167-015-3683-8

28. Webster KE, Wotherspoon S, Feller JA, McClelland JA. The effect of anterior cruciate ligament graft orientation on rotational knee kinematics. *Knee Surg Sports Traumatol Arthrosc*. (2013) 21:2113–20. doi: 10.1007/s00167-012-2310-1

29. Zampeli F, Ntoulia A, Giotis D, Tsiaras VA, Argyropoulou M, Pappas E, et al. Correlation between anterior cruciate ligament graft obliquity and tibial rotation during dynamic pivoting activities in patients with anatomic anterior cruciate ligament reconstruction: an in vivo examination. *Arthroscopy*. (2012) 28:234–46. doi: 10.1016/j.arthro.2011.08.285

30. Zampeli F, Terzidis I, Espregueira-Mendes J, Georgoulis JD, Bernard M, Pappas E, et al. Restoring tibiofemoral alignment during ACL reconstruction results in better knee biomechanics. *Knee Surg Sports Traumatol Arthrosc*. (2018) 26:1367–74. doi: 10.1007/s00167-017-4742-0

31. Noyes FR, Huser LE, Levy MS. The effect of an ACL reconstruction in controlling rotational knee stability in knees with intact and physiologic laxity of secondary restraints as defined by tibiofemoral compartment translations and graft forces. *J Bone Joint Surg Am*. (2018) 100:586–97. doi: 10.2106/JBJS.16.01412

32. Littlefield CP, Belk JW, Houck DA, Kraeutler MJ, LaPrade RF, Chahla J, et al. The anterolateral ligament of the knee: an updated systematic review of anatomy, biomechanics, and clinical outcomes. *Arthroscopy*. (2021) 37:1654–66. doi: 10.1016/j.arthro.2020.12.190

33. Marom N, Ouanezar H, Jahandar H, Zayyad ZA, Fraychineaud T, Hurwit D, et al. Lateral extra-articular tenodesis reduces anterior cruciate ligament graft force and anterior tibial translation in response to applied pivoting and anterior drawer loads. *Am J Sports Med*. (2020) 48:3183–93. doi: 10.1177/0363546520959322

frontiers | Frontiers in Surgery

TYPE Original Research
PUBLISHED 13 October 2022
DOI 10.3389/fsurg.2022.991476

Check for updates

OPEN ACCESS

EDITED BY
Huiwu Li,
Shanghai Ninth People's Hospital, China

REVIEWED BY
Jia Hua,
University College London, United Kingdom
Guoan Li,
Newton Wellesley Hospital, United States

*CORRESPONDENCE
Min Wang
wangmin@tmmu.edu.cn
Cheng-Kung Cheng
ckcheng2009@gmail.com

SPECIALTY SECTION
This article was submitted to Orthopedic Surgery, a section of the journal Frontiers in Surgery

RECEIVED 11 July 2022
ACCEPTED 26 September 2022
PUBLISHED 13 October 2022

CITATION
Luan Y, Zhang M, Ran T, Wang H, Fang C, Nie M, Wang M and Cheng C-K (2022) Correlation between component alignment and short-term clinical outcomes after total knee arthroplasty. Front. Surg. 9:991476.
doi: 10.3389/fsurg.2022.991476

COPYRIGHT
© 2022 Luan, Zhang, Ran, Wang, Fang, Nie, Wang and Cheng. This is an open-access article distributed under the terms of the Creative Commons Attribution License (CC BY). The use, distribution or reproduction in other forums is permitted, provided the original author(s) and the copyright owner(s) are credited and that the original publication in this journal is cited, in accordance with accepted academic practice. No use, distribution or reproduction is permitted which does not comply with these terms.

Correlation between component alignment and short-term clinical outcomes after total knee arthroplasty

Yichao Luan[1], Min Zhang[1], Tianfei Ran[2], Huizhi Wang[3], Chaohua Fang[3,4], Maodan Nie[3], Min Wang[2]* and Cheng-Kung Cheng[1,3]*

[1]School of Biological Science and Medical Engineering, Beihang University, Beijing, China, [2]Department of Orthopaedics, Xinqiao Hospital, Army Military Medical University, Chongqing, China, [3]School of Biomedical Engineering, Shanghai Jiao Tong University, Shanghai, China, [4]Department of Joint Surgery, Ningbo No.6 Hospital, Ningbo, China

Objective: This study aimed to investigate the correlation between component alignment and short-term clinical outcomes after total knee arthroplasty (TKA).
Methods: 50 TKA patients from a regional hospital were enrolled in the study. The following component alignments were measured from radiological data acquired within 1 week after surgery: hip-knee-ankle angle (HKA), medial distal femoral angle (MDFA), medial proximal tibial angle (MPTA), femoral flexion-extension angle (FEA), tibial slope angle (TSA), femoral rotational angle (FRA) and tibial rotational angle (TRA). The Hospital for Special Surgery (HSS) knee scoring system was used to assess clinical outcomes after 1 year, with patients being divided into three groups (excellent, good and not good) according to the HSS scores. Difference analysis and linear correlation analysis were used for the statistical analysis.
Results: The results showed significant differences in MDFA ($p = 0.050$) and FEA ($p = 0.001$) among the three patient groups. It was also found that the total HSS had only a moderate correlation with FEA ($r = 0.572$, $p < 0.001$), but FEA had a positive linear correlation with pain scores ($r = 0.347$, $p = 0.013$), function scores ($r = 0.535$, $p = 0.000$), ROM scores ($r = 0.368$, $p = 0.009$), muscle scores ($r = 0.354$, $p = 0.012$) and stability scores ($r = 0.312$, $p = 0.028$). A larger MDFA was associated with lower FE deformity scores ($r = -0.289$, $p = 0.042$) and the TSA had a positive influence on the ROM ($r = 0.436$, $p = 0.002$). Also, changes in FRA produced a consequent change in the FE deformity score ($r = 0.312$, $p = 0.027$), and the muscle strength scores increased as TRA increased ($r = 0.402$, $p = 0.004$).
Conclusion: The results show that the FEA plays a significant role in clinical outcomes after TKA. Surgical techniques and tools may need to be improved to accurately adjust the FEA to improve joint functionality and patient satisfaction.

Abbreviations
TKA, total knee arthroplasty; HKA, hip-knee-ankle angle; MDFA, medial distal femoral angle; MPTA, medial proximal tibial angle; FEA, femoral flexion-extension angle; TSA, tibial slope angle; FRA, femoral rotational angle; TRA, tibial rotational angle; HSS, Hospital for Special Surgery knee scoring system; PS, posterior-stabilized; TEA, trans-epicondylar axis; AP, anterior-posterior; PCL, posterior condylar line; TCA, tibial component axis; TTA, tibial tuberosity axis; GC, geometrical center; FMA, femoral mechanical axis; CTL, condylar tangent line; BTB, border of tibial baseplate; TMA, tibial mechanical axis; JL, joint line; FAA, femoral anatomical axis; DCL, distal cutting line; TAA, tibial anatomical axis

KEYWORDS
total knee arthroplasty, component alignment, clinical outcomes, outlier rate, linear correlation

Introduction

Total knee arthroplasty (TKA) is the most effective treatment for severe arthritis of the knee joint. However, about 20% of patients are reportedly dissatisfied with the outcome because of joint pain or restricted function (1, 2). Malalignment of the knee prosthesis, which possibly results from inadequate determination of anatomical landmarks, the thickness of the saw blade and surgeon experience (3–5) have been reported as some of the main reasons for dissatisfaction and even revision (6, 7). Previous studies found that malalignment of knee prostheses can cause patellofemoral mal-tracking and incongruence with the femoral-insert interface, which may cause postoperative complications such as anterior knee pain and patellar subluxation (8, 9). The alignment of the prosthesis also influences the biomechanics and kinematics of the knee joint, such as stress on the ligaments, anterior-posterior translation of the femoral component and polyethylene wear (10–14).

Mechanical alignment is considered to create a biomechanically friendly environment in the knee joint that aims to position both the femoral and tibial components perpendicular to the mechanical axis. This method of aligning the components has been proven to produce good clinical and functional outcomes as well as long survivorship (15, 16). Some surgeons have suggested that the "safe zone" for the hip-knee-ankle (HKA) angle is with tibiofemoral alignment on the coronal plane being 180° ± 3° (17, 18). Patients aligned in this zone have reported better clinical outcomes (19), but, in contrast, some studies found no difference in outcomes or survivorship regardless if the alignment is within the "safe zone" (20, 21). Moreover, it has been reported that the "safe zone" may not be applicable to modern personalized alignment strategies (22). Complicating the discussion, differences in component alignment on the sagittal and transverse planes can also have a considerable impact on the joint. Some studies have shown that maintaining component alignment within 3° on the sagittal or transverse planes will not significantly affect the clinical outcomes (23, 24). However, opposing results have also been reported in other literature (25, 26). Few studies have examined the correlation between clinical outcomes and the alignment of knee components on all three planes (transverse, frontal and sagittal) in the same cohort of patients.

Recent advances in navigation, patient-specific instrumentation and robotics have improved surgical precision, but many surgeons still prefer conventional techniques because of the longer surgical time, higher cost and lack of qualifiable improvements in clinical outcome with the more advanced methods (27–30), a possible reason might be the greater attention to coronal alignment rather than also considering the sagittal and transverse planes, as well as unclear correlations between planar alignment and clinical outcomes. Therefore, this study aimed to investigate the correlation between the clinical scores and component alignment on all three planes (transverse, frontal and sagittal) using radiological measurements and clinical follow-up. It was hypothesized that there was a linear correlation between the alignment and clinical scores.

Materials and methods

Patients

This retrospective research was approved by our institutional ethics committee and all patients provided informed consent before involvement. This study retrospectively assessed all primary TKA procedures performed in a regional hospital between June 2019 and December 2020. In total, 276 TKA procedures were considered. The exclusion criteria of this study were as follows: (1) patients preoperatively diagnosed with rheumatoid arthritis or traumatic arthritis; (2) patients with served extra-articular deformities, trauma or other joint diseases; (3) patients treated with bilateral TKA; (4) patients imaged more than 1 week after the procedure; (5) patients followed up less than 1 year after surgery. After exclusions, 50 patients (Female:Male = 42:8) were enrolled in this study including 24 left knees and 26 right knees. The age of these patients was 68.40 ± 8.73 years old.

Surgical procedures

All subjects were implanted with a posterior-stabilized (PS) knee system (Vanguard, Zimmer Biomet, USA) by an experienced senior knee surgeon following the approved guidelines for this prosthesis. The anteromedial incision and medial parapatellar approach were adopted for all TKA procedures and the prostheses were positioned using mechanical alignment. After cutting the distal femur, an intramedullary rod was placed into the femur along the anatomical axis. A valgus angle between the anatomical axis and mechanical axis was set according to pre-operative radiographs to ensure the cutting plane lay perpendicular to

the mechanical axis. On the sagittal plane, the cutting line was perpendicular to the rod. The size of the femoral component was determined using the AP sizer and a 4-in-1 cutting block was placed when the slot was parallel to the trans-epicondylar axis (TEA). The location of the block was checked according to the anterior reference, and the distal femur was resected before the PS box was prepared following the surgical guidelines.

The extramedullary method was used for tibial resection. The cutting plane was perpendicular to the mechanical axis of the tibia on the coronal plane with a 5-degree slope on the sagittal plane. The size of the tibial component was confirmed following the best tibial coverage in both AP and medial-lateral (ML) directions. Rotational alignment of the tibial component was determined with the tibial trail under the knee flexion. The patella was repaired to an appropriate shape instead of the resurfacing.

Radiographic assessment

Full leg weight-bearing anterior-posterior (AP) radiographs were taken preoperatively to measure the angle between the mechanical and anatomical axis, and lateral radiographs were used to estimate the required size of femoral component. The standard anteroposterior and lateral radiographs and the artifact-reducing CT images of the knee joint were taken routinely within 1 week after surgery. On the coronal plane, the hip-knee-ankle angle (HKA), medial distal femoral angle and medial proximal tibial angle were used to assess joint alignment (31). The femoral mechanical axis was defined as a line connecting the centers of the femoral head and knee joint, and the tibial mechanical axis was a line connecting the centers of the knee joint and ankle joint. The medial angle between the mechanical axis of the femur and tibia was taken as the HKA, the medial angle between the mechanical axis and condylar tangent line of the femoral component was MDFA, and the angle between the mechanical axis and the border of the tibial baseplate was the MPTA (**Figure 1**). The femoral flexion-extension angle (FEA) and tibial slope angle (TSA) were used to evaluate alignment on the sagittal plane (24), with the anatomical axis being the line that connected the midpoints of the outer cortical diameter at 5 and 15 cm proximal to the joint line on the femur and tibia (32). The anterior angle between the femoral anatomical axis and the distal cutting line was the FEA, and the posterior angle between the tibial anatomical axis and the border of the tibial baseplate was the TSA (**Figure 2**). On the transverse plane, the femoral rotational angle (FRA) and tibial rotation angle (TRA) were used to identify the alignments. The angle between TEA and the posterior condylar line (PCL) was FRA (**Figure 3A**). The TRA was determined by the tibial component axis (TCA) and tibial tuberosity axis (TTA)

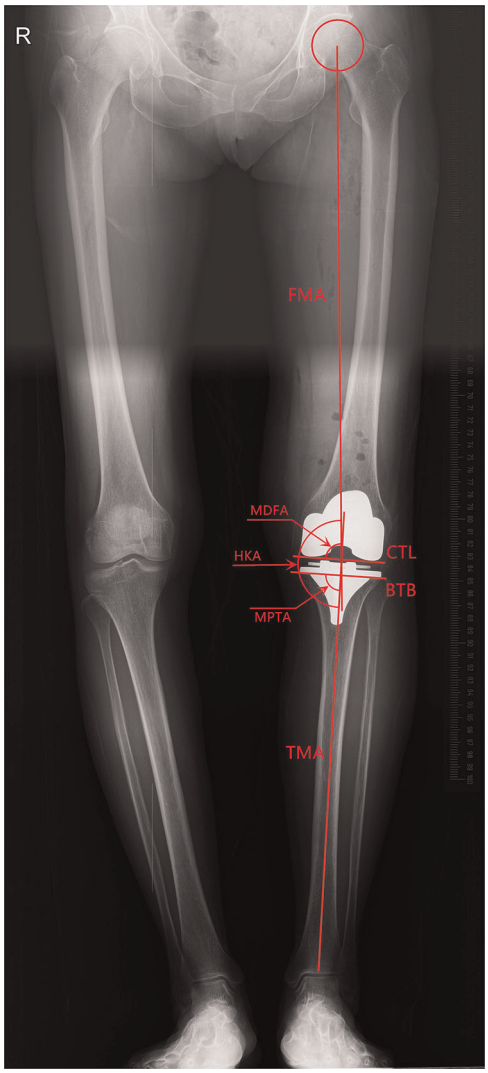

FIGURE 1
Measurement on the coronal plane (FMA, femoral mechanical axis: a line connecting the centers of the femoral head and knee joint; CTL, condylar tangent line; BTB, border of tibial baseplate; TMA, tibial mechanical axis: a line connecting the centers of the knee joint and ankle joint; MDFA, medical distal femoral angle; MPTA, medical proximal tibial angle; HKA, medical angle between FMA and TMA).

(**Figure 3D**). TCA was the mid-perpendicular line of the tibial posterior border (TPB) (**Figure 3B**). TTA was the line connecting the geometrical center (GC) (**Figure 3C**) of an ellipse of best fit around the proximal tibia just below the metal base plate and the center of the most prominent part of the tibial tuberosity (9). Neutral tibial rotational alignment was considered to be 18° internal rotation from TTA to TCA (33). Alignment errors were calculated as the difference between the preoperative surgical plan (HKA = 180°, MDFA = MPTA = FEA = 90°, TSA = 85°, FRA = 0°, TRA = 18°) and actual measurements from radiographs, and the outlier was

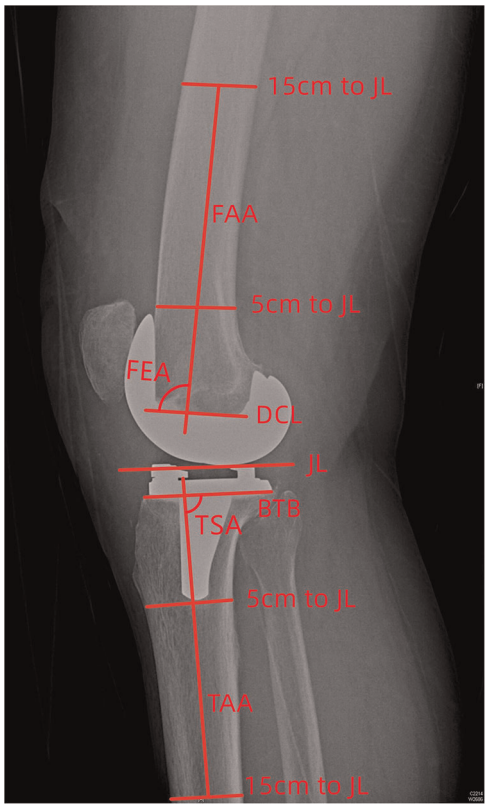

FIGURE 2
Measurement on the sagittal plane (JL, joint line; FAA, femoral anatomical axis; DCL, distal cutting line; BTB, border of tibial baseplate; TAA, tibial anatomical axis; FEA, femoral flexion-extension angle; TSA, tibial posterior slope angle).

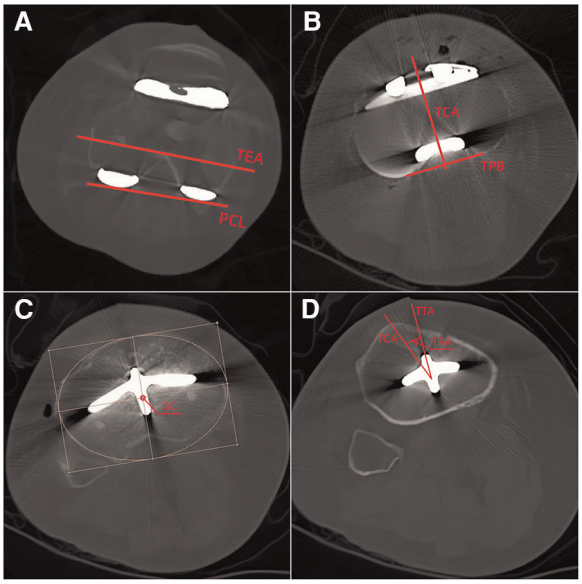

FIGURE 3
Measurement on the transverse plane (**A**: TEA, trans-epicondyle axis; PCL, posterior condylar line; **B**: TPB, tibial posterior border; TCA, tibial component axis: the mid-perpendicular line of the TPB; **C**: GC, geometrical center; **D**: TRA, tibial rotational angle).

considered as the errors more than 3° (17, 18). The outlier rate was the ratio of number of outlier cases to the total cases. The angles on the coronal (HKA, MDFA, MPTA) and sagittal (FEA, TSA) planes were measured by Picpick 5.0 (NGWIN, Korea) while the angles on the transverse plane (FRA, TRA) were measured by Mimics 21.0 (Materialise, Belgium). All measurements were recorded to an accuracy of 0.1°. Each angle was measured three times, with the average being considered the result for that angle.

Post-operative follow-up and evaluation

All patients were followed up by physical examination in the outpatient department for at least 12 months after surgery. The Hospital for Special Surgery knee scoring system (HSS) was selected to assess the clinical outcome (34). The HSS score consisted of six sections, including pain (30 scores), function (22 scores), range of motion (18 scores), muscle force (10 scores), flexion-extension deformity (10 scores) and stability (10 scores). The maximum score achievable is 100 which is the sum of the six sections. The patients were divided into three groups according to their HSS scores. Scores between 85 and 100 were considered excellent (Group A), scores between 84 and 70 points were considered good (Group B), and scores less than 69 points were considered not good (Group C) (34).

Statistical analysis

All statistical analyses were performed using IBM SPSS Statistics 26 (SPSS Inc, Chicago, USA). Power analysis was used to calculate the sample size. The power level was set as 80% with a 0.05 significance level, and the effect size was set as 0.44 (35). The analysis indicated that 43 participants were needed to provide a statistical power of 80%. The Kolmogorov-Smirnov test was used to test the normality of all data and data was regarded as a normal distribution when the significance was greater than 0.05. Quantitative data was expressed as a mean ± standard deviation. The linear correlation between joint alignments (HKA, MDFA, MPTA, FEA, TSA, FRA, TRA) and HSS scores, both the total score and section scores, was analyzed by Pearson analysis when the variable was distributed normally, and by Spearman analysis when the variable was not normally distributed. The correlation coefficient (r) assumes any value from −1 to 1, with an $|r|$ value of less than 0.4 being considered a weak correlation, moderate correlations when $|r|$ is between 0.4 and 0.7, and strong correlations when $|r|$ is more than 0.7.

Difference in alignment among the groups were assessed using a Kruskal-Wallis test. A p-value less than 0.05 was considered significant.

Results

Measurement results

The pre-operative HKA for the patient cohort was 174.10° ± 8.66° and the follow-up time was 16.94 ± 3.61 months. Joint alignment on the three measurement planes is shown in Table 1. On the coronal plane, the post-operative HKA was 179.46° ± 3.36° and presented as varus alignment, which was defined as an angle of less than 180°. The MDFA and MPTA were 89.08° ± 2.59° and 89.78° ± 1.68° respectively, which were similarly considered to be in varus alignment if the angle was less than 90°. On the sagittal plane, the FEA was 91.67° ± 2.18°, with an angle of more than 90° being considered extension. The TSA was 86.20° ± 1.77°, which represents a posterior slope when the angle is less than 90°. On the transverse plane, the FRA and TRA were 1.58° ± 2.83° and 3.32° ± 4.92° respectively, with positive values representing external alignment. The total HSS score and the score from each section are shown in Table 2.

The outlier rates for all the post-operative alignments were calculated. The results showed that FEA had the highest rate (42%) in all alignments (Table 3).

TABLE 1 Measurement results of post-operative joint alignment.

	Mean	SD	Range
Pre-HKA (°)	174.1	8.7	156.1–198.6
Post-HKA (°)	179.5	3.4	173.2–187.5
MDFA (°)	89.1	2.6	83.8–93.5
MPTA (°)	89.8	1.7	86.0–93.6
FEA (°)	91.7	2.2	86.9–96.8
TSA (°)	86.2	1.8	82.9–89.8
FRA (°)	1.6	2.8	−5.6–7.5
TTA (°)	3.3	4.9	−7.7–12.6

TABLE 2 HSS scores of all patients.

HHS	Mean	SD	Range
Total	84.7	9.5	63.0–97.0
Pain	26.1	3.8	15.0–30.0
Function	18.3	3.3	8.0–22.0
ROM	12.2	2.2	5.0–16.0
Muscle strength	9.4	1.4	4.0–10.0
FE deformity	9.1	1.8	5.0–10.0
Stability	9.6	1.2	5.0–10.0

TABLE 3 Outlier rates of component alignment (%).

HKA	MDFA	MPTA	FEA	TSA	FRA
40	34	10	42	18	36

Linear correlation analysis of joint alignment and HSS scores

The correlation coefficients (r) and associated p-values are shown in Table 4. The results show that the FEA had a positive linear correlation with the total HSS score (Figure 4, $r = 0.572$, $p = 0.000$), pain score ($r = 0.347$, $p = 0.013$), function score ($r = 0.535$, $p = 0.000$), ROM score ($r = 0.368$, $p = 0.009$), muscle score ($r = 0.354$, $p = 0.012$) and stability score ($r = 0.312$, $p = 0.028$). Larger values for MDFA were associated with lower FE deformity scores ($r = -0.289$, $p = 0.042$) and the TSA had a positive influence on the ROM scores ($r = 0.436$, $p = 0.002$). Also, it was found that different FRA would result in the different FE deformity scores ($r = 0.312$, $p = 0.027$), and the muscle strength score increased as the TRA increased ($r = 0.402$, $p = 0.004$). Positive correlations between results were confirmed when the r-value was greater than 0.

Difference test results

The patients were divided into different groups according to the total HSS score. There were 28 patients in Group A, 16 patients in Group B, 6 patients in Group C. Patient age, pre-operative HKA, alignments on the three planes for the three groups were assessed using a Kruskal Wallis test. The results revealed significant differences in MDFA ($p = 0.050$) and FEA ($p = 0.001$) between the groups. Except for the parameters mentioned, no significant differences were detected between other measurements ($p > 0.050$). All results are detailed in Table 5.

Discussion

The main finding of this study was that there were significant differences in MDFA and FEA between the three groups with excellent, good and not good scores. It was also found that the total HSS only had a moderate correlation with FEA. Meanwhile, the outlier rate of FEA was the highest among all alignments within the same patient cohort.

This study found similar correlations between alignments and clinical outcomes as previous studies. Kastner et al. demonstrated that the sagittal alignment of femoral components is significantly correlated with the range of motion (36), which supports the associated between FEA and the ROM scores in this present study. Scott et al. found that

TABLE 4 Results of correlation analysis between alignments and clinical scores.

Independent		Dependent						
		Total HSS	Pain	Function	ROM	Muscle strength	FE deformity	Stability
Post-HKA	*r*	−0.085	0.004	−0.062	0.001	−0.047	−0.101	−0.055
	p	0.558	0.980	0.669	0.995	0.744	0.484	0.702
MDFA	*r*	−0.228	−0.050	−0.016	−0.063	−0.153	**−0.289**	−0.135
	p	0.111	0.728	0.913	0.665	0.289	**0.042**	0.349
MPTA	*r*	−0.071	−0.063	−0.198	−0.007	−0.135	0.172	0.118
	p	0.626	0.666	0.168	0.963	0.352	0.232	0.412
FEA	*r*	**0.572**	**0.347**	**0.535**	**0.368**	**0.354**	0.258	**0.312**
	p	**<0.001**	**0.013**	**<0.001**	**0.009**	**0.012**	0.070	**0.028**
TSA	*r*	0.188	0.009	0.214	**0.436**	0.170	0.007	−0.106
	p	0.191	0.952	0.135	**0.002**	0.237	0.962	0.466
FRA	*r*	0.223	0.059	0.180	0.057	−0.008	**0.313**	0.183
	p	0.120	0.685	0.211	0.696	0.955	**0.027**	0.204
TRA	*r*	0.070	−0.007	−0.104	−0.143	**0.402**	0.201	0.063
	p	0.627	0.963	0.474	0.323	**0.004**	0.162	0.663

The bold values represents statistically significant results.

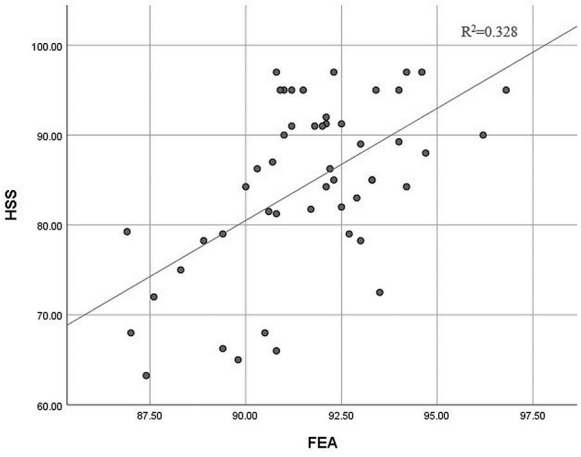

FIGURE 4
Correlation between HSS and FEA (HSS, hospital for special surgery knee scores; FEA, femoral flexion-extension angle).

TABLE 5 The results of the Kruskal-Wallis test between different groups.

	Group A		Group B		Group C		*p*
	Mean	SD	Mean	SD	Mean	SD	
Age	68.54	9.57	68.24	7.94	70.33	4.23	0.892
Pre-HKA	173.05	8.63	175.11	8.78	177.65	5.25	0.303
Post-HKA	178.97	2.67	180.00	4.13	181.57	4.39	0.413
MDFA	88.91	2.39	89.15	2.84	91.63	1.98	**0.050**
MPTA	89.54	1.20	90.16	2.17	89.93	2.52	0.499
FEA	92.62	1.66	90.50	2.24	89.15	1.59	**0.001**
TSA	86.31	2.07	86.18	1.21	85.70	1.63	0.858
FRA	2.08	2.14	0.81	3.49	−0.72	3.66	0.244
TRA	4.05	4.23	2.37	5.80	2.75	5.06	0.550

The bold values represents statistically significant results.

the alignment of the femoral component on the sagittal plane was associated with anterior knee pain, and femoral component extension was a major risk factor (37). Similarly, this study found a significant correlation between FEA and pain score. Meanwhile, the functional scores had a moderate correlation with FEA, which is somewhat supported by Okamoto's study that good femoral sagittal alignment leads to better joint function (38). In this study, the FEA was also correlated with muscle strength and stability. Koh et al. reported that the quadriceps force, collateral ligament force and patella-femoral contact stress decreased as the angle between the axis of the femoral component and anterior cortex became smaller (39). This indicates that changes in the biomechanical environment around the knee may affect muscle strength and joint stability. Also, the significant correlation between FE-deformity scores and MDFA and FRA is supported by a study by Matziolis et al. detailing that distal femoral resection influences the flexion deformity of knee joint (40).

In this study, the FEA had the highest outlier rate, which is similar to findings from previous studies (**Table 6**). It is common for surgeons to attempt to align the femoral component when the cutting line is perpendicular to the anatomical axis on the sagittal plane and avoid the notch of the anterior cortical bone (48). However, it is not easy to identify the anatomical axis during conventional operations. When an intramedullary rod is used to represent the anatomical axis of the femur, errors with positioning of the entry point and insertion direction might lead to the rod being offset from the true axis. Such differences may also

TABLE 6 Comparison of outlier rates from published studies (%).

Year	Author	Cases	HKA	MDFA	MPTA	FEA	TSA	FRA
	Present study	50	40.00	34.00	10.00	42.00	18.00	36.00
2017	Ueyama (41)	75	-	13.30	4.00	21.30	8.00	-
2014	Huang (42)	37	27.10	27.10	2.70	43.20	0.00	10.90
2014	Chen (43)	72	27.80	50.00	25.00	36.10	16.70	-
2014	Kotela (44)	46	30.43	26.09	19.57	47.82	19.56	-
2014	Yan (45)	30	53.30	23.30	20.00	56.70	13.30	-
2014	Victor (46)	64	28.10	14.10	3.10	48.40	3.10	23.00
2013	Boonen (47)	82	18.00	13.00	2.00	65.00	28.00	-

contribute to malalignment on the coronal plane. While variations in radiographic assessments could also influence the results, when using the anatomical axis and anterior cortical axis to evaluate femoral alignment on the sagittal plane, Jenny et al. reported little difference between the two axes and any variation in readings will likely have little clinical relevance (32). Tibial rotational alignment is considered one of the most controversial alignment methods in TKA because of the different reference landmarks used for the tibia and difference methods of alignment (4). This study performed a tibial trial during rotational alignment of the tibial component to confirm proper positioning, but this led to an unclear target of TRA value, and hence the outlier rate of TRA was not calculated.

The results showed a correlation between femoral component alignment on the sagittal plane (FEA) and complications after TKA, including pain, flexion contracture, and a restricted range of motion. A 10-year follow-up study by Scott et al. found sagittal plane positioning of the femoral component to be associated with long-term anterior knee pain, and it was suggested that femoral component extension might be a major risk factor for knee pain (37). Okamoto et al. found that FEA was significantly different between groups with differing degrees of flexion contracture, and they reported that FEA and body height were independent predictive risk factors for residual flexion contracture of more than 10° (38). Changes in the mechanical and kinematic environment in the knee joint resulting from different FEA were a likely reason for these complications.

The sagittal positioning of the femoral component is recognized as an important factor in knee joint mechanics and kinematics. It was reported that the femoral flexion-extension angle influenced the femorotibial contact position in the knee flexion which changed the arm of the quadriceps force and patellofemoral (PF) contact force (49). Using finite element models, Koh et al. investigated how variations in the FEA impacted knee mechanics and kinematics, and found the femorotibial contact points were positioned more posteriorly with larger FEA angles, and the quadriceps force, as well as the PF contact force, was reduced because of the decreased lever arm. It was suggested that placing the prosthesis in slight flexion could be an effective alternative technique to enable positive biomechanical effects with TKA (39, 50). Besides, the discrepancy of medial and lateral collateral ligaments between different femoral flexion-extension angles, the collateral ligament force decreased as the femoral component flexed during the knee bending. Large amounts of sagittal femoral component extension may be harmful to the collateral ligament. Errors in femoral component sagittal alignment contribute to imbalanced soft tissue that leads to instability and a limited range of motion (51). However, while these factors may improve clinical outcomes, they must also be considered when evaluating differences between studies and patient satisfaction.

Although digital techniques such as navigation, custom instrumentation and robotics have been commercially available and widely used for a number of years, conventional surgical techniques are still common because of the additional surgical time and costs associated with more advanced methods (27, 29, 30, 52). Moreover, mechanical alignment is regarded as one of the best approaches to TKA, with many studies demonstrating acceptable joint kinematics when the error of coronal alignment is less than 3°. However, contrasting studies have also reported that coronal alignment is not an accurate predictor of clinical outcomes and maintaining alignment within $0 \pm 3°$ is not a "safe zone" when using more modern personalized alignment strategies (22, 53). The sagittal alignment for TKA, especially for the femoral component needs more consideration, and the surgical procedures and tools need to be improved to allow for more precise alignment.

There are also some limitations in this study. First, 50 TKA patients were enrolled in the study because of the considerable time and cost associated with patient examination. However, the sample size was sufficient according to the power analysis to assess the correlations between alignments and clinical scores. Moreover, the minimum follow-up time was 12 months. Future studies may consider longer-term follow-up.

Conclusion

A significant and moderate correlation was found between FEA and the HSS score, and the FEA had the highest outlier rate. This suggests that FEA should be carefully considered when planning TKA and implant positioning. Surgical techniques and tools, especially for conventional surgery, need to be enhanced, to improve surgical accuracy and patient satisfaction.

Data availability statement

The original contributions presented in the study are included in the article/Supplementary Material, further inquiries can be directed to the corresponding author/s.

Ethics statement

The studies involving human participants were reviewed and approved by Medical Ethics Committee of the Second Affiliated Hospital of PLA Army Military Medical University. The patients/participants provided their written informed consent to participate in this study. Written informed consent was obtained from the individual(s) for the publication of any potentially identifiable images or data included in this article.

Author contributions

CKC: conceptualization, methodology, project administration, supervision, writing-review and editing. MW: conceptualization, resources, supervision, writing-review and editing. YL: formal analysis, investigation, data curation, writing-original draft preparation, writing-review and editing. MZ: formal analysis, data curation, writing-original draft preparation, writing-review and editing. TR: data curation. HW, MN and CF: investigation, review and editing. All authors have agreed to be personally accountable for their own contributions and ensure that questions related to the accuracy and integrity of any part of the work have been appropriately investigated and resolved with reference to the literature when needed. All authors contributed to the article and approved the submitted version.

Funding

This research was supported by the Science and Technology Innovation and Application Development Project of Chongqing (2021MSXM197) and Ningbo Public Welfare Science and Technology project (2022S064).

Acknowledgments

We would like to thank Colin McClean for his assistance with editing this manuscript.

Conflict of interest

The authors declare that the research was conducted in the absence of any commercial or financial relationships that could be construed as a potential conflict of interest.

Publisher's note

All claims expressed in this article are solely those of the authors and do not necessarily represent those of their affiliated organizations, or those of the publisher, the editors and the reviewers. Any product that may be evaluated in this article, or claim that may be made by its manufacturer, is not guaranteed or endorsed by the publisher.

References

1. Hamel MB, Toth M, Legedza A, Rosen MP. Joint replacement surgery in elderly patients with severe osteoarthritis of the hip or knee: decision making, postoperative recovery, and clinical outcomes. *Arch Intern Med.* (2008) 168 (13):1430–40. doi: 10.1001/archinte.168.13.1430

2. Bourne RB, Chesworth BM, Davis AM, Mahomed NN, Charron KD. Patient satisfaction after total knee arthroplasty: who is satisfied and who is not? *Clin Orthop Relat Res.* (2010) 468(1):57–63. doi: 10.1007/s11999-009-1119-9

3. Peltola M, Malmivaara A, Paavola M. Learning curve for new technology? A nationwide register-based study of 46,363 total knee arthroplasties. *J Bone Joint Surg Am.* (2013) 95(23):2097–103. doi: 10.2106/jbjs.L.01296

4. Saffarini M, Nover L, Tandogan R, Becker R, Moser LB, Hirschmann MT, et al. The original akagi line is the most reliable: a systematic review of landmarks for rotational alignment of the tibial component in Tka. *Knee Surg Sports Traumatol Arthrosc.* (2019) 27(4):1018–27. doi: 10.1007/s00167-018-5131-z.

5. Yau WP, Chiu KY. Cutting errors in total knee replacement: assessment by computer assisted surgery. *Knee Surg Sports Traumatol Arthrosc.* (2008) 16 (7):670–3. doi: 10.1007/s00167-008-0550-x

6. Thiele K, Perka C, Matziolis G, Mayr HO, Sostheim M, Hube R. Current failure mechanisms after knee arthroplasty have changed: polyethylene wear is less common in revision surgery. *J Bone Joint Surg Am.* (2015) 97(9):715–20. doi: 10.2106/jbjs.M.01534

7. Ben-Shlomo Y, Blom A, Boulton C, Brittain R, Clark E, Craig R, et al. *National joint registry annual reports. The National Joint Registry 17th Annual Report 2020.* London: National Joint Registry © National Joint Registry (2020).

8. Berger RA, Crossett LS, Jacobs JJ, Rubash HE. Malrotation causing patellofemoral complications after total knee arthroplasty. *Clin Orthop Relat Res.* (1998) 356:144–53. doi: 10.1097/00003086-199811000-00021

9. Nicoll D, Rowley DI. Internal rotational error of the tibial component is a major cause of pain after total knee replacement. *J Bone Joint Surg Br*. (2010) 92(9):1238–44. doi: 10.1302/0301-620x.92b9.23516

10. Liau JJ, Cheng CK, Huang CH, Lo WH. The effect of malalignment on stresses in polyethylene component of total knee prostheses–a finite element analysis. *Clin Biomech*. (2002) 17(2):140–6. doi: 10.1016/s0268-0033(01)00109-7

11. Johnston H, Abdelgaied A, Pandit H, Fisher J, Jennings LM. The effect of surgical alignment and soft tissue conditions on the kinematics and wear of a fixed bearing total knee replacement. *J Mech Behav Biomed Mater*. (2019) 100:103386. doi: 10.1016/j.jmbbm.2019.103386

12. Wang ZW, Wen L, Luan YC, Ma DS, Dong X, Cheng CK, et al. Restoration of joint inclination in total knee arthroplasty offers little improvement in joint kinematics in neutrally aligned extremities. *Front Bioeng Biotechnol*. (2021) 9:673275. doi: 10.3389/fbioe.2021.673275

13. Fang C, Luan Y, Wang Z, Shao L, Qu T, Cheng CK. Moderate external rotation of tibial component generates more natural kinematics than internal rotation after total knee arthroplasty. *Front Bioeng Biotechnol*. (2022) 10:910311. doi: 10.3389/fbioe.2022.910311

14. Ro J, Ro DH, Kang Y, Han HS, Shin CS. Biomechanical effect of coronal alignment and ligament laxity in total knee arthroplasty: a simulation study. *Front Bioeng Biotechnol*. (2022) 10:851495. doi: 10.3389/fbioe.2022.851495

15. Choong PF, Dowsey MM, Stoney JD. Does accurate anatomical alignment result in better function and quality of life? Comparing conventional and computer-assisted total knee arthroplasty. *J Arthroplasty*. (2009) 24(4):560–9. doi: 10.1016/j.arth.2008.02.018

16. Cherian JJ, Kapadia BH, Banerjee S, Jauregui JJ, Issa K, Mont MA. Mechanical, anatomical, and kinematic axis in Tka: concepts and practical applications. *Curr Rev Musculoskelet Med*. (2014) 7(2):89–95. doi: 10.1007/s12178-014-9218-y

17. Bonner TJ, Eardley WG, Patterson P, Gregg PJ. The effect of post-operative mechanical axis alignment on the survival of primary total knee replacements after a follow-up of 15 years. *J Bone Joint Surg Br*. (2011) 93(9):1217–22. doi: 10.1302/0301-620x.93b9.26573

18. Abdel MP, Oussedik S, Parratte S, Lustig S, Haddad FS. Coronal alignment in total knee replacement: historical review, contemporary analysis, and future direction. *Bone Joint J*. (2014) 96-b(7):857–62. doi: 10.1302/0301-620x.96b7.33946

19. Slevin O, Hirschmann A, Schiapparelli FF, Amsler F, Huegli RW, Hirschmann MT. Neutral alignment leads to higher knee society scores after total knee arthroplasty in preoperatively non-varus patients: a prospective clinical study using 3D-CT. *Knee Surg Sports Traumatol Arthrosc*. (2018) 26(6):1602–9. doi: 10.1007/s00167-017-4744-y

20. Mugnai R, Zambianchi F, Digennaro V, Marcovigi A, Tarallo L, Del Giovane C, et al. Clinical outcome is not affected by total knee arthroplasty alignment. *Knee Surg Sports Traumatol Arthrosc*. (2016) 24(10):3339–45. doi: 10.1007/s00167-016-4094-1

21. Abdel MP, Ollivier M, Parratte S, Trousdale RT, Berry DJ, Pagnano MW. Effect of postoperative mechanical axis alignment on survival and functional outcomes of modern total knee arthroplasties with cement: a concise follow-up at 20 years. *J Bone Joint Surg Am*. (2018) 100(6):472–8. doi: 10.2106/jbjs.16.01587

22. Schelker BL, Nowakowski AM, Hirschmann MT. What is the "safe zone" for transition of coronal alignment from systematic to a more personalised one in total knee arthroplasty? A systematic review. *Knee Surg Sports Traumatol Arthrosc*. (2022) 30(2):419–27. doi: 10.1007/s00167-021-06811-5

23. Kim YH, Park JW, Kim JS, Park SD. The relationship between the survival of total knee arthroplasty and postoperative coronal, sagittal and rotational alignment of knee prosthesis. *Int Orthop*. (2014) 38(2):379–85. doi: 10.1007/s00264-013-2097-9

24. Ahmed I, Paraoan V, Bhatt D, Mishra B, Khatri C, Griffin D, et al. Tibial component sizing and alignment of tkr components does not significantly affect patient reported outcome measures at six months. A case series of 474 participants. *Int J Surg*. (2018) 52:67–73. doi: 10.1016/j.ijsu.2018.02.039

25. Thielemann FW, Konstantinids L, Herget GW, Knothe D, Helwig P, Sudkamp NP, et al. Effect of rotational component alignment on clinical outcome 5 to 7 years after tka with the Columbus knee system. *Orthopedics*. (2016) 39(3 Suppl):S50-5. doi: 10.3928/01477447-20160509-17

26. Panni AS, Ascione F, Rossini M, Braile A, Corona K, Vasso M, et al. Tibial internal rotation negatively affects clinical outcomes in total knee arthroplasty: a systematic review. *Knee Surg Sports Traumatol Arthrosc*. (2018) 26(6):1636–44. doi: 10.1007/s00167-017-4823-0

27. Yang JH, Dahuja A, Kim JK, Yun SH, Yoon JR. Alignment in knee flexion position during navigation-assisted total knee arthroplasty. *Knee Surg Sports Traumatol Arthrosc*. (2016) 24(8):2422–9. doi: 10.1007/s00167-015-3589-5

28. Giannotti S, Sacchetti F, Citarelli C, Bottai V, Bianchi N, Agostini G, et al. Single-use, patient-specific instrumentation technology in knee arthroplasty: a comparative study between standard instrumentation and psi efficiency system. *Musculoskelet Surg*. (2020) 104(2):195–200. doi: 10.1007/s12306-019-00612-3

29. Onggo JR, Onggo JD, De Steiger R, Hau R. Robotic-assisted total knee arthroplasty is comparable to conventional total knee arthroplasty: a meta-analysis and systematic review. *Arch Orthop Trauma Surg*. (2020) 140(10):1533–49. doi: 10.1007/s00402-020-03512-5

30. Batailler C, Fernandez A, Swan J, Servien E, Haddad FS, Catani F, et al. Mako CT-based robotic arm-assisted system is a reliable procedure for total knee arthroplasty: a systematic review. *Knee Surg Sports Traumatol Arthrosc*. (2021) 29(11):3585–98. doi: 10.1007/s00167-020-06283-z

31. Abane L, Zaoui A, Anract P, Lefevre N, Herman S, Hamadouche M. Can a single-use and patient-specific instrumentation be reliably used in primary total knee arthroplasty? A multicenter controlled study. *J Arthroplasty*. (2018) 33(7):2111–8. doi: 10.1016/j.arth.2018.02.038

32. Jenny JY, Barbe B. Small differences between anatomical and mechanical sagittal femur axes: a radiological and navigated study of 50 patients. *Arch Orthop Trauma Surg*. (2012) 132(7):1053–7. doi: 10.1007/s00402-012-1500-0

33. Berger RA, Crossett LS. Determining the rotation of thefemoral and tibial components in total knee arthroplasty: a computer tomography technique. *Oper Tech Orthop*. (1998) 8(3):128–33. doi: 10.1016/S1048-6666(98)80022-0

34. Alicea J. Knee scores in total knee arthroplasty. In: GR Scuderi, AJ Tria, editors. *Surgical techniques in total knee arthroplasty*. New York, NY: Springer New York (2002). p. 31–8.

35. Valkering KP, Breugem SJ, van den Bekerom MP, Tuinebreijer WE, van Geenen RC. Effect of rotational alignment on outcome of total knee arthroplasty. *Acta Orthop*. (2015) 86(4):432–9. doi: 10.3109/17453674.2015.1022438

36. Kastner N, Sternbauer S, Friesenbichler J, Vielgut I, Wolf M, Glehr M, et al. Impact of the tibial slope on range of motion after low-contact-stress, mobile-bearing, total knee arthroplasty. *Int Orthop*. (2014) 38(2):291–5. doi: 10.1007/s00264-013-2242-5

37. Scott CEH, Clement ND, Yapp LZ, MacDonald DJ, Patton JT, Burnett R. Association between femoral component sagittal positioning and anterior knee pain in total knee arthroplasty: a 10-year case-control follow-up study of a cruciate-retaining single-radius design. *J Bone Joint Surg Am*. (2019) 101(17):1575–85. doi: 10.2106/jbjs.18.01096

38. Okamoto Y, Otsuki S, Nakajima M, Jotoku T, Wakama H, Neo M. Sagittal alignment of the femoral component and patient height are associated with persisting flexion contracture after primary total knee arthroplasty. *J Arthroplasty*. (2019) 34(7):1476–82. doi: 10.1016/j.arth.2019.02.051

39. Koh YG, Hong HT, Lee HY, Kim HJ, Kang KT. Influence of variation in sagittal placement of the femoral component after cruciate-retaining total knee arthroplasty. *J Knee Surg*. (2021) 34(4):444–51. doi: 10.1055/s-0039-1696958

40. Matziolis G, Loos M, Böhle S, Schwerdt C, Roehner E, Heinecke M. Effect of additional distal femoral resection on flexion deformity in posterior-stabilized total knee arthroplasty. *Knee Surg Sports Traumatol Arthrosc*. (2020) 28(9):2924–9. doi: 10.1007/s00167-019-05675-0

41. Ueyama H, Matsui Y, Minoda Y, Matsuura M, Nakamura H. Using accelerometer-based portable navigation to perform accurate total knee arthroplasty bone resection in Asian patients. *Orthopedics*. (2017) 40(3):e465–e72. doi: 10.3928/01477447-20170223-01

42. Huang TW, Peng KT, Huang KC, Lee MS, Hsu RW. Differences in component and limb alignment between computer-assisted and conventional surgery total knee arthroplasty. *Knee Surg Sports Traumatol Arthrosc*. (2014) 22(12):2954–61. doi: 10.1007/s00167-014-3331-8

43. Chen X, Wang H, Cai Y, Zhu Q, Zhu J. Sagittal component alignment is less reliable than coronal component alignment in a Chinese population undergoing navigated tka. *J Orthop Surg Res*. (2014) 9:51. doi: 10.1186/s13018-014-0051-1

44. Kotela A, Kotela I. Patient-specific computed tomography based instrumentation in total knee arthroplasty: a prospective randomized controlled study. *Int Orthop*. (2014) 38(10):2099–107. doi: 10.1007/s00264-014-2399-6

45. Yan CH, Chiu KY, Ng FY, Chan PK, Fang CX. Comparison between patient-specific instruments and conventional instruments and computer navigation in total knee arthroplasty: a randomized controlled trial. *Knee Surg Sports Traumatol Arthrosc*. (2015) 23(12):3637–45. doi: 10.1007/s00167-014-3264-2

46. Victor J, Dujardin J, Vandenneucker H, Arnout N, Bellemans J. Patient-specific guides do not improve accuracy in total knee arthroplasty: a prospective randomized controlled trial. *Clin Orthop Relat Res*. (2014) 472(1):263–71. doi: 10.1007/s11999-013-2997-4

47. Boonen B, Schotanus MG, Kerens B, van der Weegen W, van Drumpt RA, Kort NP. Intra-operative results and radiological outcome of conventional and patient-specific surgery in total knee arthroplasty: a multicentre, randomised controlled trial. *Knee Surg Sports Traumatol Arthrosc*. (2013) 21(10):2206–12. doi: 10.1007/s00167-013-2620-y

48. Gromov K, Korchi M, Thomsen MG, Husted H, Troelsen A. What is the optimal alignment of the tibial and femoral components in knee arthroplasty? *Acta Orthop*. (2014) 85(5):480–7. doi: 10.3109/17453674.2014.940573

49. Browne C, Hermida JC, Bergula A, Colwell Jr. CW, D'Lima DD. Patellofemoral forces after total knee arthroplasty: effect of extensor moment arm. *Knee*. (2005) 12(2):81–8. doi: 10.1016/j.knee.2004.05.006

50. Kang KT, Koh YG, Son J, Kwon OR, Park KK. Flexed femoral component improves kinematics and biomechanical effect in posterior stabilized total knee arthroplasty. *Knee Surg Sports Traumatol Arthrosc*. (2019) 27(4):1174–81. doi: 10.1007/s00167-018-5093-1

51. Koh YG, Lee JA, Lee HY, Suh DS, Park JH, Kang KT. Finite element analysis of femoral component sagittal alignment in mobile-bearing total knee arthroplasty. *Bio-Med Mater Eng*. (2022) 33(3):195–207. doi: 10.3233/bme-211280

52. Zheng G, Nolte LP. Computer-assisted orthopedic surgery: current state and future perspective. *Front Surg*. (2015) 2:66. doi: 10.3389/fsurg.2015.00066

53. Zhu S, Zhang X, Chen X, Wang Y, Li S, Qian W, et al. Degree of coronal alignment correction can't predict knee function in total knee replacement. *BMC Surg*. (2021) 21(1):383. doi: 10.1186/s12893-021-01372-3

frontiers | Frontiers in Surgery

TYPE Original Research
PUBLISHED 13 October 2022
DOI 10.3389/fsurg.2022.1035681

Check for updates

OPEN ACCESS

EDITED BY
Tsung-Yuan Tsai,
Shanghai Jiao Tong University, China

REVIEWED BY
Xing Du,
First Affiliated Hospital of Chongqing Medical University, China
Wei Zhang,
Ningbo University, China
Zhongkai Zhang,
Shandong Provincial Hospital, China

*CORRESPONDENCE
Xin Liu
Biasas@aliyun.com

SPECIALTY SECTION
This article was submitted to Orthopedic Surgery, a section of the journal Frontiers in Surgery

RECEIVED 03 September 2022
ACCEPTED 26 September 2022
PUBLISHED 13 October 2022

CITATION
Yang D, Liu X, Zhou Y, Xu Y and Huang Q (2022) A novel scoring system to predict the residual back pain after percutaneous kyphoplasty for osteoporotic vertebral compression fracture. Front. Surg. 9:1035681. doi: 10.3389/fsurg.2022.1035681

COPYRIGHT
© 2022 Yang, Liu, Zhou, Xu and Huang. This is an open-access article distributed under the terms of the Creative Commons Attribution License (CC BY). The use, distribution or reproduction in other forums is permitted, provided the original author(s) and the copyright owner(s) are credited and that the original publication in this journal is cited, in accordance with accepted academic practice. No use, distribution or reproduction is permitted which does not comply with these terms.

A novel scoring system to predict the residual back pain after percutaneous kyphoplasty for osteoporotic vertebral compression fracture

Dongjun Yang, Xin Liu*, Yang Zhou, Yong Xu and Qiangkai Huang

Department of Orthopedics, Second People's Hospital of Chengdu, Chengdu, China

Objective: To establish a scoring system to predict the residual back pain after percutaneous kyphoplasty (PKP) for osteoporotic vertebral compression fracture (OVCF).

Materials and methods: We retrospectively reviewed the clinical records of 98 patients who were diagnosed of single-vertebral OVCF and underwent PKP surgery in our department from January 2015 to December 2017. The following clinical characteristics including age, gender, disease course, fracture location, fracture type, segmental kyphosis, and bone cement volume were all recorded, and the effects of these factors on postoperative pain (at 1-month and 6-month postoperative) were also analyzed respectively. Based on 6-month postoperative VAS score, the included patients were divided into two groups, namely the residual back pain group (19 patients) and the non-residual back pain group (79 patients). The independent risk factors of residual back pain after PKP were screened and the scoring system was established by the multivariate logistic regression analysis. The performance of this scoring system was also prospectively validated using the clinical data of 45 patients with single-vertebral OVCF from January 2018 to December 2019.

Results: The scoring system was consist of five clinical characteristics which were confirmed as significant predictors of residual back pain after PKP, namely, age ≥60 years ($P = 0.021$), fracture location = thoracic or lumbar ($P = 0.002$), fracture type = OF4 type ($P = 0.018$), segmental kyphosis ≥20° ($P = 0.014$), and bone cement volume <5 ml ($P = 0.001$). Patients in the residual back pain group showed a significant higher score than the non-residual back pain group (6.84 ± 1.71 vs. 2.66 ± 1.97, $t = 8.499$, $P < 0.001$), and the optimal cut-off value for the scoring system was 5 points. The sensitivity and specificity of the scoring system for predicting residual back pain after PKP were 84.21% and 87.34%, respectively, in derivation set and 78.57% and 83.87% in validation set.

Conclusion: This novel scoring system showed satisfactory diagnostic efficacy in predicting residual back pain after PKP for single-vertebral OVCF. Patients with the score of 5–9 had a high risk of postoperative residual back pain, while the patients with score of 0–4 was low.

KEYWORDS

osteoporotic vertebral compression fracture (OVCF), percutaneous kyphoplasty (PKP), residual back pain, prediction, scoring system

Introduction

Osteoporosis is a systemic bone disease manifested by the decrease of bone density and quality, the destruction of bone micro-structure, and the increase of bone fragility, and often result in fractures (1). Osteoporotic vertebral compression fracture (OVCF) is the most common fracture type in osteoporosis patients. With the improvement of average life expectancy and the aggravation of population aging, the incidence of OVCF is increasing year by year (2). OVCF often leads to back pain, spinal kyphosis and even paralysis, thus seriously affect patients' quality of life (3).

The treatment of OCVF included conservative treatment and surgical treatment. Conservative treatment mainly included bed rest, wearing waist brace, and analgesic drugs (4). However, patients' adherence to strict bed rest was not high and patients may suffer high risk of gastrointestinal bleeding due to the use of nonsteroidal anti-inflammatory drugs (NSAIDs) (5). Surgical treatment mainly included percutaneous vertebroplasty (PVP) and percutaneous kyphoplasty (PKP). Compared with PVP, PKP was reported with low risk of bone cement leakage and good ability of kyphosis correction, and thus is most commonly used at present (6, 7).

It was reported PKP can effectively relieve pain, and thus promote the early activities after surgery, shorten the time in bed, and reduce the risk of postoperative complications (8). Therefore, whether an OVCF patient can achieve effective pain relief after PKP was the focus of the attentions of both surgeons and patients (9). However, most of current studies focused on PKP-related complications, such as bone cement leakage and recurrent vertebral fractures (10, 11). Although the risk factors for non-relief of pain after PKP was reported (12), surgeons can hardly objectively and accurately predict the pain relief after PKP due to the so many reported risk factors and different effects of each risk factor on pain relief.

Therefore, we conducted this study to identify the clinical characteristics which can predict residual back pain and develop a novel scoring system to help spinal surgeon to predict residual back pain after PKP. We also validated the performance of this scoring system and confirmed its satisfactory ability in predicting residual back pain after PKP in OVCF.

Materials and methods

This study was approved by the Ethics Committee of the Second People's Hospital of Chengdu and carried out in accordance with the Declaration of Helsinki. All of the participants provided their written informed consent to participate in this study. The work has been reported in line with the STARD criteria (13).

Derivation of the scoring system

Patients selection

We retrospectively reviewed the medical records of hospitalized patients diagnosed of OVCF in our department from January 2015 to December 2017 to form the derivation set.

Inclusion criteria: (1) Acute single-vertebral OVCF (high signal in lipid suppressor sequence on MRI imaging); (2) Bone mineral density (BMD) examination (dual-energy x-ray absorption) confirmed osteoporosis (T score ≤ -2.5); (3) The fracture type was OF2, OF3, or OF4 according to the Classification of Osteoporotic Thoracolumbar recommended by the Spine Section of the German Society for Orthopaedics and Trauma (DGOU) (14).

Exclusion Criteria: (1) Previous history of spinal surgery; (2) Long-term use of analgesics before hospitalization, such as NSAIDs, opioids; (3) Pathologic vertebral fracture caused by tumor, infection; (4) Less than 12-month follow-up or incomplete medical record data.

According to the patients selection criteria, a total of 98 patients were finally included in the derivation set with 29 males and 69 females. The average age of the included patients was 64.72 ± 7.89 years and the average disease course was 3.01 ± 1.45 months. The detailed clinical characteristics of the included patients were shown in **Table 1**.

TABLE 1 Clinical characteristics of the included patients.

Characteristic	Value
Number of patients (*n*)	98
Age (year, mean ± SD)	64.72 ± 7.89
Gender (*n*, %)	
Male	29 (29.59%)
Female	69 (70.41%)
Course of disease (month, mean ± SD)	3.01 ± 1.45
Fracture location (*n*, %)	
Thoracic vertebrae (T_4–T_9)	7 (7.14%)
Thoracolumbar vertebrae (T_{10}–L_2)	77 (78.57%)
Lumbar vertebrae (L_3–L_5)	14 (14.29%)
Fracture type (*n*, %)	
OF2/OF3 type	41 (41.84%)
OF4 type	57 (58.16%)
Segmental kyphosis (*n*, %)	
<20°	60 (61.22%)
≥20°	38 (38.78%)
Bone cement volume (*n*, %)	
<5 ml	44 (44.90%)
≥5 ml	54 (55.10%)
VAS (score, mean ± SD)	
Preoperative	8.45 ± 0.89
1 month postoperative	4.56 ± 0.76
6 months postoperative	5.18 ± 0.74

Data collection

Based on previous studies and our experience, we included the following predictors for residual back pain after PKP. In addition, postoperative VAS scores at different follow-up time were also recorded.

(1) Patient related data: (a) Age of patient: age ≥60 years or <60 years; (b) Gender of patient: male or female; (c) Disease course: ≥6 weeks or <6 weeks.
(2) Preoperative imaging data: (a) Fracture location: thoracic vertebrae (T_4–T_9), thoracolumbar vertebrae (T_{10}–L_2), or lumbar vertebrae (L_3–L_5); (b) Fracture type: OF3 type, OF3 type, or OF4 type; (c) Segmental kyphosis: the kyphosis angle was defined as the angle between the superior and inferior endplates of the fractured vertebra, kyphosis angle <20° or ≥20°.
(3) Surgery related data: bone cement volume <5 ml or ≥5 ml.
(4) Follow-up outcomes: VAS score at preoperatively, 1 month postoperatively, and 6 months postoperatively. Postoperative residual back pain was defined as the VAS score at 6 months postoperatively was more than four or the patients still need analgesic medication to contribute a good sleep.

Development of the scoring system

Firstly, the effects of these clinical characteristics, including age, gender, course of disease, fracture location, fracture type, segmental kyphosis, and bone cement volume, on postoperative pain (at 1 month and 6 months postoperatively) were all analyzed respectively. Secondly, all the included patients were divided into two groups, namely, non-residual back pain group and residual back pain group according to the 6-month postoperative follow-up outcomes. Next, multivariate logistic regression analysis was performed. According to the results of multivariate logistic regression analysis, the indexes with $P < 0.05$ were considered the final predictors for postoperative residual back pain and, thus, determined as the items of the scoring system. Then, we established the weighted score of each item based on the relative size of Odds Ratio (OR) according to the method reported by previous research (15). Finally, we identified the appropriate cut-off points for the scoring system using ROC curves corresponding to the point on the curve nearest the upper left corner of the ROC graph.

Validation of the scoring system

From January 2018 to December 2019, we prospectively included patients to validate the accuracy of the scoring system. The following criteria were used to select patients to form the validation set. Inclusion criteria: (1) MRI suggested acute single-vertebral OVCF; (3) BMD examination showed T score ≤−2.5; (4) OF2, OF3, or OF4 type fracture. Exclusion Criteria: Exclusion Criteria: (1) Previous history of spinal surgery; (2) Long-term use of analgesics before hospitalization; (3) Pathologic vertebral fracture caused by tumor, infection.

Patients signed informed consent and then underwent PKP surgery. Before discharge, surgeon predicted whether the patient will suffer from residual back pain at 6 months postoperatively according to the scoring system (predictive outcome). At 6 months after surgery, the patient will be assessed whether they truly develop residual back pain (true outcome). The accuracy of the scoring system was evaluated by comparing the consistency between the predictive outcome and the true outcome.

Statistical analysis

The effects of clinical characteristics on postoperative back pain at different follow-up point were analyzed by independent-samples *t*-test. The significant predictors of residual back pain at 6 months postoperatively were evaluated by multivariate logistic regression analysis. The items of the scoring system were determined by multivariate logistic regression, and the weighted score of each item was based on the relative size of the OR. The optimal cut-off point was made by using ROC curves. $P < 0.05$ was set of statistical significance. The SPSS version 10.0 software was used for statistical analysis.

Results

Derivation of the scoring system

It was showed that age ≥60 years ($P = 0.03$ and $P = 0.02$, respectively), course of disease ≥6 weeks ($P < 0.001$ and $P < 0.001$, respectively), fracture location = thoracic or lumbar ($P < 0.001$ and $P = 0.002$, respectively), fracture type = OF4 type ($P = 0.04$ and $P = 0.03$, respectively), segmental kyphosis ≥20° ($P < 0.001$ and $P < 0.001$, respectively), and bone cement volume <5 ml ($P = 0.03$ and $P = 0.004$, respectively), all had negative effects on postoperative back pain at both 1 month and 6 months postoperatively (**Figure 1**).

According to the back pain at 6 months postoperatively, 19 patients suffered residual back pain while 79 patients did not, and the incidence of postoperative residual back pain was 19.39%. Multivariate logistic regression analysis showed five clinical characteristics, namely, age ≥60 years ($P = 0.021$), fracture location = thoracic or lumbar ($P = 0.002$), fracture type = OF4 type ($P = 0.018$), segmental kyphosis ≥20° ($P = 0.014$), and bone cement volume <5 ml ($P = 0.001$) were significant predictors of postoperative residual back pain (**Table 2**).

We developed a scoring system based on these five clinical characteristics that were confirmed significant predictors of

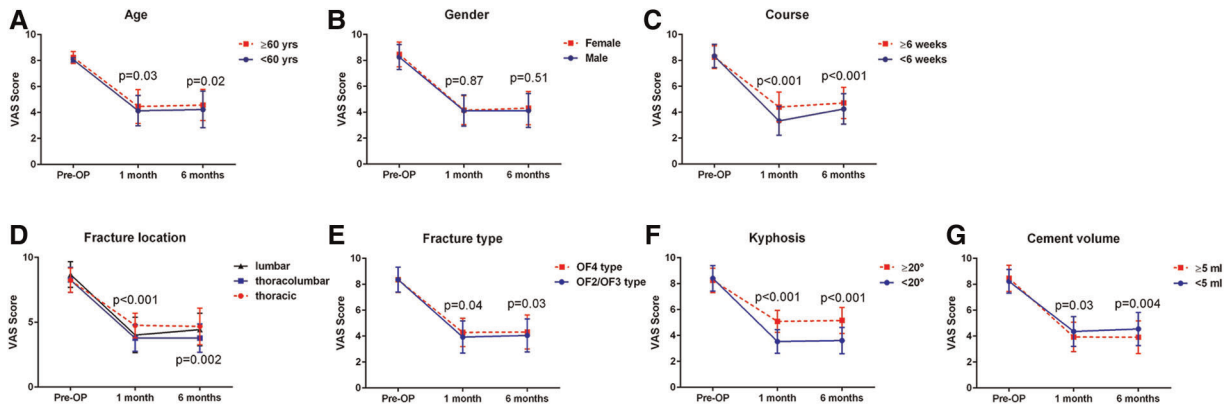

FIGURE 1
The effects of clinical characteristics on postoperative back pain at different follow-up point. (A), age; (B), gender; (C), course of disease; (D), fracture location; (E), fracture type; (F), segmental kyphosis; (G), cement volume.

TABLE 2 Multivariate logistic regression analysis of the risk factors of residual back pain after PKP.

Factors	Regression coefficient (β)	OR	*P*-value
Age ≥60 years	0.590	1.804	0.021
Fracture location = thoracic or lumbar	0.626	1.870	0.002
Fracture type = OF4 type	0.149	1.161	0.018
Segmental kyphosis ≥20°	0.720	2.054	0.014
Bone cement volume <5 ml	0.881	2.413	0.001

TABLE 3 The scoring system for predicting residual back pain after PKP.

Variables	Score
Age	
≥60 years	2
<60 years	0
Fracture location	
Thoracic or lumbar vertebrae	2
Thoracolumbar vertebrae	0
Fracture type	
OF4 type	1
OF2 or OF3 type	0
Segmental kyphosis	
≥20°	2
<20°	0
Bone cement volume	
<5 ml	2
≥5 ml	0

postoperative residual back pain. The variables were given the weighted scores according to the relative value of the OR in multivariate logistic regression analysis: age ≥60 years, fracture location = thoracic or lumbar, fracture type = OF4 type, segmental kyphosis ≥20°, and bone cement volume <5 ml were weighted as 2 points, 2 points, 1 point, 2 points, and 2 points, respectively. The score was then calculated by determining the total number of points, ranging from 0 to 9 (Table 3).

A histogram distribution of the score values was shown in Figure 2. Remarkably, residual back pain group showed a significant higher score than non-residual back pain group (6.84 ± 1.71 vs. 2.66 ± 1.97, $t = 8.499$, $P < 0.001$). The optimal cut-off value of the predictive scoring system was 5 points, and the area under curve (AUC) was 0.931 (95% CI, 0.876–0.985, $P < 0.001$) (Figure 3).

Validation of the scoring system

Finally, a total of 45 patients were prospectively included in the validation set, including 14 cases in residual back pain group group and 31 cases in non-residual back pain group according to the 6-month postoperative follow-up outcomes. Comparison of the performance of the score system on derivation set and validation set was shown in Table 4. Based on the cut-off value of 5 points, the sensitivity and specificity of the scoring system for predicting postoperative residual back pain were 84.21% and 87.34%, respectively, in derivation set and 78.57% and 83.87% in validation set.

Discussion

In this study, we first evaluated the clinical efficacy of PKP for OVCF. During the 6-month follow-up, we found that PKP was an effective procedure, with significant short-term relief

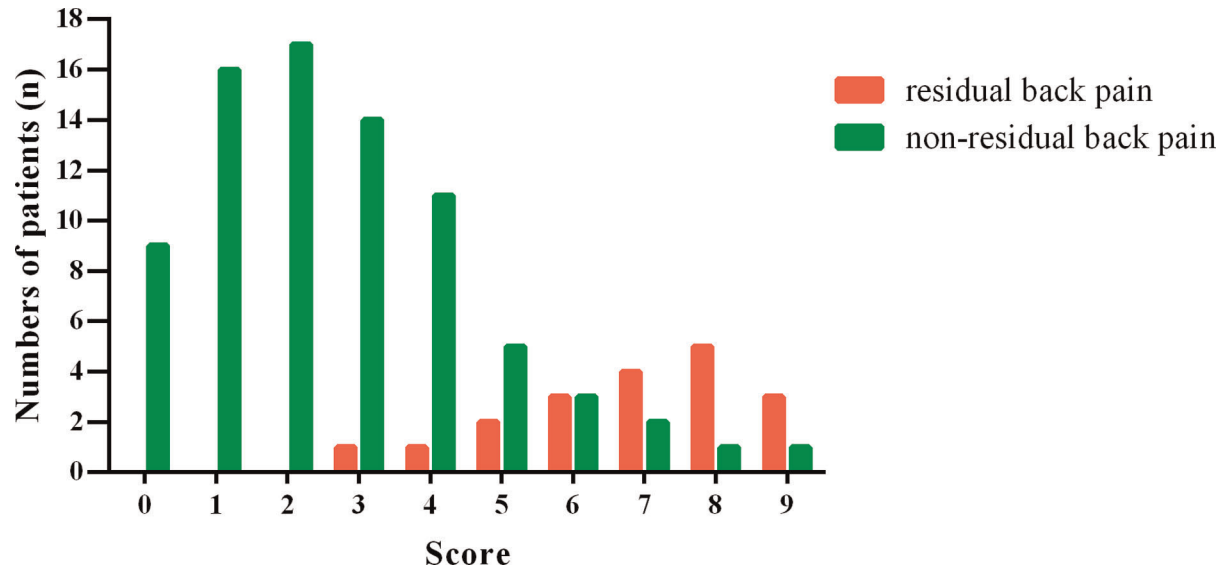

FIGURE 2
Histogram distribution of residual back pain group and non-residual back pain group for each score of the scoring system.

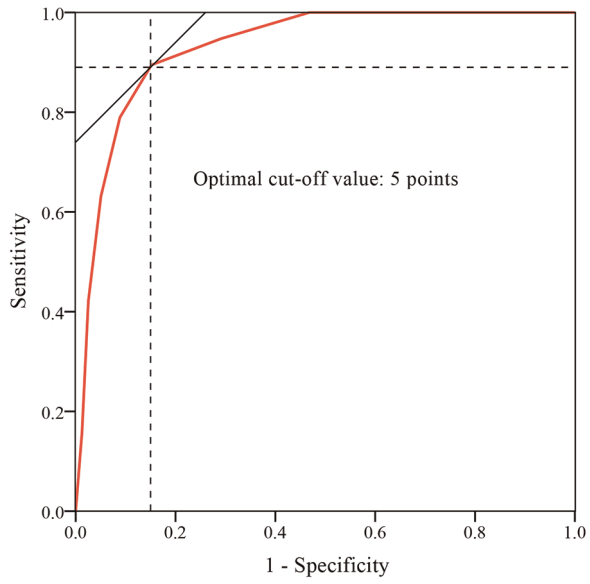

FIGURE 3
ROC curve analysis of the scoring system. The optimal cut-off point based on the ROC curve analysis of scores was 5 points.

of patients' pain symptoms. Although the VAS score of at 6 months postoperativbely was higher than that at 1 month postoperatively, the difference was not statistically significant, and the VAS score at 6 months postoperativbely was significantly lower than that before surgery, which further confirmed the efficacy of PKP for OVCF.

Moreover, we further analyzed the predictors of postoperative residual back pain. We found that the postoperative residual back pain 6 months after PKP was more obvious in OVCF patients aged ≥60 years than in patients aged <60 years. There might be the following reasons: (a) the degree of osteoporosis was more serious in the elderly (16); (b) the elderly had poor tolerance to surgical trauma and thus had slow postoperative recovery, long hospital stay and high risk of postoperative complications (17). This result was consistent with Yimin et al. who suggested that younger age was favorable factor for the prognosis of PKP (18). Diel et al. analyzed the prognostic factors of 1408 patients with vertebral fractures (including traumatic, pathological and osteoporotic) after PKP, and found that male patients had a higher risk of re-fracture after PKP (19). However, our present study found no significant difference in VAS scores between male and female OVCF patients. This may be because Diel et al. included vertebral fractures caused by multiple causes in their study, while our study only included vertebral fractures caused by osteoporosis. Yimin et al. suggested that PKP treatment within the first 6 weeks after fracture can achieve good pain relief (18). Our study found no significant relationship between course of disease and pain relief. This may be because Yimin et al.'s conclusions were drawn through literature review, and there may be publication bias.

In addition, the results of this study showed that there were significant differences in pain relief in different types of OVCF. First of all, patients with OF2 or OF3 type fracture had more obvious pain relief, while patients with OF4 type fracture had higher VAS scores after PKP. Secondly, we also found that OVCF patients with kyphosis had higher postoperative VAS scores and less pain relief. We speculate that this may be related to the severity of vertebral fracture (20), namely, burst

TABLE 4 Comparison of performance of the scoring system on derivation set and validation set.

		Predictive outcome					
		Derivation set			Validation set		
		Residual back pain (score ≥5)	Non-residual back pain (score ≤4)	Total	Residual back pain (score ≥5)	Non-residual back pain (score ≤4)	Total
True outcome	residual back pain	16	3	19	11	3	14
	non-residual back pain	10	69	79	5	26	31
	Total	26	72	98	16	29	45
Sensitivity (%)			84.21			78.57	
Specificity (%)			87.34			83.87	

fracture (or vertebral posterior margin fracture) and combined kyphosis suggested severe injury violence and vertebral fracture. In addition, we found that patients with thoracolumbar vertebral fracture had more obvious pain relief after PKP, while patients with thoracic or lumbar vertebral fracture had higher postoperative VAS scores, which may be related to higher anatomical stability of thoracic vertebral segments (21). By analyzing 27 patients with malignant vertebral fractures, Papanastassiou et al. also found that thoracic vertebral fractures had poor pain relief after PKP treatment (22). DGOU divided OVCF into 5 types (OF1–5) according to the injury of the posterior wall of the fracture vertebra. It was found that compared with OF4 and 5 types fractures, OF1–3 types fractures had better pain relief after PVP (23, 24), which was consistent with the findings of our present study. Therefore, we speculated that for patients with severe vertebral fractures (such as complete burst fractures), the addition of bone cement-assisted fixation on the basis of internal fixation may achieve better pain relief (25).

Surgical factors are important factors affecting the postoperative pain. Röder et al. conducted a retrospective analysis of 276 patients with single-segment vertebral fractures, and found that bone cement volume was an important factor influencing pain relief after PKP (OR = 0.36), meanwhile, they suggested that bone cement volume in PKP should be >4.5 ml in order to better relieve the pain (26). The above conclusions were consistent with our present study, which showed that bone cement volume <5 ml was a risk factor of residual back pain after PKP (OR = 2.412). Several studies suggested that there was a dose-effect relationship between pain relief and the bone cement volume, however, several studies showed a wireless relationship between the pain relief and the bone cement volume (27, 28). Al-ali et al. believed that neither the amount of bone cement and the leakage of bone cement to intervertebral disc had correlation with pain relief after PKP (29). The main reasons were as follows (30, 31): (a) different definitions of pain relief in these studies; (b) different sites of vertebral fractures were included in each study; (c) the evaluation indexes of bone cement volume are different. Therefore, in our opinion, when PKP was used for OVCF, the optimal bone cement volume should be individual (32). When the bone cement volume is low, the pain relief may not be satisfactory, while when the bone cement volume is too high, the risk of complications may be increased, such as bone cement leakage and adjacent vertebral fractures.

There are some limitations of our study. First, it was a retrospective study. Second, the number of patients included in this study was small and the postoperative follow-up time was short. Third, this study did not evaluate other factors that might affect postoperative pain relief, such as comorbidities.

In summary, our study suggested that PKP can significantly relieve pain in OVCF patients. Age ≥60 years, fracture location = thoracic or lumbar, fracture type = OF4 type, segmental kyphosis ≥20°, and bone cement volume <5 ml were the predictors for residual back pain after PKP. Due to the limitations of the study, further studies are needed to confirm the above conclusion.

Data availability statement

The raw data supporting the conclusions of this article will be made available by the authors, without undue reservation.

Ethics statement

The studies involving human participants were reviewed and approved by the Ethics Committee of the Second People's Hospital of Chengdu. The patients/participants provided their written informed consent to participate in this study.

Author contributions

Conception and design: DY and XL. Data analysis and interpretation: DY, XL, and YZ. Data collection and management: DY, XL, YX, and QH. Manuscript writing and

critical revisions: all authors. Overall responsibility: XL. All authors contributed to the article and approved the submitted version.

Conflict of interest

The authors declare that the research was conducted in the absence of any commercial or financial relationships that could be construed as a potential conflict of interest.

Publisher's note

All claims expressed in this article are solely those of the authors and do not necessarily represent those of their affiliated organizations, or those of the publisher, the editors and the reviewers. Any product that may be evaluated in this article, or claim that may be made by its manufacturer, is not guaranteed or endorsed by the publisher.

References

1. Clynes MA, Harvey NC, Curtis EM, Fuggle NR, Dennison EM, Cooper C. The epidemiology of osteoporosis. *Br Med Bull*. (2020) 133(1):105–17. doi: 10.1093/bmb/ldaa005

2. Yu F, Xia W. The epidemiology of osteoporosis, associated fragility fractures, and management gap in China. *Arch Osteoporos*. (2019) 14(1):32. doi: 10.1007/s11657-018-0549-y

3. Hoyt D, Urits I, Orhurhu V, Orhurhu MS, Callan J, Powell J, et al. Current concepts in the management of vertebral compression fractures. *Curr Pain Headache Rep*. (2020) 24(5):16. doi: 10.1007/s11916-020-00849-9

4. Longo UG, Loppini M, Denaro L, et al. Osteoporotic vertebral fractures: current concepts of conservative care. *Br Med Bull*. (2012) 102:171–89. doi: 10.1093/bmb/ldr048

5. Longo UG, Loppini M, Denaro L, Maffulli N, Denaro V. Osteoporotic vertebral fractures: predictive factors for conservative treatment failure. A systematic review. *Eur Spine J*. (2018) 27(10):2565–76. doi: 10.1007/s00586-017-5340-z

6. Chang X, Lv YF, Chen B, Li HY, Han XB, Yang K, et al. Vertebroplasty versus kyphoplasty in osteoporotic vertebral compression fracture: a meta-analysis of prospective comparative studies. *Int Orthop*. (2015) 39(3):491–500. doi: 10.1007/s00264-014-2525-5

7. Xu Z, Hao D, Dong L, Yan L, He B. Surgical options for symptomatic old osteoporotic vertebral compression fractures: a retrospective study of 238 cases. *BMC Surg*. (2021) 21(1):22. doi: 10.1186/s12893-020-01013-1

8. Zhang B, Li T, Wang Z. Efficacy and complications of different surgical modalities of treating osteoporotic spinal compression fracture in the elderly. *Am J Transl Res*. (2022) 14(1):364–72.

9. Nikoobakht M, Gerszten PC, Shojaei SF, Shojaei H. Percutaneous balloon kyphoplasty in the treatment of vertebral compression fractures: a single-center analysis of pain and quality of life outcomes. *Br J Neurosurg*. (2021) 35(2):166–9. doi: 10.1080/02688697.2020.1777254

10. Zhan Y, Jiang J, Liao H, Tan H, Yang K. Risk factors for cement leakage after vertebroplasty or kyphoplasty: a meta-analysis of published evidence. *World Neurosurg*. (2017) 101:633–42. doi: 10.1016/j.wneu.2017.01.124

11. Yang S, Liu Y, Yang H, Zou J. Risk factors and correlation of secondary adjacent vertebral compression fracture in percutaneous kyphoplasty. *Int J Surg*. (2016) 36(Pt A):138–42. doi: 10.1016/j.ijsu.2016.10.030

12. Li Y, Yue J, Huang M, Lin J, Huang C, Chen J, et al. Risk factors for postoperative residual back pain after percutaneous kyphoplasty for osteoporotic vertebral compression fractures. *Eur Spine J*. (2020) 29(10):2568–75. doi: 10.1007/s00586-020-06493-6

13. Bossuyt PM, Reitsma JB, Bruns DE, Gatsonis CA, Glasziou PP, Irwig L, et al. STARD 2015: an updated list of essential items for reporting diagnostic accuracy studies. *Br Med J*:(2015) 351:h5527. doi: 10.1136/bmj.h5527

14. Schnake KJ, Blattert TR, Hahn P, Franck A, Hartmann F, Ullrich B, et al. Classification of osteoporotic thoracolumbar spine fractures: recommendations of the spine section of the German society for orthopaedics and trauma (DGOU). *Global Spine J*. (2018) 8(2 Suppl):46S–9S. doi: 10.1177/2192568217717972

15. Du X, She Y, Ou Y, Zhu Y, Luo W, Jiang D. A scoring system for outpatient orthopedist to preliminarily distinguish spinal metastasis from spinal tuberculosis: a retrospective analysis of 141 patients. *Dis Markers*. (2021) 2021:6640254. doi: 10.1155/2021/6640254

16. Shen Y, Huang X, Wu J, Lin X, Zhou X, Zhu Z, et al. The global burden of osteoporosis, low bone mass, and its related fracture in 204 countries and territories, 1990-2019. *Front Endocrinol (Lausanne)*. (2022) 13:882241. doi: 10.3389/fendo.2022.882241

17. Wang MY, Widi G, Levi AD. The safety profile of lumbar spinal surgery in elderly patients 85 years and older. *Neurosurg Focus*. (2015) 39(4):E3. doi: 10.3171/2015.7.FOCUS15180

18. Yimin Y, Zhiwei R, Wei M, Jha R. Current status of percutaneous vertebroplasty and percutaneous kyphoplasty–a review. *Med Sci Monit*. (2013) 19:826–36. doi: 10.12659/MSM.889479

19. Diel P, Freiburghaus L, Röder C, Benneker LM, Popp A, Perler G, et al. Safety, effectiveness and predictors for early reoperation in therapeutic and prophylactic vertebroplasty: short-term results of a prospective case series of patients with osteoporotic vertebral fractures. *Eur Spine J*. (2012) 21(Suppl. 6 (Suppl. 6)):S792–9. doi: 10.1007/s00586-011-1989-x

20. Zhang H, Yang B, Hao D, Wang B, He B, Sun H, et al. Pain location is associated with fracture type in acute osteoporotic thoracolumbar vertebral fracture: a prospective observational study. *Pain Med*. (2022) 23(2):263–8. doi: 10.1093/pm/pnab229

21. Jin H, Ma X, Liu Y, Liu M, Yin X, Fan W, et al. Back pain from painful osteoporotic vertebral fractures: discrepancy between the actual fracture location and the location suggested by patient-reported pain or physical examination findings. *Osteoporos Int*. (2020) 31(9):1721–32. doi: 10.1007/s00198-020-05434-9

22. Papanastassiou ID, Filis AK, Gerochristou MA, Vrionis FD. Controversial issues in kyphoplasty and vertebroplasty in malignant vertebral fractures. *Cancer Control*. (2014) 21(2):151–7. doi: 10.1177/107327481402100208

23. Verheyden AP, Spiegl UJ, Ekkerlein H, Gercek E, Hauck S, Josten C, et al. Treatment of fractures of the thoracolumbar spine: recommendations of the spine section of the German society for orthopaedics and trauma (DGOU). *Global Spine J*. (2018) 8(2 Suppl):34S–45S. doi: 10.1177/2192568218771668

24. Schönrogge M, Lahodski V, Otto R, Adolf D, Damm R, Sitte-Zöllner A, et al. Inter- and intraobserver reliabilities and critical analysis of the osteoporotic fracture classification of osteoporotic vertebral body fractures. *Eur Spine J*. (2022) 31(9):2431–8. doi: 10.1007/s00586-022-07201-2

25. Liao JC, Chen WJ. Short-segment instrumentation with fractured vertebrae augmentation by screws and bone substitute for thoracolumbar unstable burst fractures. *Biomed Res Int*. (2019) 2019:4780426. doi: 10.1155/2019/4780426

26. Röder C, Boszczyk B, Perler G, Aghayev E, Külling F, Maestretti G. Cement volume is the most important modifiable predictor for pain relief in BKP: results from SWISSspine, a nationwide registry. *Eur Spine J*. (2013) 22(10):2241–8. doi: 10.1007/s00586-013-2869-3

27. Fu Z, Hu X, Wu Y, Zhou Z. Is there a dose-response relationship of cement volume with cement leakage and pain relief after vertebroplasty? *Dose Response*. (2016) 14(4):1559325816682867. doi: 10.1177/1559325816682867

28. He X, Li H, Meng Y, Huang Y, Hao DJ, Wu Q, et al. Percutaneous kyphoplasty evaluated by cement volume and distribution: an analysis of clinical data. *Pain Physician*. (2016) 19(7):495–506.

29. Al-Ali F, Barrow T, Luke K. Vertebroplasty: what is important and what is not. *AJNR Am J Neuroradiol*. (2009) 30(10):1835–9. doi: 10.3174/ajnr.A1732

30. Sun HB, Jing XS, Liu YZ, Qi M, Wang XK, Hai Y. The optimal volume fraction in percutaneous vertebroplasty evaluated by pain relief, cement dispersion, and cement leakage: a prospective cohort study of 130 patients with painful osteoporotic vertebral compression fracture in the thoracolumbar vertebra. *World Neurosurg*. (2018) 114:e677–88. doi: 10.1016/j.wneu.2018.03.050

31. Nieuwenhuijse MJ, Bollen L, van Erkel AR, Dijkstra PD. Optimal intravertebral cement volume in percutaneous vertebroplasty for painful osteoporotic vertebral compression fractures. *Spine (Phila Pa 1976)*. (2012) 37 (20):1747–55. doi: 10.1097/BRS.0b013e318254871c

32. Jin YJ, Yoon SH, Park KW, Chung SK, Kim KJ, Yeom JS, et al. The volumetric analysis of cement in vertebroplasty: relationship with clinical outcome and complications. *Spine (Phila Pa 1976)*. (2011) 36(12):E761–72. doi: 10.1097/BRS.0b013e3181fc914e

frontiers | Frontiers in Surgery

TYPE Original Research
PUBLISHED 14 October 2022
DOI 10.3389/fsurg.2022.1000074

Check for updates

OPEN ACCESS

EDITED BY
Tengbo Yu,
The Affiliated Hospital of Qingdao University, China

REVIEWED BY
Yeon Soo Lee,
Catholic University of Daegu, South Korea
Shaobai Wang,
Shanghai University of Sport, China

*CORRESPONDENCE
Yong Xia
yxia@nwpu.edu.cn
Wei Wang
dr.wangwei@xjtu.edu.cn

SPECIALTY SECTION
This article was submitted to Orthopedic Surgery, a section of the journal Frontiers in Surgery

†These authors have contributed equally to this work and share second authorship

RECEIVED 21 July 2022
ACCEPTED 27 September 2022
PUBLISHED 14 October 2022

CITATION
Alkhatatbeh T, Wang JL, Zhang WJ, Li YW, Xia Y and Wang W (2022) A new automatic stitching method for full-length lower limb radiography. Front. Surg. 9:1000074.
doi: 10.3389/fsurg.2022.1000074

COPYRIGHT
© 2022 Alkhatatbeh, Wang, Zhang, Li, Xia and Wang. This is an open-access article distributed under the terms of the Creative Commons Attribution License (CC BY). The use, distribution or reproduction in other forums is permitted, provided the original author(s) and the copyright owner(s) are credited and that the original publication in this journal is cited, in accordance with accepted academic practice. No use, distribution or reproduction is permitted which does not comply with these terms.

A new automatic stitching method for full-length lower limb radiography

Tariq Alkhatatbeh[1], Jia Lin Wang[1†], Wei Jia Zhang[2†], Yong Wei Li[1], Yong Xia[2*] and Wei Wang[1*]

[1]Department of Bone and Joint Surgery, The Second Affiliated Hospital of Xi'an Jiaotong University, Xi'an, China, [2]School of Computer Science and Engineering, National Engineering Laboratory for Integrated Aero-Space-Ground-Ocean Big Data Application Technology, Northwestern Polytechnical University Youyi Campus of Northwestern Polytechnical University, Xi'an, China

Full-length lower limb x-rays are used to diagnose and plan surgical procedures, such as Total Knee Arthroplasty (TKA) and High Tibial Osteotomy (HTO). Due to the size limitation of digital radiography (DR), panoramic x-ray images cannot be obtained in a single exposure, necessitating multiple exposures and image stitching. In favor of manually constructing full-length x-ray images, we propose a new feature-based automated method for stitching together x-ray images. This new method is based on Canny algorithm, which detects and aligns bone edges before fusing them using a Wavelet form domain. Twenty-eight sets of lower limb x-ray images obtained from our hospital have been stitched and evaluated. The hip, knee, and ankle (HKA) angle was computed in two different ways then compared to manually stitched x-ray images by an expert. The stitching time was only three seconds, and the *P*-value was $P = 0.974$, and an accuracy rate of 100% was found. This method demonstrated greater precision and speed than both manually stitched x-ray images and previously published methods.

KEYWORDS

x-ray image stitching, feature detection, canny algorithm, full-length lower limb radiography, radiography stitching, panoramic radiography

Introduction

High Tibial Osteotomy (HTO) and Total Knee Arthroplasty (TKA) are frequent and effective surgical interventions for the treatment of osteoarthritis. Planning and evaluating these interventions requires a full-length x-ray image of the lower extremity (1). X-ray images of the lower limb consist of three parts: the hip, the knee, and the ankle. Due to the size limitation of digital radiography (DR), a full-length limb cannot be captured at once, necessitating multiple exposures that produce multiple radiographs that must be combined and fused (2). X-ray image stitching was developed to assist in joining x-ray images and displaying the desired portion in a single image. Conventional stitching generally requires an expert to independently input, align, and merge x-ray images (3), but this process may be compromised or troubled under heavy workloads (4). Therefore, researchers developed automated x-ray stitching that utilized various factors and features to achieve its purpose. Based on the method applied, automated x-ray stitching can be classified as either pixel-based or feature-based (5). Several pixel-based methods had previously been

introduced; in 2013, Samsudin proposed a method that used MACE's filter to obtain the overlapping region between two x-ray images of the hand, then stitched them together. An accuracy of 80% was found and his method required a 30 percent overlapping region for successful stitching, which was not always present (5). Similarly, Yang presented in 2016 another pixel-based method that used a phase correlation, a quick way to register x-ray images (6). This method estimated the relative translation between two x-ray images with an overlapping region and then stitched them together. It was only used to combine two x-ray images simultaneously with an accuracy rate of 90%. Therefore, their efficacy in regards to lower limb x-ray stitching cannot be demonstrated. In 2018, Ben Zekri proposed a new automated stitching method based on features using a Sobel derivative that detected bone edges and shafts to determine the overlapping region and complete the stitching. The Hip, Knee, and Ankle angle was calculated and compared to x-ray images created by an expert to evaluate his method. The results obtained were extremely promising as accuracy rate was found to be 100%, but the overall stitching time of 15 s was relatively lengthy (7). Aside from these, another method used a ruler to help align the x-ray images (8), and one more was built around a c-arm mobile x-ray device (9). And this defeats the purpose of having a dependent and reliable automated x-ray image stitching method for lower limb x-rays. Therefore, a method of precise and rapid stitching must be developed. This method could be of a significant importance economically, as it reduces the need of expensive advanced DR systems that may not be available everywhere; which reflects to more affordable and accessible options for both patients and surgeons. Besides, it could aid Orthopedic technicians with their workloads by reducing the time and effort needed for manual x-ray stitching.

The Canny algorithm is a well-known edge detector that was introduced in 1986; it can detect the edges of objects with a low error rate, discarding false edges and ensuring accurate detection (10). In this study, we propose a new Canny-based method for stitching x-ray images of the lower limb. Our method relies solely on the accurate and rapid detection of lower limb bone edges to align and proceed with the stitching. Unlike previous methods, this minimizes the need for additional equipment or materials such as rulers or external markers. We can simultaneously manipulate not only two but three x-ray images, which are required to create a full-length x-ray image of the lower limb.

Materials and methods

Data of patients

To perform this experiment, a total of 28 patents' lower limb x-ray images were collected from the database of Xi'an Jiaotong University's second affiliated hospital in JPG form. A hip, a knee, and an ankle,with each image dimension of 3408*3320 pixels, and a resolution of 150*150; and a full-length lower limb x-ray image stitched by an expert were included in each set of these x-ray radiographs.The DR system used was Sedecal "NOVA FA" that had a flat panel detector. The distance between the x-ray source and the patient was 150 CM. In total, 112 images were utilized for this study. The Second Affiliated Hospital of Xi'an Jiaotong University has granted permission for this study to collect and use patient information. This hospital's x-ray system was a linear system in which the x-ray source moved from top to bottom to capture images.

Data processing steps

To perform the desired x-ray stitching, the following four steps were taken: (1) Image input: hip, knee, and ankle x-ray images were selected and input. Each image was down-sampled to decrease its file size and increase its processing speed. (2) Detection of features: A Gaussian filter was initially used to smooth the images and reduce noise. This would aid in the detection of bone edges. Then, we applied the Canny Algorithm to detect the lower limb bone edges. (3) Overlapping region estimation: Based on horizontal shifting, we computed the image position transformation (x -direction offset and y -direction offset) to find the overlapping region. (4) Stitching of x-ray images: A Wavelet transform domain was used to stitch and merge all the images and create a full-length x-ray image.

Image input

The full x-ray image of the lower limb consists of three parts: the hip, knee, and ankle images. To construct image stitching successfully, we must first input these three x-ray images in the specified order. Images then were down-sampled in size to enhance the processing speed.

Features detection

As noise can mislead any edges detection algorithm, it was essential to apply a 5*5 Gaussian filter first to remove and reduce the noise. Bone edges were then extracted using the Canny algorithm. Assuming that the original image was a two-dimensional (2D) matrix $I \in \mathbb{R}^{H \times W}$, then $I_{x,y}$ represents the first x column and y the pixel value of the row. The edge information graph $E_{x,y} \in \{0, 1\}$ indicated whether the corresponding position of the original image was an edge or not (1 is an edge, 0 for non-edge). **Figure 1** shows the edges detected after applying the Canny algorithm to x-ray images.

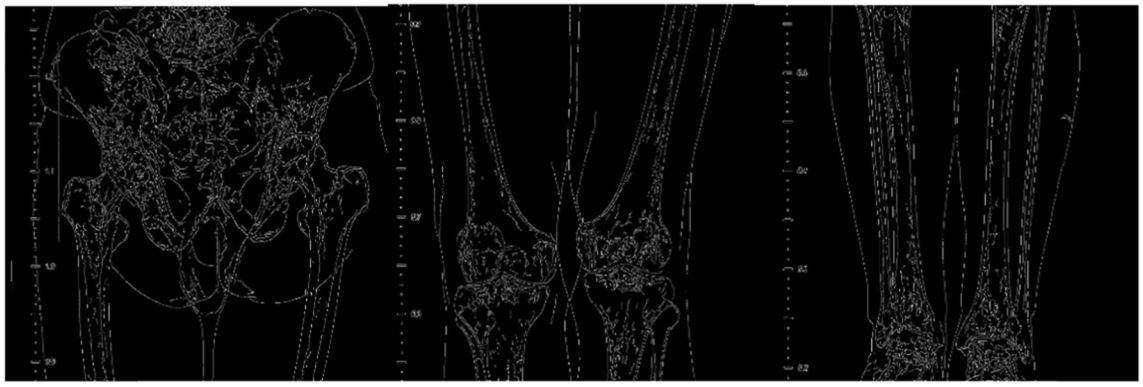

FIGURE 1
Three parts that consist the full-length lower limb x-ray image, the hip, the knee and the ankle, edges extracted by canny algorithm.

Overlapping region estimation

Since the patients were required to stand still during the collection of x-ray images of the lower limbs, this study assumed that there was no rotation perspective or other transformations in the images; therefore, our method was only based on horizontal shifting, which neglects any vertical shifting. This study only needed to calculate the image position transformation (x -direction offset and y -direction offset) to find the overlapping region.

After extracting features using the Canny algorithm, this study calculated the distance D $D_{x,y}$ as follows:

$$D_{x,y} = \underset{x',y'}{\operatorname{argmin}} \sqrt{(x-x')^2 + (y-y')^2}, (E_{x',y'} = 1)$$

$D_{x,y}$ represents the distance to the nearest edge (x, y).

In the matching process, this study used the overlapping region of the two images to evaluate the registration quality of the two images. The overlapping area of the two images is two equal-sized areas. If their edge map and distance map is considered as E^1, E^2 and D^1, D^2, then the specified matching distance A is:

$$A = \frac{\sum_{x,y} E^1_{x,y} D^2_{x,y}}{\sum_{x,y} E^1_{x,y}} + \frac{\sum_{x,y} E^2_{x,y} D^1_{x,y}}{\sum_{x,y} E^2_{x,y}}$$

The closer the overlapping area is the better the two images match. The algorithm needs to traverse all the registration parameters and calculate the corresponding distance to find the smallest distance A, making A the smallest registration parameter; this study had taken it as the final registration result. **Figure 2** illustrates how edges are registered after being detected.

FIGURE 2
Bone edge registration, after edges were extracted using canny algorithm; and to determine the true bone edge, the bright areas are excluded as they are considered far from edges.

X-ray image stitching

After determining the overlapping region, one of the most critical aspects of successful image stitching is how to combine the images, making this step crucial. Wavelet transformations are used in a wide range of applications, often replacing the Fourier Transform. Image compression, feature extraction, image denoising, and other medical image technologies benefit from Wavelet Transforms (WT) (11). Hence, this study used the wavelet transform domain stitching method to merge x-ray images together. Assuming that the overlapping areas of the two images were I^1, I^2, and their

FIGURE 3
A full-length lower limb x-ray radiograph stitched using the proposed method based on canny algorithm.

FIGURE 4
HKA angle calculated manually using angle meter. A mid-femur-head point is estimated, a mid-knee joint point and a mid-ankle joint point were estimated to get the HKA angle.

wavelet transform coefficients were W^1, W^2, respectively, the wavelet coefficients of the same scale were aligned:

$$W_i = \theta W_i^1 + (1 - \theta) W_i^2$$

After the aligning was completed, the wavelet transform was applied to produce the stitching result, as shown in **Figure 3**.

HKA angle calculation

HKA angle is a commonly used angle in lower limb surgical interventions and planning (1, 12); therefore, we employ it to assess the quality of our stitching. The HKA angle calculations were performed manually and automatically.

In accordance with the criteria outlined in this book (12) for calculating the HKA angle, we first manually calculated the angle. Three distinct users were given the same set of x-ray images of the lower limb. Using an iPad application called Angle meter version 1.9, they estimated the midpoint of the femur, knee, and ankle and then calculated the HKA angle for each of the provided images. This app has a rating of 4.6 stars on the Apple store; it can measure angles from any image, but in this study, it was used to measure the HKA angle from the stitched x-ray images.

Second, the automated HKA angle calculation was performed on a Windows computer using Python and the RCNN algorithm (Region-Based Convolutional Neural Networks). RCNN employs selective search to identify candidate bounding-box object regions (a region of interest) (13). Each of these regions' convolutional network options is then extracted for classification. Utilized in our research to automatically calculate the HKA for the purpose of the experiment.

Analytics

We determined the *P*-value by performing a *T*-test on SPSS (Statistical Package for the Social Sciences) on all the HKA angle values obtained manually and automatically for the x-ray images stitched using this method and those constructed manually by an expert. A positive *P*-value (>0.05) indicates that there is no statistically significant difference between the HKA angles of the stitched x-ray images and those obtained by an expert. In addition, analysis of variance (ANOVA) and the *T*-test were used to examine the mean difference. Python, a conventional programming language, was used to execute the Canny algorithm and apply the steps of our method. This study utilized a Windows 10 computer with 16GB of RAM and an i7 processor.

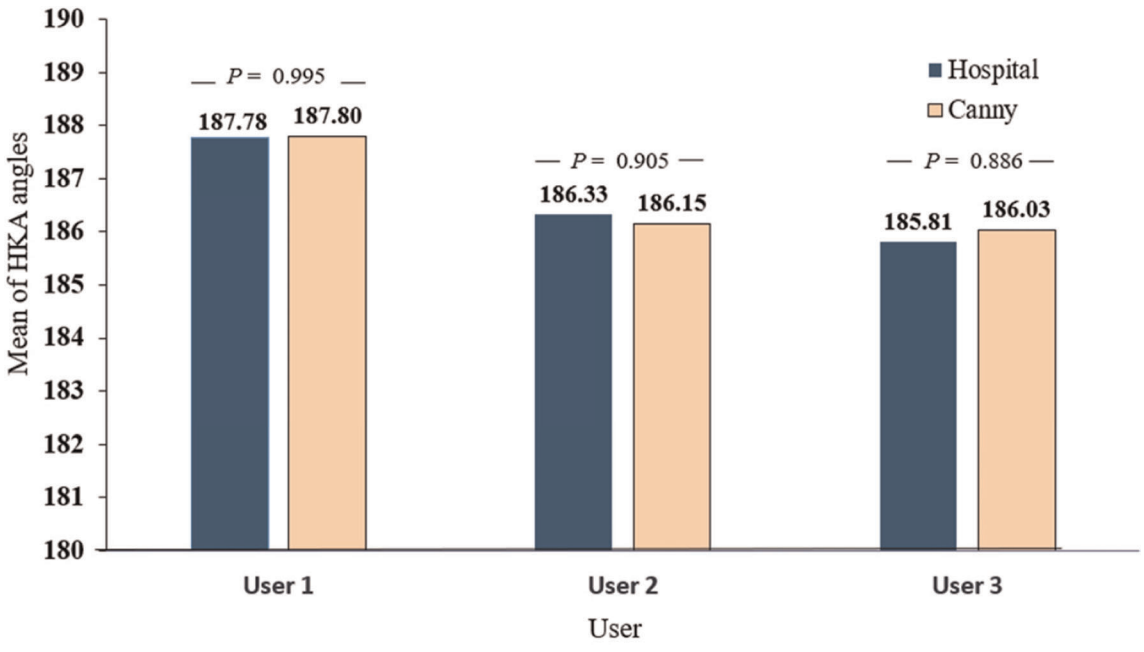

FIGURE 5
Manually measured HKA angles comparison for three different users between x-ray images stitched by an expert and acquired from the hospital and x-ray images stitched using our method based on canny algorithm.

Results

Manual HKA angle calculation outcomes

Using the Angle Meter APP on an iPad, three separate users manually measured the HKA angle for both images stitched by an expert and others obtained using Canny; Figure 4 depicts an example of the angle measurement result. We then compared the mean HKA angles between all images stitched with this method and those stitched by an expert and found $P = 0.995$ for user 1, $P = 0.905$ for user 2, and $P = 0.886$ for user 3. Figure 5 shows the difference in means. We then used ANOVA on SPSS to compare the mean to the standard deviation between the three different users, as shown in Table 1.

Automated HKA angle calculation outcomes

On a Windows computer running Python and using RCNN, we automatically calculated the HKA angle for both sets of images obtained by Canny and stitched by an expert. An example of the result is displayed in Figure 6. After measuring the HKA angle automatically, we ran a *T*-test on SPSS to compare the means to the standard deviation and determined whether there was any significant difference or not. Hence, we found $P = 0.974$ as can be seen in Table 2 and Figure 7.

Discussion

In this study, we propose a new stitching method for lower limb x-ray images that are both efficient and accurate and is based on the detection of anatomical features. To evaluate this method, we first stitched 28 sets of lower limb x-ray images obtained from the Second affiliated hospital of Xi'an Jiaotong University, and then measured the HKA angles both manually and automatically. We have used HKA angle as a reference point because its practical and it is what full-length x-rays are

TABLE 1 The mean compared to the standard deviation for both x-ray images obtained from the hospital and were constructed by an expert and the ones stitched using our method based on canny by three different users.

Variable	User 1 ($n = 28$)	User 2 ($n = 28$)	User 3 ($n = 28$)	*P*-value
Hospital, mean ± SD	187.78 ± 1.19	186.34 ± 1.14	185.81 ± 1.10	**0.010**
Canny, mean ± SD	187.80 ± 1.18	186.15 ± 1.13	186.03 ± 1.08	**0.020**

FIGURE 6
HKA angle calculated automatically using RCNN.

TABLE 2 The mean compared to the standard deviation for auto-calculated HKA angles using *t*-test for both images obtained from the hospital that were constructed by an expert and others stitched using our method based on canny.

Variable	Automatic ($n = 28$)	*P*- value
Hospital, mean ± SD	186.45 ± 1.09	0.974
Canny, mean ± SD	186.40 ± 1.09	

used for. Using the calculated angles, we tested the data with the *T*-test; when comparing the means, the *P*-value was positive (>0.05). And when the mean was compared to the standard deviation, the *P*-value was also positive (>0.05). Which indicates no significant difference between the stitched x-ray images and the ones manually constructed by an expert. As we are merely depending on bone edges to stitch images, only 3 s are required to successfully construct a full-length x-ray image using our method. In Table 3, we compared several previous stitching techniques pertaining to the same topic. In 2013, Samsudain presented a pixel-based method to stitch x-ray images automatically. His technique utilized the MACE filter to detect x-ray images' edges and corners; then, it estimated the overlapping region between two images and performed stitching accordingly. This method was applied only on a pair of x-ray images of a hand, and it was found 80% accurate. In 2016, Yang implemented a correlation coefficient (CC) for x-ray image edge detection, which is also based on a pixel-based image stitching. His study was mainly focused on scoliosis patients and their x-ray images. Despite his fair accuracy rate of 90%, his method was not evaluated for lower limb x-ray stitching. In 2018, Ben Zekri applied a feature-based x-ray image stitching algorithm that used Sobel kernel and a second derivative filter that detected lower limb bone edges and estimated the bone shaft. This robust image stitching method took 15 s to create a panoramic x-ray image. His method was tested on a big database of lower limb x-ray images and was found to have a 100% accuracy rate. But we believe that using bone edges alone is both sufficient and fast to create a panoramic x-ray image of the lower limb as demonstrated in our study where we also obtained a 100% accuracy rate while reducing the time to three seconds only. In general we can say that Pixel-based stitching, despite being faster, it less accurate than feature-based method. Nonetheless, a key advantage of feature-based stitching is that it can stitch multiple x-ray images at once, in this case its three images that are required to construct a full-length radiograph of the lower limb. This method is more time-consuming, but it produces superior results.

In some of the stitched images using our method, we found a distortion in the ruler's markings, as can be seen in Figure 8 to the right. Though, manual stitching depends on external markers as stated earlier, and in our hospital's case, that marker is a ruler. But that is not always sufficient as seen in the image stitched by an expert to the left in Figure 8. As the expert depends mainly on the markers to perform his stitching, this could present some anatomical mismatching or slight distortion. On the other hand, our method solely uses anatomical features to perform the stitching with superior performance. This phenomen can be explained in Figure 9. As linear x-ray systems have the x-ray source moving vertically from top to bottom, and while the patient and the markers used are fixed at one position. The ruler is captured from different angles, thus, using it as the only factor to stitch

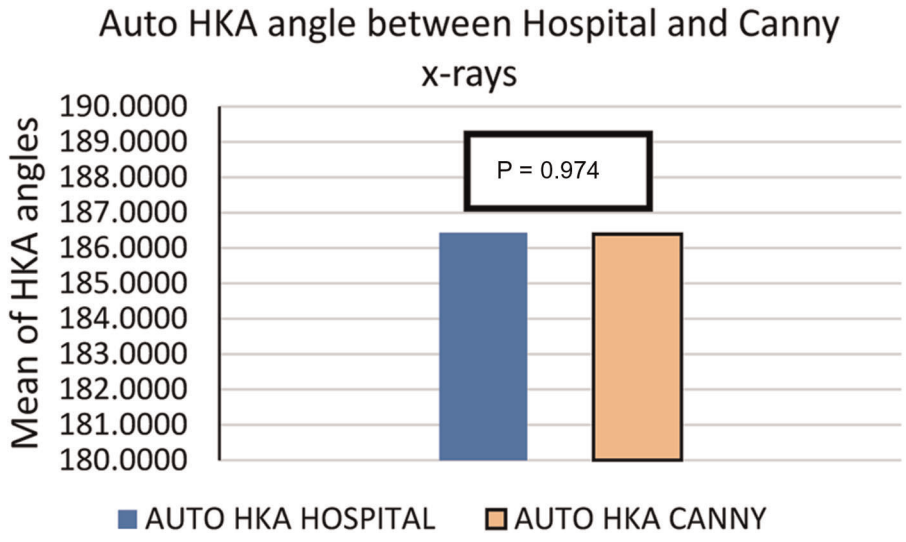

FIGURE 7
The mean of HKA angles for 28 sets of x-ray images stitched using our method and the x-ray radiographs obtained from the hospital directly, which were stitched by an expert.

TABLE 3 A comparison between different stitching methods and their efficacy.

Name	Year	Method	Images	Accuracy	Time	Rotation/scaling/ translation
Samsudain	2013	Pixel-based method (MACE filter)	2 images of a hand were used	80%	2.2 s	No
Yang	2016	Pixel-based method (multiple correlation coefficient)	2 images of the spine were used	90%	1.9 s	Rotation, scaling and translation
Ben Zekri	2018	Feature-based method (sobel algorithm)	3 lower limb images, the hip, the knee, and the ankle	100%	15 s	Scaling and rotation
Tariq	2021	Feature-based method (canny algorithm)	3 lower limb images, the hip, the knee, and the ankle	100%	3 s	No
Manual (used by the hospital of this study)	N/A	Expert stitching manually	3 lower limb images, the hip, the knee, and the ankle	100%	90 s	Rotation, scaling and translation

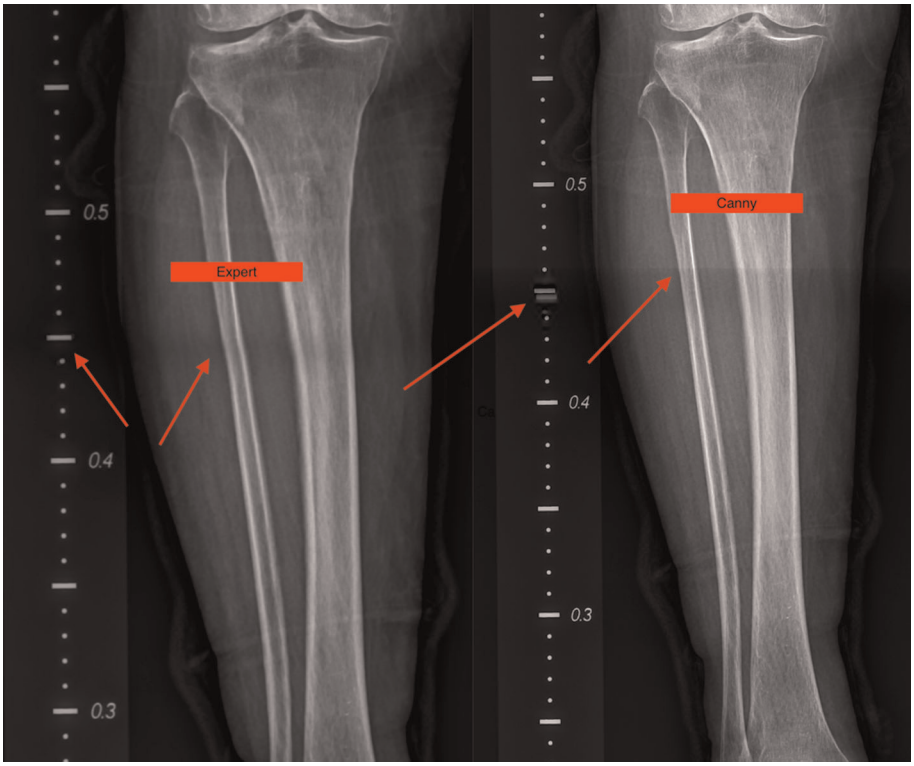

FIGURE 8
A slight distortion can be seen on the ruler's markers in the image obtained by canny to the right while maintaining accurate anatomical features. Whereas, no distortion in the ruler markers' can be seen in the image stitched by an expert to the left but a slight distortion in the anatomical features in present.

x-ray radiographs could present such an anatomical distortion as in Figure 8 to the left. Whereas using our method, the findings don't represent a distortion in the anatomical features, and that indeed further proves that our method is even more accurate when compared to this manual method.

This study has several limitations, including the inability to scale or rotate x-ray images prior to stitching. However, as previously explained, this is irrelevant because patients must remain still and immobile during the image capture process, eliminating the possibility of shifting or transitioning. Moreover, the tests were only conducted on x-ray images from the Second Affiliated Hospital of Xi'an Jiaotong University, so we do not know the effectiveness of this method on x-ray images from other sources.

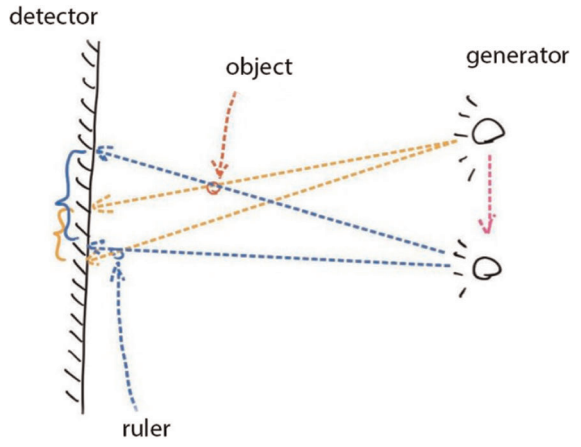

FIGURE 9
During the x-ray image capturing process, the source has to move from top to bottom to take multiple images; this means that the ruler markers' is captured from two different angles. Once the images are stitched according to features and not ruler markers', a slight distortion can be seen in the markers. It does not represent a real distortion in the stitching of our method, but it verifies that our method solely depends on anatomical features to perform stitching and that its more accurate.

Conclusion

This study proposes a new method for stitching x-ray images of the lower limb. Our method reduces overall processing time while maintaining a high level of accuracy which is 100%. Using the Canny algorithm to detect bone edges that exist within the x-ray image itself makes this method extremely user-friendly and eliminates the need for additional markers or rulers. In conclusion, this method is a reliable technique for stitching x-ray images of the lower limb.

Data availability statement

The raw data supporting the conclusions of this article will be made available by the authors, without undue reservation.

Author contributions

TA designed, planned the research, and wrote the manuscript. JLW helped collect the images needed for the experiment, and YWL helped edit the manuscript and gave suggestions. YX and WJZ helped perform the investigation and provided technical support. WW supervised and guided the whole study. All authors contributed to the article and approved the submitted version.

Funding

This work was jointly supported by the National Key Research and Development Program of China (2019YFC0120602); National Natural Science Foundation of China (82072522); Shaanxi Province Colleges and Universities Joint Medical-Industrial Cross-Project (2020GXLH-Y-001); State Administration of Traditional Chinese Medicine Clinical Collaborative Innovation Project of Integrated Traditional Chinese and Western Medicine (GZY-KJS-2021-002); Shaanxi Provincial Administration of Traditional Chinese Medicine Clinical Collaborative Innovation Project of Integrated Traditional Chinese and Western Medicine (2020-ZXY-003).

Conflict of interest

The authors declare that the research was conducted in the absence of any commercial or financial relationships that could be construed as a potential conflict of interest.

Publisher's note

All claims expressed in this article are solely those of the authors and do not necessarily represent those of their affiliated organizations, or those of the publisher, the editors and the reviewers. Any product that may be evaluated in this article, or claim that may be made by its manufacturer, is not guaranteed or endorsed by the publisher.

References

1. Cooke TD, Li J, Scudamore RA. Radiographic assessment of bony contributions to knee deformity. *Orthop Clin North Am.* (1994) 25(3):387–93. doi: 10.1016/S0030-5898(20)31923-4

2. Cooke TD, Scudamore RA, Bryant JT, Sorbie C, Siu D, Fisher B. A quantitative approach to radiography of the lower limb. Principles and applications. *J Bone Joint Surg Br.* (1991) 73(5):715–20. doi: 10.1302/0301-620X.73B5.1894656

3. Bassi S, Baldini S, Rebuffat C, Sarti R, Ferretti F. First test on three stitching methods with digital detectors used in radiography. *Radiol Phys Technol.* (2013) 6 (1):187–96. doi: 10.1007/s12194-012-0187-9

4. Jordan JM, Sowers MF, Messier SP, Bradley J, Arangio G, Katz JN, et al. Methodologic issues in clinical trials for prevention or risk reduction in osteoarthritis. *Osteoarthritis Cartilage.* (2011) 19(5):500–8. doi: 10.1016/j.joca.2010.10.031

5. Samsudin S, Adwan S, Arof H, Mokhtar N, Ibrahim F. Development of automated image stitching system for radiographic images. *J Digit Imaging.* (2013) 26(2):361–70. doi: 10.1007/s10278-012-9483-5

6. Yang F, He Y, Deng ZS, Yan A. Improvement of automated image stitching system for DR x-ray images. *Comput Biol Med.* (2016) 71:108–14. doi: 10.1016/j.compbiomed.2016.01.026

7. Ben-Zikri YK, Yaniv ZR. A marker-free registration method for standing x-ray panorama reconstruction for hip-knee-ankle axis deformity assesment. *Comput Meth Biomech Biomed*. (2018) 7(4):464–78. doi: 10.1080/21681163.2018.1537859

8. Gooßen A, Schlüter M, Hensel M, Pralow T, Grigat R-R, editors. *Ruler-Based automatic stitching of spatially overlapping radiographs. Bildverarbeitung für die medizin*. Berlin, Heidelberg: Springer Berlin Heidelberg (2008). p. 192–6.

9. Wang L, Traub J, Heining SM, Benhimane S, Euler E, Graumann R, et al. Long bone x-ray image stitching using camera augmented mobile C-arm. *Med Image Comput Comput Assist Interv*. (2008) 11(Pt 2):578–86. doi: 10.1007/978-3-540-85990-1_69

10. Canny J. A computational approach to edge detection. *IEEE Trans Pattern Anal Mach Intell*. (1986) PAMI-8(6):679–98. doi: 10.1109/TPAMI.1986.4767851

11. Barbhuiya AHMJI, Hemachandran K. Wavelet tranformations & its Major applications in digital image processing. *Int J Eng Res Technol*. (2013) 02(03). doi: 10.17577/IJERTV2IS3538

12. Krackow KA. *The measurement and analysis of axial deformity of the knee*. Mahwah, New Jersey: Homer Stryker Center. (2008).

13. Ren S, He K, Girshick RB, Sun J. Faster R-CNN: towards real-time object detection with region proposal networks. *IEEE Trans Pattern Anal Mach Intell*. (2015) 39:1137–49. doi: 10.1109/TPAMI.2016.2577031

frontiers | Frontiers in Surgery

TYPE Original Research
PUBLISHED 14 October 2022
DOI 10.3389/fsurg.2022.956696

Check for updates

OPEN ACCESS

EDITED BY
Tengbo Yu,
The Affiliated Hospital of Qingdao University, China

REVIEWED BY
Osvaldo Mazza,
Bambino Gesù Children's Hospital (IRCCS), Italy
Biagio Zampogna,
Policlinico Universitario Campus Bio-Medico, Italy

*CORRESPONDENCE
Xinyu Liu
newyuliu@163.com
Lianlei Wang
wllspine@163.com

†These authors have contributed equally to this work

SPECIALTY SECTION
This article was submitted to Orthopedic Surgery, a section of the journal Frontiers in Surgery

RECEIVED 30 May 2022
ACCEPTED 27 September 2022
PUBLISHED 14 October 2022

CITATION
Wang Z, Tian Y, Li C, Li D, Ibrahim Y, Yuan S, Wang X, Tang J, Zhang S, Wang L and Liu X (2022) Radiographic risk factors for degenerative lumbar spondylolisthesis: A comparison with healthy control subjects. Front. Surg. 9:956696. doi: 10.3389/fsurg.2022.956696

COPYRIGHT
© 2022 Wang, Tian, Li, Li, Ibrahim, Yuan, Wang, Tang, Zhang, Wang and Liu. This is an open-access article distributed under the terms of the Creative Commons Attribution License (CC BY). The use, distribution or reproduction in other forums is permitted, provided the original author(s) and the copyright owner(s) are credited and that the original publication in this journal is cited, in accordance with accepted academic practice. No use, distribution or reproduction is permitted which does not comply with these terms.

Radiographic risk factors for degenerative lumbar spondylolisthesis: A comparison with healthy control subjects

Zheng Wang†, Yonghao Tian†, Chao Li, Donglai Li, Yakubu Ibrahim, Suomao Yuan, Xia Wang, Juan Tang, Shijun Zhang, Lianlei Wang* and Xinyu Liu*

Department of Orthopedics, Qilu Hospital, Cheeloo College of Medicine, Shandong University, Jinan, Shandong, China

Objective: To evaluate the radiologic parameters of degenerative lumbar spondylolisthesis (DLS) and determine the radiographic risk factors for DLS by making comparisons with healthy control subjects.

Methods: Seventy-five patients with L4/5 DLS (Meyerding grade I) and 53 healthy control subjects were analyzed. The L1-S1 disc height index (DHI), L4/5 facet joint angle (FJA), and relative cross-sectional area (RCSA) of paravertebral muscles were measured in both groups. The initial L4/5 DHI (iDHI) before the onset of DLS were estimated based on the L3/4 DHI of the DLS group and DHI of the control group. The sagittal parameters of DLS were also included in this study.

Results: The DHI of L4/5 was lower in the DLS group than in the control group ($P < 0.05$), but the DHI of the L1-L4 segments were much higher than in the control group ($P < 0.05$). The initial L4/5 DHI and FJA of the DLS group were significantly higher than those of the control group ($P < 0.05$). The RCSA of the paravertebral muscles were smaller in the DLS group than in the control group ($P < 0.05$). Binary logistic regression analysis showed that iDHI, FJA, and RCSA of the total paraspinal muscles were risk factors for DLS. The cutoff values for iDHI, FJA, and RCSA were 0.504, 56.968°, and 1.991 respectively. The iDHI was associated with lumbar lordosis (LL), while L4/5 DHI was associated with the RCSA of the multifidus muscle and psoas major muscle ($P < 0.05$).

Conclusion: A large initial lumbar disc height, large FJA, and paravertebral muscle atrophy may be risk factors for DLS.

KEYWORDS

degenerative lumbar spondylolisthesis, disc height, facet joint, paraspinal muscle, radiographic risk factors

Abbreviations

DHI, disc height index; iDHI, initial L4/5 disc height index; FJA, facet joint angel; RCSA, relatve cross-sectional area; T-RCSA, relatve cross-sectional area of total paraspinal muscles; PI, pelvic incidence; PT, pelvic tilt; SS, sacral slope; LL, lumbar lordosis.

Introduction

Spondylolisthesis involves an anterior migration or slip of a vertebra in relation to the next caudal vertebra. Macnab (1) described spondylolisthesis with an intact neural arch — "pseudo-spondylolisthesis". The term "degenerative spondylolisthesis" was coined by Newman and Stone (2) in 1955, who noted that slippage of vertebrae with an intact neural arch was the result of degenerative arthritis of the lumbar facet joints.

Pope (3) defined spinal instability as displacement of the vertebral bodies due to loss of supportability of the constraining structures, such as the intervertebral discs and facet joints. Vernon-Roberts (4) postulated that degenerative changes of the spine are initiated by structural disorders associated with aging, degeneration, and disc prolapse. Subsequent local or overall disc height decrease leads to forward tilt of the upper vertebral body around the axis of the facet joint, resulting in vertebral instability, facet joint degeneration, osteophyte proliferation, and a series of subsequent changes (5).

The imaging characteristics and risk factors of degenerative lumbar spondylolisthesis (DLS) have been previously investigated. The reported risk factors include female sex (6), lumbar spine degeneration (higher Pfirrmann grade, kyphotic deformity of the sacrum, and facet sclerosis grade) (7–9), more sagittally-oriented facets (10, 11), lumbar lordosis angle, lumbar index (12, 13), shorter transverse process (14), decreased anterior disc height (13), and multifidus muscle atrophy (15). A prospective observation and case-control study with 15-year follow-up in Japan showed a 14% (25/180) incidence of *de novo* DLS during the 15-year period. Progression of the L4 slip (≥3 mm) was observed in 23 participants after 15 years. The significant risk factors for L4 slip progression were identified as age less than 60 years, female sex, lumbar axis sacral distance, facet sagittalization, and existence of slip at baseline (16).

Previous studies have found that the higher and less degenerated have greater intervertebral mobility (17, 18), and disc height decreased at the lesion segment in patients with DLS (13). However, the initial disc height before the lesion has not been studied. The purposes of this study were to investigate the radiographic risk factors of DLS and explore the relationships between intervertebral disc height and other imaging parameters in patients with DLS. We accomplished these by comparing differences in the L1-S1 disc height index (DHI), initial L4/5 disc height index (iDHI), facet joint angle (FJA), and relative cross-sectional area (RCSA) of the paraspinal muscle between patients with and without DLS.

Materials and methods

Inclusion and exclusion criteria

This study was approved by the ethics committee of Qilu Hospital of Shandong University and performed in accordance with the Helsinki Declaration. The inclusion criteria were as follows: (1) DLS with Meyerding grade I slippage at L4/5 level; (2) an age between 50 and 70 years; (3) complete pre- and post-operative imaging information (lumbar lateral x-ray, computed tomography, and magnetic resonance imaging data). The exclusion criteria were as follows: (1) lumbar coronal deformity, spine fractures, spine infections, trauma, tumors, and hip and lower extremity disorders; (2) history of previous spinal and/or limb surgery; (3) systemic diseases. The x-ray, CT and MRI of DLS patients and normal subjects were shown in **Figure 1**.

General information

The DLS group included 75 patients with L4/5 DLS who received treatment between January 2015 and October 2021 (33 men, 42 women; mean age, 60.4 ± 6.4 years). The control group consisted of 53 participants (23 men, 30 women; mean age, 58.4 ± 5.4 years). The authors counted and compared the BMI (body mass index) and the number of smokers in the two groups.

Radiographic measurements

DHI

Sagittal T2-weighted magnetic resonance images of the lumbar spine were used for measurement of the anterior edge height (A) and posterior edge height (B) of the L4/5 intervertebral disc, which was performed using Image J software (NIH Corp., Bethesda, USA). The L4 vertebra height (C) and L5 vertebra height (D) were also measured. DHI was calculated as (A + B)/(C + D), to exclude the influence of individual height and weight differences on intervertebral disc height (**Figure 2**) (19–21). The DHI of L1/2, L2/3, L3/4, and L5/S1 were measured using the same method.

The L4/5 to L3/4 intervertebral height ratio in Chinese individuals is about 1.14 (22). The ratio of the L4/5 to L3/4 disc height in our control group measured by the method described in the literature (22) was 1.16, which is similar to the published results. Using the L3/4 DHI of the DLS group and the ratio of L3/4 to L4/5 DHI (1.18) of the control group, the initial L4/5 DHI (iDHI) of the DLS group was calculated as L3/4 DHI × 1.18.

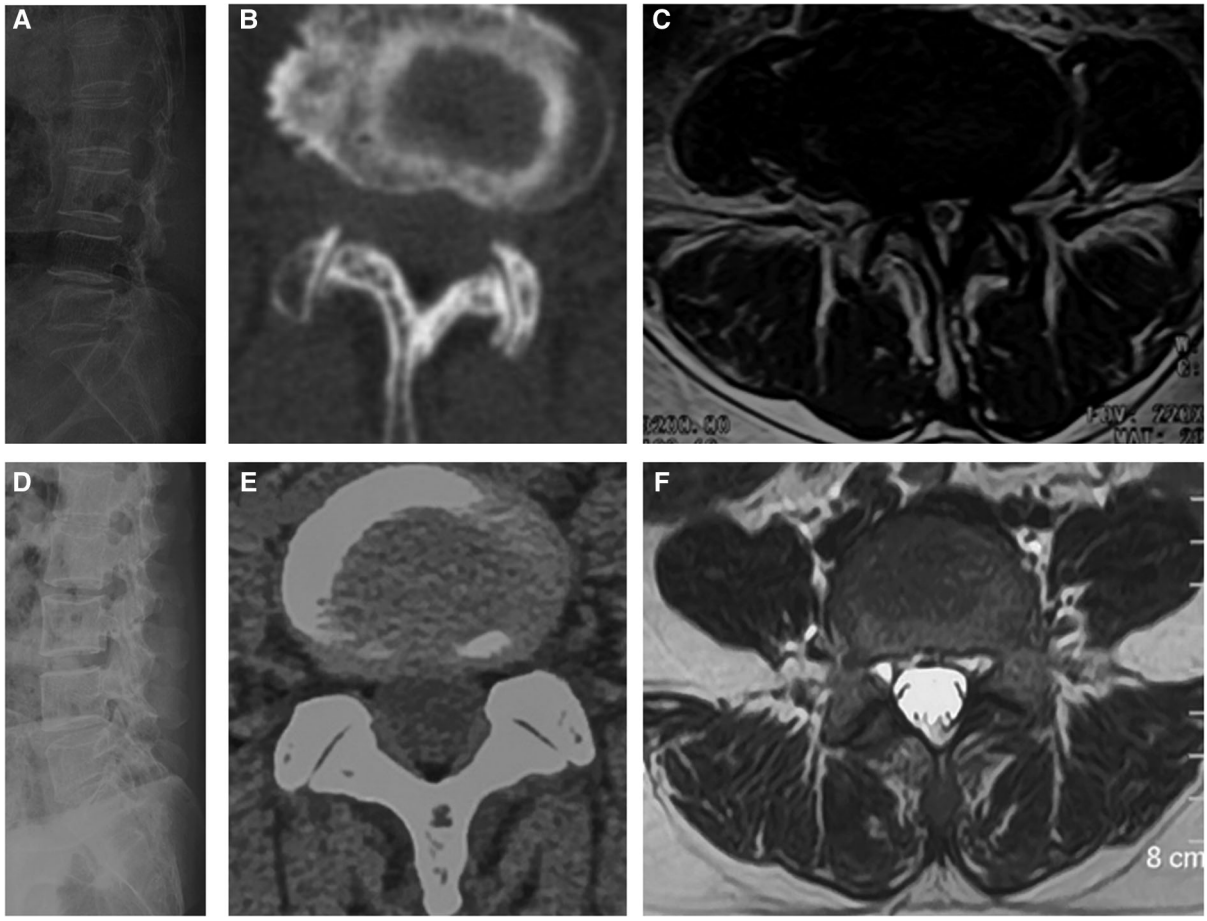

FIGURE 1
(A, B and C) are x-ray, CT and MRI of DLS patients, respectively. (D, E and F) are x-ray, CT and MRI of Normal subjects respectively.

FJA

An axial computed tomography image of the lumbar spine was used for FJA measurement. The middle of the L4/5 vertebral space was identified parallel to the end plate level of the lower edge of L4, and the angle of the connection between the two highest points of the posterior edge of the vertebral body and the connection between the anterior wall of the upper facet and the posterior wall of the lower facet was measured. The right-side FJA was denoted as A and the left as B, and the average angle of both sides was calculated as (A + B)/2 (23) (**Figure 3**). The average bilateral FJAs were compared between the DLS and control groups. The differences in the average angle were also compared between men and women in the DLS group and the control group.

Relative cross-sectional area (RCSA) of paravertebral muscle

An axial T2-weighted magnetic resonance image of the lumbar spine was used to calculate the CSA of paravertebral muscle. The middle of the L4/5 intervertebral space was taken parallel to the end plate of the lower edge of L4. The CSAs of the bilateral psoas major, multifidus, and erector spinae muscles were measured using ImageJ software, and the CSA of each muscle was defined as the boundary of the deep fascia surrounding the innermost muscle. The lower edge of the L4 vertebral body was identified and the CSA of the L4 vertebral body was measured as VCSA. The relative CSA (RCSA) of each paraspinal muscle was calculated and the interactions of height and weight differences on the paraspinal muscle CSA were excluded. The RCSAs were calculated as PCSA/VCSA for psoas major muscle, MCSA/VCSA for multifidus muscle, and ECSA/VCSA for erector spinae muscle (**Figure 4**). The sum of the RCSAs of the three paraspinal muscles defined the total paraspinal muscle RCSA(T-RCSA) (24). The bilateral average value was taken.

Lumbosacral sagittal parameters

All patients underwent a full-spine x-ray examination. Radiological parameters investigated included (1) lumbar lordosis (LL)—the Cobb's angle between the superior endplate

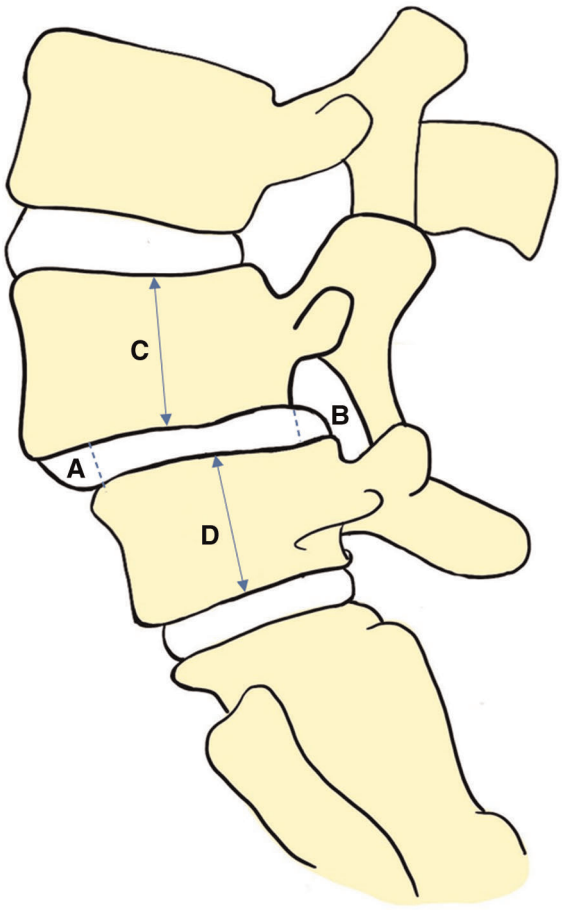

FIGURE 2
Measurement method of intervertebral disc height index: (A + B)/(C + D).

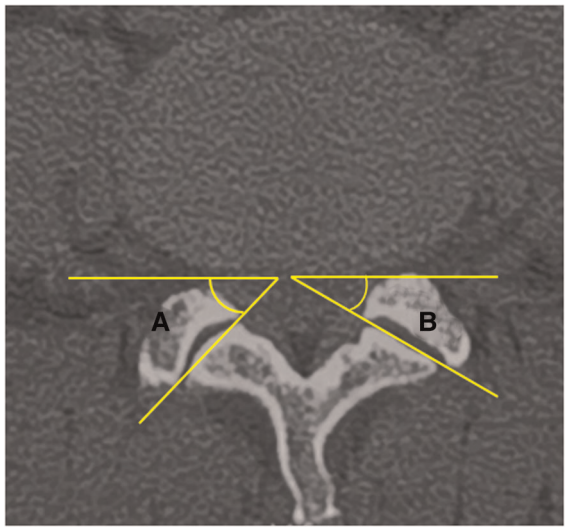

FIGURE 3
Measurement method of facet joint angle: (A + B)/2.

of L1 and S1; (2) pelvic incidence (PI)—the angle between the line perpendicular to the sacral plate at its midpoint and the line connecting this point to the axis of the femoral head; (3) pelvic tilt (PT)—the angle between the vertical line and the line connecting the midpoint of the sacral plate to the axis of the femoral head; and (4) sacral slope (SS)—the angle between the sacral plate and the horizontal line. Lordotic angles were noted as positive, and kyphotic ones as negative (25). The measurement methods are shown in Figure 5.

Statistical analysis

SPSS 22.0 (IBM Corp., Armonk, NY, USA) was used for statistical analysis. Measurement data are expressed as mean ± standard deviation. Independent-samples *t*-tests were used to analyze data with a normal distribution. The imaging parameters of the two groups were analyzed using binary logistic regression with the initial L4/5 DHI, FJA, and total paraspinal muscle RCSA included as independent variables in the binary logistic regression model. Because of a high degree of collinearity between the L4/5 DHI and other data, L4/5 DHI was not included in this model. The odds ratios (ORs), 95% confidence intervals (CIs), and *P*-values of each parameter were calculated using this model. Receiver operating characteristics (ROC) and Youden's index were used to calculate cutoff values for risk factors. In the DLS group, Pearson's correlation was used to determine the correlation between the L4/5 DHI and other parameters, and the correlation between the initial L4/5 DHI and lumbosacral sagittal parameters. A *P* value of <0.05 was considered statistically significant. The inclusion test level was $\alpha = 0.05$.

Results

The demographic data of the two groups are shown in Table 1. There were no statistically significant differences in age, sex, BMI or number of smokers between the two groups ($P > 0.05$).

DHI

The DHI of L4/5 were lower in the DLS group than in the control group ($P < 0.05$; Table 1), whereas the DHI of L1-4 and L5/S1 segments were higher in the DLS group than in the control group ($P < 0.05$). The ratio of the L4/5 to L3/4 DHI were lower in the DLS group than in the control group ($P < 0.05$). The initial L4/5 DHI was significantly higher in the DLS group (0.53 ± 0.11) than in the control group (0.41 ± 0.07) ($P < 0.05$; Table 1).

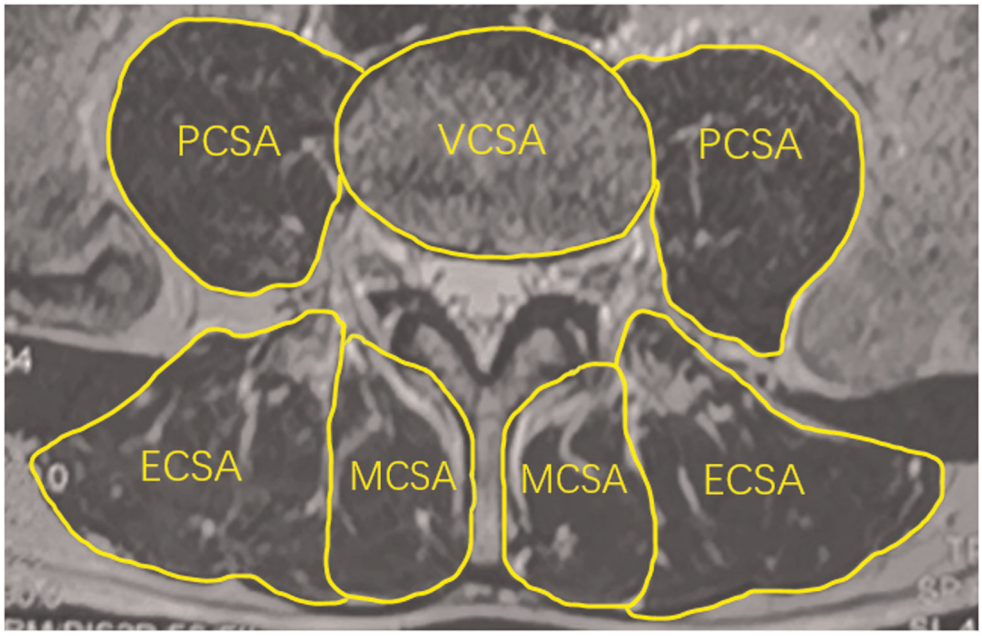

FIGURE 4
Measurement method of relative cross-sectional area of paraspinal muscles. MCSA, the CSA of multifidus muscle; ECSA, the CSA of erector spinae muscle; PCSA, the CSA of psoas major muscle; VCSA, the CSA of the L4 vertebral body.

FJA

The L4/5 FJA was higher in the DLS group than in the control group ($P < 0.05$; Table 1), but there was no significant difference between the bilateral FJA in the two groups ($P < 0.05$; Table 2). There was no significant difference between men and women in the DLS group and the control group ($P < 0.05$).

RCSA of paravertebral muscle

The RCSAs of three paravertebral muscles (multifidus, erector spinae, and psoas major) were smaller in the DLS group than in the control group (all $P < 0.05$; Table 1).

Lumbosacral sagittal parameters

The mean values of PT, PI, LL, SS, and PI-LL in the DLS group were 23.2 ± 7.7°, 52.8 ± 10.3°, 45.0 ± 12.9°, 29.5 ± 8.5°, and 7.7 ± 11.8°, respectively (Table 3).

Correlations between the radiographic parameters

The initial L4/5 DHI showed a significant positive correlation with LL ($r = 0.361$, $P < 0.05$; Table 3), but no significant correlation with PI, PT, SS, or PI-LL ($P > 0.05$). L4/5 DHI showed significant positive correlations with L2/3 DHI ($r = 0.470$, $P < 0.05$; Table 4; Figure 6), L3/4 DHI ($r = 0.529$, $P < 0.05$; Figure 6), and L5/S1 DHI ($r = 0.463$, $P < 0.05$; Figure 6) in the DLS group, but no significant correlation with L1/2 DHI ($P > 0.05$). L4/5 DHI showed significant positive correlations with the RCSA of the multifidus muscle ($r = 0.390$, $P < 0.05$) and psoas major muscle ($r = 0.294$, $P < 0.05$; Table 4, Figure 6), but no significant correlation with the RCSA of the erector spinae muscle ($P > 0.05$).

Radiographic risk factors for DLS

The risk factors for DLS were initial L4/5 DHI (OR = 1.443, 95% CI = 1.081–1.927, $P = 0.013$), FJA (OR = 1.845, 95% CI = 1.210–2.813, $P = 0.004$), and RCSA of the total paravertebral muscle (OR = 0.495, 95% CI = 0.289–0.847, $P = 0.010$; Table 5).

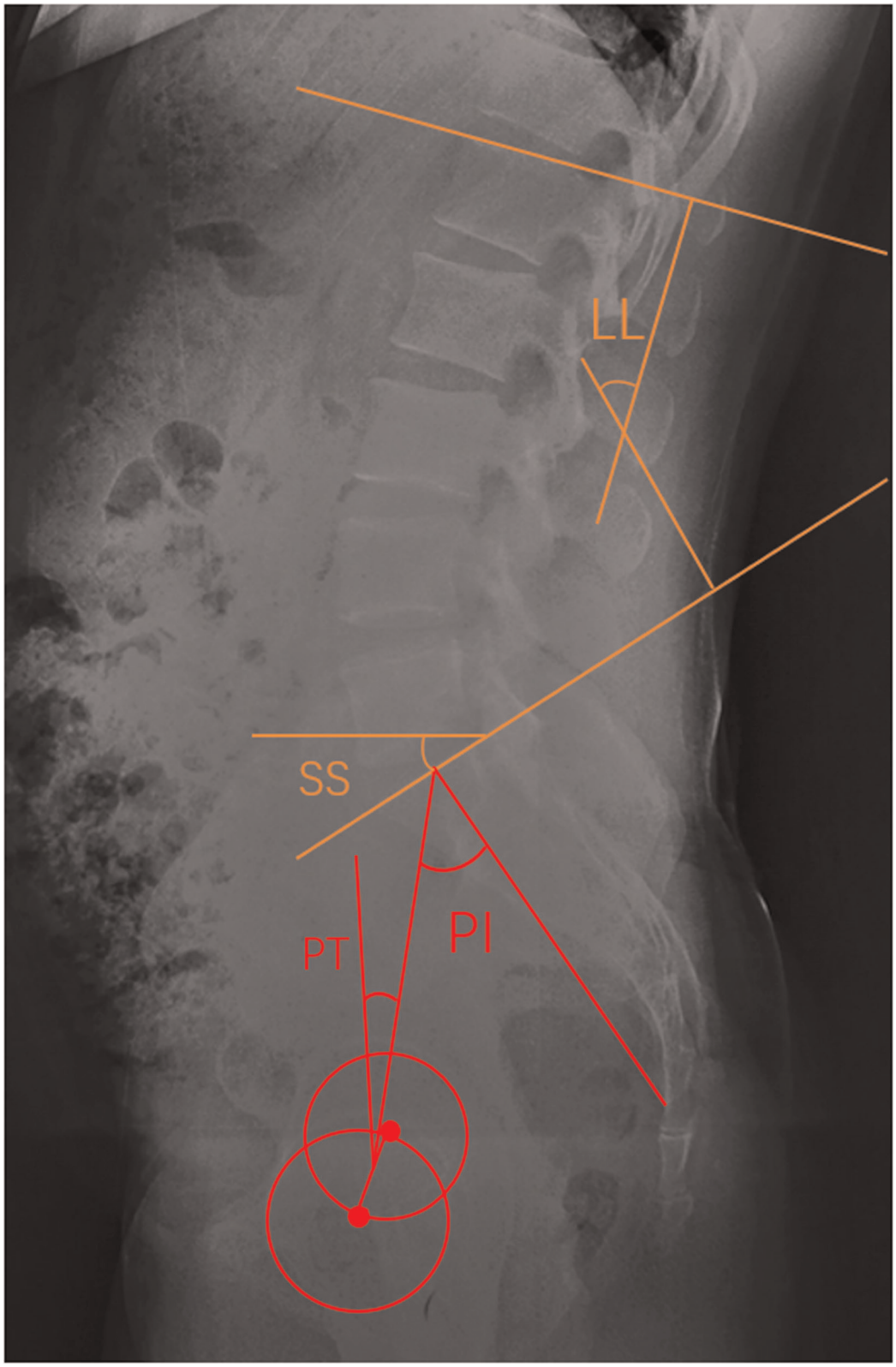

FIGURE 5
The lumbosacral sagittal parameters, included PI, PT, LL and SS.

TABLE 1 Comparison of results between two groups ($\bar{x} \pm s$).

	DLS group	Control group	*P* value
Age (years)	60.4 ± 6.4	58.4 ± 5.4	0.096
Sex (men: women)	33:42	20:33	0.479
BMI	23.6 ± 4.5	23.4 ± 4.9	0.851
Smokers (%)	15 (20%)	9 (16.7%)	0.666
DHI			
L1/2	0.35 ± 0.05	0.26 ± 0.03	0.000*
L2/3	0.39 ± 0.073	0.29 ± 0.04	0.000*
L3/4	0.44 ± 0.10	0.34 ± 0.06	0.000*
L4/5	0.35 ± 0.13	0.41 ± 0.07	0.017*
Ratio of L4/5 to L3/4	0.80 ± 0.26	1.18 ± 0.15	0.000*
L5/S1	0.40 ± 0.09	0.36 ± 0.09	0.019*
Initial L4/5 DHI	0.53 ± 0.11	0.41 ± 0.07	0.000*
FJA (°)	63.95 ± 9.99	44.64 ± 7.94	0.000*
RCSA			
Multifidus muscle	0.44 ± 0.12	0.58 ± 0.11	0.000*
Erector spine muscle	0.79 ± 0.18	0.90 ± 0.24	0.010*
Psoas major muscle	0.55 ± 0.20	0.71 ± 0.18	0.000*

DLS, degenerative lumbar spondylolisthesis; BMI, body mass index; DHI, disc height index; FJA, Facet joint angle; CSA, Cross sectional area; RCSA, Relative cross sectional area.
The level of statistical significance was set at 0.05.
*$P < 0.05$.

TABLE 2 Comparison of FJA in the two groups ($\bar{x} \pm s$).

	Right side	Left side	*P* value
DLS group	65.19 ± 10.98	62.71 ± 11.29	0.270
Control group	46.01 ± 8.78	43.28 ± 9.03	0.129
	Male	Female	*P* value
DLS group	63.84 ± 10.26	64.03 ± 9.97	0.950
Control group	43.45 ± 8.68	45.65 ± 7.27	0.333

DLS, degenerative lumbar spondylolisthesis; FJA, Facet joint angle.
The level of statistical significance was set at 0.05.
*$P < 0.05$.

ROC curves and Youden's indices of the risk factors

For the prediction of DLS, the area under the ROC curve (AUC) of the initial L4/5 DHI was 0.812 (standard error, 0.042; $P = 0.000$; 95% CI = 0.729–0.895; Table 5, Figure 7). With a cutoff value of 0.504, the sensitivity, specificity, and Youden's index of the iDHI were 58.0%, 94.0%, and 0.52 respectively, (Table 5). The AUC of FJA was 0.936 (standard error, 0.025; $P = 0.000$; 95% CI = 0.888–0.984; Table 5, Figure 7), and with a cutoff value of 56.968, the sensitivity, specificity, and Youden's index were 76.0%, 98.0%, and 0.74, respectively (Table 5).

The AUC of the total paraspinal muscle RCSA was 0.236 (standard error, 0.048; $P = 0.000$; 95% CI = 0.142–0.330). After adjusting the test direction, the AUC was 0.764 and the cutoff value 1.991, providing sensitivity, specificity, and Youden's index of 70.0%, 76.0%, and 0.46, respectively.

TABLE 3 Correlation between initial L4/5 DHI and lumbosacral sagittal parameters.

	Mean value (°)	*R* value	*P* value
PT	23.2 ± 7.7	0.042	0.795
PI	52.8 ± 10.3	0.226	0.162
LL	45.0 ± 12.9	0.361	0.022*
SS	29.5 ± 8.5	0.143	0.236
PI-LL	7.7 ± 11.8	−1.98	0.220

PI, pelvic incidence; PT, pelvic tilt; SS, sacral slope; LL, lumbar lordosis.
*The level of statistical significance was set at 0.05.

TABLE 4 Correlation between L4/5 DHI and other imaging parameters.

	R value	*P* value
DHI		
L1/2	0.017	0.907
L2/3	0.470	0.001*
L3/4	0.529	0.000*
L5/S1	0.463	0.001*
FJA	0.028	0.849
RCSA		
Multifidus muscle	0.390	0.005*
Erector spine muscle	0.187	0.194
Psoas major muscle	0.294	0.038*

DHI, disc height index; FJA, facet joint angle; RCSA, relative cross sectional area of total paraspinal muscle.
The level of statistical significance was set at 0.05.
*$P < 0.05$.

Discussion

Our study showed that a large initial lumbar DHI, a large FJA, and paravertebral muscle atrophy are risk factors for DLS.

Similar to previous studies (14), we found that the DHI of L4/5 was much lower in patients with DLS than in healthy control subjects. Berlemann (7) found that the severity of lumbar spondylolisthesis was significantly negatively correlated with disc height after lesion occurrence, and was associated with the sagittal alignment of the L4/5 facet joint. The decreased disc height and volume were mainly caused by disc degeneration (26), with DLS patients having a high degree of disc degeneration (10). To date, most studies only focused on the disc height of the affected level, ignoring the disc height of upper and lower segments. In our clinical practice, we noted that the adjacent disc height is usually high in patients with DLS, and therefore wondered whether the

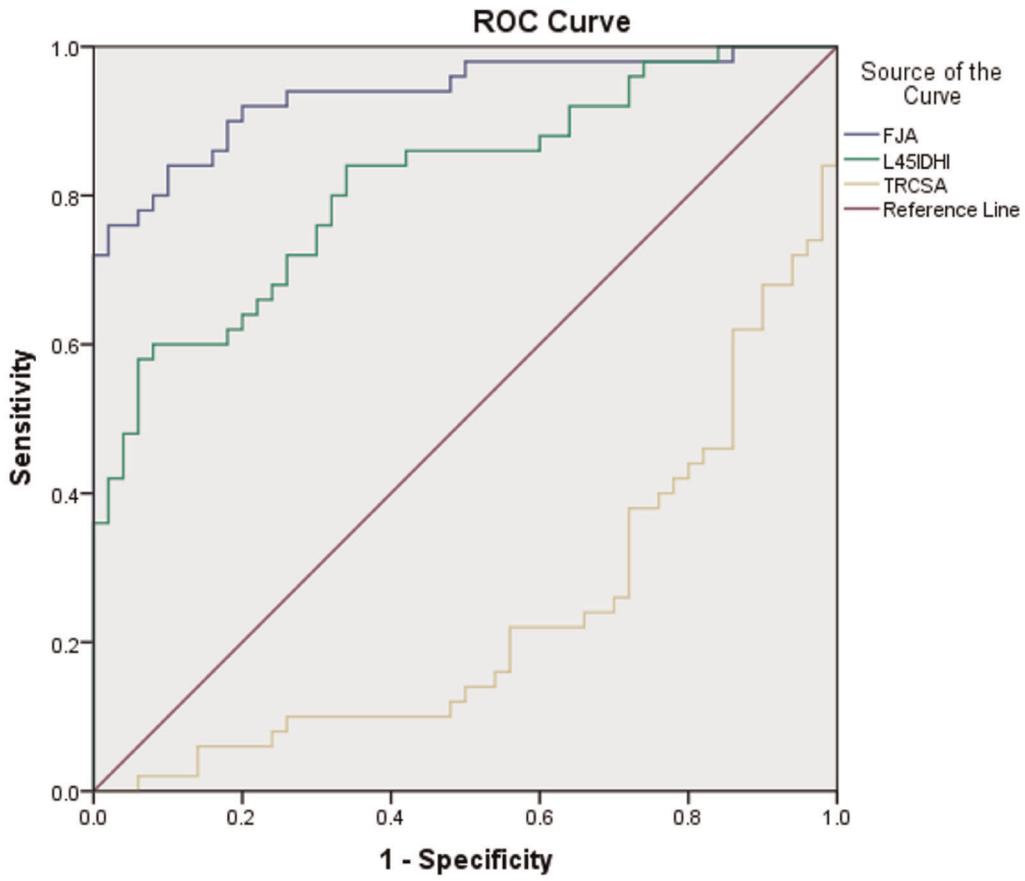

FIGURE 6
Receiver operating characteristics curve. IDHI: initial L4/5 disc height index, FJA: facet joint angle, TRCSA: relative cross-sectional area of total paraspinal muscle.

initial intervertebral height might be related to the occurrence of DLS.

In healthy Chinese individuals, the L4/5 to L3/4 intervertebral height ratio is about 1.14 (22). The ratio of the L4/5 to L3/4 disc height in our control group measured by the method described in the literature (22) was 1.16, which is similar to the published results. Thus, we consider our estimates of initial L4/5 DHI to be reliable and suitable for statistical analysis. Our estimated initial L4/5 DHI in the DLS group was significantly higher than the measured L4/5 DHI in the control group, and L1-4 and L5/S1 DHIs were also significantly higher in the DLS group than in the control group. Logistic regression showed that patients with a large initial L4/5 DHI were more prone to DLS, with an optimal cutoff value of 0.505. Therefore, the authors stipulated that this initial higher intervertebral height at the affected level may play an important role in slip progression in DLS, and act as a risk factor for DLS. When the spine is over-extended and over-flexed, a higher disc height is associated with lower disc stiffness and a greater risk of deformation, which may be related to disc geometry, calcification, or degenerative changes (27). As a result, the posterior column of the spine bears a greater load during activity, and the small joint capsule and ligament will withstand greater stretch tension (28). Many authors have measured spinal mobility with respect to the effect of age and disc degeneration (29). Lumbar mobility is determined by the geometry and material properties of the intervertebral structures, the higher discs and less degenerated dics have greater intervertebral mobility (17). Studies have shown that discs can undergo rapid deformation in response to changes in pressure, and the rapid deformation was associated with nucleus pulposus and endplate flow. Thus, high discs with greater mobility and deformability have more intense nucleus pulposus flow and are more susceptible to disc degeneration (18). When the discs and facet joints are unstable, the lumbar spine is subjected to shear forces, resulting in grade 1 DLS (30). As the disc degenerates, the disc height decreases, the supporting pressure effect and spinal flexibility decreases as a result (17).

TABLE 5 Logistic regression analysis between 2 groups.

	OR	95% CI		*P* value
Initial L4/5 DHI	1.443	1.081–1.927		0.013*
FJA	1.845	1.210–2.813		0.004*
T-RCSA	0.495	0.289–0.847		0.010*
ROC curve	**AUC**	**Standard error**	***P* value**	**95% CI**
Initial L4/5 DHI	0.812	0.042	0.000*	0.729–0.895
FJA	0.936	0.025	0.000*	0.888–0.984
T-RCSA	0.236	0.048	0.000*	0.142–0.330
Cutoff value and Yuden index	**Cutoff value**	**Sensitivity**	**Specificity**	**Yuden index**
Initial L4/5 DHI	0.504	58.0%	94.0%	0.52
FJA	56.968	76.0%	98.0%	0.74
T-RCSA	1.991	70.0%	76.0%	0.46

DHI, disc height index; FJA, facet joint angle; T-RCSA, relative cross-sectional area of total paraspinal muscle.
The level of statistical significance was set at 0.05.
*$P < 0.05$.

Among lumbosacral sagittal parameters, a large LL and PI were found to be significant predictors of L4 DLS by some researchers (31), with a cutoff value of 45.0° for LL, the same value as the mean LL of the DLS patients in the current study. We also analyzed the initial L4/5 DHI and lumbosacral sagittal parameters and found a significant positive correlation between the initial L4/5 DHI and LL. Therefore, the higher disc height is associated with lumbar instability. The LL of patients with DLS is larger than that of age-matched subjects without DLS (16, 31). This larger LL causes L4 to become the apex of LL and applies greater shear force that increases spinal instability, causing DLS.

Many studies showed that sagittally-oriented facets at L4/5 may be a risk factor for DLS (32). Coronal facet surfaces can withstand greater shear forces than sagittal facet surfaces. Therefore, the intervertebral discs and capsular ligaments of sagittal facet joints are more susceptible to further damage due to anterior-posterior shear forces. In our study, the FJA of patients with DLS was significantly larger than that of control subjects of the same age. The cutoff value for the angle as a risk factor was 57°. Abnormal morphology of the lumbar articular processes is a predisposing factor for the development of DLS. Although many studies have revealed sagittal deviation of the facet joints in DLS, it is difficult to

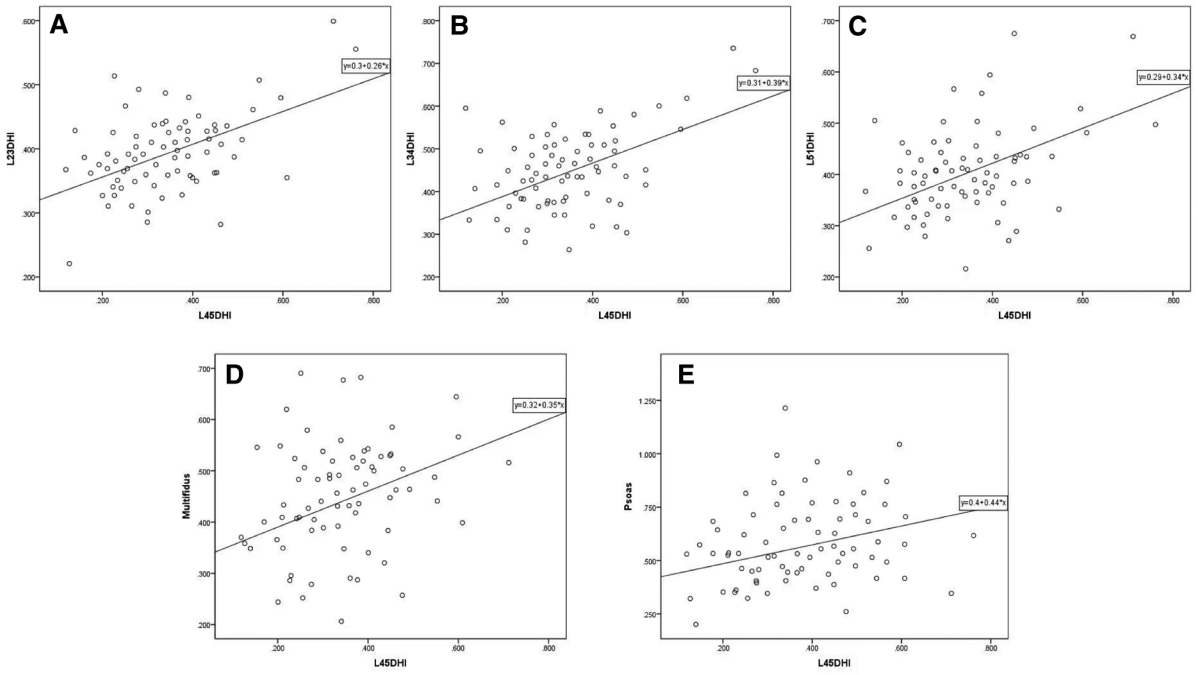

FIGURE 7
Scatter plot of L4/5 DHI and other imaging parameters in DLS group. (**A**, **B**, **C**) L4/5 DHI showed significant positive correlations with L2/3 DHI ($r = 0.470$, $P < 0.05$), L3/4 DHI ($r = 0.529$, $P < 0.05$), and L5/S1 DHI ($r = 0.463$, $P < 0.05$) in the DLS group. (**D**, **E**) L4/5 DHI showed significant positive correlations with the RCSA of the multifidus muscle ($r = 0.390$, $P < 0.05$) and psoas major muscle ($r = 0.294$, $P < 0.05$). DHI: disc height index, Multifidus: relative cross-sectional area of multifidus muscle, Psoas: relative cross-sectional area of psoas major muscle.

demonstrate that this is a preexisting factor for lumbar spondylolisthesis. Our study also showed no correlation between FJA and DHI. Moreover, joint asymmetry can lead to uneven stresses on the small joints and uneven distribution of pressure and biomechanical forces on the intervertebral discs, which can eventually lead to DLS. Current studies report the incidence of joint asymmetry to be between 40% and 70%, with L4/5 being the most commonly affected segment (33). Some authors have found that joint asymmetry is significantly associated with DLS (11, 34). Devanand found that facet angle sagittalization was significantly associated with the L5-S1 level in men and the L4-5 level in women (35). However, we did not find a significant difference in bilateral FJA between the DLS and control group, and no significant difference was found between men and women in either the DLS or control group.

The paraspinal muscles, including the multifidus, erector spinae, and psoas major, are very important for maintaining spine stability and lumbar lordosis (36). In patients with DLS, both the degree of multifidus atrophy and the T2 signal intensity are increased, suggesting that fat infiltration reduces muscle strength and may lead to instability of adjacent vertebrae (15). In this study, the RCSA of the multifidus muscle in the affected segment was significantly smaller than that in the control group, suggesting that multifidus muscle atrophy occurred in patients with spondylolisthesis. Furthermore, atrophy of the erector spinae and psoas major muscles was also observed in the DLS group, and our statistical analysis showed a decreased total paraspinal muscle area (with a cutoff value of 1.991 for prediction of DLS), which facilitated the occurrence of DLS.

In patients with LDH or spinal stenosis, the degree of disc degeneration is positively correlated with paraspinal atrophy (36, 37), and a smaller intervertebral space in DLS is associated with a greater degree of vertebral slippage (7, 38), resulting in more severe squeezing or pulling of nerve roots. When the dorsal ramus nerve is covered and compressed by scar tissue after surgery, the local paraspinal muscles of the corresponding segment will undergo denervation atrophy (39). Tamai et al. (40) found that multifidus atrophy was related to the severity of lumbar spondylolisthesis and that intervertebral disc degeneration could interact with paravertebral muscle fat infiltration. Our results also indicate that a lower DH is associated with paraspinal muscle atrophy.

The current study also has several limitations. First, this study is a retrospective study, there are certain limitations in the study of the pathogenesis of degenerative lumbar spondylolisthesis and the order of changes in imaging parameters. More prospective studies and basic studies such as physiology, pathology, anatomy, cytology, and ergonomics may be needed for further explorations. Second, the small sample size significantly limits the generalizability of the results to a wider population. Thirdly, as the study has been conducted on a Chinese population, it is possible that the external validity of the results may not be applicable to other populations with different anthropometric characteristics.

Conclusions

A large initial lumbar disc height, large FJA, and paravertebral muscle atrophy may be risk factors for DLS.

Data availability statement

The raw data supporting the conclusions of this article will be made available by the authors, without undue reservation.

Ethics statement

Written informed consent was obtained from the individual(s) for the publication of any potentially identifiable images or data included in this article.

Author contributions

ZW and YT contributed equally to the main manuscript text and prepared figures. All authors contributed to the article and approved the submitted version.

Funding

This work was supported in part by the National Nature Science Foundation (81874022 and 82172483 to Xinyu Liu; 82102522 to Lianlei Wang) and Shandong Natural Science Foundation (ZR202102210113 to Lianlei Wang).

Conflict of interest

The authors declare that the research was conducted in the absence of any commercial or financial relationships that could be construed as a potential conflict of interest.

Publisher's note

All claims expressed in this article are solely those of the authors and do not necessarily represent those of their affiliated organizations, or those of the publisher, the editors and the reviewers. Any product that may be evaluated in this article, or claim that may be made by its manufacturer, is not guaranteed or endorsed by the publisher.

References

1. Macnab I. Spondylolisthesis with an intact neural arch; the so-called Pseudo-spondylolisthesis. *J Bone Jt Surg Br Vol.* (1950) 32-b(3):325–33. doi: 10.1302/0301-620x.32b3.325

2. Fitzgerald JA, Newman PH. Degenerative spondylolisthesis. *J Bone Jt Surg Br Vol.* (1976) 58(2):184–92. doi: 10.1302/0301-620x.58b2.932080

3. Pope MH, Panjabi M. Biomechanical definitions of spinal instability. *Spine.* (1985) 10(3):255–6. doi: 10.1097/00007632-198504000-00013

4. Vernon-Roberts B, Pirie CJ. Degenerative changes in the intervertebral discs of the lumbar Spine and their sequelae. *Rheumatol Rehabil.* (1977) 16(1):13–21. doi: 10.1093/rheumatology/16.1.13

5. Takashima H, Takebayashi T, Yoshimoto M, Terashima Y, Ida K, Shishido H, et al. Investigation of intervertebral disc and facet joint in lumbar spondylolisthesis using T2 mapping. *Magn Reson Med Sci.* (2014) 13(4):261–6. doi: 10.2463/mrms.2013-0099

6. Vogt MT, Rubin D, Valentin RS, Palermo L, Donaldson 3rd WF, Nevitt M, et al. Lumbar olisthesis and lower back symptoms in elderly white women. The study of osteoporotic fractures. *Spine.* (1998) 23(23):2640–7. doi: 10.1097/00007632-199812010-00020

7. Berlemann U, Jeszenszky DJ, Bühler DW, Harms J. The role of lumbar lordosis, vertebral End-plate inclination, disc height, and facet orientation in degenerative spondylolisthesis. *J Spinal Disord.* (1999) 12(1):68–73. doi: 10.1097/00002517-199902000-00011

8. Postacchini F, Perugia D. Degenerative lumbar spondylolisthesis. Part I: etiology, pathogenesis, pathomorphology, and clinical features. *Ital J Orthop Traumatol.* (1991) 17(2):165–73.

9. Takahashi K, Yamagata M, Takayanagi K, Tauchi T, Hatakeyama K, Moriya H. Changes of the Sacrum in severe spondylolisthesis: a possible key pathology of the disorder. *J Orthop Sci.* (2000) 5(1):18–24. doi: 10.1007/s007760050004

10. Grannum S, Torrie PA, Miller A, Harding IJ. Risk factors for the development of a mobile degenerative spondylolisthesis at L4-L5. *Spine Deform.* (2015) 3(1):98–104. doi: 10.1016/j.jspd.2014.06.012

11. Dai LY. Orientation and tropism of lumbar facet joints in degenerative spondylolisthesis. *Int Orthop.* (2001) 25(1):40–2. doi: 10.1007/s002640000201

12. Antoniades SB, Hammerberg KW, DeWald RL. Sagittal plane configuration of the Sacrum in spondylolisthesis. *Spine.* (2000) 25(9):1085–91. doi: 10.1097/00007632-200005010-00008

13. Chen IR, Wei TS. Disc height and lumbar Index as independent predictors of degenerative spondylolisthesis in middle-aged women with low back pain. *Spine.* (2009) 34(13):1402–9. doi: 10.1097/BRS.0b013e31817b8fbd

14. Aihara T, Takahashi K, Yamagata M, Moriya H, Shimada Y. Does the iliolumbar ligament prevent anterior displacement of the fifth lumbar vertebra with defects of the pars? *J Bone Jt Surg Br Vol.* (2000) 82(6):846–50. doi: 10.1302/0301-620x.82b6.10302

15. Wang G, Karki SB, Xu S, Hu Z, Chen J, Zhou Z, et al. Quantitative mri and x-ray analysis of disc degeneration and paraspinal muscle changes in degenerative spondylolisthesis. *J Back Musculoskelet Rehabil.* (2015) 28(2):277–85. doi: 10.3233/bmr-140515

16. Enyo Y, Yoshimura N, Yamada H, Hashizume H, Yoshida M. Radiographic natural course of lumbar degenerative spondylolisthesis and its risk factors related to the progression and onset in a 15-year community-based cohort study: the miyama study. *J Orthop Sci.* (2015) 20(6):978–84. doi: 10.1007/s00776-015-0759-8

17. Mimura M, Panjabi MM, Oxland TR, Crisco JJ, Yamamoto I, Vasavada A. Disc degeneration affects the multidirectional flexibility of the lumbar spine. *Spine.* (1994) 19(12):1371–80. doi: 10.1097/00007632-199406000-00011

18. O'Connell GD, Jacobs NT, Sen S, Vresilovic EJ, Elliott DM. Axial creep loading and unloaded recovery of the human intervertebral disc and the effect of degeneration. *J Mech Behav Biomed Mater.* (2011) 4(7):933–42. doi: 10.1016/j.jmbbm.2011.02.002

19. Welsch GH, Trattnig S, Paternostro-Sluga T, Bohndorf K, Goed S, Stelzeneder D, et al. Parametric T2 and T2* mapping techniques to visualize intervertebral disc degeneration in patients with low back pain: initial results on the clinical use of 3.0 tesla mri. *Skeletal Radiol.* (2011) 40(5):543–51. doi: 10.1007/s00256-010-1036-8

20. Xue Q, Hang G. Roentgenographic study of cervical spine degeneration. *Orthop Surg.* (1994) 09:530–3. doi: 10.3760/cma.j.issn.0253-2352.1994.09.106

21. Jarman JP, Arpinar VE, Baruah D, Klein AP, Maiman DJ, Muftuler LT. Intervertebral disc height loss demonstrates the threshold of Major pathological changes during degeneration. *Eur Spine J.* (2015) 24(9):1944–50. doi: 10.1007/s00586-014-3564-8

22. Bai W, Gu H, Liao Z, Liu W. The measurement of Normal lumbar intervertebral discs and its significance. *Chen J Clin Anat.* (2013) 31(05):505–10. doi: 10.13418/j.issn.1001-165x.2013.05.019

23. Guo M, Kong C, Sun S, Sun X, Li X, Lu S. Predictors of L4-L5 degenerative lumbar spondylolisthesis: l4 inclination angle and facet joint angle. *World Neurosurg.* (2019) 130:e680–e6. doi: 10.1016/j.wneu.2019.06.188

24. Love TW, Fagan AB, Fraser RD. Degenerative spondylolisthesis. Developmental or acquired? *J Bone Jt Surg Br Vol.* (1999) 81(4):670–4. doi: 10.1302/0301-620x.81b4.9682

25. Jia J, Zhao Y, Liu X. Impact of sagittal imbalance correction on clinical outcomes in patients undergoing mis-tlif for lss. *Clin Neurol Neurosurg.* (2019) 181:119–26. doi: 10.1016/j.clineuro.2019.04.017

26. Pfirrmann CW, Metzdorf A, Elfering A, Hodler J, Boos N. Effect of aging and degeneration on disc volume and shape: a quantitative study in asymptomatic volunteers. *J Orthop Sci.* (2006) 24(5):1086–94. doi: 10.1002/jor.20113

27. Sawa AGU, Lehrman JN, Crawford NR, Kelly BP. Variations among human lumbar spine segments and their relationships to in vitro biomechanics: a retrospective analysis of 281 motion segments from 85 cadaveric spines. *Int J Spine Surg.* (2020) 14(2):140–50. doi: 10.14444/7021

28. Dreischarf M, Schmidt H, Putzier M, Zander T. Biomechanics of the L5-S1 motion segment after total disc replacement - influence of iatrogenic distraction, implant positioning and preoperative disc height on the range of motion and loading of facet joints. *J Biomech.* (2015) 48(12):3283–91. doi: 10.1016/j.jbiomech.2015.06.023

29. Moll JM, Wright V. Normal Range of spinal mobility. An objective clinical study. *Ann Rheum Dis.* (1971) 30(4):381–6. doi: 10.1136/ard.30.4.381

30. Melnyk AD, Kingwell SP, Zhu Q, Chak JD, Cripton PA, Fisher CG, et al. An in vitro model of degenerative lumbar spondylolisthesis. *Spine.* (2013) 38(14):E870–877. doi: 10.1097/BRS.0b013e3182945897

31. Nakamae T, Nakanishi K, Kamei N, Adachi N. The correlation between sagittal spinopelvic alignment and degree of lumbar degenerative spondylolisthesis. *J Orthop Sci.* (2019) 24(6):969–73. doi: 10.1016/j.jos.2019.08.021

32. Wang H, Wu Z. Association between irregular alteration of facet orientation and degenerative lumbar spondylolisthesis. *World Neurosurg.* (2019) 131:e298–302. doi: 10.1016/j.wneu.2019.07.141

33. Binder DS, Nampiaparampil DE. The provocative lumbar facet joint. *Curr Rev Musculoskelet Med.* (2009) 2(1):15–24. doi: 10.1007/s12178-008-9039-y

34. Gao T, Lai Q, Zhou S, Liu X, Liu Y, Zhan P, et al. Correlation between facet tropism and lumbar degenerative disease: a retrospective analysis. *BMC Musculoskelet Disord.* (2017) 18(1):483. doi: 10.1186/s12891-017-1849-x

35. Degulmadi D, Dave BR, Krishnan A. Age- and sex-related changes in facet orientation and tropism in lower lumbar spine: an mri study of 600 patients. *Eur Spine J.* (2019) 28(5):961–6. doi: 10.1007/s00586-019-05953-y

36. Sun D, Liu P, Cheng J, Ma Z, Liu J, Qin T. Correlation between intervertebral disc degeneration, paraspinal muscle atrophy, and lumbar facet joints degeneration in patients with lumbar disc herniation. *BMC Musculoskelet Disord.* (2017) 18(1):167. doi: 10.1186/s12891-017-1522-4

37. Miki T, Naoki F, Takashima H, Takebayashi T. Associations between paraspinal muscle morphology, disc degeneration, and clinical features in patients with lumbar spinal stenosis. *Prog in Rehabil Med.* (2020) 5:20200015. doi: 10.2490/prm.20200015

38. Saraste H, Broström LA, Aparisi T. Prognostic radiographic aspects of spondylolisthesis. *Acta Radiol Diagn (Stockh).* (1984) 25(5):427–32. doi: 10.1177/028418518402500515

39. Sihvonen T, Herno A, Paljärvi L, Airaksinen O, Partanen J, Tapaninaho A. Local denervation atrophy of paraspinal muscles in postoperative failed back syndrome. *Spine.* (1993) 18(5):575–81. doi: 10.1097/00007632-199304000-00009

40. Tamai K, Chen J, Stone M, Arakelyan A, Paholpak P, Nakamura H, et al. The evaluation of lumbar paraspinal muscle quantity and quality using the goutallier classification and lumbar indentation value. *Eur Spine J.* (2018) 27(5):1005–12. doi: 10.1007/s00586-018-5485-4

frontiers | Frontiers in Surgery

TYPE Methods
PUBLISHED 14 October 2022
DOI 10.3389/fsurg.2022.1000404

Check for updates

OPEN ACCESS

EDITED BY
Huiwu Li,
Shanghai Ninth People's Hospital, China

REVIEWED BY
Chung-Hwan Chen,
Kaohsiung Medical University, Taiwan
Osvaldo Mazza,
Bambino Gesù Children's Hospital (IRCCS), Italy

*CORRESPONDENCE
Chen-Kun Liaw
chenkunliaw@tmu.edu.tw;
chenkunliaw@gmail.com

SPECIALTY SECTION
This article was submitted to Orthopedic Surgery, a section of the journal Frontiers in Surgery

RECEIVED 22 July 2022
ACCEPTED 20 September 2022
PUBLISHED 14 October 2022

CITATION
Chen C-K, Wu T-Y, Liao Y-C, Fuh C-S, Chen K-H, Weng P-W, Wang J-Y, Chen C-Y, Huang Y-M, Chen C-P, Chu Y-L, Yeh K-L, Yu C-H, Wu H-K, Lin W-P, Liou T-H, Wu M-S and Liaw C-K (2022) Mathematical model of distal radius orientation.
Front. Surg. 9:1000404.
doi: 10.3389/fsurg.2022.1000404

COPYRIGHT
© 2022 Chen, Wu, Liao, Fuh, Chen, Weng, Wang, Chen, Huang, Chen, Chu, Yeh, Yu, Wu, Lin, Liou, Wu and Liaw. This is an open-access article distributed under the terms of the Creative Commons Attribution License (CC BY). The use, distribution or reproduction in other forums is permitted, provided the original author(s) and the copyright owner(s) are credited and that the original publication in this journal is cited, in accordance with accepted academic practice. No use, distribution or reproduction is permitted which does not comply with these terms.

Mathematical model of distal radius orientation

Cheng-Kuang Chen[1,2], Tai-Yin Wu[3,4,5], Yu-Ciao Liao[6], Chiou-Shann Fuh[6], Kuan-Hao Chen[7,8], Pei-Wei Weng[7,8,9], Jr-Yi Wang[7,8], Chih-Yu Chen[7,8,9,10], Yu-Min Huang[7,8], Chung-Pei Chen[11], Yo-Lun Chu[1,2,12], Kuei-Lin Yeh[6,13,14], Ching-Hsiao Yu[15,16], Hung-Kang Wu[15,16,17], Wei-Peng Lin[16,18], Tsan-Hon Liou[19], Mai-Szu Wu[20] and Chen-Kun Liaw[7,8,9,21]*

[1]Department of Orthopedics, Shin Kong Wu Ho-Su Memorial Hospital, Taipei, Taiwan, [2]Department of Biomedical Engineering, National Taiwan University, Taipei, Taiwan, [3]Department of Family Medicine, Zhongxing Branch, Taipei City Hospital, Taipei, Taiwan, [4]Institute of Epidemiology and Preventive Medicine, National Taiwan University, Taipei, Taiwan, [5]General Education Center, University of Taipei, Taipei, Taiwan, [6]Institute of Computer Science and Information Engineering, National Taiwan University, Taipei, Taiwan, [7]Department of Orthopedics, School of Medicine, College of Medicine, Taipei Medical University, Taipei City, Taiwan, [8]Department of Orthopedics, Shuang Ho Hospital, Taipei Medical University, New Taipei City, Taiwan, [9]Graduate Institute of Biomedical Optomechatronics, College of Biomedical Engineering; Research Center of Biomedical Device, Taipei Medical University, Taipei City, Taiwan, [10]International Ph.D. Program in Biomedical Engineering, College of Biomedical Engineering, Taipei Medical University, Taipei, Taiwan, [11]Department of Orthopedics, Cathay General Hospital, Taipei, Taiwan, [12]School of Medicine, College of Medicine, Fu Jen Catholic University, New Taipei City, Taiwan, [13]Department of Orthopaedics, Ditmanson Medical Foundation Chia-Yi Christian Hospital, Chia-Yi City, Taiwan, [14]Department of Long-Term Care and Management, WuFeng University, Chiayi County, Taiwan, [15]Department of Orthopaedic Surgery, Taoyuan General Hospital, Ministry of Health and Welfare, Taoyuan City, Taiwan, [16]Department of Orthopaedic Surgery, National Taiwan University Hospital, Taipei City, Taiwan, [17]Department of Nursing, Yuanpei University of Medical Technology, Hsinchu City, Taiwan, [18]Department of Orthopedics, Postal Hospital, Taipei, Taiwan, [19]Department of Physical Medicine and Rehabilitation, School of Medicine, College of Medicine, Taipei Medical University, Taipei City, Taiwan, [20]Division of Nephrology, School of Medicine, College of Medicine, Taipei Medical University, Taipei City, Taiwan, [21]TMU Biodesign Center, Taipei Medical University, Taipei, Taiwan

Distal radius orientation is important in evaluating Colles' fracture. In most cases, the wrist was protected by a bandage, splint, or cast. Therefore, it was difficult for the radiology technician to take perfect anteroposterior and lateral view radiographs. In this study, we build a mathematical model and calculate the pronation angle needed to produce dorsal tilt, which is a volar tilt in a perfect lateral view radiograph. The formulas are all incorporated into Excel to facilitate usage.

KEYWORDS
distal radius volar tilt, distal radius inclination, supination, pronation, rotation matrix

Introduction

Reduction and the indications for the operation of Colles' fracture usually require the guidance of x-rays. These x-rays include wrist anteroposterior and lateral views evaluating volar (palmar) tilt and radial inclination (1–4). These two parameters are in fact three-dimensional. We see patients with dorsal tilt in some lateral view radiographs and volar tilt in others frequently.

Figure 1 showed a patient with normal anatomy. However, the lateral view showed dorsal tilt.

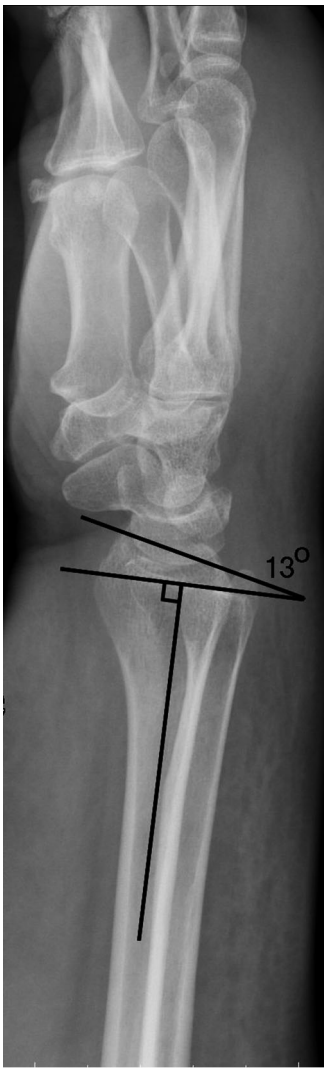

FIGURE 1
Wrist lateral view of a healthy Normal radius which showed dorsal tilt.

These findings raised some questions:

1. What is the mathematical model of distal radius?
2. When does the lateral view show dorsal tilt in normal distal radius?

Methods

The orientation of distal radius cartilage is three-dimensional. We must have a spatial concept when measuring it. Usually, it is presented by volar tilt and radial inclination. Using vector mathematics, we can present its orientation with a normal vector. First, we assume a 3D coordinate system.

The z-axis is aligned by the axis of the radial shaft and directed from the elbow toward the distal radius. The x-axis is directed from the ulnar side toward the radial side. The y-axis

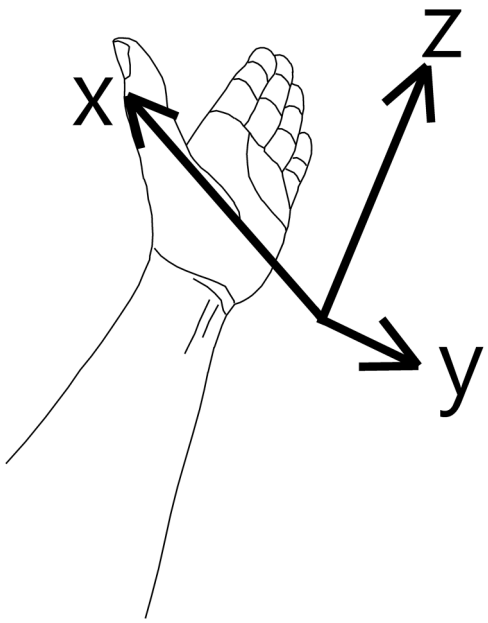

FIGURE 2
3D coordinate system we used in this study.

is from the dorsal toward the volar side (Figure 2). Volar tilt is θ. The inclination is ψ.

Now we can get the distal radius orientation vector by trigonometric mathematics with the same principle (5).

Distal radius orientation normal vector (unit vector) $= (-\cos\theta\sin\varphi,\ \sin\theta\cos\varphi,\ \cos\theta\cos\varphi)$

In clinical practice, we usually take x-rays with some rotation around the z-axis, either supination or pronation. Thus, we use the rotation matrix to simulate this situation,

$$Rz(a) = \begin{bmatrix} \cos(a) & -\sin(a) & 0 \\ \sin(a) & \cos(a) & 0 \\ 0 & 0 & 1 \end{bmatrix}$$

where "a" = rotation around the z-axis or pronation angle. A positive value means pronation and negative means supination.

Thus, the normal vector after rotation "a" angle around the z-axis becomes the multiplication of the two matrixes,

$$\begin{bmatrix} \cos(a) & -\sin(a) & 0 \\ \sin(a) & \cos(a) & 0 \\ 0 & 0 & 1 \end{bmatrix} \begin{bmatrix} -\cos\theta\sin\varphi \\ \sin\theta\cos\varphi \\ \cos\theta\cos\varphi \end{bmatrix}$$

And the results after multiplication are

Distal radius orientation normal vector(unit vector) $=$
$(-\cos\theta\sin\varphi\cos a - \sin\theta\cos\varphi\sin a,$
$-\cos\theta\sin\varphi\sin a + \sin\theta\cos\varphi\cos a,\ \cos\theta\cos\varphi)$

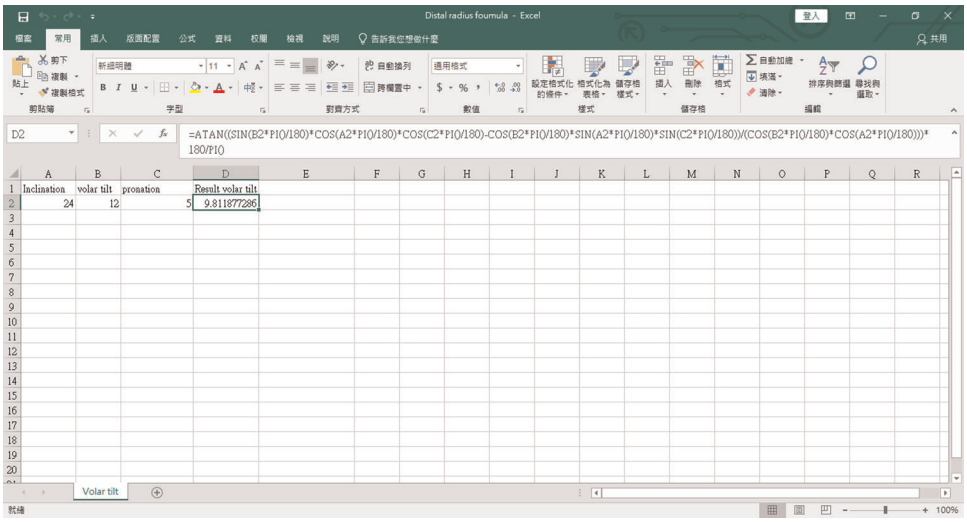

FIGURE 3
The excel program for the mathematical formula. The source code is as follows: "=ATAN((SIN(B2*PI()/180)*COS(A2*PI()/180)*COS(C2*PI()/180)-COS(B2*PI()/180)*SIN(A2*PI()/180)*SIN(C2*PI()/180))/(COS(B2*PI()/180)*COS(A2*PI()/180)))*180/PI()". Readers can copy and paste the code directly.

After pronating rotation "a" angle, the volar tilt becomes

Volar tilt after pronating rotation "a"

$=\tan^{-1}$ (Y component on normal vector/Z component of the normal vector)

$=\tan^{-1}((-\cos\theta\sin\varphi\sin a+\sin\theta\cos\varphi\cos a)\cos\theta\cos\varphi))$.

This formula is incorporated into the Excel file (attachment file) (Figure 3.)

Because $\cos\theta\ \cos\varphi>0$,

Thus if $(-\cos\theta\ \sin\varphi\ \sin a+\sin\theta\ \cos\varphi\ \cos a)>0$, it is volar tilt;

if $((-\cos\theta\ \sin\varphi\ \sin a+\sin\theta\ \cos\varphi\ \cos a)<0$, it is dorsal tilt.

Then, we get the following:

If $\tan\theta>\tan\varphi\ \tan a$, it is volar tilt;
if $\tan\theta<\tan\varphi\ \tan a$, it is dorsal tilt.

or

if $\tan a<\tan\theta\ \cot\varphi$, it is volar tilt;
if $\tan a>\tan\theta\ \cot\varphi$, it is dorsal tilt.

We then get the result as follows:

If pronation (a) $>\tan^{-1}\ \tan\theta\ \cot\varphi)$, it changed from volar tilt to dorsal tilt. We incorporated it into excel. The excel file is attached.

We also incorporated the formula "pronation $=\tan^{-1}(\tan\theta\ \cot\varphi))$" into the Excel file (**supplementary material**).

If we input the normal parameters, inclination 24°, and volar tilt 12°, we get the result. It showed 25.5°, which means if the patient pronates its wrist larger than 25.5°, the x-ray will show dorsal tilt.

Results and discussion

We considered the distal radius articular surface a plane and built a mathematical model of its normal vector. We used this model and calculated the pronation angle, 25.5°, needed to have dorsal tilt in normal patients.

Its clinical importance cannot be overlooked. In practice, Orthopedics doctors can have every radiograph in perfect projection. We should always keep in mind that the radiographs are in fact three-dimensional.

In Figure 1, there are two solid pieces of evidence of pronation. First, the radial styloid is moved toward the volar side. Second, the ulna is moved toward the dorsal side.

In clinical practice, excessive pronation on the lateral radiograph of the wrist usually happened during the postoperative examination while excessive bandage (with splint or cast) confused the radiology technician. The confusing results also perplexed the surgeon. Our results can solve this clinical problem.

Conclusions

We build a mathematical model for evaluating distal radius orientation and we found that the volar tilt will become dorsal

tilt if the pronation is larger than 25.5°. Further study may be needed to determine precision.

Data availability statement

The original contributions presented in the study are included in the article/**Supplementary Material**, further inquiries can be directed to the corresponding author/s.

Ethics statement

The above study has been approved by expedited review process of the TMU-Joint Institutional Review Board (TMU-JIRB No: N202108038). Written informed consent for participation was not required for this study in accordance with national legislation and institutional requirements.

Author contributions

C-KL, T-YW, and Y-CL conceptualized the study. C-KL, P-WW, J-YW, C-YC, K-HC, and Y-MH helped acquired the funding. Y-CL derived the mathematics. C-SF, C-PC, Y-LC, C-KC, and K-LY wrote the algorithm. C-HY, H-KW, W-PL, T-HL, M-SW, and Y-MH simulated data and tested. C-KC, T-YW, and Y-CL wrote the paper. All authors contributed to the article and approved the submitted version.

Funding

This work was funded by grants from the Taiwan Ministry of Science and Technology under grant number 109-2314-B-038 -029.

Conflict of interest

The authors declare that the research was conducted in the absence of any commercial or financial relationships that could be construed as a potential conflict of interest.

Publisher's note

All claims expressed in this article are solely those of the authors and do not necessarily represent those of their affiliated organizations, or those of the publisher, the editors and the reviewers. Any product that may be evaluated in this article, or claim that may be made by its manufacturer, is not guaranteed or endorsed by the publisher.

Supplementary material

The Supplementary Material for this article can be found online at: https://www.frontiersin.org/articles/10.3389/fsurg.2022.1000404/full#supplementary-material.

References

1. Raittio L, Launonen AP, Hevonkorpi T, Luokkala T, Kukkonen J, Reito A, et al. Two casting methods compared in patients with Colles' fracture: a pragmatic, randomized controlled trial. *PLoS One*. (2020) 15(5):e0232153. doi: 10.1371/journal.pone.0232153

2. Reyes-Aldasoro CC, Ngan KH, Ananda A, d'Avila Garcez A, Appelboam A, Knapp KM. Geometric semi-automatic analysis of radiographs of Colles' fractures. *PLoS One*. (2020) 15(9):e0238926. doi: 10.1371/journal.pone.0238926

3. Yokota H, Yasui M, Hirai S, Hatayama N, Ohshima S, Nakano T, et al. Evaluation of the pressure on the dorsal surface of the distal radius using a cadaveric and computational model: clinical considerations in intersection syndrome and Colles' fracture. *Anat Sci Int*. (2020) 95(1):38–46. doi: 10.1007/s12565-019-00491-5

4. Zenke Y, Furukawa K, Furukawa H, Maekawa K, Tajima T, Yamanaka Y, et al. Radiographic measurements as a predictor of correction loss in conservative treatment of Colles' fracture. *J Uoeh*. (2019) 41(2):139–44. doi: 10.7888/juoeh.41.139

5. Liaw C-K, Wu T-Y, Hou S-M, Yang R-S, Fuh C-S. How to evaluate three dimensional angle error from plain radiographs. *J Arthroplasty*. (2013) 28 (10):1788–90. doi: 10.1016/j.arth.2013.05.023

frontiers | Frontiers in Surgery

TYPE Original Research
PUBLISHED 18 October 2022
DOI 10.3389/fsurg.2022.998590

Check for updates

OPEN ACCESS

EDITED BY
Tsung-Yuan Tsai,
Shanghai Jiao Tong University, China

REVIEWED BY
Jun-Young Kim,
Catholic University of Daegu, South Korea
Vincenzo Ricci,
University of Bologna, Italy

*CORRESPONDENCE
Jinli Zhao
happyzjl2009@163.com

†These authors have contributed equally to this work and share first authorship

SPECIALTY SECTION
This article was submitted to Orthopedic Surgery, a section of the journal Frontiers in Surgery

RECEIVED 20 July 2022
ACCEPTED 28 September 2022
PUBLISHED 18 October 2022

CITATION
Guan H, Wu Q, Zhou Y, Fan X, Zheng K, Si T and Zhao J (2022) A retrospective study of ultrasound-guided intervention for frozen shoulder in the frozen stage.
Front. Surg. 9:998590.
doi: 10.3389/fsurg.2022.998590

COPYRIGHT
© 2022 Guan, Wu, Zhou, Fan, Zheng, Si and Zhao. This is an open-access article distributed under the terms of the Creative Commons Attribution License (CC BY). The use, distribution or reproduction in other forums is permitted, provided the original author(s) and the copyright owner(s) are credited and that the original publication in this journal is cited, in accordance with accepted academic practice. No use, distribution or reproduction is permitted which does not comply with these terms.

A retrospective study of ultrasound-guided intervention for frozen shoulder in the frozen stage

Haitao Guan[1,2†], Qinfeng Wu[3†], Yuan Zhou[4], Xing Fan[1], Kun Zheng[1], Tong Si[2] and Jinli Zhao[5*]

[1]Department of Ultrasonography, Suzhou Science & Technology Town Hospital, Suzhou, China, [2]Department of Ultrasonography, Nantong Third People's Hospital, Nantong, China, [3]Department of Rehabilitation, Suzhou Science & Technology Town Hospital, Suzhou, China, [4]Department of Pain, Affiliated Hospital of Nantong University, Nantong, China, [5]Department of Imaging, Affiliated Hospital of Nantong University, Nantong, China

Background: To investigate the clinical value of ultrasound (US)-guided intervention for frozen shoulder (FS) in the frozen stage.
Methods: This study included 40 patients who had primary FS in the frozen stage and were evaluated by US. These 40 patients have all received conservative treatment elsewhere, and no satisfactory results have been achieved, with no improvement in active and passive movement angles, and no improvement in scores within 3 months. Therefore, their previous treatment was set as comparison. All patients underwent US-guided shoulder joint capsule distension by injection of sterilized water. Of these participants, 22 patients with scapulohumeral periarthritis received a compound betamethasone injection, and 14 patients with thickened coracohumeral ligaments (CHLs) underwent acupotomy lysis, and the remaining 4 patients had no extra treatments. The Constant-Murley score (CMS) was evaluated before and after the operation and analysed for each patient.
Results: Before treatment, the indices for the thickening of the subaxillary joint capsule, subacromial bursa (with or without effusion), long head of the biceps brachii tendon (LHBBT) and CHL were 40, 22, 16 and 14, respectively. After treatment, all the indices were significantly decreased (all $P < 0.010$) except for that of the LHBBT ($P = 0.123$). The patients' CMSs improved, with the median total CMS increasing from 59 points (interquartile range: 53–64 points) to 86 points (interquartile range: 78–90 points) ($P < 0.010$). While the internal rotation (Ir) of the shoulder joint did not improve (FDRs < 0.50), abduction, forward flexion (Ff) and external rotation (Er) improved significantly (all FDRs = 1.00).
Conclusion: Compared with conservative treatment, US-guided intervention for FS in the frozen stage is highly effective and of great clinical value.

KEYWORDS

frozen shoulder, frozen stage, ultrasound-guided intervention, ultrasound evaluation of the shoulder joint, Constant-Murley score

Introduction

Frozen shoulder (FS) is also known as 50-year shoulder, scapulohumeral periarthritis and shoulder contracture syndrome. FS is characterized by pain and is accompanied by shoulder dyskinesia, which gradually worsens. Notably, FS includes three stages: the freezing stage, frozen stage and thawing stage. Patients in the freezing stage can recover on their own after conservative treatment (1–3). However (4, 5), the frozen stage, which is associated with pain and stiffness, can recur and continue for decades (1), which has a significant impact on patients' quality of life, especially middle-aged and elderly patients. However, the treatment of FS in the frozen stage is particularly difficult in the clinical setting. With the widespread application of ultrasound (US) in myology and osteology, US plays an increasingly important role in the diagnosis and treatment of shoulder diseases (6, 7). However, previous studies have emphasized local treatment and ignored the use of holistic treatment (8). Although many patients have no pain after treatment, they are unable to recover their previous exercise ability. In this study, our team performed comprehensive US evaluations of the patients' diseased shoulder joints. On this basis, the FS treatment plan was formulated, and its clinical value was analysed.

Materials and methods

This retrospective study was approved by the Institutional Ethics Committee of the Nantong third people's hospital. All patients signed an informed consent form before treatment. All of the study protocols adhered to the principles of the Declaration of Helsinki for medical research.

Patients

From January 2018 to October 2021, FS patients were recruited for this study from Nantong third people's hospital. The inclusion criteria were as follows. (1) The patient had chronic primary FS contracture syndrome and were in the frozen stage. (2) The patient had at least two sets of movements that were limited during active and passive movement, with a range of motion (ROM) of less than 30°. The exclusion criteria were as follows. (1) The patient had metabolic syndrome or diabetes. (2)The patient had an abnormal shoulder bone structure. (3) The patient had a history of shoulder fracture or rotator cuff injury. (4) The patient had secondary FS with other pathogenic factors. (5) The patient had symptoms of muscle atrophy and showed decreased muscle strength. Symptoms and specific scores of patients prior to participation in this study were recorded.

Procedures

US evaluation

All US examinations were conducted by an experienced radiologist (G.H.T., with 10 years of experience) with a US (Arietta 850, Hitachi, Tokyo, Japan) transducer (frequency range: 6–15 MHz). The patient was in a sitting position, and the long head of the biceps brachii tendon (LHBBT), the LHBBT sheath (normal thickness is 1.7 ± 1.6 mm), the subscapular tendon, the supraspinatus tendon, the infraspinatus tendon, the teres minor tendon, the coracohumeral ligament (CHL, 3.08 ± 1.32 mm), the subacromial bursa (0.59 ± 0.17 mm), the rotator interval, the bursae around the rotator cuff, and the subaxillary joint capsule (2.21 ± 0.37 mm) were examined successively according to the US examination method described for the shoulder joint in the Musculoskeletal Ultrasound Technical Guidelines, as recommended by the European Society of Musculoskeletal Radiology (9–12); The dates of all US examinations were recorded along with the results. During the above process, attention was given to observing whether there was pain and dyskinesia caused by an impingement in the shoulder joint cavity or the peripheral capsular ligamentous complex and if there were other pathogenic factors present. The ultrasonographic manifestations of FS include contracture and thickening of the capsule, thickening of the rotator cuff space, thickening of the CHL, and thickening of or effusion from the bursae around the rotator cuff.

US-guided intervention treatment

The patients received US-guided intervention treatments during the first, second and fourth weeks (13). After a patient was placed in a lateral recumbent position, the skin was disinfected with povidone iodine, and 0.5% lidocaine was injected for local anaesthesia. Under US guidance, a 22 G injection needle (Kindly, Zhejiang, China) that was connected to a single-use Luer lock syringe (Kindly, Shanghai, China) was inserted into the shoulder joint cavity by a posterior approach. A 10–15 ml volume of sterile water was injected to slowly expand the shoulder joint cavity. When the thickness of the subacromial bursa, the sheath of the LHBBT, or the rotator interval was more than 2 mm, the patient was injected with 1 ml of 10% compound betamethasone. In this manner, the shoulder joint cavity was expanded by water injection under US guidance during the first treatment (**Figures 1**, **2**). Intra-plane injection technique was adopted to conduct the ultrasound-guided subacromial bursa injection. The drug started being slowly pushed out when the bone puncture needle tip reached the subacromial bursa space, and the drug was slowly injected into the subacromial bursa along the injection path from the outside to the inside. The injection was ended until the drug can flow in and out of the

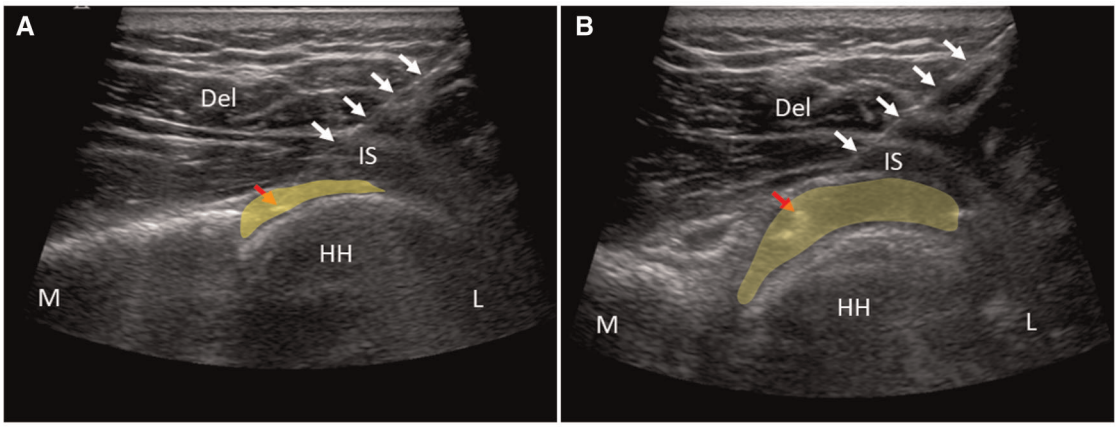

FIGURE 1
US-guided shoulder joint cavity injection and before (A) and after (B) distension treatment. Del, deltoid muscle; HH, humeral head; IS, infraspinatus tendon; L, lateral; M, medial. White arrows indicate the injection needle. Red arrow points at the tip of injection needle. The highlighted yellow area indicates the shoulder joint cavity.

subacromial bursa to form a bar-shaped anechoic. When the thickness of the CHL exceeded 3 mm (14), the patient underwent an US-guided acupotomy (diameter: 0.6 mm, ZhongWu, Jiangsu, China) lysis of the CHL during the first treatment. The coracoid process of the CHL was longitudinally thinned and transversely striped by an acupotome three times under sonographic guidance (**Figure 3**) (15). When a small acupotome was inserted into the coracohumeral ligament under ultrasound guidance, attention should be paid not to damage other structures in the subthoracic space.

Shoulder joint Constant-Murley score (CMS)

The shoulder joint CMS provided scores for factors, including pain, daily living activity and the range of motion of the shoulder joint, before and after US-guided treatment (16).

Statistical analyses

R software (version 4.0.2) was used for the statistical analysis. The normality of the data was tested by the Shapiro–Wilk test. The continuous variables that were normally distributed were expressed as the mean ± standard deviations ($\bar{x} \pm S$), and the data that were nonnormally distributed were expressed as medians and interquartile ranges (IQR, 25th–75th percentile). Categorical variables are expressed as counts and percentages. The normally distributed data were compared by using the independent samples t test. The Mann–Whitney U test was used to compare the mean values before and after treatment of the same group or between two groups. The difference in nonnormally distributed variables was compared among multiple groups by using the Kruskal–Wallis test, and the difference between the groups was compared by using the Mann–Whitney U test. The nominal P value was corrected for multiple comparisons by using the Benjamini–Hochberg method. $P < 0.050$ was considered statistically significant.

Results

US evaluation of FS

A total of 40 patients were included in this study; 17 males (42.5%) and 23 females (57.5%), and they had a mean age of 53.0 ± 9.6 years (range, 32–75 years). Before treatment, the median thickness of the subaxillary joint capsule was 3.1 mm (IQR: 2.8–3.8 mm) in 40 patients, and colour Doppler US showed that there was no obvious blood flow signal in the contracted synovium of the capsule. Among them, 22 patients were diagnosed with thickening of the shoulder space with or without effusion, so ultrasound-guided local glucocorticoid injection was added. Fourteen patients were diagnosed with coracohumeral ligament thickening, so ultrasound-guided coracohumeral ligament acupotomy was performed. Four patients were only diagnosed with thickening of the shoulder joint capsule, so only ultrasound-guided injection of sterile water into the shoulder joint cavity was performed. The subacromial bursa (with or without effusion) was thickened in 20 patients, with a median thickness of 2.5 mm (IQR: 2.0–3.5 mm). The LHBBT sheath (with or without effusion) was thickened in 16 patients, and the median thickness of the LHBBT sheath was 6.3 mm (IQR: 2.4–10.0 mm). The median

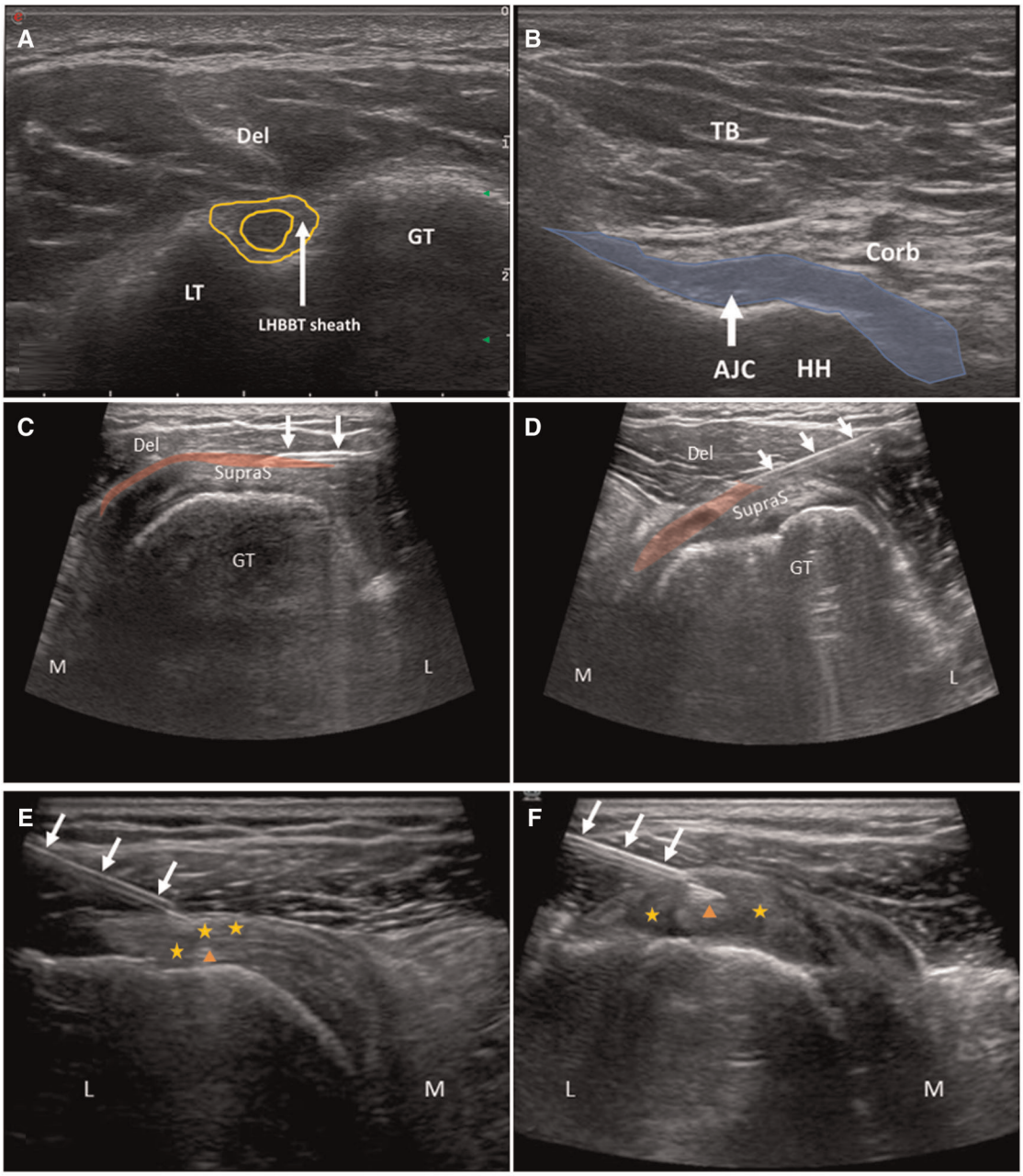

FIGURE 2
A,B are ultrasound images for diagnosis. C (before injection) and D (after injection) are US-guided injection into the subacromial Bursa. E (before injection) and F (after injection) are intrathecal injection into the LHBBT sheath. Del, deltoid muscle; TB, Triceps brachii; Corb, coracobrachialis; AJC, axillary joint capsule; HH, humeral head; GT, greater tubercle of humerus; LT, lesser tubercle of humerus; SupraS, supraspinatus tendon; L, lateral; M, medial; yellow star, rotator interval; orange triangle, the long head of the biceps brachii tendon (LHBBT); highlighted red area, subacromial Bursa. White arrows indicate the injection needle.

thickness of the CHL was 4.5 mm (IQR: 4.2–4.8 mm) in 14 patients. After treatment, all of the values in the aforementioned indices were significantly lower than the values before treatment (all $P < 0.010$, Table 1), except for the thickness of the LHBBT sheath (with or without effusion) ($P = 0.123$).

Evaluation on the motion range of the shoulder joint

Before treatment, evaluation of the shoulder joint CMS showed that the median pain score of the patients was 10 points (IQR: 5–10 points), the median score for daily living

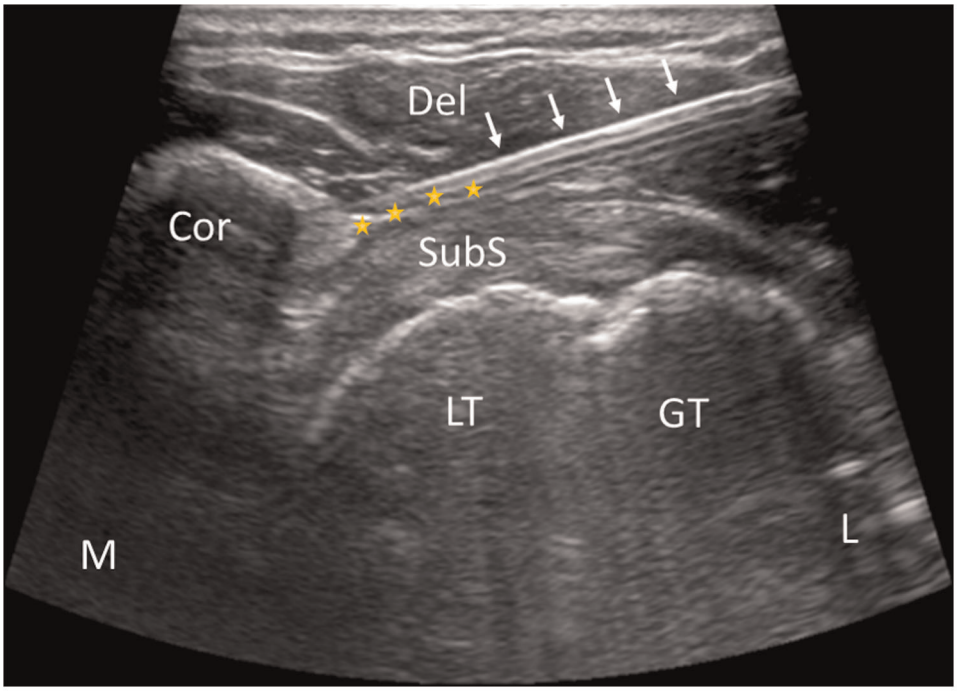

FIGURE 3
US-guided acupotome lysis of coracohumeral ligaments. Cor, coracoideus; Del, deltoid muscle; GT, greater tubercle of humerus; LT, lesser tubercle of humerus; SubS, subscapularis tendon; L, lateral; M, medial; yellow star, coracohumeral ligament. White arrows indicate the acupotome.

TABLE 1 Comparison of the US evaluation results before and after treatment.

	Before treatment	After treatment	*P*
Thickness of the subaxillary joint capsule	3.1 (2.8–3.8)	2.1 (1.5–2.5)	<0.001*
Thickening of the subacromial bursa (with or without effusion)	2.5 (2.0–3.5)	2 (1.9–2.3)	0.009*
Thickness of the LHBBT (with or without effusion)	6.3 (2.4–10.0)	2.5 (2.0–3.8)	0.123
Thickness of the CHL	4.5 (4.2–4.8)	2.5 (2.3–3.4)	0.001*

Data are presented as the median (25th, 75th).
*Statistically significant difference.

activity was 11 points (IQR: 7–13 points), and the median score for active range of motion was 16 points (IQR: 12–20 points). After treatment, all aforementioned scores were significantly improved (all $P < 0.010$). Specifically, the median pain score increased to 15 points (IQR: 10–15 points), the median score for daily living activity increased to 18 points (IQR: 16–20 points), and the median score for active range of motion increased to 28 points (IQR: 24–34 points). The median total CMS of the patients increased from 59 points (IQR: 53–64 points) before treatment to 86 points (IQR: 78–90 points) after treatment ($P < 0.010$) (Table 2).

TABLE 2 Comparison of the CMS of the patients before and after treatment.

	Before treatment	After treatment	*P*
Pain (15 points)	10 (5–10)	15 (10–15)	<0.001*
Daily living activity (20 points)	11 (7–13)	18 (16–20)	<0.001*
Activity level (10 points)	5 (3–6)	9.5 (8–10)	<0.001*
Restricted work (4 points)	2 (0–2)	4 (2–4)	<0.001*
Restricted entertainment (4 points)	2 (2–4)	4 (4–4)	<0.001*
Affected sleep (2 points)	1 (0–1)	2 (1–2)	<0.001*
Position reached by painless movement (10 points)	6 (4–8)	8 (8–10)	<0.001*
Angle and score of the active range of motion (40 points)	16 (12–20)	28 (24–34)	<0.001*
Flexion (10 points)	6 (4–8)	10 (8–10)	<0.001*
Abduction (10 points)	4 (2–4)	8 (6–8)	<0.001*
External rotation (10 points)	4 (2–6)	8 (6–8)	<0.001*
Internal rotation (10 points)	2 (2–4)	4 (4–6)	<0.001*
Flexion (angle)	120 (90–123)	170 (150–180)	<0.001*
Abduction (angle)	90 (60–90)	138 (100–153)	<0.001*
Muscle force evaluation (25 points)	25	25	
Total constant score (100 points)	59 (53–64)	86 (78–90)	<0.001*

Data are presented as the median (25th, 75th).
*Statistically significant difference.

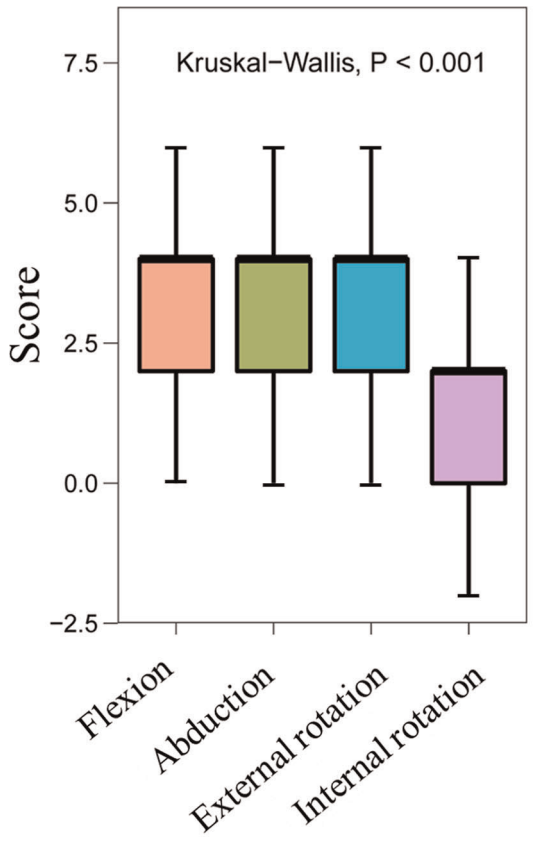

FIGURE 4
Box chart showing the degree of improvement in the scores of four indices involving the active range of motion.

According to the angle and score of the active ROM in the CMS table, our team found that every subindex (forward flexion (Ff), abduction, external rotation (Er) and internal rotation (Ir)) was significantly improved ($P < 0.010$). The median score for Ff increased from 6 points (IQR: 4–8 points) to 10 points (IQR: 8–10 points), and its median angle increased from 120° (IQR: 90°–123°) to 170° (IQR: 150°–180°). The median score for abduction increased from 4 points (IQR: 2–4 points) to 8 points (IQR: 6–8 points), and its median angle increased from 90° (IQR: 60°–90°) to 138° (IQR: 100°–153°). The median score for Er increased from 4 points (IQR: 2–6 points) to 8 points (IQR: 6–8 points), while the median score for Ir increased from 2 points (IQR: 2–4 points) to 4 points (IQR: 4–6 points) (Table 2). Although there were significant differences in the four index scores that involve the active range of motion of the patients before and after treatment ($P < 0.010$), the degree of improvement of each index was different. It should be emphasized that Ff, abduction and Er showed greater improvement (all FDRs = 1) than Ir (FDRs < 0.050) (Figure 4).

Comparison of the treatment efficacy of the CHL between the thickening group and the nonthickening group

The patients were divided into the thickening group ($n = 14$) and the nonthickening group ($n = 26$) according to whether the thickening of the patient's CHL was more than 3 mm. In the thickening group, the after-treatment scores of various indices associated with the active range of motion improved compared to the values before treatment ($P < 0.010$). Specifically, the median score for Ff increased from 5 points (IQR: 4–6 points) to 10 points (IQR: 7–10 points), and its median angle increased from 90° (IQR: 80°–120°) to 160° (IQR: 121°–179°). The median score for abduction increased from 2 points (IQR: 2–4 points) to 6 points (IQR: 4–8 points), and its median angle increased from 60° (IQR: 45°–65°) to 110° (IQR: 90°–143°). The median score for Er increased from 3 points (IQR: 2–6 points) to 6 points (IQR: 6–8 points), while the median score for Ir increased from 2 points (IQR: 0–2 points) to 4 points (IQR: 2–4 points). The median total score for the active range of motion increased from 12 points (IQR: 9–18 points) to 24 points (IQR: 20–30 points) (Table 3).

In the nonthickening group, the median score for Ff increased from 6 points (IQR: 5–8 points) to 10 points (IQR: 8–10 points), and its median angle increased from 120° (IQR: 90°–146°) to 175° (IQR: 150°–180°). The median score for abduction increased from 4 points (IQR: 4–6 points) to 8 points (IQR: 6–8 points), and its median angle increased from 90° (IQR: 65°–90°) to 150° (IQR: 120°–158°). The median score for Er increased from 4 points (IQR: 2–6 points) to 8 points (IQR: 6–8 points), while the median score for Ir increased from 2 points (IQR: 2–4 points) to 4 points (IQR: 4–6 points). The median total score for the active range of motion increased from 17 points (IQR: 15–24 points) to 29 points (IQR: 26–34 points) (Table 4).

TABLE 3 Comparison of the active range of motion in the thickening group before and after treatment.

	Before treatment	After treatment	*P*
Angle and score of the active range of motion	12 (9–18)	24 (20–30)	0.001*
Flexion (10 points)	5 (4–6)	10 (7–10)	<0.001*
Abduction (10 points)	2 (2–4)	6 (4–8)	<0.001*
External rotation (10 points)	3 (2–6)	6 (6–8)	0.001*
Internal rotation (10 points)	2 (0–2)	4 (2–4)	0.004*
Flexion (angle)	90 (80–120)	160 (121–179)	0.002*
Abduction (angle)	60 (45–65)	110 (90–143)	0.002*

Data are presented as the median (25th, 75th).
*Statistically significant difference.

TABLE 4 Comparison of the active range of motion in the nonthickening group before and after treatment.

	Before treatment	After treatment	*P*
Angle and score of the active range of motion ($n = 40$)	17 (15–24)	29 (26–34)	<0.001*
Flexion (10 points)	6 (5–8)	10 (8–10)	<0.001*
Abduction (10 points)	4 (4–6)	8 (6–8)	<0.001*
External rotation (10 points)	4 (2–6)	8 (6–8)	<0.001*
Internal rotation (10 points)	2 (2–4)	4 (4–6)	<0.001*
Flexion (angle)	120 (90–146)	175 (150–180)	<0.001*
Abduction (angle)	90 (65–90)	150 (120–158)	<0.001*

Data are presented as the median (25th, 75th).
*Statistically significant difference.

TABLE 5 Comparison of the improvements in the active range of motion between the thickening group and the nonthickening group before and after treatment.

	Thickening group	Nonthickening group	*P*
Angle and score of the active range of motion ($n = 40$)	12 (10–16)	12 (8–14)	0.404
Flexion (10 points)	4 (4–4)	4 (2–4)	0.188
Abduction (10 points)	4 (2–4)	4 (2–4)	0.867
External rotation (10 points)	2 (2–4)	4 (2–4)	0.672
Internal rotation (10 points)	2 (1–2)	2 (0–2)	0.618
Flexion (angle)	60 (45–60)	55 (30–61)	0.718
Abduction (angle)	50 (35–75)	55 (30–64)	0.917

Data are presented as the median (25th, 75th).

After treatment, there was no significant difference in the improvement of the active range of activity between the thickening group and the nonthickening group (all $P > 0.050$) (Table 5).

Discussion

The pathogenesis of FS is unclear. It may be related to continuous tension in the patient's posture and the patient's emotions, or related to an increase in a variety of inflammatory factors (17, 18). The disease includes the freezing stage, frozen stage and thawing stage (5). Although FS is self-limiting, some patients may experience the frozen stage for decades, and the condition can recur. In this study, our team focused on patients with FS in the frozen stage. There are various treatments for FS (16, 19–22), such as acupuncture, massage, release of the shoulder joint cavity under brachial plexus block, arthroscopic release of the shoulder joint capsule, and high-dose oral steroids. However, the efficacy of these treatments is uncertain. Lu et al. (23) found that US-guided distension of the shoulder joint cavity had good efficacy for the treatment of FS. However, in the frozen stage, CHL thickness correlates negatively with the Er and Ir ranges of the shoulder (14), and FS patients with thickening of the CHL do not achieve good improvement of shoulder ROM using this method alone (24). Many studies have shown that steroid drugs can effectively control pain associated with FS (25), but these drugs are relatively short acting (26, 27). Traditional or single US-guided injection therapy is not the best method to treat FS, especially for patients in the frozen stage. Preoperative US evaluation is very important. The ultimate aim of US-guided intervention should be to improve the overall function of the shoulder joint.

During the active and passive movement of the shoulder joint, US can dynamically determine whether the sliding trajectory and the structures around the tender points are abnormal, and these evaluations cannot be obtained by magnetic resonance imaging or other imaging examinations. The US manifestations of FS include contracture and thickening of the subaxillary joint capsule, thickening of the coracobrachial tendon, coracoacromial ligament and scapulohumeral periarthritis (28, 29). US-guided interventional treatment is increasingly applied as an FS therapy and has shown a good curative effect. Several studies have shown that the range of motion of the shoulder joint in patients with primary FS is significantly improved after an US-guided shoulder joint injection (30, 31). However, there are few reports on the application of US-guided treatment for FS patients in the frozen stage.

In terms of improving the shoulder joint function, the short- and medium-term efficacy of an US-guided shoulder joint injection combined with joint capsule distension is significantly better than that of a simple shoulder joint injection (23, 32, 33). A study by Cheng et al. (23, 34) showed that three consecutive US-guided shoulder joint injections combined with joint capsule distension was an effective method for the treatment of FS. Therefore, in this study, our team also used a series of three consecutive US-guided shoulder joint injections combined with joint capsule distension. Ultrasound images showed subacromial bursitis when the thickness of the synovium and/or effusion is greater than 2 mm. It can be diagnosed as long head biceps tenosynovitis or inflammation of the rotator cuff space when local thickening and hypoechoic reduction and the long head of the biceps brachii tendon sheath or rotator cuff space, and the thickness of the synovium and/or effusion is greater than 2 mm. Therefore, we believe that there is inflammation when the thickness of the peri-shoulder space is greater than 2 mm, and local glucocorticoid injection under ultrasound guidance is performed (35). The normal volume of the shoulder joint cavity is approximately 20 ml, but in patients with shoulder

contracture syndrome, the volume is often reduced due to intra-articular synovial contracture. In this study, 10–15 ml sterilized water was injected into the shoulder joint cavity. The injection dose that is used depends on the patient's tolerance level. In patients with FS, fibrosis and thickening of the capsule were the main features that were seen in the shoulder joint cavity. Colour Doppler US showed that there was no obvious blood flow signal in the contracted synovium of the shoulder capsule, which means there was no evidence of inflammation in the capsule. A study showed that shoulder joint capsule distension with sterilized water is effective for release training (33). The expansion of the shoulder joint cavity by injecting sterile water is mainly to mechanically separate the adhering joint cavity and increase the range of motion, which was proved a good long-term effect. Therefore, only sterilized water was used for the joint injections in this study.

Inflammation, indicated by signs such as effusion and reduced tendon clearance space, can be identified when an US evaluation is performed to evaluate the soft tissue around the shoulder joint and the rotator cuff tendon clearance. Several studies have shown that synovitis can be effectively controlled by steroids (26, 27). Therefore, US-guided steroid injections into the soft tissue around the shoulder joint and rotator cuff tendon clearance may also be effective. However, the curative efficacy of these US-guided local injections is variable. This may be because the compound betamethasone injection is a lipid-soluble granular suspension. This limits the drug from being applied evenly on the synovial membranes or in the interstitial spaces with adhesions due to the lack of flow, which prevents the drug from reaching some places. Therefore, to solve the above problems, our team shook it well before the injection. During the injection, the needle was inserted into the gap or synovium, and the drug was slowly injected, with mild pressure being applied when any resistance was encountered. The injection was stopped when an arc-shaped anechoic region appeared in the injection area (36).

The CHL is often found to be thickened in FS patients. When the CHL is thickened up to 3.0 mm, there is a high likelihood for the existence of FS. The thickening of the CHL is highly correlated with adhesions, inflammation, and stability of the shoulder joint (14). The CHL is stiffer in the frozen stage than in the freezing stage (24). Some studies have shown that US-guided release of the CHL is effective in FS patients (37, 38). Under US guidance, our team made vertical cuts in the CHL at the coracoid process with a small needle knife in 14 patients with thickened CHLs; this procedure achieved a good curative effect.

In this study, US-guided FS intervention treatment was performed based on static and dynamic US evaluations, and a holistic treatment was emphasized. The CMS of the shoulder joint, especially the daily living activity score, was significantly improved after the operation. The Ff, abduction and Er of the shoulder joint were significantly improved, but the Ir was not improved. The reason may be that Ir is a compound action, and the patients' symptoms improved slowly due to severe adhesions and fibrosis of the shoulder joint during the frozen stage. Two patients were found severe fibrosis of the shoulder joint cavity during the operations. Besides, this study ignored the assessment of the patient's posture, but rounded shoulder posture is one of the most common structural abnormalities of the shoulder complex, involving increased cervical anteversion and increased upper thoracic retroversion, resulting in shoulder and scapula herniation, as well as increase in inferior rotation and anterior tilt. Patients with frozen shoulder typically have a rounded shoulder with adducted and internally rotated glenohumeral joints, and a contracture of the joint capsule (39, 40). After the expansion of the shoulder joint, the joint capsule contracture improved and the range of motion increased, but the patient's rounded shoulder did not change. When the adduction and internal rotation test was performed, the subacromial rotation and anteversion of the scapula were limited, and the subacromial space was insufficient, which could cause pain and limitation (41). Therefore, it is suggested that the patients with frozen shoulder still need to adjust their posture through manipulation and training after the release of the joint capsule and related ligaments in order to comprehensively improve the shoulder joint function.

In conclusion, US-guided intervention of FS patients in the frozen stage is convenient and effective; this procedure has high application value and should be promoted in clinical practice.

Limitations

The internal rotation is affected by the coracobrachialis muscle, infraspinatus muscle, and teres minor muscle. For the thickening and nonthickening group, the internal rotation of CMS did not improve, Potential approaches to operate the muscles or further improve this score need be explored in the future. Severe adhesions and fibrosis of the shoulder joint might be one of the reasons, and this need be further studied.

Data availability statement

The raw data supporting the conclusions of this article will be made available by the authors, without undue reservation.

Ethics statement

The studies involving human participants were reviewed and approved by Institutional Ethics Committee of Nantong third people's hospital. The patients/participants provided their written informed consent to participate in this study.

Written informed consent was obtained from the individual(s) for the publication of any potentially identifiable images or data included in this article.

Author contributions

HG, QW and JZ designed and conceptualized the study. HG and QW conducted the operation and collected the data. HG and JZ drafted and revised the manuscript, performed the data analysis and interpretations. YZ, XF, KZ and TS collected and processed the data. All authors contributed to the article and approved the submitted version.

Funding

This work was supported by Nantong Min Sheng Science and Technology Project (MS12020040) and Senior Health Research Project of Jiangsu Provincial Health Commission (LKM2022061).

Conflict of interest

The authors declare that the research was conducted in the absence of any commercial or financial relationships that could be construed as a potential conflict of interest.

Publisher's note

All claims expressed in this article are solely those of the authors and do not necessarily represent those of their affiliated organizations, or those of the publisher, the editors and the reviewers. Any product that may be evaluated in this article, or claim that may be made by its manufacturer, is not guaranteed or endorsed by the publisher.

References

1. Diercks RL, Stevens M. Gentle thawing of the frozen shoulder: a prospective study of supervised neglect versus intensive physical therapy in seventy-seven patients with frozen shoulder syndrome followed up for two years. *J Should Elbow Surg*. (2004) 13(5):499–502. doi: 10.1016/j.jse.2004.03.002

2. Cho C-H, Bae K-C, Kim D-H. Treatment strategy for frozen shoulder. *Clin Orthop Surg*. (2019) 11(3):249–57. doi: 10.4055/cios.2019.11.3.249

3. Shaffer B, Tibone J, Kerlan RK. Frozen shoulder. A long-term follow-up. *J Bone Joint Surg Am*. (1992) 74(5):738–46. doi: 10.2106/00004623-199274050-00013

4. Li W, Lu N, Xu H, Wang H, Huang J. Case control study of risk factors for frozen shoulder in China. *Int J Rheum Dis*. (2015) 18(5):508–13. doi: 10.1111/1756-185X.12246

5. Pandey V, Madi S. Clinical guidelines in the management of frozen shoulder: an update! *Indian J Orthop*. (2021) 55(2):299–309. doi: 10.1007/s43465-021-00351-3

6. Tao W, Fu Y, Hai-Xin S, Yan D, Jian-Hua L. The application of sonography in shoulder pain evaluation and injection treatment after stroke: a systematic review. *J Phys Ther Sci*. (2015) 27(9):3007–10. doi: 10.1589/jpts.27.3007

7. Sconfienza LM, Adriaensen M, Albano D, Allen G, Aparisi Gómez MP, Bazzocchi A, et al. Clinical indications for image-guided interventional procedures in the musculoskeletal system: a Delphi-based consensus paper from the European society of musculoskeletal radiology (ESSR)—part I, shoulder. *Eur Radiol*. (2020) 30(2):903–13. doi: 10.1007/s00330-019-06419-x

8. Balazs CGC. In frozen shoulder, US-guided versus blind administration of intra-articular corticosteroid injections increased accuracy of injections but did not improve clinical outcomes at 12 weeks. *JBJS*. (2021) 103(22):2144. doi: 10.2106/JBJS.21.01007

9. Sconfienza LM, Albano D, Allen G, Bazzocchi A, Bignotti B, Chianca V, et al. Clinical indications for musculoskeletal ultrasound updated in 2017 by European society of musculoskeletal radiology (ESSR) consensus. *Eur Radiol*. (2018) 28 (12):5338–51. doi: 10.1007/s00330-018-5474-3

10. Ricci V, Chang K-V, Güvener O, Mezian K, Kara M, Leblebicioğlu G, et al. EURO-MUSCULUS/USPRM dynamic ultrasound protocols for shoulder. *Am J Phys Med Rehab*. (2022) 101(3):e29–36. doi: 10.1097/PHM.0000000000001833

11. Carbone S, Napoli A, Gumina S. MRI of adhesive capsulitis of the shoulder: distension of the bursa in the superior subscapularis recess is a suggestive sign of the pathology. *Eur J Radiol*. (2014) 83(2):345–8. doi: 10.1016/j.ejrad.2013.10.017

12. Park I, Lee H-J, Kim S-E, Bae S-H, Lee K-Y, Park K-S, et al. Evaluation of the effusion within biceps long head tendon sheath using ultrasonography. *Clin Orthop Surg*. (2015) 7(3):351–8. doi: 10.4055/cios.2015.7.3.351

13. Shen Q, Sun Y, Feng H, Xu S, Jiang T. The differential diagnosis of benign and malignant in mass type breast diseases based on the real-time monitoring of full-angle ultrasonic shear wave elastography. *Chin J Ultrasono*. (2019) 28:981–5. doi: 10.3760/cma.j.issn.10044477.2019.11.011

14. Wu PY, Hsu PC, Chen TN, Huang JR, Chou CL, Wang JC. Evaluating correlations of coracohumeral ligament thickness with restricted shoulder range of motion and clinical duration of adhesive capsulitis with ultrasound measurements. *PM R*. (2021) 13(5):461–9. doi: 10.1002/pmrj.12432

15. Ricci V, Mezian K, Naňka O, Özçakar L. Assessing/imaging the subcoracoid space: from anatomy to dynamic sonography. *J Ultrasound Med*. (2021) 41:2149–55. doi: 10.1002/jum.15898

16. Constant C, Murley A. A clinical method of functional assessment of the shoulder. *Clin Orthop Relat Res*. (1987) 214:160–4. doi: 10.1097/00003086-198701000-00023

17. Jump CM, Duke K, Malik RA, Charalambous CP. Frozen shoulder: a systematic review of cellular, molecular, and metabolic findings. *JBJS Rev*. (2021) 9(1):e19. doi: 10.2106/JBJS.RVW.19.00153

18. Green HD, Jones A, Evans JP, Wood AR, Beaumont RN, Tyrrell J, et al. A genome-wide association study identifies 5 loci associated with frozen shoulder and implicates diabetes as a causal risk factor. *PLoS Genet*. (2021) 17(6): e1009577. doi: 10.1371/journal.pgen.1009577

19. Challoumas D, Biddle M, McLean M, Millar NL. Comparison of treatments for frozen shoulder: a systematic review and meta-analysis. *JAMA Network Open*. (2020) 3(12):e2029581-e. doi: 10.1001/jamanetworkopen.2020.29581

20. Maund E, Craig D, Suekarran S, Neilson A, Wright K, Brealey S, et al. Management of frozen shoulder: a systematic review and cost-effectiveness analysis. *Health Technol Assess*. (2012) 16(11):1–264. doi: 10.3310/hta16110

21. Zhang J, Zhong S, Tan T, Li J, Liu S, Cheng R, et al. Comparative efficacy and patient-specific moderating factors of nonsurgical treatment strategies for frozen shoulder: an updated systematic review and network meta-analysis. *Am J Sports Med*. (2021) 49(6):1669–79. doi: 10.1177/0363546520956293

22. Boutefnouchet T, Jordan R, Bhabra G, Modi C, Saithna A. Comparison of outcomes following arthroscopic capsular release for idiopathic, diabetic and secondary shoulder adhesive capsulitis: a systematic review. *Orthopaed Traumatol Surg Res*. (2019) 105(5):839–46. doi: 10.1016/j.otsr.2019.02.014

23. Xuanyan G, Man LU, Fanding HE, Yanyan WU, Kai C, Lei W, et al. Ultrasound-guided joint injection combined with capsular distension for treatment of frozen shoulder. *Chin J Med Imaging Technol*. (2018) 34:1081–4. doi: 10.13929/j.1003-3289.201712107

24. Xu H, Zhang Y, Wang C. Ultrasound-guided hydrodilatation of glenohumeral joint combined with acupotomy for treatment of frozen shoulder. *J Back Musculoskelet Rehabil*. (2022) 35:1–8. doi: 10.3233/BMR-210272

25. Atici T, Ermutlu C, Akesen S, Özyalçin A. High-dose short-course oral corticosteroid protocol for treatment of primary frozen shoulder: a retrospective cohort study. *J Int Med Res*. (2021) 49(7):03000605211024875. doi: 10.1177/03000605211024875

26. Kim Y-S, Lee H-J, Lee D-H, Choi K-Y. Comparison of high-and low-dose intra-articular triamcinolone acetonide injection for treatment of primary shoulder stiffness: a prospective randomized trial. *J Should Elbow Surg*. (2017) 26(2):209–15. doi: 10.1016/j.jse.2016.09.034

27. Kim K-H, Suh J-W, Oh KY. The effect of intra-articular hyaluronate and tramadol injection on patients with adhesive capsulitis of the shoulder. *J Back Musculoskelet Rehabil*. (2017) 30(4):913–20. doi: 10.3233/BMR-160641

28. Lee J-G, Peo H, Cho J-H, Cho C-H, Kim D-K, Kim D-H. Dynamic ultrasonographic measurement of inferior joint capsule thickness in patients with unilateral frozen shoulder. *Diagnostics*. (2021) 11(5):898. doi: 10.3390/diagnostics11050898

29. Kim DH, Cho C-H, Sung DH. Ultrasound measurements of axillary recess capsule thickness in unilateral frozen shoulder: study of correlation with MRI measurements. *Skeletal Radiol*. (2018) 47(11):1491–7. doi: 10.1007/s00256-018-2959-8

30. Cho C-H, Min B-W, Bae K-C, Lee K-J, Kim DH. A prospective double-blind randomized trial on ultrasound-guided versus blind intra-articular corticosteroid injections for primary frozen shoulder. *Bone Joint J*. (2021) 103(2):353–9. doi: 10.1302/0301-620X.103B2.BJJ-2020-0755.R1

31. Gaba E, Sethi J, Bhardwaj M. Effect of interferential therapy over ultrasound therapy with common protocol of manual therapy in grade-II frozen shoulder. *J Exercise Sci Physiother*. (2020) 16(2):23–31. doi: 10.18376/jesp/2020/v16/i2/157454

32. Koraman E, Turkmen I, Uygur E, Poyanlı O. A multisite injection is more effective than a single glenohumeral injection of corticosteroid in the treatment of primary frozen shoulder: a randomized controlled trial. *Arthroscopy*. (2021) 37(7):2031–40. doi: 10.1016/j.arthro.2021.01.069

33. Hagiwara Y, Kanazawa K, Ando A, Sekiguchi T, Koide M, Yabe Y, et al. Effects of joint capsular release on range of motion in patients with frozen shoulder. *J Should Elbow Surg*. (2020) 29(9):1836–42. doi: 10.1016/j.jse.2020.01.085

34. Cheng XQ, Lu M, Zhang ZQ, Guo XY, He FD, Chen K. Treatment of frozen shoulder by ultrasound-guided intra-articular injection combined with expansion. *Chin J Ultrasound Imaging*. (2017 Oct) 26(10):895–8. doi: 10.3760/cma.j.issn.10044477.2017.10.017

35. Valley VT, Stahmer SA. Targeted musculoarticular sonography in the detection of joint effusions. *Acad Emerg Med*. (2001) 8(4):361–7. doi: 10.1111/j.1553-2712.2001.tb02114.x

36. Ricci V, Galletti S, Chang KV, Özçakar L. Ultrasound imaging and guidance in the management of adhesive bursopathy of the shoulder: a video demonstration. *J Ultrasound Med*. (2020) 39(3):633–5. doi: 10.1002/jum.15117

37. Yukata K, Goto T, Sakai T, Fujii H, Hamawaki J, Yasui N. Ultrasound-guided coracohumeral ligament release. *Orthopaed Traumatol Surg Res*. (2018) 104(6):823–7. doi: 10.1016/j.otsr.2018.01.016

38. Liu XC, Zhang P, Zhang XL. Primary clinical outcomes of ultrasound guided selective release with needle knifes for frozen shoulder. *Orthoped J China*. (2020) 28(24):4. doi: 10.3977/j.issn.1005-8478.2020.24.11

39. Kim M-K, Lee JC, Yoo K-T. The effects of shoulder stabilization exercises and pectoralis minor stretching on balance and maximal shoulder muscle strength of healthy young adults with round shoulder posture. *J Phys Ther Sci*. (2018) 30(3):373–80. doi: 10.1589/jpts.30.373

40. An T-G, Lee H-S, Park S-W, Seon H-C. Effect of nordic walking on depression and physical function in the elderly with high-risk of depression. *J Korean Soc Phys Med*. (2020) 15(4):11–20. doi: 10.13066/kspm.2020.15.4.11

41. Tahran Ö, Yeşilyaprak SS. Effects of modified posterior shoulder stretching exercises on shoulder mobility, pain, and dysfunction in patients with subacromial impingement syndrome. *Sports Health*. (2020) 12(2):139–48. doi: 10.1177/1941738119900532

frontiers | Frontiers in Surgery

TYPE Original Research
PUBLISHED 18 October 2022
DOI 10.3389/fsurg.2022.956877

Check for updates

OPEN ACCESS

EDITED BY
Huiwu Li,
Shanghai Ninth People's Hospital, China

REVIEWED BY
Wei Chen,
The Third Hospital of Hebei Medical University, China
Zhiyong Hou,
Third Hospital of Hebei Medical University, China

*CORRESPONDENCE
Yun-fa Yang
eyyangyunfa@scut.edu.cn

SPECIALTY SECTION
This article was submitted to Orthopedic Surgery, a section of the journal Frontiers in Surgery

RECEIVED 31 May 2022
ACCEPTED 22 September 2022
PUBLISHED 18 October 2022

CITATION
Yang Y-f, Huang J-w, Gao X-s and Xu Z-h (2022) Eccentric distance zone analysis system: New regional evaluation of cephalic fixator tip location for predicting cut-out in geriatric intertrochanteric fractures with internal fixation. Front. Surg. 9:956877.
doi: 10.3389/fsurg.2022.956877

COPYRIGHT
© 2022 Yang, Huang, Gao and Xu. This is an open-access article distributed under the terms of the Creative Commons Attribution License (CC BY). The use, distribution or reproduction in other forums is permitted, provided the original author(s) and the copyright owner(s) are credited and that the original publication in this journal is cited, in accordance with accepted academic practice. No use, distribution or reproduction is permitted which does not comply with these terms.

Eccentric distance zone analysis system: New regional evaluation of cephalic fixator tip location for predicting cut-out in geriatric intertrochanteric fractures with internal fixation

Yun-fa Yang*, Jian-wen Huang, Xiao-sheng Gao and Zhong-he Xu

Department of Orthopaedic Surgery, Guangzhou First People's Hospital, the Second Affiliated Hospital, School of Medicine, South China University of Technology, Guangzhou, China

Objective: The aim of this study was to investigate an eccentric distance (ED) zone analysis system for regional evaluation of the cephalic fixator tip based on the ED of the cephalic fixator tip referenced to the radius of its own femoral head to predict cut-out in intertrochanteric fractures (ITF) with internal fixation.
Methods: First, we assumed all the femoral heads were regular spheres with the radius (R_{FD}) of "3" for a complete match of the Cleveland zone system and calculated the ED of the cephalic fixator tip by measuring the distances from the cephalic fixator tip to the geometric central axis in the femoral neck and head on both anteroposterior (AP) view and lateral view radiographs. Second, we defined the maximum transverse section of the femoral head into three zones named ED Zone A with ED less than "1," Zone B with ED ranging in "1–2," and Zone C with ED ranging in "2–3" in turns by concentric circles (circles A, B, and C) with the radius of 1/3, 2/3, and 3/3 times of R_{FD}, respectively. Third, we evaluated the ED zones according to the ED and location of the cephalic fixator tip in the eligible 123 ITF patients with single-screw cephalomedullary nail (SCMN) fixation and then analyzed the correlation between the cut-out rate and the ED zones.
Results: The cut-out rates in ED Zones A, B, and C were 4.17%, 38.46%, and 100%, respectively. Multivariate logistic regression indicated that ED Zone A had at least a 14 times lower rate of cut-out compared with ED Zone B. The cephalic fixator tip located in ED Zone A has a lower cut-out rate than that in Cleveland Zone 5. The cut-out rate in ED Zone A is significantly lower than that in the region inside Cleveland Zone 5 but outside ED Zone A.
Conclusion: ED zone analysis system is a reliable regional evaluation of the cephalic fixator tip position for predicting cut-out in geriatric ITF patients with SCMN fixations and potentially an artificial intelligence measurement during surgery. For decreasing the cut-out rate, the cephalic fixator tip should be located in ED Zone A.

KEYWORDS

eccentric distance zone analysis system, intertrochanteric fractures, internal fixation, cut-out, artificial intelligence

Introduction

The incidence of intertrochanteric fractures (ITF) is increasing every year due to the aging population globally. The social burden of ITF significantly increases because of their existing comorbidities, mortality, and bedridden complications resulting in aging (1, 2). Generally, surgical treatment is the first choice for geriatric ITF patients unless there are contraindications to surgery. Nowadays, cephalomedullary nails have been commonly used for ITF due to their biomechanical advantages and good clinical outcomes. However, postoperative implant failures (such as cut-out), which occur in 1.85%–20.5% (1, 3–6), remain a great challenge to orthopedists.

Actually, cut-out is highly associated with the placement of the cephalic fixator tip (7–15). Furthermore, the cephalic fixator should locate in the geometric center of the transversal surface of the femoral head. Kyle et al. suggested that a cephalic fixator should place centrally within the femoral head because the region was the connection area of compression and tension trabeculae (16). Jenkins et al. demonstrated that the strongest and thickest trabecular bone was in the center of the femoral head by microarchitectural evaluation (17), and optimal fixation would be achieved if the cephalic fixator was placed at the neck axis and the center of the femoral head (17). Similarly, Liu et al. confirmed that the highest bone mineral density (BMD) of the proximal femur was in the femoral head, particularly in the middle of the femoral head by quantitative computed tomography, which showed that the cephalic fixator should be placed in the central region of the femoral head for maximum holding power (18). Actually, the Cleveland zone system is easily available for the surgeon to evaluate the intraoperative cephalic fixator placement (3, 16, 17, 19–22).

However, cut-out still occurs in patients who had the cephalic fixator tip in Cleveland Zone 5. Our previous study has confirmed that the probability of cut-out increased dramatically with the increase of eccentric distance (ED) of the cephalic fixator tip, and the best cut-off value of ED for predicting cut-out is "1.022" with a sensitivity of 73.3% and a specificity of 86.1% by the receiver operating characteristic (ROC) analysis (area under the curve, AUC = 0.867, $p < 0.001$) when we assumed all the femoral heads were regular spheres and the radius (R_{FD}) as "3" for a complete match of the Cleveland zone system (23). The mechanical effect of the cephalic fixator tip in Cleveland Zone 5 is different because the ED of the marginal region of Cleveland Zone 5 is much bigger, and that is probably why cut-out still occurs in patients for whom the cephalic fixator tip located in Cleveland Zone 5. Consequently, the geometric center region in the femoral head should be a circle but not a square. Because on a central–central principle in an approximate sphere—the femoral head, a circling zone is better to describe the center zone than a square zone of the Cleveland zone system. We need the right tool to evaluate the cephalic fixator tip position to ensure that the cephalic fixator tip is exactly located in the geometric center region in the femoral head to prevent cut-out.

Therefore, we hypothesized that the placement of cephalic fixator tips with different EDs should have different cut-out risks. We aimed to (1) design an ED zone analysis system for measurement of cephalic fixator tip position, (2) look for the optimal center–center region of the femoral head, and (3) potentially verify the artificial intelligence (AI) applicability of the ED zone analysis system in predicting the cut-out rate in ITF patients with internal fixation during surgery.

Materials and methods

We designed an ED zone analysis system and analyzed the correlation between the cut-out rate and the ED zones of the cephalic fixator tip location in ITF patients with internal fixation.

ED zone analysis system

First, we assumed the femoral head was a regular sphere and standardized all the radius of the femoral head (R_{FD}) to be "3" (R_{FD} = "3") no matter how big the R_{FD} was for a complete match of the Cleveland zone system, easy comparison of the ED, and convenient identification for artificial intelligence based on the study by Yang et al. (23).

Second, we calculated the ED of the cephalic fixator tip using the distances from the cephalic fixator tip to the geometric central axis in the femoral neck and head on both lateral view radiograph ($x = x_0/R_{lat} \times R_{FD}$) and anteroposterior (AP) view radiograph ($y = y_0/R_{ap} \times R_{FD}$) that resulted in "$ED = (x^2+y^2)^{1/2}$" based on our previous study (**Figure 1**) (23). The femoral neck geometric central axis was a straight line through both the femoral head geometric center and the femoral neck geometric center (24). "x_0, y_0, R_{ap}, R_{lat}" were actual measured values. The value of "x" or "y" was defined as positive if the cephalic fixator tip was on the superior or posterior, and as negative if the cephalic fixator tip was inferior or anterior referencing the axis of the femoral head. Thus, we could intuitively locate the tip of the cephalic fixator in the coordinate diagram of the femoral head and easily calculate the ED. ED of the tip point (x,y) is the distance from the circle center to the point of (x,y). (**Figure 2**)

Third, we designed the ED zone analysis system. In this system, we defined the maximum transversal section of the femoral head into three zones named ED Zone A (center zone), B (subcenter zone), and C (remote zone) in turns by three concentric circles (circles A, B, and C) with the radius of 1/3, 2/3, and 3/3 times of R_{FD}, respectively (R_A, R_B, and R_C

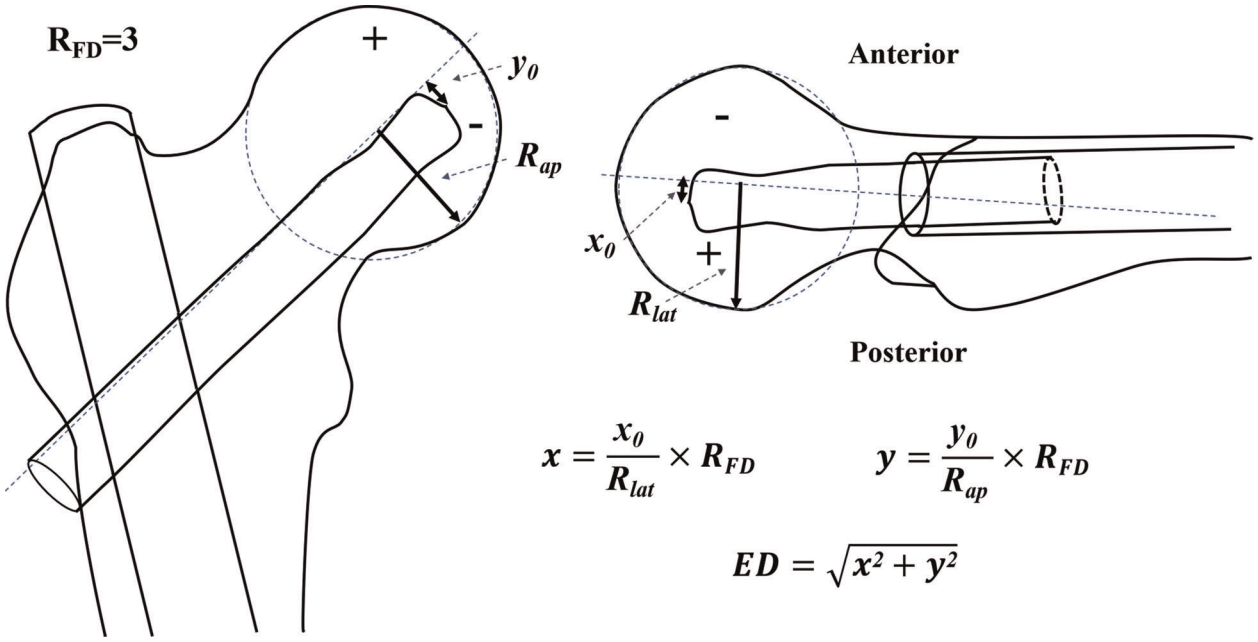

FIGURE 1
The measurement and calculation of ED based on our previous study (23). No matter how big the radius of the femoral head (R_{FD}) was, we standardized the R_{FD} as "3" (R_{FD} = "3," without any unit) for a good match with the Cleveland zone system and easy calculation. "x_0, y_0, R_{ap}, R_{lat}" were the actual measured values. The ED of the cephalic fixators was calculated by the distances from the cephalic fixator tip to the geometric central axis in the femoral neck and head on both the AP view radiograph ($y = y_0/R_{ap} \times R_{FD}$) and the lateral view radiograph ($x = x_0/R_{lat} \times R_{FD}$) resulted in ED = $(x^2 + y^2)^{1/2}$. The value of "x" or "y" was defined as positive if the cephalic fixator tip was on the superior or posterior, and as negative if the cephalic fixator tip was on the inferior or anterior when compared with the axis of femoral head. ED, eccentric distance.

were "1," "2," and "3" accordingly because R_{FD} = "3") for evaluating the location of cephalic fixator tip. Therefore, the ED in Zones A, B, and C ranged as "0–1," "1–2," and "2–3," respectively. To accurately analyze the cephalic fixator tip placements, we could further subdivide the femoral head into four quadrants (Q1, 2, 3, and 4) in this system (**Figure 2**).

Primary verification of ED zone analysis system in geriatric ITF patients

We verified the ED zone analysis system in patients with ITF treated surgically and followed up in our hospital between September 2016 and August 2020 (approved by the Ethics Committee of our Hospital) retrospectively. There were 187 ITF patients who were treated and followed up in our hospital during this period.

The exclusion criteria are as follows: (1) age <65 years, (2) pathological fractures, (3) loss of preoperative or postoperative radiographs, (4) internal fixation was dual-screw cephalomedullary nail or plate system, and (5) patients without any implant failures during radiological follow-up of less than 6 months.

The eligible ITF patients were divided into the Cut-out group and the Non-Cut-out group according to whether the cephalic fixator cut-out or not. We located the tip of the cephalic fixator in the coordinate diagram (an x–y plot) of the femoral head and evaluated the cephalic fixator tip position by individually measuring the ED of the cephalic fixator tip in ITF patients with single-screw cephalomedullary nail (SCMN) fixation. Then, we assessed all the cephalic fixator tip positions in ED Zones A, B, and C according to the ED of the cephalic fixator tip. Finally, we analyzed the correlation between the cut-out rates and the ED zones (**Figure 3**).

The clinical data including age, gender, fracture site, fractures classifications according to the AO Foundation and Orthopaedic Trauma Association system (AO/OTA), American Society of Anesthesiologists (ASA) classification, anesthesia, fixation type, reduction quality, Cleveland zone system, and ED zones of cephalic fixator tip (cephalic fixator tip position based on ED zone analysis system) were analyzed.

All the radiological parameters were evaluated by two observers (J-wH and X-sG). Fracture classification was determined using preoperative AP radiographs by the AO/OTA system (2018 version) (25). Bone qualities were evaluated using the Singh index on preoperative AP radiographs (26). Reduction qualities were graded into three conditions (poor, acceptable, and good) based on the criteria developed by Baumgaertner et al. (27).

The relation between the ED zones and the cut-out rate (the rate of cut-out and pending cut-out) was analyzed. The definition of cut-out was the upper extrusion of the cephalic fixator from the femoral head. The pending cut-out was the presence of over 20° decrease of neck-shaft angle (NSA) on the AP view with no cephalic fixator penetration in the last radiographic follow-up compared with the NSA at the first radiograph right after the surgery.

Statistical analysis

The occurrence of cut-out was defined as the dependent variable. Univariate analysis of continuous and categorical variables was performed using Student's *t*-test and χ^2 test, respectively. All of the significant variables in the univariate analysis ($p < 0.1$) and potential variates (such as age, gender, fracture type, and reduction quality if $p < 0.2$ in univariate analysis) were entered into multivariate logistic models. The Hosmer–Lemeshow goodness-of-fit test (H–L test) was used to evaluate if the models fit the data. The fitting curve was used for the correlation between the ED zones and the probability of cut-out. All analyses above were performed using SPSS (IBM SPSS Statistic for Windows, Version 25.0, IBM Corp, Armonk, NY, United States). All tests were two-sided, and statistical significance was defined as the *p*-value below 0.05. The ROC curves were performed to assess the cut-off value and the reliability of the ED zone analysis system in predicting the cut-out rate with MedCalc® Statistical Software version 19.5.6 (MedCalc Software Ltd, Ostend, Belgium).

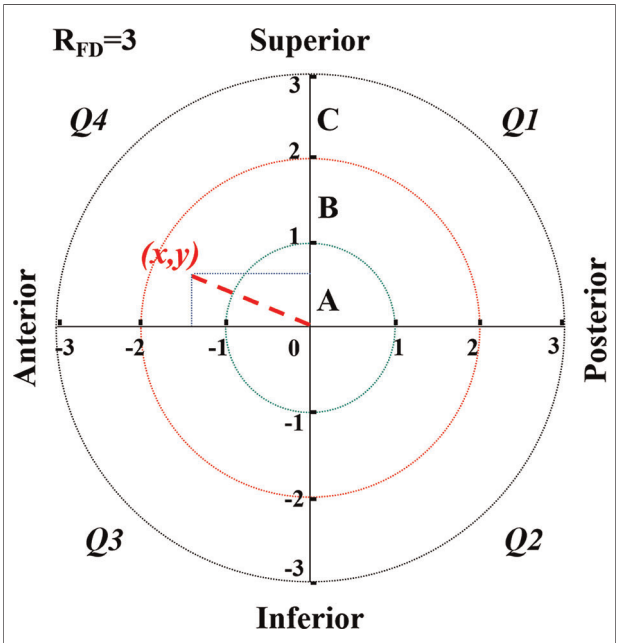

FIGURE 2
ED zone analysis system is just like the coordinate graph (an *x*–*y* plot). In this system, no matter how big the radius of the femoral head (R_{FD}) was, we standardized the R_{FD} as "3" (R_{FD} = "3," without any unit) for a good match with the Cleveland zone system and easy calculation. We defined the femoral head into three zones named Zone A (remote zone), B (subcenter zone), and C (center zone) in turns by three concentric circles (circle A, B, and C) with the radius of 3/3, 2/3, and 1/3 times of R_{FD}, respectively (R_A, R_B, and R_C was "3," "2," and "1," accordingly). The femoral head was divided into four quadrants (Q1, 2, 3, and 4). ED of the tip point (*x*, *y*) is the distance from the circle center to the point of (*x*,*y*). ED, eccentric distance.

Results

A total of 123 eligible geriatric ITF patients with SCMN fixation were included in this full analysis. The 123 patients (43 males and 80 females) aged 80.4 ± 8.4 years. The mean follow-up was 11.8 months (range, 6–48 months). Overall, 15 ITF patients were found with a cut-out (7 of cut-out and 8 of pending cut-out, Cut-out group). The remaining 108 ITF patients were without cut-out (Non-Cut-out group).

The cephalic fixator tip placement evaluated by the ED zone analysis system and Cleveland zone system are shown in Figure 3. In the ED zone analysis system, 96 cephalic fixator tips (in 96 hips of 96 patients) were located in ED Zone A (center zone), 26 cephalic fixator tips (in 26 hips) in ED Zone B (subcenter zone), and 1 cephalic fixator tip (in 1 hip) in ED Zone C (remote zone). The cut-out rates in ED Zones A, B, and C were 4.17%, 38.46%, and 100%, respectively. The cephalic fixator tip position in ED Zone A has a lower cut-out rate than that in Cleveland Zone 5 (cut-out rate: $R_{EDZoneA} = 4.17\%$, $R_{ClevelandZone5} = 7.62\%$). The cut-out rate in ED Zone A is significantly lower than that in the region inside Cleveland Zone 5 but outside ED Zone A (Fisher exact test, $p = 0.0016$) (Figure 3).

In the univariate system (Table 1), no significant differences were found in age, gender, fracture site, fracture classification, anesthesia, ASA classification, fixation type, and reduction quality. Cephalic fixator placements evaluated by the ED zone analysis system had significant differences for cut-out ($p < 0.001$).

In the multivariate analysis, the age, gender, fracture type, reduction quality, and ED zone system were included. Only the ED zone analysis system was independently associated with the cut-out (Table 2). The ED Zone B (subcenter zone) had an over 14 times higher rate of cut-out when compared with the corresponding center zone [ED Zone A, adjusted odds ratio (OR) = 14.38, 95% confidence interval (CI), 4.02–51.55, $p < 0.001$].

The diagnostic effect of ED zone A, of which the AUC was 0.788 ($p < 0.001$), indicated that the cephalic fixator tip position located in ED Zone A (center zone) could significantly reduce the cut-out rate (Figure 4A). Compared with the Cleveland

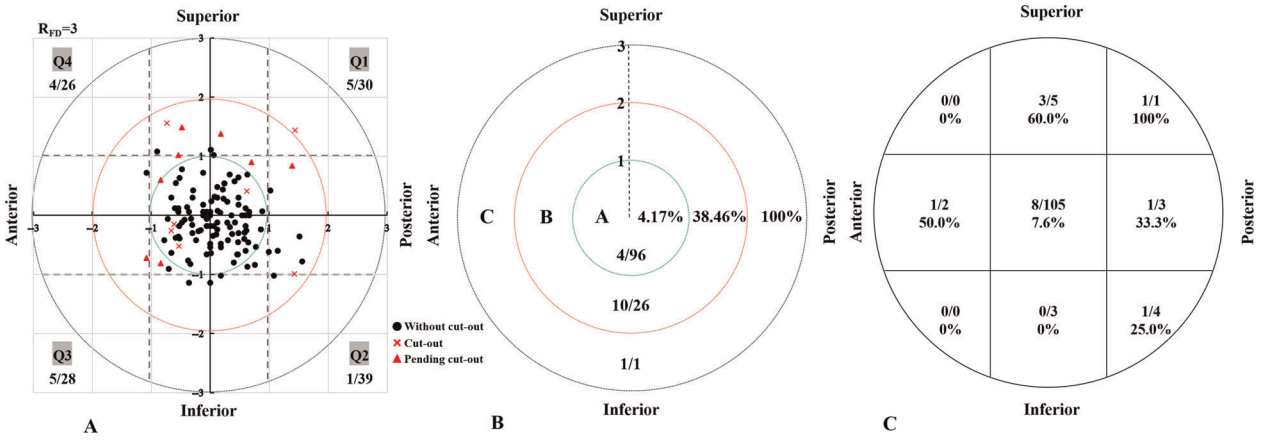

FIGURE 3
The distribution of cephalic fixator tip placements according to the ED zone analysis system (**A**), the rate of cut-out in each zones based on ED zone analysis system (**B**), and the rate of cut-out in each zones based on Cleveland zone system (**C**). Cephalic fixator position in ED Zone A has lower cut-out rate than that in the Cleveland Zone 5 (cut-out rate: $R_{EDZoneC} = 4.17\%$, $R_{ClevelandZone5} = 7.62\%$). The cut-out rate in ED Zone A is significant lower than that in the region inside the Cleveland Zone 5 but outside the ED Zone A ($p = 0.0016$). ED, eccentric distance.

center zone (Zone 5), ED center zone (ED Zone A) had significant low cut-out rate (AUC of ED center was 0.788; AUC of Cleveland center was 0.673; $p = 0.048$) (**Figure 4B**). Compared with the Cleveland noncentral zone (all the zone outside of Zone 5), Cleveland center (Zone 5) has no significant low cut-out rate by multivariate logistic regression analysis (Adjusted OR = 6.513; 95% CI, 0.617 to 68.790; $p = 0.119$). However, the ED center (ED Zone A) has a significant low cut-out rate in comparing with the ED noncentral zone (Zone C and B) (Adjusted OR = 10.026; 95% CI, 2.236 to 44.950; $p = 0.003$) (**Table 3**).

We made further subdivisions in ED Zone B. In terms of the subdivided ED Zone B, the cut-out rates in the ED Zones B_1, B_2, B_3, and B_4 were 50% (3/6), 10% (1/10), 50% (3/6), and 66.7% (4/6), respectively.

Discussion

The occurrence of the cut-out in geriatric ITF with cephalomedullary nailing is highly associated with implant placement, particularly the location of the cephalic fixator tip within the femoral head. The center–center principle was the leading principle of the cephalic fixator tip position (3, 17, 28, 29). However, precise tools were still lacking to measure the real center region in the femoral head in the literature. Thus, we design a new evaluation tool based on measuring the ED of the cephalic fixator tip, the ED zone analysis system, to resolve the problems above and verify its reliability. In this study, we find that the ED zone analysis system is a reliable evaluation tool for the measurement of the cephalic fixator tip position in predicting the cut-out rate in geriatric ITF patients with SCMN fixation. The rate of cut-out rises with the increasing ED. Clinically, the "real" center region should be in Zone A based on the ED zone analysis system. We can potentially use the ED zone analysis system in artificial intelligence measurements just during internal fixation surgeries.

ED zone analysis system can precisely predict the cut-out rate

The cut-out rates in ED Zones A, B, and C were 4.17%, 38.46%, and 100%, respectively. ED center zone (ED Zone A) had at least a 14 times lower rate of cut-out compared with the ED subcenter zone (ED Zone B) by multivariate logistic regression ($p < 0.001$). Positioning the cephalic fixator tip in the femoral head as centrally as possible could decrease the cut-out rate even if it was accompanied by the slightly superior or anterior placement. Moreover, the "slightly superior or anterior" can be determined quantitatively by this system. Therefore, the ED zone analysis system is significantly accurate for predicting cut-out.

ED zone A may be the best location of the cephalic fixator tip

Our previous study has confirmed that the probability of cut-out increased dramatically with the increase of ED, and the best cut-off value of ED for predicting cut-out is "1.022" with a sensitivity of 73.3% and a specificity of 86.1% by the

TABLE 1 Univariate analysis of collected data.

Factor	Overall ($n = 123$)	Non-Cut-out group ($n = 108$)	Cut-out group ($n = 15$)	p-value	OR (95% CI)
Age (mean ± SD)	80.4 ± 8.40	80.3 ± 8.43	81.1 ± 8.46	0.744[a]	1.01 (0.95–1.08)
Gender				0.255[b]	2.35 (0.63–8.84)
Male	43 (35.0)	40 (37.0)	3 (20.0)		
Female	80 (65.0)	68 (63.0)	12 (80.0)		
Fracture site				0.781[b]	1.27 (0.43–3.77)
Left	71 (57.7)	63 (58.3)	8 (53.3)		
Right	52 (42.3)	45 (41.7)	7 (46.7)		
AO/OTA classification				0.108[b]	NA
31A1	62 (50.4)	58 (53.7)	4 (26.7)		
31A2	56 (45.5)	46 (42.6)	10 (66.7)		
31A3	5 (4.1)	4 (3.7)	1 (6.6)		
Anesthesia				0.598[b]	1.96 (0.42–9.27)
Spinal	95 (77.2)	82 (75.9)	13 (86.7)		
General	28 (22.8)	26 (24.1)	2 (13.3)		
ASA				0.719[b]	NA
2	54 (43.9)	46 (42.6)	8 (53.3)		
3	66 (53.7)	59 (57.4)	7 (46.7)		
4	3 (2.4)	3 (2.8)	0 (0.0)		
Fixation type (%)				0.559[b]	1.39 (0.46–4.21)
Blade	41 (33.3)	35 (32.4)	6 (40.0)		
Screw	82 (66.7)	73 (67.6)	9 (60.0)		
Reduction quality				0.176[b]	NA
Good	54 (43.9)	50 (46.3)	4 (26.7)		
Acceptable	47 (38.2)	38 (35.2)	9 (60.0)		
Poor	22 (17.9)	20 (18.5)	2 (13.3)		
Cleveland zone system				**0.002**[b]	6.39 (1.99–20.57)
Zone 5	105 (85.4)	97 (89.8)	8 (53.3)		
The other zones	18 (14.6)	11 (10.2)	7 (46.7)		
ED zone analysis system				**<0.001**[b,c]	15.81 (4.48–55.83)
Zone A	96 (78.0)	92 (85.2)	4 (26.6)	**<0.001**[b,d]	14.38 (4.02–51.55)
Zone B	26 (21.2)	16 (14.8)	10 (66.7)		
Zone C	1 (0.8)	0 (0)	1 (6.7)		

AO/OTA, AO Foundation and Orthopaedic Trauma Association; ASA, American Society of Anesthesiologists; ED, eccentric distance; OR, odds ratio; CI, confidence interval; NA, not applicable.
The bold values represent significant difference between the two groups.
[a]Student's t-test for continuous variables.
[b]Chi-square test for categorical variables.
[c]The reference category is Zone A (comparing with Zone B and C).
[d]The reference category is Zone A (comparing with Zone B).

ROC analysis (23). All the ED in ED Zone A (ED center) are less than "1" (less than the best cut-off value of ED), and the cut-out rate in ED Zone A was only 4.17% (in other words, the cephalic fixator tip placed in ED Zone A had a non-cut-out rate over 95%). The cephalic fixator tip located in ED Zone A had at least a 14 times lower rate of cut-out compared with that in the ED subcenter zone (ED Zone B) by multivariate logistic regression ($p < 0.001$). Consequently, ED Zone A may be the best location for the cephalic fixator tip.

Furthermore, ED Zone A showed higher reliability than the Cleveland Zone 5 dose. First, compared with the Cleveland center zone (Zone 5), ED Zone A had a significantly low cut-out rate by ROC analysis (AUC: 0.788 vs. 0.673; $p = 0.048$). There is some difference in biomechanics heterogeneity in ED Zone A when compared with Cleveland Zone 5 because ED Zone A covers just the region of the internally tangent circle of Cleveland Zone 5. In comparison with ED Zone A, the biomechanical effects of cephalic fixator tips in the

nonoverlapping parts of the two zones, the margins of Cleveland Zone 5, are probably more similar to the adjacent regions of other noncentral zones. The cephalic fixator tips located in these margin regions have a much higher risk of secondary movement or rotation than those in ED Zone A. Second, based on the central–central principle, ED Zone A is more intuitive and easier to understand and fit with observation habits in describing the geometric center of the femoral head than Cleveland Zone 5. In this study, we found that four in nine cases (4/9, 44.44%) with a cut-out located in the region of Cleveland Zone 5 while just outside of ED Zone A.

Considering that different cephalic fixator tip placements had the same ED, we further subdivided ED Zone B into four quadrants for better clinical usage. We found the low rate of cut-out was in the inferior-posterior region (ED Zone B_2). Many studies had also demonstrated that central or inferior on AP view and central or posterior on lateral view within the femoral head were optimal options to prevent cut-out (13, 27,

TABLE 2 Multivariate logistic regression analysis.

Factor	*β* value	*p*-value	Adjusted OR	95% CI lower	95% CI upper
Unstable fracture	0.470	0.540	1.600	0.355	7.201
poor reduction	1.110	0.495	3.033	0.125	73.665
Cleveland noncentral zone[a]	1.874	0.119	6.513	0.617	68.790
ED noncentral zone[b]	2.305	**0.003**	10.026	2.236	44.950

ED, eccentric distance; OR, odds ratio; CI, confidence interval.
The bold values represent significant difference between the two groups.
[a]Cleveland noncentral zone means the other zones except zone 5, the reference category is Cleveland zone 5.
[b]ED noncentral zone means ED zone C and B, the reference category is ED zone A.

TABLE 3 Reliability between two independent observers for measuring variables.

Variable	ICC or κ	95% CI	Reliability
Singh index	0.682	0.573–0.767	Excellent
Fracture classification	0.788	0.709–0.847	Excellent
Reduction quality	0.809	0.709–0.909	Almost perfect
Cleveland zone	0.669	0.565–0.773	Excellent
Cleveland center	0.745	0.641–0.829	Excellent
ED value	0.943	0.701–0.978	Almost perfect
ED center	0.763	0.624–0.902	Excellent

ED, Eccentric distance; CI, confidence interval; ICC, intraclass correlation coefficient; κ, Kappa coefficient.

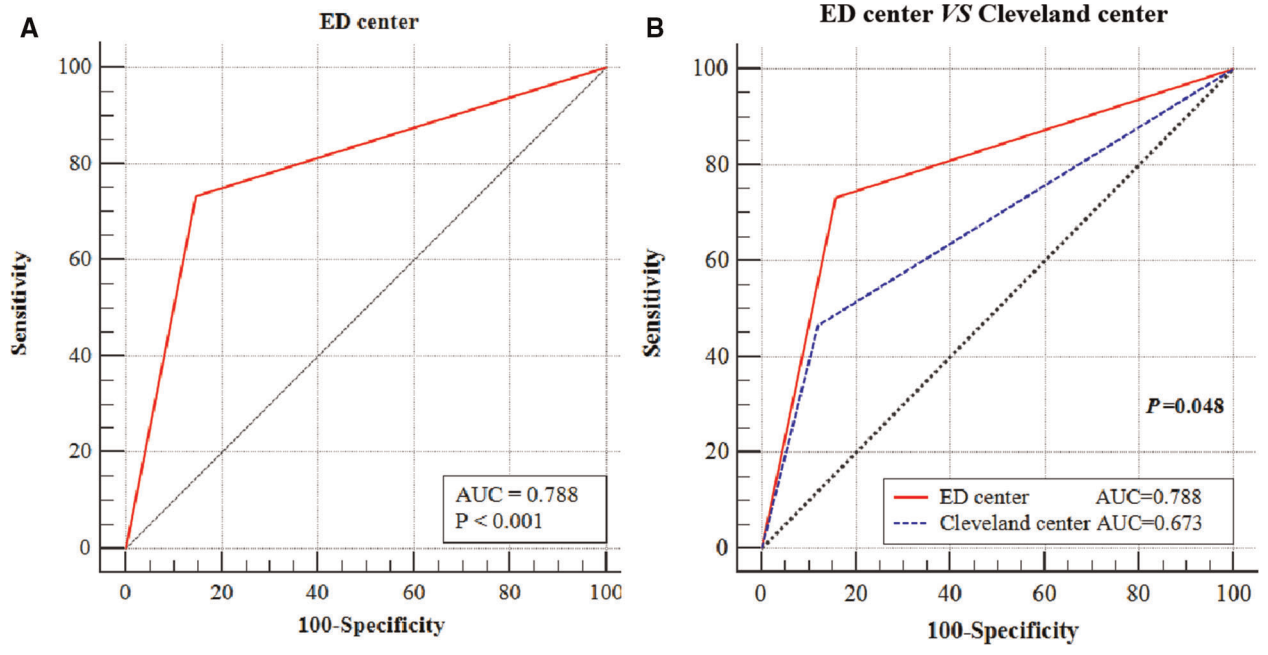

FIGURE 4
The graph shows the ROC analysis of ED zone C. The ED center (ED Zone C) was reliable in predicting cut-out (AUC = 0.788, $p < 0.001$) (**A**). Compared with the Cleveland center zone (Zone 5), ED center zone (ED Zone C) had significant low cut-out rate (AUC of ED center was 0.788; AUC of Cleveland center was 0.673; $p = 0.048$) (**B**). ROC, receiver operating characteristic; ED, eccentric distance; AUC, area under the curve.

29–33). The reason for the discrepancies between the previous conclusions and our results probably is that not all the cases with cut-out previously were in ED Zone B_2 but the more marginal locations with much bigger ED. As for the other regions of ED Zone B (ED Zones B_1, B_3, and B_4), there were no significant differences in the cut-out rate, which may be attributed to the small number of cases (only 26 cases in ED Zone B).

In terms of the ED Zone C, it was excessively eccentric to place the cephalic fixator tip in this region. Only one case was found in ED Zone C, which was observed with cut-out. With the assistance of the C-arm and cephalic fixator insertion principle, an overlarge ED was almost impossible in clinical practice. We should not finish the operation with an extremely ED of cephalic fixator tip position on AP or lateral view unless the patient's poor general condition.

Therefore, the ED Zone A could be the excellent position of the cephalic fixator tip.

ED zone analysis system may potentially be an AI application during surgery

The ED zone analysis system can be easily used because the measurement and the numerical relationship of the ED are completely matched the Cleveland zone system and the calculation of the ED only based on the AP view and the lateral view radiographs. In addition, the ED is a relative value measurement (the measurement with no complicated formula, regardless of magnification), which provides convenience in clinical usage. If we can set up the relative software of the ED zone analysis system in the C-arm x-ray machine, we may even use the ED zone analysis system in AI measurement just during surgeries.

Limitations or weaknesses

However, there are still some limitations or weaknesses in this study. First, the design of ED zones is based on the ideal condition that the femoral head is a regular sphere. Second, we only verify the applicability of the ED zone analysis system in the single-screw cephalomedullary nails, resulting in the conclusion that may not be suitable for other types of internal fixations for the treatment of ITF. Third, we have not considered the quantitative osteoporosis assessment of the femoral head and the depth of cephalic fixator tips in the femoral head in geriatric ITF patients accurately. Thus, further studies are necessary to verify the clinical applicability of the ED zone analysis system and its clinical significance.

Conclusions

The ED zone analysis system is a new reliable evaluation tool and potentially an AI application for measuring the cephalic fixator tip position in predicting cut-out in geriatric ITF patients with SCMN fixation. The cut-out rate rises with increasing ED. For decreasing the cut-out rate, the cephalic fixator tip should be located in ED Zone A (the center of the femoral head).

Data availability statement

The raw data supporting the conclusions of this article will be made available by the authors, without undue reservation.

Ethics statement

The studies involving human participants were reviewed and approved by the Ethics Committee of Guangzhou First People's Hospital (K-2020-106-01). The patients/participants provided their written informed consent to participate in this study.

Author contributions

All authors contributed to the study conception and design. The study was designed by Y-fY. Material preparation, data collection, and analysis were performed by J-wH, X-sG, and Z-hX. The first draft of the manuscript was written by J-wH and was revised by Y-fY. All authors contributed to the article and approved the submitted version.

Conflict of interest

The authors declare that the research was conducted in the absence of any commercial or financial relationships that could be construed as a potential conflict of interest.

Publisher's note

All claims expressed in this article are solely those of the authors and do not necessarily represent those of their affiliated organizations, or those of the publisher, the editors and the reviewers. Any product that may be evaluated in this article, or claim that may be made by its manufacturer, is not guaranteed or endorsed by the publisher.

References

1. Yam M, Kang BJ, Chawla A, Zhang W, Way LG, Xavier RPA, et al. Cephalomedullary blade cut-ins: a poorly understood phenomenon. *Arch Orthop Trauma Surg*. (2020) 140(12):1939–45. doi: 10.1007/s00402-020-03439-x

2. Yang YF, Huang JW, Gao XS, Liu ZL, Wang JW, Xu ZH. The correlation between timing of surgery and the need for RBC transfusions in the geriatric intertrochanteric fracture population. *Geriatr Orthop Surg Rehabil*. (2021) 27 (12):2151459321998614. doi: 10.1177/2151459321998614

3. Caruso G, Bonomo M, Valpiani G, Salvatori G, Gildone A, Lorusso V, et al. A six-year retrospective analysis of cut-out risk predictors in cephalomedullary nailing for pertrochanteric fractures: can the tip-apex distance (TAD) still be considered the best parameter? *Bone Joint Res*. (2017) 6(8):481–8. doi: 10.1302/2046-3758.68.BJR-2016-0299.R1

4. Khanna V, Tiwari M. Significance of tip apex distance in intertrochanteric fracture femur managed with proximal femoral nailing. *Orthop Traumatol Surg Res*. (2021) 107(6):103009. doi: 10.1016/j.otsr.2021.103009

5. Mao W, Ni H, Li L, He Y, Chen X, Tang H, et al. Comparison of Baumgaertner and Chang reduction quality criteria for the assessment of trochanteric fractures. *Bone Joint Res*. (2019) 8(10):502–8. doi: 10.1302/2046-3758.810.BJR-2019-0032.R1

6. Lee SR, Kim ST, Yoon MG, Moon MS, Heo JH. The stability score of the intramedullary nailed intertrochanteric fractures: stability of nailed fracture and postoperative patient mobilization. *Clin Orthop Surg*. (2013) 5(1):10–8. doi: 10.4055/cios.2013.5.1.10

7. Huang JW, Gao XS, Yang YF. Risk factors for cut-outs in geriatric intertrochanteric fractures with cephalomedullary nailing after obtaining acceptable reduction: a case-control study. *BMC Musculoskelet Disord*. (2022) 23(1):354. doi: 10.1186/s12891-022-05296-8

8. Yang YF, Huang JW, Gao XS. CalTAD is the key evaluation tool for measurement of cephalic fixation position for predicting cut-out in geriatric intertrochanteric fracture patients with internal fixations after achieving acceptable reduction. *Geriatr Orthop Surg Rehabil*. (2022) 29 (13):21514593221083820. doi: 10.1177/21514593221083820

9. Law GW, Wong YR, Gardner A, Ng YH. Intramedullary nailing confers an increased risk of medial migration compared to dynamic hip screw fixation in unstable intertrochanteric hip fractures. *Injury*. (2021) 52(11):3440–5. doi: 10.1016/j.injury.2021.01.011

10. Huang JW, Gao XS, Yang YF. Early prediction of implant failures in geriatric intertrochanteric fractures with single-screw cephalomedullary nailing fixation. *Injury*. (2022) 53(2):576–83. doi: 10.1016/j.injury.2021.12.031

11. Yoon YC, Oh CW, Sim JA, Oh JK. Intraoperative assessment of reduction quality during nail fixation of intertrochanteric fractures. *Injury*. (2020) 51 (2):400–6. doi: 10.1016/j.injury.2019.10.087

12. Warschawski Y, Ankori R, Rutenberg TF, Steinberg EL, Atzmon R, Drexler M. Expandable proximal femoral nail versus gamma proximal femoral nail for the treatment of hip reverse oblique fractures. *Arch Orthop Trauma Surg*. (2022) 142 (5):777–85. doi: 10.1007/s00402-020-03726-7

13. Zhang W, Antony Xavier RP, Decruz J, Chen YD, Park DH. Risk factors for mechanical failure of intertrochanteric fractures after fixation with proximal femoral nail antirotation (PFNA II): a study in a Southeast Asian population. *Arch Orthop Trauma Surg*. (2021) 141(4):569–75. doi: 10.1007/s00402-020-03399-2

14. Sivakumar A, Thewlis D, Ladurner A, Edwards S, Rickman M. Proximal femoral nail unlocked versus locked (ProFNUL): a protocol for a multicentre, parallel-armed randomised controlled trial for the effect of femoral nail mode of lag screw locking and screw configuration in the treatment of intertrochanteric femur fractures. *BMJ Open*. (2020) 10(2):e032640. doi: 10.1136/bmjopen-2019-032640

15. Mitsuzawa S, Matsuda S. Cement distribution and initial fixability of trochanteric fixation nail advanced (TFNA) helical blades. *Injury*. (2022) 53 (3):1184–9. doi: 10.1016/j.injury.2021.10.028

16. Kyle RF, Cabanela ME, Russell TA, Swiontkowski MF, Winquist RA, Zuckerman JD, et al. Fractures of the proximal part of the femur. *Instr Course Lect*. (1995) 44:227–53. PMID: 7797861

17. Jenkins PJ, Ramaesh R, Pankaj P, Patton JT, Howie CR, Goffin JM, et al. A micro-architectural evaluation of osteoporotic human femoral heads to guide implant placement in proximal femoral fractures. *Acta Orthop*. (2013) 84 (5):453–9. doi: 10.3109/17453674.2013.842432

18. Liu G, Ge J, Zheng X, Wu C, Yan Q, Yang H, et al. Proximal femur lag screw placement based on bone mineral density determined by quantitative computed tomography. *Exp Ther Med*. (2020) 19(4):2720–4. doi: 10.3892/etm.2020.8480

19. Turgut A, Kalenderer Ö, Karapınar L, Kumbaracı M, Akkan HA, Ağuş H. Which factor is most important for occurrence of cutout complications in patients treated with proximal femoral nail antirotation? Retrospective analysis of 298 patients. *Arch Orthop Trauma Surg*. (2016) 136(5):623–30. doi: 10.1007/s00402-016-2410-3

20. Kane P, Vopat B, Heard W, Thakur N, Paller D, Koruprolu S, et al. Is tip apex distance as important as we think? A biomechanical study examining optimal lag screw placement. *Clin Orthop Relat Res*. (2014) 472(8):2492–8. doi: 10.1007/s11999-014-3594-x

21. Bojan AJ, Beimel C, Taglang G, Collin D, Ekholm C, Jönsson A. Critical factors in cut-out complication after Gamma Nail treatment of proximal femoral fractures. *BMC Musculoskelet Disord*. (2013) 14:1. doi: 10.1186/1471-2474-14-1

22. Lenich A, Bachmeier S, Prantl L, Nerlich M, Hammer J, Mayr E, et al. Is the rotation of the femoral head a potential initiation for cutting out? A theoretical and experimental approach. *BMC Musculoskelet Disord*. (2011) 12:79. doi: 10.1186/1471-2474-12-79

23. Yang YF, Huang JW, Gao XS, Xu ZH. The correlation between cutout and eccentric distance (ED) of the cephalic fixator tip in geriatric intertrochanteric fractures with internal fixation. *J Orthop Surg Res*. (2022) 17(1):263. doi: 10.1186/s13018-022-03153-x

24. Wilson JD, Eardley W, Odak S, Jennings A. To what degree is digital imaging reliable? Validation of femoral neck shaft angle measurement in the era of picture archiving and communication systems. *Br J Radiol*. (2011) 84 (1000):375–9. doi: 10.1259/bjr/29690721

25. Meinberg EG, Agel J, Roberts CS, Karam MD, Kellam JF. Fracture and dislocation classification compendium—2018. *J Orthop Trauma*. (2018) 32 (Suppl 1):s1–s170. doi: 10.1097/BOT.0000000000001063

26. Singh M, Nagrath AR, Maini PS. Changes in trabecular pattern of the upper end of the femur as an index of osteoporosis. *J Bone Joint Surg Am*. (1970) 52 (3):457–67. doi: 10.2106/00004623-197052030-00005

27. Baumgaertner MR, Curtin SL, Lindskog DM. Intramedullary versus extramedullary fixation for the treatment of intertrochanteric hip fractures. *Clin Orthop Relat Res*. 1998, (348):87–94. doi: 10.1097/00003086-199803000-00015

28. Cleveland M, Bosworth DM, Thompson FR, Wilson HJ, Ishizuka T. A ten-year analysis of intertrochanteric fractures of the femur. *J Bone Joint Surg Am*. (1959) 41-A:1399–408. doi: 10.2106/00004623-195941080-00003

29. Baumgaertner MR, Curtin SL, Lindskog DM, Keggi JM. The value of the tip-apex distance in predicting failure of fixation of peritrochanteric fractures of the hip. *J Bone Joint Surg Am*. (1995) 77(7):1058–64. doi: 10.2106/00004623-199507000-00012

30. Goffin JM, Pankaj P, Simpson AH. The importance of lag screw position for the stabilization of trochanteric fractures with a sliding hip screw: a subject-specific finite element study. *J Orthop Res*. (2013) 31(4):596–600. doi: 10.1002/jor.22266

31. Kaufer H. Mechanics of the treatment of hip injuries. *Clin Orthop Relat Res*. (1980) 146:53–61. doi: 10.1097/00003086-198001000-00008

32. Davis TR, Sher JL, Horsman A, Simpson M, Porter BB, Checketts RG. Intertrochanteric femoral fractures. Mechanical failure after internal fixation. *J Bone Joint Surg Br*. (1990) 72(1):26–31. doi: 10.1302/0301-620X.72B1.2298790

33. De Bruijn K, den Hartog D, Tuinebreijer W, Roukema G. Reliability of predictors for screw cutout in intertrochanteric hip fractures. *J Bone Joint Surg Am*. (2012) 94(14):1266–72. doi: 10.2106/JBJS.K.00357

frontiers | Frontiers in Surgery

TYPE Original Research
PUBLISHED 28 October 2022
DOI 10.3389/fsurg.2022.1041105

Check for updates

OPEN ACCESS

EDITED BY
Yan Yu,
Tongji University School of Medicine, China

REVIEWED BY
Giovanna Pavone,
University of Foggia, Italy
Zhao Lang,
Beijing Jishuitan Hospital, China

*CORRESPONDENCE
Jincai Yang
jincaiy2008@163.com
Peng Yin
yinpeng3904@126.com

SPECIALTY SECTION
This article was submitted to Orthopedic Surgery, a section of the journal Frontiers in Surgery

RECEIVED 10 September 2022
ACCEPTED 03 October 2022
PUBLISHED 28 October 2022

CITATION
Pang D, Yang J, Hai Y, Fan Z, Gao H and Yin P (2022) Changes in paraspinal muscles and facet joints after percutaneous endoscopic transforaminal lumbar interbody fusion for the treatment of lumbar spinal stenosis: A 3-year follow-up.
Front. Surg. 9:1041105.
doi: 10.3389/fsurg.2022.1041105

COPYRIGHT
© 2022 Pang, Yang, Hai, Fan, Gao and Yin. This is an open-access article distributed under the terms of the Creative Commons Attribution License (CC BY). The use, distribution or reproduction in other forums is permitted, provided the original author(s) and the copyright owner(s) are credited and that the original publication in this journal is cited, in accordance with accepted academic practice. No use, distribution or reproduction is permitted which does not comply with these terms.

Changes in paraspinal muscles and facet joints after percutaneous endoscopic transforaminal lumbar interbody fusion for the treatment of lumbar spinal stenosis: A 3-year follow-up

Daming Pang, Jincai Yang*, Yong Hai, Zhexuan Fan, Haifeng Gao and Peng Yin*

Department of Spine Surgery, Affiliated Beijing Chaoyang Hospital of Capital Medical University, Beijing, China

Objectives: This study investigates the changes in the paraspinal muscles of lumbar spinal stenosis patients after percutaneous endoscopic transforaminal lumbar interbody fusion (PE-TLIF).

Methods: Thirty-three patients from Beijing Chaoyang Hospital who had L4/5 segment lumbar spinal stenosis between January, 2017 and January, 2019were included in this study. Patient-reported outcomes including the visual analog scale scores for back pain and leg pain (VAS-BP and VAS-LP, respectively) and the Oswestry disability index (ODI) scores at pre-operation and 1-week, 3-month, 12-month, and (at least) 3-year follow-up (the final follow-up) were evaluated. Computed tomography (CT) was performed at the 12-month follow-up, 24-month follow-up, and the final follow-up after surgery. Multifidus (MF) muscle functional cross-sectional area (FCSA) and fat infiltration (FI) were evaluated, and the degree of adjacent facet joint degeneration was evaluated using Pathria scores.

Results: All patients underwent at least a 3-year follow-up period. The VAS-BP, VAS-LP, and ODI were significantly lower at 1-week, 3-month, 12-month, and 3-year follow-up than at pre-operation ($P < 0.05$). At the 3-year follow-up, no differences were found in FCSA and FI for any patient's MF muscle at the lower third of the vertebral body (L3) above the operation level ($P > 0.05$), and there was no statistical difference in the central plane of the L3/4 and L5/S1 vertebral facet joints at pre-operation, 12-month, 24-month, and 3-month follow-up ($P > 0.05$).

Conclusions: PE-TLIF can provide satisfactory clinical outcomes for patients with lumbar spinal stenosis. Furthermore, the technique may also reduce the injury on the paravertebral muscles, especially the MF muscle, as well as on adjacent facet joints.

Abbreviation

PE-TLIF, percutaneous endoscopic transforaminal lumbar interbody fusion; VAS-LBP, visual analogue scale on lumbar pain; VAS-LP, visual analogue scale on leg pain; ODI, oswestry disability index; CT, computed tomography; MF, multifidus; FCSA, functional cross-sectional area; FI, fat infiltration; LSS, lumbar spinal stenosis; SAP, superior articular process; ROI, regions of interest; ASD, adjacent segment degeneration; USFJ, upper segment facet joints; LSFJ, lower segment facet joints.

KEYWORDS
transforaminal lumbar interbody fusion, endoscopy, paraspinal muscles atrophy, functional cross-sectional area, spondylolisthesis

Background

Since the 1990s, traditional open surgery has been widely used to treat Lumbar spinal stenosis (LSS) (1), a condition that affects 47.2% of people worldwide (2). However, paraspinal muscle atrophy, especially the multifidus (MF), and degeneration of the facet joints are frequently observed as a complication of the procedure during follow-up, due traditional open surgery's lack of protection of the paraspinal muscles and facet joints (3). Paraspinal muscles such as the MF and facet joints play an important role in maintaining the stability of lumbar vertebrae (4), and injuries to these structures can lead to chronic back pain (4–8). Therefore, finding effective treatments for stenosis that reduce the chance of injuries to these structures is of paramount importance.

Clinical trials have shown that minimally invasive interbody fusions are effective at reducing muscle injuries (9). In 2002, Foley and Lefkowitz introduced minimally invasive fusion technology for the first time, and the technique exhibited clear advantages in reduced trauma, wound size, and hospitalization time (10). However, the MIS-TLIF technique uses screws in a similar way to conventional open surgery, and this method can too often lead to the injury of the medial branch of the dorsal ramus, increasing the possibility of MF atrophy. As a result, surgeons have begun to attempt percutaneous screw fixation in lumbar surgery.

By applying a minimally invasive approach and developing spinal endoscopic techniques, we have developed some novel techniques for performing percutaneous endoscopic transforaminal lumbar interbody fusion. Furthermore, we have developed a guided superior articular process (SAP) resection device that can excise the articular processes precisely and reduce iatrogenic injury (11, 12). Thus, the objective of this study is to evaluate the changes in paraspinal muscles and facet joint degeneration after PE-TLIF and a follow-up period of at least 3 years in order to assess the clinical value of PE-TLIF in the treatment of lumbar spinal stenosis.

Materials and methods

Patient population

This retrospective study was performed at Beijing Chaoyang Hospital and included 33 patients who were diagnosed with lumbar spinal stenosis according their symptoms, clinical signs, and medical images and subsequently underwent PE-TLIF between January, 2017 and January, 2019. Inclusion criteria were as follows: (1) degenerative instability on the L4/5 level and LSS; (2) receipt of PE-TLIF treatment; and (3) a follow-up period of at least 3 years. Exclusion criteria were: (1) receipt of previous spinal surgery and (2) suffering from infection, trauma, or spondylolisthesis. This study was approved by the Ethics Committee of Beijing Chaoyang Hospital.

Surgical technique

The specific procedure is detailed in our previous research (12).

Data collection

In order to examine the changes in paraspinal muscles and facet joints degeneration after PE-TLIF, we obtained MF functional cross-sectional area (FCSA) (13) and fat infiltration (FI) measurements from axial CT axial images at the lower third of the vertebral body (L3) above the operation level (L4/5) before surgery and 12 months, 24 months, and 3 years (or final follow-up if longer than 3 years) after surgery to avoid any artifacts produced by the screws themselves. In addition, to prevent interference from the nearby fat, bony structures, and other soft tissues, we measured the MF FCSA and FI using purpose-built software from GE Healthcare (United States) according to the manufacturer's selection method for muscle regions of interest (ROI) (**Figure 1**) (14). The FI rate was graded according to the degree to which MF muscle was replaced by adipose tissue: "0" for estimates of normal or no obvious FI within the muscle, "1" for <10% FI, "2" for 10%–50% FI, and "3" for >50% FI. We obtained the total segmental value for FI by summing the left and right values.

The central planes of the L3/4 and L5/S1 vertebral facet joints were qualitatively evaluated using the Pathria grading system in axial scanning CT imaging (15), and once again we obtained the total segmental scores for each level by summing the left and right Pathria scores for that level. Clinical effects, including the visual analog scale scores (VAS) for back pain and leg pain (VAS-LBP and VAS-LP, respectively) and the Oswestry disability index (ODI), were evaluated at

FIGURE 1
Measurement of the MF FCSA in an atrophied muscle.

pre-operation, and at the 1-week, 3-month, 12-month and final follow-ups.

Statistical analyses

All data were analyzed using SPSS 21.0 software. We used the Friedman rank-sum test for nominal data and repeated measures analysis of variance for continuous data in order to test MF functional cross-sectional area. For each test, we considered a $P < 0.05$ to indicate a statistically significant result.

Results

Patient demographics

A total of 33 patients were included in this study. There were 13 male and 20 female patients, and the mean age of patients was 61.0 ± 8.9 years (range, 45–82 years). All patients received a follow-up period of at least 3 years, and the average follow-up period was 41.7 ± 3.5 months. The mean body mass index (BMI) was 23.5 ± 3.9 kg/m^2, and the average operation time was 208.7 ± 28.5 min. Mean blood loss from the operation was 138.2 ± 83.5 ml, and the average postoperative rest time for each patient was 17.9 ± 2.2 days (see Table 1 and Figure 2).

TABLE 1 Characteristics of patients.

Characteristics	*n*
Gender	
Male	13
Female	20
Age (years)	59.0 ± 8.9
BMI (kg/m^2)	23.5 ± 3.9
Average incision length (cm)	8.7 ± 2.5
Operation time (min)	208.7 ± 28.5
Intraoperative blood loss (ml)	138.2 ± 83.5
Postoperative rest time (days)	17.9 ± 2.2
Follow-up period (months)	41.7 ± 3.5

Postoperative outcomes

The ODI score decreased from 62% (56,65) at pre-operation to 24% (20,30) at 3-month follow-up, 12% (9.5,16.5) at 12-month follow-up, and 8% (4,15.5) at final follow-up. The VAS-LBP decreased from 7 (7,8) at pre-operation to 3 (2,3) at 1-week follow-up, 1 (1,2) at 3-month follow-up, 1 (0,2) at 12-month follow-up, and 1 (0,1) at final follow-up. Similarly, the VAS-LP decreased from 6 (5,7) at pre-operation to 2 (1,3) at 1-week follow-up, 1 (1,2) at 3-month follow-up, 1 (0,2) at 12-month follow-up, and 0 (0,1) at final follow-up (Table 2). Compared to the preoperative FCSA of the MF, the postoperative FCSA of the MF for any follow-up stage was not statistically different ($P > 0.05$). Furthermore, the median preoperative MF muscle FI was 2, the median 12-month postoperative MF muscle FI was 3, the median 24-month postoperative MF muscle FI was 3, and the median final follow-up MF muscle FI was 3. None of these differences were statistically different from 0 ($P > 0.05$) (Table 3).

The postoperative upper segment facet joint scores at 12 months and 24 months were also not statistically different compared to pre-operation ($P > 0.05$), and compared to the preoperative lower segment facet joint score, the postoperative lower segment facet joint scores at 12 months and 24 months were not statistically different either ($P > 0.05$) (Table 4). Finally, intervertebral fusion was completed in all patients after 12 months, according to the Bridwell criteria (16), Grade I in 13 cases, Grade II in 16 cases, and Grade III in 4cases.

Discussion

The focus of our study was on the effects of PE-TLIF for single segment LSS on the MF and facet joints. During the follow-up period for this procedure, we found that use of the PE-TLIF technique provided adequate protection for the MF and adjacent facet joints. Additionally, the PE-TLIF surgery significantly improved the ODI and VAS for all patients, indicating that the clinical symptoms of the patients had been effectively relieved.

The MF is the most important stabilizing muscle of the spine and is located in the deepest part of the spinal column.

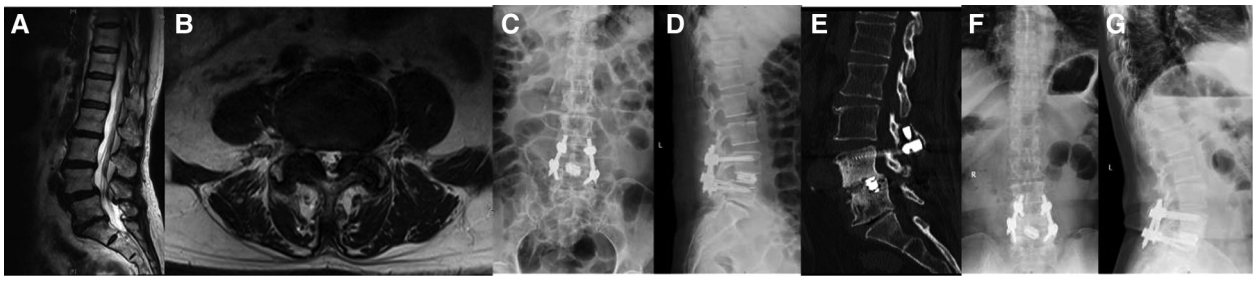

FIGURE 2
A 69-year-old female. Preoperative VAS-LBP: 6; Preoperative VAS-LP: 8; Preoperative ODI: 70%. (**A**, **B**) A L4/5 spinal stenosis identified in the preoperative MRI. (**C**, **D**) A good implantation position shown by x-rays taken a week after the operation. (**E**) At 12 months after the surgery, a CT scan image revealed a standard lumbar fusion. (**F**, **G**) The final x-ray images indicated that the implantation occurred in a good position.

TABLE 2 Comparison of indicators related to efficacy evaluation before and after PE-TLIF.

n = 33	VAS-LBP	VAS-LP	ODI (%)
Pre-operation	7 (7,8)	6 (5,7)	62 (56,65)
Post-1 w	3 (2,3)*	2 (1,3)*	–
Post-3 m	1 (1,2)*	1 (1,2)*	24 (20,30)*
Post-12 m	1 (0,2)*	1 (0,1)*	12 (9.5,16.5)*
Final follow-up	1 (0,1)*	0 (0,1)*	8 (4,15.5)*

Note. *Compared to pre-operation, $P < 0.05$.

TABLE 3 Preoperative and postoperative paraspinal muscle parameters.

	Preoperative	Post-12 m	Post-24 m	Final follow-up
FCSA of the MF	(568.09 ± 49.82)	(557.12 ± 51.31)*	(558.55 ± 53.37)*	(537.51 ± 55.11)*
FI of the MF	2 (2,3)	3 (2,3)*	3 (2,3)*	3 (3,3)*

Note. *Compared to pre-operation, $P > 0.05$.

TABLE 4 Preoperative and postoperative scores of the segment facet joints.

	Preoperative	Post-12 m	Post-24 m	Final follow-up
USFJ	5 (4,6)	5 (4,6)*	5 (4,5)*	5 (4,6)*
LSFJ	5 (4,6)	5 (4,5)*	5 (4,6)*	5 (4,7)*

Note. *Compared to pre-operation, $P > 0.05$.

During spinal movement, two-thirds of stabilizing stiffness is provided by the MF. In lumbar surgery, it is necessary to protect paraspinal muscles.

The traditional posterior surgery has great trauma, which causes direct damage to the paraspinal muscles in the process of muscle stripping. In addition, Tsutsumimoto et al. (17) believe that the continuous stretch of the paraspinal muscle caused by the retractor increases the pressure of the paraspinal muscle and affects the blood perfusion of the capillaries of the paraspinal muscle in traditional open surgery. This ischemic change of paraspinal muscles will eventually lead to functional changes of paraspinal muscles and muscle atrophy. The PE-TLIF technology we have developed has the advantages of smaller incision size and reduced paravertebral muscle dissection, which reduces the direct injury to the paraspinal muscle and the influence on the blood circulation of the paraspinal muscle. Moreover, through the analysis of the morphological changes of the multifidus in MRI after the injury of the the medial branch of the dorsal ramus after operation, it is considered that the muscle atrophy after lumbar surgery is related to the iatrogenic injury of the medial branch of the dorsal ramus (18–21). According to anatomy, it was found that the MF was innervated only by the medial branch. Traditional posterior open surgery increases the probability of injury of this nerve and the possibility of denervated atrophy of MF. In order to reduce the risk of the nerve injury, different from the traditional posterior lumbar interbody fusion and minimally invasive fusion technique, we chose to use the percutaneous method. According to Regev et al. (22), percutaneous screw placement can reduce the incidence of indirect injury to the medial branch nerve from 84% to 20%.

In order to evaluate the changes of MF after PE-TLIF, we compared the FCSA and FI rate of MF at pre-operation, 12-month follow-up, 24-month follow-up, and at final follow-up. Some studies have shown that the decrease of muscle volume and the increase of fat deposition are the main characteristics of paraspinal muscle degeneration (23, 24). Kang et al. confirmed by MRI that the degree of paraspinal muscle degeneration can be reflected by the decrease of paraspinal muscle FCSA and FI (25). In our study, we used FCSA and FI to assess the degree of MF atrophy by CT axial images. FCSA assessed by CT has high intraclass correlation with MRI according to Hu et al. (26). Due to interference from the metal artifacts, however, the MF had to

be measured in selected axial images (27). The results showed that the FI rate of the MF muscles did not change significantly at 12 months, 24 months, or the final follow-up after surgery. Some studies have reported that the function of the MF can be affected after operation (28, 29), but in this study we found no difference in the FCSA of the MF at 12 months, 24 months, or the final follow-up after PE-TLIF.

In order to help us perform this novel procedure, we have invented a cannula with a hook-shaped front. This tool can effectively remove part of the articular process and protect local tissue. By reducing intraoperative trauma, the impact on adjacent segments can be reduced. The adjacent segmental facet joint scores of the 33 patients in this study were not statistically different from their preoperative scores. In our study, all the patients achieved satisfactory clinical results, and their postoperative lumbar pain was significantly reduced. No obvious degeneration of adjacent facet joint was found at least 3 years after operation, but for long-term results, it is necessary to analyze the effects of degeneration and operation on adjacent segments, so as to evaluate the results of PE-TLIF. However, this study has several limitations. First, the study was retrospective and single-center in design, and it was neither randomized nor controlled. Second, the sample size was small. Finally, we couldn't estimate the effects of our procedure on the muscles at the fusion level due to the interference from the metal artifacts.

Conclusion

Our novel PE-TLIF can provide satisfactory clinical outcomes for patients with lumbar spinal stenosis. By the avoiding direct injury to the paraspinal muscle and the traction of the paraspinal muscle, and reducing the injury probability of the medial dorsal branch, Our PE-TLIF can adequately protect the MF and reduce the degeneration of the adjacent facet joints.

Data availability statement

The original contributions presented in the study are included in the article/Supplementary Material, further inquiries can be directed to the corresponding author/s.

Ethics statement

The studies involving human participants were reviewed and approved by the Ethics Committee of Beijing Chaoyang Hospital. The patients/participants provided their written informed consent to participate in this study. Written informed consent was obtained from the individual(s) for the publication of any potentially identifiable images or data included in this article.

Author contributions

PY, JY, YH, and DP contributed to the design and operation of the study. HG and ZF were in charge of data collection. DP and HG collected follow-up information specifically. DP contributed to the graphics and statistical analysis. All authors contributed to the article and approved the submitted version.

Acknowledgments

The authors thank AiMi Academic Services (www.aimieditor.com) for English language editing and review services.

Conflict of interest

The authors declare that the research was conducted in the absence of any commercial or financial relationships that could be construed as a potential conflict of interest.

Publisher's note

All claims expressed in this article are solely those of the authors and do not necessarily represent those of their affiliated organizations, or those of the publisher, the editors and the reviewers. Any product that may be evaluated in this article, or claim that may be made by its manufacturer, is not guaranteed or endorsed by the publisher.

References

1. Farrokhi MR, Yadollahikhales G, Gholami M, Mousavi SR, Mesbahi AR, Asadi-Pooya AA. Clinical outcomes of posterolateral fusion vs. Posterior lumbar interbody fusion in patients with lumbar spinal stenosis and degenerative instability. *Pain Phy.* (2018) 21:383–406. doi: 10.36076/ppj.2018.4.383.

2. Cole AA. Fusion for lumbar spinal stenosis? *BMJ.* (2016) 353:i3145. doi: 10.1136/bmj.i3145.

3. Fan SW, Hu ZJ, Fang XQ, Zhao FD, Huang Y, Yu HJ. Comparison of paraspinal muscle injury in one-level lumbar posterior inter-body fusion: modified minimally invasive and traditional open approaches. *Orthop Surg.* (2010) 2:194–200. doi: 10.1111/j.1757-7861.2010.00086.x.

4. Freeman MD, Woodham MA, Woodham AW. The role of the lumbar multifidus in chronic low back pain: a review. *PM R.* (2010) 2:142–6, 1-167. doi: 10.1016/j.pmrj.2009.11.006.

5. Lee JC, Cha JG, Kim Y, Kim YI, Shin BJ. Quantitative analysis of back muscle degeneration in the patients with the degenerative lumbar flat back using a digital image analysis: comparison with the normal controls. *Spine (Phila Pa 1976)*. (2008) 33:318–25. doi: 10.1097/BRS.0b013e318162458f.

6. Shafaq N, Suzuki A, Matsumura A, Terai H, Toyoda H, Yasuda H, et al. Asymmetric degeneration of paravertebral muscles in patients with degenerative lumbar scoliosis. *Spine (Phila Pa 1976)*. (2012) 37:1398–406. doi: 10.1097/BRS.0b013e31824c767e.

7. Sihvonen T, Herno A, Paljärvi L, Airaksinen O, Partanen J, Tapaninaho A. Local denervation atrophy of paraspinal muscles in postoperative failed back syndrome. *Spine (Phila Pa 1976)*. (1993) 18:575–81. doi: 10.1097/00007632-199304000-00009.

8. Cho SM, Kim SH, Ha SK, Kim SD, Lim DJ, Cha J, et al. Paraspinal muscle changes after single-level posterior lumbar fusion: volumetric analyses and literature review. *BMC Musculoskelet Disord*. (2020) 21:73. doi: 10.1186/s12891-020-3104-0.

9. Schwender JD, Holly LT, Rouben DP, Foley KT. Minimally invasive transforaminal lumbar interbody fusion (TLIF): technical feasibility and initial results. *J Spinal Disord Tech*. (2005) 18(Suppl):S1–6. doi: 10.1097/01.bsd.0000132291.50455.d0.

10. Foley KT, Lefkowitz MA. Advances in minimally invasive spine surgery. *Clin Neurosurg*. (2002) 49:499–517.

11. Yang J, Liu C, Hai Y, Yin P, Zhou L, Zhang Y, et al. Percutaneous endoscopic transforaminal lumbar interbody fusion for the treatment of lumbar spinal stenosis: preliminary report of seven cases with 12-month follow-up. *Biomed Res Int*. (2019) 2019:3091459. doi: 10.1155/2019/3091459.

12. Yin P, Gao H, Zhou L, Pang D, Hai Y, Yang J. Enhanced recovery after an innovative percutaneous endoscopic transforaminal lumbar interbody fusion for the treatment of lumbar spinal stenosis: a prospective observational study. *Pain Res Manag*. (2021) 2021:7921662. doi: 10.1155/2021/7921662.

13. Yoo JS, Min SH, Yoon SH, Hwang CH. Paraspinal muscle changes of unilateral multilevel minimally invasive transforaminal interbody fusion. *J Orthop Surg Res*. (2014) 9:130. doi: 10.1186/s13018-014-0130-3.

14. Crawford RJ, Cornwall J, Abbott R, Elliott JM. Manually defining regions of interest when quantifying paravertebral muscles fatty infiltration from axial magnetic resonance imaging: a proposed method for the lumbar spine with anatomical cross-reference. *BMC Musculoskelet Disord*. (2017) 18:25. doi: 10.1186/s12891-016-1378-z.

15. Pathria M, Sartoris DJ, Resnick D. Osteoarthritis of the facet joints: accuracy of oblique radiographic assessment. *Radiol*. (1987) 164:227–30. doi: 10.1148/radiology.164.1.3588910.

16. Bridwell KH, Lenke LG, McEnery KW, Baldus C, Blanke K. Anterior fresh frozen structural allografts in the thoracic and lumbar spine. Do they work if combined with posterior fusion and instrumentation in adult patients with kyphosis or anterior column defects? *Spine (Phila Pa 1976)*. (1995) 20:1410–8. doi: 10.1097/00007632-199506020-00014.

17. Tsutsumimoto T, Shimogata M, Ohta H, Misawa H. Mini-open versus conventional open posterior lumbar interbody fusion for the treatment of lumbar degenerative spondylolisthesis: comparison of paraspinal muscle damage and slip reduction. *Spine (Phila Pa 1976)*. (2009) 34:1923–8. doi: 10.1097/BRS.0b013e3181a9d28e.

18. Hultman G, Nordin M, Saraste H, Ohlsèn H. Body composition, endurance, strength, cross-sectional area, and density of MM erector spinae in men with and without low back pain. *J Spinal Disord*. (1993) 6:114–23. doi: 10.1097/00002517-199304000-00004.

19. Barker KL, Shamley DR, Jackson D. Changes in the cross-sectional area of multifidus and psoas in patients with unilateral back pain: the relationship to pain and disability. *Spine (Phila Pa 1976)*. (2004) 29:E515–9. doi: 10.1097/01.brs.0000144405.11661.eb.

20. Hansen L, de Zee M, Rasmussen J, Andersen TB, Wong C, Simonsen EB. Anatomy and biomechanics of the back muscles in the lumbar spine with reference to biomechanical modeling. *Spine (Phila Pa 1976)*. (2006) 31:1888–99. doi: 10.1097/01.brs.0000229232.66090.58.

21. Tsutsumimoto T, Shimogata M, Ohta H, Misawa H. Mini-open versus conventional open posterior lumbar interbody fusion for the treatment of lumbar degenerative spondylolisthesis: comparison of paraspinal muscle damage and slip reduction. *Spine (Phila Pa 1976)*. (2009) 34:1923–8. doi: 10.1097/BRS.0b013e3181a9d28e.

22. Regev GJ, Lee YP, Taylor WR, Garfin SR, Kim CW. Nerve injury to the posterior rami medial branch during the insertion of pedicle screws: comparison of mini-open versus percutaneous pedicle screw insertion techniques. *Spine (Phila Pa 1976)*. (2009) 34:1239–42. doi: 10.1097/BRS.0b013e31819e2c5c.

23. Fan SW, Hu ZJ, Fang XQ, Zhao FD, Huang Y, Yu HJ. Comparison of paraspinal muscle injury in one-level lumbar posterior inter-body fusion: modified minimally invasive and traditional open approaches. *Orthop Surg*. (2010) 2:194–200. doi: 10.1111/j.1757-7861.2010.00086.x.

24. Kameyama K, Ohba T, Endo T, Katsu M, Koji F, Kensuke K, et al. Radiological assessment of postoperative paraspinal muscle changes after lumbar interbody fusion with or without minimally invasive techniques. *Global Spine J*. (2021):302288682. doi: 10.1177/2192568221994794.

25. Kang CH, Shin MJ, Kim SM, Lee SH, Lee CS. MRI Of paraspinal muscles in lumbar degenerative kyphosis patients and control patients with chronic low back pain. *Clin Radiol*. (2007) 62:479–86. doi: 10.1016/j.crad.2006.12.002.

26. Hu ZJ, He J, Zhao FD, Fang XQ, Zhou LN, Fan SW. An assessment of the intra- and inter-reliability of the lumbar paraspinal muscle parameters using CT scan and magnetic resonance imaging. *Spine (Phila Pa 1976)*. (2011) 36:E868–74. doi: 10.1097/BRS.0b013e3181ef6b51.

27. He W, He D, Sun Y, Xing Y, Liu M, Wen J, et al. Quantitative analysis of paraspinal muscle atrophy after oblique lateral interbody fusion alone vs. Combined with percutaneous pedicle screw fixation in patients with spondylolisthesis. *BMC Musculoskelet Disord*. (2020) 21:30. doi: 10.1186/s12891-020-3051-9.

28. Fan SW, Hu ZJ, Fang XQ, Zhao FD, Huang Y, Yu HJ. Comparison of paraspinal muscle injury in one-level lumbar posterior inter-body fusion: modified minimally invasive and traditional open approaches. *Orthop Surg*. (2010) 2:194–200. doi: 10.1111/j.1757-7861.2010.00086.x.

29. Zhu HF, Wang GL, Zhou ZJ, Fan SW. Prospective study of long-term effect between multifidus muscle bundle and conventional open approach in one-level posterior lumbar interbody fusion. *Orthop Surg*. (2018) 10:296–305. doi: 10.1111/os.12402.

frontiers | Frontiers in Surgery

TYPE Brief Research Report
PUBLISHED 30 November 2022
DOI 10.3389/fsurg.2022.1011432

Check for updates

OPEN ACCESS

EDITED BY
Yan Yu,
Tongji University School of Medicine, China

REVIEWED BY
Suk Kyoon Song,
Catholic University of Daegu, South Korea
Rongshan Cheng,
Shanghai Jiao Tong University, China

*CORRESPONDENCE
Yoon Hyuk Kim,
yoonhkim@khu.ac.kr

†These authors have contributed equally to this work and share first authorship

SPECIALTY SECTION
This article was submitted to Orthopedic Surgery, a section of the journal Frontiers in Surgery

RECEIVED 04 August 2022
ACCEPTED 03 November 2022
PUBLISHED 30 November 2022

CITATION
Kim K, Wei R and Kim YH (2022) Reliability in measurement of three-dimensional anterior pelvic plane orientation by registration with an inertial measurement unit.
Front. Surg. 9:1011432.
doi: 10.3389/fsurg.2022.1011432

COPYRIGHT
© 2022 Kim, Wei and Kim. This is an open-access article distributed under the terms of the Creative Commons Attribution License (CC BY). The use, distribution or reproduction in other forums is permitted, provided the original author(s) and the copyright owner(s) are credited and that the original publication in this journal is cited, in accordance with accepted academic practice. No use, distribution or reproduction is permitted which does not comply with these terms.

Reliability in measurement of three-dimensional anterior pelvic plane orientation by registration with an inertial measurement unit

Kyungsoo Kim[1†], Ruoyu Wei[2†] and Yoon Hyuk Kim[2,3*]

[1]Department of Applied Mathematics, Kyung Hee University, Yongin, South Korea, [2]Department of Mechanical Engineering, Kyung Hee University, Yongin, South Korea, [3]Integrated Education Institute for Frontier Science and Technology (BK21 Four), Kyung Hee University, Yongin, South Korea

It is strongly challenging to obtain functional movement of the pelvis based on the three-dimensional (3D) dynamic anterior pelvic plane (APP) orientation information. This study provided the 3D APP orientation measurement technique by registration with an inertial measurement unit (IMU), and its reliability was tested. The local coordinate systems of the APP and the IMU sensor were registered using two images of the pelvic part from the frontal and left sagittal views in a neutral standing posture. Then, the measurement errors in the APP orientation were analyzed by comparing the values obtained from manually measured four points in the IMU sensor and the known exact values in 10 different postures. Moreover, the errors between values obtained from manually measured three anatomical points and the known exact values were also compared. The average errors were quite small (less than 0.6°) when measuring from three anatomical points and were acceptable (1.6°–3.4°) when measuring from four points in the IMU sensor. These results indicate that the measurement of APP direction using four points in the IMU sensor could be considered reliable in terms of intra-participant and inter-participant. The present technique to register the IMU sensor position and the APP direction by taking X-ray images from the frontal and sagittal directions can be fundamental information to measure the APP direction during dynamic motion when the IMU position is obtained from the IMU sensor data instead of the four-point location information.

KEYWORDS

anterior pelvic plane, orientation, inertial measurement units, registration, hip

Introduction

Total hip arthroplasty (THA) is a highly successful surgical intervention to restore the hip joint function and relieve pain in patients with symptomatic end-stage osteoarthritis (OA) of the hip (1). THA is also the primary treatment method for femoral neck fracture and osteonecrosis of femoral head (1). The anterior pelvic plane (APP) formed by the bilateral anterior superior iliac spines and the upper margin of the pubic symphysis was regarded as an anatomical reference for the navigation

system during THA (2, 3). The pelvic tilt (PT) was defined as the angle of the APP relative to a vertical axis, and many reports denoted a certain relationship between PT and acetabular anteversion and lumbar back deformity (4, 5).

Several useful radiological-imaging techniques have been reported to obtain the APP orientation (6–12). Radiological imaging was limited to a certain posture and it merely provided the frontal and sagittal views (6–10). The computed tomography and ultrasound device can provide a three-dimensional (3D) reconstruction of the pelvic bony model to analyze the normal direction of the APP plane, but these methods easily led to APP orientation errors because of soft-tissue thickness (6–10). The EOS imaging system can provide a high-quality image and is reliable for assessing the APP orientation with lower radiation (11, 12). However, it can only provide a static posture and is also difficult to maintain in proper position while taking measurements. Therefore, a 3D pelvis-motion measurement system will be useful in clinical fields since it can resolve certain weaknesses in previous technologies.

Recently, inertial measurement units (IMUs) have been widely utilized in clinical and rehabilitation settings. The IMU is a small electric device that measures velocity and acceleration, angular velocity and acceleration, and orientation of the body using accelerometers, gyroscopes, and/or magnetometers (13–17). Functional movement of the lumbar spine was measured with the IMUs for assessment of movement-related disorders (13). The IMU-based wearable device has been used for measuring spinal shape and posture (14–16) and performing sport motion analysis (17). Moreover, the PT was analyzed using one IMU sensor (18, 19). However, it is strongly challenging to obtain functional movement of the 3D dynamic APP orientation information. This study provided the 3D APP orientation measurement technique by registration with an IMU, and its reliability was tested.

Materials and methods

The 3D orientation of APP can be represented by two linearly independent vectors: a normal vector to APP and a vector included in the APP (20). The following procedure aims to find two vectors to represent the APP from the position information of the IMU sensor.

The local coordinate system for the IMU sensor can be defined by four points (end points of the horizontal and vertical bars attached to the IMU sensor), while the local coordinate system for the APP can be defined by three points (two anterior superior iliac spine points and a marginal point on the pubic tubercles). Two images of the pelvic part from the frontal and left sagittal views in a neutral standing posture were used to register the local coordinate systems of the APP and the IMU sensor (**Figure 1A**). The two images were obtained by virtually projecting a 3D pelvic bony model with the IMU sensor from the frontal and left sagittal views, where the 3D pelvic model was developed in our previous study (21). Those images included the four points (P_1, P_2, P_3, and P_4) from the IMU sensor and the three points (P_5, P_6, and P_7) from the APP. Here, P_1 and P_2 were the top and bottom end points of the vertical bar, and P_3 and P_4 were the left and right end points of the horizontal bar. P_5 and P_7 were the left and right anterior superior iliac spine points, and P_6 was the marginal point on the pubic tubercles. The x-, y-, and z-axes in the global coordinate system were from left to right, from back to front, and from bottom to top, respectively.

In the frontal and left sagittal figures, the top left corner points were set as the origins O_F and O_S. Next, the horizontal and vertical distances in pixel from O_F to P_i $(1 \le i \le 7)$ were defined by $\mathrm{NF}_{i,1}$ and $\mathrm{NF}_{i,2}$. Similarly, the horizontal and vertical distances in pixel from O_S to P_i $(1 \le i \le 7)$ were $\mathrm{NS}_{i,1}$ and $\mathrm{NS}_{i,2}$.

Let us define $v_1 = \overrightarrow{P_2P_1}$ and $v_2 = \overrightarrow{P_3P_4}$ for the local coordinate system of the IMU sensor and $v_3 = \overrightarrow{P_5P_7}$ and $v_4 = \overrightarrow{P_5P_6}$ for the local coordinate system of the APP. However, the scales of the frontal and left sagittal figures may not match. Since the real distance of P_1 and P_2 in the z-direction in each figure should be the same, $\mathrm{UF} = \mathrm{NF}_{2,2} - \mathrm{NF}_{1,2}$ and $\mathrm{US} = \mathrm{NS}_{2,2} - \mathrm{NS}_{1,2}$ represented the same length. By assuming the UF and US as a unit length in each figure, the vector $\overrightarrow{P_iP_j}$ can be obtained with $\mathrm{NF}_{i,1}$, $\mathrm{NF}_{i,2}$, $\mathrm{NS}_{i,1}$, and $\mathrm{NS}_{i,2}$ $(1 \le i \le 7)$ as

$$\overrightarrow{P_iP_j} = \left[\frac{\mathrm{NF}_{i,1} - \mathrm{NF}_{j,1}}{\mathrm{UF}}, \frac{\mathrm{NS}_{i,1} - \mathrm{NS}_{j,1}}{\mathrm{US}}, \frac{1}{2}\left(\frac{\mathrm{NF}_{i,2} - \mathrm{NF}_{j,2}}{\mathrm{UF}} + \frac{\mathrm{NS}_{i,2} - \mathrm{NS}_{j,2}}{\mathrm{US}}\right)\right]$$

where the x-component and y-component are normalized by the UF and US, respectively, and the z-component is the mean of z-components normalized by the UF and US. Then, $v_1 = \overrightarrow{P_2P_1}$, $v_2 = \overrightarrow{P_3P_4}$, $v_3 = \overrightarrow{P_5P_7}$, and $v_4 = \overrightarrow{P_5P_6}$ are represented by

$$v_1 = \overrightarrow{P_2P_1} = \left[\frac{\mathrm{NF}_{2,1} - \mathrm{NF}_{1,1}}{\mathrm{UF}}, \frac{\mathrm{NS}_{2,1} - \mathrm{NS}_{1,1}}{\mathrm{US}}, \frac{1}{2}\left(\frac{\mathrm{NF}_{2,2} - \mathrm{NF}_{1,2}}{\mathrm{UF}} + \frac{\mathrm{NS}_{2,2} - \mathrm{NS}_{1,2}}{\mathrm{US}}\right)\right]$$

$$v_2 = \overrightarrow{P_3P_4} = \left[\frac{\mathrm{NF}_{3,1} - \mathrm{NF}_{4,1}}{\mathrm{UF}}, \frac{\mathrm{NS}_{3,1} - \mathrm{NS}_{4,1}}{\mathrm{US}}, \frac{1}{2}\left(\frac{\mathrm{NF}_{3,2} - \mathrm{NF}_{4,2}}{\mathrm{UF}} + \frac{\mathrm{NS}_{3,2} - \mathrm{NS}_{4,2}}{\mathrm{US}}\right)\right]$$

$$v_3 = \overrightarrow{P_5P_7} = \left[\frac{\mathrm{NF}_{5,1} - \mathrm{NF}_{7,1}}{\mathrm{UF}}, \frac{\mathrm{NS}_{5,1} - \mathrm{NS}_{7,1}}{\mathrm{US}}, \frac{1}{2}\left(\frac{\mathrm{NF}_{5,2} - \mathrm{NF}_{7,2}}{\mathrm{UF}} + \frac{\mathrm{NS}_{5,2} - \mathrm{NS}_{7,2}}{\mathrm{US}}\right)\right]$$

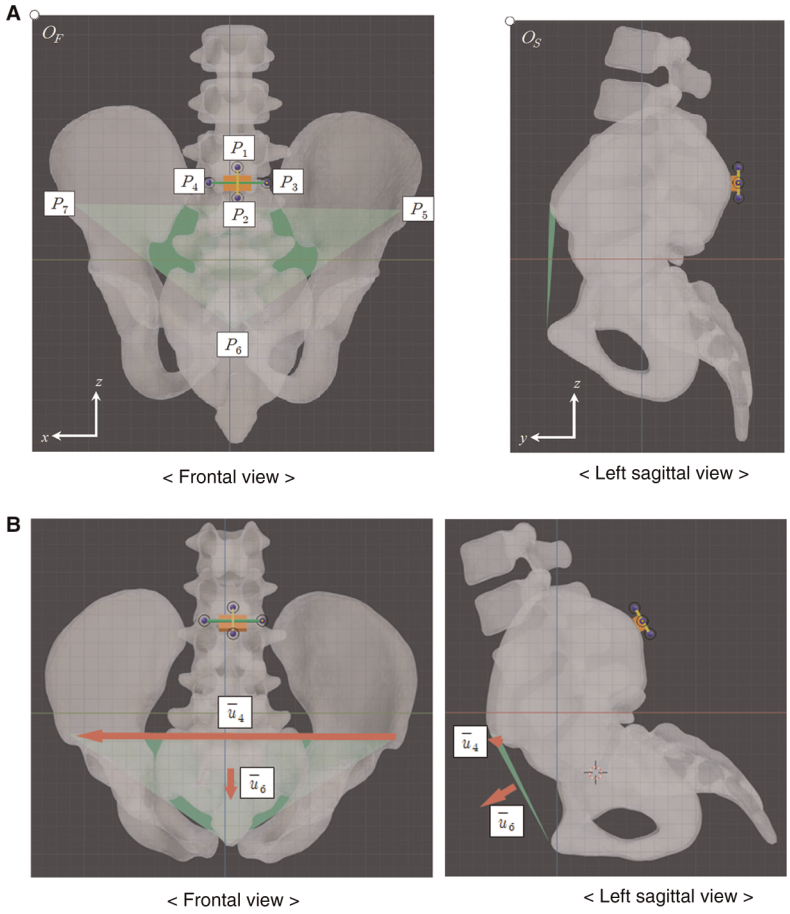

FIGURE 1
Frontal and left sagittal images of pelvic model, including the IMU sensor and the APP. (A) Neutral standing posture. (B) Flexion 30° posture.

$$v_4 = \overrightarrow{P_5P_6} = \left[\frac{NF_{5,1} - NF_{6,1}}{UF}, \frac{NS_{5,1} - NS_{6,1}}{US}, \frac{1}{2}\left(\frac{NF_{5,2} - NF_{6,2}}{UF} + \frac{NS_{5,2} - NS_{6,2}}{US}\right)\right]$$

Three unit vectors, $u_1 = v_1/||v_1||$, $u_2 = v_2/||v_2||$, and $u_3 = u_1 \times u_2$, construct an orthonormal basis for the local coordinate system of the IMU sensor. Let the 3×3 matrix U_0 be $U_0 = [u_1 : u_2 : u_3]$. Moreover, another three unit vectors, $u_4 = v_3/||v_3||$, $u_5 = v_4/||v_4||$, and $u_6 = u_4 \times u_5$, represent the APP orientation, where u_6 is the normal vector to the APP, and u_4 is a vector included in the APP from left to right anatomical points. Two vectors, u_6 and u_4, are used as reference unit vectors to estimate the APP orientation in other postures.

To geometrically understand u_6 and u_4, the latitude and longitude concepts are introduced. The latitude θ_{Lat} of a vector is defined as an angle between the vector and the xy-plane, where the $+z$ direction is +90° and the $-z$ direction is −90°. The longitude θ_{Long} of a vector is defined as an angle between the vector and zx-plane, where the x-direction is 0° and the y direction is 90° (Figure 2).

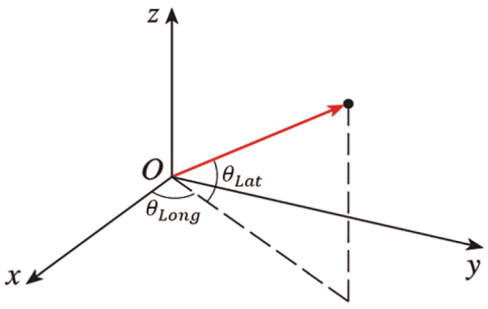

FIGURE 2
Definition of the latitude and longitude of a vector.

In an arbitrary posture, the normal vector to the APP and the vector from the left to right anatomical points can be estimated when frontal and left sagittal figures are given, only including the four end points in bars attached to the IMU sensor. Let the four points be $\bar{P}_1$, $\bar{P}_2$, $\bar{P}_3$, and $\bar{P}_4$. As in the neutral standing

posture, three unit vectors, $\bar{u}_1$, $\bar{u}_2$, and $\bar{u}_3$, can be obtained and construct an orthonormal basis for the local coordinate system of the IMU sensor in an arbitrary posture. Let the 3×3 matrix U be $U = [\bar{u}_1 : \bar{u}_2 : \bar{u}_3]$. Under the assumption that the IMU sensor and the APP were attached to the pelvis, the normal vector to the APP $\bar{u}_6$ and the vector from left to right anatomical point $\bar{u}_4$ in the arbitrary posture can be estimated as $\bar{u}_6 = UU_0^{-1}u_6$ and $\bar{u}_4 = UU_0^{-1}u_4$ (Figure 1B). Let α_{Lat} and α_{Long} be the latitude and longitude of $\bar{u}_6$, and β_{Lat}, and β_{Long} be the latitude and longitude of $\bar{u}_4$.

Two vectors, $\bar{u}_6$ and $\bar{u}_4$, also can be obtained using $\bar{P}_5$, $\bar{P}_6$, and $\bar{P}_7$, which are three anatomical points in the arbitrary posture. Two calculation methods should result in the same vectors based on the fundamental linear algebra. However, there may be measurement errors when obtaining P_i and $\bar{P}_i$ $(1 \leq i \leq 7)$ since the pixel values of points are manually measured.

To investigate the reliability in measuring the 3D APP orientation only using positional information from one IMU sensor, 10 volunteers (26.1 ± 3.5 years old, visual acuity 0.86 ± 0.45) participated in the test experiment with the written informed consent. An Android tablet (Samsung Galaxy Tab S3 9.7, Korea) was used to collect point data and touch pencil was used to mark the four points in the IMU sensors and the three anatomical points (Figure 3). Each participant clicked seven points on frontal and left sagittal images from eleven different image sets and repeated the experiment five times with randomly reordered image sets.

FIGURE 3
Android tablet/pencil used in the experiment.

The 11 image sets were obtained using the 3D pelvic bony model: (1) neutral standing posture, (2) flexion 15°, (3) extension 15°, (4) extension 30°, (5) right rotation 15°, (6) right rotation 30°, (7) left bending 15°, (8) left bending 30°, (9) extension 15° and right rotation 15°, (10) right rotation 15° and left bending 15°, and (11) extension 15° and right bending 15°. First, the 3D pelvic bony model (21) with the IMU sensor was set to the given posture among the 11 postures using commercial CAD software. The images were then taken by projecting the 3D model from frontal and left sagittal views. Thus, the exact values of α_{Lat}, α_{Long}, β_{Lat}, and β_{Long} in a given posture were known. Then, the measurement errors in α_{Lat}, α_{Long}, β_{Lat}, and β_{Long} were analyzed by comparing the values obtained from manually measured four points in the IMU sensor and the known exact values. Moreover, the errors between values obtained from manually measured three anatomical points and the known exact values were also compared. The average errors of all participants' results from five trials were analyzed. The interclass correlation coefficients (ICCs) among 10 participants for α_{Lat}, α_{Long}, β_{Lat}, and β_{Long} were investigated in each measurement cases, using four points in the IMU sensor and using three anatomical points.

Results

Table 1 shows the average and standard deviation (SD) of errors in α_{Lat}, α_{Long}, β_{Lat}, and β_{Long} of 11 image sets for each participant when the error was calculated from three anatomical points. Additionally, the average ± SD of 10

TABLE 1 Errors from manually measured three anatomical points (unit: °).

Participant	Error in α_{Lat}		Error in α_{Long}		Error in β_{Lat}		Error in β_{Long}	
	Average	SD	Average	SD	Average	SD	Average	SD
1	0.3	0.2	0.3	0.3	0.2	0.1	0.3	0.4
2	0.8	0.4	0.8	0.6	0.4	0.3	0.7	0.6
3	0.7	0.5	0.5	0.4	0.3	0.2	0.5	0.4
4	0.7	0.3	0.7	0.7	0.3	0.3	0.7	0.7
5	0.5	0.3	0.5	0.4	0.3	0.3	0.4	0.4
6	0.7	0.4	0.7	0.8	0.5	0.5	0.6	0.8
7	0.5	0.2	0.4	0.5	0.3	0.2	0.4	0.5
8	0.7	0.3	0.5	0.4	0.3	0.2	0.5	0.4
9	0.6	0.2	0.4	0.3	0.2	0.1	0.4	0.3
10	0.4	0.1	0.3	0.3	0.2	0.1	0.3	0.3
Average ± SD	0.6 ± 0.2	0.3 ± 0.1	0.5 ± 0.2	0.5 ± 0.2	0.3 ± 0.1	0.2 ± 0.1	0.5 ± 0.2	0.5 ± 0.2

TABLE 2 Errors from manually measured four points in the IMU sensor (unit: °).

Participant	Error in α_{Lat}		Error in α_{Long}		Error in β_{Lat}		Error in β_{Long}	
	Average	SD	Average	SD	Average	SD	Average	SD
1	3.3	0.6	1.0	0.6	1.3	0.3	1.2	0.7
2	3.7	1.4	3.1	2.0	1.6	0.7	3.0	1.6
3	3.3	0.3	1.7	1.0	1.7	1.0	1.9	1.1
4	3.8	1.0	3.2	1.4	2.2	1.1	3.2	1.8
5	3.3	0.9	1.9	1.0	1.7	0.6	1.9	1.0
6	4.0	1.6	3.8	1.4	2.5	0.7	3.7	1.7
7	3.0	0.8	1.4	1.1	1.3	0.4	1.7	0.9
8	3.6	1.2	1.6	0.7	1.6	0.5	1.6	0.7
9	3.3	0.7	1.2	0.7	1.1	0.3	1.4	0.6
10	3.1	0.5	1.2	1.0	1.4	0.4	1.6	0.8
Average ± SD	3.4 ± 0.3	0.9 ± 0.4	2.0 ± 1.0	1.1 ± 0.4	1.6 ± 0.4	0.6 ± 0.2	2.1 ± 0.8	1.1 ± 0.4

averages were provided as 0.6° ± 0.2°, 0.5° ± 0.2°, 0.3° ± 0.1°, and 0.5° ± 0.2°, while the average ± SD of 10 SDs were 0.3° ± 0.1°, 0.5° ± 0.2°, 0.2° ± 0.1°, and 0.5° ± 0.2° in α_{Lat}, α_{Long}, β_{Lat}, and β_{Long}. All averages and SDs were less than 1°. The ICCs among 10 participants for α_{Lat}, α_{Long}, β_{Lat}, and β_{Long} were 0.9954, 0.9058, 0.9967, and 0.9979, respectively.

Table 2 shows the average and SD of errors in α_{Lat}, α_{Long}, β_{Lat}, and β_{Long} of 11 image sets for each participant when using four points in the IMU sensor. The average ± SD of 10 averages were also presented as 3.4° ± 0.3°, 2.0° ± 1.0°, 1.6° ± 0.4°, and 2.1° ± 0.8°, while the average ± SD of 10 SDs were 0.9° ± 0.4°, 1.1° ± 0.4°, 0.6° ± 0.2°, and 1.1° ± 0.4° in α_{Lat}, α_{Long}, β_{Lat}, and β_{Long}. The maximum average and SD of errors were 4.0° in α_{Lat} for participant 6 and 2.0° in α_{Long} for participant 2. The ICCs among 10 participants for α_{Lat}, α_{Long}, β_{Lat}, and β_{Long} were 0.9933, 0.9668, 0.9933, and 0.9671, respectively.

Discussion

In measuring from three anatomical points, the average errors in α_{Lat}, α_{Long}, β_{Lat}, and β_{Long} were quite small (less than 0.6°). The SDs for the image set and the participant, which were related to the variability according to the image set and the participant, were also very small (less than 0.3° and 0.5°). Moreover, the ICCs for four angles were greater than 0.9. These results indicate that the measurement of the APP direction using three anatomical points could be considered accurate; thus, it can be used as the true value of APP direction due to the difficulty in the direct measurement of the APP direction in a common clinical setting.

In measuring from four points in the IMU sensor, the average errors in α_{Lat}, α_{Long}, β_{Lat}, and β_{Long} were acceptable (1.6°–3.4°) in comparison with errors or variations (2°–10°) provided in previous studies (2, 19, 22). Lewinnek et al. proposed 10° of margin in inclination and an anteversion of cup position in THA as a safe zone (2). Wang et al. demonstrated seventy-five percent of the errors across all measurements were within 5° of the radiograph measurements (19). Kalteis et al. showed that the precision of acetabular cup inclination and anteversion were 3° and 10° with plain X-rays, while those were approximately 2° with CT-scan (22). In addition, the SDs for the image set and the participant, which were related to the variability according to the image set and the participant, were also very small (less than 1.4° and 1.1°). Similar to the measurement from three anatomical points, the ICCs for four angles were greater than 0.9. These results also indicate that the measurement of APP direction using four points in the IMU sensor could be considered reliable in terms of intra-participant and inter-participant.

The technique presented in this study, the registration of the IMU sensor position and the APP direction determined from three anatomical points and four IMU points by taking X-ray images from the frontal and sagittal directions, can be applied to measure the APP direction during dynamic motion when the IMU position is obtained from the IMU sensor data instead of the four-point location information. In future study, the registration of the IMU position from four points and the IMU position data from the three inside sensors (accelerometers, gyroscopes, and magnetometer) can be completely obtained by calculating the orthonormal matrix from the local coordinate system in the IMU sensor position to that in the IMU sensor data. Then, the APP direction can be predicted from the IMU sensor data.

There were limitations in this study. Various anatomical and biomechanical factors, which could generate additional error such as the soft tissue tension, contracture, and skin movement as well as the body mass index and pelvic deformation, should be considered in order to enhance the clinical relevance. In addition, more participants can improve statistical confidence since the sample size of study (10 participants) was relatively small.

Conclusion

This study provided the 3D APP orientation measurement technique by registration with an IMU, and its reliability was tested. The measurement errors in the APP orientation were analyzed by comparing the values obtained from manually measured four points in the IMU sensor and the known exact values in different postures. Moreover, the errors between values obtained from manually measured three anatomical points and the known exact values were also compared. The average errors were quite small when measuring from three anatomical points and were acceptable when measuring from four points in the IMU sensor. The ICCs among participants were greater than 0.9 in both measurements. These results indicate that the measurement of APP direction using four points in the IMU sensor could be considered reliable in terms of intra-participant and inter-participant. The present technique to register the IMU sensor position and the APP direction by taking X-ray images from the frontal and sagittal directions can be fundamental information to measure the APP direction during dynamic motion when the IMU position is obtained from the IMU sensor data instead of the four-point location information.

Data availability statement

The raw data supporting the conclusions of this article will be made available by the authors, without undue reservation.

Author contributions

KK and YK contributed to conception and design and RW contributed to acquisition of data. KK, RW, and YK performed analysis and interpretation of data. All authors contributed to the article and approved the submitted version.

Funding

This work was supported by the National Research Foundation of Korea (NRF) grants funded by the Korea government (MSIP) (NRF-2017R1A2B1010492 and NRF-2021R1A2C1011825).

Conflict of interest

The authors declare that the research was conducted in the absence of any commercial or financial relationships that could be construed as a potential conflict of interest.

Publisher's note

All claims expressed in this article are solely those of the authors and do not necessarily represent those of their affiliated organizations, or those of the publisher, the editors and the reviewers. Any product that may be evaluated in this article, or claim that may be made by its manufacturer, is not guaranteed or endorsed by the publisher.

References

1. Ferguson RJ, Palmer AJ, Taylor A, Porter ML, Malchau H, Glyn-Jones S. Hip replacement. *Lancet*. (2018) 392(10158):1662–71. doi: 10.1016/S0140-6736(18)31777-X

2. Lewinnek GE, Lewis JL, Tarr R, Compere CL, Zimmerman JR. Dislocations after total hip-replacement arthroplasties. *J Bone Joint Surg Am*. (1978) 60(2):217–20. doi: 10.2106/00004623-197860020-00014

3. Blondel B, Parratte S, Tropiano P, Pauly V, Aubaniac JM, Argenson JN. Pelvic tilt measurement before and after total hip arthroplasty. *Orthop Traumatol Surg Res*. (2009) 95(8):568–72. doi: 10.1016/j.otsr.2009.08.004

4. Roussouly P, Pinheiro-Franco JL. Biomechanical analysis of the spino-pelvic organization and adaptation in pathology. *Eur Spine J*. (2011) 20(Supp 5):609–18. doi: 10.1007/s00586-011-1928-x

5. Yang G, Li Y, Zhang H. The influence of pelvic tilt on the anteversion angle of the acetabular prosthesis. *Orthop Surg*. (2019) 11(5):762–9. doi: 10.1111/os.12543

6. DiGioia AM, Hafez MA, Jaramaz B, Levison TJ, Moody JE. Functional pelvic orientation measured from lateral standing and sitting radiographs. *Clin Orthop Relat Res*. (2006) 453:272–6. doi: 10.1097/01.blo.0000238862.92356.45

7. Nishihara S, Sugano N, Nishii T, Ohzono K, Yoshikawa H. Measurements of pelvic flexion angle using three-dimensional computed tomography. *Clin Orthop Relat Res*. (2003) 411:140–51. doi: 10.1097/01.blo.0000069891.31220.fd

8. Lee YS, Yoon TR. Error in acetabular socket alignment due to the thick anterior pelvic soft tissues. *J Arthroplasty*. (2008) 23(5):699–706. doi: 10.1016/j.arth.2007.06.012

9. Babisch JW, Layher F, Amiot LP. The rationale for tilt adjusted acetabular cup navigation. *J Bone Joint Surg Am*. (2008) 90(2):357–65. doi: 10.2106/JBJS.F.00628

10. Fritz B, Agten CA, Boldt FK, Zingg PO, Pfirrmann CWA, Sutter R. Acetabular coverage differs between standing and supine positions: model-based assessment of low-dose biplanar radiographs and comparison with CT. *Eur Radiol*. (2019) 29(10):5691–9. doi: 10.1007/s00330-019-06136-5

11. Lazennec JY, Rousseau MA, Rangel A, Gorin M, Belicourt C, Brusson A, et al. Pelvis and total hip arthroplasty acetabular component orientations in sitting and standing positions: measurements reproductibility with EOS imaging system versus conventional radiographies. *Orthop Traumatol Surg Res*. (2011) 97(4):373–80. doi: 10.1016/j.otsr.2011.02.006

12. Thelen T, Thelen P, Demezon H, Aunoble S, Le Huec J-C. Normative 3D acetabular orientation measurements by the low-dose EOS imaging system in 102 asymptomatic subjects in standing position: analyses by side, gender, pelvic incidence and reproducibility. *Orthop Traumatol Surg Res*. (2017) 103(2):209–15. doi: 10.1016/j.otsr.2016.11.010

13. Beangea KHE, Chan ADC, Beaudette SM, Graham RB. Concurrent validity of a wearable IMU for objective assessments of functional movement quality and

control of the lumbar spine. *J Biomech*. (2019) 97(3):109356. doi: 10.1016/j.jbiomech.2019.109356

14. Wong WY, Wong MS. Trunk posture monitoring with inertial sensors. *Eur Spine J*. (2008) 17(5):743–53. doi: 10.1007/s00586-008-0586-0

15. Voinea G-D, Butnariu S, Mogan G. Measurement and geometric modelling of human spine posture for medical rehabilitation purposes using a wearable monitoring system based on inertial sensors. *Sensors*. (2016) 17(1):3. doi: 10.3390/s17010003

16. Stollenwerk K, Müller J, Hinkenjann A, Krüger B. Analyzing spinal shape changes during posture training using a wearable device. *Sensors*. (2019) 19 (16):3625. doi: 10.3390/s19163625

17. Khuyagbaatar B, Purevsuren T, Kim YH. Kinematic determinants of performance parameters during golf swing. *Proc Inst Mech Eng H*. (2019) 233 (5):554–61. doi: 10.1177/0954411919838643

18. Wada T, Nagahara R, Gleadhill S, Ishizuka T, Ohnuma H, Ohgi Y. Measurement of pelvic orientation angles during sprinting using a single inertial sensor. *Proc AMIA Annu Fall Symp*. (2020) 49:10. doi: 10.3390/proceedings2020049010

19. Wang X, Qureshi A, Vepa A, Rahman U, Palit A, Williams MA, et al. A sensor-based screening tool for identifying high pelvic mobility in patients due to undergo total hip arthroplasty. *Sensors*. (2020) 20(21):6182. doi: 10.3390/s20216182

20. Stewart J, Clegg D, Watson S. *Calculus*. 9th ed. Boston: Cengage Learning (2020).

21. Khurelbaatar T, Kim K, Kim YH. A cervico-thoraco-lumbar multibody dynamic model for the estimation of joint loads and muscle forces. *J Biomech Eng*. (2015) 137(11):111001. doi: 10.1115/1.4031351

22. Kalteis TA, Handel M, Herbst B, Grifka J, Renkawitz T. In vitro investigation of the influence of pelvic tilt on acetabular cup alignment. *J Arthroplasty*. (2009) 24(1):152–7. doi: 10.1016/j.arth.2007.12.014

frontiers | Frontiers in Surgery

TYPE Original Research
PUBLISHED 26 December 2022
DOI 10.3389/fsurg.2022.997848

Check for updates

OPEN ACCESS

EDITED BY
Ronald Mark Gillies,
Medical Device Research Australia, Australia

REVIEWED BY
Rongshan Cheng,
Shanghai Jiao Tong University, China
Ye Ye,
Luoyang Orthopedic Traumatological Hospital, China

*CORRESPONDENCE
Yeon Soo Lee
✉ biomechanics.yslee@gmail.com
Seung-Hoon Baek
✉ sbaek@knu.ac.kr

SPECIALTY SECTION
This article was submitted to Orthopedic Surgery, a section of the journal Frontiers in Surgery

RECEIVED 19 July 2022
ACCEPTED 21 November 2022
PUBLISHED 26 December 2022

CITATION
Min Lee J, Baek S-H and Soo Lee Y (2022) Vital protocols for PolyWare™ measurement reliability and accuracy.
Front. Surg. 9:997848.
doi: 10.3389/fsurg.2022.997848

COPYRIGHT
© 2022 Min Lee, Baek and Soo Lee. This is an open-access article distributed under the terms of the Creative Commons Attribution License (CC BY). The use, distribution or reproduction in other forums is permitted, provided the original author(s) and the copyright owner(s) are credited and that the original publication in this journal is cited, in accordance with accepted academic practice. No use, distribution or reproduction is permitted which does not comply with these terms.

Vital protocols for PolyWare™ measurement reliability and accuracy

Jong Min Lee[1], Seung-Hoon Baek[2]* and Yeon Soo Lee[1]*

[1]Department of BioMedical Engineering, School of BioMedical Science, Daegu Catholic University, Gyungbuk, South Korea, [2]Department of Orthopedic Surgery, School of Medicine, Kyungpook National University, Kyungpook National University Hospital, Daegu, South Korea

Background and objective: PolyWare™ software (PW) has been exclusively used in the majority of polyethylene wear studies of total hip arthroplasty (THA). PW measurements can be significantly inaccurate and unrepeatable, depending on imaging conditions or subjective manipulation choices. In this regard, this study aims to shed light on the conditions needed to achieve the best accuracy and reliability of PW measurements.
Methods: The experiment looked at how PW fluctuated based on several measurement conditions. x-ray images of in-vitro THA prostheses were acquired under a clinical x-ray scanning condition. A linear wear rate of 6.67 mm was simulated in combination with an acetabular lateral inclination of 36.6° and anteversion of 9.0°.
Results: Among all the imported x-ray images, those with a resolution of 1,076 × 1,076 exhibited the best standard deviation in wear measurements as small as 0.01 mm and the lowest frequencies of blurriness. The edge detection area specified as non-square and off the femoral head center exhibited the most blurriness. The x-ray image that scans a femoral head eccentrically placed by 15 cm superior to the x-ray beam center led to a maximum acetabular anteversion measurement error of 5.3°.
Conclusion: Because PW has been the only polyethylene wear measurement tool used, identifying its sources of error and devising a countermeasure are of the utmost importance. The results call for PW users to observe the following measurement protocols: (1) the original x-ray image must be a 1,076 × 1,076 square; (2) the edge detection area must be specified as a square with edge lengths of 5 times the diameter of the femoral head, centered at the femoral head center; and (3) the femoral head center or acetabular center must be positioned as close to the center line of the x-ray beam as possible when scanning.

KEYWORDS

total hip arthroplasty (THA), PolyWare (PW), polyethylene wear, anteversion, lateral inclination

1. Introduction

Wear debris-induced osteolysis and implant loosening are the primary causes limiting implant longevity after total hip arthroplasty (THA) (1, 2). Additionally, proper acetabular cup (AC) placement in THA is essential to reduce implant wear and dislocation. Thus, early detection of the complications *via* accurate measurement

of wear rate and AC alignment during routine check-ups is of paramount clinical value (3–8).

Previous studies have demonstrated the high accuracy of PolyWare™ software (PW) in measuring wear rate or cup orientation (9). Even though reliable interactive computerized methods for measurements based on 2D AP x-ray images or 2D-3D registration methods have been proposed (7, 10), the majority of them have not been commercialized. In contrast, for decades PW has been the only commercially available tool to quantify THA polyethylene wear, due to its ease of use and lack of need for bead insertion or dual x-ray scanners. Because PW matches 3D sphere models representing the AC and femoral head (FH) onto the silhouettes of the AC and FH on x-ray images, it can measure the anteversion and the lateral tilt of the AC alongside polyethylene wear.

However, we found that PW measurement results can be significantly inaccurate depending on factors such as the observer's technical preferences and the features of x-ray images. Various error messages have frequently been encountered during our PW measurements due to unknown causes and PW spontaneously shutting down during measurements. The authors have categorized these errors into intrinsic and extrinsic, according to their dependency on PW performance. We believe that some errors can be reduced by optimizing the observer's choices or skill: ***Ext1***) PW's extrinsic error as a result of the original x-ray images being imported at an improper size; ***Ext2***) PW's extrinsic error as a result of the object's eccentric location away from the x-ray source-to-detector center line; ***Int1***) PW's intrinsic error, i.e., PW's functional limitation which is unable to fix the measurement error due to the asymmetrical specification of the edge detection area.

Because PW has been the only polyethylene wear measurement tool used, identifying the sources of its errors and developing a countermeasure is critical for THA research. In this regard, the current study has two aims. The first is to experimentally assess PW's extrinsic and intrinsic errors (***Ext1***, ***Ext2***, and ***Int1***). The second is to provide three technical empirical guidelines that clinicians or researchers can use.

2. Materials and methods

2.1. Study design

The experiments parametrically investigated the effects of three potential error-causing factors: the size of the original x-ray image (*S*), the eccentric placement of the THA implants with respect to the x-ray source-to-detector center line (*E*), and the geometric characteristics of edge detection area definition (*G*). The *S*, *E*, and *G* factors correspond to ***Ext1***, ***Ext2***, and ***Int1***, respectively. Figure 1 shows the overall layout of the current study. To ensure the highest level of reliability for PW measurements, the three best parameters for *S*, *E*, and *G* were ultimately identified.

2.2. Materials

2.2.1. THA prosthesis

The employed THA prosthesis set was composed of a Biolox® Delt ϕ28 mm femoral head (CeramTec®, Plochingen, Germany), a Trilogy® ϕ58 mm acetabular cup (Zimmer Biomet®, Warsaw, IN, USA), a Bencox® stem (CorenTec®, Cheon-An, Korea), and a Longevity® liner (Zimmer Biomet®, Warsaw, IN, USA). According to the authors' experience with PolyWare measurements, the edge detection of the prostheses in x-ray images was independent of the prosthesis size. The majority of THA femoral heads have sizes between 26 and 36 mm, large enough to accurately detect the edge of the prostheses and locate the femoral head and acetabular component centers.

2.2.2. Wear measurement software

A software called PolyWare™, v.8 (Draftware Inc., IN, USA) for radiographic measuring was used for evaluation. A PW measurement compares the analysis results of any two follow-up times. Figure 2 shows the measurement process for PW. The follow-up times can be postop (1–14 days from THA), intervals of 3 months, 6 months, 1 year, and annual increments after that. The results of the analysis include the polyethylene liner wear and the anteversion and lateral inclination of the AC. The liner wear is calculated as the difference in distance between the FH center and the AC center from the initial to the final follow-up times. The initial and final follow-up times in a PW measurement correspond to earlier and later, respectively.

2.2.3. x-ray images

The images of the THA prostheses were obtained using a clinical x-ray scanner (Innovision SH, DongKang Co., Rep. Korea). The perpendicular distance from the x-ray beam source to the detector panel was fixed at 115 cm. These scanning conditions were maintained because nonuniformity in the distance or scanning direction of the beam source to the detector can lead to different results. All x-ray images were first acquired in DICOM format at a resolution of $3{,}020 \times 3{,}020$ pixels. They were converted to TIFF format because PW software v.8 only analyzes TIFF images or converts DICOM images into TIFF ones automatically inside the software.

2.2.4. Computers

The incidence of errors in PW work may be affected by computer performance. In this regard, a laptop PC and a desktop PC with different performance levels were tested (Table 1).

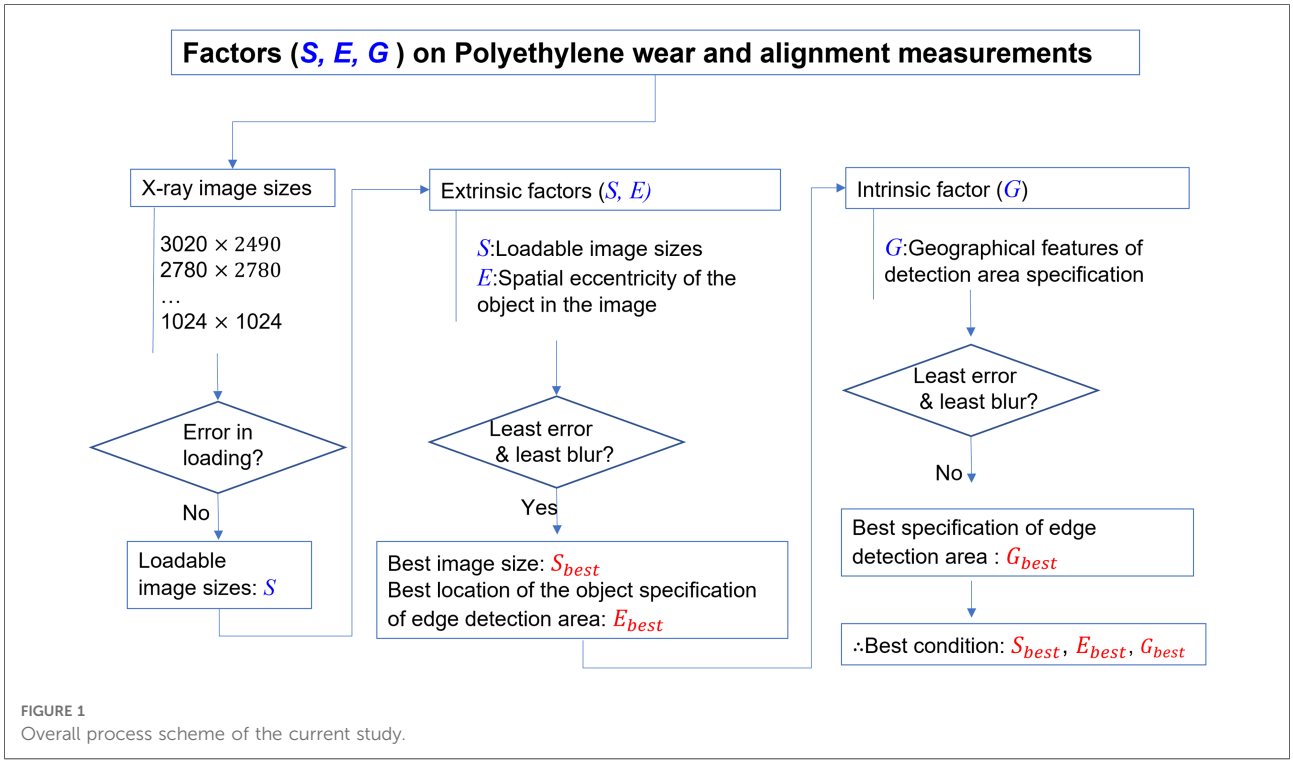

FIGURE 1
Overall process scheme of the current study.

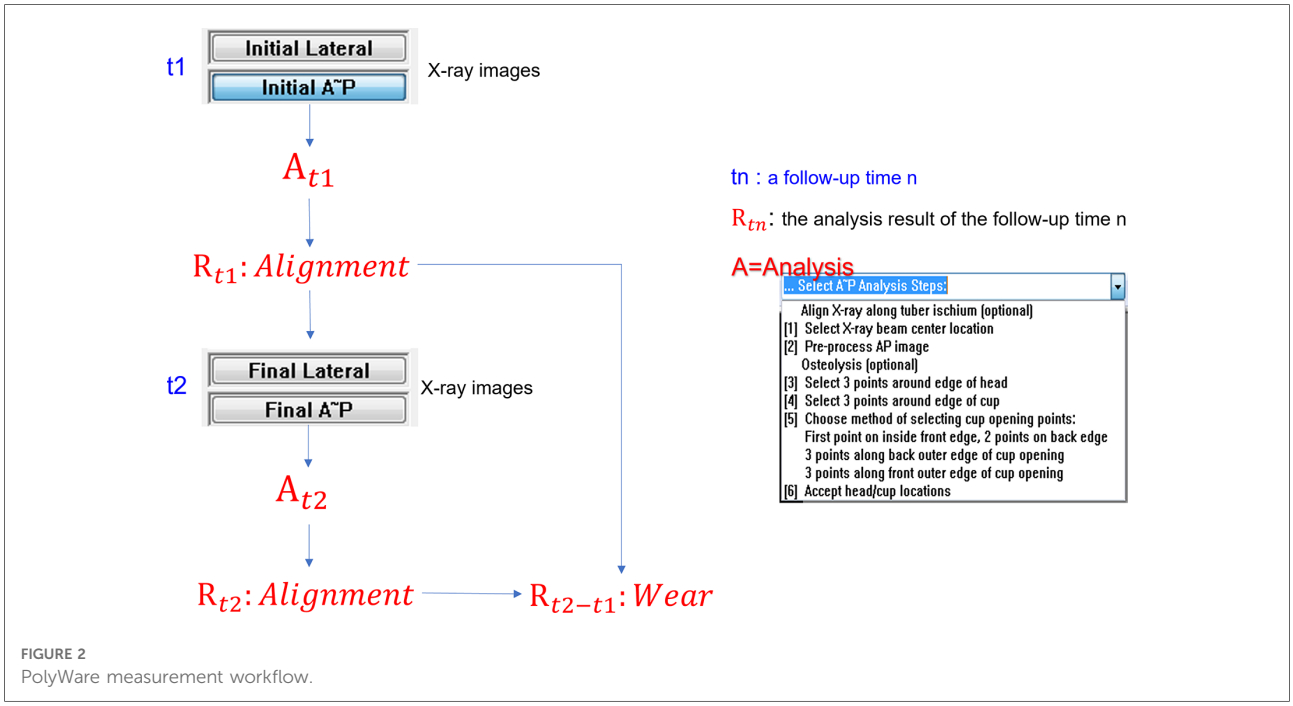

FIGURE 2
PolyWare measurement workflow.

2.2.5. Experimental simulation setup for polyethylene wear and AC alignment

Wear was replicated by translating the femoral component. The initial position of the prosthesis matched the condition in which the FH fully contacts the AC, while the final position was intended as a translation of the FH by 6.67 mm along the normal direction to the equatorial plane of the AC. x-ray images were collected before (initial) and after (final) the translation of the FH component

TABLE 1 Specifications of the laptop and the desktop personal computers (PCs).

	Manufacturer, model	OS	RAM	CPU	Memory	Graphics
Laptop PC	Laptop PC NT270E5R, Samsung Electronics Co., Ltd., Suwon, South Korea.	Windows 7 (32bit)	8 GB	Intel Core i5 4200U	DDR 3 8 GB	Intel HD Graphics 4400, Shared memory
Desktop PC	Desktop PC, Custom-built	Windows 10 (64bit)	16 GB	Intel Core i7 4930K	DDR 3 16 GB	NVIDIA GeForce GTX 750, 1GB

(Figure 3). To secure the spatial link between the FH and the AC at the initial and final positions during the x-ray, alginate, an irreversible hydrocolloid, was used. Alginate powder and water were mixed in a plastic case. The mixture was left at room temperature up until the alginate started to solidify. The components of the hip prosthesis were then positioned over the alginate. The alginate foam hardened into the native shape of the prosthetic frame in 1 min.

2.2.6. Measurement of true polyethylene wear and AC alignment

A CAD measurement was used to determine the true translation of the simulated wear. The original x-ray images of resolution 3,020 × 3,020, with the FH center located at their center, are imported into CAD software, Solidworks (Dassault Systèmes, Vélizy-Villacoublay Cedex, France). The change in the intercenter distance between the femoral head and the acetabular cup was used to calculate polyethylene wear with respect to the known diameter of the FH. Additionally, the lateral tilt of the acetabular cup was calculated as the angle between the horizontal line (also known as the medial-lateral line) and the line connecting the medial-most and lateral-most points (Figure 4). AC anteversion was calculated with the Lewinnek method (11). The true translation of the FH was 6.67 mm, and the true lateral inclination and AC anteversion were 36.6° and 9.0°, respectively.

2.3. Compatibility of x-ray image sizes with PW

2.3.1. Image loading error

When loading the x-ray images into PW, all x-ray images with a resolution of 3,020 × 3,020 or higher led to an error message. This was known as an "image loading error." Image size is determined by several parameters, such as file format, level of color/gray expression, and resolution. Because all of the x-ray images in our study were in TIFF format with a 256 grey level, the only parameter affecting image size was resolution. Various image resolutions were tested to assess their compatibility with PW during the image loading process. The original x-ray image had a resolution of 3,020 × 3,020 and captured the FH at its center. It was subsequently shrunk to several lower-resolution images, the lowest being 1,024 × 1,024 (Table 2).

2.4. Effect of spatial eccentricity of the objects in the original x-ray images

2.4.1. Test setups for spatial eccentricity modes

The distance from the x-ray beam source to an object grew as it moved away from it on a transverse plane, yet the

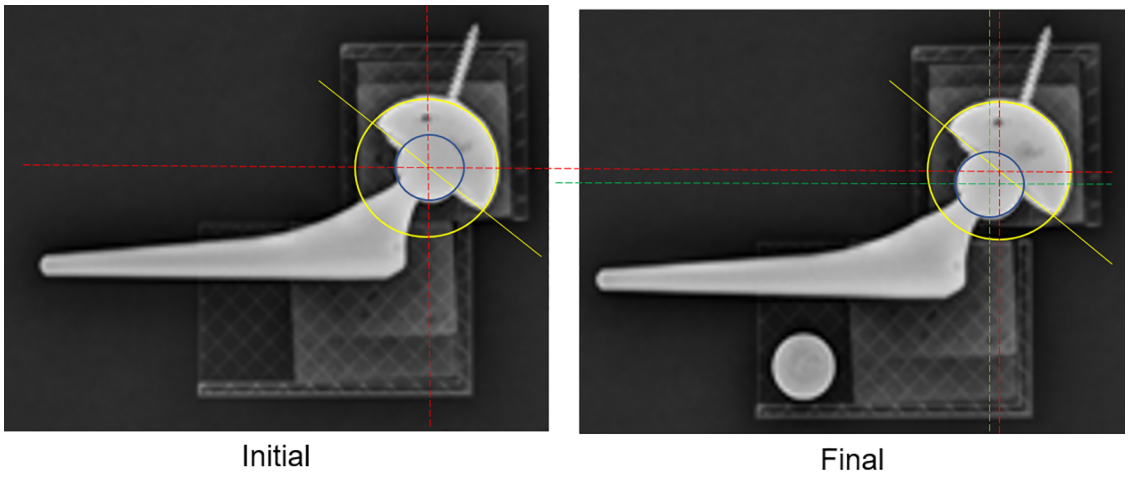

FIGURE 3
x-ray images of the initial (left) and final (right) positions, simulating cup wear by a 6.67 mm translation of the femoral stem normal to the equator plane of the AC.

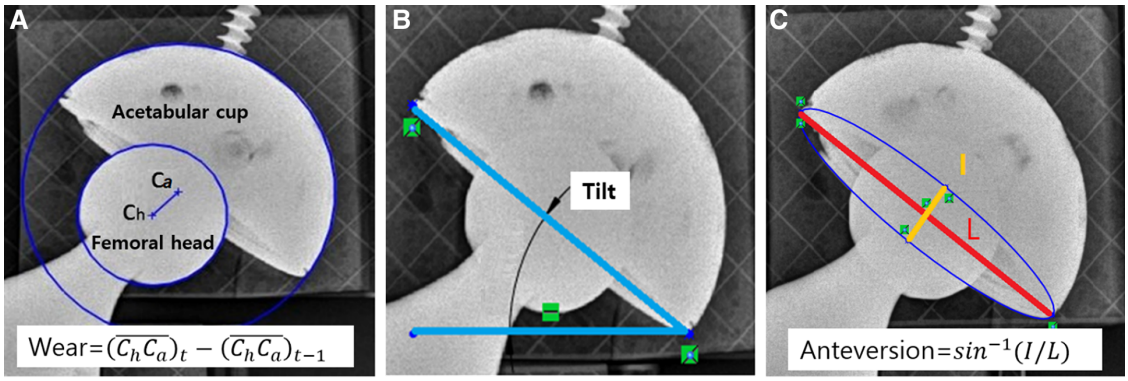

FIGURE 4
Measured values for PolyWare evaluation. (A) AC liner wear, (B) AC lateral tilt, and (C) AC anteversion.

perspective viewing angle of the object field decreased (12). As a result, the object's silhouette shape was projected differently on a detector plane, and PW measurements would give different results. We defined spatial eccentricity as the translational deviation of the FH center from the original x-ray image's middle on the same plane normal to the vector passing the x-ray source and detector centers.

Nine spatial eccentricity modes were set up *via* translating the THA prosthesis on the x-ray detector. With respect to the central location mode (O), other eight modes were specified *via* translating the prosthesis by 15 cm in left, right, superior, and/or inferior directions relative to the center placement mode (O) (**Figure 5**). The central mode (O) indicates the location of the center of the FH within the x-ray beam. All of the x-ray images used for the eccentricity tests had a resolution of 1,076 × 1,076. Without applying any rotation, the same wear of 6.67 mm was reproduced in each of the nine modes. The angular alignments of AC and acetabular liner wear should be measured at the same values because the prosthesis was only translated without rotation at all nine eccentricity modes.

2.5. PW compatibility of geometric features of the user-specified edge detection area

The pre-processing step termed "a pre-processing anteroposterior (AP) image" removes the superfluous region from the initially loaded AP x-ray images for measurements in a set of PW analyses. When a user assigns a rectangular area by dragging the cursor from a point to its matching diagonal point, PW magnifies the interior of the rectangle to the size of a full working window. This step only assigns the regions required for FH and AC edge detection, allowing for a more accurate, quicker analysis. Following this, PW performs edge detection for this rectangular area.

2.5.1. Blurring of the edge detection area

Even though images were loaded into PW without any errors, PW occasionally returned a blur in the selected region during the pre-process AP step. The blur was intuitively recognizable, as in **Figure 6**. However, the condition in which the image blur occurs is not revealed. Standard imaging did not change the gray expression of the original x-ray image. By contrast, the blurred imaging rendered the entire edge detection area of the gray expression considerably whiter and blurrier. It was necessary to prevent the circumstances leading up to the blur. Numerous tests indicated that the placement of the user-specified edge detection area significantly affected the blurring. The frequency of the blur decreased when the center of the detection area was set as being closer to the FH center. Consequently, we hypothesized that the image blur is directly affected by the location of the FH in the edge detection area. Therefore, the following three configurations of the edge detection area were set up (**Figure 7**).

- Head-centered $5D_h \times 5D_h$ square: the first configuration involves assigning the area as a square with edge lengths corresponding to five times the diameter of the FH (D_h) and centered at the center of the FH component.
- Head-centered $7D_h \times 7D_h$ square: the second configuration has the same profile as that of the first method, although its edge lengths are seven times the diameter of the FH component (D_h).
- Not head-centered, non-square: the final configuration is a random specification because it is neither square-shaped nor centered at the FH center. The non-square specification indicates that the observer specifies the areas in non-squared rectangles and improvised sizes.

TABLE 2 Polyware compatibility tests of multiple TIFF x-ray image sizes.

Image	Resolution	1,024 × 1,024	1,076 × 1,076	1,200 × 1,200	1,300 × 1,300	1,400 × 1,400	1,500 × 1,500	1,800 × 1,800	2,494 × 2,494	2,780 × 2,780	3,020 × 3,020
	Gray bits	8	8	8	8	8	8	8	8	8	8
	Size (KB)	1,060	1,220	1,499	1,742	1,994	2,253	3,433	5.978	7,202	26,721
Loading Error ratio (in the desktop PC)		0/10	**0**/10	**0**/10	0/10	0/10	0/10	8/10	10/10	10/10	10/10
Loading Error ratio (in the laptop PC)		0/10	**0**/10	**0**/10	0/10	0/10	0/10	8/10	10/10	10/10	10/10
Blur ratio in the edge detection image (identical in both PCs)		5/10	2/10	4/10	6/10	5/10	5/10	2/2	NA	NA	NA
Wear (mm) True = 6.67 of All cases		6.88 (0.50)	6.79 (0.01)	6.42 (0.42)	6.64 (0.52)	6.70 (0.14)	6.61 (0.29)	6.49 (0.66)	NA	NA	NA
Wear (mm) True = 6.67 of Non-blur cases only		6.60 (0.00)	6.79 (0.00)	6.24 (0.17)	6.27 (0.28)	6.68 (0.01)	6.46 (0.25)	NA	NA	NA	NA
Lateral tilt (°) True = 36.70° of All cases		36.5 (0.8)	36.0 (0.5)	36.5 (0.5)	36.2 (0.4)	36.2 (0.4)	36.4 (0.6)	36.5 (0.9)	NA	NA	NA
Lateral tilt (°) True = 36.70° of Non-blur cases only		36.3 (0.7)	36.0 (0.6)	36.6 (0.6)	36.3 (0.3)	36.0 (0.4)	36.3 (0.4)	NA	NA	NA	NA
Anteversion (°) True = −9.0° of All cases		−8.7 (0.4)	−8.6 (0.7)	−8.3 (0.3)	−8.7 (0.8)	−8.8 (0.5)	−8.7 (0.7)	−8.5 (0.1)	NA	NA	NA
Anteversion (°) True = −9.0° of Non-blur cases only		−8.5 (0.2)	−8.6 (0.8)	−8.5 (0.2)	−8.9 (0.9)	−9.0 (0.5)	−8.5 (0.7)	NA	NA	NA	NA

NA, not available since none of the measurement trials were successful or possible. The wear, lateral tilt, and anteversion were obtained from the only successful measurements without any blur phenomenon in both the initial and final images. These tests were performed for the x-ray image whose midpoint coincides with the center of the femoral head (*O* in Figure 5).

For this edge detection area specification test, x-ray images with a resolution of 1,076 × 1,076 were used. The image resolution of 1,076 × 1,076 was selected because it was found to be the most compatible resolution with PW (presented in the "Results" section).

3. Results

3.1. Image loading error vs. loaded image size

Concerning the image loading error, images with a resolution equal to or higher than 1,800 × 1,800 frequently failed while loading the initial or final x-ray images (Table 2). Each resolution image was tested ten times. All the images of resolutions corresponding to 2,494 × 2,494, 2,780 × 2,780, or 3,020 × 3,020 failed at being loaded into PW, i.e., the loading error rate was 10/10 = 1. The image loading error rate for 1,800 × 1,800 resolution images was 8/10. Conversely, all images with a resolution of 1,500 × 1,500 or lower were successfully loaded into PW with no errors.

In terms of occurrence rate, the image loading error was identical for the desktop PC and laptop PC (Table 2). Therefore, the PW image loading error did not depend on computer performance.

3.2. Blurring of the edge detection image vs. loaded image size

Only images that had been successfully loaded in PW could be used in the edge detection process. For all the images successfully loaded into PW, the edge detection area was specified in the head-centered $5D_h \times 5D_h$ square.

When the edge detection area specified an error, all two successfully loaded 1,800 × 1,800 resolution images became blurry (Table 2). In contrast, images with a resolution of 1,076 × 1,076 exhibited a 2/10 blur ratio, which corresponded to the lowest blur occurrence rate among all resolutions.

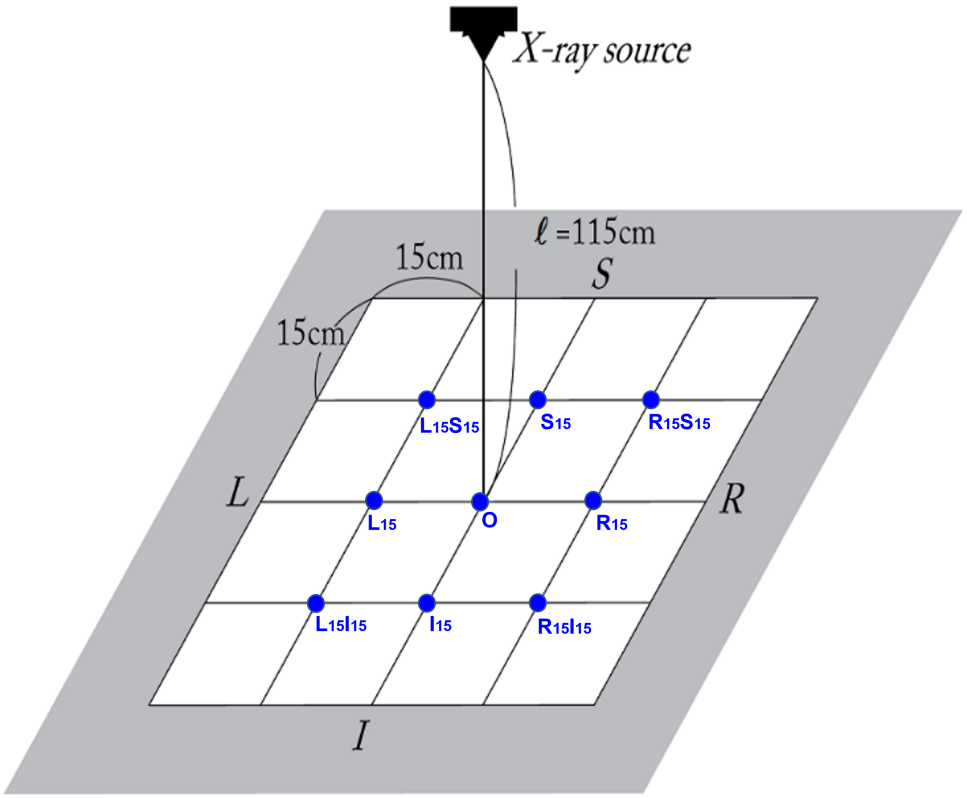

FIGURE 5
Eccentricity comparison test setup, i.e., nine spatial eccentricity modes. With respect to the center of the x-ray detector, nine spatial eccentricity locations of the THA prostheses were set up to figure out how the eccentricity of the component location affected PolyWare measurement results.

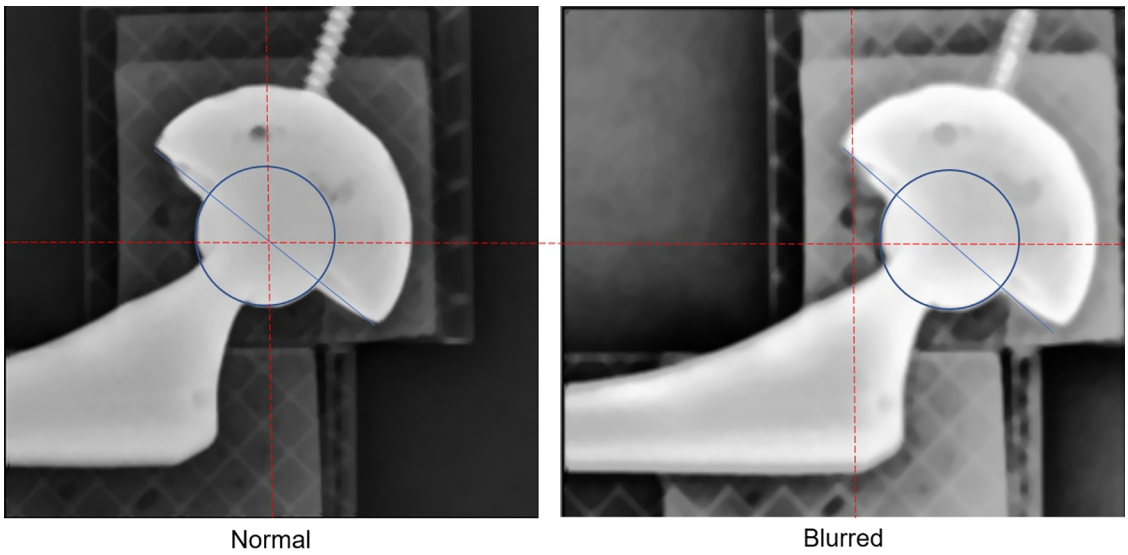

FIGURE 6
The blur of the edge detection area. For the same x-ray image, different specifications of rectangular edge detection areas result in different image sharpness. The left one is normal, but the right one is blurred. In the normal case, the rectangular edge detection area is specified such that its center is at the very center of the femoral head. In the blurred case the rectangular edge detection area is specified so that its center is considerably off the center of the femoral head, causing the edge detection area to blur.

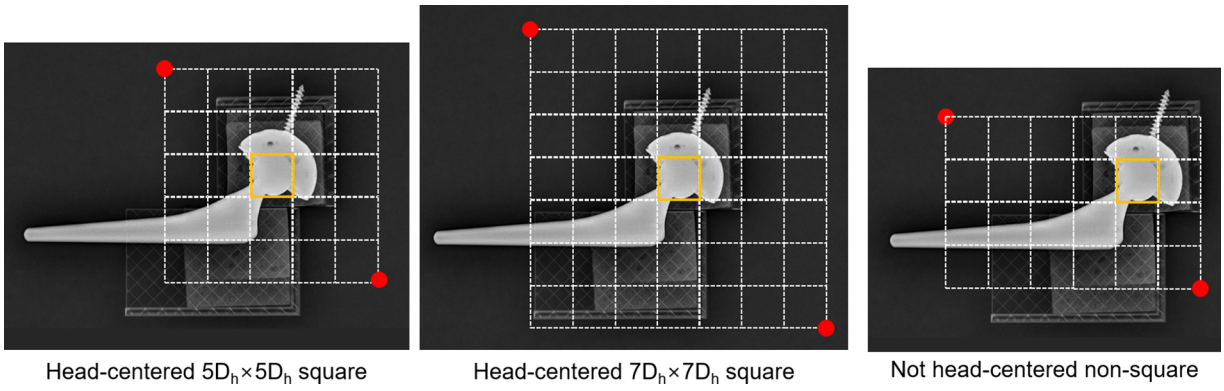

FIGURE 7
Three ways of specifying the edge detection area. The edge detection area was assigned as a rectangle whose edge lengths were 5 times ($5D_h$) square, 7 times ($7D_h$) square of the diameter of the femoral head component (D_h), or non-square. The square areas specified were centered in the middle of the FH, whereas non-square ones were off the FH center.

3.3. PW-compatible geometric features of the edge detection area specification

The effects of the edge detection area's geometric feature were assessed with only the X-ray images with a resolution of 1076×1076, because all the images with this resolution were successfully loaded into PW and exhibited the least blur in the edge detection process. The incidence across 10 trials served as a measure of the blur's occurrence rate. The blur indicates that the original image is degraded by the blur created while specifying the edge detection area, and edge detection will be processed for the degraded image.

The reliability of measurements was evaluated by the incidence of blurs or unexpected errors, as shown in **Table 3**. When the edge detection area was specified as a square with its center in the center of the FH on x-ray images, PW measurements showed more reliability as opposed to when the center of the area was described being as randomly located off the center of the FH. The edge detection operation is terminated by an unexpected error, which indicates that the edge detection procedure returned an error message without any explanation.

Ten trials of the not-head-centered, non-squared specification resulted in three unexpected errors and five blurs at the edge detection procedure. When it comes to blurring, the $7D_h \times 7D_h$ square specification showed two blur incidents in ten trials, whereas the $5D_h \times 5D_h$ square specification showed one blur incident in 10 trials. The wear values of both square specifications (including all the blur and non-blur situations) corresponded to 6.79 (0.00) mm, which was extremely close to the true value of 6.67 mm. In comparison, 10 trials with not-head-centered, non-squared specifications produced three unexpected errors and five blurs during the edge detection procedure. The wear of the non-head-centered random non-square specification was 6.92 (0.15) mm, which was less accurate and precise than the squared specifications.

3.4. Effect of the prosthesis's eccentric placement at the time of the x-ray scanning

The eccentricity tests were performed with only the images with a resolution of 1,076 × 1,076, and their edge detection area specification was the head-centered $5D_h \times 5D_h$ square. The PW measurements for each eccentricity mode were averaged from ten trials. **Table 4** shows the wear amount and alignment measurement results for the nine different eccentricity modes.

The spatial eccentricity of the prosthesis from the original x-ray image center led to inaccurate results in wear measurement. L_{15}, $R_{15}S_{15}$, $R_{15}I_{15}$, and $L_{15}I_{15}$ eccentricities resulted in an error of approximately 0.42 mm, and the I_{15} eccentricity resulted in an error of approximately 0.67 mm. $L_{15}S_{15}$ and R_{15} resulted in an error of 0.50 mm.

AC anteversion measurements were considerably inaccurate due to any eccentricity in all directions, and, in particular, the maximum error appearing at $L_{15}I_{15}$ mode by 5.4° (=14.4°–9.0°). S_{15} and I_{15} eccentricity modes resulted in anteversion measurement errors of 4.3° and −3.6°, respectively.

4. Discussion

In the study, we are faced with the very uncomfortable fact that some of the published PW measuring studies may not be valid if they did not acknowledge and fix the errors our research revealed. In light of our findings, we advise

TABLE 3 The measured wear for different area specifications (true wear = 6.67 mm).

	Head-centered				Not head-centered	
	$5D_h \times 5D_h$ square		$7D_h \times 7D_h$ square		Non-square	
Trials	Trouble	Wear (mm)	Trouble	Wear (mm)	Trouble	Wear (mm)
1	No	6.79	No	6.79	No	7.05
2	Blur	7.76	No	6.79	Error	NA
3	No	6.79	No	6.79	Blur	7.75
4	No	6.79	No	6.79	No	6.79
5	No	6.79	No	6.79	Blur	6.12
6	No	6.79	Blur	6.12	Error	NA
7	No	6.79	Blur	6.12	Blur	7.98
8	No	6.79	No	6.79	Blur	6.12
9	No	6.79	No	6.79	Error	NA
10	No	6.79	No	6.79	Blur	6.12
Total	Error: 0 Blur: 1	6.89 (0.31) of all 6.79 (0.00) of 9 N-blurs 7.76 of 1 blur	Error: 0 Blur: 2	6.66 (0.28) of all 6.79 (0.00) of 8 N-blurs 6.12 (0.00) of 2 blurs	Error: 3 Blur: 5	6.85 (0.79) of all 6.92 (0.18) of 2 N-blurs 6.82 (0.96) of 5 Blurs

NA, not available since none of the measurement trials were successful or possible. These tests were performed for the x-ray image whose midpoint coincides with the center of the femoral head (O in Figure 5). The symbol D_h denotes the diameter of the femoral head component.

polyethylene wear researchers to use the following three PW measurement protocols.

4.1. Finding 1: Optimal size for original x-ray images (S_{best})

Regarding the image loading problem, all images with a resolution of $1{,}500 \times 1{,}500$ or lower were successfully loaded into PW without any errors. Particularly, images with a resolution of $1{,}076 \times 1{,}076$ showed a two-to-ten (2/10) blur occurring ratio that was the lowest among all image resolutions. In practical situations, an original image transferred from a medical modality may be non-square ($1{,}076 \times 1{,}500$ or $1{,}200 \times 1{,}100$, for example). In this instance, we recommend cropping it into a square with the original image's center at the center, changing its pixel size to $1{,}076 \times 1{,}076$. Therefore, an x-ray image with a resolution of $1{,}076 \times 1{,}076$ is optimally compatible with the PW measurement, i.e., $S_{best} = 1{,}076 \times 1{,}076$.

TABLE 4 PolyWare measurement results for nine spatial eccentricity modes.

Eccentricity mode	Liner wear, mm True = 6.67	Lateral tilt, True = 36.7	Anteversion, True = −9.0
O	6.79 (0.00)	36.3 (0.3)	9.0 (0.6)
L_{15}	6.25 (0.00)	36.2 (0.6)	11.1 (0.7)
$L_{15}S_{15}$	6.52 (0.00)	36.2 (0.2)	7.9 (0.6)
S_{15}	6.79 (0.00)	36.7 (0.3)	4.7 (0.5)
$R_{15}S_{15}$	6.25 (0.00)	37.2 (0.3)	1.5 (0.2)
R_{15}	6.52 (0.00)	37.2 (0.3)	5.9 (0.6)
$R_{15}I_{15}$	6.25 (0.00)	37.2 (0.3)	9.8 (0.4)
I_{15}	6.00 (0.00)	37.1 (0.5)	12.6 (0.4)
$L_{15}I_{15}$	6.25 (0.00)	37.2 (0.4)	14.4 (0.3)

L, *R*, *S*, and *I* in the eccentricity mode represent left, right, superior, and inferior, respectively. The subscript 15 in the eccentricity mode indicates a translational distance of 15 mm.

4.2. Finding 2: Optimal location of the THA prosthesis on the original x-ray images (E_{best})

The eccentricity of the FH location from the x-ray beam center line significantly reduced the accuracy of the liner wear and AC anteversion measurements. The errors in **Figures 8**, **9** are mean deviations from the true wear and anteversion values recalculated from **Table 3**, respectively. It is clear that an eccentric placement of the prosthesis with respect to the x-ray beam center line leads to errors in the liner wear and AC anteversion. Because the prosthesis was placed superiorly or inferiorly in relation to the x-ray beam source, the anteversion specifically showed a greater inaccuracy. Unless the FH was placed extremely close to the central x-ray

beamline at the x-ray scanning instant, the anteversion measurement by PW was unreliable.

To determine why the eccentric prosthesis placement significantly affected the anteversion, we measured the anteversion of the virtual x-ray images generated by simulating a projection of the hip prosthesis 3D CAD model in a perspective view. The perspective view simulation was made with 3D CAD software, i.e., Rapidform 2006® (INUSTechnology, Seoul, Korea). With a source-to-detector distance of 394 cm, Rapidform 2006 creates a virtual perspective image in which the proximal edge of a 100 cm × 100 cm × 100 cm cube is projected as 130 cm on the detector plane. Figure 10 demonstrates changes in liner wear based on superior and inferior eccentricity modes. The anteversion was calculated *via* the Lewinnek method (11). The superior and inferior 15 cm eccentricity modes were 4.3° and 3.6° of over- and under-anteversion, respectively. From our CAD measurement using Rapidform, it is postulated that PW uses the Lewinnek method to calculate acetabular anteversion. It is concluded that the acetabular measurement is only valid when the center of the FH (or similarly, the center of the AC) is placed very close to the center line of the x-ray beam. As a result, eccentricity significantly impairs the accuracy of measurements of wear and acetabular anteversion; thus, the FH center should be positioned along the center line of the x-ray beam (E_{best} = O).

4.3. Finding 3: Optimal specification of the edge detection area (G_{best})

The pre-process AP image in PW measurements required cutting out unnecessary portions from the originally loaded image. The image remaining after the pre-processing was used for edge detection of the FH and AC. The occurrence of image blur was influenced by the geometric characteristics of the region that users had specified for the pre-processing. The geometric features of the selected area include size and symmetry with respect to the center of the

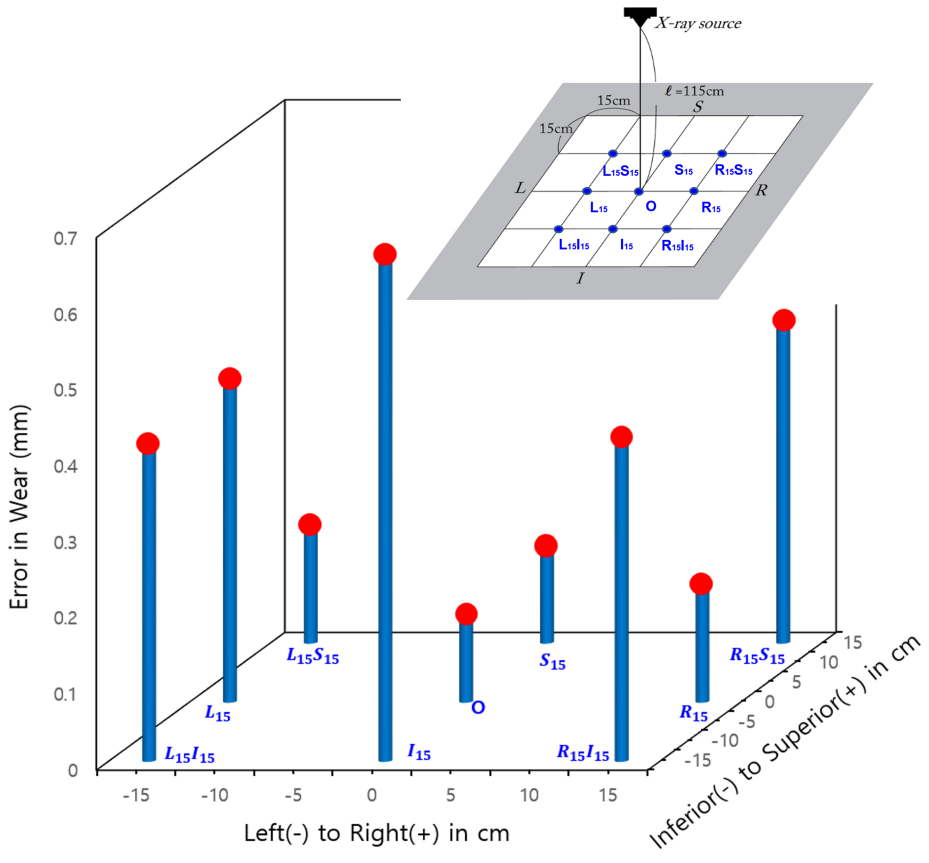

FIGURE 8
The error (in absolute values) in the wear of the femoral head's spatial eccentricity modes in the original x-rays.

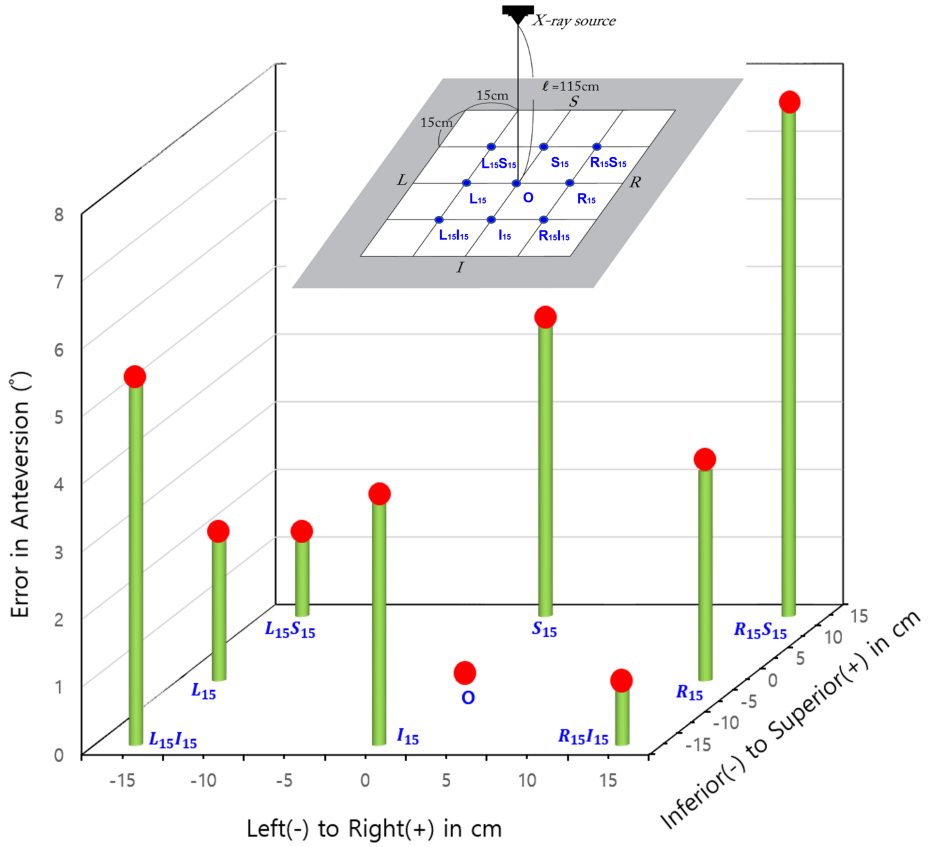

FIGURE 9
Errors (in absolute values) in the acetabular anteversion for the femoral head's spatial eccentricity modes in the original x-rays.

FH. In the current study, the asymmetry of the specified area increased the likelihood of a blur. Because the magnified process image can be more accurately analyzed for edge detection, the head-centered $5D_h \times 5D_h$ square is preferable to the head-centered $7D_h \times 7D_h$ square. In this sense, we postulate that a head-centered $3D_h \times 3D_h$ square would also be preferable. The optimal geometric specification mode of the image processing for edge detection corresponds to the head-centered $5D_h \times 5D_h$ square, i.e., G_{best} = head-centered $5D_h \times 5D_h$ square or probably the head-centered $3D_h \times 3D_h$ square.

The current research presents several limitations. First, because the study only used prostheses rather than including real tissues such as bones and soft tissues, the x-ray images used here are clinically impractical. There should be a small occlusion when tissues are absent around the prostheses; as a result, the outline of the prostheses will be more visible than when tissues are present. However, the current study aims to evaluate measurement accuracy. To assess accuracy, the true wear rate was translated into a precise simulation, and we compared the measured values to that true rate. Real clinical patient hip images cannot provide a true wear value since we are not allowed to measure the true AC wear of living individuals by surgically opening them and taking direct measurements. Additionally, the accuracy was also hindered by the difficulty of standardizing complex human tissue shapes and material compositions around THA prostheses during each x-ray scanning. Hence, in the current study, x-ray images were obtained without considering human tissues, to control accurately wear simulation by translating the femoral component. In future studies, a simulation may be developed to represent tissues around the prostheses. Second, the resolution and aspect ratio of the original x-ray images that were tested did not cover all possible variations. Clinical x-ray images may have a variety of resolutions or aspect ratios. Additionally, although PW automatically squared the imported images, practically obtained original x-ray images may not be. However, the aspect ratio will be irrelevant if the x-ray image has a resolution of 1,500 ×

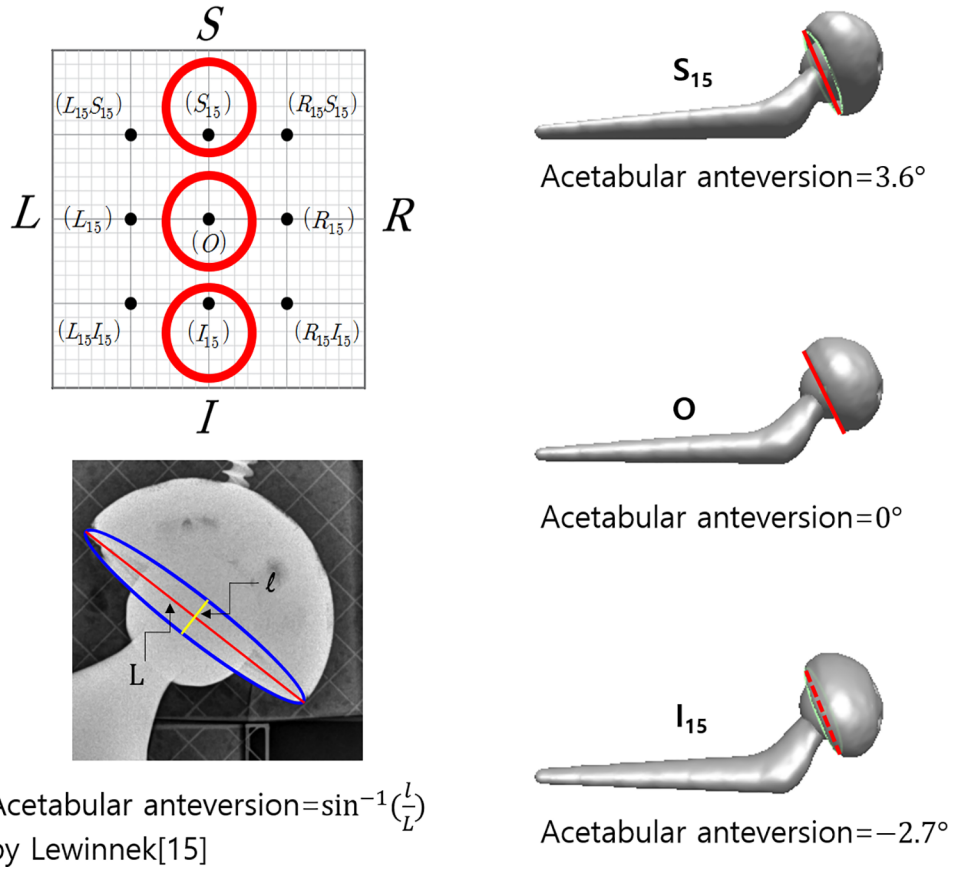

FIGURE 10
Measurement of acetabular anteversion using CAD to investigate the effect of the eccentricity of the prosthesis from the center of the x-ray beam on the acetabular anteversion. The same x-ray images used for polyethylene measurements were also used for the measurement using CAD software, i.e., Rapidform 2006® (INUSTechnology, Seoul, Korea). The superior and inferior placements of the prosthesis bring about errors in acetabular anteversion by the nature of perspective x-ray imaging.

1,500 or lower. Thirdly, the current study investigated only one type of THA prosthesis, i.e., THA using fourth-generation ceramic-on-polyethylene articulations. When it comes to opacity in x-ray scanning, fourth-generation ceramic-on-polyethylene and metal-on-polyethylene are comparable since their liners are made of polyethylene. However, if the liners are made of radio-opaque materials like metal or fourth-generation ceramics, it can be difficult to identify the outline of the femoral head. It must be noted that PW compares patient x-ray images to measure the volume of polyethylene material worn away from the bearing surfaces of orthopedic hip implants over time (http://www.draftware.com/html/polyware.htm). Hence, PW can only be used the measure polyethylene wear.

The authors are aware of no published research that has investigated the error sources and their solutions in PW measurements. Recent literature has reported that manual measurements of the digital x-ray screen and PW measurement are comparable when it comes to measuring AC anteversion (9, 13). However, it should be highlighted that since there is no way for them to measure true polyethylene wear in living THA patients, their study only reports repeatability and not accuracy. When it comes to wear, comparing our findings with existing literature is quite limited.

5. Conclusion

Because PW has been the only polyethylene wear measurement tool used, identifying its sources of error and devising a countermeasure is of the utmost importance. For the best accuracy and reliability in PolyWare™ measurements, this study strongly recommends following the methodology proposed. Otherwise, the validity of the PW measurements cannot be reliably determined.

Data availability statement

The original contributions presented in the study are included in the article/Supplementary Material, further inquiries can be directed to the corresponding author.

Author contributions

JM carried out the experiments and data analysis, and S-HB conceived the idea for the study and participated in the manuscript writing. Additionally, YS conducted experiments, interpreted their results and wrote the manuscript. All authors contributed to the article and approved the submitted version.

Conflict of interest

The authors declare that the research was conducted in the absence of any commercial or financial relationships that could be construed as a potential conflict of interest.

Publisher's note

All claims expressed in this article are solely those of the authors and do not necessarily represent those of their affiliated organizations, or those of the publisher, the editors and the reviewers. Any product that may be evaluated in this article, or claim that may be made by its manufacturer, is not guaranteed or endorsed by the publisher.

References

1. Bozic KJ, Kurtz SM, Lau E, Ong K, Vail TP, Berry DJ. "The epidemiology of revision total hip arthroplasty in the United States". *J Bone Joint Surg* . (2009) 91 (1):128–33. doi: 10.2106/JBJS.H.00155

2. Shen C, Tang Z-H, Hu J-Z, Zou G-Y, Xiao R-C, Yan D-X. "Does cross-linked polyethylene decrease the revision rate of total hip arthroplasty compared with conventional polyethylene? A Meta-Analysis". *Orthop Traumatol: Surg Res.* (2014) 100(7):745–50. doi: 10.1016/j.otsr.2014.07.015

3. Biedermann R, Tonin A, Krismer M, Rachbauer F, Eibl G, Stöckl B. "Reducing the risk of dislocation after total hip arthroplasty: the effect of orientation of the acetabular component". *J Bone Joint Surg Br.* (2005) 87 (6):762–9. doi: 10.1302/0301-620X.87B6.14745

4. D'lima DD, Urquhart AG, Buehler KO, Walker RH, Colwell Jr CW. "The effect of the orientation of the acetabular and femoral components on the range of motion of the hip at different head-neck ratios". *J Bone Joint Surg* . (2000) 82(3):315–21. doi: 10.2106/00004623-200003000-00003

5. Dumbleton JH, Manley MT, Edidin AA. "A literature review of the association between wear rate and osteolysis in total hip arthroplasty". *J Arthroplasty.* (2002) 17(5):649–61. doi: 10.1054/arth.2002.33664

6. Kennedy J, Rogers W, Soffe K, Sullivan R, Griffen D, Sheehan L. "Effect of acetabular component orientation on recurrent dislocation, pelvic osteolysis, polyethylene wear, and component migration". *J Arthroplasty.* (1998) 13 (5):530–4. doi: 10.1016/S0883-5403(98)90052-3

7. Kerrigan CS, Mckenna SJ, Ricketts IW, Wigderowitz C. "Automated assessment of polyethylene wear in cemented acetabular components using anteroposterior radiographs of total hip replacements". *Comput Med Imaging Graph.* (2008) 32(3):221–38. doi: 10.1016/j.compmedimag.2007.12.002

8. Wan Z, Boutary M, Dorr LD. "The influence of acetabular component position on wear in total hip arthroplasty". *J Arthroplasty.* (2008) 23(1):51–6. doi: 10.1016/j.arth.2007.06.008

9. Shin W, Lee S, Lee K, Cho H, Lee J, Suh K. "The reliability and accuracy of measuring anteversion of the acetabular component on plain anteroposterior and lateral radiographs after total hip arthroplasty". *Bone Joint J.* (2015) 97(5):611–6. doi: 10.1302/0301-620X.97B5.34735

10. Zheng G. "Effective incorporating spatial information in a mutual information based 3D–2D registration of a CT volume to x-ray images". *Comput Med Imaging Graph.* (2010) 34(7):553–62. doi: 10.1016/j.compmedimag.2010.03.004

11. Lewinnek GE, Lewis J, Tarr R, Compere C, Zimmerman J. "Dislocations after total hip-replacement arthroplasties". *J Bone Joint Surg Am.* (1978) 60 (2):217–20. doi: 10.2106/00004623-197860020-00014

12. Kerr DA. "The proper pivot point for panoramic photography". *Pumpkin.* (2008) 2(8):1–15.

13. Park YS, Shin WC, Lee SM, Kwak SH, Bae JY, Suh KT. "The best method for evaluating anteversion of the acetabular component after total hip arthroplasty on plain radiographs". *J Orthop Surg Res.* (2018) 13(1):66. doi: 10.1186/s13018-018-0767-4

frontiers | Frontiers in Surgery

TYPE Original Research
PUBLISHED 06 January 2023
DOI 10.3389/fsurg.2022.1065189

Check for updates

OPEN ACCESS

EDITED BY
Huiwu Li,
Shanghai Ninth People's Hospital, China

REVIEWED BY
Yansong Qi,
Inner Mongolia People's Hospital, China
Liyuan Tao,
Peking University Third Hospital, China

*CORRESPONDENCE
Yueming Song
sym_cd@163.com

SPECIALTY SECTION
This article was submitted to Orthopedic Surgery, a section of the journal Frontiers in Surgery

RECEIVED 09 October 2022
ACCEPTED 09 November 2022
PUBLISHED 06 January 2023

CITATION
Li Z, Yang H, Zhou C, Xiu P, Yang X, Wang L, Feng G, Liu L and Song Y (2023) Nomogram for predicting the distal adding-on phenomenon in severe and rigid scoliosis.
Front. Surg. 9:1065189.
doi: 10.3389/fsurg.2022.1065189

COPYRIGHT
© 2023 Li, Yang, Zhou, Xiu, Yang, Wang, Feng, Liu and Song. This is an open-access article distributed under the terms of the Creative Commons Attribution License (CC BY). The use, distribution or reproduction in other forums is permitted, provided the original author(s) and the copyright owner(s) are credited and that the original publication in this journal is cited, in accordance with accepted academic practice. No use, distribution or reproduction is permitted which does not comply with these terms.

Nomogram for predicting the distal adding-on phenomenon in severe and rigid scoliosis

Zhongyang Li, Huiliang Yang, Chunguang Zhou, Peng Xiu, Xi Yang, Lei Wang, Ganjun Feng, Limin Liu and Yueming Song*

Department of Orthopedic Surgery and Orthopedic Research Institute, West China Hospital, Sichuan University, Chengdu, China

Background: The distal adding-on phenomenon has attracted extensive discussion in the field of spine surgery due to the continual occurrence after scoliosis correction. Previous work has mainly focused on adolescent idiopathic scoliosis (AIS), and a relatively high number of theories for the mechanism of the distal adding-on phenomenon has been proposed for these kinds of patients. Severe and rigid scoliosis, as a special disease form, has a unique etiology, clinical manifestations and internal mechanisms distinct from those of AIS. Given the uniqueness of this disease, the mechanism and causes of the distal adding-on phenomenon have been infrequently studied in depth.

Objective: To define clinical and radiological factors associated with distal adding-on in patients with severe and rigid scoliosis.

Methods: Radiographic parameters and demographic data of patients with severe and rigid scoliosis were evaluated preoperatively, after posterior instrumentation and fusion surgery, and at the final follow-up *via* radiographs. According to the appearance of distal adding-on at the final follow-up, the patients were grouped into the Adding-on and the Non-adding-on groups. Various radiological parameters were analyzed in stepwise multivariate logistic regression to identify the variables associated with distal adding-on, which were then incorporated into a nomogram. The predictive performance and calibration of the nomograms for distal adding-on were assessed using C statistics and calibration plots.

Results: 93 patients (21 in the Adding-on and 72 in the Non-adding-on group) were included. The incidence of distal adding-on was 22.6%. The variables associated with distal adding-on were the anterior release, posterior internal distraction, and later posterior spinal fusion (IP) procedure, the posterior vertebral column resection and posterior spinal fusion (PVCR) procedure, postoperative apical vertebral translation (Post-AVT) and preoperative slope of the line linking the pedicles on the concave side of the upper- and lower-end vertebrae (Tan α). Combining these factors, the nomogram achieved a concordance index of 0.92 in predicting distal adding-on and had well-fitted calibration curves.

Conclusions: For patient with a negative Tanα in severe and rigid scoliosis, the risk of distal adding-on tended to increase, and it is recommended to give priority to IP or PVCR. In the final correction, a smaller Post-AVT should not be pursued excessively.

KEYWORDS

distal adding-on, nomogram, internal distraction, severe and rigid scoliosis, scoliosis

Introduction

Severe and rigid scoliosis is a special disease form of scoliosis with a unique etiology, clinical manifestations and internal mechanisms, presenting as a complex and progressive spinal deformity with many distinctive features. It is generally recognized that patients with severe and rigid scoliosis possess a main curve of more than 80° on normal radiographs and the flexibility of less than 30% on bending radiographs (1, 2).

The distal adding-on phenomenon has attracted extensive discussion in the field of spine surgery due to the continual occurrence after scoliosis correction. It is defined as a progressive increase of the number of vertebrae contained distally within the main curve linked with either an increase in the deviation of the first vertebra below instrumentation from the center sacral vertical line (CSVL) of more than 5 mm or an increase in the angulation of the first disc of more than 5° at a minimum 2-year follow-up (3).

Previous work on the distal adding-on phenomenon has mainly focused on AIS patients, and a relatively high number of theories have been proposed for its mechanism in these kinds of patients (4, 5). Given the unique presentation of severe and rigid scoliosis, however, the mechanism and causes of the distal adding-on phenomenon are rarely studied in depth. Consequently, the objective of the present study was to define clinical and radiological factors associated with distal adding-on in severe and rigid scoliosis using patient data from a single center. Especially, we tried to create and internally validate a nomogram to predict the distal adding-on phenomenon in this disease.

Patients and methods

Patients

This study was approved by the ethics committee of West China Hospital of Sichuan University and all patients signed the informed consent. This study was conducted in strict accordance with relevant guidelines and regulations. A review was performed on all patients retrospectively with severe and rigid thoracic or thoracolumbar scoliosis who underwent anterior release and posterior spinal fusion (APSF), anterior release, posterior internal distraction, and later posterior spinal fusion (IP), and the posterior vertebral column resection and posterior spinal fusion (PVCR) at our medical center from January 2008 to June 2018. The inclusion criteria were as follows: (1) main thoracic or thoracolumbar curve greater than 80° and flexibility of less than 30% on bending radiographs, (2) a minimum of two years of follow-up, and (3) no history of spine surgery. The distal adding-on was defined as (1) lowest instrumented vertebra (LIV)-central sacral vertical line (CSVL) > 10 mm, (2) LIV + 1-CSVL > 5 mm, and (3) disc angle of LIV + 1 > 5°. Patients who met at least one criterion were included in the Adding-on group. Altogether, 93 patients (21 in the Adding-on group and 72 in the Non-adding-on group) were included in the present study. General information, including sex, age, and Risser classification, was collected from the patients. Radiographic assessment was performed using full-length anteroposterior (AP) lateral radiographs and passive lateral bending radiographs acquired preoperatively, postoperatively, and at the final follow-up.

Surgical procedures

All procedures were performed by two senior spine surgeons (L.M.L. and Y.M.S.), and somatosensory evoked potentials and motor evoked potentials were performed. Patients received 3 kinds of surgery (anterior release and posterior spinal fusion (APSF); anterior release, posterior internal distraction, and later posterior spinal fusion (IP); posterior vertebral column resection and spinal fusion (PVCR). The APSF consisted of anterior approach surgery and later posterior spinal fusion. The anterior release involves a thoracic incision and the convex side of the area was resected. The patients were taken to lateral position with the main curve upward to undergo the anterior release. Thoroughly remove the intervertebral disc and the fibrous connective tissue to ensure adequate loosening of the spine. And then expose and remove the rib adhere to the uppermost level of the spine to be approached (6). After anterior release, the patient was converted to prone position for posterior spinal fusion.

For the IP procedure, after anterior release, the patients were turned to prone position for posterior internal distraction. Make two small incisions to expose the vertebral body at the caudal and caudal to be fixed. Subperiosteal dissection was performed to expose the facet and transverse process on the concave side of the spine. To select at least 2 fixing points at the caudal and caudal end respectively to ensure fully fixation. After implanting pedicle screws at the fixed point, 2 pre-bent titanium rods were selected. The long distraction rod passed subcutaneously and connected to the pedicle screw at the cranial end and the short distraction rod was connected with the pedicle screw at the caudal end. Then, connect the two rods through the domino connector (Medtronic, Fort Worth, TX) and lock the pedicle screw cap. After locking the screw caps on the medial side of the domino connector, distraction between the distal pedicle screw and the domino connector was performed. Next, to lock the screw caps on the lateral side and loosen the screw caps on the medial side of the domino connector. Perform a similar distraction between the

domino connector and the rod holder (7). During the distraction process, the abnormal evoked potential should be avoided as much as possible. During each distraction, we allow a few minutes of stress relaxation between multiple distractions. One to four weeks after traction, posterior spinal fusion was performed.

For the PVCR procedure, after the general anesthesia, the patients were turned to a prone position with the autologous blood transfusion. Along the spinous process of the predetermined fusion segment, an arc-shaped incision was used to open the skin and subcutaneous tissue. The paraspinal muscles were stripped along the spinous process to the subperiosteal sides on both sides, the supraspinous ligaments of the upper and lower vertebrae of the scheduled fusion levels are preserved, and the lamina and the upper and lower articular processes of the scheduled fusion levels were completely exposed. In the process of screw placement, the lower articular process of the corresponding vertebral body was excised at the same time, and the cartilage surface of the upper articular process was scraped off to obtain adequate release of the spine and facilitating the fusion. Except for the predetermined osteotomy segment, pedicle screws were implanted. After the screw placement completed, C-arm fluoroscopy was performed to check the internal fixation. After the pedicle placement, the spinous process, lamina, bilateral articular process and transverse process of the vertebral body scheduled for osteotomy was excised, and the spinous process, lamina and bilateral articular process of the upper and lower 1–2 vertebral bodies were removed to achieve decompression of the spinal cord and nerve roots., the convex side osteotomy of the vertebral body was performed first followed by the decompression. After resection of the vertebral body, the osteotomy surface and spinal nerve were carefully checked. After the correction operation, the C-arm fluoroscopy was performed to confirm that the implant was stable and in a good position.

Radiographic evaluation

Double-blind parameter measurements were performed by two experienced spine surgeons, and the measured parameters were averaged as the final result. The Adding-on and Non-adding-on groups were compared according to these variables: operation time, screw number, fusion length, estimated blood loss, follow-up duration, and radiographic parameters. Radiographic parameters included the primary curve, cranial curve, caudal curve, thoracic kyphosis, lumbar lordosis, thoracic apical vertebral translation (AVT), coronal balance (CB), clavicular angle (CA), coracoid height difference (CHD), clavicle-rib intersection difference (CRID), radiographic shoulder height (RSH), sagittal vertical axis (SVA) and slope of the line connecting the pedicles on the concave side of the upper and lower-end vertebrae (Tan α). To evaluate CB, draw a vertical plumb line from the midpoint of the C7 vertebral body to measure the horizontal distance between the plumb line and the midline of the sacrum. The SVA was determined by measuring the horizontal distance of the C7 plumb line to the posterior superior corner of the sacrum. The CA was determined by measuring the angle between the lines connecting the highest point of the clavicle on the horizontal plane. The CHD was determined by measuring the difference in height between horizontal lines passing through the upper edge of each coracoid process; negative values indicate right shoulder elevation, while positive values indicate left shoulder elevation. The CRID was determined by the height difference between the horizontal lines passing through the intersection of the upper edge of the clavicle and the outer edge of the second rib on both sides. The RSH was determined by the difference of soft tissue shadows directly above the acromioclavicular joint on standing anteroposterior films. The absolute values were used to check any deviation from the normal value, regardless of the direction of the shoulder (8–10). To assess Tan α, a line linking the pedicles on the concave side of the upper- and lower-end vertebrae was drawn, and the tangent of the angle between this line and the vertical plumb line was calculated.

Statistical analysis

Continuous variables are represented as the mean (SD) and were compared using an unpaired, 2-tailed t test. The categorical variables were compared through the $\chi 2$ or Fisher exact test. The significance of each variable in the training cohort was evaluated by univariate logistic regression analysis to investigate the independent risk factors of distal adding-on. Variables significantly associated with distal adding-on were included for the stepwise multivariate analysis. Based on the results of multivariable logistic regression analysis, the nomogram was developed through the rms R package, version 3.0 (http://www.r-project.org/). The nomograph is based on scaling each regression coefficient in the multiple logistic regression into a score of 0–100 points. The effect of the variable with the highest β coefficient is designated as 100 points. Add these points to get the total number of points, and then convert it into a prediction probability.

For the clinical use of the model, the total scores of each patient were calculated according to the nomogram. Receiver operating characteristic (ROC) curve analysis was used to get the optimal cutoff values, which were depended on maximizing the Youden index (i.e., sensitivity + specificity−1). The accuracy of the best cutoff value was assessed with the sensitivity, specificity, predictive values, and likelihood ratios. In the univariate analyses, $p < 0.05$ was considered to be significant statistically. In the stepwise multivariate analysis,

$p < 0.1$ was considered to have a trend statistically. All of the analyses were performed by SAS, version 9.1 (SAS Institute Inc.) and R, version 3.0 (11, 12).

Results

Altogether, 93 patients (21 in the Adding-on and 72 in the Non-adding-on group) were included in this study. The incidence of distal adding-on was 22.6% in the study. The mean age at surgery in the Adding-on group and the Non-adding-on group was 17.6 ± 3.9 years and 17.7 ± 3.9 years, respectively. The Risser grades in the Adding-on and Non-adding-on group were 3.2 ± 0.7 and 3.4 ± 0.9, respectively, and no significant difference was found. There was no significant difference in operation time, fusion length, screw number, estimated blood loss, or follow-up duration between the two groups. There was no significant difference in the main curve preoperatively, postoperatively, or at the final follow-up between the two groups (Table 1).

The characteristics of the primary thoracic curve, including the Cobb angle and flexibility, were similar in both groups. The Adding-on group had a stiffer cranial compensatory curve preoperatively ($p < 0.05$). In the Adding-on and the Non-adding-on group, the average angles of the caudal compensatory curve were 26.9° ± 12.4° and 20.1° ± 10.1°, respectively ($p = 0.01$). At the final follow-up, the average angles of the caudal compensatory curves were 26.2° ± 13.0° and 18.1° ± 9.9°, and a significant difference was found ($p = 0.01$). No significant difference in CB between the two groups either preoperatively or postoperatively was found. At the final follow-up, the average CB in the two groups was 20.8 ± 16.8 mm and 13.2 ± 13.5 mm, respectively ($p = 0.04$). In the SVA, there was no significant difference between the two groups preoperatively, postoperatively or at the final follow-up. Preoperatively, the average CA was 4.6 ± 2.9 mm and 2.9 ± 3.1 mm in the Adding-on and the Non-adding-on groups, respectively, and a significant difference was found ($p = 0.03$). In the CA, no significant difference was found postoperatively or at the final follow-up. The CHD, the CRID and the RSH preoperatively, postoperatively, or at the final follow-up. There was no significant difference in the incidence of thoracic kyphosis or lumbar lordosis. The average Post-AVT in the Adding-on and the Non-adding-on group were 17.8 ± 9.2 mm and 23.9 ± 12.5 mm, respectively ($p = 0.04$). At the final follow-up, the average Post-AVT was 15.5 ± 9.5 mm and 26.6 ± 13.2 mm, respectively ($p = 0.00$). Preoperatively, the average Tan α in the Adding-on group and the Non-adding-on group was −0.11 ± 0.28 and 0.01 ± 0.24, respectively ($p = 0.04$).

The LIV-last-touched vertebra (LTV) averaged 0.9 ± 0.8 levels and 1.1 ± 1.2 levels, and the LIV-last substantially touching vertebra (LSTV) averaged 0.6 ± 1.0 levels and 1.0 ± 1.1 levels in the Adding-on and the Non-adding-on group, respectively, with no significant differences. The LIV-lower-end vertebra (LEV) averaged 2.1 ± 0.9 levels and 2.5 ± 0.5 levels, the LIV-neutral vertebra (NV) averaged −1.3 ± 1.0 levels and −0.4 ± 0.7 levels, and the LIV-stable vertebra (SV) averaged −0.4 ± 1.1 levels and −0.6 ± 0.5 levels in the Adding-on and the Non-adding-on group, respectively, with no significant difference (Table 2).

Established risk factors, as well as clinical and radiological characteristics of adding-on, were selected as candidate variables for the prediction model. The variables associated with distal adding-on included the operation, including IP (OR: 0.02; 95% CI: 0–0.18; $p = 0.001$) and PVCR (OR: 0.08; 95% CI: 0.01–0.56; $p = 0.011$). Post-AVT (OR: 0.9; 95% CI: 0.83–0.97; $p = 0.008$) and Tan α (OR: 0.07; 95% CI: 0–1.45;

TABLE 1 Patient characteristics and outcomes between the two groups.

	Adding-on	Non-adding-on	*p* value*
No. of patient	21	72	
Age (yr)	17.6 (13–28)	17.7 (8–25)	0.87
Gender			
Male	12	42	0.59
Female	9	30	
Risser grade	3.2 (1.5–4)	3.4 (0–4)	0.31
Flexibility (%)			
Main curve	14.1 (4–23)	15.1 (4–27)	0.54
Cranial compensatory curve	32.9 (8–68)	15.9 (4–71)	0.02*
Caudal compensatory curve	35.9 (17–47)	42.5 (2–75)	0.23
Direction of main curve			
Left	6	15	0.32
Right	15	57	
No. of screw	14.2 (12–16)	13.6 (12–16)	0.32
No. of fused level	13.5 (12–15)	14.2 (13–15)	0.45
Op. time (min)	392 (417–515)	453 (390–515)	0.72
Estimated blood loss (ml)	1,182 (765–1,432)	1,092 (800–1,650)	0.78
Follow-up (mon)	39.2 (25–76)	42.5 (24–80)	0.82
Operation			
APSF	11	10	
IP	4	41	0.00
PVCR	6	21	
Etiology			
IS	19	58	
SMS	2	12	0.40
CS	0	2	

APSF, Anterior release and posterior spinal fusion; IP, anterior release, posterior internal distraction, and subsequent posterior spinal fusion; PVCR, the posterior vertebral column resection and posterior spinal fusion; IS, Idiopathic scoliosis; SMS, syringomyelia-associated scoliosis; CS, Congenital scoliosis.
*$p < 0.05$

TABLE 2 Radiographic parameters in the two groups.

	Adding-on	Non-adding on	*p* value
Main curve (deg)			
Pre-operative	98.1 (85–120)	104.3 (85–135)	0.06
Post-operative	37.5 (23–60)	39.1 (24–48)	0.46
Follow-up	39.6 (20–58)	40.2 (20–54)	0.58
Loss of correction	2.1 (−6–12)	1.4 (−10–14)	0.71
Cranial compensatory curve (deg)			
Pre-operative	42.8 (15–64)	49.2 (20–72)	0.10
Post-operative	24.4 (10–47)	29.3 (3–53)	0.11
Follow-up	23.9 (8–38)	27.4 (0–47)	0.22
Caudal compensatory curve (deg)			
Pre-operative	49.0 (29–74)	50.3 (21–80)	0.71
Post-operative	26.9 (5–48)	20.1 (5–47)	0.01*
Follow-up	26.2 (5–47)	18.1 (5–52)	0.01*
Thoracic AVT (mm)			
Pre-operative	77.4 (70–90)	80.2 (50–100)	0.30
Post-operative	17.8 (5–40)	23.9 (5–40)	0.04*
Follow-up	15.5 (5–40)	26.6 (10–45)	0.00*
Thoracic kyphosis (T5-T12) (deg)			
Pre-operative	53.3 (24–90)	50.7 (10–115)	0.68
Post-operative	28.2 (18–40)	31.6 (10–60)	0.18
Follow-up	28.8 (18–51)	29.6 (10–58)	0.77
Lumbar lordosis (T12-S1) (deg)			
Pre-operative	57.8 (49–74)	59.6 (31–90)	0.72
Post-operative	45.1 (31–59)	44.3 (8–62)	0.78
Follow-up	45.3 (36–54)	45.2 (5–69)	0.97
Coronal balance (mm)			
Pre-operative	11.2 (0–50)	13.8 (0–50)	0.45
Post-operative	17.9 (0–42)	13.3 (0–60)	0.20
Follow-up	20.8 (0–38)	13.2 (0–43)	0.04*
Sagittal vertical axis (mm)			
Pre-operative	24.8 (0–70)	18.5 (0–65)	0.18
Post-operative	21.9 (0–80)	14.8 (0–60)	0.09
Follow-up	14.8 (0–30)	19.9 (0–70)	0.22
CA (deg)			
Pre-operative	4.6 (0–9)	2.9 (0–14)	0.03*
Post-operative	4.8 (0–15)	3.4 (0–9)	0.10
Follow-up	3.6 (0–5)	3.2 (0–10)	0.52
CHD (mm)			
Pre-operative	12.1 (0–28)	8.7 (0–45)	0.17
Post-operative	11.7 (0–28)	12.8 (0–32)	0.63
Follow-up	7.3 (0–20)	9.6 (0–30)	0.27
CRID (mm)			
Pre-operative	3.9 (0–13)	4.0 (0–15)	0.91
Post-operative	3.4 (0–18)	3.9 (0–13)	0.49
Follow-up	4.1 (0–12)	4.2 (0–13)	0.96
RSH (mm)			
Pre-operative	9.6 (0–29)	8.1 (0–30)	0.52
Post-operative	11.9 (0–32)	10.0 (0–28)	0.40
Follow-up	9.1 (4–30)	7.9 (4–25)	0.43
Tan α (deg)	−0.11 (−0.55–0.28)	0.01 (−0.67–0.31)	0.04*
LIV-LTV (level)	0.9 (0–2)	1.1 (0–3)	0.62
LIV-LSTV (level)	0.6 (−1–2)	1.0 (0–3)	0.39
LIV-LEV (level)	2.1 (1–3)	2.5 (1–3)	0.32
LIV-NV (level)	−1.3 (−3–0)	−0.4 (−1–2)	0.07
LIV-SV (level)	−0.4 (−2–1)	−0.6 (−1–0)	0.68

AVT, apical vertebra translation; CA, Clavicular angle; CHD, Coracoid height difference; CRID, Clavicle-rib cage intersection difference; RSH, Radiographic shoulder height; Tan α, the slope of the line connecting the pedicles on the concave side of the upper and lower end vertebrae; LIV, lower instrumented vertebra; LTV, last touching vertebra; LSTV, last substantially touching vertebra; LEV, lower end vertebra; NV, neutral vertebra; SV, stable vertebra.
*$p < 0.05$

$p = 0.085$) were additional related factors (Table 3). Combining these factors, the nomogram achieved a concordance index of 0.92 in predicting distal adding-on and had well-fitted calibration curves (Figure 1).

Discussion

In this study, all patients with severe and rigid scoliosis had a main curve of more than 80° on normal radiographs and the flexibility of less than 30% on bending radiographs. The incidence of distal adding-on was approximately 22.6% at a minimum 2-year follow-up, which is lower than that reported in the literature (3). For common AIS patients with a smaller curve, the incidence of distal adding-on has been reported to be 2%–13% (13). There are many hypotheses regarding the causes of distal adding-on in common AIS (14–17). However, severe and rigid scoliosis, as a special disease form, has a unique etiology, clinical manifestations and internal mechanisms that are different from those of AIS. Consequently, the mechanism and causes of the distal adding-on phenomenon have rarely been studied in depth.

TABLE 3 Independent prognostic factors of distal adding-on.

Characteristics	SE	OR	CI	*p**
IP	1.12	0.02	0–0.18	0.001*
PVCR	0.98	0.08	0.01–0.56	0.011*
Post-AVT	0.04	0.90	0.83–0.97	0.008*
Tan α (deg)	1.57	0.07	0–1.45	0.085*

IP, anterior release, posterior internal distraction, and subsequent posterior spinal fusion; PVCR, the posterior vertebral column resection and posterior spinal fusion; AVT, the apical vertebra translation.
*$p < 0.1$

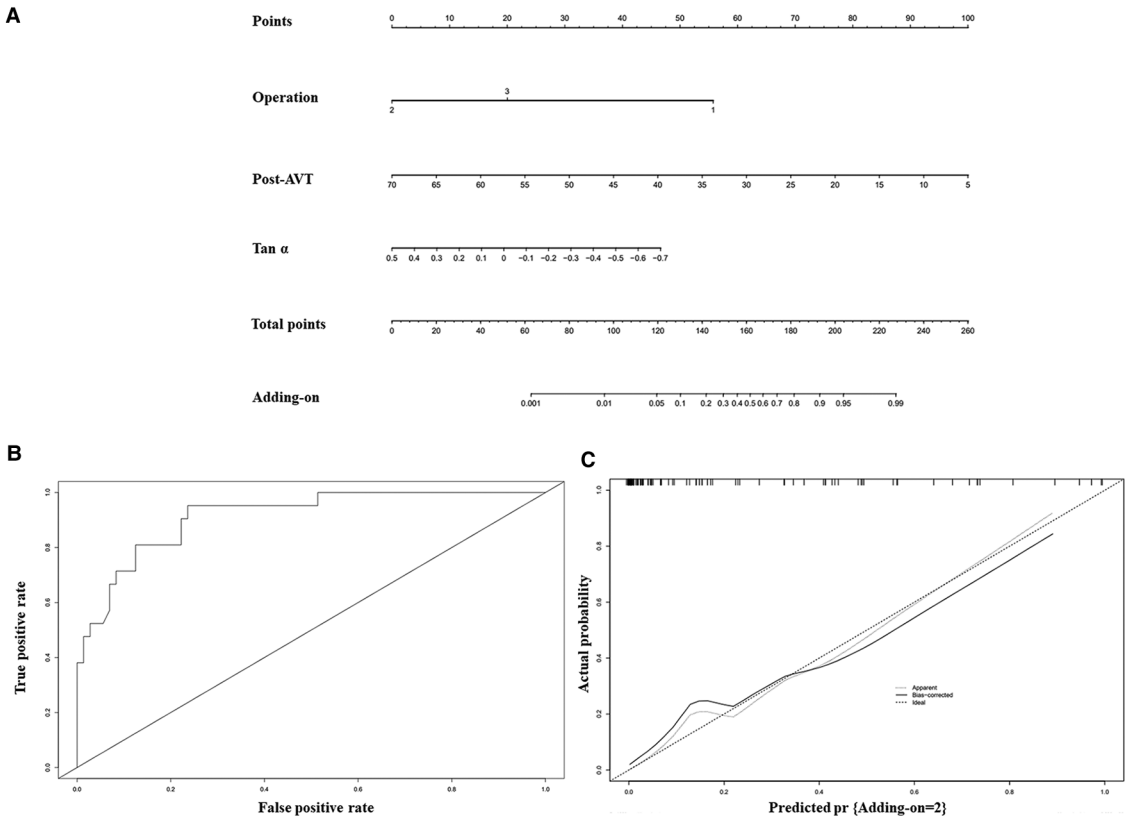

FIGURE 1
A nomogram for predicting the adding-on phenomenon was created based on independent prognostic factors (A). To use the nomogram, find the position of each variable on the corresponding axis, draw a line to the points axis for the number of points, add the points from all of the variables, and draw a line from the total points axis to determine the probabilities of the adding-on phenomenon. The operation 1, 2 and 3 represent APSF, IP, and PVCR respectively. The ROC curve (area under the curve 0.92) (B) and the calibration (C) indicate that the model performs well.

Skeletal maturity is thought to be related to the occurrence of distal adding-on, and some researchers believe that lower skeletal maturity may also be associated (18). In this study, no obvious difference in the Risser grade was found, which may be because the patient reached bone maturity at the time of operation. Therefore, further research is needed to confirm this theory. Another factor to consider is the etiology of the patients, as treatment strategies may vary widely under different etiologies. Different etiologies can also lead to more confounding factors, complicating the study of distal adding-on in scoliosis. There are some related studies comparing scoliosis with different etiologies. A classic study by Sha et al. compared outcomes after spinal fusion surgery in syringomyelia-associated scoliosis (SMS) and AIS patients and found that despite the differences in preoperative status, AIS and SMS patients had comparable clinical and radiographic outcomes (19). Nevertheless, there is little data on distal adding-on in these patients. In this study, the etiology was not identified in severe and rigid scoliosis as a predictor of distal adding-on, which may mainly be limited by the sample size of syringomyelia-associated scoliosis and congenital scoliosis (CS).

According to our study, the correction rate of the primary curve was similar, and therefore distal adding-on caused by overcorrection was not observed. Notably, Post-AVT was associated with distal adding-on in the stepwise logistic regression analysis. As the degree of Post-AVT decreases, the probability of adding-on increases according to the nomogram. We hypothesize that as the degree of Post-AVT decreases, the body trunk requires greater compensatory force at the caudal side to maintain body balance. When this compensatory force exceeds a certain critical value, adding-on may appear, which may also explain why the CB and caudal disc angle in the Adding-on group were greater at the last follow-up. During the process of body trunk dynamic balance restoration, the CB and caudal disc angle may change to achieve somatic balance. Except for the cause of the caudal side, the shoulder balance needs to be observed because it is closely related to distal adding-on in AIS patients, especially in Lenke type II. In previous studies, distal adding-on was shown to play a positive

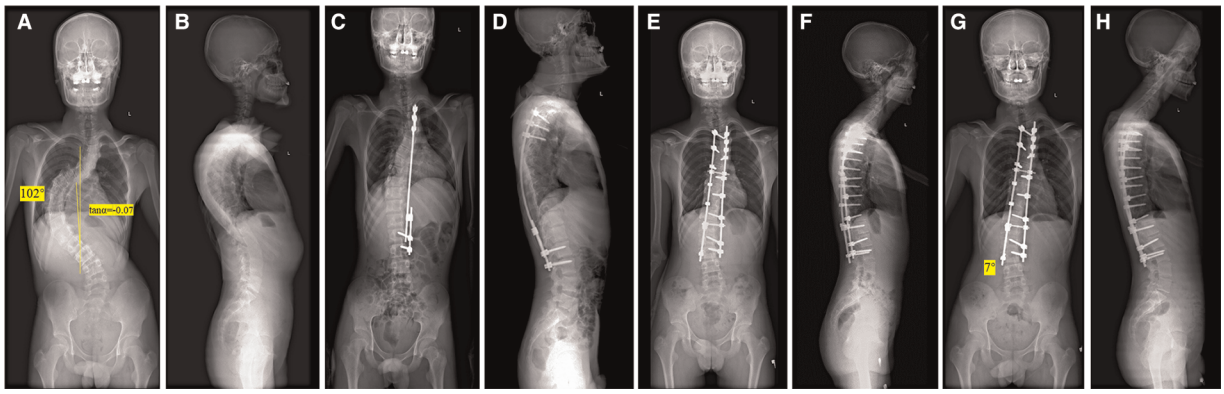

FIGURE 2
A 15-year-old boy with a severe and rigid thoracic curve (**A**,**B**). The radiographs demonstrate a thoracic curve angle of 102°, and the slope of the line connecting the pedicles on the concave side of the upper- and lower-end vertebrae (Tan α) is −0.07. After-distraction posteroanterior (**C**) and lateral (**D**) radiographs demonstrate well-maintained global coronal and sagittal balance. Postoperative posteroanterior (**E**) and lateral (**F**) radiographs following posterior spinal fusion from T2 to L3 demonstrate well-maintained global coronal and sagittal balance. Radiographs made at the final follow-up (**G**,**H**) reveal the appearance of the distal adding-on phenomenon with an intervertebral space angle below the LIV of 7°.

role in maintaining shoulder balance (20). However, no significant correlation was observed in the parameters of shoulder balance, including CA, CHD, CRID, and RSH, between the groups with and without distal adding-on in this study. One possible explanation is that the relationship between the shoulder balance and distal adding-on is so weak that it is difficult to identify in severe and rigid scoliosis.

Another highly controversial issue is the relationship between LIV and LTV, LSTV, LEV, NV, and SV. Substantial evidence suggests that inappropriate LIV selection may lead to distal adding-on (15, 21). It is currently recognized that LIV should be extended to or beyond the LTV/LSTV to prevent distal adding-on. In most patients in our study, the instrumented levels were extended to or beyond the LTV/LSTV; therefore, relevant evidence still needs to be further explored.

Notably, the preoperative Tan α in severe and rigid scoliosis was found to be related to distal adding-on. According to the nomogram, as the preoperative Tan α decreased from positive to negative values, the probability of distal adding-on increased. This phenomenon shares many similarities with the previously proposed S-line in Lenke type 5C but differs in its definition and essence (22). In Lenke type 5C AIS patients, spine surgeons change the S-line from a positive to a negative condition with one of a number of techniques to avoid postoperative coronal decompensation. This demonstrates that

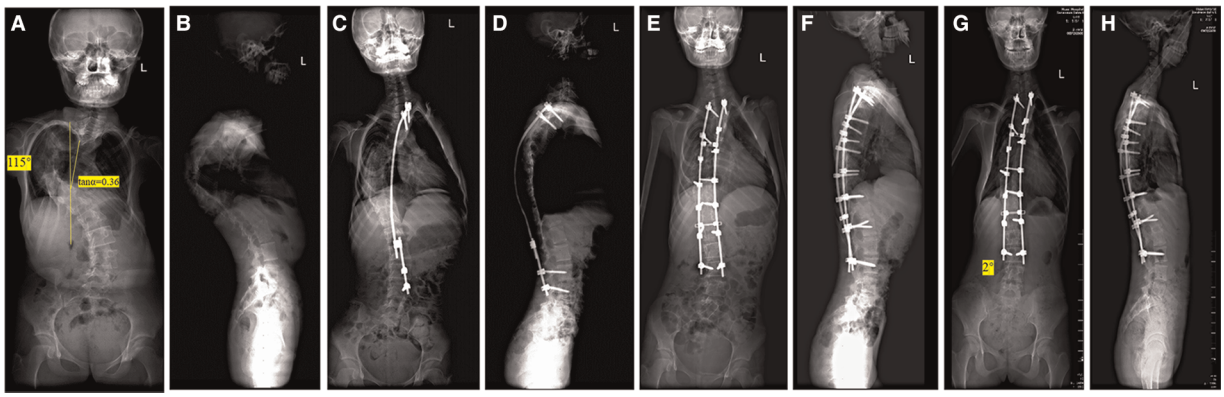

FIGURE 3
A 16-year-old girl with a severe and rigid thoracic curve (**A**,**B**). The radiographs demonstrate a thoracic curve angle of 115°, and the slope of the line connecting the pedicles on the concave side of the upper- and lower-end vertebrae (Tan α) is 0.36. After-distraction posteroanterior (**C**) and lateral (**D**) radiographs demonstrate well-maintained global coronal and sagittal balance. Postoperative posteroanterior (**E**) and lateral (**F**) radiographs following posterior spinal fusion from T2 to L3 demonstrate well-maintained global coronal and sagittal balance. Radiographs made at the final follow-up (**G**,**H**) reveal well-maintained global coronal and sagittal balance with absence of the distal adding-on phenomenon.

connecting lines such as the S-line play a role in predicting or reflecting the state of body trunk dynamic balance restoration. Similarly, the preoperative Tan α predicted distal adding-on at the last follow-up. Our data include a 15-year-old boy and the radiographs demonstrated a thoracic curve of 102° and a Tan α of −0.07. Radiographs made 2 years after surgery revealed the appearance of the distal adding-on phenomenon with an intervertebral space angle below the LIV of 7° (**Figure 2**). In 16-year-old girl and the radiographs demonstrated a thoracic curve of 115° and a Tan α of 0.36). Two years after surgery, radiographs made obtained well-maintained global coronal and sagittal balance with the absence of distal adding on (**Figure 3**). We hypothesize that as the preoperative Tan α decreases from positive to negative, the stress area maintaining body trunk balance on the caudal side moves down, and under similar instrumented levels, the stress exceeds a certain acceptable critical value, decompensation occurs in the body trunk, and distal adding-on soon develops.

Among the three surgical approaches, the IP procedure demonstrated the best effect on preventing distal adding-on, followed by PVCR; APSF was the most likely to increase the probability of distal adding-on. Compared with APSF, IP and PVCR can release the internal stress of the spine to a greater extent and thus largely prevent the occurrence of distal adding-on. We combined the indications for distal adding on to create a nomogram, whose results suggest that when the preoperative Tan α is a negative value, spine surgeons should select the appropriate LIV and prioritize IP and PVCR for preventing the occurrence of distal adding-on. And during the correction process, a smaller Post-AVT should not be overly pursued.

This study has several limitations. First, it was a single-center study performed retrospectively. Second, patients with main lumbar curvature were excluded from this study; therefore, not all types of severe and rigid scoliosis were analyzed. Finally, there were no related data on the Research Society-22 score for evaluating the clinical outcome. Finally, the patients in the data set possessed their own characteristics, and the treatment methods also involved the characteristics of the center. Therefore, whether it is effective in other larger data sets still needs further verification and further research should be conducted to optimize these deficiencies.

Conclusion

In conclusion, by combining associated factors of distal adding-on in severe and rigid scoliosis patients, a nomogram was constructed. The operation, Post-AVT and Tan α were identified as predictors of distal adding-on. For patient with a negative Tanα in severe and rigid scoliosis, the risk of distal adding-on tended to increase, and it is recommended to give priority to IP or PVCR. In the final correction, a smaller Post-AVT should not be pursued excessively.

Data availability statement

The original contributions presented in the study are included in the article/Supplementary Material, further inquiries can be directed to the corresponding author/s.

Ethics statement

Written informed consent was obtained from the individual(s) for the publication of any potentially identifiable images or data included in this article.

Author contributions

All authors listed have made substantial, direct, and intellectual contribution to this work and approved for publication. All authors contributed to the article and approved the submitted version.

Funding

This study was supported in part by The Science and Technology Project of the Health Planning Committee of Sichuan (grant no. 21PJ036), and Chengdu Science and Technology Project (grant no. 2021-YF05-00743-SN) and National Natural Science Foundation of China (grant no. 82102521).

Acknowledgments

The authors would like to thank AJE (www.aje.com) for English language editing.

Conflict of interest

The authors declare that the research was conducted in the absence of any commercial or financial relationships that could be construed as a potential conflict of interest.

Publisher's note

All claims expressed in this article are solely those of the authors and do not necessarily represent those of their affiliated organizations, or those of the publisher, the editors and the reviewers. Any product that may be evaluated in this article, or claim that may be made by its manufacturer, is not guaranteed or endorsed by the publisher.

References

1. Koller H, Zenner J, Gajic V, Meier O, Ferraris L, Hitzl WJESJ. The impact of halo-gravity traction on curve rigidity and pulmonary function in the treatment of severe and rigid scoliosis and kyphoscoliosis: a clinical study and narrative review of the literature. *Eur Spine J*. (2012) 21(3):514–29. doi: 10.1007/s00586-011-2046-5

2. Sucato DJ. Management of severe spinal deformity scoliosis and kyphosis. *Spine*. (2019) 35(25):2186–92. doi: 10.1097/brs.0b013e3181feab19

3. Lei Z, Yong H, Yuan S, Su Q, Ning FJS. Distal adding-on and risk factors in severe and rigid scoliosis. *Spine*. (2016) 42(3):160. doi: 10.1097/BRS.0000000000001684

4. Wang Y, Bünger CE, Zhang Y, Wu C, Hansen ES. Distal adding-on in lenke 1a scoliosis. *Spine*. (2013) 38(6):490–5. doi: 10.1097/BRS.0b013e318273ed11

5. Roye BD, Matsumoto H, Fano AN, Marciano GF, Lyer RR, Body A, et al. Distal adding-on in adolescent idiopathic scoliosis results in diminished health-related quality of life at 10 years following posterior spinal fusion. *J Spine Deformity*. (2021) 10(3):515–26. doi: 10.1007/s43390-021-00432-1

6. Suk SI, Kim JH, Cho KJ, Kim SS, Han LJESJ. Is anterior release necessary in severe scoliosis treated by posterior segmental pedicle screw fixation? *Eur Spine J*. (2007) 16:1359–65. doi: 10.1007/s00586-007-0334-x

7. Zhou C, Liu L, Song Y, Liu H, Li T, Gong Q, et al. Anterior release internal distraction and posterior spinal fusion for severe and rigid scoliosis. *Spine*. (2013) 38(22):1411–7. doi: 10.1097/BRS.0b013e3182a3cd90

8. Marks M, Petcharaporn M, Betz RR, Clements D, Lenke L, Newton PO. Outcomes of surgical treatment in male versus female adolescent idiopathic scoliosis patients. *Spine*. (2007) 32(5):544–9. doi: 10.1097/01.brs.0000256908.51822.6e

9. Legaye J, Duvalbeaupère G. Sagittal plane alignment of the spine and gravity: a radiological and clinical evaluation. *Acta Orthop Belg*. (2005) 71(2):213–20.

10. Hong JY, Suh SW, Modi HN, Yang JH, Park SY. Analysis of factors that affect shoulder balance after correction surgery in scoliosis: a global analysis of all the curvature types. *Eur Spine J*. (2013) 22(6):1273–85. doi: 10.1007/s00586-013-2697-5

11. Yuhree K, Georgios A, Jason D, Thuy B, Lauren M, Shishir K, et al. Nomograms to predict recurrence-free and overall survival after curative resection of adrenocortical carcinoma. *JAMA Surg*. (2016) 151(4):365–73. doi: 10.1001/jamasurg.2015.4516

12. Zhengqing L, Jun L, Dong W, Yong X, Qing W, Si A, et al. Nomogram for preoperative estimation of microvascular invasion risk in hepatitis B virus–related hepatocellular carcinoma within the milan criteria. *JAMA Surg*. (2016) 151(4):356–63. doi: 10.1001/jamasurg.2015.4257

13. Wang Y, Hansen ES, Høy K, Wu C, Bünger CE. Distal adding-on phenomenon in lenke 1a scoliosis: risk factor identification and treatment strategy comparison. *Spine*. (2011) 36(14):1113–22. doi: 10.1097/BRS.0b013e3181f51e95

14. Wang Y, Bünger CE, Zhang YQ, Wu CS, Li HS. Distal adding-on in lenke 1a scoliosis: how to more effectively determine the onset of distal adding-on. *Spine*. (2013) 36(6):490–5. doi: 10.1097/BRS.0b013e318273ed11

15. Matsumoto M, Watanabe K, Hosogane N, Kawakami N, Tsuji T, Uno K, et al. Postoperative distal adding-on and related factors in lenke type 1a curve. *Spine*. (2013) 38(9):737–44. doi: 10.1097/BRS.0b013e318279b666

16. Wang Y, Bünger C, Zhang Y, Wu C, Li H, Hansen ES. Distal adding on in lenke 1a scoliosis: what causes it? how can it be prevented? *Spine Deform*. (2014) 2(4):301–7. doi: 10.1016/j.jspd.2014.04.003

17. Xiaodong Q, Chao X, Leilei X, Fei S, Huang Y, Yong Q, et al. Natural history of postoperative adding-on in adolescent idiopathic scoliosis: what are the risk factors for progressive adding-on? *Biomed Res Int*. (2018) 2018:1–8. doi: 10.1155/2018/3247010

18. Schlechter J, Newton P, Upasani V, Yaszay B, Lenke L, Betz R, et al. P130. Risk factors for distal adding-on identified: what to watch out for. *Spine J*. (2008) 8(5-supp-S):164S. doi: 10.1016/j.spinee.2008.06.772

19. Sha S, Yong Q, Sun W, Xiao H, Zhu W, Zhu Z, et al. Does surgical correction of right thoracic scoliosis in syringomyelia produce outcomes similar to those in adolescent idiopathic scoliosis? *J Bone Joint Surg Am*. (2016) 98:295–302. doi: 10.2106/JBJS.O.00428

20. Cao K, Watanabe K, Hosogane N, Toyama Y, Yonezawa I, Machida M, et al. Association of postoperative shoulder balance with adding-on in lenke type ii adolescent idiopathic scoliosis. *Spine*. (2014) 39(12):E705. doi: 10.1097/BRS.0000000000000325

21. Suk SI, Lee SM, Chung ER, Kim JH, Kim WJ, Sohn HMJS. Determination of distal fusion level with segmental pedicle screw fixation in single thoracic idiopathic scoliosis. *Spine*. (2003) 28(5):484–91. doi: 10.1097/01.BRS.0000048653.75549.40

22. Zhang T, Shu S, Jing W, Gu Q, Bao HJESJ. Optimizing the fusion level for lenke 5c adolescent idiopathic scoliosis: is the S-line a validated and reproducible tool to predict coronal decompensation? *Euro Spine J*. (2021) 1:1–8. doi: 10.1007/s00586-021-06781-9

frontiers | Frontiers in Surgery

TYPE Original Research
PUBLISHED 06 January 2023
DOI 10.3389/fsurg.2022.1047603

Check for updates

OPEN ACCESS

EDITED BY
Yan Yu,
Tongji University School of Medicine, China

REVIEWED BY
Yuhui Chen,
Southern Medical University, China
Xianyue Shen,
Second Affiliated Hospital of Jilin University, China
Song Wang,
Tianjin Hospital, China

*CORRESPONDENCE
Peifu Tang
pftang301@163.com
Licheng Zhang
zhanglicheng@301hospital.com.cn
Jiantao Li
lijiantao618@163.com

†These authors have contributed equally to this work

SPECIALTY SECTION
This article was submitted to Orthopedic Surgery, a section of the journal Frontiers in Surgery

RECEIVED 18 September 2022
ACCEPTED 07 November 2022
PUBLISHED 06 January 2023

CITATION
Xu G, Wang D, Zhang H, Xu C, Li H, Zhang W, Li J, Zhang L and Tang P (2023) Prediction of osteoporosis from proximal femoral cortical bone thickness and Hounsfield unit value with clinical significance.
Front. Surg. 9:1047603.
doi: 10.3389/fsurg.2022.1047603

COPYRIGHT
© 2023 Xu, Wang, Zhang, Xu, Li, Zhang, Li, Zhang and Tang. This is an open-access article distributed under the terms of the Creative Commons Attribution License (CC BY). The use, distribution or reproduction in other forums is permitted, provided the original author(s) and the copyright owner(s) are credited and that the original publication in this journal is cited, in accordance with accepted academic practice. No use, distribution or reproduction is permitted which does not comply with these terms.

Prediction of osteoporosis from proximal femoral cortical bone thickness and Hounsfield unit value with clinical significance

Gaoxiang Xu[1,2,3†], Daofeng Wang[1,2,3†], Hao Zhang[2,3†], Cheng Xu[2,3], Hua Li[2,3], Wupeng Zhang[2,3,4], Jiantao Li[2,3*], Licheng Zhang[2,3*] and Peifu Tang[2,3*]

[1]Medical School of Chinese PLA, Chinese PLA General Hospital, Beijing, China, [2]Department of Orthopedics, The Fourth Medical Center, Chinese PLA General Hospital, Beijing, China, [3]National Clinical Research Center for Orthopedics, Sports Medicine and Rehabilitation, Chinese PLA General Hospital, Beijing, China, [4]School of Medicine, Nankai University, Tianjin, China

Background: Utilizing dual-energy x-ray absorptiometry (DXA) to assess bone mineral density (BMD) was not routine in many clinical scenarios, leading to missed diagnoses of osteoporosis. The objective of this study is to obtain effective parameters from hip computer tomography (CT) to screen patients with osteoporosis and predict their clinical outcomes.
Methods: A total of 375 patients with hip CT scans for intertrochanteric fracture were included. Among them, 56 patients possessed the data of both hip CT scans and DXA and were settled as a training group. The cortical bone thickness (CTh) and Hounsfield unit (HU) values were abstracted from 31 regions of interest (ROIs) of the proximal femur. In the training group, the correlations between these parameters and BMD were investigated, and their diagnostic efficiency of osteoporosis was assessed. Finally, 375 patients were divided into osteoporotic and nonosteoporotic groups based on the optimal cut-off values, and the clinical difference between subgroups was evaluated.
Results: The CTh value of ROI 21 and the HU value of ROI 14 were moderately correlated with the hip BMD [$r = 0.475$ and 0.445 ($p < 0.001$), respectively]. The best diagnostic effect could be obtained by defining osteoporosis as CTh value < 3.19 mm in ROI 21 or HU value < 424.97 HU in ROI 14, with accuracies of 0.821 and 0.883, sensitivities of 84% and 76%, and specificities of 71% and 87%, respectively. The clinical outcome of the nonosteoporotic group was better than that of the osteoporotic group regardless of the division criteria.
Conclusion: The CTh and HU values of specific cortex sites in the proximal femur were positively correlated with BMD of DXA at the hip. Thresholds for osteoporosis based on CTh and HU values could be utilized to screen osteoporosis and predict clinical outcomes.

KEYWORDS
osteoporosis, bone mineral density, proximal femur, cortical bone thickness, Hounsfield unit

Introduction

Osteoporosis, an age-related illness marked by reduced bone mineral density (BMD) and microarchitectural deterioration, could lead to a series of osteoporotic fractures (1). In the global population over 50 years old, 33% of women and 20% of men would encounter one or more osteoporotic fractures (2). The mortality rate within 1 year was as high as 20%, and the permanent disability rate was as high as 50% (3). Meanwhile, due to reduced bone strength, the incidence of postoperative complications of osteoporotic fractures was significantly higher than that of nonosteoporotic fractures (4, 5). These cost the China healthcare system approximately 18.9 billion dollars annually (6). Thus, an early screening of osteoporosis would be advantageous to allocate considerable resources for preventing osteoporotic fractures and postoperative complications without exceeding those incurred following these problems (7).

Dual-energy x-ray absorptiometry (DXA) and quantitative computed tomography (QCT) have been applied to identify osteoporosis as the gold standard (8). BMD assessed in exact areas of the hip or lumbar spine was commonly utilized to evaluate bone health and fracture risk (9). However, the lack of both tests in primary medical institutions, the untimely examination of patients in senior medical institutions, and the additional medical costs resulting from routine examination make many patients easily missed. Therefore, how to apply the existing imaging data to screen osteoporosis to avoid the occurrence of osteoporotic fractures and postoperative complications has attracted high attention of researchers.

Cortical thickness could be more easily acquired in routine orthopedic radiographic examinations, and this value in the proximal femur has been proven to be correlated with BMD and of ability to predict osteoporosis (10). However, which part of the proximal femur possessed the highest predictive value had been seldom discussed. Additionally, the correlation between HU values of the cortex and BMD was unclear. In addition, no study has explored the correlation between these parameters and clinical outcomes.

Thus, we attracted cortical bone thickness (CTh) and Hounsfield unit (HU) values from the cortical bone in hip computed tomography (CT) to evaluate the correlation between these parameters and BMD. This study aimed to (1) investigate the correlation between the anatomical parameters of cortical bone and BMD assessed with DXA scans; (2) calculate the sensitivity, specificity, and area under the curve (AUC) of the parameters with higher correlation to predict osteoporosis; and (3) evaluate the clinical differences between osteoporotic and nonosteoporotic patients with intertrochanteric fractures divided by the cut-off values with optimal diagnostic efficiency.

Materials and methods

Patient selection

Nine hundred and sixty-three patients with intertrochanteric fractures were admitted to our hospital from September 2009 to March 2017. According to the inclusion and exclusion process shown in **Figure 1**, 375 patients were included for clinical evaluation. Among them, 56 patients that had received CT scans from a CT machine (Siemens AG, Erlangen, Germany) and a contemporary DXA (with a Hologic Discovery system) at the unaffected hip and lumber spine at our institution within 1 month were identified for the calculation of correlation between BMD and anatomical parameters and the diagnosis efficiency of osteoporosis. This study was approved by the institutional review board (S2020-114-01).

Region of interest for cortical bone

Patient hip CT data in the Digital Imaging and Communications in Medicine (DICOM) format were imported in Mimics 20.0 (Materialise, Belgium), and bone tissue was separated by the threshold value of 0–350 HU displaying the outline of bone clearly. Then, according to our previous study (11), 31 regions of interest (ROIs) that best reflect the stress distribution pattern in the proximal femur were defined to abstract the CTh and HU values of cortical bone.

Femoral neck

The bottom and subcephalic sites of the femoral neck were determined using the method described by Sparks et al.(12) and Zhang et al. (13). Furthermore, the middle site of the femoral neck was determined. Then, Sections 1–3 at the above sites perpendicular to the femoral neck axis were established (**Figure 2**). According to the method of our previous study (11), the ROIs of upper, lower, anterior, and posterior cortical bone in each section were determined as follows: the longest line between the upper and lower walls (purple line) and the longest line between the anterior and posterior walls (green line) were drawn and intersected with cortical bone, resulting in the intersections regarded as the ROIs 1–12 of cortical bone in each section of the femoral neck to extract CTh and HU values (**Figures 3A–C**). Then, the relevance between BMD and these parameters was analyzed.

Femoral shaft

By the method described by Zhang et al. (14), five sections perpendicular to the femoral shaft axis were determined: S4 at

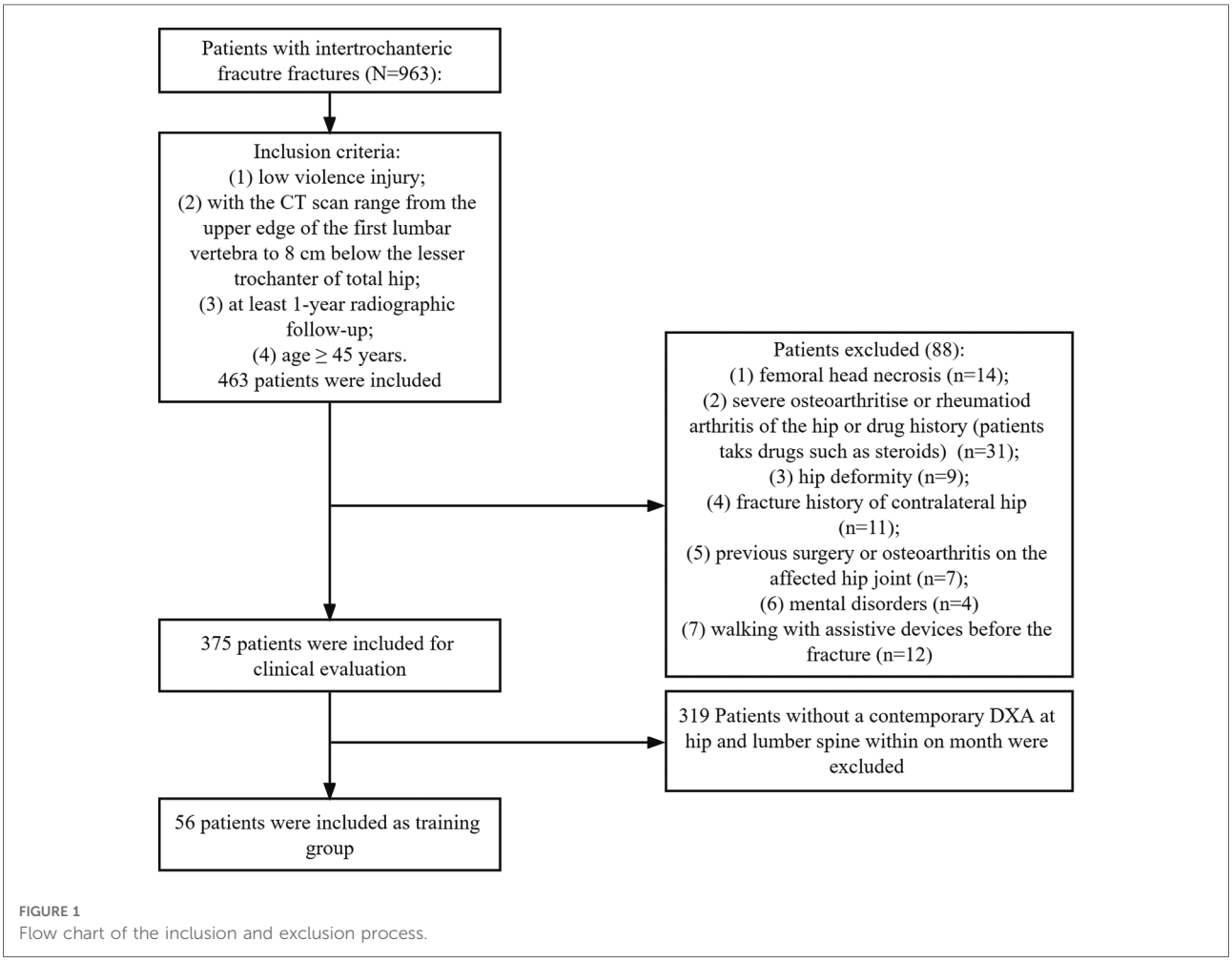

FIGURE 1
Flow chart of the inclusion and exclusion process.

20 mm above the upper edge of the femoral lesser trochanter, S5 at the upper edge of the femoral lesser trochanter, S6 at the vertex of the femoral lesser trochanter, S7 at the lower edge of the femoral lesser trochanter, and S8 at the 20 mm below the vertex of the femoral lesser trochanter (**Figure 2**). According to the method of our previous study (11), in each section, the longest line (red line) between the medial and lateral walls and the longest line (yellow line) between the anterior and posterior walls were drawn to determine the ROIs 13–31 in each section of the femoral shaft to extract CTh and HU values (**Figures 3D–H**). Since it intersected with the femoral head, the medial wall of S4 was excluded.

Subgroup analysis

BMD values of the lumbar spine (L1–4) and healthy hip sites were measured by a DXA scanner. According to the World Health Organization criteria: a patient with T-value at any region less than −2.5 was diagnosed with osteoporosis. Then, the sensitivity, specificity, positive predictive value, and negative predictive value of CTh and HU values in different areas for screening osteoporosis were assessed.

Clinical evaluation

After the cut-off values with optimal diagnostic efficiency of osteoporosis were determined, 375 patients with intertrochanteric hip fracture were divided into osteoporosis and nonosteoporosis groups. The demographic information, functional parameters, and complications of different groups were collected for clinical evaluation.

Functional parameters

Timed Up and Go (TUG) test (15), the Functional Independence Measure (FIM) (16), 2-min walk test (2MWT) (17), and Parker–Palmer scores (18) were obtained in medical records and used to assess the physical function at the final follow-up.

Complications

Implant breakage, reduction loss, nonunion, excessive sliding, cut-out, periprosthetic fracture, infection, and loss of

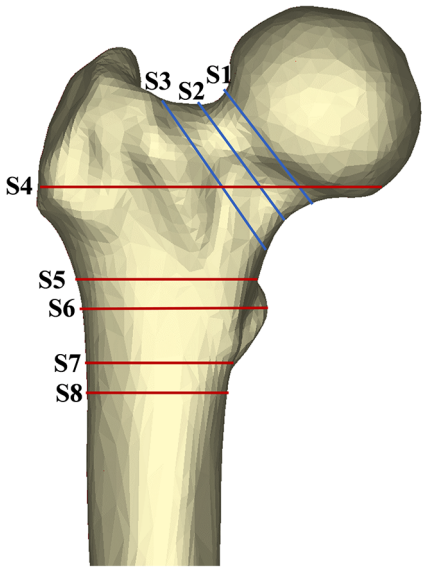

FIGURE 2
Area of exploration in proximal femoral region. The femoral neck was divided by axial S1–3 (sections at the subcephalic, middle, and bottom sites of the femoral neck, respectively). Similarly, the shaft region was divided by S4–8 (sections at 20 mm above the upper edge of the femoral lesser trochanter, the upper edge of the femoral lesser trochanter, the vertex of the femoral lesser trochanter, the lower edge of the femoral lesser trochanter, and the 20 mm below the vertex of the femoral lesser trochanter, respectively).

mobility were recorded as complications. Reduction loss was defined as a change of femoral neck-shaft angle >10°, and excessive sliding was defined as a sliding distance ≥10 mm in postoperative radiography follow-up (19).

Reliability analysis

The intraclass correlation coefficient (ICC) was used to assess the reliability of the measurement methods established in this study. The CTh and HU values were measured twice independently at 2-week intervals by an orthopedic surgeon blinded to the result of the DXA scan. Independent measurements were performed by other two orthopedic colleagues within a 2-week period. The interobserver and intraobserver correlation coefficients were then calculated.

Statistical analysis

Statistical analysis was conducted using the SPSS software (version 26.0, IBM, Armonk, NY, United States) and R package (3.6.3 version, statistical analysis and visualization). Student's *t*-test was utilized to analyze the continuous data conforming to nonosteoporosis distribution, or a nonparametric rank sum test was used. Chi-square analysis or Fisher's exact test was performed for categorical variables. Pearson's correlation coefficient (*r*) was utilized to test the association between CTh

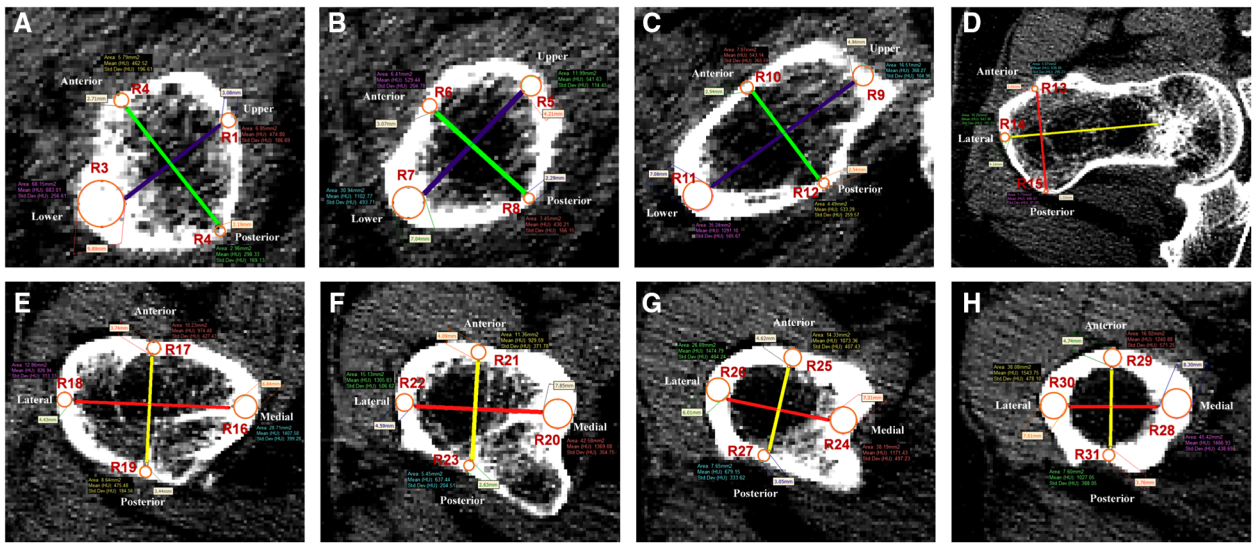

FIGURE 3
Thirty-one regions of interest were defined in the femoral neck and shaft regions. (**A–C**) Femoral neck region. Purple line was the longest diameter between the upper and lower walls of femoral neck. Green line was the longest diameter between the anterior and posterior walls of femoral neck. R1–12 were defined as the measurement points of S1–3. (**D–H**) Femoral shaft region. Red line was the longest diameter between the medial and lateral walls of the femoral shaft. Yellow line was the longest diameter between the anterior and posterior walls of the femoral shaft. R13–31 were defined as the measurement points of S4–8.

value, HU value, and BMD. The receiver operating characteristic (ROC) curve was used to determine the diagnostic efficiency of the parameters of ROIs for osteoporosis. The cut-off values of variables were determined by calculating AUC. Then, sensitivity, specificity, positive predictive value, and negative predictive value were calculated. The level of statistical significance was defined as $p < 0.05$.

Results

Correlation between hip BMD, CTh, and HU values

Fifty-six patients (40 female and 16 male) with a mean age of 82 ± 9 years were enrolled for the calculation of Pearson's correlation coefficient and the diagnostic efficiency of osteoporosis in our study. The mean BMD values of the hip and lumbar spine were 0.57 ± 0.19 and 0.82 ± 0.16 g/cm^2, respectively. Other characteristics are shown in **Table 1**.

Correlation between hip BMD and CTh values

There was a moderate correlation between hip BMD and the CTh value of ROI 16 ($r = 0.523$, $p < 0.001$), ROI 21 ($r = 0.475$, $p < 0.001$), ROI 23 ($r = 0.501$, $p < 0.001$), ROI 25 ($r = 0.480$, $p < 0.001$), and ROI 28 ($r = 0.457$, $p = 0.001$) (**Table 2**). The mean CTh value and the correlation between other CTh values and BMD are summarized in **Supplementary Tables S1, 2**.

Correlation between hip BMD and HU values

The moderate correlation was found between hip BMD and the HU values of ROI 14 ($r = 0.445$, $p = 0.001$), ROI 23 ($r = 0.449$, $p = 0.001$), ROI 27 ($r = 0.481$, $p < 0.001$), and ROI 29 ($r = 0.446$, $p = 0.001$) (**Table 2**). The mean HU value and the correlation between other HU values and BMD were summarized in **Supplementary Tables S1, 2**.

TABLE 1 The characteristics of the patients with a DXA at the hip and lumber spine.

Characteristic		
General information	Mean age, years	81.91 ± 9.05
	Gender (female/male), *n* (%)	40 (71.4)/16 (28.6)
	Femur side (right/left), *n* (%)	27 (48.2)/29 (51.8)
	Mean BMI, kg/m^2	23 ± 3.9
Mean BMD, g/cm^2	Hip	0.57 ± 0.19
	Lumbar spine (L1–L4)	0.82 ± 0.16
Mean T-score, g/cm^2	Hip	−2.70 ± 1.37
	Lumbar spine (L1–L4)	−2.18 ± 1.37

DXA, dual-energy x-ray absorptiometry; BMI, body mass index; BMD, bone mineral density.

Correlation between lumber BMD, CTh, and HU values

The correlations between lumber BMD, CTh, and HU values at 31 ROIs were weak, so we summarized the correlation between these parameters in 31 ROIs and lumber BMD in **Supplementary Tables S1, 2**.

ROC and AUC

The CTh and HU values with greater *r* values were used to evaluate ROC and AUC. Among them, the CTh of ROI 21 and HU of ROI 14 showed superior diagnostic accuracy for screening osteoporosis, as AUC were 0.82 (0.71– 0.93) and 0.88 (0.80– 0.97), respectively (**Figure 4**). The cut-off value for the CTh value of ROI 21 was 3.19 mm, with a sensitivity of 84% and a specificity of 71%. The cut-off value for the HU value of ROI 14 was 424.97 HU, with a sensitivity of 76% and a specificity of 87% (**Table 3**). Other CTh values of 18 ROIs and HU values of 10 ROIs were confirmed to be weaker diagnostic efficiency (displayed in **Supplementary Table S3, 4**).

Clinical evaluation

Three hundred and seventy-five patients (240 female and 135 male) with a mean age of 77.81 ± 9.44 years were included for clinical evaluation. Their demographic information is shown in **Table 5**. Based on the cut-off value

TABLE 2 Correlation between CTh and HU values of the proximal femur and hip BMD.

Variables	Regions	Measurement	Correlation	
			r	*p*
CTh (mm)	ROI 16	6.01 ± 1.39	0.523	<0.001
	ROI 21	3.37 ± 0.84	0.475	<0.001
	ROI 23	2.67 ± 0.81	0.501	<0.001
	ROI 25	3.91 ± 1.03	0.480	<0.001
	ROI 28	6.39 ± 1.39	0.457	0.001
HU values (HU)	ROI 14	419.48 ± 135.38	0.445	0.001
	ROI 23	474.74 ± 122.65	0.449	0.001
	ROI 27	570.09 ± 139.75	0.481	<0.001
	ROI 29	919.90 ± 170.33	0.446	0.001

CTh, cortical bone thickness; HU, Hounsfield unit; BMD, bone mineral density; ROI, region of interest.

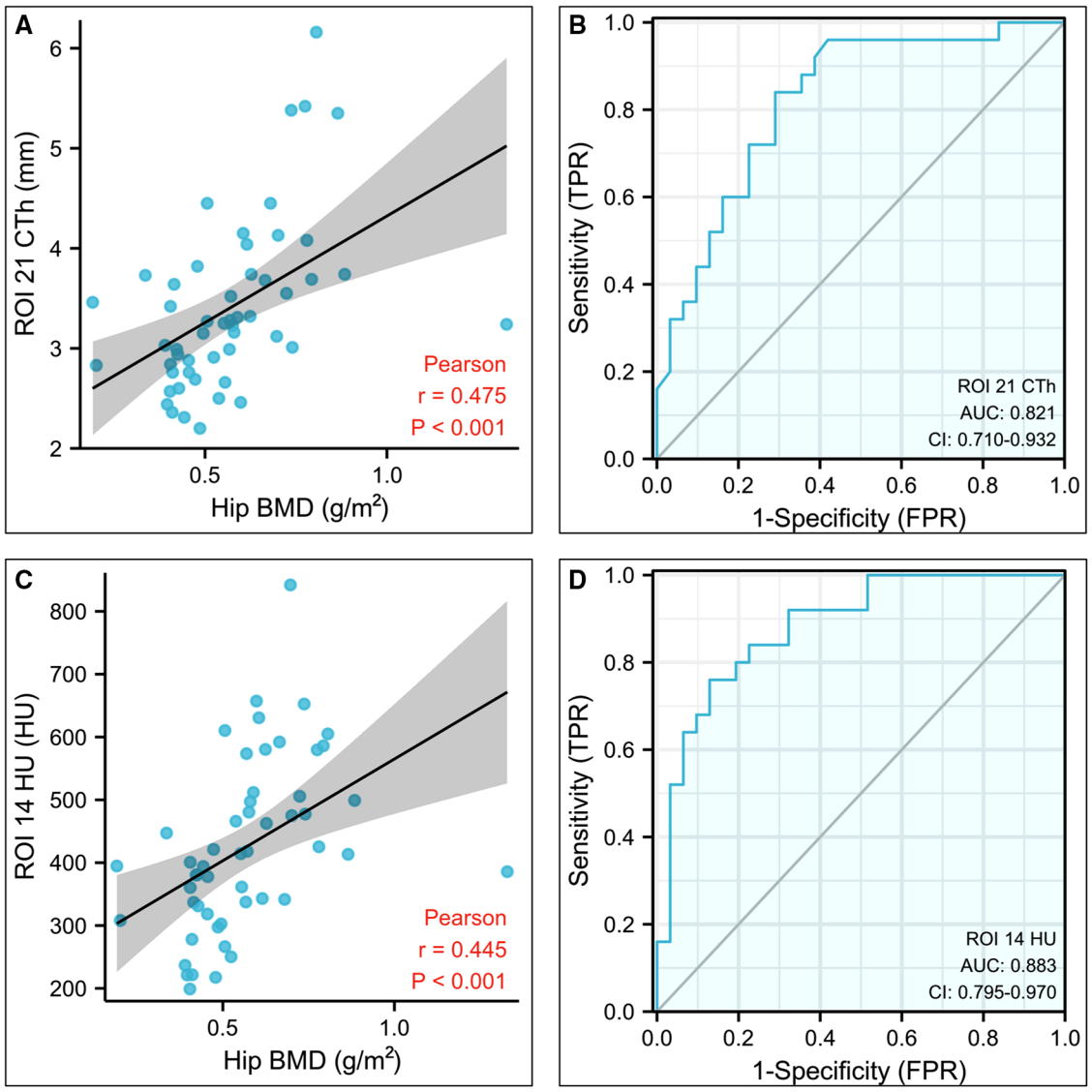

FIGURE 4
Statistical analysis results of the CTh value of the region of interest (ROI) 21 and HU value of the ROI 14. (**A**) Plot illustrating the correlation between the CTh value of ROI 21 and hip bone mineral density. (**B**) Diagnostic efficiency of the CTh value of ROI 21 for osteoporosis. (**C**) Plot illustrating the correlation between the HU value of ROI 14 and hip bone mineral density. (**D**) Diagnostic efficiency of the HU value of ROI 14 for osteoporosis. CTh, cortical bone thickness; HU, Hounsfield unit; ROI, region of interest.

TABLE 3 Diagnostic efficiency of ROI 21 CTh and ROI 14 HU value for osteoporosis.

Parameters	Diagnosis for nonosteoporosis						
	AUC	95% CI	Cut-off	Se	Sp	PV+	PV−
ROI 21 CTh	0.821	0.710–0.932	3.185	0.84	0.71	0.7	0.846
ROI 14 HU	0.883	0.795–0.970	424.97	0.76	0.871	0.826	0.818

ROI, region of interest; CTh, cortical bone thickness; HU, Hounsfield unit; AUC, area under the curve; Se, sensitivity; Sp, specificity; PV+, positive predictive value; PV−, negative predictive value.

of CTh value at ROI 21, 375 patients were divided into the osteoporosis group ($n = 180$) and the nonosteoporosis group ($n = 195$). Based on the cut-off value of 424.97 HU at ROI 14, 375 patients were divided into the osteoporosis group ($n = 183$) and the nonosteoporosis group ($n = 192$). There was a correlation between the two diagnostic methods of osteoporosis, but there was no difference between them (Table 4). The incidence of postoperative complications in the osteoporosis group was higher than that in the nonosteoporosis group divided by the CTh value at ROI 21

TABLE 4 Correlation and difference analysis of two diagnostic methods based on the cut-off values of ROI 21 CTh and ROI 14 HU value for osteoporosis.

Method	Statistics	*p* value
Fisher's test	23.198	0.000
McNemar's test	0.858	0.4

ROI, region of interest; CTh, cortical bone thickness; HU, Hounsfield unit.

($p < 0.05$) (Table 5). The number of patients who got FIM parameters and Parker–Palmer scores is shown in Table 6. The proportion of patients completing the TUG and 2MWT is shown in Table 7. The FIM parameters and Parker–Palmer scores of the nonosteoporosis group were higher than those of the osteoporosis group divided by the HU value of ROI 14 ($p < 0.05$) (Table 6).

The reliability of measurement

The intraclass correlation coefficient (ICC) was 0.803–0.965 for interobserver reliability and 0.814–0.970 for intraobserver reliability (Figure 5; Supplementary Figures S1–4).

Discussion

Our research reflected that CTh and HU in the exact areas of the proximal femur could be reliable indexes for screening osteoporosis, verifying that BMD could be assessed from other image data. The above two methods had the same diagnostic rate for osteoporosis and could replace each other (Table 4). And osteoporosis and nonosteoporosis groups divided by the above cut-off values displayed distinct differences in clinical outcomes. Meanwhile, the measurement methods of CTh and HU values showed excellent interrater and intrarater reliability. Therefore, our study provided clinicians with an effective and convenient method for screening osteoporosis and predicting clinical outcomes.

In this study, we found that the CTh and HU values of the cortex in the proximal femur pronouncedly corresponded with hip BMD but were weakly associated with lumbar spine BMD. This could be explained by the fact that these anatomic parameters were extracted from the hip not the lumbar spine. Furthermore, BMD of hip DXA correlated better with these parameters in the intertrochanteric region (ROIs 13–27) than those in the femoral neck (ROIs 1–12) and shaft (ROIs 28–31) regions, suggesting that the CTh and HU values of the intertrochanteric region were more suitable for predicting bone

TABLE 5 Patient demographics and complications by the group.

Parameters		ROI 21 CTh (mm)		P1 value	ROI 14 HU value (HU)		P2 value
		≥3.19 (*n* = 180)	<3.19 (*n* = 195)		≥424.97 (*n* = 192)	<424.97 (*n* = 183)	
Sex	Female	95	145	<0.001	106	134	<0.001
	Male	85	50		86	49	
Side	Left	88	103	0.447	97	94	0.870
	Right	92	92		95	89	
Age (year)		76.48 ± 10.22	79.04 ± 8.50	0.009	76.26 ± 10.43	79.45 ± 7.98	0.001
Height (cm)		164.71 ± 8.68	160.71 ± 7.40	<0.001	164.29 ± 8.32	160.89 ± 7.87	<0.001
Weight (kg)		64.24 ± 12.27	57.85 ± 11.27	<0.001	63.70 ± 12.42	58.00 ± 11.23	<0.001
BMI (kg/m^2)		23.60 ± 3.77	22.35 ± 3.84	0.002	23.52 ± 3.86	22.35 ± 3.76	0.003
AO classification, *n*	A1	60	56	0.568	59	57	0.992
	A2	100	119		113	106	
	A3	20	21		22	21	
Fixation type	Gamma3	6	11	0.562	11	6	0.088
	Intertan	17	18		23	12	
	PFNA	157	166		158	165	
Complications, *n*		12	24	0.037	18	18	0.880
	Loss of reduction	3	0		2	1	
	Excessive sliding of the cephalic nail	1	4		3	2	
	Cut-out	0	3		1	2	
	Implant breakage	3	1		3	1	
	Nonunion	0	1		1	0	
	Infection	1	2		3	0	
	Periprosthetic fracture	0	4		2	2	
	Loss of mobility	2	5		1	6	
	Contralateral hip fracture	2	4		2	4	

ROI, region of interest; CTh, cortical bone thickness; HU, Hounsfield unit; BMI, body mass index; AO, arbeitsgemeinschaftfür osteosynthesefragen; PFNA, proximal femoral nail antirotation.

TABLE 6 Functional ability by the group.

Group	Numbers that got the parameters, *n* (%)	Functional independence measure Mean ± SD	Parker–Palmer score Mean ± SD
ROI 21 CTh (mm)			
≥3.19 (*n* = 180)	148 (82.2%)	97.57 ± 20.00	6.76 ± 2.13
<3.19 (*n* = 195)	164 (84.1%)	96.07 ± 17.32	6.84 ± 1.88
P1 value	0.627	0.483	0.731
ROI 14 HU value			
≥ 424.97 (*n* = 192)	159 (82.8%)	99.23 ± 16.79	7.02 ± 1.87
<424.97 (*n* = 183)	153 (83.6%)	94.24 ± 20.09	6.57 ± 2.11
P2 value	0.837	0.018	0.047

ROI, region of interest; CTh, cortical bone thickness; HU, Hounsfield unit.

TABLE 7 Performance-based functional ability by the group measured using the 2-min walk test and Timed Up and Go test.

Group	2-min Walk Test (m)		Timed Up and Go Test (s)	
	Proportion who completed test, *n* (%)	Mean ± SD	Proportion who completed test, *n* (%)	Mean ± SD
ROI 21 CTh (mm)				
≥3.19 (*n* = 180)	136 (75.6%)	67.03 ± 24.08	139 (77.2%)	18.70 ± 10.60
<3.19 (*n* = 195)	155 (79.5%)	62.15 ± 21.87	156 (80.0%)	18.47 ± 7.56
P1 value	0.362	0.071	0.512	0.834
ROI 14 HU value				
≥ 424.97 (*n* = 192)	151 (78.6%)	66.72 ± 22.59	154 (80.2%)	19.09 ± 8.85
<424.97 (*n* = 183)	140 (76.5%)	61.96 ± 23.30	141 (77.0%)	18.11 ± 9.34
P2 value	0.619	0.079	0.455	0.356

ROI, region of interest; CTh, cortical bone thickness; HU, Hounsfield unit.

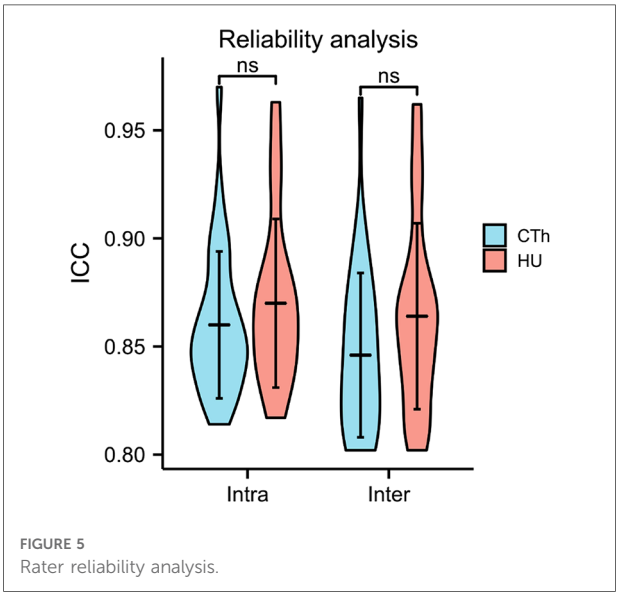

FIGURE 5
Rater reliability analysis.

quality. We believed that this difference mainly resulted from the intertrochanteric region, as the separation zone between the cortical and cancellous bone of the proximal femur, was more sensitive to deterioration of bone quality. In addition, Tang et al. (11, 20–22) proposed the "triangular stability theory" of the proximal femur and pointed out that the proximal femur was stabilized by a structural mechanical model formed by the medial, lateral, and upper sides. The ROI 14 was located at the cortex of the vastus lateralis ridge, which was the junction between the lateral and upper sides. The ROI 21 was located at the anterior wall at the vertex of the lesser trochanter, which was the junction between the lateral and medial sides. Both regions could effectively predict BMD and mechanical stability and might prevent the occurrence of osteoporotic fractures and postoperative complications.

Clinically, a simple and reliable method for screening osteoporosis was vital for the early prevention of osteoporotic fracture and the optimal choice of surgical scheme. Therefore, the concept of "opportunistic osteoporosis screening" was proposed and popularized (23). Mather et al. (24), Patterson et al. (25), and Ye et al. (26) analyzed the correlation between BMD and the cortical bone thickness of proximal humerus, distal tibia, and distal radius on x-ray, respectively, and verified that the cortical bone thickness of different sites could be used to screen osteoporosis. Wagner et al. (27) and Schreiber et al. (23) measured the HU values of cancellous portions of the distal ulna and radius from wrist CT scans to glean additional information

for predicting bone quality. Then, Ehresman et al. (28) utilized a novel MRI-based score, the Vertebral Bone Quality score, to predict osteoporosis and proposed this score to be a significant predictor of osteoporosis with an accuracy of 81%. Compared with the above previous studies, a strength of this study was that hip CT of femoral intertrochanteric fracture was a routine examination and accurately reflected a person's true anatomy. Another strength of this study was that these measurement parameters were all abstracted from the hip, which was the site with the most serious consequences of osteoporotic fractures, such as femoral neck and intertrochanteric fractures (29). To our knowledge, no study has conducted a correlation analysis between these parameters and BMD. Thus, our method would provide the clinician with a novel prospect to assess BMD.

Meanwhile, our study evaluated the clinical difference between osteoporosis and nonosteoporosis groups divided by the cut-off values. When the group was divided by the cut-off value of CTh in ROI 21, the osteoporotic group occupied a higher incidence of complications. Due to reduced BMD and microarchitectural deterioration, the mechanical strength of osteoporotic cancellous bone significantly decreased, resulting in that osteoporotic bone could not resist normal screw pullout strength and insertional torque (4, 30). When the normal load was applied to osteoporotic cancellous bone, the proximal femur would have the tendency of varus, and the stress between implant and bone tended to be concentrated, leading to a higher incidence of complications (30). Previous studies also confirmed that patients with osteoporotic fractures occupied a higher rate of complications (31). However, there was no statistical difference in the incidence of complications between different groups divided by the cut-off value of HU in ROI 14 ($p > 0.05$), which might result from the lower sensitivity of the cut-off value of HU in ROI 14 led to more misdiagnosis of actual osteoporotic patients. Thus, the cut-off value of CTh in ROI 21 was suggested as the optimal index for predicting clinical outcomes. After the osteoporotic patients were selected, the initiation of osteoporotic treatment should be considered for preventing the happen of osteoporotic fractures (32). Also, some implants with better mechanical stability, such as medial sustain nail based on femoral proximal triangular stability theory (33), should be adopted to prevent the happening of complications.

Our study had some limitations. First, the sample size was small, but this would not likely have dramatic effects on our results since the excellent measuring reliability and significant results. Second, this study only involved the patient experiencing intertrochanteric fracture, so the result of the study might not apply to the general population. Third, only Chinese was selected in our study and the result might not be generalizable to all races. Despite these limitations, this study provided a useful method for screening for osteoporosis and provided guidance for clinical treatment.

In conclusion, the CTh of ROI 21 and HU value of ROI 14 were simple and effective screening indexes to predict BMD, which could help clinicians prevent the happen of osteoporotic fractures and postoperative complications.

Data availability statement

The raw data supporting the conclusions of this article will be made available by the authors, without undue reservation.

Ethics statement

The studies involving human participants were reviewed and approved by the Medical Ethics Committee of Chinese PLA General Hospital (S2020-114-04).

Author contributions

Conception: PT, LZ, and JL. Collection, measurement, and analysis of data: GX, DW, HZ, and CX. Preparation of the manuscript: GX, DW, and HZ. Revision for important intellectual content: GX, HL, and WZ. Supervision: PT, LZ, and JL. All authors contributed to the article and approved the submitted version.

Funding

This work was supported by the Beijing Natural Science Foundation (Grant 7222180) and the 13th Five-year Plan for Key Discipline Construction Project of PLA (A350109). We declare that no funds, grants, or other support were received during the preparation of this manuscript.

Acknowledgments

The authors thank Miss Dou Xiong for her guidance on measurement methods.

Conflict of interest

The authors declare that the research was conducted in the absence of any commercial or financial relationships that could be construed as a potential conflict of interest.

Publisher's note

All claims expressed in this article are solely those of the authors and do not necessarily represent those of

their affiliated organizations, or those of the publisher, the editors and the reviewers. Any product that may be evaluated in this article, or claim that may be made by its manufacturer, is not guaranteed or endorsed by the publisher.

Supplementary material

The Supplementary Material for this article can be found online at: https://www.frontiersin.org/articles/10.3389/fsurg.2022.1047603/full#supplementary-material.

References

1. Compston JE, McClung MR, Leslie WD. Osteoporosis. *Lancet*. (2019) 393:364–76. doi: 10.1016/S0140-6736(18)32112-3

2. Bliuc D, Nguyen ND, Milch VE, Nguyen TV, Eisman JA, Center JR. Mortality risk associated with low-trauma osteoporotic fracture and subsequent fracture in men and women. *JAMA*. (2009) 301:513–21. doi: 10.1001/jama.2009.50

3. Liu R, Chao A, Wang K, Wu J. Incidence and risk factors of medical complications and direct medical costs after osteoporotic fracture among patients in China. *Arch Osteoporos*. (2018) 13:12. doi: 10.1007/s11657-018-0429-5

4. von Rüden C, Augat P. Failure of fracture fixation in osteoporotic bone. *Injury*. (2016) 47(Suppl 2):S3–10. doi: 10.1016/S0020-1383(16)47002-6

5. Hollensteiner M, Sandriesser S, Bliven E, von Rüden C, Augat P. Biomechanics of osteoporotic fracture fixation. *Curr Osteoporos Rep*. (2019) 17:363–74. doi: 10.1007/s11914-019-00535-9

6. Si L, Winzenberg TM, Jiang Q, Chen M, Palmer AJ. Projection of osteoporosis-related fractures and costs in China: 2010-2050. *Osteoporos Int*. (2015) 26:1929–37. doi: 10.1007/s00198-015-3093-2

7. Majumdar SR. A T-2 translational research perspective on interventions to improve post-fracture osteoporosis care. *Osteoporos Int*. (2011) 22(Suppl 3):471–6. doi: 10.1007/s00198-011-1700-4

8. Xiongfeng T, Cheng Z, Meng H, Chi M, Deming G, Huan Q, et al. One novel phantom-less quantitative computed tomography system for auto-diagnosis of osteoporosis utilizes low-dose chest computed tomography obtained for COVID-19 screening. *Front Bioeng Biotechnol*. (2022) 10:856753. doi: 10.3389/fbioe.2022.856753

9. Rajapakse CS, Farid AR, Kargilis DC, Jones BC, Lee JS, Johncola AJ, et al. MRI-based assessment of proximal femur strength compared to mechanical testing. *Bone*. (2020) 133:115227. doi: 10.1016/j.bone.2020.115227

10. Baumgärtner R, Heeren N, Quast D, Babst R, Brunner A. Is the cortical thickness index a valid parameter to assess bone mineral density in geriatric patients with hip fractures. *Arch Orthop Trauma Surg*. (2015) 135:805–10. doi: 10.1007/s00402-015-2202-1

11. Xu G, Li J, Xu C, Xiong D, Li H, Wang D, et al. Triangular mechanical structure of the proximal femur. *Orthop Surg*. (2022) 14:3047–60. doi: 10.1111/os.13498

12. Sparks CA, Decker SJ, Ford JM. Three-dimensional morphological analysis of sex, age, and symmetry of proximal femurs from computed tomography: application to total hip arthroplasty. *Clin Anat*. (2020) 33:731–8. doi: 10.1002/ca.23496

13. Zhang RY, Su XY, Zhao JX, Li JT, Zhang LC, Tang PF. Three-dimensional morphological analysis of the femoral neck torsion angle-an anatomical study. *J Orthop Surg Res*. (2020) 15:192. doi: 10.1186/s13018-020-01712-8

14. Zhang Q, Liu H, Chen W, Li X, Song Z, Pan J, et al. Radiologic measurement of lesser trochanter and its clinical significance in Chinese. *Skeletal Radiol*. (2009) 38:1175–81. doi: 10.1007/s00256-009-0662-5

15. Morris S, Morris ME, Iansek R. Reliability of measurements obtained with the timed "up & go" test in people with Parkinson disease. *Phys Ther*. (2001) 81:810–8. doi: 10.1093/ptj/81.2.810

16. Granger CV. The emerging science of functional assessment: our tool for outcomes analysis. *Arch Phys Med Rehabil*. (1998) 79:235–40. doi: 10.1016/s0003-9993(98)90000-4

17. Butland RJ, Pang J, Gross ER, Woodcock AA, Geddes DM. Two-, six-, and 12-minute walking tests in respiratory disease. *Br Med J (Clin Res Ed)*. (1982) 284:1607–8. doi: 10.1136/bmj.284.6329.1607

18. Parker MJ, Palmer CR. A new mobility score for predicting mortality after hip fracture. *J Bone Joint Surg Br*. (1993) 75:797–8. doi: 10.1302/0301-620X.75B5.8376443

19. Li J, Tang S, Zhang H, Li Z, Deng W, Zhao C, et al. Clustering of morphological fracture lines for identifying intertrochanteric fracture classification with Hausdorff distance-based K-means approach. *Injury*. (2019) 50:939–49. doi: 10.1016/j.injury.2019.03.032

20. Chen H, Li J, Chang Z, Liang X, Tang P. Treatment of femoral neck nonunion with a new fixation construct through the Watson-Jones approach. *J Orthop Translat*. (2019) 19:126–32. doi: 10.1016/j.jot.2019.04.004

21. Li J, Yin P, Zhang L, Chen H, Tang P. Medial anatomical buttress plate in treating displaced femoral neck fracture a finite element analysis. *Injury*. (2019) 50:1895–900. doi: 10.1016/j.injury.2019.08.024

22. Li J, Zhang L, Zhang H, Yin P, Lei M, Wang G, et al. Effect of reduction quality on postoperative outcomes in 31-A2 intertrochanteric fractures following intramedullary fixation: a retrospective study based on computerised tomography findings. *Int Orthop*. (2019) 43:1951–9. doi: 10.1007/s00264-018-4098-1

23. Schreiber JJ, Gausden EB, Anderson PA, Carlson MG, Weiland AJ. Opportunistic osteoporosis screening—gleaning additional information from diagnostic wrist CT scans. *J Bone Joint Surg Am*. (2015) 97:1095–100. doi: 10.2106/JBJS.N.01230

24. Mather J, MacDermid JC, Faber KJ, Athwal GS. Proximal humerus cortical bone thickness correlates with bone mineral density and can clinically rule out osteoporosis. *J Shoulder Elbow Surg*. (2013) 22:732–8. doi: 10.1016/j.jse.2012.08.018

25. Patterson J, Rungprai C, Den Hartog T, Gao Y, Amendola A, Phisitkul P, et al. Cortical bone thickness of the distal part of the tibia predicts bone mineral density. *J Bone Joint Surg Am*. (2016) 98:751–60. doi: 10.2106/JBJS.15.00795

26. Ye C, Guo Y, Zheng Y, Wu Z, Chen K, Zhang X, et al. Distal radial cortical bone thickness correlates with bone mineral density and can predict osteoporosis: a cohort study. *Injury*. (2020) 51:2617–21. doi: 10.1016/j.injury.2020.08.018

27. Wagner SC, Dworak TC, Grimm PD, Balazs GC, Tintle SM. Measurement of distal ulnar Hounsfield units accurately predicts bone mineral density of the forearm. *J Bone Joint Surg Am*. (2017) 99:e38. doi: 10.2106/JBJS.15.01244

28. Ehresman J, Pennington Z, Schilling A, Lubelski D, Ahmed AK, Cottrill E, et al. Novel MRI-based score for assessment of bone density in operative spine patients. *Spine J*. (2020) 20:556–62. doi: 10.1016/j.spinee.2019.10.018

29. Nieves JW, Bilezikian JP, Lane JM, Einhorn TA, Wang Y, Steinbuch M, et al. Fragility fractures of the hip and femur: incidence and patient characteristics. *Osteoporos Int*. (2010) 21:399–408. doi: 10.1007/s00198-009-0962-6

30. Nazarian A, Muller J, Zurakowski D, Müller R, Snyder BD. Densitometric, morphometric and mechanical distributions in the human proximal femur. *J Biomech*. (2007) 40:2573–9. doi: 10.1016/j.jbiomech.2006.11.022

31. Adler RA. Update on osteoporosis in men. *Best Pract Res Clin Endocrinol Metab*. (2018) 32:759–72. doi: 10.1016/j.beem.2018.05.007

32. Cosman F, de Beur SJ, LeBoff MS, Lewiecki EM, Tanner B, Randall S, et al. Clinician's guide to prevention and treatment of osteoporosis. *Osteoporos Int*. (2014) 25:2359–81. doi: 10.1007/s00198-014-2794-2

33. Li J, Han L, Zhang H, Zhao Z, Su X, Zhou J, et al. Medial sustainable nail versus proximal femoral nail antirotation in treating AO/OTA 31-A2.3 fractures: finite element analysis and biomechanical evaluation. *Injury*. (2019) 50:648–56. doi: 10.1016/j.injury.2019.02.008

frontiers | Frontiers in Surgery

TYPE Original Research
PUBLISHED 06 January 2023
DOI 10.3389/fsurg.2022.1070324

Check for updates

OPEN ACCESS

EDITED BY
Huiwu Li,
Shanghai Ninth People's Hospital, China

REVIEWED BY
Hai-jun Wang,
Peking University Third Hospital, China
Kun Mi,
Guangxi International Zhuang Medical Hospital, China

*CORRESPONDENCE
Yongsheng Xu
xys_sportsmedicine@126.com
Yansong Qi
malaqinfu@126.com

†These authors have contributed equally to this work and share first authorship

SPECIALTY SECTION
This article was submitted to Orthopedic Surgery, a section of the journal Frontiers in Surgery

RECEIVED 14 October 2022
ACCEPTED 07 November 2022
PUBLISHED 06 January 2023

CITATION
Wang X, Qi Y, Bao H and Xu Y (2023) Application of the 3D-MRI on post-operative graft assessment in adolescent patients with ACL reconstruction: A minimal 2-year follow-up. Front. Surg. 9:1070324. doi: 10.3389/fsurg.2022.1070324

COPYRIGHT
© 2023 Wang, Qi, Bao and Xu. This is an open-access article distributed under the terms of the Creative Commons Attribution License (CC BY). The use, distribution or reproduction in other forums is permitted, provided the original author(s) and the copyright owner(s) are credited and that the original publication in this journal is cited, in accordance with accepted academic practice. No use, distribution or reproduction is permitted which does not comply with these terms.

Application of the 3D-MRI on post-operative graft assessment in adolescent patients with ACL reconstruction: A minimal 2-year follow-up

Xiaona Wang[1†], Yansong Qi[2*†], Huricha Bao[2] and Yongsheng Xu[2*]

[1]Department of Imaging Medicine, Inner Mongolia People's Hospital, Hohhot, China, [2]Department of Orthopedics (Sports Medicine Center), Inner Mongolia People's Hospital, Hohhot, China

Background: The purpose of the present study was to assess the prognostic morphological changes of the reconstructed hamstring auto-grafts by using reconstructed three-dimensional MRI (3D-MRI) in adolescent patients with ACLR.

Methods: 22 adolescent patients (less than 17 years old) were retrospective included between January 1, 2018, and October 31, 2020, in our department. The patients were divided into 2 subgroups: subgroup A (<14 years old) and subgroup B (≥14 years old). 3D-MRI was used to detect the total cross-sectional area (TCA) and long-to-short axis (LSA) ratio of the reconstructed ACL graft at the proximal, mid-point, and distal regions. The minimal follow-up was 2 years.

Results: The averaged follow-up of subgroup A and B was 37.8 ± 5.6 and 37.6 ± 6.5 months, respectively. Comparing to the initial graft (ACLR operation), the TCA of reconstructed ACL was increased by 30.6% on average, and the TCAs at proximal, mid-point, and distal regions were increased by 56.4%, 50.0%, and 17.7%, respectively, inner-group comparisons showed that the TCAs of the 3 region in subgroup A were all increased at the follow-up ($P = 0.002$) ($P < 0.001$) ($P < 0.001$), however, only increased mid-point ($P = 0.024$) and distal TCAs ($P < 0.001$) were found in subgroup B. Comparing to the native ACL, the proximal LSA ratio in subgroup A was comparable, while it was lower in subgroup B than the native ACL ($P = 0.004$), the distal LSA ratios in the 2 subgroups were both lower than the native ACL ($P = 0.004$) ($P = 0.006$).

Conclusions: 3D-MRI assessment can exactly identify the morphological changes of the graft in adolescent patients with ACLR, the TCA of the constructed ACL was increased compared to the initial graft, however, the LSA ratio was still lower than the native ACL. Younger adolescent patients may have a better potential on the ligamentization after ACLR than the older adolescent patients.

KEYWORDS

three-dimensional MRI, adolescent, ACL reconstruction, morphology, cross-sectional area, long-to-short axis ratio, ligamentization

Introduction

In recent years, the incidence of anterior cruciate ligament (ACL) rupture is progressing at a greater rate in the pediatric and adolescent population, in comparison with adults (1–3). Considerable attention needs to be paid on the treatment of ACL rupture in this skeletally immature adolescent population. ACL reconstruction (ACLR) has become the gold standard of treatment for the adolescent population seeking to return to sports (4). The hamstring tendon auto-graft is preferred in the ACLR for adolescent patients, which avoids the damage from open epiphysis by the bone-patellar tendon-bone (BPTB) graft (5, 6). Young age, the smaller size of the auto-graft, and higher activity level were considered to be the risk factors related to ACL re-rupture and clinical failures in adolescent patients (7, 8).

Reconstructed three-dimensional MRI (3D-MRI) is a new objective imaging assessment for ALCR (9). The latest study has reported that using 3D-MRI on assessment of the reconstructed ACL showed a substantial intra- and inter-observer agreement (10). It has also been shown that 3D-MRI identification of the reconstructed ACL compares favorably and can be used interchangeably with the anatomic identification of cadaveric ACL (11). Given that prediction of the diameter of the semitendinosus and gracilis tendon from adolescent patients may represent insufficient graft strength (12), the objective assessments of the reconstructed ACL tendon in post-operation are of great significance to clinical practice.

Although several different ACLR techniques are available for skeletally immature patients, however, the optimal surgical technique for ACLR in younger children is still controversial at present (13). One of the main reasons is lacking the objective imaging assessments of the reconstructed ACL tendon in post-operation follow-ups. The purpose of this study was to assess the prognostic morphological changes of the reconstructed hamstring auto-grafts by using 3D-MRI in adolescent patients with ACLR.

Methods

Patient involvement

This was a self-control clinical study. Adolescent patients diagnosed with ACL rupture were included between January 1, 2018, and October 31, 2020, in our department. The inclusion criteria: (1) patients younger than 17 years old; (2) with open physis diagnosed through knee radiographs images at the time of surgery (14); (3) single-bundle trans-physeal ACLR with hamstring grafts; (4) follow-up more than 2 years. The exclusion criteria: (1) multi-ligament injury; (2) ACL re-rupture; (3) history of lower extremity fracture, ligament rupture, and operations; (4) systematic diseases, such as rheumatoid arthritis, and motor-nerve system diseases. The included patients were recruited retrospectively with the recorded contact information. The patients were divided into 2 subgroups: subgroup A (patients < 14 years old) and subgroup B (patients ≥ 14 years old).

Ethics approval was obtained before the enrolment of patients into the study. Our study was conducted following the international ethical standards required for publication (15).

ALCR operation

The trans-physeal reconstruction techniques using autologous single-bundle hamstring grafts were applied to all the patients by the senior author.

The procedure was performed under combined spinal-epidural anesthesia with the arthroscopic assessment, which allowed the treatment of associated injuries. Meniscal lesions were either sutured or resected. After harvesting the semitendinosus and gracilis, tendons were cleaned of muscle insertion. Grafts were tightened and half-folded to be prepared for insertion into the patient's knee (16). Before implantation, a circular millimeter ruler was used to measure the diameter of the graft at its middle point, which will be located inside the joint. During the surgical procedure, the positioning of the femoral and tibial tunnel was based on the anatomic center of the native ACL footprint after removing the remnant (17). According to the size of previously measured grafts, the tibial and femoral tunnels were reamed through the central epiphysis independently. Afterward, the four-strand semitendinosus and gracilis tendon was taken care of to fill in both tunnels. On the femoral side, standard far-posterior tunnel placement was undertaken with suspensory fixation using an EndobuttonCL (Smith & Nephew). Double staples were used for tibial fixation. All 22 patients were rehabilitated with braces according to the same guidelines by physical therapists, emphasizing early full extension and range of motion.

Follow-ups

The follow-up started when the ACLR was completed. The end was re-rupture/death/missing, whichever occurred first. The minimum follow-up was 2 year (y). General characteristics included: sex, age, surgery duration (the injury time before the operation), and follow-up time, other clinical information included: associated injuries (meniscus tear, cartilage, and other injuries) and complications. The clinical assessments of the outcomes of ACLR included: knee 3D-MRI, as well as the subjective scoring systems of knee function, which were

performed at 1 and 2y follow-ups. All of the follow-up data was checked and entered into the database by two independent researchers, and a double-entry is also carried out for control of quality.

3D-MRI Assessment

The 3D-MRI was performed by a radiologist with 5 years of experience in knee MRI images. At the follow-ups, 3D-MRI was utilized for bilateral knees with 1-mm slice thickness T2 weighted images with no fat suppression (GE, 3.0 T Signa HDxt at resolution 512*512 pixels bitmap). The images were introduced into AW Server 2.0 (GE Health Care) to reconstruct three-dimensional models. A reference line passing through the geometric centroid of the entire graft was identified.

Graft size assessment

Grafts measurements in 3D-MRI were performed separately by 2 researchers (a radiologist with 5 years of experience in knee MRI images and a sports medicine doctor with more than 10 years of clinical experience). Perpendicular planes to the central axis of ACL were marked at 25% (proximal), 50% (mid-point), and 75% (distal) of the ligament's overall length (from the femoral attachment to the tibial attachment), to create 3 cross-sectional slices (**Figures 1A,B**). The total cross-sectional area (TCA) was calculated, $TCA = \pi^*(\text{averaged diameter of the 3 slices}/2)^2$. The TCA provides information about the size of the graft, which could be compared to the initial size recorded during surgery. At each cross-section slice, outline of the cross-sectional area of ACL graft was carefully identified to extract the LSA (**Figures 1C,D**), and the long-to-short-axis (LSA) ratio was calculated. LSA ratio

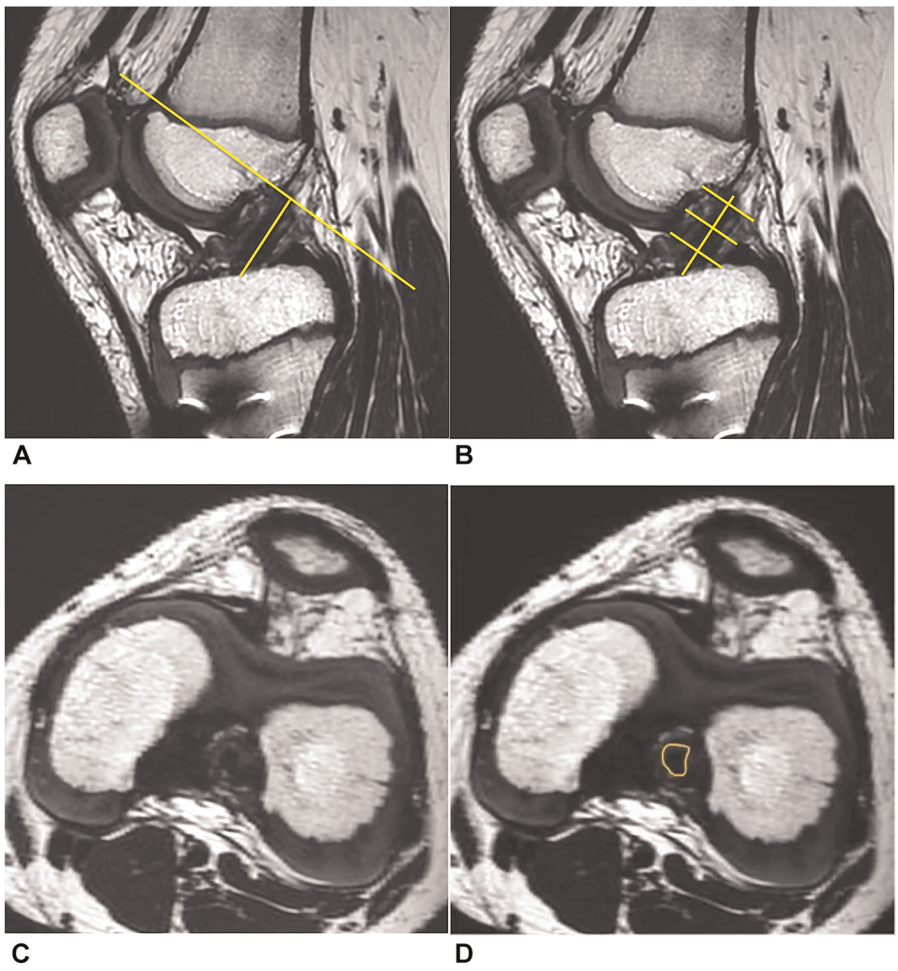

FIGURE 1
3D-MRI assessment of the ACL. (**A**) A reference line across the center of the entire ACL graft and a perpendicular plane. (**B**) The 2nd, 3rd, and 4th slices represented three evenly spaced cross-sectional slices (at 25%, 50%, and 75% of the ligament's overall length from the femoral attachment to the tibial attachment). (**C**) Cross-section of ACL graft at the mid-point location. (**D**) Outline of the cross-sectional area.

provides insight into the shape of the transverse section, whereby a ratio of 1:1 implies a round ligament.

To compare those parameters of the ACL graft with the native ACL, the same procedure was applied to the contralateral knee at the same time point.

Statistical analysis

Continuous data were expressed as mean ± SD, and the comparisons were processed by the paired *t*-tests and Levene variance homogeneity tests. Count data were expressed as number (n) and rate (/), and comparisons of the count data were processed by the Chi-square test or Fisher's exact test. The level of significance was set at 0.05. All of the statistical analyses were performed using SPSS 20.0 (SPSS Inc., 2009, Chicago, IL, USA).

Results

Basic characteristics

Finally, 22 adolescent patients meeting all the criteria were included. Subgroup A (<14 years old) consisted of 9 patients: 5 suffered a sprain of the knee when doing competitive sports, 4 sprained the knee by themselves when doing un-competitive sports, such as skiing and skating; subgroup B (≥14 years old) consisted of 13 patients: 6 suffered a sprain of the knee when doing competitive sports, 3 sprained the knee by themselves when doing un-competitive sports, 2 slipped and sprained the knee by themselves during daily routine, and 2 were caused by vehicle accidents. The general characteristics and clinical information of the 2 subgroups were listed below (**Table 1**), and no complication of abnormal bone growth or angular deformity was observed during the follow-up period.

TABLE 1 Basic characteristics of the subgroups in adolescent patients with ACLR.

Characteristics	Subgroup A (<14 years old)	Subgroup B (≥14 years old)
Enrolled subjects (*n*)	9	13
Sex (male/female)	7/2	8/5
Age (year)	12.0 ± 1.1	15.7 ± 1.2
BMI	22.17 ± 1.23	22.25 ± 1.51
Surgery duration (week)	2.1 ± 2.9	3.7 ± 4.5
Meniscus injury (with/without)	1/8	2/11
MCL injury (with/without)	1/8	1/12
Graft diameter (mm)	7.86 ± 0.23	7.82 ± 0.25
Follow-up time (month)	37.8 ± 5.6	37.6 ± 6.5

Note: BMI, Body Mass Index; ACLR, anterior cruciate ligament reconstruction; MCL, medial collateral ligament.

TCA comparison between the initial graft and follow-up

The sizes of the ACL grafts were increased at the 3 slices of 3D-MRI at the follow-up in all of the patients (**Figure 2**), and the TCA at proximal, mid-point, and distal regions were increased by 56.4%, 50.0%, and 17.7%, respectively. The maximal increase was observed in the proximal region, while the increase in the distal region was relatively less. Averagely, the TCA of ACL graft was increased by 30.6% in post-operation at a minimal 2y follow-up.

Inner-group comparisons of Subgroup A showed that the TCA of reconstructed ACL at the proximal, mid-point, and distal regions were increased at minimal 2y follow-up compared to the initial state at ACLR operation, however, only increased TCA of reconstructed ACL at the mid-point and distal regions were found in Subgroup B at minimal 2y follow-up compared to the initial state (**Table 2**).

LSA comparison between the reconstructed ACL and native ACL

Inner-group comparisons showed that the proximal LSA ratio of reconstructed ACL in subgroup A was comparable with the native ACL on the healthy contralateral side, while the proximal LSA ratio of reconstructed ACL in subgroup B was lower than that of the native ACL; the mid-point LSA ratio of reconstructed ACL did not have significant difference with the native ACL in the 2 subgroups; the distal LSA ratios of reconstructed ACL in the 2 subgroups were lower than that of the native ACL (**Table 3**).

Discussion

It has been reported the incidence of ACL rupture in adolescents has increased with a peak at 17 years old (18). Since ACLR results in higher joint stability and lower risks of additional meniscal and chondral injuries in adolescent patients, compared to non-operative or delayed operative treatment (4), ACLR has become the gold standard of treatment for adolescent patients. Objective imaging assessments of the reconstructed ACL tendon in post-operation follow-ups were relatively rare in present studies. As the morphology parameters of the reconstructed ACL are closely associated with the function and outcome, for example, the TCA and LSA ratio, the 3D-MRI assessment is of great significance to clinical practice.

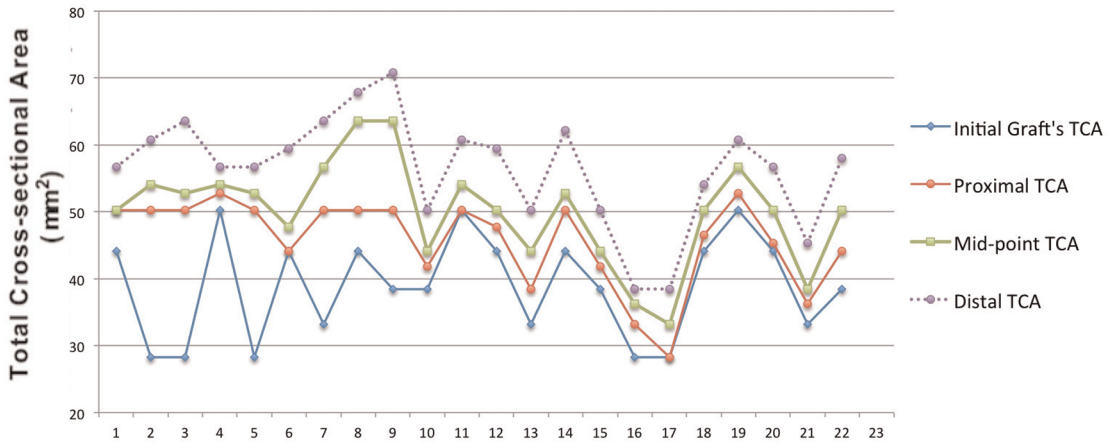

FIGURE 2
Self-control comparisons of TCA between the initial graft and follow-up in each patient the largest growths were found in the distal TCAs (blue) in all patients, and then the mid-point (green) and distal (Red) TCAs, respectively.

TABLE 2 TCA comparisons between the initial graft and follow-up in the 2 subgroups.

TCA	Subgroup A (<14 years old)			Subgroup B (≥14 years old)		
	Initial Graft	Reconstructed ACL	*P* value	Initial Graft	Reconstructed ACL	*P* value
Proximal TCA (mm^2)	37.68 ± 8.45	49.85 ± 2.29	$t = -4.107$ $P = 0.002$**	39.64 ± 7.38	42.84 ± 7.21	$t = -1.117$ $P = 0.275$
Mid-point TCA (mm^2)	37.68 ± 8.45	55.07 ± 5.44	$t = -5.191$ $P < 0.001$**	39.64 ± 7.38	46.53 ± 7.19	$t = -2.412$ $P = 0.024$*
Distal TCA (mm^2)	37.68 ± 8.45	61.81 ± 5.12	$t = -7.329$ $P < 0.001$**	39.64 ± 7.38	52.69 ± 8.11	$t = -4.291$ $P < 0.001$**

Note: $P < 0.01$.
**$P < 0.05$.
*Total cross-sectional area (TCA).

TABLE 3 LSA comparisons between the reconstructed ACL and native ACL at follow-up.

LSA	Subgroup A (<14 years old)			Subgroup B (≥14 years old)		
	Native ACL	Reconstructed ACL	*P* value	Native ACL	Reconstructed ACL	*P* value
Proximal LSA ratio	1.29 ± 0.10	1.39 ± 0.16	$t = -1.634$ $P = 0.122$	1.21 ± 0.18	1.43 ± 0.17	$t = -3.138$ $P = 0.004$**
Mid-point LSA ratio	1.67 ± 0.13	1.54 ± 0.14	$t = 2.028$ $P = 0.060$	1.60 ± 0.14	1.61 ± 0.17	$t = -0.173$ $P = 0.864$
Distal LSA ratio	2.59 ± 0.17	2.07 ± 0.39	$t = 3.683$ $P = 0.004$**	2.52 ± 0.16	2.10 ± 0.45	$t = 3.218$ $P = 0.006$**

Note: $P < 0.01$.
**Long-to-short-axis.

The present study found that the 3D-MRI assessment can exactly identify the morphological changes of the graft in adolescent patients. Most adolescents become skeletally mature over 17 years old (19). Our results showed that compared with the initial size at surgery, the TCA of the graft based on 3D-MRI was shown to increase by 30.6% on average at a minimal 2y follow-up in this population. The increasing percentage of TCA at three slices from proximal, mid-point and distal regions were increased by 56.4%, 50.0%, and 17.7%, respectively. The TCA provides information about graft size. It has been proved that the TCA of graft measured by MRI in post-operation was well correlated with those directly measured during the ACLR operation (20). In order to assess the size changes of the reconstructed ACL in long-term

TABLE 4 Motor function comparisons between the subgroups at the follow-up.

Motor function	Subgroup A (< 14 years old)	Subgroup B (≫ 14 years old)	*P* value
			$t = 1.184$
Lysholm	86.22 ± 2.91	84.31 ± 4.19	
			$P = 0.250$
			$t = 1.774$
IKDC	87.22 ± 4.18	84.69 ± 2.53	
			$P = 0.091$
	yes 9	yes 13	
Return to sports			$P = 1.000$
	no 0	no 0	

prognosis, we compared the TCA measured by 3D-MRIs at the follow-up with the data of graft measured during the ACLR operation. Similar to our results, Min et al. also showed that the diameter of the autologous patellar tendon graft increased by 70% in 23 patients, which was measured in an oblique axial image directly scanned with 1.5 T MR (21). Hamada et al. showed that measured in an oblique coronal ACL image, the graft cross-sectional area increased by 29% at 12 months after surgery (20). The increasing size of the ACL graft in this study could be attributed to the process of ligamentization (22), during which the graft underwent remodeling and became hypertrophy. Our study suggests that the 3D-MRI assessment can exactly identify the morphological changes of the graft in adolescent patients. The present study also found a difference in the graft ligamentization process between the 2 subgroups based on the different age distribution. Our results showed that compared to the initial graft, the proximal, mid-point, and distal TCA of reconstructed ACL were all increased in patients < 14 years old, while only the mid-point and distal TCA were increased in patients ≥ 14 years old, which suggested that adolescent patient with younger age may have a better potential on ligamentization after ACLR.

The LSA ratio is another morphological parameter extracted from the 3D-MRI, which indicates the transverse section shape of the graft, and a ratio of 1:1 implies a cylindrical ligament. Our results showed that the proximal, mid-point and distal LSA ratios were beyond the initial ratio (1:1, at the ALCR operation), what's more, were gradually increased. It suggests that LSA ratios measured in 3D-MRI demonstrate that the cross-sectional shape of the intra-articular graft has changed from the original cylindrical shape to a fan-shaped flat ligament, and 3D-MRI assessment can exactly identify the morphological changes in the graft's ligamentization process in adolescent patients. Our results found that the LSAs of the constructed ACL in the 2 subgroups were lower than the native ACL, which suggested the constructed ACL was prone to cylindrical compared to the native ACL with a flatter fan-shaped. It has been reported that the constructed ACL was more cylindrical compared with the native ACL (9, 23), and a cylindrical ACL may cause impingement on PCL and femoral notch (9, 24). Therefore, the double-bundle ACLR with a more similar shape to the native ACL can avoid those disadvantages (25), and 3D-MRI has the benefit of assessing the morphological characteristics of post-operative ligamentization in adolescent patients. In addition, the present study also found a difference in the LSA between the 2 subgroups. Our results showed that the proximal LSA ratio of reconstructed ACL in patients < 14 years old was comparable with the native ACL, while the proximal LSA ratio of reconstructed ACL in patients ≥ 14 years old was higher than that of the native ACL. The proximal LSA ratio indicates the transverse section shape of the foot-print region of the graft. Our results suggested that adolescent patients with younger age can result in a more similar footprint shape to the native ACL.

The limitations of our study were as follows: (1) this was a retrospective study, and the relatively small sample size and variable follow-up periods might result in bias of the results, especially for the results based on two subgroups; (2) lack of observation on the dynamic changes of the ACL graft in post-operation. Further longitudinal studies with more samples and follow-up points are required to explore more valuable morphology changes in adolescent patients with ACLR.

Conclusion

3D-MRI assessment can exactly identify the morphological changes of the graft in adolescent patients with ACLR, the TCA of the constructed ACL was increased compared to the initial graft, however, the LSA of the constructed ACL was still lower than the native ACL at a minimal 2y follow-up. Younger adolescent patients (<14 years old) may have a better potential on the ligamentization after ACLR than the older adolescent patients (≥14 years old).

Data availability statement

The original contributions presented in the study are included in the article/Supplementary Material, further inquiries can be directed to the corresponding author/s.

Ethics statement

The studies involving human participants were reviewed and approved by the Ethics Committee of Clinical Investigation in the Inner Mongolia People's Hospital. Written informed consent to participate in this study was provided by the

participants' legal guardian/next of kin. Written informed consent was obtained from the individual(s), and minor(s)' legal guardian/next of kin, for the publication of any potentially identifiable images or data included in this article.

Author contributions

XW wrote the first version of the manuscript. YQ participated in critical revision of the manuscript for intellectual content and sorted out and screened the relevant literatures. HB revised the paper, YX designed the outline and revised the paper. All authors contributed to the article and approved the submitted version.

Funding

This study was supported by the National Natural Science Foundation of China (grant numbers: 81560374, 81960399), the Natural Science Foundation of Inner Mongolia (grant numbers: 2017MS08136, 2018BS08002, 2020MS03064), and the Doctoral Research Start-up Fund Project of Inner Mongolia People's Hospital (grant number: 2019BS04).

Acknowledgments

The authors would like to thank Yi Ding (M.D., Ph.D., Post-doc) from Department of Orthopaedic Surgery of Beijing Tiantan Hospital for the professional English language assistance and the statistics support.

Conflict of interest

The authors declare that the research was conducted in the absence of any commercial or financial relationships that could be construed as a potential conflict of interest.

Publisher's note

All claims expressed in this article are solely those of the authors and do not necessarily represent those of their affiliated organizations, or those of the publisher, the editors and the reviewers. Any product that may be evaluated in this article, or claim that may be made by its manufacturer, is not guaranteed or endorsed by the publisher.

References

1. Weitz FK, Sillanpää PJ, Mattila VM. The incidence of paediatric ACL injury is increasing in Finland. *Knee Surg Sports Traumatol Arthrosc.* (2020) 28:363–8. doi: 10.1007/s00167-019-05553-9

2. Bram JT, Magee LC, Mehta NN, Patel NM, Ganley TJ. Anterior cruciate ligament injury incidence in adolescent athletes: a systematic review and meta-analysis. *Am J Sports Med.* (2021) 49:1962–72. doi: 10.1177/0363546520959619

3. Nogaro MC, Abram SGF, Alvand A, Bottomley N, Jackson WFM, Price A. Paediatric and adolescent anterior cruciate ligament reconstruction surgery: results from a national cohort of 16,000 patients over 20 years. *Bone Joint J.* (2020) 102-B:239–45. doi: 10.1302/0301-620X.102B2.BJJ-2019-0420.R2

4. James EW, Dawkins BJ, Schachne JM, Ganley TJ, Kocher MS, Anderson CN, et al. Early oper- ative versus delayed operative versus nonoperative treatment of pediatric and adolescent anterior cruciate ligament injuries: a systematic review and meta-analysis. *Am J Sports Med.* (2021) 49:4008–17. doi: 10.1177/0363546521990817

5. Leys T, Salmon L, Waller A, Linklater J, Pinczewski L. Clinical results and risk factors for reinjury 15 years after anterior cruciate ligament reconstruction: a prospective study of hamstring and patellar tendon grafts. *Am J Sports Med.* (2012) 40:595–605. doi: 10.1177/0363546511430375

6. Pinczewski LA, Lyman J, Salmon LJ, Russell VJ, Roe J, Linklater J. A 10-year comparison of anterior cruciate ligament reconstructions with hamstring tendon and patellar tendon autograft: a controlled, prospective trial. *Am J Sports Med.* (2007) 35:564–74. doi: 10.1177/0363546506296042

7. Magnussen RA, Lawrence JT, West RL, Toth AP, Taylor DC, Garrett WE. Graft size and patient age are predictors of early revision after anterior cruciate ligament reconstruction with hamstring autograft. *Arthroscopy.* (2012) 28:526–31. doi: 10.1016/j.arthro.2011.11.024

8. Webster KE, Feller JA, Leigh WB, Richmond AK. Younger patients are at increased risk for graft rupture and contralateral injury after anterior cruciate ligament reconstruction. *Am J Sports Med.* (2014) 42:641–7. doi: 10.1177/0363546513517540

9. Thein R, Spitzer E, Doyle J, Khamaisy S, Nawabi DH, Chawla H, et al. The ACL graft has different cross-sectional dimensions compared with the native ACL: implications for graft impingement. *Am J Sports Med.* (2016) 44:2097–105. doi: 10.1177/0363546516645531

10. Sivakumaran T, Jaffer R, Marwan Y, Hart A, Radu A, Burman M, et al. Reliability of anatomic bony landmark localization of the ACL femoral footprint using 3D MRI. *Orthop J Sports Med.* (2021) 9(10):23259671211042603. doi: 10.1177/23259671211042603

11. Han Y, Kurzencwyg D, Hart A, Powell T, Martineau PA. Measuring the anterior cruciate ligament's Footprints by three-dimensional magnetic resonance imaging. *Knee Surg Sports Traumatol Arthrosc.* (2012) 20(5):986–95. doi: 10.1007/s00167-011-1690-y

12. Cruz AI J, Fabricant PD, Seeley MA, Ganley TJ, Lawrence JT. Change in size of hamstring grafts during preparation for ACL reconstruction: effect of tension and circumferential compression on graft diameter. *J Bone Joint Surg Am.* (2016) 98:484–9. doi: 10.2106/JBJS.15.00802

13. Moksnes H, Grindem H. Prevention and rehabilitation of paediatric anterior cruciate ligament injuries. *Knee Surg Sports Traumatol Arthrosc.* (2016) 24:730–6. doi: 10.1007/s00167-015-3856-5

14. O'Connor JE, Bogue C, Spence LD, Last J. A method to establish the relationship between chronological age and stage of union from radiographic assessment of epiphyseal fusion at the knee: an Irish population study. *J Anat.* (2008) 212:198–209. doi: 10.1111/j.1469-7580.2007.00847.x

15. Harriss DJ, Macsween A, Atkinson G. Standards for ethics in sport and exercise science research: 2018 update. *Int J Sports Med.* (2017) 38:1126–31. doi: 10.1055/s-0043-124001

16. Guillard C, Lintz F, Odri GA, Vogeli D, Colin F, Collon S, et al. Effects of graft pretensioning in anterior cruciate ligament reconstruction. *Knee Surg Sports Traumatol Arthrosc.* (2012) 20:2208–13. doi: 10.1007/s00167-011-1833-1

17. Marchand JB, Ruiz N, Coupry A, Bowen M, Robert H. Do graft diameter or patient age influence the results of ACL reconstruction? *Knee Surg Sports Traumatol Arthrosc.* (2016) 24:2998–3004. doi: 10.1007/s00167-015-3608-6

18. Dodwell ER, Lamont LE, Green DW, Pan TJ, Marx RG, Lyman S. 20 Years of pediatric anterior cruciate ligament reconstruction in New York state. *Am J Sports Med.* (2014) 42:675–80. doi: 10.1177/0363546513518412

19. O'Connor JE, Coyle J, Spence LD, Last J. Epiphyseal maturity indicators at the knee and their relationship to chronological age: results of an Irish population study. *Clin Anat.* (2013) 26:755–67. doi: 10.1002/ca.22122

20. Hamada M, Shino K, Horibe S, Mitsuoka T, Toritsuka Y, Nakamura N. Changes in cross-sectional area of hamstring anterior cruciate ligament grafts as a function of time following transplantation. *Arthroscopy*. (2005) 21:917–22. doi: 10.1016/j.arthro.2005.05.006

21. Min BH, Chung WY, Cho JH. Magnetic resonance imaging of reconstructed anterior cruciate ligament. *Clin Orthop Relat Res*. (2001) 393:237–43. doi: 10.1097/00003086-200112000-00026

22. Amiel D, Kleiner JB, Roux RD, Harwood FL, Akeson WH. The phenomenon of "ligamentization": anterior cruciate ligament reconstruction with autogenous patellar tendon. *J Orthop Res*. (1986) 4:162–72. doi: 10.1002/jor.1100040204

23. Smigielski R, Zdanowicz U, Drwiega M, Ciszek B, Ciszkowska-Lyson B, Siebold R. Ribbon like appearance of the midsubstance fibres of the anterior cruciate ligament close to its femoral insertion site: a cadaveric study including 111 knees. *Knee Surg Sports Traumatol Arthrosc*. (2015) 23:3143–50. doi: 10.1007/s00167-014-3146-7

24. Iriuchishima T, Shirakura K, Fu FH. Graft impingement in anterior cruciate ligament reconstruction. *Knee Surg Sports Traumatol Arthrosc*. (2013) 21:664–70. doi: 10.1007/s00167-012-2014-6

25. Triantafyllidi E, Paschos NK, Goussia A, Barkoula NM, Exarchos DA, Matikas TE, et al. The shape and the thickness of the anterior cruciate ligament along its length in relation to the posterior cruciate ligament: a cadaveric study. *Arthroscopy*. (2013) 29:1963–73. doi: 10.1016/j.arthro.2013.09.007

frontiers | Frontiers in Surgery

TYPE Methods
PUBLISHED 06 January 2023
DOI 10.3389/fsurg.2022.951820

Check for updates

OPEN ACCESS

EDITED BY
Tsung-Yuan Tsai,
Shanghai Jiao Tong University, China

REVIEWED BY
Chen Zhu,
The First Affiliated Hospital of University of Science and Technology of China Anhui Provincial Hospital, China
Xiaowei Yu,
Shanghai Jiao Tong University, China

*CORRESPONDENCE
Feng Qiao
qiaofenghhyy@163.com

SPECIALTY SECTION
This article was submitted to Orthopedic Surgery, a section of the journal Frontiers in Surgery

RECEIVED 24 May 2022
ACCEPTED 27 September 2022
PUBLISHED 06 January 2023

CITATION
Lu Y, Wang X, Yang B, Xu Z, Zhang B, Jia B, He J, Qi L, Wang M and Qiao F (2023) Application of SolidWorks software in preoperative planning of high tibial osteotomy.
Front. Surg. 9:951820.
doi: 10.3389/fsurg.2022.951820

COPYRIGHT
© 2023 Lu, Wang, Yang, Xu, Zhang, Jia, He, Qi, Wang and Qiao. This is an open-access article distributed under the terms of the Creative Commons Attribution License (CC BY). The use, distribution or reproduction in other forums is permitted, provided the original author(s) and the copyright owner(s) are credited and that the original publication in this journal is cited, in accordance with accepted academic practice. No use, distribution or reproduction is permitted which does not comply with these terms.

Application of SolidWorks software in preoperative planning of high tibial osteotomy

Yufeng Lu[1], Xue Wang[2], Bo Yang[3], Zhaochen Xu[1], Baogang Zhang[1], Bin Jia[1], Jinlong He[1], Liang Qi[1], Min Wang[1] and Feng Qiao[1]*

[1]Department of Integrated Traditional Chinese Medicine (TCM) and Western Medicine Orthopedics, Honghui Hospital, Xi'an Jiaotong University, Xi'an, China, [2]Department of Emergency Medicine, Affiliated Hospital of Shaanxi University of Traditional Chinese Medicine, Xianyang, China, [3]Graduate School, Xi'an Medical University, Xi'an, China

Purpose: Open-wedge high tibial osteotomy (HTO) is a common surgical treatment for medial osteoarthritis in young and active patients. The accuracy of osteotomy is closely associated with postoperative efficacy. The accuracy of digital preoperative planning is higher than that of the preoperative manual measurement and several computer software with varying accuracy and convenience are used for digital preoperative planning. This study aimed to use the SolidWorks software for HTO preoperative planning and to determine its accuracy and reliability in HTO preoperative planning.

Methods: We reviewed the data of 28 patients with 54 with medial compartment knee arthritis who underwent open-wedge HTO preoperative planning using SolidWorks between June 2019 and March 2021. The standard anteroposterior standing whole-leg radiographs were assessed before and 6 weeks after the surgery. The correction angle, weight-bearing line (WBL) ratio, mechanical femorotibial angle (mFTA), and medial proximal tibial angle (MPTA) before and after the surgery were compared. The clinical results were evaluated using the Knee Society score.

Results: At 6 weeks after the surgery, the WBL ratio was corrected from 16.8% to 50.5%, mFTA was corrected from 6.4° varus to 1.2° valgus, and MPTA was corrected from 83.4° to 89.3°. No significant difference was observed between the predicted correction angle before the surgery and the correction angle measured 6 weeks after the surgery ($t = -1.745$, $p = 0.087$). The knee score and function score of Knee Society increased from 76.4 and 80.7 before surgery to 95.0 and 95.7, respectively.

Conclusions: The SolidWorks software showed high accuracy and reliability in preoperative planning of open-wedge HTO in patients with medial compartment knee arthritis.

KEYWORDS

open-wedge high tibial osteotomy, solidworks, preoperative planning, correction angle, weight-bearing line ratio

Introduction

High tibial osteotomy (HTO) is an effective method for the treatment of medial single-compartment knee osteoarthritis as it corrects the weight-bearing line (WBL) of the lower limbs (1). Currently, lateral closing wedge HTO and open-wedge HTO (OWHTO) are most commonly used. Compared with lateral closing wedge HTO, OWHTO is less traumatic, simpler, more convenient for the intraoperative adjustment of lower limb alignment, more accurate in deformity correction, and easily convertible to total knee arthroplasty without the need for fibula osteotomy (2). OWHTO is widely used and has achieved a favorable outcome in young and active patients with medial compartment knee arthritis.

Previous studies have reported that the accuracy of limb alignment correction is important in determining the success of HTO. Both over-correction and under-correction can affect the clinical outcome and survival rate of patients with medial compartment knee arthritis after HTO. According to the biomechanical studies performed by Hsu et al. (3), the medial compartment of the knee joint with a 1.2° mechanical femorotibial angle (mFTA) varus deformity can share 75% of the weight in a single-leg weight-bearing. To improve the accuracy of OWHTO, designing the correction angle and the opening gap preoperatively is necessary to determine the target WBL passing through a certain point of the tibial plateau in standing whole-leg radiographs. Currently, the most commonly used preoperative planning methods are the Miniaci method (4–7), Dugdale–Noyes method (8, 9), and Coventry method (10). Studies have reported that the Miniaci method is reliable, convenient, and simple to measure the opening angle and gap. It is most commonly used for OWHTO preoperative planning. Because of the wide applications of the picture archiving and communication system (PACS), orthographic images can be magnified at desirable magnification using the computer, thus making radiographic measurement convenient in preoperative planning. Studies have reported that the use of PACS for preoperative planning is highly reliable (11–13). In recent years, several computer software has originated to assist surgeons in HTO preoperative planning, such as the Materialise OrthoView software, Osteotomy Master (14), Biomet Orthosize, mediCAD (15, 16), and PreOPlan (16), which can be used to import patients' full-length orthographic images of lower limbs to calculate the opening angle and gap of the osteotomy. The accuracy of osteotomy has been greatly improved using these techniques. Recently, computer navigation (17) and three-D printing individualized osteotomy templates (18) have been developed to improve the accuracy of osteotomy but they are expensive and cumbersome for preoperative planning.

Since 2019, researchers are using the SolidWorks software in our institution for OWHTO preoperative planning, and good results have been achieved. This study aimed to evaluate the accuracy and reliability of the SolidWorks software for preoperative planning in patients undergoing medial OWHTO by comparing the preoperative and postoperative WBL ratio and opening angle.

Patients and methods

The study protocol was approved by the Institutional Review Board of our hospital (approval no. 202109009). Written informed consent was obtained from all participants.

We reviewed the medial open-wedge HTO performed by our center from June 2019 to April 2021.

The subject inclusion criteria were as follows: (1) age <45 years, (2) preoperative plan to use the SolidWorks software, (3) preoperative planning to design the knee joint weight line at 50% of the tibial plateau, and (4) knee varus deformity, varus <15°, knee joint Medial pain, osteoarthritis grade K-L 0-I grade; and (5) no restriction of the knee joint movement.

The study exclusion criteria were as follows: (1) presence of lesions in the lateral compartment of the knee joint; (2) knee joint ligament injuries, including medial and lateral laxity, instability of varus and valgus, and anterior and posterior cruciate ligament injuries; (3) obese patients, with BMI >30 kg/m^2, and (4) inflammation arthritis such as rheumatoid arthritis.

Using these criteria, 54 knees of 28 patients (15 women and 13 men) were included. There were a total of 26 left knees and 28 right knees. Of the 26 bilateral HTOs, 25 were performed bilaterally at one stage. One case underwent a procedure on the right side first, followed by that on the left side after 5 months. The mean patient age at the time of index operation was 32.6 ± 7.7 years (range: 18–44 years). The mean follow-up was 25.6 ± 6.8 months (range: 4–26 months) (**Table 1**).

Preoperative planning

The preoperative plan was completed by a senior orthopedic surgeon Qiao Feng. All patients were taken preoperatively with a standard anteroposterior full-length lower limb weight-bearing radiography.

TABLE 1 Patient demographics.

Characteristics	
Knees/patients	54/28
Ages (years)	32.6 ± 7.7
Male/female	13/15
Side (right/left)	28/26
Height (cm)	165.4 ± 8.2
Weight (kg)	61.1 ± 11.0
BMI (kg/m^2)	22.1 ± 2.5
Follow-up (month)	25.6 ± 6.8

We input the standard plain AP standing whole-leg radiographs into the SolidWorks 2016 (Dassault Systemes, USA) and corrected the radiograph magnification so that the software measured according to the scale marked on the radiograph.

The following measurements were made:

1. Draw a line from the center of the femoral head to the midpoint of the tibial plateau and extend it distally beyond the ankle joint. We defined this line as the target weight-bearing line (Figure 1).
2. Mark the lateral hinge point. We selected a point 15-mm distal to the lateral tibial plateau and an 8-mm medial to the proximal lateral cortex of the tibia as the lateral hinge point. Make a concentric circle with a lateral hinge point as the center, passing through the center of the ankle joint and the target weight-bearing line (Figure 2).
3. The osteotomy site was marked. We took the medial edge of the tibial plateau as the center, with a radius of 40 mm for the concentric circles, and the intersection with the medial cortex of the tibia was marked as the osteotomy site (Figure 3).
4. A line was made connecting the lateral hinge point and the center of the ankle joint, with a line connecting the lateral

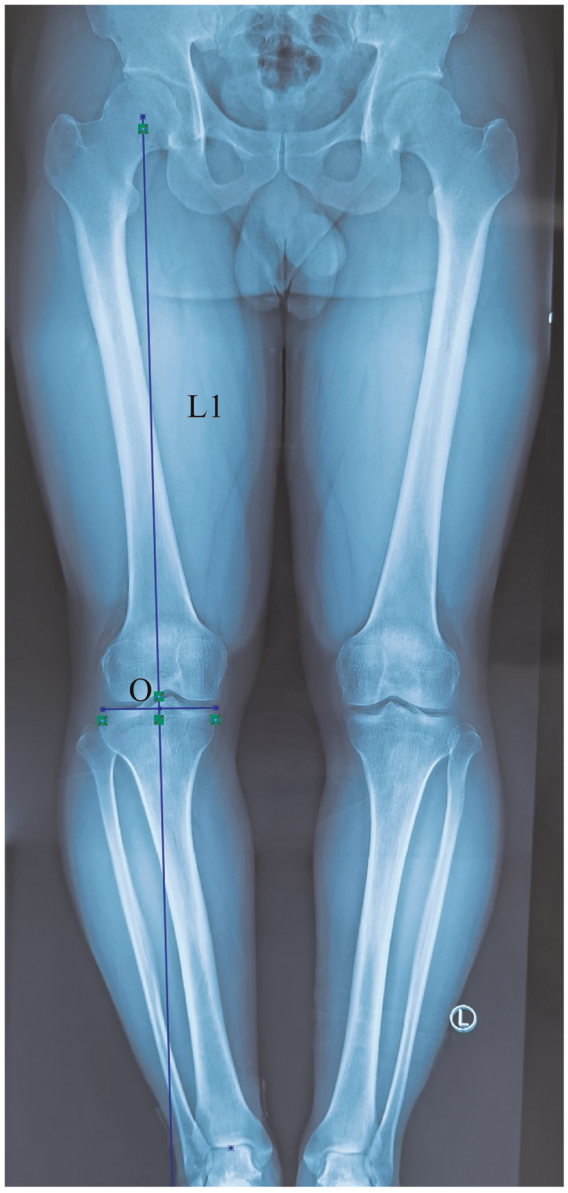

FIGURE 1
The target weight-bearing point (O) was set at 50% of the tibial plateau, and L1 represents the target weight-bearing line.

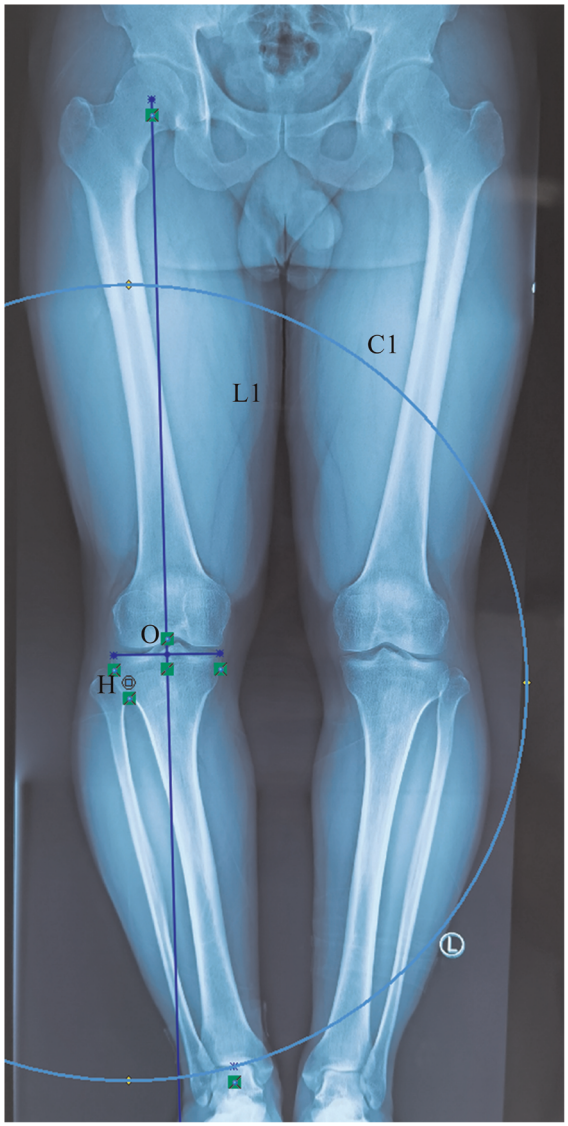

FIGURE 2
The site 15-mm distal to the lateral tibial plateau and 8-mm medial to the lateral cortex of the proximal tibia were selected as the hinge point (H). With point H as the center, a concentric circle was drawn through the center of the ankle joint (C1).

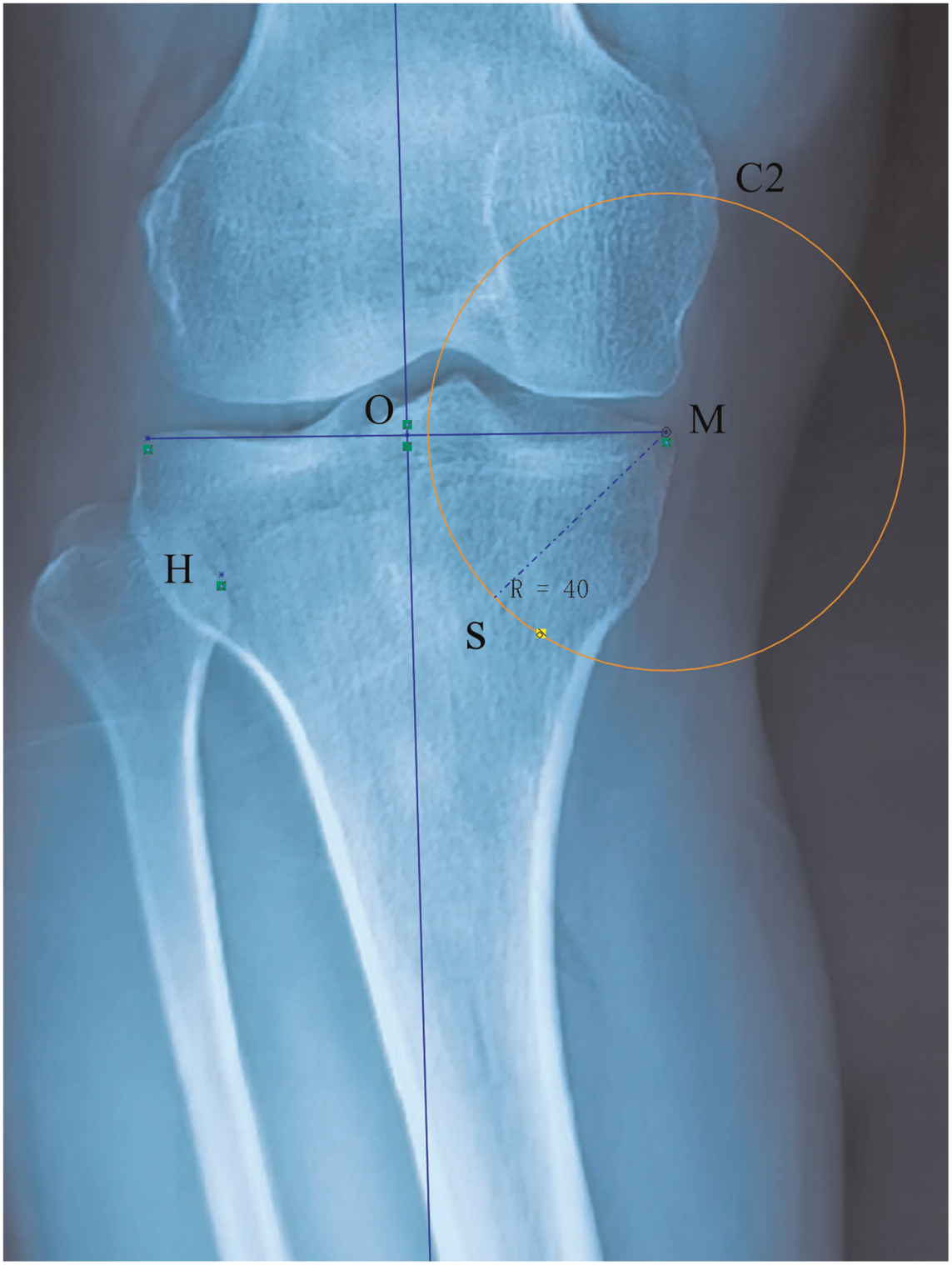

FIGURE 3
Point M represents the medial border of the tibial plateau. With M as the center and a concentric circle was drawn with a radius of 40 mm, which intersected at point S of the medial cortex of the tibia. Point S was selected as the osteotomy site.

hinge point and the intersection of the target weight-bearing line and the circle. The angle formed by the two lines served as the predicted correction angle.

5. Concentric circle was made with the lateral hinge point as the center and pass through the osteotomy site, and intersects the target WBL and the line from the lateral hinge point to the center of the ankle joint. The distance between the two intersection points was considered as the predicted correction gap (Figure 4).

Surgical techniques

All surgeries were performed by the same senior orthopedic surgeon. The patient was asked to lay down in a supine position, the affected limb was routinely disinfected, and the tourniquet was applied. Create a longitudinal incision on the anterior medial side of the tibia with a length of 4 cm–6 cm. The skin was cut subcutaneously and the deep fascia sequentially. The 4-cm distal end of the medial tibial plateau was used as the osteotomy site (using a 4-cm long-cut Kirschner wire to determine under fluoroscopy), and a ϕ 2.0 Kirschner wire was inserted oriented medially to laterally, to the target hinge point (approximately 15-mm distal to the lateral tibial plateau, 8-mm inside the outer edge of the tibia). After fluoroscopy confirmed the correct position, the osteotomy line parallel to the tibial slope on the sagittal plane was marked. The pes anserinus tendons were dissected and the superficial medial collateral ligament was freed and retracted along the

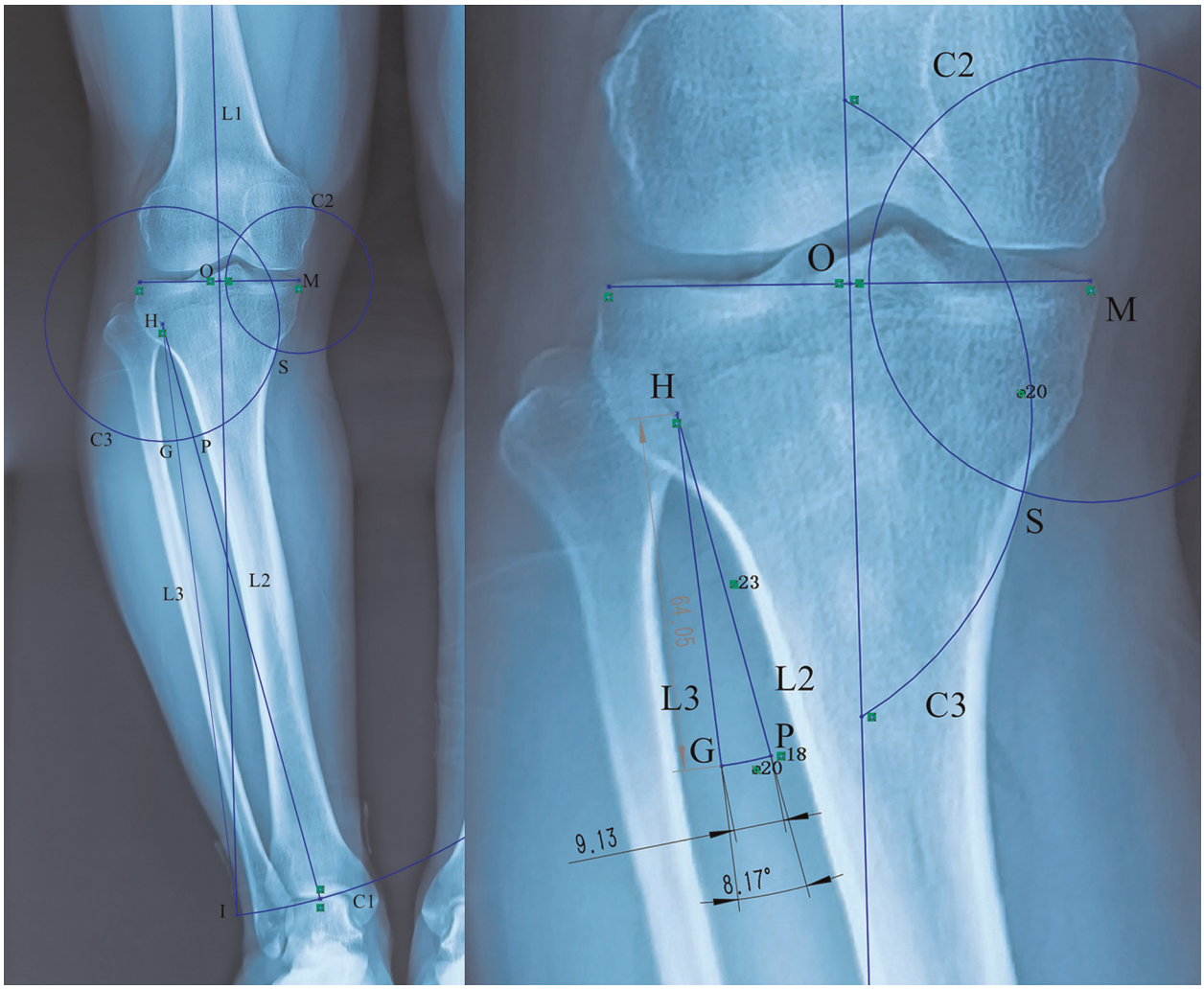

FIGURE 4
The H point was used as the center, and the distance from the H point to the ankle joint center (L2) was used as the radius to draw a concentric circle, L1 intersected at the I point, and line segment HI (L3) was drawn. The angle formed by L2 and L3 indicates the correction angle. Taking point H as the center, HS was used as the radius to draw a concentric circle that intersected L2 at point P and L3 at point G, while the length of the line segment PG indicated the length of the correction gap.

designed osteotomy line. Next, 2 Kirschner wires were inserted again on the marked osteotomy line, and 1 Kirschner wire was inserted into the posterior side of the tibial tubercle. After a blunt retractor was inserted posterior to the medial collateral ligament and the tibia to protect the neurovascular structures posterior to the incision line, an oscillating saw with 0.9-mm-thick saw blade was used to perform biplane osteotomy. During the sawing process, as per the preoperative plan, the sawing depth was controlled by the length scale of the saw blade. Then, stepwise insertion of 3–5 coupled chisels was performed into the osteotomy line and the spreader was finally used to gradually open out the medial cortex carefully, and then a trimmed tape was prepared during the operation, keeping the length exactly equal to the distance calculated preoperatively using the SolidWorks plus Saw blade thickness. When the opening reached the target distance, the laminar spreader was inserted into the posteromedial cortex of the tibia to maintain the realignment position. Finally, the TomoFix plate and locking screws (TomoFix, Synthes GmbH, Switzerland) were used to fix the osteotomized tibia. We did not use intraoperative fluoroscopy to examine the mechanical axis. The pes anserinus was not reconstructed when the wound was closed. If the tension of the medial collateral ligament was excessively large, the pie-crusting technique was used to loosen it until the tension was appropriate. None of the patients' lateral hinges were broken during the operation. We performed structural bone grafting for an opening distance >15 mm. On the first day after the operation, quadriceps and range-of-motion exercises were initiated. Full weight-bearing was allowed on the second day of surgery.

Radiographic measures

All measurements were performed on the AP standing whole-leg radiographs using picture archiving and communication systems (PACS) (Synapse, Fujifilm Inc., Tokyo Japan) before surgery and at 6 -weeks postoperative follow-up. (1) The percentage of the WBL passing through the tibial plateau (calculated from the medial plateau) (**Figure 5**); the acceptable postoperative range was set to 50 ± 5% (range: 45%–55%), and percentages lower or higher than this range were defined as under- or over-correction, respectively. (2) Mechanical femorotibial angle (mFTA). (3) Mechanical medial proximal tibial angle (mMPTA). (4) The correction angle. (5) Preoperative correction distance. Due to the occlusion of the plate, the correction distance of the osteotomy site on the medial tibia cannot be measured after the operation.

All measurements were performed by 2 observers who did not participate in the operation. After 3 weeks, the measurement was performed again. The intraclass correlation coefficient (ICC) was applied to determine the reliability of the measurement. The ICC values were characterized as follows: poor agreement (<0.40), fair to good agreement (0.40–0.75), and excellent agreement beyond chance (>0.75). The measurement data used the mean value of the first measurement of the 2 observers.

Clinical evaluation

Clinical outcome assessment used the knee social score (KSS) pre-operatively and at the final follow-up. The KSS comprises two parts: a knee score, which includes pain, stability, and a range of motion (ROM), and a function score, which includes the patient's ability to walk and climb stairs and the need for ambulatory aids.

Statistical analysis

Statistical analysis was performed using PASW Statistics ver.18.0 (SPSS Inc., Chicago, IL, USA). All measurement data were expressed as mean ± standard deviation. The paired *t*-test was used to compare the preoperative and postoperative parameters. $P < 0.05$ was set to indicate a statistically significant difference.

Results

The Kolmogorov–Smirnov test showed that all data followed the normal distribution pattern. ICC and interclass correlation coefficients for the reproducibility of all parameters were >80% (**Table 2**).

The WBL ratio on the tibial plateau was corrected from the preoperative mean of 16.8% ± 13.0% (range, −37.3% to 36.7%) to the postoperative mean of 50.5% ± 4.4% (range, 40.6% to 62.3%) ($t = 53$, $p < 0.001$) (**Table 3**).

Forty-three knees of correction were found to be within the acceptable range (79.6%, 49.3% ± 2.6%), 2 knees were under-corrected (3.7%, 41.8% ± 1.7%), and 9 knees were over-corrected (16.7%, 58.1% ± 1.8%) based on the WBL on the tibial plateau.

The mFTA was varus 6.4 ± 2.8° before the surgery and valgus 1.2 ± 1.3° after the surgery (**Table 3**). The preoperatively planned opening angle was 8.5 ± 3.5°, and the postoperative measurement correction angle was 8.8 ± 2.9°. No statistical difference was observed in the preoperative opening angle and postoperative correction angle ($t = 1.745$, $P = 0.087$) (**Table 3**). The average planned preoperative opening gap was 8.9 ± 3.7 mm. The KSS was significantly improved after the surgery (95.0 ± 3.6)

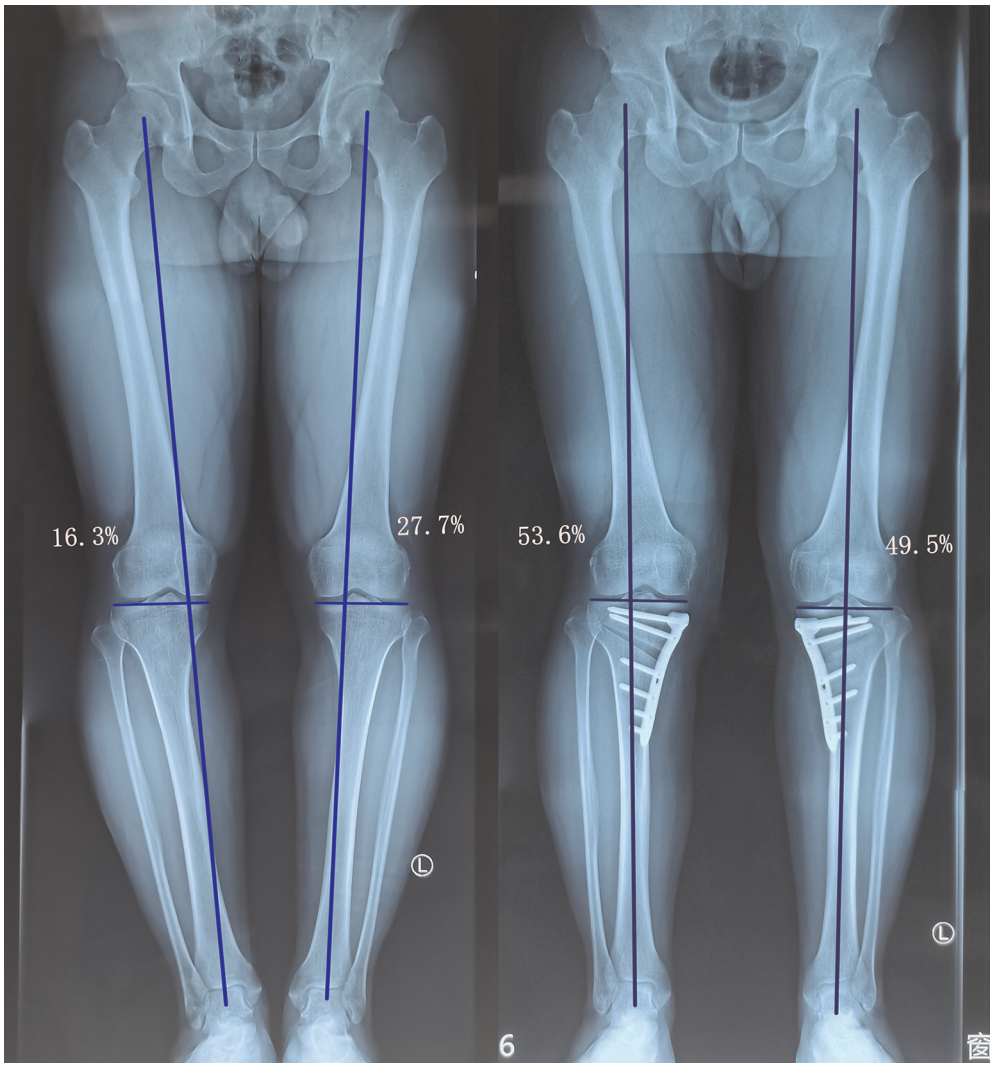

FIGURE 5
A 37-year-old man presented with medial compartment osteoarthritis (K-L grade I) and varus deformity in both knees. The WBL ratios of the left and right sides were 27.7% and 16.3% preoperatively, and 49.5% and 53.6% postoperatively, respectively.

TABLE 2 Intraclass correlation coefficient of radiographic parameters.

	Intrarater agreement	Interrater agreement
Preop. WBL	0.97	0.95
Postop. WBL	0.91	0.95
Preop. MPTA	0.99	0.87
Postop. MPTA	0.87	0.83
Postop. wedge angle	0.95	0.89
Preop. mFTA	0.97	0.90
Postop. mFTA	0.96	0.89

compared with the preoperative KSS (76.4 ± 8.2). The functional score was improved after the surgery (95.7 ± 4.9) compared with the preoperative functional score (80.7 ± 9.1) (Table 3).

Discussion

Digital preoperative planning has become the mainstream in OWHTO. He et al. (14) used the OsteoMaster software for preoperative planning, and the operation time and the number of x-ray fluoroscopy were significantly reduced compared with the traditional Miniaci method. The accuracy, depth, open height, correction angle, FTA, and WBL ratio of osteotomy were not reduced compared with the traditional Miniaci method. Kim et al. (11) used PACS technology for preoperative planning of open-wedge HTO and used the Miniaci method to measure the preoperative tibial plateau WBL ratio, correcting angle, and opening distance and to compare them with those of the last postoperative follow-up. No statistical difference was found between parameters

TABLE 3 Results of HTO using the SolidWorks methods.

		T value	*P* value
Weight-bearing line (%)			
Preoperative	16.8 ± 13.0	53	<0.001
Postoperative	50.5 ± 4.4		
Wedge angle (°)			
Preoperative	8.5 ± 3.5	−1.745	0.087
Postoperative	8.8 ± 2.9		
Mechanical femur-tibia angle (°)			
Preoperative	varus 6.4 ± 2.8	−18.605	<0.001
Postoperative	valgus 1.2 ± 1.3		
Mechanical medial proximal tibial angle (°)			
Preoperative	83.4 ± 2.7	−14.818	<0.001
Postoperative	89.3 ± 1.9		
Knee Society knee score			
Preoperative	76.4 ± 8.2	−18.843	<0.001
Postoperative	95.0 ± 3.6		
Knee Society function score			
Preoperative	80.7 ± 9.1	−15.165	<0.001
Postoperative	95.7 ± 4.9		

obtained by preoperative planning and postoperative x-ray radiography, indicating that PACS technology can be used for HTO preoperative planning.

Lee et al. (19) used the PACS-photoshop method and the Real-size paper template method for OWHTO preoperative planning, compared the two methods prospectively, and found that the former is highly reliable. Later, they (20) reviewed 72 cases treated by open-wedge HTO using the PACS-Photoshop method for preoperative planning. The postoperative measurement average correction gap was 10.8 mm; the correction gap of <10.8 mm was divided into one group, and that higher than 10.8 mm was divided into another group. By comparing the postoperative correction gap with the measured preoperative correction gap, they found that when the correction gap is large, the difference between the postoperative and preoperative WBL ratios increases. However, it did not deviate toward the side of either over-correction or under-correction. Schröter et al. (16) studied the inter-group reliability of the digital software PreOPlan and mediCAD for open-wedge HTO preoperative planning and found that both the software preoperative plans have a high degree of inter-group reliability, and are unaffected by the experience of the measurer. They (15) used the mediCAD digital software for OWHTO preoperative planning and closed distal femur osteotomy (DFO) preoperative planning for severe knee varus osteoarthritis, and good imaging and clinical results were obtained.

Some studies recently reported the use of 3D-planned patient-specific instrumentation (PSI) (21) and navigation system (22) to perform open-wedge HTO and a more accurate WBL ratio, especially tibial slope was obtained. However, Tardy et al. (23) performed a multi-center non-randomized controlled prospective observational study by comparing the parameters of 126 patients in the navigation group, PSI group, and traditional group using the Miniaci method in 11 centers. The results showed that none of the 3 techniques were superior in achieving target correction at 1 year. All the 3 techniques were reliable and precise in HTO planning.

The SolidWorks software is a powerful engineering drawing software. We have developed its imaging measurement function in the medical field. SolidWorks can mark equidistant points by making concentric circles. When SolidWorks measures the length, the accuracy can reach 0.0000001 mm and when it measures the angle, the accuracy can reach 0.0001°. However, the accuracy of PACS measuring length is only 0.01 mm, while the accuracy of measuring angle length is 1°. SolidWorks uses the principle that all radii of concentric circles are equal in length to reduce the measurement steps and the measurement errors. Compared with PACS, SolidWorks not only reduced the errors and improved the accuracy of the measurement but also reduced the measurement steps and improved the efficiency of the measurement. When compared to other 2D digital measurement software, SolidWorks measurement accuracy is the highest.

When open-wedge HTO is used to treat medial knee osteoarthritis, the optimal position of the lower limb WBL on the tibial plateau is debatable. Most studies (4, 5, 11, 14, 18, 22) have used the Fujisawa point as the target load line passing point of the tibial plateau. We used the Fujisawa point as the target point for performing open-wedge HTO in patients aged >45 years and having K-L grade II or higher for medial knee osteoarthritis. However, young and active patients <45 years of age and K-L grade did not exceed grade I for medial knee osteoarthritis when 50% of the tibial plateau was the target point. The short-term results of all cases were desirable but the long-term results will need follow-up.

Yoon et al. (5) compared the use of PACS for preoperative planning and intraoperative use of a cable method for open-wedge HTO using the tibial plateau target WBL ratio ±5° as the acceptable range of correction and found that the acceptable range of the intraoperative wire method was 55%, whereas that of the PACS method was 71.8%. Miniaci et al. (24) reported that only 50% of their cases were within the acceptable range (±10%) of correction after proximal tibial osteotomy. Kim et al. (11) used the PACS method for preoperative planning of OWHTO, and the acceptable range of correction (±5%) after surgery was 70%, under-correction was 20%, and over-correction was 10%. Using the SolidWorks software, we achieved the acceptable WBL ratio (±5%) of 79.6%, the under-correction of 3.7%, and the over-correction of 16.7%. The advantage of using the SolidWorks method is that fluoroscopy is not required to determine the alignment of the lower extremities during the surgery, thus reducing the x-ray radiation damage and the surgical time.

This study has several limitations. First, this study is a retrospective study having a small sample size and short follow-up time. Further studies using a large sample size and more patients are required to confirm the study findings. It would be best to perform a prospective randomized controlled study with a longer follow-up time to obtain more reliable results. Second, Sabharwal et al. (25) reported that the standing full-length anteroposterior radiograph magnification rate of the lower limbs was 4.6%. Their minimum patient-to-tube distance was 203 cm, whereas the minimum distance in our image center was 180 cm. Therefore, our magnification may be greater, which may be the reason for obtaining overall large values including the WBL ratio. Third, during the surgery, we controlled the posterior slope of the tibia by making the sagittal plane osteotomy line parallel to the tibial joint line and ensuring that the two osteotomy planes of the tibial tubercle were parallel. However, we did not compare the posterior tibial slope before and after the surgery. Finally, we kept the WBL in the center of the tibial plateau, which is debatable.

Conclusion

The SolidWorks software showed high accuracy and reliability in preoperative planning of open-wedge HTO in patients with medial compartment knee arthritis.

Data availability statement

The raw data supporting the conclusions of this article will be made available by the authors, without undue reservation.

Ethics statement

The studies involving human participants were reviewed and approved by the Institutional Review Board of Xi'an Honghui Hospital (approval no. 202109009). The patients/participants provided their written informed consent to participate in this study. Written informed consent was obtained from the individual(s) for the publication of any potentially identifiable images or data included in this article.

Author contributions

LY participated in the study design, and drafted the manuscript. XZ, ZB, JB, QL, and WM followed up with patients and provided the data. WX and HJ performed postoperative radiograph measurements. YB Interpreted and analyzed the data. QF designed the study and supervised the whole study process, and helped to review the manuscript. All authors contributed to the article and approved the submitted version.

Funding

The study was supported by a grant from Shaanxi Provincial Key Research and Development Project (CN) (grant no. 2019SF-214) and Traditional Chinese Medicine Inheritance and Innovation and "Qin Medicine" Development Key Scientific Research Project (2021-04-22-006).

Conflict of interest

The authors declare that the research was conducted in the absence of any commercial or financial relationships that could be construed as a potential conflict of interest.

Publisher's note

All claims expressed in this article are solely those of the authors and do not necessarily represent those of their affiliated organizations, or those of the publisher, the editors and the reviewers. Any product that may be evaluated in this article, or claim that may be made by its manufacturer, is not guaranteed or endorsed by the publisher.

Supplementary material

The Supplementary Material for this article can be found online at: https://www.frontiersin.org/articles/10.3389/fsurg.2022.951820/full#supplementary-material.

References

1. Lee OS, Ahn S, Ahn JH, Teo SH, Lee YS. Effectiveness of concurrent procedures during high tibial osteotomy for medial compartment osteoarthritis: a systematic review and meta-analysis. *Arch Orthop Trauma Surg*. (2018) 138 (2):227–36. doi: 10.1007/s00402-017-2826-4

2. Wu L, Lin J, Jin Z, Cai X, Gao W. Comparison of clinical and radiological outcomes between opening-wedge and closing-wedge high tibial osteotomy: a comprehensive meta-analysis. *PLoS One*. (2017) 12(2):e0171700. doi: 10.1371/journal.pone.0171700

3. Hsu RW, Himeno S, Coventry MB, Chao EY. Normal Axial alignment of the lower extremity and load-bearing distribution at the knee. *Clin Orthop Relat Res*. (1990) 255:215–27. doi: 10.1097/00003086-199006000-00029

4. Elson DW, Petheram TG, Dawson MJ. High reliability in digital planning of medial opening wedge high tibial osteotomy, using Miniaci's method. *Knee Surg Sports Traumatol Arthrosc*. (2015) 23(7):2041–8. doi: 10.1007/s00167-014-2920-x

5. Yoon SD, Zhang G, Kim HJ, Lee BJ, Kyung HS. Comparison of cable method and Miniaci method using picture archiving and communication system in preoperative planning for open wedge high tibial osteotomy. *Knee Surg Relat Res*. (2016) 28(4):283–8. doi: 10.5792/ksrr.16.052

6. Jiang X, Xie K, Han X, Ai S, Wu H, Wang L, et al. HKA angle-A reliable planning parameter for high tibial osteotomy: a theoretical analysis using standing whole-leg radiographs. *J Knee Surg*. (2022) 35(1):54–60. doi: 10.1055/s-0040-1712945

7. Blackburn J, Ansari A, Porteous A, Murray J. Reliability of two techniques and training level of the observer in measuring the correction angle when planning a high tibial osteotomy. *Knee*. (2018) 25(1):130–4. doi: 10.1016/j.knee.2017.11.007

8. Herman BV, Giffin JR. High tibial osteotomy in the ACL-deficient knee with medial compartment osteoarthritis. *J Orthop Traumatol*. (2016) 17(3):277–85. doi: 10.1007/s10195-016-0413-z

9. Sivertsen EA, Vik J, Meland ASV, Nerhus TK. The Dugdale planning method for high tibial osteotomies underestimates the correction angle compared to the Miniaci method. *Knee Surg Sports Traumatol Arthrosc*. (2021). doi: 10.1007/s00167-021-06663-z. [Epub ahead of print]

10. Coventry MB, Ilstrup DM, Wallrichs SL. Proximal tibial osteotomy. A critical long-term study of eighty-seven cases. *J Bone Joint Surg Am*. (1993) 75 (2):196–201. doi: 10.2106/00004623-199302000-00006

11. Kim HJ, Lee HJ, Shin JY, Park KH, Min SG, Kyung HS. Preoperative planning using the picture archiving and communication system technique in high tibial osteotomy. *J Orthop Surg (Hong Kong)*. (2017) 25 (1):2309499016684701. doi: 10.1177/2309499016684701

12. Kim YT, Choi JY, Lee JK, Lee YM, Kim JI. Coronal tibiofemoral subluxation is a risk factor for postoperative overcorrection in high tibial osteotomy. *Knee*. (2019) 26(4):832–7. doi: 10.1016/j.knee.2019.05.011

13. Kim JE, Kim DH, Lee JI, Choi HG, Jung YS, Lee SH, et al. Difference of preoperative varus-valgus stress radiograph is effective for the correction accuracy in the preoperative planning during opening-wedge high tibial osteotomy. *Knee Surg Sports Traumatol Arthrosc*. (2021) 4:1035–44. doi: 10.1007/s00167-020-06076-4

14. He A, Mao Y, Zhou Y, Kong Q, Zhang H, Chen Y, et al. Preoperative planning by osteotomy master software helps to improve the accuracy of target limb alignment in high tibial osteotomy. *J Orthop Surg Res*. (2020) 15(1):504. doi: 10.1186/s13018-020-02033-6

15. Schröter S, Nakayama H, Yoshiya S, Stöckle U, Ateschrang A, Gruhn J. Development of the double level osteotomy in severe varus osteoarthritis showed good outcome by preventing oblique joint line. *Arch Orthop Trauma Surg*. (2019) 139(4):519–27. doi: 10.1007/s00402-018-3068-9

16. Schröter S, Ihle C, Mueller J, Lobenhoffer P, Stöckle U, van Heerwaarden R. Digital planning of high tibial osteotomy. Interrater reliability by using two different software. *Knee Surg Sports Traumatol Arthrosc*. (2013) 21(1):189–96. doi: 10.1007/s00167-012-2114-3

17. Schröter S, Ihle C, Elson DW, Döbele S, Stöckle U, Ateschrang A. Surgical accuracy in high tibial osteotomy: coronal equivalence of computer navigation and gap measurement. *Knee Surg Sports Traumatol Arthrosc*. (2016) 24(11):3410–7. doi: 10.1007/s00167-016-3983-7

18. Kuriyama S, Morimoto N, Shimoto T, Takemoto M, Nakamura S, Nishitani K, et al. Clinical efficacy of preoperative 3D planning for reducing surgical errors during open-wedge high tibial osteotomy. *J Orthop Res*. (2019) 37(4):898–907. doi: 10.1002/jor.24263

19. Lee YS, Kim MK, Byun HW, Kim SB, Kim JG. Reliability of the imaging software in the preoperative planning of the open-wedge high tibial osteotomy. *Knee Surg Sports Traumatol Arthrosc*. (2015) 23(3):846–51. doi: 10.1007/s00167-013-2700-z

20. Lee OS, Lee ES, Lee YS. Disparity between preoperative target correction amount and postoperative correction amount in open wedge high tibial osteotomy. *Knee Surg Relat Res*. (2019) 31(2):126–31. doi: 10.5792/ksrr.18.034

21. Kim HJ, Park J, Shin JY, Park IH, Park KH, Kyung HS. More accurate correction can be obtained using a three-dimensional printed model in open-wedge high tibial osteotomy. *Knee Surg Sports Traumatol Arthrosc*. (2018) 26 (11):3452–8. doi: 10.1007/s00167-018-4927-1

22. Ribeiro CH, Severino NR. Moraes de barros fucs PM. Opening wedge high tibial osteotomy: navigation system compared to the conventional technique in a controlled clinical study. *Int Orthop*. (2014) 38(8):1627–31. doi: 10.1007/s00264-014-2341-y

23. Tardy N, Steltzlen C, Bouguennec N, Cartier JL, Mertl P, Batailler C, et al. Is patient-specific instrumentation more precise than conventional techniques and navigation in achieving planned correction in high tibial osteotomy? *Orthop Traumatol Surg Res*. (2020) 106(8S):S231–6. doi: 10.1016/j.otsr.2020.08.009

24. Miniaci A, Ballmer FT, Ballmer PM, Jakob RP. Proximal tibial osteotomy. A new fixation device. *Clin Orthop Relat Res*. (1989) 246:250–9. doi: 10.1097/00003086-198909000-00035

25. Sabharwal S, Zhao C, McKeon JJ, McClemens E, Edgar M, Behrens F. Computed radiographic measurement of limb-length discrepancy. Full-length standing anteroposterior radiograph compared with scanogram. *J Bone Joint Surg Am*. (2006) 88(10):2243–51. doi: 10.2106/JBJS.E.01179

frontiers | Frontiers in Surgery

TYPE Original Research
PUBLISHED 17 January 2023
DOI 10.3389/fsurg.2022.1003879

Check for updates

OPEN ACCESS

EDITED BY
Yan Yu,
Tongji University School of Medicine, China

REVIEWED BY
Jun-Young Kim,
Catholic University of Daegu, Korea
Shaojie Tang,
Xi'an University of Posts and Telecommunications, China

*CORRESPONDENCE
Fangyuan Yu
✉ yufy-1@163.com

†These authors have contributed equally to this work and share first authorship

SPECIALTY SECTION
This article was submitted to Orthopedic Surgery, a section of the journal Frontiers in Surgery

RECEIVED 26 July 2022
ACCEPTED 21 December 2022
PUBLISHED 17 January 2023

CITATION
Li P, Xie C, Liu Y, Wen Z, Nan S and Yu F (2023) Quantitative analysis of local microcirculation changes in early osteonecrosis of femoral head: DCE-MRI findings.
Front. Surg. 9:1003879.
doi: 10.3389/fsurg.2022.1003879

COPYRIGHT
© 2023 Li, Xie, Liu, Wen, Nan and Yu. This is an open-access article distributed under the terms of the Creative Commons Attribution License (CC BY). The use, distribution or reproduction in other forums is permitted, provided the original author(s) and the copyright owner(s) are credited and that the original publication in this journal is cited, in accordance with accepted academic practice. No use, distribution or reproduction is permitted which does not comply with these terms.

Quantitative analysis of local microcirculation changes in early osteonecrosis of femoral head: DCE-MRI findings

Pinxue Li[1†], Congqin Xie[2,3†], Yubo Liu[1,2†], Zhentao Wen[4], Shaokui Nan[2,3] and Fangyuan Yu[2,3*]

[1]School of Medicine, Nankai University, Tianjin, China, [2]Department of Orthopedics, The Fourth Medical Center of PLA General Hospital, Beijing, China, [3]National Clinical Research Center for Orthopedics, Sports Medicine & Rehabilitation, Beijing, China, [4]Department of Orthopedics, Handan First Hospital, Handan, China

Aim: This study aims to quantitatively analyze the changes in local microcirculation in early osteonecrosis of the femoral head (ONFH) by dynamic contrast-enhanced (DCE) MRI and to explore the pathophysiological mechanisms of early ONFH.

Patients and Methods: We selected 49 patients (98 hips) aged 21–59 years who were clinically diagnosed with early ONFH. A total of 77 femoral heads were diagnosed with different degrees of necrosis according to the Association Research Circulation Osseous (ARCO) staging system, and 21 femoral heads were judged to be completely healthy. All patients underwent DCE-MRI scanning. Pseudocolor images and time-signal intensity curves were generated by Tissue 4D processing software. The volume transfer constant (K^{trans}), extracellular extravascular space, also known as vascular leakage (V_e), and transfer rate constant (K_{ep}) of healthy and different areas of necrotic femoral heads were measured on perfusion parameter maps. The differences and characteristics of these parameters in healthy and different areas of necrotic femoral heads were analyzed.

Results: The signal accumulation in healthy femoral heads is lower than that of necrotic femoral heads in pseudocolor images. The time-signal intensity curve of healthy femoral heads is along the horizontal direction, while they all have upward trends for different areas of necrotic femoral heads. The mean value of K^{trans} of healthy femoral heads was lower than the integration of necrotic, boundary, and other areas ($F = 3.133$, $P = .036$). The K_{ep} value of healthy femoral heads was higher than the integration of lesion areas ($F = 6.273$, $P = .001$). The mean V_e value of healthy femoral heads was smaller than that of the lesion areas ($F = 3.872$, $P = .016$). The comparisons of parameters between different areas and comparisons among healthy areas and lesion areas showed different results.

Conclusion: ONFH is a complex ischemic lesion caused by changes in local microcirculation. It mainly manifests as increased permeability of the vascular wall, blood stasis in the posterior circulation, high intraosseous pressure in the femoral head, and decreased arterial blood flow. The application of DCE-MRI scanning to quantitatively analyze the visual manifestations of microcirculation after early ONFH is an ideal method to study the microcirculation changes of necrotic femoral heads.

KEYWORDS

osteonecrosis of femoral head, dynamic contrast-enhanced MRI, vascular function parameters, microcirculation change, diagnostic value

Introduction

Many theories have been proposed to decipher the mechanism behind the development of osteonecrosis of the femoral head (ONFH), including the altered lipid metabolism and fat emboli theories (1, 2), intravascular coagulation theory (3), inhibition of angiogenesis theory (4), and elevated intracortical pressure theory (5). However, none of the above has been proven. To date, the pathophysiological characteristics of ONFH are still controversial. Little evidence has fully clarified the microcirculation changes in necrotic femoral heads.

With the continuous development of imaging, magnetic resonance (MR), as an examination method without ionizing radiation and with good soft tissue resolution, has received more attention from clinicians and patients. Especially in recent years, the continuous application and development of dynamic contrast-enhanced (DCE)-MRI technology and its postprocessing software have made it possible to detect the characteristics of angiogenesis and hemodynamics in tissues and directly reflect the changes in microcirculation at the lesion site (6). In DCE-MRI, the quantity of enhancement at the lesion site is closely related to the blood perfusion parameters in the local tissue, vascular enrichment, and the permeability of microvessels in the lesion tissue (6, 7).

DCE-MRI has been widely used in the evaluation of the diagnosis and treatment of tumors of various systems (8, 9). In recent years, the application of DCE-MRI to the musculoskeletal system has received more attention (10–12). Quantitative analysis of vascular function parameters obtained by DCE-MRI has been applied to femoral neck fractures (13), while there are few studies on the mechanism of ONFH (14). In this study, DCE-MRI was used to scan femoral head lesions. Vascular function parameters obtained by the postprocessing software workstation were used to quantitatively analyze the K^{trans}, V_e, and K_{ep} values in different areas of normal and necrotic femoral heads. Differences and characteristics of these parameters in different areas of normal and necrotic femoral heads were compared, and the changes in local microcirculation after ONFH were discussed, providing a theoretical basis for clinical treatment of the disease.

Patients and methods

Inclusion and exclusion criteria

In this study, 49 patients with ONFH diagnosed clinically according to Association Research Circulation Osseous (ARCO) staging (15) were analyzed. All patients underwent DCE-MRI scans of the femoral heads. There were 77 necrotic (16 in stage I and 61 in stage II) and 21 completely healthy femoral heads. The patients ranged in age from 21 to 59 years, with an average age of 39.3 years, including 40 males and 9 females. Among them, 13 patients had a history of steroid use, 25 patients had a history of long-term alcohol consumption, and 11 patients had no clear etiology.

The inclusion criteria required patients with (1) a diagnosis of stage I–II femoral bone necrosis according to ARCO staging; (2) ONFH not caused by joint infection or trauma; (3) no circulatory, hepatic, renal, or other system diseases and who can tolerate DCE-MRI examination; (4) ages between 20 and 60, regardless of sex; and (5) informed consent to the relevant information and risks of this study and voluntary participation in this study. The exclusion criteria required patients with (1) contraindications to MRI examination; (2) previous radiotherapy, chemotherapy, or hepatic and renal dysfunctions; and (3) no willingness to participate in the study after fully understanding the relevant situation and risks of the study. A flow diagram of included and excluded patients is provided in **Figure 1**.

DCE-MRI scanning

Dynamic enhanced MRI T1WI, T2WI, and T1 scans were performed on all patients. A Siemens Magnetom Skyra 3.0T superconducting MRI scanner (Siemens Healthineers GmbH, Erlangen, Germany) with Body 18 A 3T Tim Coil (Siemens Healthineers GmbH, Erlangen, Germany) was used. Patients were placed in a supine position with their heads first. Body 18 A 3T Tim Coil was used to cover the abdomen. The scanning center was determined to be 3 cm above the symphysis pubis. The coil was firmly fixed with the bandage to avoid artifacts.

Start with a routine hip scan: Axial T1WI [time of repetition (TR) 868 ms, time of echo (TE) 10 ms, number of slices 19, slice thickness 4.0 mm, field of view (FOV) 300 mm, number of excitation (NEX) 1, flip angle (FA) 145°], T2WI-FS (TR 3600 s, TE 77 ms, slice thickness 4.0 mm, NEX 2) sequence, Coronal T2WI-FS (TR 2300 ms,TE 33 ms, slice thickness 3.0 mm) sequence; Axial T1 dynamic enhanced scanning: T1 mapping (TR/TE 4.09 ms/1.39 ms; FOV 300 mm; slice thickness 3.5 mm; slice gap 0.3 mm, NEX 1; FA 2°/15°). Then, T1 continuous enhanced sequences (TR/TE 4.83 ms/1.87 ms, FOV 300 mm, slice thickness 3.5 mm, slice gap 0.3 mm, NEX 1, FA 15°, total scanning phases 75, total scanning time 26 min) were used in the axial position. At the end of the 5th phase of data collection, the contrast medium gadopentetate dimeglumine (Gd-DTPA) (flow rate: 2.5 mL/s, 0.2 mmol/kg) was injected into the upper elbow vein at high pressure, followed by 20 mL of normal saline, with a flow rate of 5.0 mL/s. Scan without intermittency.

Image processing

The original images obtained by DCE-MRI were sent to the Siemens Syngo (Siemens Healthineers GmbH, Erlangen, Germany) workstation. The images of the first 75 stages were selected, after contrasting medium injection, and the data were postprocessed by Tissue 4D software (Siemens Healthineers GmbH, Erlangen, Germany).

Image processing of normal femoral heads: The axial plane is the main measuring plane. The slice that can show the largest diameter of the femoral head is regarded as the best slice. The whole femoral head was selected as the region of interest (ROI), excluding the cortex. After computer processing, the time-signal intensity curve was generated to display the pseudocolor image of the ROI. The vascular function parameters K^{trans}, V_e, and K_{ep} values were calculated.

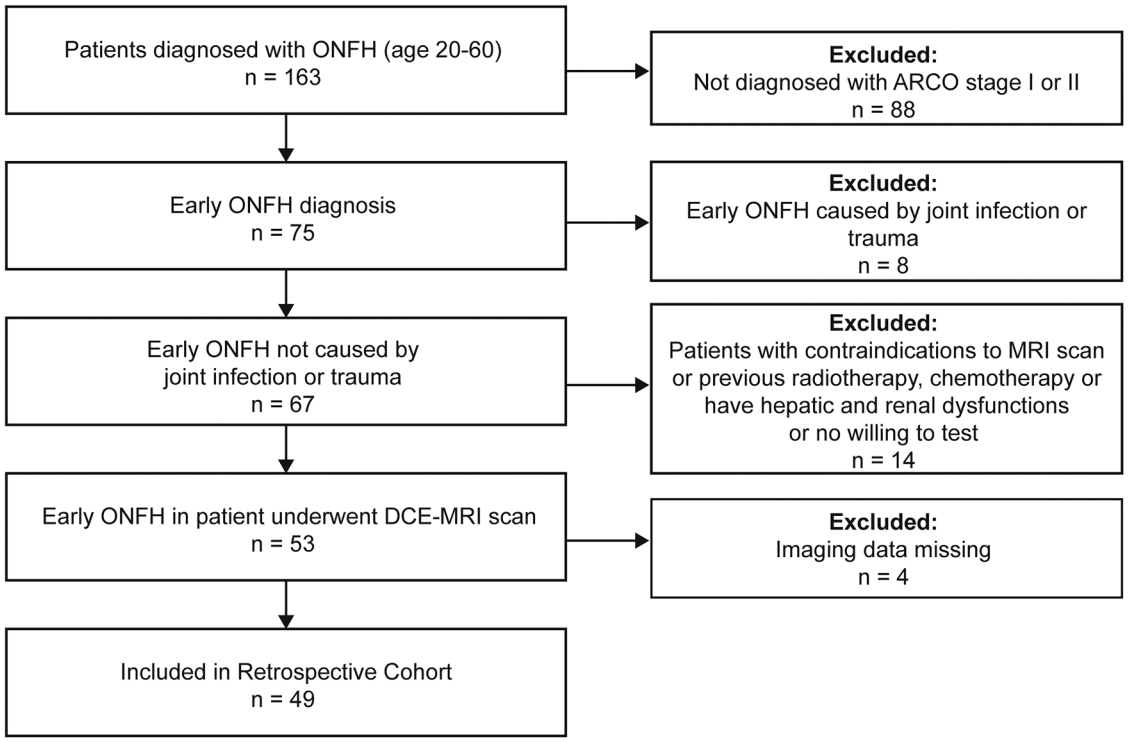

FIGURE 1
A flow diagram of included and excluded patients.

Image processing of necrotic femoral heads: (1) The axial plane is the main measuring plane. The slice with the largest lesion area is considered the best slice after image motion correction. The whole femoral head was selected as the ROI, excluding the cortex. ROI-1 (healthy femoral heads) was defined as the normal femoral head area. ROI-2 (necrotic area) was defined as the focal signal change in the subchondral area of the anterolateral weight-bearing area of the femoral head with segmental hyposignal on T1WI or "double line sign" on T2WI. ROI-3 (the boundary area or repair area) was defined as the boundary area of the necrotic area. ROI-4 (edema area) was defined as the focal signal change in the femoral head with a high signal on T2WI. After computer processing, the time-signal intensity curve was generated to display the pseudocolor image of the ROI. The vascular function parameters K^{trans}, V_e, and K_{ep} values were calculated. (2) The axial plane is the main measuring plane. The best slice is determined by image motion correction and is the slice that best shows lesions. The necrotic area, boundary area, and other areas of the necrotic femoral heads were selected as target sites. ROIs can be round or oval, including as many target areas as possible. After computer processing, the time-signal intensity curve was generated to display the pseudocolor image of the ROI. The vascular function parameters K^{trans}, V_e, K_{ep}, and iAUC were calculated.

All postprocessing of perfusion MRI images was completed by two imaging physicians with senior professional titles.

Statistical process

All tests were performed using SPSS 18.0 (IBM Corp, Armonk, NY, USA). All measurement data were tested for normality and homogeneity of variance by a single-sample K–S test and the Levene variance homogeneity test. Independent sample T tests were used to compare the overall parameters of the normal and necrotic femoral heads. Analysis of variance (ANOVA) was used to compare the parameters of normal femoral heads with those of necrotic, boundary, and other areas of necrotic femoral heads. The least-significant difference (LSD) method was used for data with homogeneity of variance, and Tamhane's T2 (M) method was used for data with unequal variance. For data with unequal variances, the independent sample T test was used to further demonstrate the comparison among groups.

All measurement data are expressed as the mean ± standard deviation. The significance level was $\alpha = 0.05$, and a P-value < .05 was considered significant in all analyses.

Results

All 49 patients who underwent DCE-MRI scanning received high-quality images that could be used for postprocessing. No errors were found in the processing of the Tissue 4D software, and there was no obvious artifact affecting the measurement of parameters and no obvious error in the obtained quantitative parameters.

Generation of pseudocolor images and time-signal curves and comparisons between healthy and necrotic femoral heads

Pseudocolor images and time-signal intensity curves of normal and necrotic femoral heads can be obtained by using

DCE-MRI scanning technology and Tissue 4D processing software (Figures 2, 3).

The mean value of K^{trans} healthy femoral heads was lower than the integration of necrotic, boundary, and other areas ($F = 3.133$, $P = .036$). The K_{ep} value of healthy femoral heads was higher than the integration of lesion areas ($F = 6.273$, $P = .001$). The mean value of V_e in healthy femoral heads was smaller than that of the lesion areas ($F = 3.872$, $P = .016$).

Comparison of quantitative parameters among the normal area, necrotic area, edema area, and boundary area of the femoral heads

The values of K^{trans}, K_{ep}, and V_e in the normal area, necrosis area, edema area, and boundary area of the femoral heads conformed to a normal distribution and homogeneity of variance. One-way ANOVA

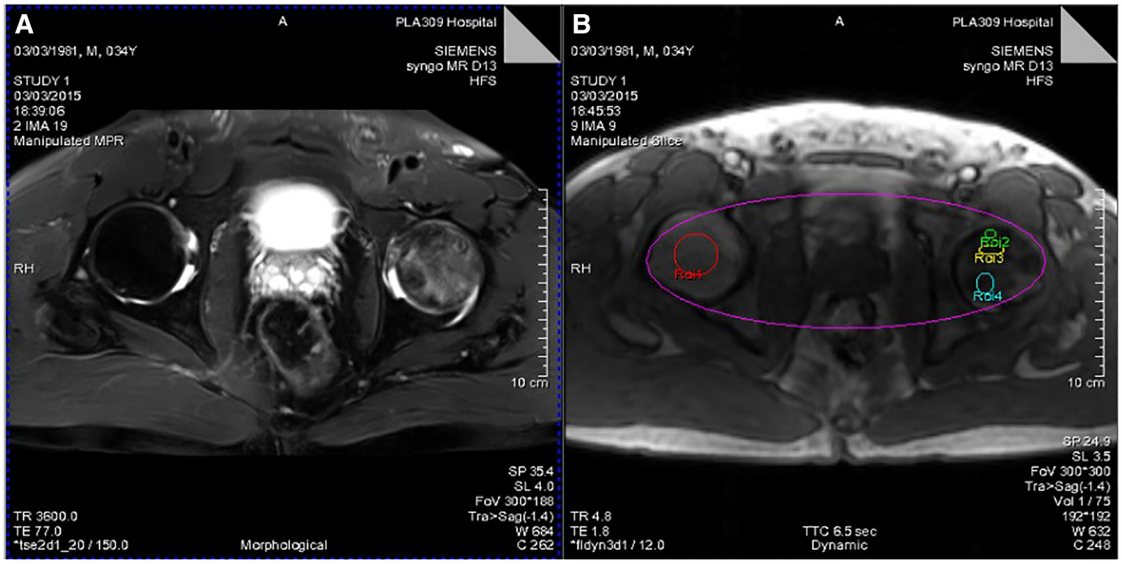

FIGURE 2
(A) T2WI lipid suppression image showing necrosis and edema of the left femoral head. (B) Different ROIs selected by Tissue 4D processing software (ROI-1, healthy femoral heads; ROI-2, necrotic area; ROI-3, boundary area; ROI-4, edema area).

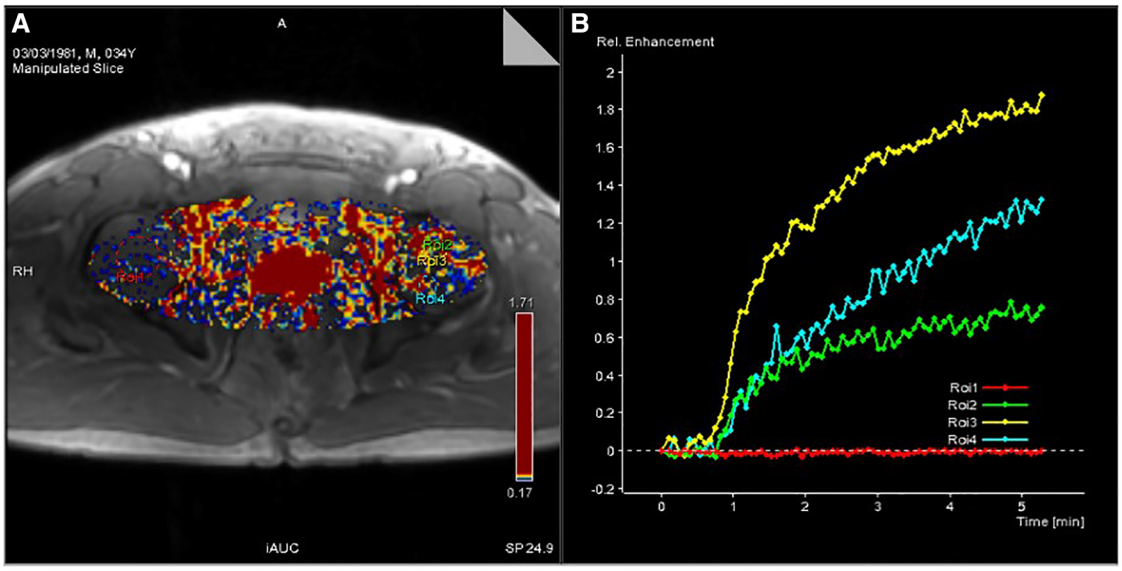

FIGURE 3
(A) Pseudocolor image processed by Tissue 4D software. (B) Time-signal intensity curve of ROIs of the four selected regions of the femoral head generated by Tissue 4D software.

revealed statistically significant effects in K^{trans} ($F = 3.133$, $P = .036$), K_{ep} ($F = 6.273$, $P = .001$), and V_e ($F = 3.872$, $P = .016$) among the normal area, necrotic area, edematous area, and boundary area of the femoral heads. The mean values of K^{trans} and V_e in the boundary area were higher than those in the necrotic area, edema area, and normal area of the femoral heads. The mean values of K^{trans} and V_e in the normal area were lower than those in the necrotic area and edema area. In the necrotic area, K^{trans} was higher and V_e was lower than those in the edema area. The K_{ep} value was the highest in the normal area, followed by the necrotic area, the edema area, and the lowest in the boundary area. In pairwise comparisons, the values of K^{trans}, K_{ep}, and V_e were statistically significant between the normal and boundary areas. The K_{ep} values were statistically significant in comparisons between normal and necrotic areas and normal and edema areas. The values of V_e were statistically significant between the necrotic and boundary areas. There was no statistical significance in pairwise comparisons among other groups ($P > .05$) (Tables 1, 2 and Figures 4–6).

Comparison of quantitative parameters between healthy and different areas of necrotic femoral heads

The values of K^{trans}, K_{ep}, and V_e in healthy femoral heads conformed to a normal distribution. Compared with necrotic and boundary areas, healthy femoral heads had significant differences in the mean values of K^{trans}, K_{ep}, and V_e. Compared with the normal area of necrotic femoral heads, only the K^{trans} difference was statistically significant, and when compared with the edema area, the K_{ep} and V_e value differences were statistically significant (Tables 3, 4).

Discussion

DCE-MRI is a widely used examination method to detect changes in microcirculation and blood circulation in relevant parts of the musculoskeletal system. The time-signal intensity curve and pseudocolor image of the target site can be obtained after processing by Tissue 4D software to semi-quantitatively describe the microcirculation characteristics of the target site. The quantitative analysis of DCE-MRI is based on the two-compartment Tofts–Kermode model, and then a series of corresponding mathematical calculations were performed to obtain the vascular functional parameters that could quantitatively reflect the changes in microcirculation and blood circulation at the target site (16–19). The parameters include the volume transfer constant (K^{trans}), extracellular extravascular space, also known as vascular leakage (V_e) and transfer rate constant (K_{ep}); K^{trans} represents the transport volume of small molecule contrast medium diffused from intravascular to extravascular space per unit time, which is mainly affected by microcirculation structure, blood flow, the transport process of contrast medium through the blood vessel wall, and the diffusion process of contrast medium in intercellular space. K_{ep} represents the amount of contrast medium returned to the blood vessel after tissue diffusion within a unit time.

Analysis of time-signal intensity curves and pseudocolor images obtained by DCE-MRI scanning

The pseudocolor image processed by Tissue 4D software (Figure 3A) indicates that the necrotic femoral head presents a high accumulation of enhanced signals, while the healthy femoral head presents a low accumulation of enhanced signals. From the

TABLE 1 Results of mean values of vascular function parameters in the normal area, necrotic area, edema area, and boundary area of femoral heads in patients with ONFH.

T1 parameters[a]	Normal area	95% CI	Necrotic area	95% CI	Edema area	95% CI	Boundary area	95% CI
	A, $n = 43$		B, $n = 64$		C, $n = 49$		D, $n = 53$	
K^{trans}	0.021 ± 0.012	0.013–0.028	0.032 ± 0.020	0.018–0.443	0.028 ± 0.033	0.003–0.059	0.052 ± 0.033	0.031–0.073
K_{ep}	4.926 ± 3.606	2.634–7.218	1.872 ± 1.820	0.715–3.028	1.027 ± 2.303	0.000–3.158	1.016 ± 1.620	0.000–0.389
V_e	0.091 ± 0.161	0.000–0.193	0.135 ± 0.139	0.045–0.224	0.224 ± 0.199	0.040–0.408	0.295 ± 0.148	0.201–0.389

ONFH, osteonecrosis of the femoral head.
[a]The unit of K^{trans} and K_{ep} is min^{-1}; V_e is constant without unit.

TABLE 2 Results of pairwise comparisons among the normal area, necrotic area, edema area, and boundary area of femoral heads in patients with ONFH.

T1 parameters	A and B	A and C	A and D	B and C	B and D	C and D
	P-value	*P*-value	*P*-value	*P*-value	*P*-value	*P*-value
K^{trans}	$P = .334$	$P = .549$	$P = .005$[a]	$P = .815$	$P = .061$	$P = .061$
K_{ep}	$P = .005$[a]	$P = .002$[a]	$P = .000$[a]	$P = .479$	$P = .404$	$P = .993$
V_e	$P = .500$	$P = .086$	$P = .003$[a]	$P = .245$	$P = .018$[a]	$P = .350$

A, normal area; B, necrotic area; C, edema area; D, boundary area; ONFH, osteonecrosis of the femoral head.
[a]The difference between the two groups were statistically significant.

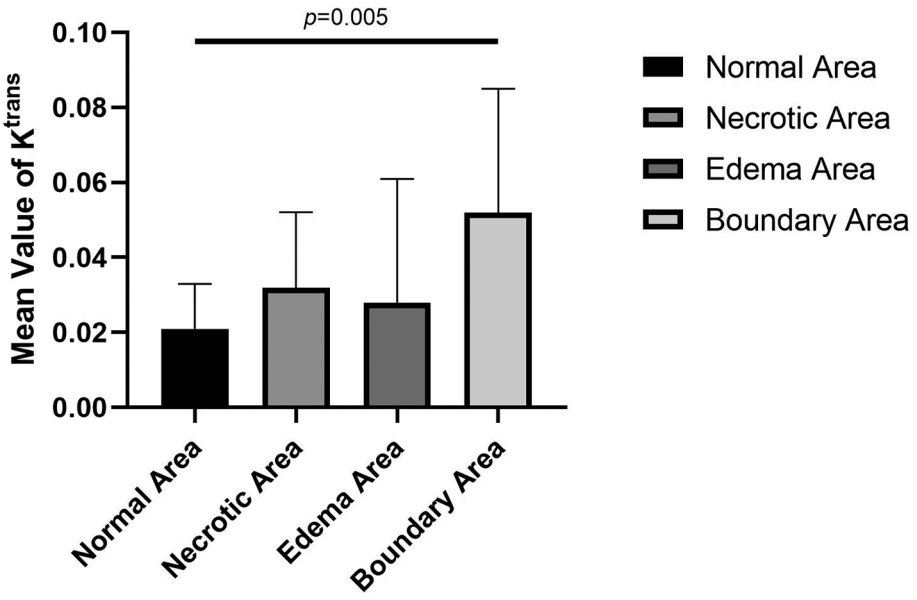

FIGURE 4
Comparison of mean values of K^{trans} of normal, necrotic, edema, and boundary areas of femoral heads in patients with ONFH.

many hypotheses about the mechanism of ONFH, the pathophysiological development will cause changes in the microcirculation of the femoral head, such as blood stasis in the posterior circulation, venous obstruction, reduced arterial blood supply, and intraosseous high pressure in the femoral head. In the pseudocolor image (Figure 3A), the high accumulation of enhancement signals after ONFH also confirmed the changes in microcirculation in the hypotheses above. Due to blood stasis in the posterior circulation after osteonecrosis, blocked venous return and high pressure in the femoral head, the permeability of the vascular wall of the microcirculation was changed. The large amount of contrast medium exuded from the blood vessels could not be effectively excluded, resulting in a high accumulation of enhanced signals. However, in healthy femoral heads, microcirculation, the vascular wall, and intraosseous pressure were all under physiological conditions, and contrast medium showed normal intake and excretion, resulting in a low accumulation of enhanced signals.

Figure 3B shows the time-signal intensity curve generated by Tissue 4D software processing the selected ROIs. The red curve is the time-signal intensity curve of ROI-1 selected in the healthy femoral head, which fluctuates in the horizontal direction, indicating the normal uptake and elimination of contrast medium. The green curve is the time-signal intensity curve of ROI-2 in the necrotic area of the selected left femoral head, which shows a slow upward trend, indicating a decrease in microcirculation vessels, poor blood circulation, less contrast medium intake, slow elimination, yet still slow accumulation of contrast medium. The yellow curve is the time-signal intensity curve of ROI-3 in the boundary area (repair area), which is located at the edge of the necrotic area of the femoral head and has the fastest upward trend and the highest signal accumulation. Due to capillary angiogenesis and high vascular permeability due to incomplete development of the neonatal capillary wall, the boundary area has the best blood supply, the fastest arrival, and the most content of contrast medium compared with other areas. Nevertheless, due to blood stasis in the microcirculation, the contrast medium is not eliminated quickly enough to generate the fastest-rising time-signal intensity curve. The blue curve is the time-signal intensity curve of ROI-4 in the edema area of the femoral head selected, which has a faster upward trend than in the necrotic area, indicating high vascular permeability and better blood supply than that in the necrotic area. Due to intercellular edema, and blood stasis in the microcirculation, the accumulation of contrast medium is relatively difficult to eliminate.

Analysis of changes in microcirculation and blood supplies among different areas of necrotic femoral heads

In this study, DCE-MRI quantitative analysis showed that the mean value of K^{trans} was the lowest in the normal area, followed by the edema area and necrotic area, and the highest value appeared in the boundary area (repair area) of necrotic femoral heads (Table 1 and Figure 4).

K^{trans} denotes the transport volume of small molecule contrast medium diffused from intravascular to extravascular within a unit time, which is influenced primarily by microcirculation structure, blood flow, contrast medium diffusion through vascular walls and intercellular spaces. Previous studies have found that an abnormal increase in the K^{trans} value is believed to be related to the microvascular density and vascular permeability of the detected site (20). Glueck et al. (21) proposed in their study that mutations in the eNOS gene are positively correlated with ONFH and could lead to incomplete structures in the vascular wall during

TABLE 3 Mean values of K^{trans}, K_{ep}, and V_e in healthy femoral heads and different areas of necrotic ones.

T1 parameters	Healthy femoral heads	Normal area	Necrotic area	Edema area	Boundary area
K^{trans}	0.012 ± 0.002	0.021 ± 0.012	0.032 ± 0.020	0.028 ± 0.033	0.052 ± 0.033
K_{ep}	4.164 ± 1.798	4.926 ± 3.606	1.872 ± 1.820	1.027 ± 2.303	1.016 ± 1.620
V_e	0.021 ± 0.014	0.091 ± 0.161	0.135 ± 0.139	0.224 ± 0.199	0.295 ± 0.148

TABLE 4 Results of pairwise comparisons between healthy femoral heads and different areas of necrotic ones, respectively (independent samples *T* test).

T1 parameters	A and E		B and E		C and E		D and E	
	t-value	*P*-value	*t*-value	*P*-value	*t*-value	*P*-value	*t*-value	*P*-value
K^{trans}	$t = 2.265$	$P = .041$[a]	$t = 1.979$	$P = .010$[a]	$t = 1.029$	$P = .328$	$t = 2.579$	$P = .021$[a]
K_{ep}	$t = 0.444$	$P = .664$	$t = -2.374$	$P = .031$[a]	$t = -2.532$	$P = .030$[a]	$t = -3.539$	$P = .003$[a]
V_e	$t = 0.940$	$P = .362$	$t = 2.776$	$P = .017$[a]	$t = 2.680$	$P = .036$[a]	$t = 4.045$	$P = .001$[a]

A, normal area; B, necrotic area; C, edema area; D, boundary area; E, healthy femoral heads.
[a]The difference between the two groups were statistically significant.

neovascularization. The mean K^{trans} value of the boundary areas of necrotic femoral heads was higher than that of the normal areas, and statistical significance was found in the pairwise comparison. This result proves that there are changes in the structures and permeability of vessel walls, including neovasculature, in necrotic femoral heads, which is in accordance with the results of Glueck et al.

The value of K_{ep} represents the amount of contrast medium flowing back through the vessels per unit time after diffusion into tissues, and it is not only related to the vascular permeability of microcirculation but also to the status of posterior circulation. When the status of the posterior circulation changes, it will directly affect the osmotic pressure on both sides of the vascular wall and then affect the reflux rate of the contrast medium and the K_{ep} value. Abnormally elevated K_{ep} values are associated with microvascular density and vascular permeability (20), and the K_{ep} value often increases or decreases simultaneously with K^{trans} in most instances. In this study, the mean value of K^{trans} in the boundary areas was higher than that in the normal areas, but the mean value of K_{ep} was lower in the boundary areas and in the necrotic and edema areas (**Table 1** and **Figure 5**). In pairwise comparisons, differences in the mean values of K_{ep} in the normal area and in other lesion areas were statistically significant, which is not exactly the same as the distribution variations in tumor tissues and normal tissues (14, 22). When ONFH develops, the permeability of microcirculation vessels will increase, but the K_{ep} value will become lower than that in healthy tissues, which is consistent with the theories and hypotheses of ONFH that, in the later stage of the disease, changes in microcirculation manifest blood stasis in the posterior circulation, blocked venous return, and result in increased intraosseous pressure. The higher osmotic pressure in blood vessels in lesion areas prevents the effective reflux of contrast medium so that the K_{ep} values become lower than those in the normal area.

V_e stands for extracellular extravascular space and has a relationship with K^{trans} and K_{ep} values as follows: $V_e = K^{trans}/K_{ep}$. Therefore, the change in the V_e value is closely related to the K^{trans} and K_{ep} values. In this study, the variation trend of the mean value of V_e gradually increased from the normal area, necrotic area, and edema area to the boundary area, which was consistent with the variation trend of K^{trans} and K_{ep} values. In pairwise comparisons of the mean values of V_e in different areas, there were statistically significant differences between normal and boundary areas and between necrotic and boundary areas. No significant differences were identified among other pairings. The change in the V_e value indirectly confirms that the above description of the pathophysiological changes in the mechanism of ONFH is correct.

Comparative analysis of changes in microcirculation and blood supplies between healthy femoral heads and different areas of necrotic femoral heads

In this study, the differences in vascular function parameters between healthy femoral heads and different areas of necrotic femoral heads were further compared. It indicates that there was no statistically significant difference in mean values of K^{trans} between healthy femoral heads and edema areas of necrotic femoral heads, whereas they both were lower than those in other areas. All pairwise comparisons of K^{trans} between healthy femoral heads and each area of necrotic femoral heads showed statistically significant differences (**Tables 3**, **4**). There was no statistical significance between healthy femoral heads and edema areas, which may be attributed to the relatively small sample size of edema areas. In the progression of ONFH, the microcirculation and vascular wall will change compared with healthy femoral heads, mainly manifested as increased permeability of the vascular wall.

The mean value of K_{ep} in healthy femoral heads is greater than those in necrotic, edema, and boundary areas of necrotic femoral heads, while V_e is smaller than the three areas. When healthy femoral heads and the three areas were compared in pairs, the results showed that the differences in K_{ep} and V_e values were all statistically significant. In the comparison between healthy femoral

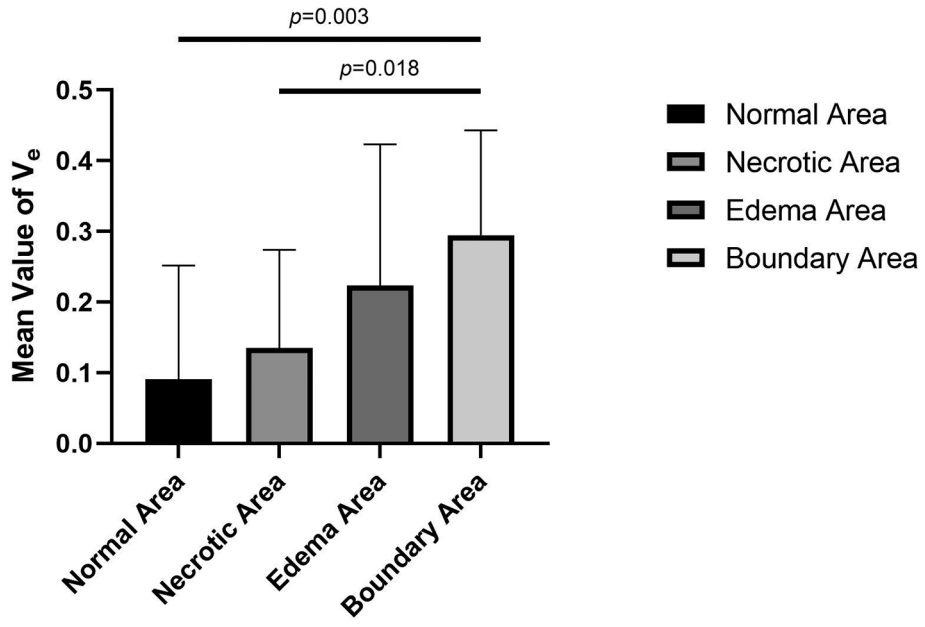

FIGURE 5
Comparison of the mean K_{ep} values in normal, necrotic, edema and boundary areas of the femoral heads in patients with ONFH.

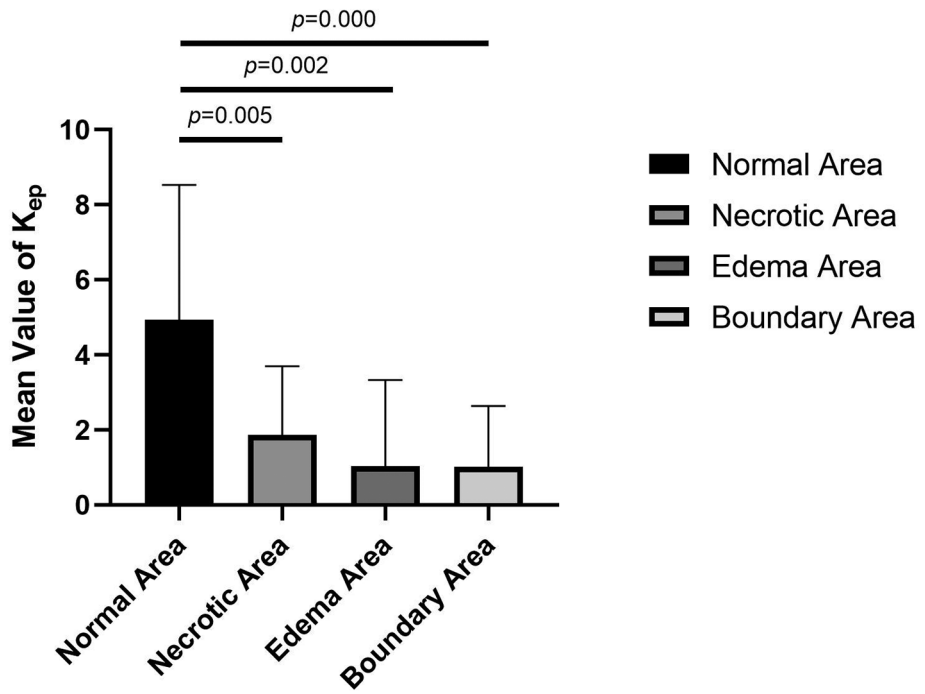

FIGURE 6
Comparison of the mean values of V_e in normal, necrotic, edema, and boundary areas of femoral heads in patients with ONFH.

heads and normal areas in necrotic femoral heads, differences in the values of K_{ep} and V_e were not statistically significant. The results again confirmed that in the process of ONFH, the microcirculation changes are mainly manifested in increased permeability of the vascular wall, blood stasis in the posterior circulation, high intraosseous pressure in the femoral head and decreased arterial blood flow.

Limitation

In this study, quantitative data between different ARCO stages were not compared and analyzed. On the other hand, the judgment of different femoral head necrosis areas, such as necrotic areas and edema areas, depends more on visual and empirical judgment and lacks objective and unified standards. Moreover,

different causes, such as alcohol-induced and steroid-induced osteonecrosis of the femoral head, were not analyzed and compared by microcirculation of the femoral head in this study. Therefore, quantitative analysis of the mechanism of femoral head necrosis using vascular function parameters obtained from DCE-MRI needs to be further explored.

Conclusion

We believe that this is the first and largest study applying DCE-MRI to early ONFH in human patients. Vascular function parameters were compared between healthy femoral heads and areas in necrotic femoral heads, which quantitively described and directly proved the pathophysiological mechanism of early ONFH. The main manifestations include increased permeability of the vascular wall, blood stasis in the posterior circulation, high intraosseous pressure in the femoral head, and decreases in arterial blood flow. All the results provide a theoretical basis for the clinical treatment of early ONFH.

Data availability statement

The original contributions presented in the study are included in the article/Supplementary Materials, further inquiries can be directed to the corresponding author/s.

Ethics statement

The studies involving human participants were reviewed and approved by The Ethics Committee of Eighth Medical Center of Chinese PLA General Hospital. The patients/participants provided their written informed consent to participate in this study. Written informed consent was obtained from the individual(s) for the publication of any potentially identifiable images or data included in this article.

Author contributions

PL and YL: designed the manuscript and wrote part of it. CX: wrote part of the manuscript with the insights of all the other authors. ZW and SN: conceptualized and generated **Tables 1–4**. FY: revised and finalized the manuscript. All authors contributed to the article and approved the submitted version.

Acknowledgments

This study was supported by the National Key R&D Program of China (2021YFC2401303), National Key R&D Program of China (2021YFC2401304) and 2022 Major Scientific Problems and Medical Technology Problems Project of China Medicine Education Association (2022KTZ006).

Conflict of interest

The authors declare that the research was conducted in the absence of any commercial or financial relationships that could be construed as a potential conflict of interest.

Publisher's note

All claims expressed in this article are solely those of the authors and do not necessarily represent those of their affiliated organizations, or those of the publisher, the editors and the reviewers. Any product that may be evaluated in this article, or claim that may be made by its manufacturer, is not guaranteed or endorsed by the publisher.

References

1. Jaffe W, Epstein M, Heyman N, Mankin H. The effect of cortisone on femoral and humeral heads in rabbits. An experimental study. *Clin Orthop Relat Res*. (1972) 82:221–8. doi: 10.1097/00003086-197201000-00029

2. Wang G, Sweet D, Reger S, Thompson R. Fat-cell changes as a mechanism of avascular necrosis of the femoral head in cortisone-treated rabbits. *J Bone Joint Surg Am*. (1977) 59:729–35. doi: 10.2106/00004623-197759060-00003

3. Jones J. Coagulopathies and osteonecrosis. *Acta Orthop Belg*. (1999) 65 Suppl 1:5–8.

4. Smith D. Is avascular necrosis of the femoral head the result of inhibition of angiogenesis? *Med Hypotheses*. (1997) 49:497–500. doi: 10.1016/S0306-9877(97)90067-0

5. Hungerford D, Lennox D. The importance of increased intraosseous pressure in the development of osteonecrosis of the femoral head: implications for treatment. *Orthop Clin North Am*. (1985) 16:635–54. doi: 10.1016/S0030-5898(20)30432-6

6. Cuenod C, Balvay D. Perfusion and vascular permeability: basic concepts and measurement in DCE-CT and DCE-MRI. *Diagn Interv Imaging*. (2013) 94:1187–204. doi: 10.1016/j.diii.2013.10.010

7. Budzik J, Lefebvre G, Forzy G, El Rafei M, Chechin D, Cotten A. Study of proximal femoral bone perfusion with 3D T1 dynamic contrast-enhanced MRI: a feasibility study. *Eur Radiol*. (2014) 24:3217–23. doi: 10.1007/s00330-014-3340-5

8. Del Grande F, Ahlawat S, Subhawong T, Fayad L. Characterization of indeterminate soft tissue masses referred for biopsy: what is the added value of contrast imaging at 3.0 Tesla? *J Magn Reson Imaging*. (2017) 45:390–400. doi: 10.1002/jmri.25361

9. van Rijswijk C, Geirnaerdt M, Hogendoorn P, Taminiau A, van Coevorden F, Zwinderman A, et al. Soft-tissue tumors: value of static and dynamic gadopentetate dimeglumine-enhanced MR imaging in prediction of malignancy. *Radiology*. (2004) 233:493–502. doi: 10.1148/radiol.2332031110

10. Riis R, Gudbergsen H, Henriksen M, Ballegaard C, Bandak E, Röttger D, et al. Synovitis assessed on static and dynamic contrast-enhanced magnetic resonance imaging and its association with pain in knee osteoarthritis: a cross-sectional study. *Eur J Radiol*. (2016) 85:1099–108. doi: 10.1016/j.ejrad.2016.03.017

11. Riis R, Gudbergsen H, Simonsen O, Henriksen M, Al-Mashkur N, Eld M, et al. The association between histological, macroscopic and magnetic resonance imaging assessed synovitis in end-stage knee osteoarthritis: a cross-sectional study. *Osteoarthr Cartil*. (2017) 25:272–80. doi: 10.1016/j.joca.2016.10.006

12. Zhang M, Zhou L, Huang N, Zeng H, Liu S, Liu L. Assessment of active and inactive sacroiliitis in patients with ankylosing spondylitis using quantitative dynamic contrast-enhanced MRI. *J Magn Reson Imaging*. (2017) 46:71–8. doi: 10.1002/jmri.25559

13. Lazaro L, Dyke J, Thacher R, Nguyen J, Helfet D, Potter H, et al. Focal osteonecrosis in the femoral head following stable anatomic fixation of displaced femoral neck fractures. *Arch Orthop Trauma Surg*. (2017) 137:1529–38. doi: 10.1007/s00402-017-2778-8

14. Sujlana P, Skrok J, Fayad L. Review of dynamic contrast-enhanced MRI: technical aspects and applications in the musculoskeletal system. *J Magn Reson Imaging*. (2018) 47:875–90. doi: 10.1002/jmri.25810

15. Yoon B, Mont M, Koo K, Chen C, Cheng E, Cui Q, et al. The 2019 revised version of association research circulation osseous staging system of osteonecrosis of the femoral head. *J Arthroplasty*. (2020) 35:933–40. doi: 10.1016/j.arth.2019.11.029

16. Riches S, Payne G, Morgan V, Sandhu S, Fisher C, Germuska M, et al. MRI in the detection of prostate cancer: combined apparent diffusion coefficient, metabolite ratio, and vascular parameters. *AJR Am J Roentgenol*. (2009) 193:1583–91. doi: 10.2214/AJR.09.2540

17. Tofts P, Kermode A. Blood brain barrier permeability in multiple sclerosis using labelled DTPA with PET, CT and MRI. *J Neurol Neurosurg Psychiatry*. (1989) 52:1019–20. doi: 10.1136/jnnp.52.8.1019

18. Hodgson R, Connolly S, Barnes T, Eyes B, Campbell R, Moots R. Pharmacokinetic modeling of dynamic contrast-enhanced MRI of the hand and wrist in rheumatoid arthritis and the response to anti-tumor necrosis factor-alpha therapy. *Magn Reson Med*. (2007) 58:482–9. doi: 10.1002/mrm.21349

19. Horsfield M, Morgan B. Algorithms for calculation of kinetic parameters from T1-weighted dynamic contrast-enhanced magnetic resonance imaging. *Magn Reson Imaging*. (2004) 20:723–9. doi: 10.1002/jmri.20161

20. Kozlowski P, Chang S, Meng R, Mädler B, Bell R, Jones E, et al. Combined prostate diffusion tensor imaging and dynamic contrast enhanced MRI at 3T – quantitative correlation with biopsy. *Magn Reson Imaging*. (2010) 28:621–8. doi: 10.1016/j.mri.2010.03.011

21. Glueck C, Freiberg R, Oghene J, Fontaine R, Wang P. Association between the T-786C eNOS polymorphism and idiopathic osteonecrosis of the head of the femur. *J Bone Joint Surg Am*. (2007) 89:2460–8. doi: 10.2106/00004623-200711000-00018

22. Zahra M, Hollingsworth K, Sala E, Lomas D, Tan L. Dynamic contrast-enhanced MRI as a predictor of tumour response to radiotherapy. *Lancet Oncol*. (2007) 8:63–74. doi: 10.1016/S1470-2045(06)71012-9

frontiers | Frontiers in Surgery

TYPE Original Research
PUBLISHED 01 March 2023
DOI 10.3389/fsurg.2023.964160

Check for updates

OPEN ACCESS

EDITED BY
Yan Yu,
Tongji University School of Medicine, China

REVIEWED BY
Biagio Zampogna,
Campus Bio-Medico University Hospital, Italy
Osvaldo Mazza,
Bambino Gesù Children's Hospital (IRCCS), Italy
Piotr Zarychta,
Silesian University of Technology, Poland

*CORRESPONDENCE
Kai-jin Guo
kaijinguo@163.com
Sheng Pan
doctorps@163.com

SPECIALTY SECTION
This article was submitted to Orthopedic Surgery, a section of the journal Frontiers in Surgery

RECEIVED 08 June 2022
ACCEPTED 23 January 2023
PUBLISHED 01 March 2023

CITATION
Zheng X, Wang Y-y-f, Jin W-y, Huang C-r, Yan Z-w, Peng D-l, Zhou S, Guo K-j and Pan S (2023) Intraindividual variance of lower limb rotation in patients with bilateral knee osteoarthritis.
Front. Surg. 10:964160.
doi: 10.3389/fsurg.2023.964160

COPYRIGHT
© 2023 Zheng, Wang, Jin, Huang, Yan, Peng, Zhou, Guo and Pan. This is an open-access article distributed under the terms of the Creative Commons Attribution License (CC BY). The use, distribution or reproduction in other forums is permitted, provided the original author(s) and the copyright owner(s) are credited and that the original publication in this journal is cited, in accordance with accepted academic practice. No use, distribution or reproduction is permitted which does not comply with these terms.

Intraindividual variance of lower limb rotation in patients with bilateral knee osteoarthritis

Xin Zheng[1], Yang-yu-fan Wang[2], Wang-yi Jin[3,4], Chao-ran Huang[4], Zi-wen Yan[4], Da-lin Peng[4], Shen Zhou[4], Kai-jin Guo[4]* and Sheng Pan[4,5]*

[1]Department of Orthopaedics, Zhujiang Hospital, Southern Medical University, Guangzhou, China, [2]State Key Laboratory of Pharmaceutical Biotechnology, Department of Sports Medicine and Adult Reconstructive Surgery, Nanjing Drum Tower Hospital, The Affiliated Hospital of Nanjing University Medical School, Nanjing, China, [3]Department of Traumatic Surgery, Changshu Hospital Affiliated to Soochow University, First Peoples' Hospital of Changshu, Changshu, China, [4]Department of Orthopaedics, The Affiliated Hospital of Xuzhou Medical University, Xuzhou, China, [5]Department of Orthopedics, The Second Affiliated Hospital of Soochow University, Suzhou, China

Purpose: To determine the side-to-side difference in intraindividual rotation alignment of patients with bilateral varus-type knee osteoarthritis (OA) and compare it with control subjects.

Methods: This retrospective study enrolled 60 patients with bilateral varus-type knee OA and 50 control subjects. All cases underwent bilateral lower limb CT angiography. Bilateral femoral and tibial rotation alignment were measured, and the overall lower limb rotation was calculated by two different methods. Method 1 was calculated by subtracting angle of the femoral torsion from the tibial torsion and method 2 was determined by relative rotation of the femoral neck angle to bimalleolar angle. The intraindividual variance and differences between the two groups were analyzed.

Results: Both OA and control samples showed significant differences between right and left for all measurements. Femoral torsion for control group was 10.4 ± 5.5°, tibial torsion was −22.1 ± 6.1°, and overall leg rotation by method 1 was −15.6 ± 7.2° and method 2 was −11.7 ± 8.2°. Femoral torsion, tibial torsion, method 1, and method 2 in the patients with OA were 8.2 ± 6.3°, −18.6 ± 4.1°, −14.9 ± 7.9°, and −10.4 ± 7.6°, respectively. Patients with OA showed a more pronounced retroversion in the femur ($p = 0.008$) and more internal rotation in the tibia ($p < 0.001$). No statistical significance of both methods was found between the two groups. Patients with OA had a greater median side-to-side absolute difference in all measurements, though the differences of both two methods of overall lower limb rotation were not statistically significant.

Conclusions: The discrepancy of side-to-side differences of bilateral lower limb rotation ought to be noticed with caution in diagnosing and treating rotational deformities of the lower limb, especially for patients with bilateral knee OA.

KEYWORDS

external, rotation, osteoarthritis, computed tomography, individual

Background

Improper rotational alignment of the lower limb may be carried over from childhood or acquired (1). Open or closed reduction and intramedullary nailing of femur and tibia fractures is a long-standing and less-invasive surgical procedure (2). Fracture commonly achieves indirect healing for the stable fixation of closed nailing, whereas the reconstruction of anatomical rotational alignment of the lower limb is of vital importance (3, 4). Contralateral healthy knee was always used as reference of rotation for reconstruction of the pre-traumatic alignment. Rotational differences of over 15°, compared to the healthy side, are considered to be unacceptable (3, 5, 6).

Computed tomography (CT) is the current gold standard for the measurements of axial rotational alignment (7). The rotational alignment is composed of four axes of femur and tibia: femoral neck axis, distal femoral condylar axis, the proximal tibial axis, and bimalleolar axis. "Ulm method" was one of the most widely accepted techniques for measuring femoral, tibial, and limb rotation described by Waidelich et al. (2). In 2011, Liodakis et al. (8) proposed an alternative method measuring the overall lower limb rotation (neck–malleolar angle) that considers the knee joint rotation angle.

It was reported that there is a significant side-to-side difference of bilateral femorotibial torsion in healthy subjects (1). Knee osteoarthritis (OA) is one of the most common forms of OA, especially in people over 50 years old. Patients with knee OA tend to combine with a deformity of the lower limbs (9). In a study of the strength of the associations of knee injury and obesity with OA in 3,885 healthy people, it was found that the incidence of bilateral osteoarthritis is 5%, which is more common than unilateral osteoarthritis (2%) (10). Günther et al. (11) also reported that in individuals who have primarily unilateral knee OA, 87.4% had radiographic evidence of bilateral OA. There was less femoral anteversion and more external torsion of tibia in patients with knee osteoarthritis than normal subjects (9, 12, 13). However, to date, there is a distinct lack of literature characterizing the side-to-side variations in rotation of the lower limbs in patients with bilateral knee OA.

The purpose of this study was to determine the side difference in intraindividual rotation alignment of patients with bilateral knee OA and to compare it to control subjects. The hypothesis was that patients with bilateral knee OA had a greater mean side-to-side absolute difference than control subjects. The finding may be beneficial to acute clinical settings as well as for orthopedist opinion.

Materials and methods

The study was approved by the hospital review board, and each patient enrolled was given a written informed consent. All cases who underwent bilateral lower limb CT angiography from January 2018 to December 2020 in our hospital were identified using the hospital's Picture Archiving and Communication System (PACS; GE Healthcare, Chicago, IL, United States) for vascular disease of lower limb. In this retrospective study, all images were judged by two experienced orthopedic surgeons and the diagnosis of OA was done *via* coronal reconstruction of CT or standard x-rays of the knee joints. Sixty patients with bilateral varus-type knee OA and 50 patients who were not diagnosed with OA but were suspected of having other lower limb diseases such as deep venous thrombosis or arterial embolism were enrolled.

Lower limb CT angiographies were done with Philips iCT256 (Philips, Netherlands). Patients were positioned in a supine state of neutral rotation with knees fully extended, feet affixed, and toes pointing upward. Scan level ranged from the ilium to the distal of the feet, including the joints of the hip, knee, and ankle with sections of 0.625 mm thickness. The image was obtained with radiation levels of 100–120 kVp for an effective mAs (20–35 mAs) duration.

For the OA group, patients were exclude if they had (1) a diagnosis other than primary knee OA, (2) the Kellgren–Lawrence (K–L) grade of either side of knee was lower than 2, (3) a significant bony deformity that restrained identification of the anatomical landmarks for measurement, (4) a history of operation on the lower limb (e.g., total hip arthroplasty, an operation for a femoral or tibial fracture, or high tibial osteotomy), and (5) amputation of the calf/thigh.

The exclusion criteria of the control subjects were (1) age younger than 18 years, (2) osteoarthritis of the hip and knee joint, (3) endoprosthesis of the hip or knee joint, (4) post-traumatic changes of the lower leg (e.g., acute fracture), (5) bony abnormalities (e.g., tumors or severe deformities), and (6) amputation of the lower leg.

All data were measured on PACS by two independent observers who were familiar with the rotational assessment of the lower limbs on the axial plane of CT images in two times with each at a 1-month interval. Four axes were measured in the lower limb: femoral neck axis, posterior condylar axis (PCA) of the distal femur, axis of the proximal tibial condyles, and bimalleolar axis. The data were recorded as an angle between the axis and the horizontal plane on PACS. Internal rotation was assigned a negative sign, and external rotation was assigned a positive sign. The angles were measured to the least 0.1°.

The femoral neck axis was defined as a line connecting the center of the femoral head and the midpoint of the femoral neck with the femoral head, isthmus of the femoral neck, and the superior border of the greater trochanter is evident in a CT cut (**Figure 1A**). This method was first proposed by Hernandez et al. (14) and validated by Liodakis et al. (8). The PCA of the distal femur was defined as a line connecting the posterior margins of the lateral and medial femoral condyles (9) (**Figure 1B**). The axis of the proximal tibial condyles was defined as a line between posterior cortices of the proximal tibial condyles, set at the plane of the apex of the fibula (1). (**Figure 1C**) The bimalleolar axis was defined as a line connecting the centers of the medial and lateral malleolus (6) (**Figure 1D**).

The following step was to calculate the rotational profile of lower limb. The femoral torsion was calculated by subtracting the posterior condylar axis from the femoral neck angle (1). Femoral anteversion and retroversion were represented by positive values and negative values, respectively. Femoral anteversion was assigned femoral external rotation of the femoral neck in relation to the PCA.

The tibial rotation was calculated by subtracting the bimalleolar angle from the angle of the proximal tibial condyles (1). Positive values indicated the internal rotation of the tibia, and negative values indicated the external rotation of the tibia. Negative values presented external rotation of baseline of the proximal posterior tibia in relation to the distal tibia.

The overall lower limb rotation had two methods as reported: method 1 was calculated by subtracting angle of the femoral torsion from the tibial torsion; method 2 was reported as the neck–malleolar angle proposed by Liodakis et al. (8) in 2011 and determined by relative rotation of the femoral neck angle to bimalleolar angle. The angle was calculated by subtracting the bimalleolar angle from the femoral neck angle. Negative values represented relative external rotation of distal tibia in relation to the proximal femur.

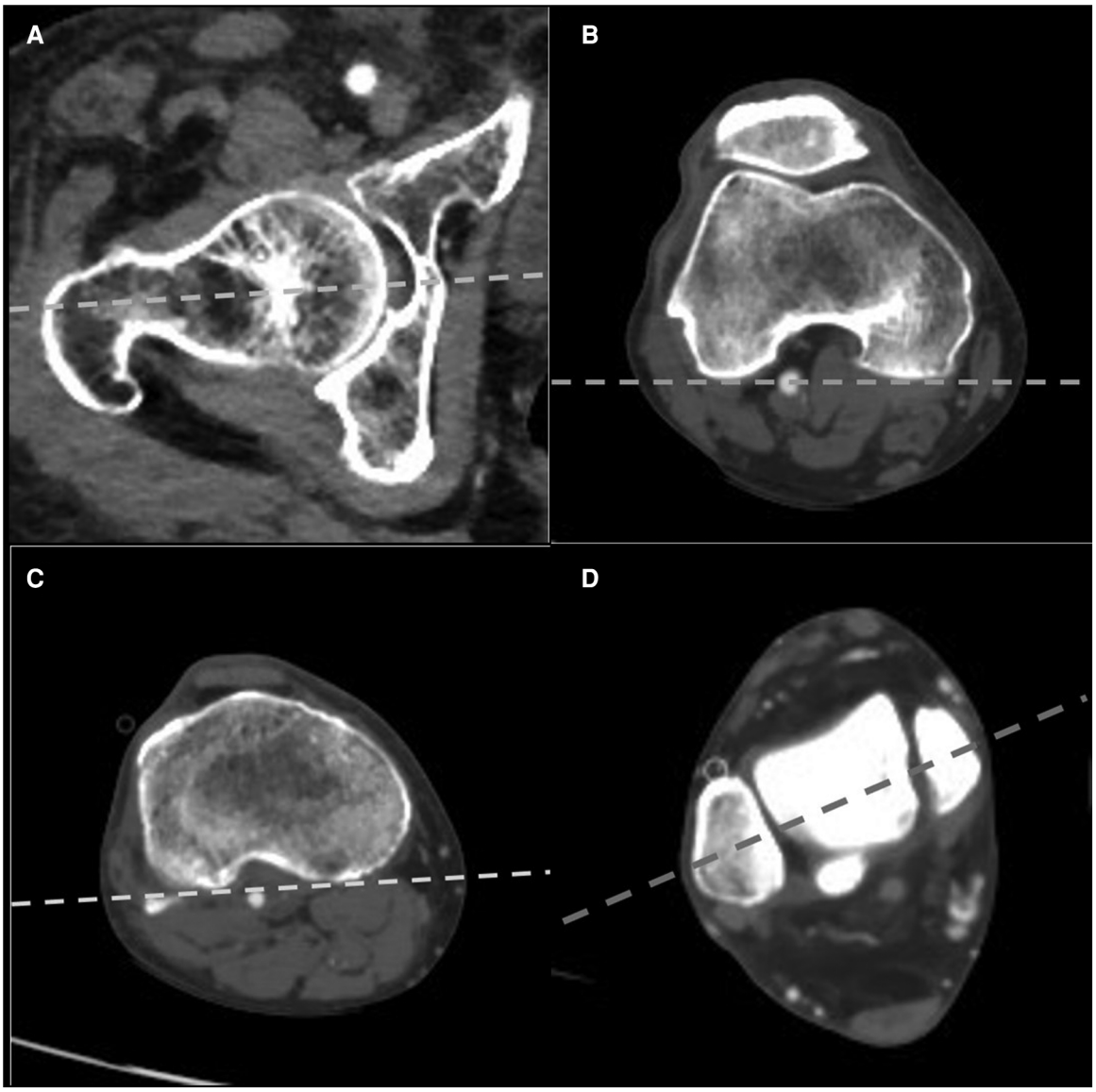

FIGURE 1
Measurement technique of lower limb rotation on CT (right limb). (**A**) Femoral neck axis. (**B**) Posterior condylar axis of the distal femur. (**C**) Axis of the proximal tibial condyles. (**D**) The bimalleolar axis. The data were recorded as an angle between the axis and horizontal baseline. CT, computed tomography.

Statistical analysis

For the OA group, an estimated sample size of at least 34 would be needed to provide 80% power for two-sided paired sample t tests, assuming an effect size index of 0.5, with a two-sided α of 0.05. Statistical analysis was performed with SPSS 25.0 (IBM, Chicago, Illinois, United States). All data were obtained by two independent observers in two times with each at a 1-month interval. The mean value of the four different measurements was used for analysis. Inter- and intraobserver reliabilities of the methods were evaluated by intraclass correlation coefficients (ICCs). ICC values greater than 0.80 indicated excellent reliability. The normality of continuous variable was calculated by the Shapiro–Wilk test. Data with normal distribution were expressed as mean and SD. Difference of variables was reported as absolute value. All variables but the side-to-side absolute difference of the lower limb rotation (both patients with OA and control subjects) were normally distributed. Two-sided paired t test was conducted to determine significant differences between right and left limb for all measurements. Independent-sample T tests or Mann–Whitney *U* test was conducted to determine the differences of the two groups or two methods of overall lower limb rotation. $p < 0.05$ was considered as statistically significant.

Results

There were no significant differences between the OA and control groups on gender ($p = 0.275$) and age ($p = 0.208$).

For all parameters, ICCs of inter- and intraobserver reliabilities were all greater than 0.90, which indicated excellent reliability.

Both OA and control samples showed significant differences between right and left for all measurements (Table 1).

Femoral torsion, tibial torsion and overall leg rotation by the two methods of the control group were provided in Table 2.

Femoral and tibial torsion in the patients with OA were 8.2 ± 6.3° and −18.6 ± 4.1°, respectively. The overall lower limb rotation calculated by method 1 and method 2 were 14.9 ± 7.9° and −10.4 ± 7.6°, respectively (Table 2). Patients with OA showed a more pronounced retroversion in the femur ($p = 0.008$) and more internal rotation in the tibia ($p < 0.001$). No statistical significance of both methods was found between bilateral varus-type knee OA group and control group (Table 2).

Patients with OA had a more evident median side-to-side absolute difference in all measurements, though the differences of two methods of overall lower limb rotation were not statistically significant (Table 2 and Figure 2).

For both OA and control groups, there were no significant differences between the two methods in terms of side-to-side absolute difference of overall lower limb rotation (Figure 3).

Discussion

This study aimed to investigate the side-to-side difference in intraindividual rotation alignment of patients with bilateral knee OA and to compare it to control subjects. The key findings of this study including the following: First, there were significant differences between right and left for all measurements of lower limb rotation in both OA group and control subjects. Second, patients with bilateral knee OA had a more evident side-to-side difference in all measurements compared with control subjects. It may be profitable to acute clinical settings or subsequent orthopedic procedures, especially for those patients with bilateral knee OA.

With regard to the reduction and fixation for fractures, the reconstruction of long bone of the lower limb into a correct rotational limb alignment is necessary (3). The healthy side is usually used as the reference to restore pre-traumatic lower limb rotation alignment (2). Side-to-side difference in the lower limb rotation was described by numerous studies (1, 15). Strecker et al. (15) analyzed the intraindividual asymmetry of lower limb rotation in 355 normal individuals. The rotation of right and left femur in individuals did not differ significantly, but there was a significant difference of rotation between right (36.46° of external torsion) and left tibia (33.07° of external torsion). It was reported that two methods identifying the overall lower limb rotation to determine the intraindividual variance of bilateral lower limb rotation in 105 healthy subjects and showed the mean side-to-side differences of 6.0 ± 4.7° in femoral and 5.7 ± 4.8° in tibial rotation. The absolute side-to-side overall lower limb rotation difference was 9.5° with both methods. Our study found the conclusion of the intraindividual side difference in bilateral "healthy" legs, though the median absolute difference of lower limb rotation was less than previous studies (1).

Traditional method measuring the overall lower limb rotation is calculated from the differences in the femoral and tibial rotation (2).

TABLE 1 Results of bilateral measurements separately shown for OA and control subjects.

	OA group ($n = 60$)			Control group ($n = 50$)		
	Left mean ° (SD)	Right mean ° (SD)	*p*-value	Left mean ° (SD)	Right mean ° (SD)	*p*-value
Femur rotation	9.0 (6.8)	7.5 (5.7)	0.003*	9.7 (5.8)	11.2 (5.3)	0.001*
Tibial rotation	−17.6 (4.1)	−19.6 (3.9)	0.001*	−23.0 (7.2)	−21.4 (4.0)	0.009*
Method 1	−13.0 (8.1)	−16.7 (7.3)	0.001*	−16.7 (8.1)	−14.6 (6.1)	0.002*
Method 2	−8.6 (7.9)	−12.2 (6.9)	0.001*	−13.3 (9.3)	−10.2 (6.9)	0.001*

OA, osteoarthritis.
*p < 0.05 [Normally distributed values were given as means and SD].

TABLE 2 Differences of measurement between OA and control subjects.

		OA (°)	Control (°)	*p*-value
Femur rotation	Overall	8.2 (6.3)	10.4 (5.5)	0.008*
	AbsΔ (right–left)	2.7 (1.4–5.1)	1.7 (1.0–2.8)	0.010*
Tibial rotation	Overall	−18.6 (4.1)	−22.1 (6.1)	0.001*
	AbsΔ (right–left)	3.9 (2.7–5.4)	2.6 (1.1–5.6)	0.030*
Method 1	Overall	−14.9 (7.9)	−15.6 (7.2)	0.490
	AbsΔ (right–left)	4.7 (3.2–6.7)	3.7 (2.1–5.4)	0.040*
Method 2	Overall	−10.4 (7.6)	−11.7 (8.2)	0.217
	AbsΔ (right–left)	5.4 (3.4–7.7)	4.7 (2.1–6.7)	0.085

OA, osteoarthritis; AbsΔ, absolute difference.
*p < 0.05 [Normally distributed values were given as means and SD; Non-normal variables were reported as median (interquartile range)].

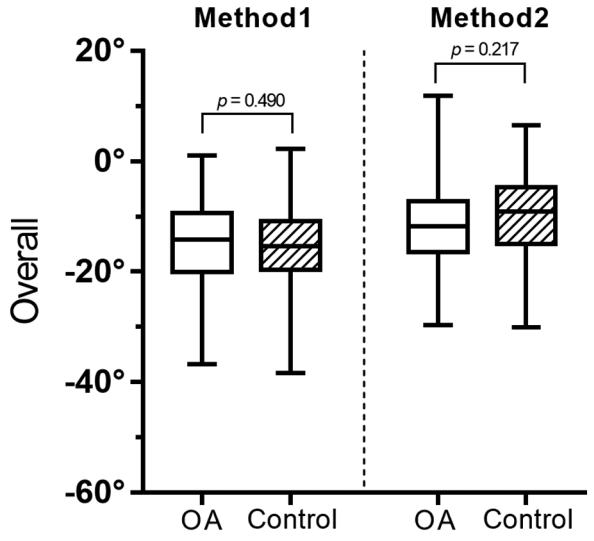

FIGURE 2
Absolute difference between methods 1 and 2 by a box-whisker plot. OA, osteoarthritis; AbsΔ, absolute difference.

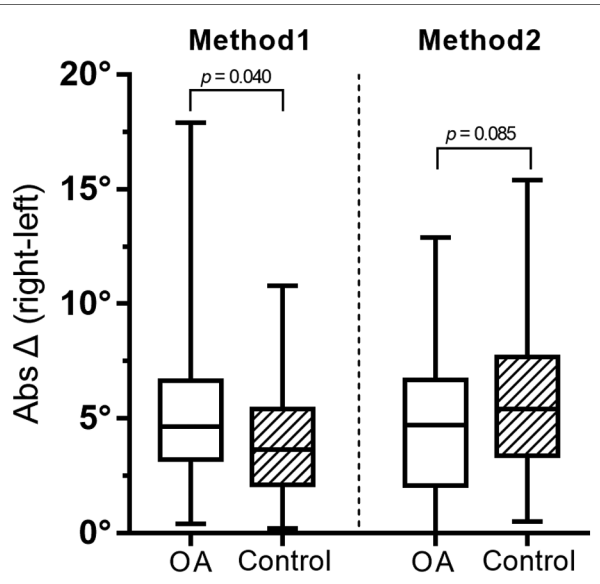

FIGURE 3
Overall results of methods 1 and 2 by a box-whisker plot. OA, osteoarthritis.

This method was regarded negligence of the variability of knee joint rotation. It is known that the magnitude of rotational shift during knee extension relies on the individual difference of the medial and lateral femoral condyles (16). The internal and external rotation of the tibia relative to the femur is minimal at full extension of the knee. Consequently, it is evident that the knee joint rotation is an important anatomical element of the overall lower limb rotation. Liodakis et al. (8) were the first to introduce an alternative method (neck–malleolar angle) for measuring overall lower limb torsion that considers the knee joint rotation angle. This method was a direct measurement of the angle between the femoral neck axis and the bimalleolar axis. They used both the traditional method and the method of neck–malleolar angle to determine the overall lower limb rotation; however, the difference between the two methods was not mentioned. Overall leg rotations calculated by two methods were compared with the study by Ries et al. (1). The absolute side-to-side differences of overall lower limb rotation by two methods were both 9.5°. The differences between both methods were not significant. Yet, absolute differences between the two methods were 3.3°. In our study, for both OA and control subjects, no significant differences between the two methods in terms of side-to-side absolute difference of overall lower limb rotation was found.

Khan et al. (17) noticed that tibial rotation reduced significantly in OA patients (19.5 ± 6.16°) compared with that in the healthy group (23.51 ± 6.34°). They also reported a significant negative correlation between varus deformity and tibial torsion ($r = -0.54$, $p < 0.02$). It was indicated that as the progression of varus deformity, tibial torsion reduced further. Chang et al. (9) divided 422 lower limbs into three groups according to the coronal alignment. In their study, as the coronal alignment changed from varus to valgus, the degree of femoral anteversion (the angle between femoral neck and PCA) and the external tibial rotation increased. However, their external tibia rotation was determined by the angle between PCA and the line connecting the most prominent points of lateral and medial malleolus. According to the study by Liodakis et al. (6), the bimalleolar methods used in our study for measuring rotation had the greatest inter- and intraobserver reliabilities. In the current study, we compared the mean rotation alignment of bilateral lower limb of OA patients with control subjects. Significant differences were found both in the femoral and tibial rotation between the two groups, but the overall lower limb rotation by two methods was not significantly different. Previous reports of lower limb rotation were in agreement with our findings, namely, those of Moussa (18), who evaluated the difference of rotational alignment patterns between OA patients and control subjects who had no knee joint problems. Moreover, in our study, all differences of bilateral lower limbs were reported as absolute values. In our view, there was no need to determine which side rotates more internally or externally.

There were several limitations of this study. First, patients with OA always have different degrees of articular cartilage erosion, which is invisible using CT. In addition, the behavior of the ligament apparatus is also hard to be determined by CT. It may be considered to recommend magnetic resonance imaging (MRI) in future studies. Second, most cases underwent lower limb CT angiography for thrombosis of lower limbs. Those were unable to represent the general normal population. Also, age-related changes in bone morphology for control subjects, therefore, cannot be ruled out. However, due to ethical considerations, we could not acquire lower limb CT angiography of healthy subjects. Finally, it was a retrospective study, the knee OA was only diagnosed by K–L grades on the coronal plane of CT reconstruction or standard short knee radiograph. We could not obtain the patients' specific clinical symptoms (e.g., pain intensity and knee function). Furthermore, we were unable to ensure the same bilateral K–L grades of knees in patients with bilateral knee OA. Further studies may consider the association between a larger sample size of symptomatic knee OA and control samples concerning lower limb rotation.

Conclusion

Compared with control subjects, patients with bilateral knee OA had a greater side-to-side absolute difference in all measurements. The discrepancy ought to be noticed with caution in diagnosing and treating rotational deformities of the lower limb, especially for patients with bilateral knee OA.

Data availability statement

The raw data supporting the conclusions of this article will be made available by the authors, without undue reservation.

Ethics statement

The studies involving human participants were reviewed and approved by the ethics board of the Affiliated Hospital of Xuzhou Medical University. The patients/participants provided their written informed consent to participate in this study. Written informed consent was obtained from the individual(s) for the publication of any potentially identifiable images or data included in this article.

Author contributions

XZ, Y-y-fW, and W-yJ contributed equally to this work. SP, K-jG, and XZ designed the study and drafted the manuscript. YW, C-rH, W-yJ, Z-wY, and SZ performed the data collection and the statistical analysis. All authors contributed to the article and approved the submitted version.

Funding

This study was supported by National Natural Science Foundation of China (82272523 and 81902244) and the Natural Science Foundation of Jiangsu Province (BK20201154).

Conflict of interest

The authors declare that the research was conducted in the absence of any commercial or financial relationships that could be construed as a potential conflict of interest.

Publisher's note

All claims expressed in this article are solely those of the authors and do not necessarily represent those of their affiliated organizations, or those of the publisher, the editors and the reviewers. Any product that may be evaluated in this article, or claim that may be made by its manufacturer, is not guaranteed or endorsed by the publisher.

References

1. Ries C, Boese CK, Ott N, Doerner J, Müller LP, Hackl M. Intra-individual variance of bilateral femoro-tibial leg rotation: a CT study of 105 healthy subjects. *Knee Surg Sports Traumatol Arthrosc.* (2021) 29:1106–13. doi: 10.1007/s00167-020-06101-6

2. Waidelich HA, Strecker W, Schneider E. Computed tomographic torsion-angle and length measurement of the lower extremity. The methods, normal values and radiation load. *Rofo.* (1992) 157:245–51. doi: 10.1055/s-2008-1033007

3. Jaarsma RL, Dfm P, Verdonschot N, Biert J, Kampen AV. Rotational malalignment after intramedullary nailing of femoral fractures. *J Orthop Trauma.* (2004) 18:403–9. doi: 10.1097/00005131-200408000-00002

4. Puloski S, Romano C, Buckley R, Powell J. Rotational malalignment of the tibia following reamed intramedullary nail fixation. *J Orthop Trauma.* (2004) 18:397–402. doi: 10.1097/00005131-200408000-00001

5. Kuo TY, Skedros JG, Bloebaum RD. Measurement of femoral anteversion by biplane radiography and computed tomography imaging: comparison with an anatomic reference. *Invest Radiol.* (2003) 38:221–9. doi: 10.1097/01.RLI.0000059542.90854.EF

6. Liodakis E, Doxastaki I, Chu K, Krettek C, Gaulke R, Citak M, et al. Reliability of the assessment of lower limb torsion using computed tomography: analysis of five different techniques. *Skeletal Radiol.* (2012) 41:305–11. doi: 10.1007/s00256-011-1185-4

7. Tomczak RJ, Guenther KP, Rieber A, Mergo P, Ros PR, Brambs HJ. MR Imaging measurement of the femoral antetorsional angle as a new technique: comparison with CT in children and adults. *AJR Am J Roentgenol.* (1997) 168:791–4. doi: 10.2214/ajr.168.3.9057536

8. Liodakis E, Aljuneidi W, Krettek C, Ettinger M, Kenawey M. The neck-malleolar angle: an alternative method for measuring total lower limb torsion that considers the knee joint rotation angle. *Skeletal Radiol.* (2011) 40:617–21. doi: 10.1007/s00256-010-1039-5

9. Chang MJ, Jeong HJ, Kang SB, Chang CB, Yoon C, Shin JY. Relationship between coronal alignment and rotational profile of lower extremity in patients with knee osteoarthritis. *J Arthroplasty.* (2018) 33:3773–7. doi: 10.1016/j.arth.2018.07.022

10. Taylor BC, Dimitris C, Mowbray JG, Gaines ST, Steensen RN. Perioperative safety of two-team simultaneous bilateral total knee arthroplasty in the obese patient. *J Orthop Surg Res.* (2010) 5:38. doi: 10.1186/1749-799X-5-38

11. Günther KP, Stürmer T, Sauerland S, Zeissig I, Sun Y, Kessler S, et al. Prevalence of generalised osteoarthritis in patients with advanced hip and knee osteoarthritis: the Ulm Osteoarthritis Study. *Ann Rheum Dis.* (1998) 57:717–23. doi: 10.1136/ard.57.12.717

12. Fujii T, Sato T, Ariumi A, Omori G, Koga Y, Endo N. A comparative study of weight-bearing and non-weight-bearing 3-dimensional lower extremity alignment in knee osteoarthritis. *J Orthop Sci.* (2020) 25:874–9. doi: 10.1016/j.jos.2019.11.012

13. Harris SJ, Cobb JP, Jeffers L, Puthumanapully PK, Amis AA. A morphometric study of normal and varus knees. *Knee Surg Sports Traumatol Arthrosc.* (2014) 22:2891–9. doi: 10.1007/s00167-014-3337-2

14. Hernandez RJ, Tachdjian MO, Poznanski AK, Dias LS. CT determination of femoral torsion. *AJR Am J Roentgenol.* (1981) 137:97–101. doi: 10.2214/ajr.137.1.97

15. Strecker W, Keppler P, Gebhard F, Kinzl L. Length and torsion of the lower limb. *J Bone Joint Surg Br.* (1997) 79:1019–23. doi: 10.1302/0301-620X.79B6.0791019

16. Nagao N, Tachibana T, Mizuno K. The rotational angle in osteoarthritic knees. *Int Orthop.* (1998) 22:282–7. doi: 10.1007/s002640050261

17. Khan MS, Seon JK, Song EK. Rotational profile of lower limb and axis for tibial component alignment in varus osteoarthritic knees. *J Arthroplasty.* (2012) 27:797–802. doi: 10.1016/j.arth.2011.08.016

18. Moussa M. Rotational malalignment and femoral torsion in osteoarthritic knees with patellofemoral joint involvement. A CT scan study. *Clin Orthop Relat Res.* (1994) 304:176–83. doi: 10.1097/00003086-199407000-00027

frontiers | Frontiers in Surgery

TYPE Original Research
PUBLISHED 03 May 2023
DOI 10.3389/fsurg.2023.1134129

Check for updates

OPEN ACCESS

EDITED BY
Yan Yu,
Tongji University School of Medicine, China

REVIEWED BY
Lei Zhang,
Southwest Medical University, China
Xiao Hu,
Tongji Hospital Affiliated to Tongji University, China

*CORRESPONDENCE
Yaokai Gan
✉ Ganyk2004@126.com
Yifei Yao
✉ yifeiyao@sjtu.edu.cn

RECEIVED 29 December 2022
ACCEPTED 13 April 2023
PUBLISHED 03 May 2023

CITATION
Yu L, Jia J, Lakshminarayanan K, Li Y, Gan Y and Yao Y (2023) A finite element analysis of the carpal arch with various locations of carpal tunnel release.
Front. Surg. 10:1134129.
doi: 10.3389/fsurg.2023.1134129

COPYRIGHT
© 2023 Yu, Jia, Lakshminarayanan, Li, Gan and Yao. This is an open-access article distributed under the terms of the Creative Commons Attribution License (CC BY). The use, distribution or reproduction in other forums is permitted, provided the original author(s) and the copyright owner(s) are credited and that the original publication in this journal is cited, in accordance with accepted academic practice. No use, distribution or reproduction is permitted which does not comply with these terms.

A finite element analysis of the carpal arch with various locations of carpal tunnel release

Lu Yu[1], Jingyi Jia[1], Kishor Lakshminarayanan[2], Yiming Li[3], Yaokai Gan[3]* and Yifei Yao[1]*

[1]School of Biomedical Engineering, Shanghai Jiao Tong University, Shanghai, China, [2]Department of Sensors and Biomedical Engineering, Vellore Institute of Technology, Vellore, Tamil Nadu, India, [3]Orthopedic Department, Shanghai Ninth People's Hospital, Shanghai Jiao Tong University School of Medicine, Shanghai, China

Objective: The purpose of this study was to investigate the effects of the location of transverse carpal ligament (TCL) transection on the biomechanical property of the carpal arch structure. It was hypothesized that carpal tunnel release would lead to an increase of the carpal arch compliance (CAC) in a location-dependent manner.
Methods: A pseudo-3D finite element model of the volar carpal arch at the distal carpal tunnel was used to simulate arch area change under different intratunnel pressures (0–72 mmHg) after TCL transection at different locations along the transverse direction of the TCL.
Results: The CAC of the intact carpal arch was 0.092 mm^2/mmHg, and the simulated transections ranging from 8 mm ulnarly to 8 mm radially from the center point of the TCL led to increased CACs that were 2.6–3.7 times of that of the intact carpal arch. The CACs after radial transections were greater than those ulnarly transected carpal arches.
Conclusion: The TCL transection in the radial region was biomechanically favorable in reducing carpal tunnel constraint for median nerve decompression.

KEYWORDS

carpal tunnel release, carpal arch compliance, transverse carpal ligament, finite element analysis, median nerve compression

1. Introduction

Carpal tunnel syndrome (CTS) is currently the most common upper-extremity compression neuropathy with prevalence rates varying between 1% and 5% of the general population in the United States (1). Elevated carpal tunnel pressure is commonly noted as the cause for the median nerve neuropathy (2–4). Structurally, the carpal tunnel is formed by the transverse carpal ligament (TCL) as its volar border and the interconnected carpal bones as its medial, lateral, and dorsal borders (5). The tunnel is crowded with the median nerve and nine digital flexor tendons, predisposing the median nerve to mechanical compression by the TCL (6). Clinically, if a conservative treatment fails, a surgical release of the carpal tunnel through TCL transection is performed so that the carpal tunnel becomes more compliant to accommodate the elevated pressure.

As a standard surgical treatment for carpal tunnel syndrome, carpal tunnel release (CTR) increases carpal tunnel volume (7–9), thereby decreases carpal tunnel pressure (10) and restores median nerve shape (11). The surgical approaches are mainly divided into two aspects: the open carpal tunnel release (OCTR) and endoscopic carpal tunnel release (ECTR). Surgical release of the transverse carpal ligament for the treatment of posttraumatic median nerve compression was first described in 1933 (12). The split of the

transverse carpal ligament in a patient with CTS using endoscopy for the first time was not reported until 1987, and the endoscopic surgical approach has since been introduced (13).

Omokawa et al. investigated the anatomical course of the ulnar artery and its branches in relation to the TCL, as well as the position of the median nerve in 24 fresh cadaver hands. Their findings suggested that when performing surgery, transecting the TCL at a point roughly 5 mm radial to the radial margin of the hook of hamate may reduce postoperative bleeding and prevent inadvertent damage to the blood vessels and nerves (14). Z-lengthening is a surgical technique that has been developed as an alternative to the traditional complete incision carpal tunnel release surgery (15). In the Z-lengthening procedure, the surgeon creates a series of cuts in a zigzag pattern on the transverse carpal ligament to increase the available space for the compressed median nerve. Unlike complete severing, the Z-lengthening technique ensures that the ligament remains intact. Compared to the traditional carpal tunnel surgery, the Z-lengthening technique offers several advantages such as a smaller incision resulting in reduced pain and faster healing. In addition, this procedure has a lower incidence of complications such as damage to nearby nerves or blood vessels. As a result, Z-lengthening is an effective and safe surgical approach to treating carpal tunnel syndrome that can significantly enhance the quality of life for those affected by this condition (16). A previous study proposed a modified Z-lengthening technique that includes a distal flap on the radial side and a proximal flap on the ulnar side to avoid the hamulus insertion in the hamate bone and improve outcomes for carpal tunnel syndrome (17, 18). A meta-analysis of randomized controlled trials supported the effectiveness of Z-lengthening over the conventional TCL release for long-term functional improvement (19). Some research studies show better manual function and short-term grip strength with preserved TCL continuity comparing to complete cut of the ligament (20, 21). Therefore, TCL Z-lengthening has been proposed to preserve the TCL continuity and the first flexor tendon pulley, which is more effective than complete division. The ECTR has smaller cut incisions and better cosmetic results than the OCTR, but also has higher technical barriers and is associated with incomplete release of the transverse carpal ligament and neurovascular injury (16).

Notably, the volar carpal arch formed by the TCL contributes to the majority (93%) of the postoperative increase in the tunnel area (8). In a cadaveric study of the relationship between carpal tunnel cross-sectional area and intratunnel pressure, Kim et al. showed that carpal tunnel compliance after carpal tunnel release was nine times of that in the intact carpal tunnel (22).

Currently, the finite element (FE) model of the carpal tunnel is mainly pseudo-3D. Liong et al. established a patient-specific finite element model to analyze the relationship between repetitive finger flexion and the stress experienced on the nerve. The results show that the tendon volar movements (index finger and thumb flexion) impose larger stresses on the nerve than dorsal movements (middle finger flexion) (23). Walia et al. established a planar geometric model of carpal bones at the hamate level to analyze the best direction of the force for the maximization of the carpal arch area (CAA), so as to decrease the median nerve compression. The results showed that the maximal area occurred at 138° (volar-radial) relative to the hamate-to-trapezium axis (24). Mouzakis et al. simulated the computer work effects on the carpal arch area through finite element analysis. The results showed that the mouse work can introduce large deformation in the median nerve area, and the keyboard work can introduce a considerable and uneven axial lengthening of the nerve (25). Although there are many finite element models for studying carpal tunnel syndrome, they are currently mainly used to simulate the onset of symptoms, and few of them simulate the procedure of release surgery.

Although carpal tunnel release is a commonly performed surgical procedure for symptom relief in patients with CTS, the location of TCL transection can vary, and the implication of the transection variation on carpal tunnel biomechanics is unclear. The purpose of the current study was to investigate the effect of the location of TCL transection on the structural compliance of the distal carpal tunnel using a FE model. We hypothesized that carpal arch compliance (CAC) at the distal carpal tunnel would be dependent on the transection locations.

2. Materials and methods

2.1. Finite element modeling

The FE analysis in the current study was based on our previously developed pseudo-3D volar carpal arch structure at the distal tunnel level using computer-aided design modeling (SolidWorks 2012, Dassault Systems, Waltham, MA, United States) and then being exported to ABAQUS CAE (v6.10, Simulia, Providence, RI, United States) for FE analysis (26). Briefly, the model included the hamate bone, trapezium bone, thenar muscles, skin, fat, and TCL (**Figure 1A**). The skin and fat were modeled as a single skin–fat tissue. All tissue parts were manually segmented on transverse planar B-mode ultrasound images of the distal carpal tunnel of a cadaveric hand (male; left; age 74 years; height 177 cm; weight 95 kg). The specimen that had been thawed at room temperature prior to the test was placed in a supine, anatomically neutral position on the wrist. High-frequency (17 MHz) B-mode ultrasound images were acquired distal to the carpal tunnel using a linear array 18L6 HD transducer aligned in the transverse plane of the distal carpal tunnel along the line connecting the hook of hamate and ridge of trapezium. After acquiring the ultrasound images, the contours of thenar muscles, skin, fat, TCL, and the volar boundary of the hamate bone and trapezium bone were manually segmented and extracted with the use of the gray value threshold in ImageJ 1.46r (National Institutes of Health, Bethesda, MD, United States).

The elastic modulus of the hamate and trapezium bones was assumed as 10 GPa with a Poisson's ratio of 0.3 (27). The TCL was modeled as linearly elastic and anisotropic with a volar-dorsal elastic modulus of 0.5 MPa and a transverse elastic modulus of 5.5 MPa (28) with a Poisson's ratio of 0.4.

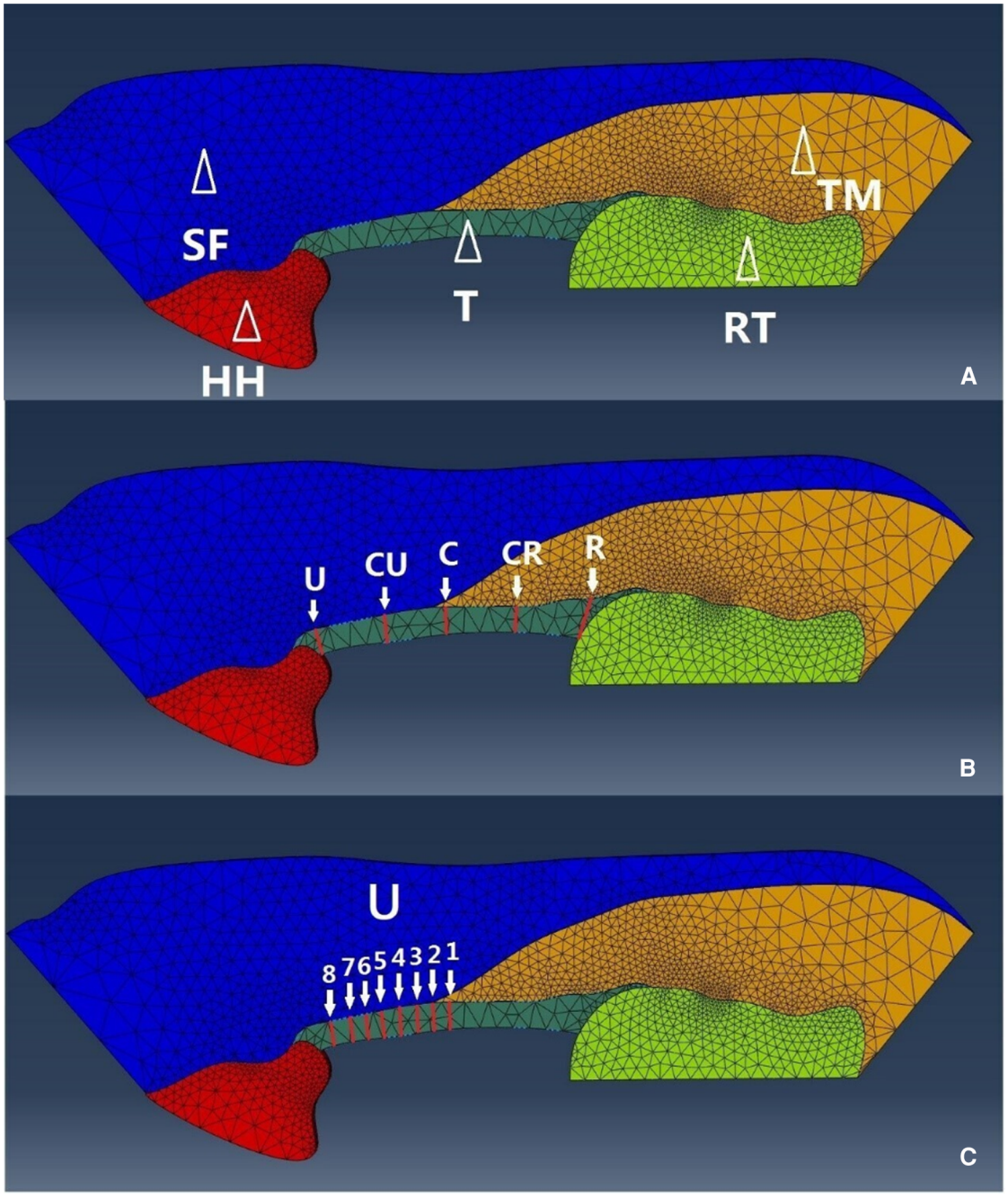

FIGURE 1
(A) The FE model of the volar carpal tunnel based on ultrasound image. The FE model components including the hamate bone, trapezium bone, thenar muscles, skin–fat, and TCL. SF, skin–fat; HH, hook of hamate; T, TCL; RT, ridge of trapezium; TM, thenar muscles. (B) Transection location on the TCL marked as U, ulnar; CU, central-ulnar; C, central; CR, central-radial; R, radial. (C) Transection location marked from 1 to 8 on the ulnar half of the TCL. FE, finite element; TCL, transverse carpal ligament.

Hyperelasticity of both muscle and subcutaneous tissue was determined by a neo-Hookean strain energy potential equation with an effective Poisson's ratio of 0.49. The initial shear modulus of muscle was assumed to be 0.00425 MPa (29). The initial shear modulus of skin–fat was assumed to be 0.016 MPa (30). The intratunnel pressure was varied from 0 to 72 mmHg (0, 12, 24, 36, 48, 60, and 72 mmHg) in the simulation. The stiffness of the hamate-to-trapezium was set at 11.8 N/mm transversely and 2.9 N/mm in the volar-dorsal direction (31). The interface between any two components was assumed as a "tie" contact condition. The hamate, trapezium, TCL, muscle, and skin–fat tissue were all modeled as C3D10 quadratic tetrahedral elements. Displacement boundary conditions (free in-plane and fixed out-of-plane) were applied at both the distal and proximal surfaces of all components. Other surfaces were assumed free as their displacement boundary conditions. The hamate bone was fixed in all six degrees of freedom.

A mesh convergence test was conducted on the entire model, with the maximum von Mises stress on the TCL as the reference. The results indicated that when the global size was less than 0.3, the variation of von Mises stress was within 5% (Figure 2). Therefore, a global size of 0.3 was selected with 17,165 elements in the model.

2.2. Transection of TCL

We simulated two sets of TCL transection locations. For the first set, the transections were performed at the central location (C), and 4 and 8 mm radially (CR, R) and ulnarly (CU, U) from location C (Figure 1B). The second set of transections was performed on the ulnar part of the TCL with 1 mm increment from the central location, marked as U1–U8 (Figure 1C). A mesh convergence analysis was performed using h-refinement method, where around double and triple element numbers in all components in the model with the same boundary conditions and material properties showed within 2.6% and within 3.6% error, respectively, on the result of TCL tensile strain for each transection. The carpal arch areas of the intact and transected carpal tunnels under various intratunnel pressures were determined as the area formed by the dorsal TCL boundary and the line connecting the two points at the hook of hamate and ridge of trapezium. Linear regression analyses were performed on the carpal arch area as a function of intratunnel pressures for each TCL transection. The CAC was defined as the slope of the regressed linear equation.

2.3. Model validation with pressure regulation

The hand was positioned in a supinated and neutral orientation and dissected minimally, preserving the tunnel and volar soft tissues. An incision was made 4 cm distal to the distal wrist crease and directly proximal to the second web space, allowing for the insertion of a custom-designed medical air balloon (Advanced Polymers Inc., Salem, NH, United States) to apply artificial pressure within the tunnel. The balloon was aligned along the tunnel's longitudinal axis with the assistance of an ultrasound and extended beyond the proximal and distal edges of the TCL (32). The balloon was pressurized, and a pressure gauge was used to monitor the pressure, which was set at levels ranging from 0 to 300 mmHg. At each pressure level, a B-mode ultrasound image was taken at the transverse plane of the distal carpal tunnel, along the line connecting the ridge of the trapezium and the hook of hamate. The tensile strain of the TCL was analyzed by manual tracing using the multipoint selection tool in ImageJ. The predictions of the TCL tensile strain simulation were compared to the measurements obtained from the cadaveric specimen to validate within 5% difference compared to the finite element analysis approach.

3. Results

Analysis of the CAA under different intratunnel pressures at five locations (Ulnar, Central-Ulnar, Central, Central-Radial, and

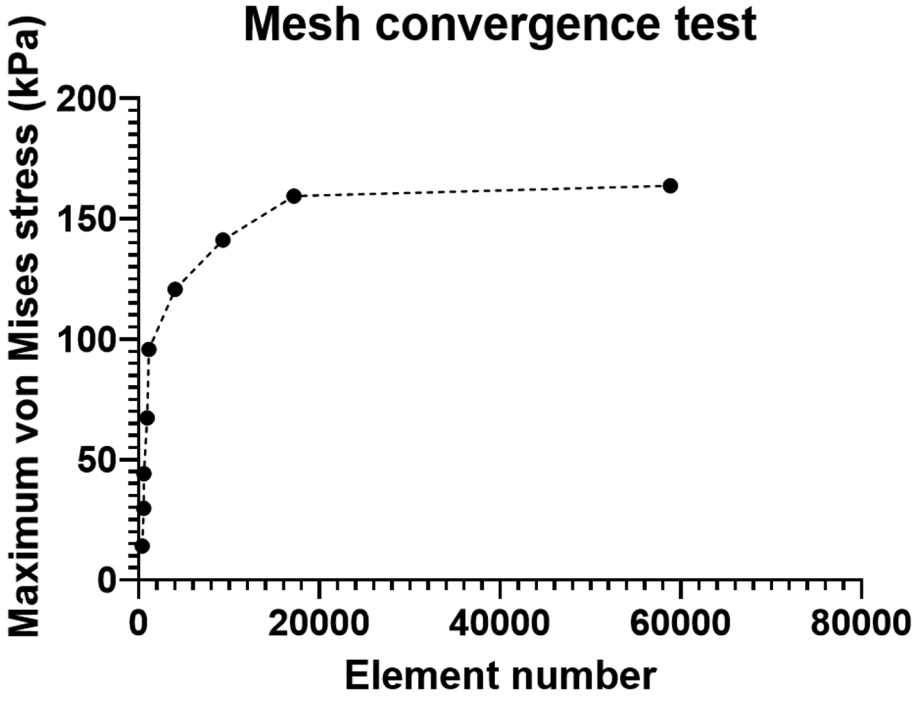

FIGURE 2
Mesh convergence test.

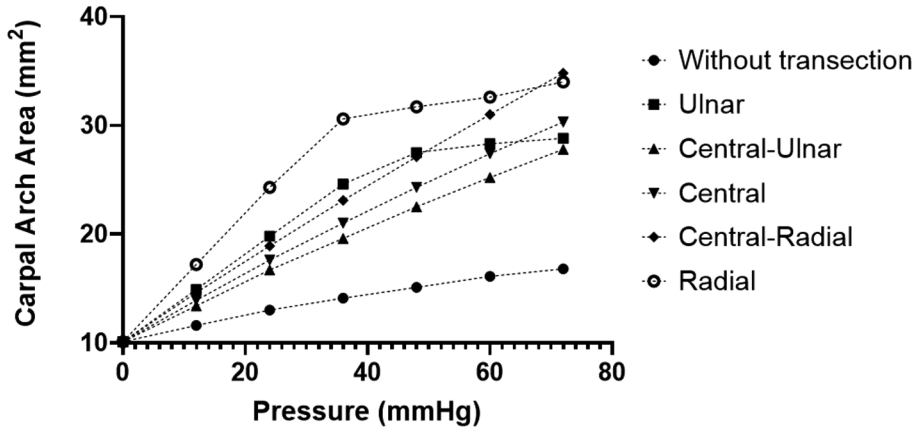

FIGURE 3
CAA with different intratunnel pressures for the intact tunnel and transected tunnel at both radial and ulnar sides. CAA, carpal arch area.

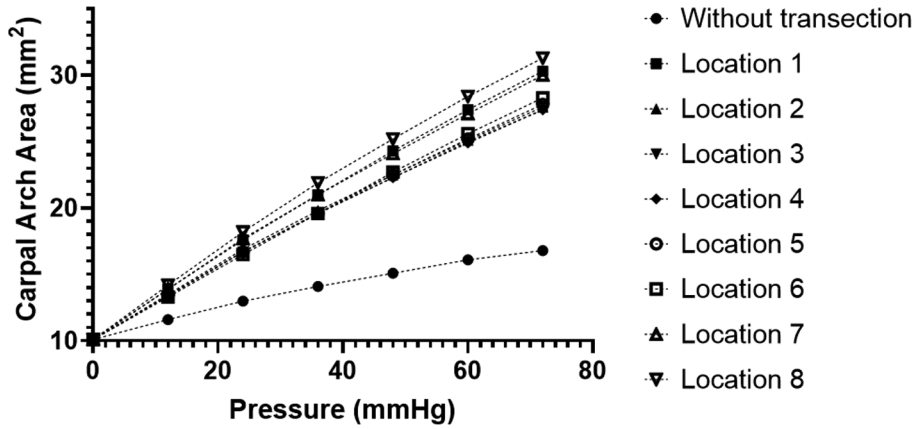

FIGURE 4
CAA with different intratunnel pressures for the intact and ulnarly transected tunnel conditions. CAA, carpal arch area.

Radial) along the transverse direction on the distal TCL is shown in Figure 3. The linear regressions on the curve of the Central-Ulnar, Central, and Central-Radial TCL transections showed a CAC of 0.25, 0.28, and 0.34 mm^2/mmHg, respectively, within the intratunnel pressure range of 0–72 mmHg (R-square value = 1.00 for each curve). The linear regressions on the curve of the Ulnar and Radial TCL transections showed 0.26 and 0.32 mm^2/mmHg, respectively, as CAC within the intratunnel pressure range of 0–72 mmHg (R-square value = 0.90 and 0.84 for the Ulnar TCL transection and Radial TCL transection, respectively). CAC without TCL transection was 0.092 mm^2/mmHg. Below 68 mmHg intratunnel pressure, radial TCL transection increased CAA the most among the five transection locations in Figure 3. Above 68 mmHg intratunnel pressure, Central-Radial TCL transection increased CAA the most (Figure 3). Central-Ulnar TCL transection increased CAA the least within the intratunnel pressure range of 0–72 mmHg. CAA increased by 18.03 mm^2, a 107% increase, below 72 mmHg intratunnel pressure at the Central-Radial TCL location after transection. CAA only increased by 10.99 mm^2, an increase of 65%, below 72 mmHg intratunnel pressure at the Central-Ulnar TCL location after transection.

During the traditional CTR, the TCL is transected on its ulnar side to avoid damage to the thenar muscle and median nerve. Analysis of CAA under different intratunnel pressures at the eight locations (Location 1–8) along the transverse direction on the ulnar half of the TCL is shown in Figure 4. The linear regressions on the curve of TCL transection at Locations 1–8 showed CAC of 0.28, 0.24, 0.24, 0.24, 0.25, 0.25, 0.27, and 0.29 mm^2/mmHg, respectively, within the intratunnel pressure range of 0–72 mmHg (R-square value = 1.00 for each curve). There was no noticeable difference in CAC (within 0.05 mm^2/mmHg) under TCL transection at Locations 1–8. At the intratunnel pressure of 72 mmHg, CAA increased by 28.77 mm^2, an increase of about 70% compared to the condition without TCL transection.

4. Discussion

It is known that carpal tunnel release leads to an augmentation of the carpal tunnel space (7–9) and a reduction of the intratunnel pressure (3, 33). Our results of increased structural compliance after simulated TCL transections corroborate the biomechanical basis of the carpal tunnel release for median nerve decompression. A compliant carpal arch is more accommodating to elevated intratunnel pressure without excessive compression on the median nerve.

The current modeling results about CAC of the intact tunnel (0.092 mm^2/mmHg) matched closely with a previous cadaveric study that examined the relationship between the intratunnel pressure and carpal arch area using MRI showing a compliance of 0.1 mm^2/mmHg (32). The change in carpal tunnel compliance after carpal tunnel release was also previously studied by Kim et al. (22), showing an increase of 56.0 mm^2 of the carpal arch area when the intratunnel pressure increased from 0 to 70 mmHg. In the current modeling study, the increase of the carpal arch area when pressure increased from 0 to 72 mmHg were 20.2 mm^2 at the central location and 17.7–24.7 mm^2 among all transection locations. Kato et al. reported that the carpal arch area increased by 82 mm^2 (from preoperative 32 mm^2 to postoperative 114 mm^2) for patients who underwent carpal tunnel release. This discrepancy in the increase of the carpal arch area might be due to that the mechanical properties of the TCL surrounding tissues might not be the same as those in the cadaveric hands.

A finite element model is particularly advantageous for the study of the biomechanical effects of various transection locations. Carpal tunnel release is traditionally in the ulnar side of the TCL along the radial border of the ring finger, which likely corresponds to the simulated U1–U5 locations in the model. Our study showed that the CAA increase stayed relatively stable under transection at different locations on the ulnar half of the TCL. In this study, we found that the determination of TCL transection location on the ulnar half of the TCL in order to create the maximal carpal tunnel space is not a key factor for surgeon's consideration.

Along the transverse direction of the distal TCL, transection on the radial TCL increases CAA more than transection on the ulnar TCL. While in surgical practice, transection on the radial half of the TCL using OCTR or ECTR can lead to damage to the thenar muscles which attach on the radial TCL. Such damage to the thenar muscles and small nerve fibers might contribute to common CTR complications such as pillar pain and persistent pinch weakness. Future techniques with TCL transection at the edge of the trapezium might be a better approach to augment the carpal tunnel if the muscle and nerve fibers can be preserved intact, which might lead to better postoperative outcomes. Recently, the OCTR with Z-lengthening reconstruction of the TCL mobilizing the ulnar and radial flaps of the transverse carpal ligament with proximal release of the ulnar flap and distal release of the radial flap showed postoperative advantages (Seitz and Lallb 2013). Z-lengthening reconstruction of the TCL releasing the radial distal TCL might create more carpal tunnel space at the distal tunnel level. The effect of radial TCL transection on carpal tunnel morphology might be a promising direction for further studies. Our study aimed to investigate the distal portion of the carpal tunnel, with the goal of establishing a theoretical basis for determining the optimal location for the distal incision in future CTR surgeries, as well as for deciding whether to preserve or transect the TCL. We discovered that a modified Z-lengthening technique with distal transection on the radial side may produce better outcomes compared to a conventional complete TCL incision. However, we also identified that there were no previous studies comparing the modified Z-lengthening with the conventional Simonetta's Z-lengthening technique, highlighting the need for further research in this area.

This study provided a basic understanding of the effect of TCL transection location on CAA and CAC. There are several limitations as follows: one limitation is that the intratunnel pressure was modeled as a constant without considering its interactive effects with TCL transection. The intratunnel pressure could decrease with the increase of CAA after TCL transection. This coupling effect warrants more investigation in the future. Another limitation is that the pseudo-3D FE model focusing on the distal level of the carpal tunnel cannot reflect the volume changes of the carpal tunnel after CTR. Future works can expand the modeling framework developed in this study to be a 3D carpal tunnel model. Finally, the FE model in this study is geometrically specimen-specific, and the future work on population-based modeling can provide more insights into the generalizability of the current results.

5. Conclusions

The radial TCL transection on carpal tunnel morphology might be a promising approach for decompression in CTS. Also, TCL transection location on the ulnar half of the TCL might not be a key factor for surgeon's consideration. Our model indicated potential benefit with radial transection location at the distal part the carpal tunnel in a modified Z-lengthening technique.

Data availability statement

The original contributions presented in the study are included in the article, further inquiries can be directed to the corresponding authors.

Ethics statement

The studies involving human participants were reviewed and approved by the Ethics Committee of the Shanghai Ninth People's Hospital. The patients/participants provided their written informed consent to participate in this study.

Author contributions

LY: formal analysis, investigation, writing-original draft preparation, writing review, and editing. JJ: formal analysis,

investigation, writing review, and editing. YL and KL: investigation, review, and editing. YG: supervision, writing review, and editing. YY: conceptualization, methodology, project administration, supervision, writing review, and editing. All authors contributed to the article and approved the submitted version.

Funding

The study described in this publication was partially supported by Key Projects of the National Defense Foundation Strengthening Plan (2020-JCJQ-ZD-264), National Natural Science Foundation of China (No. 32201067), and Shanghai Jiao Tong University "Star of Jiao Tong University" Medical-Engineering Cross Research Fund (No. YG2021QN142).

Conflict of interest

The authors declare that the research was conducted in the absence of any commercial or financial relationships that could be construed as a potential conflict of interest.

Publisher's note

All claims expressed in this article are solely those of the authors and do not necessarily represent those of their affiliated organizations, or those of the publisher, the editors and the reviewers. Any product that may be evaluated in this article, or claim that may be made by its manufacturer, is not guaranteed or endorsed by the publisher.

References

1. Dale AM, Harris-Adamson C, Rempel D, Gerr F, Hegmann K, Silverstein B, et al. Prevalence and incidence of carpal tunnel syndrome in US working populations: pooled analysis of six prospective studies. *Scand J Work Environ Health*. (2013) 39:495. doi: 10.5271/sjweh.3351

2. Alfonso C, Jann S, Massa R, Torreggiani A. Diagnosis, treatment and follow-up of the carpal tunnel syndrome: a review. *Neurol Sci*. (2010) 31:243–52. doi: 10.1007/s10072-009-0213-9

3. Diao E, Shao F, Liebenberg E, Rempel D, Lotz JC. Carpal tunnel pressure alters median nerve function in a dose-dependent manner: a rabbit model for carpal tunnel syndrome. *J Orthop Res*. (2005) 23:218–23. doi: 10.1016/j.orthres.2004.05.014

4. Szabo RM, Chidgey LK. Stress carpal tunnel pressures in patients with carpal tunnel syndrome and normal patients. *J Hand Surg*. (1989) 14:624–7. doi: 10.1016/0363-5023(89)90178-0

5. Cobb TK, Dalley BK, Posteraro RH, Lewis RC. Anatomy of the flexor retinaculum. *J Hand Surg*. (1993) 18:91–9. doi: 10.1016/0363-5023(93)90251-W

6. Armstrong TJ, Chaffin DB. Some biomechanical aspects of the carpal tunnel. *J Biomech*. (1979) 12:567–70. doi: 10.1016/0021-9290(79)90045-9

7. Ablove RH, Peimer CA, Diao E, Oliverio R, Kuhn JP. Morphologic changes following endoscopic and two-portal subcutaneous carpal tunnel release. *J Hand Surg*. (1994) 19:821–6. doi: 10.1016/0363-5023(94)90194-5

8. Kato T, Kuroshima N, Okutsu I, Ninomiya S. Effects of endoscopic release of the transverse carpal ligament on carpal canal volume. *J Hand Surg*. (1994) 19:416–9. doi: 10.1016/0363-5023(94)90055-8

9. Richman JA, Gelberman RH, Rydevik BL, Hajek PC, Braun RM, Gylys-Morin VM, et al. Carpal tunnel syndrome: morphologic changes after release of the transverse carpal ligament. *J Hand Surg*. (1989) 14:852–7. doi: 10.1016/S0363-5023(89)80089-9

10. Okutsu I, Ninomiya S, Hamanaka I, Kuroshima N, Inanami H. Measurement of pressure in the carpal canal before and after endoscopic management of carpal tunnel syndrome. *J Bone Joint Surg Am*. (1989) 71:679–83. doi: 10.2106/00004623-198971050-00006

11. El-Karabaty H, Hetzel A, Galla TJ, Horch RE, Lücking CH, Glocker FX. The effect of carpal tunnel release on median nerve flattening and nerve conduction. *Electromyogr Clin Neurophysiol*. (2005) 45:223–7. PMID: 16083145.

12. Learmonth JR. The principle of decompression in the treatment of certain diseases of peripheral nerves. *Surg Clin North Am*. (1933) 13:905–13.

13. Okutsu I, Ninomiya S, Natsuyama M, Takatori Y, Inanami H, Kuroshima N, et al. Subcutaneous operation and examination under the universal endoscope. *Nippon Seikeigeka Gakkai Zasshi*. (1987) 61:491–8.

14. Omokawa S, Tanaka Y, Ryu J, Suzuki J, Kish VL. Anatomy of the ulnar artery as it relates to the transverse carpal ligament. *J Hand Surg*. (2002) 27:101–4. doi: 10.1053/jhsu.2002.30077

15. Saravi MS, Kariminasab MH, Bari M, Ghaffari S, Razavipour M, Daneshpoor SMM, et al. A comparison of hand pain and hand function after Z-plasty reconstruction of the transverse carpal ligament with traditional median neurolysis in carpal tunnel syndrome. *Arch Bone Jt Surg*. (2016) 4:145. doi: 10.22038/ABJS.2016.6236

16. Hernández-Cortés P, Hurtado-Olmo P, O'Valle F, Pajares-López M, Catena A, Sánchez-Montesinos I, et al. Modification of intra-carpal tunnel pressure after Z-lengthening of the transverse carpal ligament. *Clin Biomech*. (2020) 80:105150. doi: 10.1016/j.clinbiomech.2020.105150

17. Castro-Menéndez M, Pagazaurtundúa-Gómez S, Pena-Paz S, Huici-Izco R, Rodríguez-Casas N, Montero-Viéites A. Z-elongation of the transverse carpal ligament vs. complete resection for the treatment of carpal tunnel syndrome. *Rev Esp Cir Ortopédica Traumatol Engl Ed*. (2016) 60:355–65. doi: 10.1016/j.recote.2016.09.002

18. Seitz WH Jr., Lall A. Open carpal tunnel release with median neurolysis and Z-plasty reconstruction of the transverse carpal ligament. *Curr Orthop Pract*. (2013) 24:53–7. doi: 10.1097/BCO.0b013e3182797ac3

19. Lai S, Zhang K, Li J, Fu W. Carpal tunnel release with versus without flexor retinaculum reconstruction for carpal tunnel syndrome at short- and long-term follow up—a meta-analysis of randomized controlled trials. *PLoS One*. (2019) 14:e0211369. doi: 10.1371/journal.pone.0211369

20. Faour Martín O, Martín Ferrero MÁ, Valverde García JA, Zuil Acosta P, Amigo Liñares L. The Simonetta technique for carpal tunnel syndrome: immediate postoperative evaluation and long-term comparative study. *Int J Orthop*. (2014) 1:109–15. doi: 10.6051/j.issn.2311-5106.2014.01.21

21. Gutiérrez-Monclus RG, Gutiérrez-Espinoza HJ, Flores-Astudillo AR, Lluch-Homedes AL, Aguirre-Jerez M. Release with or without reconstruction of the transverse carpal ligament for severe carpal tunnel syndrome: a randomized clinical trial. *J Hand Surg Eur Vol*. (2018) 43:303–9. doi: 10.1177/1753193417730260

22. Kim DH, Marquardt TL, Gabra JN, Shen ZL, Evans PJ, Seitz WH, et al. Pressure–morphology relationship of a released carpal tunnel. *J Orthop Res*. (2013) 31:616–20. doi: 10.1002/jor.22271

23. Liong K, Lahiri A, Lee S, Chia D, Biswas A, Lee HP. Finite element simulation of intra-carpal tunnel pressure: the effects of individual finger flexion and histological changes. *Int J Exp Comput Biomech*. (2015) 3:250–66. doi: 10.1504/IJECB.2015.073929

24. Walia P, Erdemir A, Li Z-M. Subject-specific finite element analysis of the carpal tunnel cross-sectional to examine tunnel area changes in response to carpal arch loading. *Clin Biomech*. (2018) 42:25–30. doi: 10.1016/j.clinbiomech.2017.01.004

25. Mouzakis DE, Rachiotis G, Zaoutsos S, Eleftheriou A, Malizos KN. Finite element simulation of the mechanical impact of computer work on the carpal tunnel syndrome. *J Biomech*. (2014) 47:2989–94. doi: 10.1016/j.jbiomech.2014.07.004

26. Yao Y, Erdemir A, Li Z-M. Finite element analysis for transverse carpal ligament tensile strain and carpal arch area. *J Biomech*. (2018) 73:210–6. doi: 10.1016/j.jbiomech.2018.04.005

27. Pistoia W, Van Rietbergen B, Lochmüller E-M, Lill CA, Eckstein F, Rüegsegger P. Estimation of distal radius failure load with micro-finite element analysis models based on three-dimensional peripheral quantitative computed tomography images. *Bone*. (2002) 30:842–8. doi: 10.1016/S8756-3282(02)00736-6

28. Holmes MW, Howarth SJ, Callaghan JP, Keir PJ. Biomechanical properties of the transverse carpal ligament under biaxial strain. *J Orthop Res*. (2012) 30:757–63. doi: 10.1002/jor.21583

29. Palevski A, Glaich I, Portnoy S, Linder-Ganz E, Gefen A. Stress relaxation of porcine gluteus muscle subjected to sudden transverse deformation as related to pressure sore modeling. *J Biomech Eng*. (2006) 128(5):782–7. doi: 10.1115/1.2264395

30. Brosh T, Arcan M. Modeling the body/chair interaction—an integrative experimental–numerical approach. *Clin Biomech*. (2000) 15:217–9. doi: 10.1016/S0268-0033(99)00073-X

31. Marquardt TL, Gabra JN, Evans PJ, Seitz WH Jr, Li Z-M. Thickness and stiffness adaptations of the transverse carpal ligament associated with carpal tunnel syndrome. *J Musculoskelet Res*. (2016) 19:1650019. doi: 10.1142/S0218957716500196

32. Li Z-M, Masters TL, Mondello TA. Area and shape changes of the carpal tunnel in response to tunnel pressure. *J Orthop Res*. (2011) 29:1951–6. doi: 10.1002/jor.21468

33. Gelberman RH, Hergenroeder PT, Hargens AR, Lundborg GN, Akeson WH. The carpal tunnel syndrome. A study of carpal canal pressures. *J Bone Joint Surg Am*. (1981) 63:380–3. doi: 10.2106/00004623-198163030-00009

Frontiers in Surgery

Explores and improves surgical practice and clinical patient management

A multidisciplinary journal which explores surgical practices - from fundamental principles to advances in microsurgery and minimally invasive techniques. It fosters innovation and improves the clinical management of patients.

Discover the latest Research Topics

See more →

Frontiers

Avenue du Tribunal-Fédéral 34
1005 Lausanne, Switzerland
frontiersin.org

Contact us

+41 (0)21 510 17 00
frontiersin.org/about/contact